

AN ASSESSMENT OF TRAILING EDGE NOISE MEASUREMENT TECHNIQUES

By

CHRISTOPHER JOHN BAHR

A DISSERTATION PRESENTED TO THE GRADUATE SCHOOL
OF THE UNIVERSITY OF FLORIDA IN PARTIAL FULFILLMENT
OF THE REQUIREMENTS FOR THE DEGREE OF
DOCTOR OF PHILOSOPHY

UNIVERSITY OF FLORIDA

2010

© 2010 Christopher John Bahr

To my parents for raising me, my wife Stephanie for supporting me, and God for inspiring me

ACKNOWLEDGMENTS

Financial support for this work was provided in part by NASA Langley Research Center, monitored by Drs. Mehdi Khorrami and Meelan Choudhari and by the Florida Center for Advanced Aero-Propulsion. I appreciate the opportunities I have had to interact with Drs. Khorrami and Choudhari, as well as the chance to work with Dr. Florence Hutcheson and Dr. David Lockard.

I would like to thank Dr. Louis N. Cattafesta III, my committee chair, for leading me through my development as a researcher. His (thorough) insistence on attention to detail has turned me into a far better experimentalist than I would have been otherwise. I would also like to thank the rest of my committee for the opportunity to work and consult with them: Dr. Mark Sheplak, Dr. Lawrence Ukeiley, and Dr. Jian Li.

I thank all of the Interdisciplinary Microsystems Group for the constant interaction and thoughtful discussions they provide. I would particularly like to acknowledge the rest of the work group class of 2003: Vijay Chandrasekharan, Tai-An Chen, Ben Griffin, Brian Homeijer and Erin Patrick McKnight. It was an honor climbing the ranks with you. I owe special thanks to Drew Wetzell, Nik Zawodny, Fei Liu and Tarik Yardibi for all the assistance they have given me with my research.

I thank my parents for nurturing my curiosity from an early age, and supporting me through my extended stay in college. I thank my wife, Stephanie, for her constant encouragement, and for keeping me grounded. Finally, I thank God for granting me the gifts He did, and for staying faithful to me through all these years.

TABLE OF CONTENTS

	<u>page</u>
ACKNOWLEDGMENTS	4
LIST OF TABLES	8
LIST OF FIGURES	9
ABSTRACT	21
CHAPTER	
1 INTRODUCTION	23
Trailing Edge Noise	24
Problem Statement	24
Existing Research	25
Theoretical development	25
Computational development	27
Experimental development	28
Research Structure	31
Existing State-of-the-Art	31
Research Objective	32
Expected Contributions	32
Research Roadmap	32
2 AEROACOUSTICS – THEORETICAL DEVELOPMENT	36
Lighthill-Based Analysis	36
Linearized Hydrodynamics	41
Howe’s Analysis	42
3 EXPERIMENTS IN TRAILING EDGE NOISE	46
Paterson, Vogt, Fink & Munch (1973)	46
Yu & Joshi (1979)	47
Brooks & Hodgson (1981)	49
Blake & Gershfeld (1988)	51
Brooks, Pope, & Marcolini (1989)	52
Hutcheson & Brooks (2002, 2004)	54
Examples of Additional Notable Work	56
Experimental Body of Work – Summary	59
4 EXPERIMENTAL METHODS AND SETUP	61
Experimental Facility – UFAFF	61

Airfoil Model	62
Model Performance	64
Steady Pressure Behavior	64
Unsteady Surface Pressures	67
Hotwire Anemometry	70
Acoustic Measurements	73
Coherence-Based Techniques	73
Coherent output power	74
Three-microphone method	80
Beamforming Techniques	90
Test Matrix	96
5 RESULTS & DISCUSSION	138
Installation Effects	138
Comparison of Two-Microphone Methods	142
Three-Microphone Method	145
Additional Linear Array Analysis	147
Beamforming Results	149
1/3 rd Octave Scaling	156
Mach Number Scaling	156
Angle of Attack Behavior	158
Instrumentation Offset	159
6 CONCLUSIONS & FUTURE WORK	200
A AIRFOIL COORDINATE DESIGN AND MEASUREMENT COMPARISON CODE	207
B ANALYSIS OF THE THREE-MICROPHONE METHOD	212
Formulation	212
Simulation & Analysis	213
C EFFECT OF MULTIPLE SOURCES ON COHERENCE-BASED ANALYSIS	231
Two-Input/Two-Output Analysis	231
Autospectral Scaling	232
Cross-Spectral Scaling	235
Coherent Output Power Behavior	236
General Monopole Multiple-Input/Multiple-Output Behavior	241
Problem Formulation	241
Simulation	249
Dipole Analysis and Comparison with Experimental Data	252
Summary	258
D ARRAY CALIBRATION IN THE PRESENCE OF ECHOES	272
Ideal Case Problem Statement	272

Ideal Case Analysis.....	273
Single Ideal Reflection	274
Analysis Options.....	279
Impulse Response Analysis.....	279
Cepstrum Alalysis.....	280
Single Ideal Reflection: Simulation.....	284
Real Experimental Conditions.....	288
Downsampling.....	293
Low Frequency Treatment.....	295
Application to Beamforming Results	297
Conclusion.....	299
E COMPARISON OF DAS AND DAMAS RESULTS.....	344
REFERENCES	359
BIOGRAPHICAL SKETCH	368

LIST OF TABLES

<u>Table</u>		<u>page</u>
1-1	Approach noise levels for a Boeing 747-400 with Pratt & Whitney Advanced Ducted Propulsor (ADP) engines.	34
4-1	Key UFAFF design characteristics.	134
4-2	UF NACA 63-215 Mod-B airfoil profile design coordinates.	135
4-3	UF NACA 63-215 Mod-B chord wise pressure tap locations.	136
4-4	Geometric and corrected microphone angles.	136
4-5	UFAFF medium-aperture array microphone design coordinates.	137
4-6	Test matrix of experiments to study measurement techniques.	137
5-1	Integrated array levels at 2,512 Hz for $M = 0.17$, 0 degree AoA for varying integration region dimensions.	198
5-2	Integrated array levels at 7,600 Hz for $M = 0.17$, 0 degree AoA for varying integration region dimensions.	198
5-3	Integrated array levels at 20,000 Hz for $M = 0.17$, 0 degree AoA for varying integration region dimensions.	199
B-1	Equation-unknown scaling for varying channel count.	230

LIST OF FIGURES

<u>Figure</u>	<u>page</u>
1-1 Schematic of major airframe noise sources.	33
1-2 Schematic of sources in the vicinity of an example trailing edge.....	33
2-1 Coordinate system for trailing edge noise analysis.....	45
4-1 Planform schematic of UFAFF showing the flow path from the garage entrance (top), through the open-jet test section and out through the fan section.	98
4-2 Isometric schematic of UFAFF.....	99
4-3 A-Weighted out-of-flow background noise comparison between different aeroacoustic flow facilities.	100
4-4 Cross section of UF NACA 63-215 Mod-B airfoil.....	101
4-5 Photograph of UF NACA 63-215 Mod-B airfoil.....	101
4-6 Photograph of UF NACA 63-215 installed in UFAFF, from below.	102
4-7 UF NACA 63-215 Mod-B profile deviation between design and measured coordinates.	103
4-8 Trailing edge profiles at varying spanwise locations.....	104
4-9 Surface error curve fits for UF NACA 63-215 Mod-B.....	105
4-10 X-Foil predicted C_p distributions for design and modified profiles, $M = 0.17$	105
4-11 C_p for -7.5° geometric AoA (-3.14° equivalent lift freestream).	106
4-12 C_p for -5° geometric AoA (-2.63° equivalent lift freestream).	106
4-13 C_p for -2.5° geometric AoA (-1.98° equivalent lift freestream).	107
4-14 C_p for 0° geometric AoA (-1.19° equivalent lift freestream).....	107
4-15 C_p for 2.5° geometric AoA (-0.65° equivalent lift freestream).....	108
4-16 C_p for 5° geometric AoA (-0.15° equivalent lift freestream).....	108
4-17 C_p for 7.5° geometric AoA (0.33° equivalent lift freestream).	109
4-18 C_p for 10° geometric AoA (0.76° equivalent lift freestream).....	109

4-19	Installed, equivalent-lift AoA scaling with geometric AoA for UF NACA 63-215.....	110
4-20	Evaluation of spanwise uniformity at zero-degree geometric AoA.....	110
4-21	Trailing edge sensor layout for the NACA 63-215 Mod-B, with orange lines representing ribbon cabling, and all dimensions in inches.	111
4-22	Map of trailing edge array spacings.....	111
4-23	Schematic of a single-wire, 2-axis traverse experiment.	112
4-24	Photograph of hotwire installation for a DU 96-W-180 airfoil, from below the model, viewing the trailing edge.....	113
4-25	Photograph of hotwire installation for a DU 96-W-180 airfoil from above the model, viewing the trailing edge.....	114
4-26	Example hotwire calibration data to be used with King’s Law.	115
4-27	Plot of mean and fluctuating boundary layer velocity profile in the trailing edge vicinity.	116
4-28	Plot of mean and fluctuating wake profile in the trailing edge vicinity.....	117
4-29	Schematic of an ideal, spatially lumped line source in a coherent power-based analysis.....	118
4-30	Block diagram for a Single-Input-Two-Output (SITO) system.....	119
4-31	Installation schematic for coherent output power measurements.	119
4-32	Coherent Output Power compared between two experiment sets.	120
4-33	Cross-channel coherence compared between two experiment sets.	120
4-34	Coherent Output Power plotted as a function of scaled frequency.....	121
4-35	Cross-channel phase angle compared between two experiment sets.....	121
4-36	Baseline experimental configuration with phased array.....	122
4-37	Experimental configuration with free field microphone located at equivalent array location in free space.	123
4-38	Experimental configuration with array horizontally offset from trailing edge by 0.25 m.	124
4-39	Experimental configuration for linear array measurements conducted prior to current body of research.....	125

4-40	Comparison of differing coherence-based noise reduction techniques.	126
4-41	Effect of shear layer correction on reliability of dipole-like assumption.	126
4-42	Phase error comparison for linear array microphones, referenced to microphone 12.	127
4-43	Phase error comparison for non-contaminated linear array microphones,	127
4-44	Comparison of power predictions from different methodologies.	128
4-45	Isometric schematic of baseline experimental configuration.	129
4-46	Layout of the UFAFF medium aperture array with acoustic treatment.	130
4-47	3 dB beamwidth of the UFAFF medium aperture array as a function of frequency.	131
4-48	PSF for medium-aperture array at 1,024 Hz.	131
4-49	PSF for medium-aperture array at 2,512 Hz.	132
4-50	PSF for medium-aperture array at 5,008 Hz.	132
4-51	PSF for medium-aperture array at 7,600 Hz.	133
4-52	PSF for medium-aperture array at 15,008 Hz.	133
4-53	PSF for medium-aperture array at 20,000 Hz.	134
5-1	Model installation effects and background noise for a Mach number of 0.10.	161
5-2	Model installation effects and background noise for a Mach number of 0.17.	161
5-3	Installation effects and background noise for upper mic, Mach number of 0.10.	162
5-4	Installation effects and background noise for upper mic, Mach number of 0.17.	162
5-5	Cepstrum comparison of installation effects for a Mach number of 0.10.	163
5-6	Cepstrum comparison of installation effects for a Mach number of 0.17.	163
5-7	Cepstrum comparison of installation effects for a Mach number of 0.17, where quefrequency has been converted to an equivalent lag distance using the measured speed of sound.	164
5-8	Cepstrum comparison of installation effects for a Mach number of $M = 0.10$, for free field microphones mounted above the model trailing edge.	165
5-9	Coherent power analysis of in-array B&K 4138 for a Mach number of 0.10.	166

5-10	Coherent power analysis of in-array B&K 4138 for a Mach number of 0.17.	166
5-11	Coherent power analysis of opposite-array G.R.A.S. 40BE for M = 0.17.	167
5-12	Coherent power analysis of free field B&K 4939 for a Mach number of 0.10.	167
5-13	Coherent power analysis of free field B&K 4939 for a Mach number of 0.17.	168
5-14	Coherent power analysis of free-field opposing G.R.A.S. 40BE for M = 0.17.	168
5-15	COP confidence intervals for the free field case for a Mach number of 0.10.	169
5-16	COP confidence intervals for the free field case for a Mach number of 0.17.	169
5-17	Ordinary coherence function computed between the upper G.R.A.S. 40BE and lower B&K 4939 trailing edge microphones for the free-field case, for two different Mach numbers.	170
5-18	Uncertainty bounds on installation effects for COP analysis, Mach number of 0.10.	171
5-19	Uncertainty bounds on installation effects for COP analysis, Mach number of 0.17.	171
5-20	Comparison of two- and three-microphone methods for array case at M = 0.10.	172
5-21	Comparison of two- and three-microphone methods for array case at M = 0.17.	172
5-22	Comparison of two- and three-microphone methods for free case at M = 0.10.	173
5-23	Comparison of two- and three-microphone methods for free case at M = 0.17.	173
5-24	Uncertainty bounds for differing methods for array case at M = 0.10.	174
5-25	Uncertainty bounds for differing methods for array case at M = 0.17.	174
5-26	Uncertainty bounds for differing methods for free field case at M = 0.10.	175
5-27	Uncertainty bounds for differing methods for free field case at M = 0.17.	175
5-28	Convergence analysis of Monte Carlo uncertainties for free field case of M = 0.10.	176
5-29	Convergence analysis of Monte Carlo uncertainties for free field case of M = 0.17.	176
5-30	Cdf of Monte Carlo results for free field case of M = 0.17 at 2,512 Hz.	177
5-31	Cdf of Monte Carlo results for free field case of M = 0.17 at 3,392 Hz.	177
5-32	Cdf of Monte Carlo results for free field case of M = 0.17 at 6,000 Hz.	178
5-33	Cdf of Monte Carlo results for free field case of M = 0.17 at 12,000 Hz.	178

5-34	Nominal and mean three-microphone methods with confidence intervals, $M = 0.10$	179
5-35	Nominal and mean three-microphone methods with confidence intervals, $M = 0.17$	179
5-36	Comparison of covariance-based fitting approaches for free field, $M = 0.17$	180
5-37	Variation of Frobenius Norm Method solution for varying internal iterations.	180
5-38	Variation of Rank-1 Method solution for varying internal iterations.	181
5-39	Variation of Maximum Likelihood Method solution for varying internal iterations.....	181
5-40	Comparison of three-microphone method and DAS for $M = 0.17$	182
5-41	Comparison of confidence interval bounds for $M = 0.17$	182
5-42	Comparison of nominal and Monte Carlo mean solutions for $M = 0.17$	183
5-43	Beam map of test section at 1,024 Hz, $M = 0.17$, 0 degree AoA.	184
5-44	Cdf of integrated Monte Carlo data at 1,024 Hz, $M = 0.17$, 0 degree AoA.	184
5-45	Beam map of test section at 2,512 Hz, $M = 0.17$, 0 degree AoA.	185
5-46	Cdf of integrated Monte Carlo data at 2,512 Hz, $M = 0.17$, 0 degree AoA.	185
5-47	Beam map of test section at 5,008 Hz, $M = 0.17$, 0 degree AoA.	186
5-48	Cdf of integrated Monte Carlo data at 5,008 Hz, $M = 0.17$, 0 degree AoA.	186
5-49	Beam map of test section at 7,600 Hz, $M = 0.17$, 0 degree AoA.	187
5-50	Cdf of integrated Monte Carlo data at 7,600 Hz, $M = 0.17$, 0 degree AoA.	187
5-51	Beam map of test section at 8,800 Hz, $M = 0.17$, 0 degree AoA.	188
5-52	Cdf of integrated Monte Carlo data at 8,800 Hz, $M = 0.17$, 0 degree AoA.	188
5-53	Beam map of test section at 15,008 Hz, $M = 0.17$, 0 degree AoA.	189
5-54	Cdf of integrated Monte Carlo data at 15,008 Hz, $M = 0.17$, 0 degree AoA.	189
5-55	Beam map of test section at 20,000 Hz, $M = 0.17$, 0 degree AoA.	190
5-56	Cdf of integrated Monte Carlo data at 20,000 Hz, $M = 0.17$, 0 degree AoA.	190
5-57	$1/3^{\text{rd}}$ octave method comparisons for a Mach number of 0.05 and 0 degree AoA.	191
5-58	$1/3^{\text{rd}}$ octave method comparisons for a Mach number of 0.07 and 0 degree AoA.	191

5-59	1/3 rd octave method comparisons for a Mach number of 0.10 and 0 degree AoA.	192
5-60	1/3 rd octave method comparisons for a Mach number of 0.12 and 0 degree AoA.	192
5-61	1/3 rd octave method comparisons for a Mach number of 0.15 and 0 degree AoA.	193
5-62	1/3 rd octave method comparisons for a Mach number of 0.17 and 0 degree AoA.	193
5-63	1/3 rd octave method comparisons for a Mach number of 0.10 at -1.5 degree AoA.	194
5-64	1/3 rd octave method comparisons for a Mach number of 0.10 at 1.5 degree AoA.	194
5-65	1/3 rd octave method comparisons for a Mach number of 0.17 at -1.5 degree AoA.	195
5-66	1/3 rd octave method comparisons for a Mach number of 0.17 at 1.5 degree AoA.	195
5-67	1/3 rd octave method comparisons for M = 0.10, 0 degree AoA with offset array.	196
5-68	1/3 rd octave method comparisons for M = 0.17, 0 degree AoA with offset array.	196
5-69	Beam map of narrowband CSM at 2,512 Hz for offset array at M = 0.17, AoA = 0.	197
5-70	Beam map of 1/3 rd octave CSM at 2,500 Hz for offset array at M = 0.17, AoA = 0.	197
6-1	Acoustic absorption coefficient of sidewalls used in UF AFF.	206
B-1	Piston in an infinite baffle, directivity pattern for $ka = 3$	218
B-2	Directivity pattern for SNR = 10, using nearest-two microphone selection.	219
B-3	Directivity pattern for SNR = 1, using nearest-two microphone selection.	219
B-4	Directivity pattern for SNR = 0.1, using nearest-two microphone selection.	220
B-5	Color maps of cross-channel coherence, SNR = 10.	220
B-6	Color maps of cross-channel coherence, SNR = 1.	221
B-7	Color maps of cross-channel coherence, SNR = 0.1.	221
B-8	Histogram of power predictions for SNR = 10.	222
B-9	Histogram of power predictions for SNR = 1.	222
B-10	Histogram of power predictions for SNR = 0.1.	223
B-11	Directivity from mean power prediction method for SNR = 10.	223
B-12	Directivity from mean power prediction method for SNR = 1.	224

B-13	Directivity from mean power prediction method for SNR = 0.1.....	224
B-14	Directivity for mean power prediction method with outlier rejection, SNR = 10.....	225
B-15	Directivity for mean power prediction method with outlier rejection, SNR = 1.....	225
B-16	Directivity for mean power prediction method with outlier rejection, SNR = 0.1.....	226
B-17	SNR data spread for microphone 10.....	226
B-18	SNR data spread for microphone 1.....	227
B-19	Histogram of estimated powers for microphone 10 and a true SNR of 0.5.....	227
B-20	Histogram of estimated powers for microphone 10 and a true SNR of 0.05.....	228
B-21	Directivity comparison for SNR = 10.....	228
B-22	Directivity comparison for SNR = 1.....	229
B-23	Directivity comparison for SNR = 0.1.....	229
C-1	Schematic of Two-Input/Two-Output system with no additive noise.....	259
C-2	Schematic of Two-Input/Two-Output system with incoherent measurement noise.....	259
C-3	TITO situation where, for monopole sources, all phase angle differences cancel.	260
C-4	Three-observer MIMO system modeling a trailing edge of incoherent sources.	261
C-5	Three-observer MIMO block diagram for the analysis of the system shown in Figure C-4.....	262
C-6	Coherence between microphones 1 and 3 based on the schematic in Figure C-4.	263
C-7	Three-microphone prediction for microphone 3 from Figure C-4.....	263
C-8	Three-observer MIMO system modeling a trailing edge of incoherent sources.	264
C-9	Coherence between microphones 1 and 3 based the schematic in Figure C-8.	265
C-10	Three-microphone prediction for microphone 3 from Figure C-8.....	265
C-11	Eight-observer MIMO system modeling a trailing edge of incoherent sources.	266
C-12	Coherence function for spanwise microphones based on schematic in Figure C-11.	267
C-13	Three-microphone predictions for microphones 2 through 4 in Figure C-11.....	267
C-14	Coherence for spanwise microphones, dipole sources located in Figure C-11.	268

C-15	Three-microphone solution, microphones 2 through 4 in Figure C-11 for dipoles.	269
C-16	Ratio of predicted power to true power for microphones in Figure C-11 for dipoles.	270
C-17	Comparison of experimental coherence with simulated source coherence between microphones 1 and 4 from Figure C-11.	271
D-1	Simplified acoustic calibration experiment with an ideal source field.	300
D-2	Block diagram of ideal acoustic calibration.	301
D-3	Acoustic calibration experiment with a single reflection.	302
D-4	Block diagram of acoustic calibration with a single reflection.	303
D-5	True frequency response magnitude of the second microphone.	303
D-6	True frequency response phase angle of the second microphone.	304
D-7	Schroeder Multisine input waveform.	304
D-8	Schroeder Multisine input power spectral density.	305
D-9	Microphone 1 power spectral density.	305
D-10	Microphone 2 power spectral density.	306
D-11	Comparison of frequency response estimate magnitudes.	306
D-12	Comparison of frequency response estimate phase angles.	307
D-13	Impulse response estimate, inverse-transformed from FRF estimate.	307
D-14	Cepstrum of impulse response estimate.	308
D-15	Cepstrum of impulse response estimate, showing the full computed record.	308
D-16	Relative FRF magnitude error for impulse response windowing.	309
D-17	Relative FRF magnitude error for cepstrum windowing.	309
D-18	FRF phase error for impulse response windowing.	310
D-19	FRF phase error for cepstrum windowing.	310
D-20	Schematic of array calibration experimental setup.	311
D-21	Multisine used in experiment, measured from function generator output.	312
D-22	Power spectral density of function generator output.	312

D-23	Power spectral density of reference B&K microphone located at array center.....	313
D-24	B&K measurement autocorrelation function, normalized to correlation coefficient.	313
D-25	Frequency response magnitude estimate for electret 1.....	314
D-26	Frequency response phase angle estimate for electret 1.....	314
D-27	Frequency response magnitude estimate for electret 63.....	315
D-28	Frequency response phase angle estimate for electret 63.....	315
D-29	Impulse response estimate between reference microphone and electret 1.....	316
D-30	Impulse response estimate between reference microphone and electret 63.....	316
D-31	Cepstrum estimate between reference microphone and electret 1.....	317
D-32	Cepstrum estimate between reference microphone and electret 63.....	317
D-33	FRF magnitude estimates for electret 1 comparing different methods.....	318
D-34	FRF phase estimates for electret 1 comparing different methods.....	318
D-35	FRF magnitude estimates for electret 63 comparing different methods.....	319
D-36	FRF phase estimates for electret 63 comparing different methods.....	319
D-37	FRF magnitude estimates for electret 1, 0.25 ms window.....	320
D-38	FRF phase estimates for electret 1, 0.25 ms window.....	320
D-39	FRF magnitude estimates for electret 63, 0.25 ms window.....	321
D-40	FRF phase estimates for electret 63, 0.25 ms window.....	321
D-41	Logarithm of the two-sided FRF magnitude between B&K and electret 63.....	322
D-42	Inverse Fourier transform of logarithmic magnitude spectrum from Figure D-41.....	322
D-43	Unwrapped two-sided FRF phase angle from B&K to electret 63.....	323
D-44	Inverse Fourier transform of imaginary phase angle from Figure D-43.....	323
D-45	Illustration of available FRF data (blue) and desired FRF calibration curve (yellow)....	324
D-46	Illustration of available FRF data and desired FRF calibration curve when decimated by 2.....	325
D-47	Downsampled logarithm of two-sided FRF from B&K microphone to electret 63.....	326

D-48	Cepstrum corresponding to Figure D-47.	326
D-49	Unwrapped downsampled phase angle from B&K to electret 63.....	327
D-50	Cepstrum corresponding to Figure D-49.	327
D-51	Window length effects for original electret 63 FRF magnitude estimate.	328
D-52	Window length effects for downsampled electret 63 FRF magnitude estimate.	328
D-53	Window length effects for original electret 63 FRF phase estimate.....	329
D-54	Window length effects for downsampled electret 63 FRF phase estimate.....	329
D-55	Low-frequency fit effect for original electret 63 FRF magnitude estimate.	330
D-56	Low-frequency fit effects for downsampled electret 63 FRF magnitude estimate.....	330
D-57	Low-frequency fit effects for original electret 63 FRF phase estimate.	331
D-58	Low-frequency fit effects for downsampled electret 63 FRF phase estimate.	331
D-59	Electret 43 phase angle estimates.	332
D-60	Plot of phase angles for electrets 1 through 63.....	332
D-61	Phase angles for electrets 1 through 63, additional acoustic treatment is applied.....	333
D-62	Phase angle estimate for an acoustically-treated case.....	333
D-63	Impulse response windowing magnitude estimate for electret 43.....	334
D-64	Downsampled impulse response windowing magnitude estimate for electret 43.....	334
D-65	Impulse response windowing phase estimate for electret 43.....	335
D-66	Downsampled impulse response windowing phase estimate for electret 43.....	335
D-67	Impulse response magnitude estimate with a 50% Tukey window.....	336
D-68	Impulse response phase estimate with a 50% Tukey window.....	336
D-69	Tukey-windowed magnitude estimate for treated calibration experiment.	337
D-70	Tukey-windowed phase estimate for treated calibration experiment.	337
D-71	Magnitude estimate comparison between untreated and treated experiments.....	338
D-72	Phase estimate comparison between untreated and treated experiments.....	338

D-73	Medium-aperture array calibration experiment beam map at 1120 Hz.	339
D-74	Ideal calibrated response for experiment beam map at 1120 Hz.	339
D-75	Uncalibrated beam map of offset speaker at 1120 Hz.	340
D-76	Calibrated beam map of offset speaker at 1120 Hz.	340
D-77	Beam map of offset speaker at 1120 Hz, calibrated with new technique.	341
D-78	Uncalibrated beam map of medium aperture array data at 10 kHz.	341
D-79	Calibrated beam map of medium aperture array data at 10 kHz.	342
D-80	Uncalibrated beam map of medium aperture array data at 20 kHz.	342
D-81	Calibrated beam map of medium aperture array data at 20 kHz.	343
E-1	Comparison of nominal DAS and DAMAS outputs.....	349
E-2	Comparison of DAMAS output to DAS uncertainty bounds.	349
E-3	Reduced scan plane DAMAS solution for 1,024 Hz.	350
E-4	Full test section scan plane DAMAS solution for 1,024 Hz.....	350
E-5	Reduced scan plane DAMAS solution for 2,512 Hz.	351
E-6	Full test section scan plane DAMAS solution for 2,512 Hz.....	351
E-7	Reduced scan plane DAMAS solution for 5,008 Hz.	352
E-8	Full test section scan plane DAMAS solution for 5,008 Hz.....	352
E-9	Reduced scan plane DAMAS solution for 7,600 Hz.	353
E-10	Full test section scan plane DAMAS solution for 7,600 Hz.....	353
E-11	Reduced scan plane DAMAS solution for 8,800 Hz.	354
E-12	Full test section scan plane DAMAS solution for 8,800 Hz.....	354
E-13	Reduced scan plane DAMAS solution for 15,008 Hz.	355
E-14	Full test section scan plane DAMAS solution for 15,008 Hz.....	355
E-15	Reduced scan plane DAMAS solution for 20,000 Hz.	356
E-16	Full test section scan plane DAMAS solution for 20,000 Hz.....	356

E-17	Full test section scan plane DAMAS solution for 20,000 Hz with 5,000 iterations.....	357
E-18	Full test section scan plane DAMAS solution for 20,000 Hz with 10,000 iterations.....	357
E-19	1/3 rd octave comparison of DAMAS beam map regions with DAS and NAFNoise.....	358

Abstract of Dissertation Presented to the Graduate School
of the University of Florida in Partial Fulfillment of the
Requirements for the Degree of Doctor of Philosophy

AN ASSESSMENT OF TRAILING EDGE NOISE MEASUREMENT TECHNIQUES

By

Christopher John Bahr

May 2010

Chair: Louis N. Cattafesta, III
Major: Aerospace Engineering

Aircraft noise is a subject of great concern, both to aircraft designers and community planners. As air travel becomes more prevalent and populations near airports increase, noise generated by aircraft during take-off and landing must be addressed. To this end, much research has gone into quantifying and reducing the strength of major contributors to aircraft noise, such as jet engines, high-lift devices and landing gear. However, as these sources are reduced, a new tier of sources grows in relative importance.

Trailing edge noise is the next major noise source which needs to be addressed if aircraft designers wish to continue their trend of making quieter aircraft with each new generation. This noise source, due to the scattering of pressure fluctuations in the wing boundary layer and near wake by the rear edge of the wing, is not fully understood, even after over thirty years of research. While theoretical models exist, developing measurement tools to validate the models is not a trivial task. Experiments performed decades ago, which were thought to have provided satisfactory data to designers, are now found to have significant flaws in their results due to instrumentation limitations. Modern experimental methods can readily show the weaknesses in the older analysis techniques, but no comprehensive set of new tools is currently available for quantifying and analyzing trailing edge noise.

This dissertation seeks to provide such a tool set by first reviewing the existing body of theoretical and experimental work, and then reviewing the major methodologies available. Existing methodologies are reformulated with additional analysis, and optimal measurement schemes are proposed. A library of acoustic data for a NACA 63-215 Mod-B airfoil is obtained, with the intent of benchmarking this tool set with respect to older results using coherent power techniques, and building a library of new ones using both coherent power and beamforming techniques. Results show that the studied techniques predict similar levels when airfoil noise is the dominant source in the facility. When distributed background noise sources are dominant, nominal prediction methods do not agree, but method uncertainties become sufficiently large that exact level estimates are identified as unreliable.

CHAPTER 1 INTRODUCTION

Since the inception of commercial flight, excess noise from air travel has been a major concern for communities near airports. Airport air traffic has increased significantly with economic growth and improving transport technology. This traffic increase, coupled with significant community expansion in the vicinity of airports, has led to the Federal Aviation Administration (FAA) regulating aircraft noise emissions [FAA 2003]. This regulation has become more stringent over time, and has led to significant research interest in the reduction of aircraft noise [Lockard & Lilley 2004; Macaraeg 1998].

Initial research on aircraft noise focused primarily on engine noise [Lockard & Lilley 2004]. However, the dramatic reduction achieved [Willshire 2003] has led to the condition where engine noise, at least during approach conditions, is of similar intensity to or less than the airframe noise generated by the aircraft [Lockard & Lilley 2004]. Airframe noise is defined as all non-propulsive noise generated by an aircraft in flight [Lilley 2001] and does not include engine/airframe interaction [Lockard & Lilley 2004]. Major sources of airframe noise at landing conditions include landing gear and high lift devices [Willshire 2003]. A schematic of major airframe noise sources on an example aircraft is shown in Figure 1-1 (contributed by Tai-An Chen). Once those primary sources are addressed, trailing edge noise from the baseline clean configuration becomes a major concern [Lockard & Lilley 2004].

The present research intends to quantify trailing edge noise from a particular airfoil model, a NACA 63-215 mod-B [Szelazek & Hicks 1979]. This model profile has been previously evaluated under various flight conditions, both acoustically and aerodynamically [Hutcheson & Brooks 2002; Hutcheson & Brooks 2004]. A more complete (with regards to previous research studies) library of analysis tools will be developed and applied to the data collected within this

research study, with the goal of assembling and assessing a set of reliable techniques for the quantification of trailing edge noise. Attention will be paid to the strengths and weaknesses of various acoustic measurement tools with a focus on their limiting assumptions in application to wind tunnel experiments. A major contribution is expected regarding the determination of the benefits and limitations of most currently-used trailing edge noise measurement methods.

This chapter begins with a definition of trailing edge noise, followed by a problem statement for the proposed research. A review of past research is presented. Theoretical work is first described, followed by a brief discussion of computational analysis, and an overview of experimental work. This is followed by a discussion of the research objectives, along with expected contributions.

Trailing Edge Noise

Trailing edge noise is generally defined as acoustic radiation induced by the combination of edge scattering of turbulent boundary layer pressure fluctuations, blunt-edge vortex shedding, and any laminar boundary layer instabilities on the rear edge of a wing or airfoil, along with any contributions from downstream wake unsteadiness [Blake & Gershfeld 1988]. Figure 1-2 is a schematic of these potential noise sources in the vicinity of a blunt, rounded trailing edge.

Trailing edge noise is present in any application involving an airfoil or exposed edge, be it in a flight condition as an aircraft wing or helicopter rotor blade, or in wind power installations as the turbine blades [Guidati, Bareiß & Wagner 1996]. In all cases, the physical noise generation mechanisms are the same (although relative power contributions may differ), as are the available acoustic analysis tools.

Problem Statement

Table 1-1 shows the importance of airframe noise relative to other aircraft noise sources when engine noise has been treated, and why airframe noise is an important consideration.

While significant research is being conducted regarding airframe noise components such as landing gear and high lift noise, the reduction in these sources is expected to fall short of anticipated FAA guidelines for acceptable community noise levels [Lockard & Lilley 2004]. To meet future approach guidelines, current low-end sources of airframe noise, of which trailing edge noise is one of the most dominant, must be addressed. In the case of wind turbines, trailing edge noise is a dominant source of noise and must be reduced in conjunction with other mechanical sources, such as the turbine gear box [Guidati *et al.* 1996]. The problem of trailing edge noise has received significant attention in the form of theoretical, computational and experimental development. The state-of-the-art regarding trailing edge noise analysis has improved significantly since the early years of theoretical studies [Ffowcs Williams & Hall 1969]. However some gaps still exist in the available research, especially regarding experimental toolsets and their potential application to the development and validation of theoretical and computational models.

Existing Research

Theoretical development

In-depth theoretical development of a trailing edge noise model can be traced back to 1959, with a Lighthill Analogy-based model [Powell 1959]. Extensions of this model focused on edge-scattering [Ffowcs Williams & Hall 1969]. Ffowcs Williams' model made use of Lighthill's Equation to describe aerodynamic noise scattered by a half-plane [Lighthill 1952].

$$\nabla^2 \rho - \frac{1}{c_0^2} \frac{\partial^2 \rho}{\partial t^2} = -\frac{1}{c_0^2} \frac{\partial^2}{\partial y_i \partial y_j} (\rho v_i v_j + p_{ij} - c_0^2 \rho \delta_{ij}) \quad (1-1)$$

Here, ρ is the thermodynamic density of the fluid, c_0 is the isentropic speed of sound, v_i is the local flow velocity, and p_{ij} is the applied stress tensor. The independent variables are t (time) and y_i (space). This equation reformulates the fluid conservation laws of mass, momentum and

energy such that a density-based wave operator on the left side of the equation exists in balance with equivalent source terms on the right side. These source terms consist of a stress tensor containing apparent turbulent stresses (the first source in parenthesis on the right), physical stresses (the second source term), and a hydrostatic pressure term for an equivalent at-rest acoustic field. Lighthill's Equation is strictly valid when the region outside of the source region, where the acoustic waves generated by the source region propagate, is isentropic and at rest. No allowance is made for feedback from the acoustic field into the source region. A dimensional analysis of this equation was first performed for jets [Lighthill 1954], and the derived scaling laws were used to determine important parameters for jet noise reduction [Lighthill 1962]. This initial evaluation of scaling involved a free-field Green's function. Subsequent analysis involved the inclusion of infinite, plane solid boundaries [Curle 1955]. While Curle's model accounted for surface pressure-doubling and source-boundary interaction, it failed to capture scattering effects from a finite-surface edge, which was later modeled as a semi-infinite half plane [Ffowcs Williams & Hall 1969].

Alternative formulations for trailing edge noise have been developed involving linearized hydrodynamic equations for flow around an airfoil [Amiet 1975; Amiet 1976; Crighton & Leppington 1971; Crighton 1972]. These formulations lack the physical exactness of Lighthill-based solutions but allow more readily for far-field noise prediction based on known turbulent surface pressure statistics in the vicinity of the trailing edge [Amiet 1976].

The aforementioned methodologies were subsequently unified, along with ad-hoc source models, as limiting cases of a more robust model [Howe 1978]. This analysis technique attempted to resolve the importance of the Kutta condition at the trailing edge and took into account source motion with respect to the trailing edge. It was later modified to include

thickness and rounding effects [Howe 1988] and then transitioned to acoustically compact chord airfoils, where interaction between the leading edge and trailing edge can be analyzed [Howe 1999; Howe 2001]. Compact assumptions can be applied when the length scales of interest, in this case the airfoil chord, are significantly smaller than the acoustic wavelengths of interest. Research involving compact-chord airfoils was used to modify Amiet's original formulation to include this interaction between the leading and trailing edges [Roger & Moreau 2005].

Computational development

A variety of computational simulations of trailing edge noise, with varying degrees of complexity, have been conducted. The simplest modeling techniques involve semi-empirical formulations, in which boundary layer parameters and mean aerodynamic properties [Drela 2001] are computed from thin airfoil theory or vortex panel methods and then substituted into linearized flow equations [Moriarty 2005; Moriarty, Guidati & Migliore 2005; Parchen 1998]. More advanced models involve computation of the hydrodynamic near-field using Reynolds-Averaged Navier Stokes (RANS) solvers before substitution into a reformulation of Lighthill's acoustic analogy [Khorrami, Berkman & Choudhari 2000; Singer *et al.* 2000a; Singer, Lockard & Brentner 2000b]. This reformulation is done using the Ffowcs Williams – Hawking Equation [Ffowcs Williams & Hawkings 1969]. The fidelity and complexity of near field computations can be increased by using large eddy simulations (LES) [Manoha, Troff & Sagaut 2000; Oberai, Roknaldin & Hughes 2002; Wang & Moin 2000]. Finally, direct numerical simulation (DNS) of the hydrodynamic near field is now possible at low Reynolds numbers using modern computing techniques [Sandberg *et al.* 2007]. DNS is the most accurate of the available computational tools, but is the most computationally expensive. Sandberg's work, for example, was limited to a chord-based Reynolds number (Re_c) of fifty thousand. This limitation means the turbulence field around the simulated airfoil cannot fully develop. Thus, turbulent pressure fluctuation

contribution to trailing edge noise, which is of major interest in full-scale applications, is not fully accounted for using DNS.

Experimental development

A large body of experimental work has been assembled to date, is summarized briefly in Table 1-2, and is discussed in detail in Chapter 3. In one of the earliest works, Paterson et al. collected data from both surface flush-mounted microphones and far field microphones [Paterson *et al.* 1973]. Experiments were conducted in a moderate Reynolds number regime on NACA 0012 and 0018 airfoils. Individual autospectra were evaluated and compared. Fink installed surface-mounted microphones in a splitter-plate airfoil and collected data from both these and far-field microphones in several locations in an open-jet wind tunnel [Fink 1975]. Data were collected with the airfoil in the center of the test section as well as mounted at the edge of the open-jet inlet in order to isolate trailing edge noise (with one-sided flow) from leading edge effects. Yu performed a similar analysis with a wall-mounted trailing edge, and also conducted shadowgraph photography of the turbulent flow field [Yu & Tam 1978; Yu & Joshi 1979]. In the first two studies, single-microphone autospectra were analyzed. The latter also used correlation analysis between surface and far field pressure transducers.

Schlinker and Amiet made an early attempt at source isolation using a directional microphone. This involved installing a standard omni-directional microphone at the focal point of an acoustic mirror to provide a directional measurement [Schlinker & Amiet 1981]. This setup reduced the influence of background noise on the microphone measurement but was only effective over a limited frequency range. Brooks and Hodgson took a different approach at roughly the same time, using a coherent output power method to evaluate coherent noise sources on a NACA 0012 airfoil [Brooks & Hodgson 1981]. Unsteady surface pressures were measured in this study as well. Subsequent studies began accounting for the effects of model lift

generation on an open jet test section facility [Brooks & Marcolini 1984]. This analysis was extended to multiple trailing edge configurations at several angles of attack [Brooks, Pope & Marcolini 1989]. Blake conducted a study on a different trailing edge model with an installation similar to that of Yu [Blake & Gershfeld 1988]. A large amount of data was collected regarding boundary layer and surface pressure scaling. Extensions of coherent power analysis have been used in more recent aeroacoustic experiments [Bahr *et al.* 2008; Mendoza, Nance & Ahuja 2008].

Meanwhile, advances were being made in noise source localization and identification. Multi-microphone phased arrays were designed for broadband measurement applications [Underbrink 1995] and leveraged for aeroacoustic experiments in an anechoic, open jet facility [Choudhari *et al.* 2002; Humphreys *et al.* 1998]. The Foundational Dutch National Aerospace Laboratory (NLR) used phased-array technology to study potential sources of noise contamination of open-jet wind tunnel facilities with side plates [Oerlemans & Sijtsma 2000]. Phased array techniques were compared to coherent power methods by Hutcheson [Hutcheson & Brooks 2002] and subsequently used to analyze a NACA 63-215 mod B model in a manner similar to the earlier Brooks, Pope and Marcolini study of a NACA 0012 [Hutcheson & Brooks 2004]. Studies were also conducted in this manner on wind turbine airfoil candidates [Oerlemans 2004].

Studies on trailing edge vortex shedding have been conducted first with coherence based microphone measurements [Kunze *et al.* 2002] and later with Particle Image Velocimetry (PIV) [Shannon, Morris & Mueller 2005]. High speed PIV has been used to capture acoustic source behavior in the vicinity of a trailing edge [Schroder *et al.* 2004]. Laser Doppler Anemometry (LDA) has also been used to capture unsteady flow fields in acoustic studies [McAlpine, Nash &

Lowson 1999; Nash, Lowson & McAlpine 1999]. Aerodynamic loading effects on the trailing edge noise sources have been considered with standard coherence techniques [Moreau & Roger 2005].

Advanced beamforming techniques have been used to attempt field analysis on airfoils. Traditional Delay-and-Sum (DAS) techniques can determine acoustic source locations, but do not provide reliable acoustic levels caused by those sources. Regional integration of DAS beam maps, with a correction based on an assumed source behavior, is one technique which has been used to determine acoustic levels due to the observed sources [Oerlemans, Broersma & Sijtsma 2007a; Oerlemans, Sijtsma & Mendez-Lopez 2007b]. Eigenvalue-decomposition methods have been considered [Sarradj 2010]. Deconvolution approaches have become another popular option in recent years, with codes such as DAMAS [Brooks & Humphreys 2006a], LORE [Ravetta, Burdisso & Ng 2009], CLEAN-SC [Sijtsma 2007], SC-DAMAS and CMF, [Yardibi *et al.* 2008] and some modified astronomical codes [Ehrenfried & Koop 2006]. Source coherence has been crudely accounted for in the DAMAS-C code [Brooks & Humphreys 2006b], as well as in LORE. This is an advancement over previous beamforming techniques, as standard beamforming algorithms assume that multiple sources are all statistically uncorrelated monopoles. These deconvolution approaches attempt to remove the effect of the finite aperture of the phased array to back out the true levels. They have been used in conjunction with traditional beamforming methods to construct hybrid broadband spectra of trailing edge noise [Shannon & Morris 2008]. Time domain extensions for broadband noise have been proposed [Dougherty & Podboy 2009]. While coherent sources are being analyzed, the effects of multipole, directional sources on beamforming analysis have yet to be fully characterized. Some modified beamforming procedures have been proposed [Bouchard, Havelock & Bouchard 2009].

In addition, some wavenumber analysis has been applied to separate higher-wavenumber turbulent fluctuations from lower-wavenumber acoustic fluctuations in a closed-wall wind tunnel [Arguillat *et al.* 2005; Koop & Ehrenfried 2008].

A practical result of the theoretical, computational and experimental analyses discussed above was the discovery that airfoil modifications can reduce trailing edge noise. One potential modification, trailing edge serrations, as discussed by Howe [Howe 1991], has been studied at NLR [Oerlemans *et al.* 2008]. Detailed, semi-empirical codes modeling trailing edge noise have been assembled [Bertsch, Dobrzynski & Guerin 2008; Nark *et al.* 2008]. Alternative techniques, such as porous airfoil design, have been evaluated [Sarradj & Geyer 2007].

Research Structure

Existing State-of-the-Art

As discussed above, there are many tools available in the analysis of trailing edge noise. While these tools can be sophisticated, the source assumptions involved in each analysis method's implementation can severely limit the validity of results. As will be discussed in Chapter 4, for instance, the Coherent Output Power method suffers from severe noise contamination effects if the source assumption of trailing edge noise, involving dominant dipole-like radiation, is violated, or if the signal-to-noise ratio (SNR) of the measurement is too low. Also, beamforming techniques, which are becoming extremely popular, suffer from aperture issues, and no standard method exists for determining integration regions of a distributed acoustic source. Different deconvolution techniques, which seek to overcome standard beamforming aperture issues, often output differing results [Yardibi *et al.* 2008].

The existing state-of-the-art lacks a standard toolbox of measurements for analysis and comparison between experimental datasets. The closest in use is by Brooks, Pope and Marcolini [Brooks *et al.* 1989], but this study was conducted with an uncambered airfoil, which while

widely-studied is of limited practical use. Also, the data set was constructed entirely with the Coherent Output Power method, and thus suffers from the limitations of that technique. A data set which, under identical experimental conditions, compares a wide variety of acoustic analysis techniques for trailing edge noise, is necessary.

Research Objective

The objective of this dissertation is to perform a suite of acoustic measurements on a classic airfoil, which is representative of the main element in a modern commercial aircraft, in a single facility. Redundant measurements will be performed with differing techniques and analyzed to attempt to isolate the individual failings of each methodology. Improved analysis techniques will be developed to minimize noise source interference in an attempt to isolate trailing-edge-related acoustic sources in each experimental set.

Expected Contributions

This research is expected to provide fundamental characterization of different aeroacoustic measurement techniques and their uncertainties. An experimental aeroacoustic analysis tool set will be produced. The data collected will be provided to the airframe noise community as a benchmark data set for their own characterization and validation of airfoils and facilities.

Research Roadmap

This dissertation will first review, in greater detail than that provided here, the fundamental theories and models of trailing edge noise in Chapter 2. In Chapter 3, a detailed discussion of existing experimental sets will be presented. This will be followed in Chapter 4 by the experimental setup for the measurements in the University of Florida Aeroacoustic Flow Facility (UFAFF), along with a discussion of the different processing techniques used here and in the literature, with emphasis on core assumptions, SNR effects and processing ambiguities. Appropriate simulation setup will be discussed in relation to each measurement technique.

UFAFF's basic design and characterization will be reviewed. In Chapter 5, the data set will be presented, followed by discussion, conclusions and future work. Appendices with detailed derivation and analysis of measurement techniques will conclude the document.

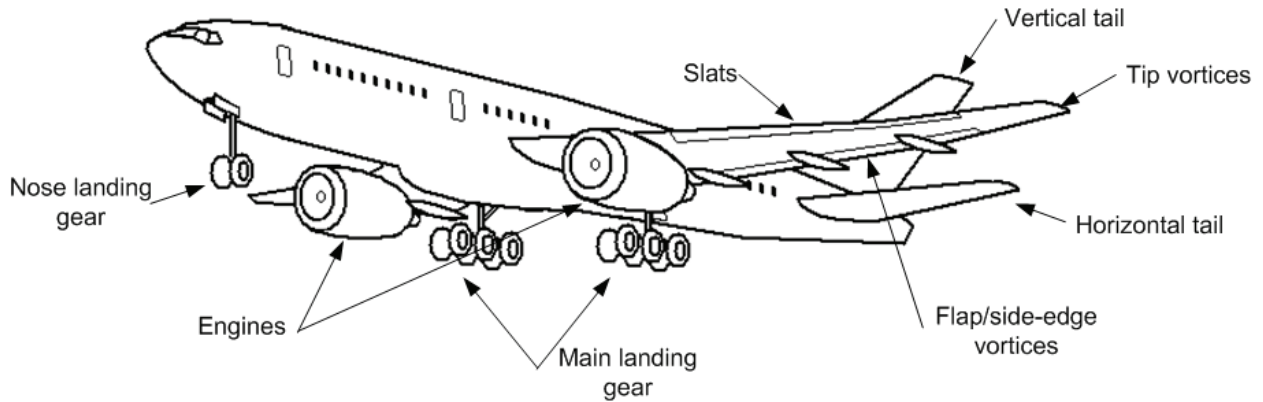


Figure 1-1. Schematic of major airframe noise sources.

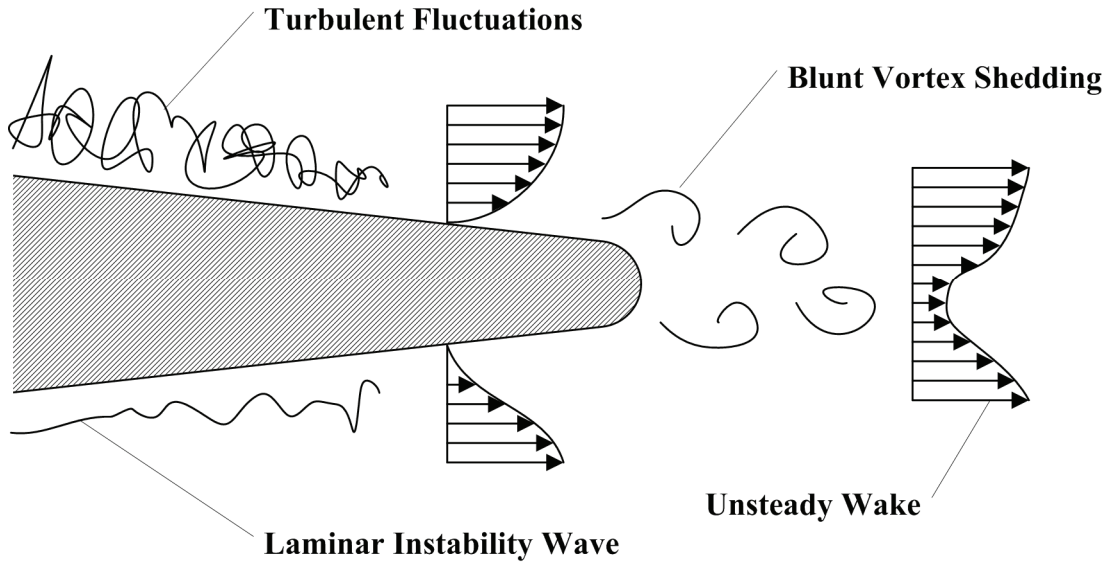


Figure 1-2. Schematic of sources in the vicinity of an example trailing edge.

Table 1-1. Approach noise levels for a Boeing 747-400 with Pratt & Whitney Advanced Ducted Propulsor (ADP) engines.

Noise Source	Effective Perceived Noise (EPN), dB
Inlet	93
Aft fan	93
Combustor	83
Turbine	78
Jet	73
Total Airframe	97
Total Aircraft Noise	100

[Golub, Rawls & Russell 2005]

Table 1-2. Summary of experimental research in trailing edge noise.

Author(s)	Year	Measurements	Limitations
Fink	1975	Single microphone	Background noise contamination
Yu & Tam, Yu & Joshi	1978, 1979	Flow visualization, correlation analysis	Limited in-flow data, noise contamination
Brooks & Hodgson	1981	Surface pressures, coherent power	Coherent power model assumptions
Schlinker & Amiet	1981	Directional microphone	Limited frequency range
Brooks & Marcolini	1984	Coherent power, open tunnel corrections	Model assumptions, open tunnel assumptions
Blake & Gershfeld	1988	Single microphone, surface pressures, boundary layer data	Background noise limitations
Brooks, Pope & Marcolini	1989	Coherent power, many model permutations	Coherent power model assumptions, no flow measurements
Oerlemans & Sijtsma	2000	Array-based Measurements	Source model assumptions, data referenced to BPM 1989
Hutcheson & Brooks	2002	Coherent power, array-based methods	Source model assumptions, data referenced to BPM 1989
Kunze & Lynch	2002	Coherent power	Source model assumptions
Hutcheson & Brooks	2004	Array-based measurements, many model permutations	Source model assumptions, data referenced to BPM 1989, limited flow data
Oerlemans	2004	Array-based measurements	Source model assumptions, data referenced to BPM 1989
Schroder & Dierksheide	2004	High speed PIV	No correlation to acoustic data
Moreau & Roger	2005	Coherent power	Coherent power model assumptions
Shannon & Morris	2005	PIV, Array-based measurements	Source model assumptions, PIV conducted in different facility from acoustics
Oerlemans, Broersma & Sijtsma	2007	Array-based measurements, field integration	Source model assumptions
Bahr et al.	2008	Coherent power and array-based measurements	Coherent power assumptions, no attempt at beamforming acoustic level analysis
Shannon & Morris	2008	Array-based measurements	Source model assumptions

CHAPTER 2
AEROACOUSTICS – THEORETICAL DEVELOPMENT

Lighthill-Based Analysis

Lighthill-based analysis techniques begin with the derivation of Lighthill's aeroacoustic equation. To start, the equations of continuity and conservation of momentum are stated, respectively [Panton 1996].

$$\frac{\partial \rho}{\partial t} + \nabla \cdot (\rho \vec{V}) = 0 \quad (2-1)$$

$$\frac{\partial (\rho \vec{V})}{\partial t} + \nabla \cdot (\vec{V} \rho \vec{V}) = -\nabla \cdot \vec{p} \quad (2-2)$$

As in Chapter 1, \vec{p} is the total stress tensor, including pressure and viscous stresses, ρ is the fluid density, and \vec{V} is the local velocity vector. These two equations can be recast in indicial notation, and the source term on the right side of the momentum equation can be moved into the divergence term on the left [Lighthill 1952].

$$\frac{\partial \rho}{\partial t} + \frac{\partial (\rho v_i)}{\partial x_i} = 0 \quad (2-3)$$

$$\frac{\partial (\rho v_i)}{\partial t} + \frac{\partial (\rho v_i v_j + p_{ij})}{\partial x_j} = 0 \quad (2-4)$$

An approximate momentum equation for a near-quiescent, inviscid flow field is defined in Equation (2-5), where un-indexed p is the thermodynamic pressure.

$$\frac{\partial (\rho v_i)}{\partial t} + \frac{\partial p}{\partial x_i} = 0 \quad (2-5)$$

The pressure in this equation can be changed to the fluid density by defining an isentropic speed of sound and applying the chain rule.

$$\frac{\partial(\rho v_i)}{\partial t} + \frac{\partial p}{\partial \rho} \frac{\partial \rho}{\partial x_i} = \frac{\partial(\rho v_i)}{\partial t} + c_0^2 \frac{\partial \rho}{\partial x_i} = 0 \quad (2-6)$$

The divergence term in Equation (2-4) can be moved to the right-hand side of the equation. The gradient term from Equation (2-6) can then be added to both sides of Equation (2-4).

$$\frac{\partial(\rho v_i)}{\partial t} + c_0^2 \frac{\partial \rho}{\partial x_i} = - \frac{\partial(\rho v_i v_j + p_{ij} - c_0^2 \delta_{ij})}{\partial x_i} \quad (2-7)$$

The source term of Equation (2-7) can be recast as a single source tensor.

$$T_{ij} = \rho v_i v_j + p_{ij} - c_0^2 \rho \delta_{ij} \quad (2-8)$$

Here, the total source tensor T_{ij} is equated to a sum of turbulent stresses, pressure stresses, and viscous stresses, minus the equivalent quiescent medium stresses.

By taking the time derivative of Equation (2-3) and subtracting the divergence of Equation (2-7), the problem can be reformulated into a single equation.

$$\frac{\partial^2 \rho}{\partial t^2} - c_0^2 \frac{\partial^2 \rho}{\partial x_i \partial x_i} = \frac{\partial^2 T_{ij}}{\partial x_i \partial x_j} \quad (2-9)$$

Equation (2-9) is a more compact restatement of Equation (1-1). An analog can be drawn between this and a homogeneous wave equation from linear acoustics [Blackstock 2000].

$$\frac{\partial^2 \rho'}{\partial t^2} - c_0^2 \frac{\partial^2 \rho'}{\partial x_i \partial x_i} = 0 \quad (2-10)$$

By comparison, Lighthill's Equation is simply a wave equation with all the usual nonlinearities of flow lumped into an inhomogeneous source term. This equation is exactly true for a continuum, under the limitation that the far field acoustic propagation is in a region of quiescent, linear lossless flow. The near field, where the source term is nonzero, can have complex, turbulent, viscous flow interactions. Solutions to Equation (2-9) generally involve assumptions of boundary conditions and the neglect of differing components of the source term to simplify

analysis. Low speed, free-field analysis of a cold turbulent jet exhausting into a quiescent medium was first conducted [Lighthill 1954], and then extended to turbulent eddies convected near a rigid, acoustically compact body [Curle 1955].

Ffowcs Williams and Hall addressed this equation in relation to scattering from a semi-infinite half plane [Ffowcs Williams & Hall 1969]. A schematic of their problem is shown in Figure 2-1. By assuming that in the Lighthill stress tensor, Equation (2-8), the viscous stresses are negligible (a valid assumption in developed turbulent flow fields away from boundaries), the second and third terms exactly balance and cancel as the remaining stresses in the second term are only nonzero on the tensor diagonal, just as in the third. This assumption leaves turbulent fluctuations as the only source. Equation (2-9) can be simplified.

$$\frac{\partial^2 \rho}{\partial t^2} - c_0^2 \frac{\partial^2 \rho}{\partial x_i \partial x_i} = \frac{\partial^2 (\rho v_i v_j)}{\partial x_i \partial x_j} \quad (2-11)$$

This wave equation has a volume source of quadrupole nature [Dowling & Ffowcs Williams 1983]. The effect of edge scattering is addressed entirely through the selection of the Green's function.

By assuming stationary behavior of turbulence in the flow field, a Fourier transform of Equation (2-11) can be taken with respect to time, reducing it to an inhomogeneous Helmholtz equation.

$$k^2 p^* + \frac{\partial^2 p^*}{\partial x_i \partial x_i} = - \left[\frac{\partial^2 (\rho v_i v_j)}{\partial x_i \partial x_j} \right]^* \quad (2-12)$$

Here, k is the acoustic wavenumber, and the * superscript denotes the Fourier-transformed functions of the stated physical quantities. The magnitude of the acoustic wavenumber, k , is related to the circular frequency of an acoustic wave, ω , through the isentropic speed of sound.

$$k = \frac{\omega}{c_0} \quad (2-13)$$

Ffowcs Williams selects an appropriate Green's function for the given equation and boundary condition, and then scales it in two ways [Ffowcs Williams & Hall 1969]. First, he addresses eddies in the near field. Assuming characteristic turbulence scales and solving for the far field acoustic intensity, I , defined in Equation (2-14) with t_{av} as the time interval of averaging and u the instantaneous acoustic velocity magnitude, as a function of space and frequency in cylindrical coordinates yields Equation (2-15).

$$I = \frac{1}{t_{av}} \int_0^{t_{av}} p u dt \quad (2-14)$$

$$I(r, \theta, z; \omega) = \frac{k^4 \sin \phi \sin^2 \left(\frac{1}{2} \theta \right) \rho_0 U^4 \alpha^2 \left\{ \frac{\cos^2}{\sin^2} \right\} \frac{\beta}{2} \nabla^2}{\pi^3 c_0 R^2 (k \bar{r}_0)^3} \quad (2-15)$$

Here, U is the mean flow velocity. The subscripted 0 terms in this equation denote the source location relative to the origin when referencing independent variables, and mean quantities for thermodynamic properties. R is the distance between the observer and source locations $|\vec{r} - \vec{r}_0|$, ∇ is the characteristic eddy volume, α is the normalized turbulence intensity, \bar{r}_0 is the distance from the turbulent eddy center to the half-plane edge, and β is the angle of the eddy center referenced from the trailing edge. The selection of sine or cosine is dependent on eddy characteristics. This formulation suppresses a term regarding the flow angle with respect to the half plane.

Suppressing directivity terms in Equation (2-15), scaling \bar{r}_0 as the turbulence characteristic correlation length scale and scaling the normalized turbulence intensity to unity

shows that this edge scattering noise follows a fifth-power law with flow velocity [Ffowcs Williams & Hall 1969].

$$I \sim \frac{\rho_0 U^5 \delta^2}{c_0^2 R^2} \quad (2-16)$$

Equation (2-16) assumes a characteristic eddy wavenumber, Equation (2-17), using a characteristic eddy radius, δ defined as the relative to the characteristic eddy volume \forall . Also, the distance from the turbulent eddy center is assumed to be of similar magnitude to the characteristic eddy size.

$$k = \frac{\pi U}{c_0 \delta} \quad (2-17)$$

For low, subsonic Mach numbers, this fifth-power scaling is more efficient at acoustic radiation than Lighthill's analysis of a free jet's eighth-power scaling [Lighthill 1954], or Curle's analysis of the sixth-power scaling of flow past a compact rigid body [Curle 1955]. Ffowcs-Williams proceeds to analyze an eddy far from an edge, and shows that the scaling becomes the same as with a free jet [Ffowcs Williams & Hall 1969].

$$I \sim \frac{\rho U^8 \delta^2}{c_0^5 R^2} \quad (2-18)$$

The implication from this analysis is that, for low Mach number flows, turbulence near the surface of a half-plane edge is far more efficient at scattering hydrodynamic pressure fluctuations into a radiating sound field than fluctuations elsewhere in the flow field. This means that the fluctuations of instability waves in a transitional boundary layer, turbulent boundary layer fluctuations, separation vortices, a turbulent near-wake of a large airfoil will be significantly louder than fluctuations further upstream on the airfoil surface, or the free fluctuations of the airfoil's turbulent far-wake. The analysis also provides some sense of source directivity, as

shown in the angular terms in Equation (2-15). The problem formulation is limited, however, in that it does not account for convection effects on sound propagation. It has also assumed, as stated before, statistically stationary behavior of the turbulence, and applied a simplistic model to the characteristic frequency content of a turbulent eddy.

Linearized Hydrodynamics

Another class of analysis of the trailing edge noise problem involves linearizing hydrodynamic equations. This process solves for source and scattered fields using a velocity potential, generally formulated in both the frequency and wavenumber domains. In addition to the assumptions required for the Lighthill-based formulations, irrotational flow is required throughout the domain of interest to allow for a velocity potential definition. In the preceding section, irrotational flow was only required in the acoustic far field. However, rotationality could be present in the source region.

Crighton set down a formulation of edge-scattered noise using the above assumptions, and recovers the fifth-power scaling of Ffowcs Williams [Crighton & Leppington 1971]. Chase presents a result for the scattered pressure field as a function of the turbulent surface pressure fluctuations near the scattering edge. [Chase 1972]. Amiet evaluated airfoil noise as a function of fluctuating surface pressure [Amiet 1975], and provided the far field pressure autospectrum as a function of surface pressure fluctuations [Amiet 1976].

$$G_{pp}(x, y, 0, \omega) = \left(\frac{\omega b z}{2\pi c_0 \sigma^2} \right)^2 l_z(\omega) d |L|^2 G_{qq}(\omega, 0) \quad (2-19)$$

Here, the far field acoustic autospectrum is subscripted p , while surface pressure fluctuations within a correlation length of the trailing edge are subscripted q . L is a term relating to airfoil compactness, l_z is the spanwise correlation length of the characteristic turbulence fluctuations, and σ is an observer distance scaled to account for convection effects. The half-chord of the

airfoil is b , and the half-span is d . While this formulation directly relates surface pressure fluctuations to far field pressure fluctuations, the computation of the airfoil compactness term can be involved. This formulation was subsequently corrected for additional leading edge effects [Amiet 1978b; Moreau & Roger 2009; Roger & Moreau 2005].

While these equations are less physically exact with regard to the nature of the source field, they do lend themselves better towards experimental validation. The determination of the true turbulent source from Lighthill's equation is experimentally difficult, as it requires knowledge of the entire turbulent velocity field as a function of space and time, requiring simultaneous multi-dimensional velocity measurements at each point in space, or at least the simultaneous turbulent correlation behavior within the region. However, unsteady surface pressure measurements in the vicinity of the airfoil trailing edge are possible using flush-mounted unsteady pressure transducers, so an approximate surface wavenumber-frequency field can be determined using homogeneous turbulent assumptions.

Howe's Analysis

Howe extended trailing edge noise analysis to include the benefits of surface pressure measurement with the exactness of Lighthill-based methods [Howe 1978]. This was done by changing the primary acoustic variable from either pressure or density to stagnation enthalpy.

Lighthill's acoustic analogy can then be re-expressed as in Equation (2-20).

$$\left\{ \frac{D}{Dt} \left(\frac{1}{c_0^2} \frac{D}{Dt} \right) + \frac{1}{c_0^2} \frac{D\vec{v}}{Dt} \cdot \nabla - \nabla^2 \right\} B = \nabla \cdot (\vec{\omega} \times \vec{v}) - \frac{1}{c_0^2} \frac{D\vec{v}}{Dt} \cdot (\vec{\omega} \times \vec{v}) \quad (2-20)$$

Here, B is the stagnation enthalpy, $\vec{\omega}$ is the vorticity vector, and the total derivatives are denoted by $D()/Dt$. The following approximations and assumptions are used in the reduction and solution of this equation.

- Isentropic flow in the far field
- Constant temperature flow
- Taylor's Hypothesis applies to turbulence in boundary layer and near wake [Tennekes & Lumley 1972]
- There is no back-reaction from the trailing edge to the upstream flow
- Eddy convection velocity is a function of local mean velocity
- Eddies moving at different convection velocities are uncorrelated
- Flow fluctuations are approximated as incompressible near the trailing edge
- Kutta-condition-induced vortex shedding is treated as a stationary vortex sheet
- The mean shear and wake convection velocities are small relative to c_0

Howe presents the far field pressure spectrum as a function of surface pressure spectrum, as well as the overall sound pressure level (OASPL) for a given observer location. The relations are presented both with and without enforcement of the Kutta condition for a flyover case.

$$\langle p_I^2 \rangle = \frac{c_\chi \rho_0^2 v^2 V^2 M_V}{2\pi} \left(\frac{Ll_z}{r^2} \right) \frac{(1 - M_0 + M_{V1}) \sin^2 \left(\frac{\theta}{2} \right) \cos^3 \beta}{(1 + M_0 \cos \theta)^3 \{1 + (M_0 - M_{V1}) \cos \theta\}^2} \quad (2-21)$$

In Equation (2-21), p_I is the far field pressure without Kutta enforcement, c_χ is the integrated, normalized source spectrum, v is the root mean square (rms) turbulent fluctuation velocity, M_V is the local Mach number, M_0 is the free stream Mach number, L is the trailing edge wetted span, β is the local surface angle at the trailing edge relative to the x-axis (or flat-plate chord line) in Figure 2-1, and M_{V1} is the x-component of the local Mach number. The Kutta condition reduces this radiated intensity by a factor dependent on the difference between the mean eddy velocity and the mean wake velocity.

Howe states that this equation reduces to the Ffowcs Williams-Hall solution when free stream and eddy convection effects are neglected. He subsequently presents a generalized model

for projecting surface pressure fluctuations to the far field. As with the previous sections, Howe shows a near-fifth-power scaling for trailing edge noise, dependent on forward flight Mach number. Howe's model also shows agreement with directivity predictions from previous research. The overall agreement between the models shows that reducing the eddy convection speed and the spanwise eddy correlation should reduce trailing edge noise radiation. With a measurement of surface pressure spectra in the vicinity of the airfoil trailing edge, far field noise can be predicted and compared with experiment, and several models of trailing edge noise can be verified. The surface pressure spectra can also be modeled with sufficient mean boundary layer measurements and existing turbulent boundary layer predictions. This is, indirectly, what some existing research attempts in relating far-field acoustic spectra to mean boundary layer properties [Brooks *et al.* 1989; Moriarty 2005].

Unfortunately, while the trailing edge noise problem has been solved for ideal cases, and even extended to more complicated geometries such as blunted and serrated trailing edges [Howe 1988; Howe 1991], much research remains. The scaling of empirical models used in design codes still requires experimental validation. For experimental validation to occur, a comprehensive, consistent set of analysis tools is required to appropriately compare results between facilities. These tools must reliably extract out real contamination effects in experiments while preserving the necessary data for theoretical model validation. While many experimental data sets have been assembled with far field noise measurements, no consistent method of acquisition and analysis has been selected. This deficiency must be addressed before theoretical model validation can be revisited. The next chapter addresses many of these data sets, discusses which measurement techniques were used, and what is lacking in each for comparison with other data sets.

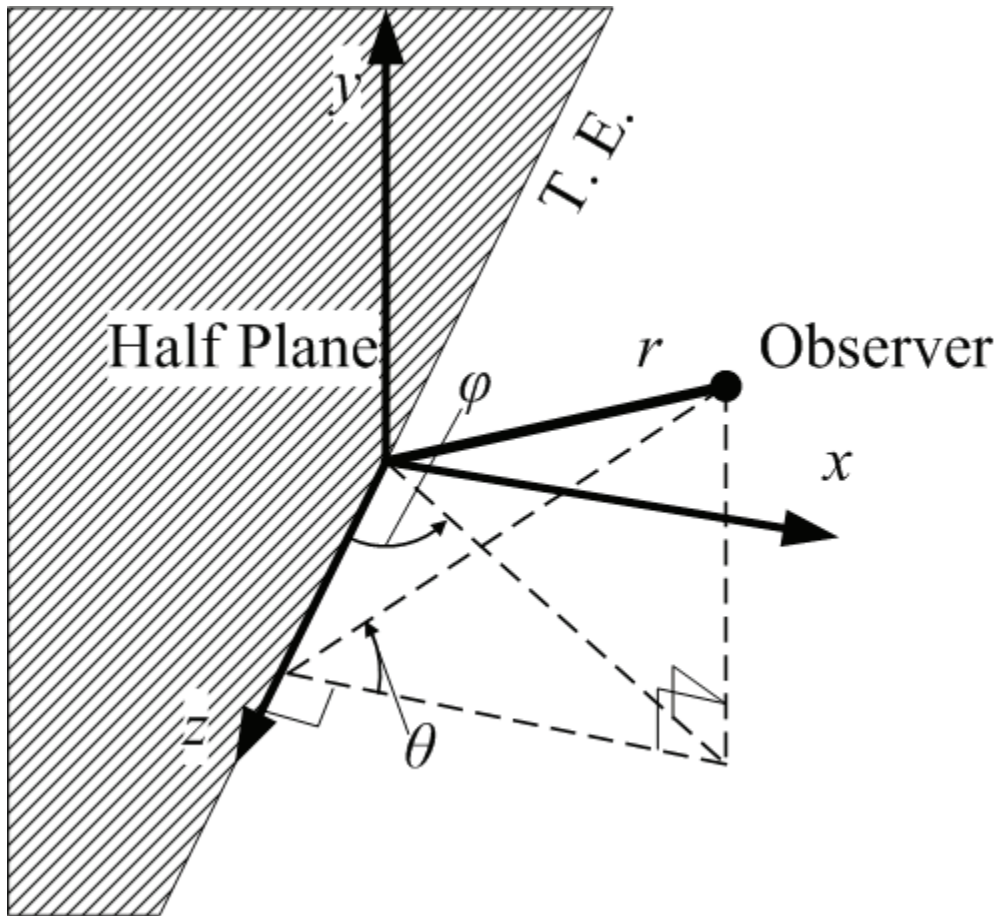


Figure 2-1. Coordinate system for trailing edge noise analysis. Adapted from Howe's work [Howe 1978].

CHAPTER 3 EXPERIMENTS IN TRAILING EDGE NOISE

Many experimental techniques have been developed for the analysis of trailing edge noise. These techniques vary in complexity from single microphone measurements to phased array methods. The following is a more extensive review of some of the major works present in the literature, as briefly discussed in Chapter 1. Analysis methods will be discussed, including the limitations of the presented experiments.

Paterson, Vogt, Fink & Munch (1973)

One of the earliest experimental works in trailing edge noise was conducted by United Aircraft Research Laboratories (UARL) and Sikorsky Aircraft Division [Paterson *et al.* 1973]. NACA 0012 and NACA 0018 models were placed in UARL's Acoustic Research Tunnel; this tunnel was an open-jet facility in an anechoic chamber, set up with sidewalls of unspecified construction to constrain flow over full-span models to two dimensions. The selected models had chords of 9", and were tested at Reynolds numbers ranging from 8×10^5 to 2.2×10^6 . Multiple angles of attack were evaluated, and were listed as geometric angles in the literature, with brief mention of required corrections due to open jet streamline curvature as defined by Pope and Harper [Pope & Harper 1966].

Models were instrumented with 1/4" microphones to measure surface pressure fluctuations. The surface microphones had protective grids removed, and the diaphragms were flush-mounted with the airfoil surface. The microphones were placed at varying chordwise locations, based on the model selection. At least one microphone on each model surface had a variable spanwise installation. The rest were installed at fixed 1/3 span locations. Additional measurements were conducted with a microphone placed in the acoustic far field, 7' above the test section centerline.

Collected data were processed individually, channel-by-channel. $1/3^{\text{rd}}$ -octave and 10 Hz binwidth narrowband spectra were computed using a variable band-pass filter. At lower Reynolds numbers, band-limited tonal behavior was detected. The tones were seen in wake hotwire data, as well. This was seen to scale as a Strouhal number, defined in Equation (3-1), with twice the laminar boundary layer thickness as a length scale. Such scaling was noted to imply a wake scale dependency. The tonal behavior was not present at higher Reynolds numbers, when the boundary layer and wake had transitioned to turbulent behavior. Trips on the airfoil suction side were found to have little effect on the tonal behavior. Trips forward of 80% chord on the pressure side suppressed the tones. At the highest Reynolds numbers, airfoil noise was indistinguishable from background tunnel noise, laying the groundwork for a need for measurement and analysis de-noising techniques for wind tunnel testing.

Yu & Joshi (1979)

In 1979, Yu and Joshi presented a study of trailing edge noise involving an airfoil in an open-jet aeroacoustic facility [Yu & Joshi 1979]. The authors used a pair of NACA 63-012 models in their experiments. Both uncambered models were identical, with chords of 0.61 m and spans of 0.3 m. One model was instrumented with surface pressure transducers, and the other was machined for smoke injection to permit flow visualization. The airfoil trailing edges were machined to razor edges, as specified in the airfoil design coordinates [Abbott & Von Doenhoff 1959]. This “razor” thickness is not defined. However, if it is assumed that blunt trailing edge shedding occurs at a Strouhal number [Panton 1996], St , of approximately 0.2 [Boldman, Brinich & Goldstein 1976], the low-speed case (30 m/s) would allow a maximum trailing edge thickness of just over 0.5 mm to be above the 10 kHz cut-off of the low-pass filter used in data acquisition.

$$St = \frac{fd}{U_{\infty}} \quad (3-1)$$

Here, d is the length scale of interest, such as trailing edge thickness, and U_∞ is the mean free stream flow velocity. Given standard caliper resolution, it can be assumed that “knife” or “razor” thickness is less than 0.5 mm. The implication of this is that the measured noise in the study would exclude any blunt shedding tones.

For this experimental set, Reynolds numbers based on model chord of 1.22×10^6 and 2.21×10^6 were considered in the surface pressure and acoustic measurements, corresponding to respective flow velocities of 29.7 m/s and 53.9 m/s. For flow visualization, analysis limitations lowered the experiment Reynolds numbers to 2.5×10^5 and 6.3×10^5 . Here, Reynolds number is defined in Equation (3-2) [Panton 1996].

$$\text{Re} = \frac{\rho U_\infty L}{\mu} \quad (3-2)$$

In Equation (3-2), ρ is the fluid density, L is the length scale of interest, and μ is the fluid dynamic viscosity. For these cases, the length scale of interest is considered to be the model chord.

Boundary layer characteristics and flow scales were measured using flow visualization. Surface pressure fluctuations on the upper and lower surfaces were collected simultaneously with far field noise measurements. It should be noted that the far field noise measurements, when analyzed using as a single microphone, could not discern trailing edge noise over facility background noise levels. Correlation-based techniques were used with surface pressure measurements, as well as microphones placed on opposite sides of the trailing edge. A 180° phase shift was seen between the suction and pressure sides of the airfoil. Surface pressures measured on the same side of the airfoil as a given far field microphone were seen to be in phase. An attempt was made to measure the effect of the Kutta condition based on phase relations from Howe [Howe 1978], but the measurement data failed to provide the necessary information. It

was hypothesized by the authors that this was due to the surface pressure measurements occurring too far from the trailing edge of the model, at 95% chord.

Brooks & Hodgson (1981)

In 1981, Brooks and Hodgson published an extensive study of trailing edge noise conducted in the Quiet Flow Facility (QFF) at NASA Langley Research Center. A NACA 0012 airfoil model, with a chord of 0.61 m and a span of 0.46 m, was used. The model trailing edge was modified using hardwood extensions. The thickest case had a trailing edge thickness of 2.5 mm, while the thinnest was defined as “sharp.” The method used to attach trailing edges led to a model chord increase of 12.7 mm for the “sharp” case. It should be noted that for the listed chord, the true defined trailing edge thickness of a NACA 0012 model is just over 1.5 mm, thus the airfoil used was actually a slightly blunted NACA 0012. The effect of this minor increase in chord was not addressed in the publication, but later work [Blake 1986] indicated that an extended model chord shifts the low-frequency cut-on where trailing edge noise becomes independent of leading edge scattering and feedback effects. All model trailing edge extensions were joined with glossy 0.08 mm thick Teflon tape. Surface pressure transducers were placed in an array along the chord and span of the airfoil, in a pattern symmetric along the upper and lower surfaces of the airfoil. The rearmost transducers were 2.54 mm, or 0.42% chord, from the trailing edge. It was noted that this distance increased as thinning trailing edge extensions were added.

An arc of Brüel and Kjær (B&K) Type 4133 free field microphones was set around the airfoil midspan. Microphone distances and angles from the trailing edge were measured geometrically and then modified for open-jet wind tunnel effects using a shear layer correction method derived by Amiet [Amiet 1978a].

Data were acquired using a 14 channel Honeywell 9600 FM analog tape recorder. Due to the large number of sensors in the experimental setup, up to five runs were required for each combination of experimental parameters. Aside from trailing edge thickness, parameters varied included mean flow velocity and model angle of attack (AoA). Not all trailing edge thicknesses were used at every AoA. The blunt trailing edge was used at zero degrees, five degrees and ten degrees; the sharp trailing edge was used for zero degrees and five degrees. The remaining trailing edge permutations were only evaluated at a zero degree AoA.

The impact of both boundary layer tripping and spanwise three-dimensional effects on the state of the boundary layer near the trailing edge was evaluated. It was noted that tripping reduced the three-dimensional effects caused by the short span of the airfoil and the presence of hard-walled side plates. Accordingly, the boundary layer was tripped for all noted studies.

Mean flow aerodynamics were analyzed for all run conditions using a moveable Pitot-rake and surface mounted Preston tubes. Both measurements confirmed two-dimensionality of the mean flow field. Boundary layer parameters, such as displacement and momentum thickness, were measured, presumably using the Pitot-rake, and computed for each run condition. Some doubt was cast on the validity of the computed displacement thicknesses, so “best fit” values were instead used for scaling purposes. This was computed by fitting a regression function to the experimental displacement thickness data using traditional known scaling laws.

Detailed statistical results of surface pressure measurements were presented in the paper. Correlation and coherence were evaluated in the chord and spanwise directions, and edge backscatter effects were discussed. That data were evaluated with respect to Corcos’ turbulent boundary layer model [Corcos 1964]. Through simplification, surface pressure data were claimed to agree with theory regarding near field pressure fluctuations near the trailing edge.

As with Yu and Joshi's work, it was determined that single microphone measurements were insufficient for determining trailing edge noise in the QFF. A coherent output power method (COP) was discussed in reference to general sources. In processing, it was assumed that trailing edge noise behaved in an antisymmetric fashion for the phase angle as had been previously shown. This allowed the simplification of the COP method and computation of a de-noised directivity pattern. The phase delay between microphones placed on opposite sides of the airfoil was computed and compared to theory. This comparison was used to determine the range over which the data were reliable. A phase relationship breakdown indicated the appropriate cut-off frequencies. Spectra were evaluated with regards to potential non-dimensional parameters, and overall sound pressure levels (OASPL) were calculated and fit to curves as functions of free stream velocity. Finally, the measured surface pressure fluctuations were used with the existing trailing edge noise models of Howe and Chase to predict radiated trailing edge noise [Chase 1975; Howe 1978]. Comparison was made with the far field acoustic measurements, and general agreement in spectral trends was seen.

Blake & Gershfeld (1988)

In 1988, Blake and Gershfeld presented a two-part comprehensive review of research conducted on trailing edge noise [Blake & Gershfeld 1988]. The first half was a review of previous theoretical and analytical work. The second half described new research conducted by the authors.

Complete information on the airfoil selection was not published in the document. A single forward-half airfoil was machined such that its aft-half could be swapped out between two trailing edges. One edge was thin, while the other was thickened to capture some vortex shedding effects. The model chord was 40 inches. Trip tape was applied at 5% chord in all

cases. Measurements were conducted in the Anechoic Flow Facility (AFF) of the David Taylor Research Center.

Unsteady surface pressures were measured, as in the previous studies. Cross correlations were computed between surface pressures and boundary layer and wake velocities. The experimental setup for the wake measurement was not provided in the publication, but given existing technology at the time, it can be assumed that hot-wire anemometry was employed. For far field noise, a pair of B&K Type 4165 half-inch microphones was placed on opposite sides of the trailing edge, as done by Brooks and Hodgson. The acoustic spectra were calculated using the COP method. Directional arrays were considered but not used, due to facility limitations, model size and the frequency range of interest.

In processing the surface pressure measurements, much attention was paid to the turbulence statistics near the model's boundary layer separation point. The airfoil trailing edge sections were selected specifically for this characteristic separation behavior, and detailed correlation and cross-spectra were presented and discussed. As with previous work, the surface pressure and far field acoustic data were used to compare experimental results with Howe's theory. Also, as with previous work, general agreement was seen between experiments and theory. The blunt trailing edge model showed better agreement, and it was claimed that this was due to the stronger radiated field.

Brooks, Pope, & Marcolini (1989)

Brooks, Pope, and Marcolini published a report in 1989 detailing their experimental research on airfoil self noise [Brooks *et al.* 1989]. The goal of this report was to generate a set of empirical codes for the prediction of airfoil self noise. The codes accounted for various components of airfoil noise such as turbulent boundary layer noise, separation noise, tip noise and vortex shedding noise. The code produced noise predictions for input parameters based on

airfoil chord, AoA, tip conditions and flow speed, as well as desired observer output locations. The output data were formatted for one-third octave bands.

To generate their empirical relations, the authors returned to the NACA 0012 airfoil design, as used by Brooks and Hodgson [Brooks & Hodgson 1981]. However, many 0012 airfoils with chords varying from 2.54 cm to 30.48 cm were machined, with “sharp” trailing edges, defined as less than 0.05 mm thick. There is no documentation on whether the standard NACA 0012 profile was extended to match this sharp condition, thus altering the original chord by a given amount or if the model was sharpened at the specified trailing edge location, and subsequently blended smoothly back along the airfoil body until the true NACA 0012 shape was recovered. No surface pressure instrumentation was used with this data set.

Flow measurements were conducted using hot wire anemometry in NASA Langley’s QFF. Boundary layer displacement and momentum thickness were calculated using three-dimensional traversing for both single-wire and cross-wire installations. Boundary layer behavior as a function of model and flight condition was one of the primary desired parameters for the code. Facility test conditions were varied such that the test section flow speed was a maximum at 71.3 m/s, and AoA varied between zero degrees and 25.2 degrees.

This experiment leveraged an open-jet correction for its calculation of model AoA based on previous work [Brooks & Marcolini 1984]. This correction is an attempt to account for the deflection of the test section’s finite jet by model lift to calculate an equivalent free stream AoA. While this does not account for details in differences of surface pressure distributions, it does find the appropriate equivalent-lift condition for an open jet exhausting into an infinite plenum. The correction utilizes a periodic formulation of potential flow vortex sheets to simulate an infinite cascade of airfoils deflecting a freestream flow. The original formulation does not allow

for a downstream jet collector turning the flow again, and thus yields questionable results in facilities with finite-length open test sections.

Acoustic measurements were conducted with half-inch free field microphones. The microphones were oriented in a manner similar to that of Brooks and Hodgson [Brooks & Hodgson 1981]. Again, the radiated sound field was computed using the COP method, and shear layer corrections were used. The measured acoustic field was compared to the boundary layer measurements for each flight condition, and scaling relations were developed. These empirical relations were converted into a Fortran code appended to the report. This was one of the first attempts at a prediction tool for trailing edge noise. Subsequent codes have refined it with more robust boundary layer predictions [Moriarty *et al.* 2005].

Hutcheson & Brooks (2002, 2004)

More recently, Hutcheson and Brooks conducted studies of trailing edge noise, attempting to leverage newer technologies [Hutcheson & Brooks 2002; Hutcheson & Brooks 2004]. These studies were again conducted in NASA Langley's QFF. The primary focus of the first body of work was to compare COP analysis to array-based techniques, while the second re-evaluated trailing edge noise using array-based techniques at different AoAs and flight speeds.

For these tests, a NACA 63-215 Mod-B airfoil was used. The model had a chord of 16", and a span of 36", and different trailing edge configurations were studied. The baseline design of a NACA 63-215 Mod-B has a sharp trailing edge [Szelazek & Hicks 1979]. As with previous work, the thickness changes altered the baseline chord, at least for some cases. In this work, that chord change was addressed and measured. The upstream distance of blending was not discussed. No surface pressure instrumentation was included.

Some of the test cases used trip tape; only tripped boundary layer experiments were presented. Test section conditions varied from Mach numbers of 0.07 to 0.17, corresponding to

Reynolds numbers varying from 6×10^5 to 1.6×10^6 , respectively. Airfoil geometric AoA was varied between -6.2 degrees and 8.8 degrees, with corrected values spanning a shorter range, depending on the experimental setup. These airfoil corrections did not account for airfoil camber. Shear layer corrections for acoustic propagation paths were also employed.

Acoustic measurements were simultaneously acquired from 35 B&K 1/8" microphones placed in the acoustic far field. Two of the microphones were situated so as to perform a COP measurement on the trailing edge of the airfoil, while the other 33 microphones were arranged in a small-aperture array designed for a wide frequency range of operation. Its small size allowed for easy traversing for directivity measurements, but also gave it very poor spatial resolution at lower frequencies of interest. A frequency-dependent per-foot weighting technique was used in an attempt to remove this aperture effect and allow for direct comparison with a COP-based microphone measurement. This technique was described in detail by Mendoza [Mendoza, Brooks & Humphreys 2002]. This weighting was employed along with diagonal removal, where the cross-spectral matrix array diagonal is set to zero to remove the influence of self-noise on microphones, and background noise subtraction, in which the measured acoustic field of an empty test section is subtracted from the airfoil's acoustic field. These will be discussed in more detail in Chapter 4.

With appropriate analysis, it was determined that for most of the frequency range of interest, array-based measurements outperformed the COP method. COP appeared to handle itself better at low frequencies, but its overlap in effectiveness with the SADA measurements was close enough that the second publication was presented using array data only. Sound pressure scaling with Mach number and AoA was presented in addition to directivity analysis.

General agreement was found with the prediction codes provided by Brooks, Pope, and Marcolini, except at high frequencies.

Examples of Additional Notable Work

A body of work involving airfoil self noise was performed in France. Research was conducted at the Laboratoire de Mécanique des Fluides et Acoustique de l'Ecole Centrale de Lyon. This facility (ECL-LMFA) has an anechoic wind tunnel [Roger & Moreau 2004] and has generated some theoretical studies evaluating trailing edge noise models [Roger & Moreau 2005]. Their research involves analysis of wind turbine airfoil profiles at lower, transitional Reynolds numbers [Moreau *et al.* 2003]. Additional experiments have been conducted to validate a modification of existing theoretical formulations [Moreau & Roger 2009].

Aerodynamic characterization was performed using surface pressure transducers. Both mean and fluctuating pressure fields were analyzed [Moreau & Roger 2005]. Detailed analysis was performed on surface pressure fluctuations using techniques from the previous stated works, as well as more spectral coherence processing allowable with modern computing. Acoustic measurements were performed with microphones placed in the far field. The facility background noise was first measured and then subtracted from the microphone measurement of the model. No additional coherence processing was performed to extract noise from the signal.

At Notre Dame, research was conducted involving an airfoil trailing edge similar to that previously used by Blake [Blake & Gershfeld 1988]. The model, a flat strut with a 0.91 m chord, was placed in Notre Dame's Anechoic Wind Tunnel (AWT) [Shannon *et al.* 2005]. A boundary layer trip was applied to the airfoil, which was tested at Reynolds numbers from 1.2×10^6 to 1.9×10^6 . Surface pressure fluctuations were measured near the trailing edge, and far field noise was simultaneously collected with a large aperture array. In a separate closed-walled facility, Particle Image Velocimetry (PIV) was used to characterize the flow field near the model trailing

edge. Observations from the phase-locked PIV measurements and the computed acoustic spectra were qualitatively compared. Noticeable facility-based contamination was observed in some of the beamforming results. Subsequent research focused on applying advanced beamforming techniques to remove the contamination of tunnel background noise in trailing edge measurements [Shannon & Morris 2008].

A significant amount of research has been conducted at NLR in the Netherlands. Some research was targeted at fundamental experimental techniques, involving characterization of sidewall effects on phased array measurements [Oerlemans & Sijtsma 2000]. It was shown that significant measurement errors can occur if sidewalls are made of a sound-hard material. Acoustically-treated sidewalls allow for much closer recovery of true acoustic source levels. Array power measurements have been another point of particular interest.

Some research was focused on simulating an ideal trailing edge to generate a frequency-dependent correction factor for peak array output levels in an attempt to evaluate absolute acoustic levels from the trailing edge noise source [Oerlemans & Sijtsma 2002]. This method was found to be dependent on trailing edge spanwise correlation scales. Subsequent research for generalized aircraft sources applied a simplified integration method where the summed power region is normalized by the array point spread function within the integration region [Oerlemans *et al.* 2007a]. A background subtraction technique, where the integrated power spectrum of the empty test section was subtracted from the integrated power spectrum of the model, was applied. It was shown through simulation and measurement that when sidelobes are within the integration region for the simulated point source, but outside of it for the actual measured source, significant level errors can occur. Coherence reduction, due to the presence of free shear layers in open-jet facilities, was also shown to contribute to underprediction of acoustic levels for larger arrays at

higher test section speeds. This was computed by comparing the array integrated levels to out-of-flow far field microphones placed in the open jet wind tunnel facility.

Additional research studied several airfoils as wind turbine candidates, and compared NACA 0012 data to previous NASA experiments [Oerlemans 2004]. Array measurement integration was conducted with a correction factor for line source behavior based on the sizing of the integration region about the mid-span of the airfoil models. Rough agreement was seen between the NLR and NASA data sets at some frequency bands, but the low frequency data saw significant disagreement. Subsequent research conducted on full-scale wind turbines summed the data in the integration region and divided by the array point spread function [Oerlemans & Sijtsma 2002]. Trailing edge serrations were shown to reduce the trailing edge noise signature.

As mentioned in the introduction, a large number of advanced beamforming techniques have been developed with the intent of improving or supplanting the standard delay-and-sum beamformer. Many of these techniques involve deconvolution, where the array aperture effects, caused by having finite samples within a finite domain of wavenumber space of the acoustic field, corrupt true images and integrated levels of acoustic sources. Most of these methods provide improved spatial resolution at the cost of computation time.

Some research has involved more novel experimental techniques. Spark photography with a schlieren system, which illuminates density gradients in a flow, has been used to study the diffraction effects of a sharp trailing edge under different flow conditions, when an acoustic wave interacts with an airfoil [Heavens 1978]. This research illuminated qualitative behavior of edge scattering with and without flow, but did not provide a method for computing absolute far field levels.

Experimental Body of Work – Summary

The discussed research contains a large variety of installations and measurement techniques. From a facility perspective, both open- and closed-test section wind tunnels have been used. The closed test section tunnels suffer from higher background noise, while the open test section facilities require shear layer corrections be applied in post-processing. Models with and without camber have been evaluated. Those without camber allow for some degree of problem simplification, since at zero angle of attack the boundary layers on the top and bottom of the model should develop near identically. Those with camber are closer to a true flight profile. Similarly, sharpened trailing edges allow for the isolation of either laminar instability noise, or turbulent broadband scattering, depending on the experiment's Reynolds number regime. Models with blunted trailing edges are more realistic in regards to true flight models.

For this body of research, however, the tunnel characteristics and model have already been determined. As discussed in Chapter 4, all experiments are performed in an open-jet wind tunnel facility on a cambered model with a blunted trailing edge. The key parameters of study are the experiment types. When comparing to previous work, many experiment types must be considered.

Acoustically, measurement techniques were sometimes as simple as a single microphone placed in the model's far field. This microphone may or may not have been directional. Pressure measurements suffered from excessive background noise levels. To overcome background noise contamination, two primary paths have been taken. One path involves applying coherence-based modeling to the trailing edge noise source and using multiple microphones to back out a coherent acoustic field. The other involves the opposite assumption of source nature, mainly that the source is composed of a series of incoherent monopoles. This assumption is used to analyze the trailing edge region using beamforming algorithms and

spatially reject noise coming from other sources. Both of these methods apply significant restrictions to the trailing edge noise source. Coherence-based techniques may break down when the acoustic field is actually generated by a collection of semi-coherent or incoherent sources. Beamforming may fail, or at least lead to incorrect level measurements, if there is a group of partially coherent sources, or the sources are not monopole in nature.

The experiments conducted in this body of research must be sufficiently broad as to cover older, single-microphone techniques, as well as modern beamforming techniques, in successive comparison. The overlap of these data with appropriately computed uncertainties will show which methods, if any, appear to provide consistent estimates of trailing edge noise.

CHAPTER 4 EXPERIMENTAL METHODS AND SETUP

The planned experiments are discussed with regard to setup. First, the wind tunnel facility characteristics will be summarized. Details on the NACA 63-215 Mod-B model, fabricated by NASA Langley Research Center (LaRC), will follow. Details will include static aerodynamic behavior of the airfoil in the University of Florida Aeroacoustic Flow Facility. These sections will be followed by a description of the experiments conducted, with previously-acquired sample data shown, demonstrating nominal agreement between the current experimental setup and previous work, as well as framing the experimental techniques to be discussed.

Experimental Facility – UFAFF

The University of Florida Aeroacoustic Flow Facility (UFAFF) is an open-jet, open-circuit wind tunnel located in the MAE-A Building of the University of Florida's Department of Mechanical and Aerospace Engineering. This facility's construction details are discussed in detail in the primary designer's dissertation [Mathew 2006] and were summarized in 2005 [Mathew *et al.* 2005]. The facility was designed for a maximum Mach number of just over 0.2, to simulate approach flight conditions. With this primary constraint in mind, the design objectives were set to leverage the existing ISO 3745 certified 100 Hz anechoic chamber [Jansson *et al.* 2002] while maximizing test section Reynolds number. The upstream portion of the facility was designed to minimize turbulence intensity, such that leading edge noise effects from turbulence ingestion would not contaminate airframe noise studies [Guidati *et al.* 1996]. Downstream sections of the facility were designed to minimize drive-system noise contamination of the test section. Acoustic foam sidewalls, 0.15 m thick S82-N manufactured by Reilly Foam, are installed on the two spanwise boundaries of the test section to constrain the open-jet flow to a quasi-two-dimensional condition. The resulting facility characteristics are

listed in Table 4-1. Figure 4-1 shows a planform view of UFAFF, and Figure 4-2 shows an isometric schematic of an example airfoil isolated in the facility test section. Background noise scaling for the facility (A-Weighted) is shown in Figure 4-3. Additional data in the figure are adapted from previous work [Duell *et al.* 2002].

Airfoil Model

A NACA 63-215 Mod-B airfoil was selected for use in trailing edge studies. This was done to allow direct comparison with modern previous research [Hutcheson & Brooks 2002; Hutcheson & Brooks 2004]. The model, fabricated by NASA Langley Research Center (LaRC), has a chord of 0.737 m, and a wetted span of the full test section, or 1.12 m. The model is composed of a carbon-fiber skin applied to metallic ribs and spars, and is hollow to allow for static pressure tubing, as well as wiring for dynamic pressure transducers. The model's full span is 1.83 m, allowing for future swept wing studies. Three hatches are built into the pressure side of the model, allowing for easy access to pressure ports and dynamic pressure transducer installations. Removable panels near the trailing edge of the model allow for quick-switch access to dynamic pressure transducer arrays. A cross-sectional plot of the airfoil profile is shown in Figure 4-4. A photograph of the model is shown in Figure 4-5. A photograph of the model's underside, installed in UFAFF, is shown in Figure 4-6, with the locations of an access hatch and a trailing edge panel.

As with the model used by Hutcheson and Brooks, the trailing edge of this model is blunted, in this case to 3.3 mm, geometrically matching one of their specific cases. XFOil [Drela 2001] was used to smoothly blend this thickness increase to the maximum-thickness point of the airfoil in the design process, thus subtly altering the overall airfoil shape. The leading-edge shape which differentiates the Mod-B from a baseline 63-215 [Szelazek & Hicks 1979] was unchanged. Coordinates for this modified airfoil shape are given in Table 4-2, and again plotted

in Figure 4-7. The profile coordinates are listed starting at the trailing edge of the model, wrapping around the leading edge (designated as the coordinate system origin) along the pressure side of the airfoil, and then back towards the trailing edge along the suction side. The trailing edge was rounded with fillets on the pressure and suction edges, each with a radius of 1.1 mm. Note that the coordinates provided in Table 4-2 do not account for skin thickness effects in the vicinity of the trailing edge. Some of this thickness issue was taken into account with the coordinate design in X-Foil though additional trailing edge thickening was seen in the quality assurance measurements, as shown in Figure 4-7 and addressed here.

Quality assurance measurements of the model were required before any experiments could be conducted, so in any analysis the true shape of the airfoil would be known, and not just the design profile. This QA was done at NASA LaRC using a coordinate measurement machine (CMM). The airfoil coordinates were mapped at 25%, 50% and 75% span. The locations of all pressure taps were also validated. To properly assess the measured profiles with respect to the design profile, a MATLAB function was written which imported all the measured and design coordinates, performed a least-squares comparison to account for any coordinate-system offsets and rotations, and then calculated local normal differences between the measurement and design coordinates. This code is presented in Appendix A. Figure 4-7 plots both the design and measured coordinates in overlay, and the surface-normal error from design. The peak absolute error was 0.16% chord and the RMS error was between 0.06% and 0.07% chord, depending on span wise chord profile location. Trailing edge deviation from design was also examined. The trailing edge is plotted for different spanwise locations in Figure 4-8. Here, 0% span would be the right side of the model when the observer is upstream of the model, facing downstream. Finally, the code performed a curve fit to the offset profiles and added the resulting smooth

polynomials, one for suction-side and one for pressure-side as plotted side-by-side in Figure 4-9, back onto the original design coordinates. This provided an “effective” airfoil shape for use in codes such as X-Foil and/or FLUENT, to assess any flow differences which may arise from the model surface error. Figure 4-10 shows the X-Foil prediction for both cases at zero angle of attack and Reynolds number of 3.0×10^6 . The data show that manufacturing deviations from the design have a minimal impact on steady aerodynamic behavior. Similarly, little impact on the overall acoustic field is expected from such deviation, but it is recorded nonetheless to allow for accurate future comparison.

Model Performance

Flow behavior around the airfoil in the facility in which acoustic measurements are performed must also be determined, to provide a complete database for the aeroacoustic dataset. As facility-to-facility differences can lead to significantly different flow behavior around identical models, having a measurement set of flow behavior is necessary for any future comparisons of datasets.

Steady Pressure Behavior

The mean flow behavior around the model can be easily evaluated by utilizing the pressure taps built into the airfoil’s surface. The airfoil has three chordwise sets of pressure taps installed at 25%, 50% and 75% span locations, to allow for mapping of the streamwise pressure distribution along the airfoil surface. The distribution of taps along the chordwise profiles was designed using an optimization routine to estimate the lift and pressure drag correctly with 47 pressure taps around the airfoil, designed by Cesar Moreno. For this model, 23 taps were allocated to the suction side, 23 to the pressure side, and one at the leading edge stagnation point. Lift simulations were conducted in X-Foil. The final design has identical tap distributions on the suction and pressure sides of the model. Tap locations are given in Table 4-3. All three

chordwise profile sets are measured to check for spanwise flow uniformity. The model also has spanwise rows of taps installed near its trailing edge on both the suction and pressure side of the airfoil. These will not be utilized in this experiment set, and will be leveraged in future work regarding quasi-three-dimensional sweep effects.

Each tap consists of a 0.028” ID metal tube connected to 0.040” ID urethane tubing. The narrow tubing was selected to minimize spatial variations in pressure across the tap hole. While this increases the time constant of the tubing and slows its response to pressure changes, it improves measurement resolution under primary experiment conditions of interest where the test section speed is constant and a large number of averages are taken.

Data were acquired using three PSI Netscanner Pressure Scanners (Model 9116). One Netscanner has a range of 10” H2O differential, while the other two have 1 PSI differential ranges. All models are accurate to 0.05% full scale. These were connected to a computer running the LabVIEW desktop environment, and data were sampled for each spanwise chord set of taps. Typically, about 500 samples were collected over 20 seconds. Uncertainty values of each tap measurement were calculated, and plotted with the pressure coefficient (C_p) distributions.

$$C_p = \frac{p - p_\infty}{\frac{1}{2} \rho U_\infty^2} \quad (4-1)$$

Equation (4-1) is valid for incompressible flow cases. All of the experiments conducted in UFADF for this research satisfy the incompressible flow assumption. In this definition of pressure coefficient, ρ is the fluid density, U_∞ is the test section velocity upstream of the airfoil, p_∞ is the test section static pressure upstream of the model, and p is the local mean surface

pressure at the tap. Dynamic pressure, the total denominator term, was measured using a pitot-static tube, by using the incompressible flow based identity given in Equation (4-2).

$$\frac{1}{2} \rho U_{\infty}^2 = p_0 - p_{\infty} \quad (4-2)$$

Here, p_0 is the flow stagnation pressure, measured by the stagnation port of the pitot probe. The static ports, similarly, measure p_{∞} . The two ports are connected to a single differential pressure transducer. The numerator in the pressure coefficient calculation was measured by connecting pressure taps to the modules, and then using a common reference pressure of the chamber static pressure for the differential measurement. Density for the test section speed computation was calculated from a local weather station's values of pressure and temperature.

Pressure distribution deviation from X-Foil prediction was expected due to open-jet wind tunnel effects, as discussed by Brooks and Marcolini [Brooks & Marcolini 1984]. Further deviation from their prediction method was also expected, due to the presence of a jet collector at the rear of the test section. An inviscid solver method which addresses both the open-jet and collector effects on model distribution has yet to be used to analyze airfoil behavior in UFAFF. Some preliminary viscous, turbulent CFD analysis of the test section has been conducted using FLUENT, but this proved to be too cumbersome for experiment planning and design.

For baseline mean aerodynamic comparison, the model was installed in the chamber and swept through a range of geometric AoAs from -7.5° to 10° , in 2.5° increments. The tunnel test section flow speed was set to 31 m/s, leading to a chord Reynolds number of 1.5×10^6 . Lift values were computed through pressure distribution integration, and substituted into X-Foil to calculate an equivalent-lift freestream AoA. Figure 4-11 through Figure 4-18 show the data for varying AoAs, compared to the prediction for an equivalent-lift freestream AoA. 95% confidence interval bars are plotted for the experimental data.

The geometric AoA vs. equivalent-lift AoA of the model is plotted in Figure 4-19. A linear regression curve is drawn through the data, generating the relation given in Equation (4-3), which has an R^2 value of 0.993.

$$\theta_{Equiv} = 0.229\theta_{Geom} - 1.37^\circ \quad (4-3)$$

Based on these measurements, it was determined that there would be much difficulty attempting to match any high-lift configurations for the airfoil model. As such, experiments were limited to -1.5° , 0° and 1.5° AoAs. The spanwise uniformity of flow about the model is demonstrated in Figure 4-20.

Unsteady Surface Pressures

An array of unsteady pressure transducers was designed and built for insertion into the trailing edge region of the UF NACA 63-215 Mod-B airfoil. Unsteady pressure measurements are of interest for comparison with previous work by many authors [Blake & Gershfeld 1988; Brooks & Hodgson 1981; Yu & Tam 1978]. The surface pressure data allow for detailed analysis of the surface pressure fluctuation structure in the vicinity of the trailing edge, evaluating such quantities as correlation length and time scales for the streamwise and spanwise directions. These measurements can also be correlated with far-field microphone measurements when the tunnel is configured for acoustic data acquisition, as well as hotwire measurements when the tunnel is configured for flow data acquisition. This correlation data, as well as the unsteady surface pressure spectra, can be used in aforementioned works [Amiet 1976; Howe 1978] for the prediction of the radiated acoustic field. While the analysis of unsteady pressure data in relation to far field acoustic data is beyond the scope of this present study, the data are acquired in conjunction with the present acoustic data for future work. As such, the airfoil's unsteady pressure measurement capability is presented here for completeness.

The trailing edge arrays consist of 14 Kulite LQ-125-5A unsteady pressure transducers. These sensors have a nominal diaphragm diameter of 0.125", an overall sensor head diameter of 0.16", and are tuned for a 5 psi pressure fluctuation range. The predicted boundary layer pressure fluctuations of 10% freestream dynamic pressure fall well within this range. Freestream dynamic pressure is simply calculated as the denominator of Equation (4-1). Unfortunately, the lack of space available in the trailing edge region of the model prevents the use of a reference pressure line. As such, the transducer selection necessitated using an absolute transducer instead of differential. Absolute transducers have a stiffer diaphragm, increasing minimum detectible pressure (MDP) fluctuations. The rated natural frequency is 150 kHz.

Each transducer is installed from the backside of the airfoil surface. The face of the transducer is seated in a cavity, which is connected to the surface of the airfoil through a pinhole opening.

The pinhole has a nominal length l of 0.01" and an area of $S = \pi(0.01")^2$. The cavity has a depth of 0.01", and diameter of 0.13", which translates to a volume V . These dimensions were used to estimate the Helmholtz resonant frequency of the cavity as approximately 16 kHz for standard atmospheric conditions.

$$f = \frac{1}{2\pi} \sqrt{\frac{c^2 S}{Vl}} \quad (4-4)$$

In Equation (4-4), c is the isentropic speed of sound.

The transducers are arranged in two 7-element L-shaped arrays. One array is located on the suction surface of the airfoil, and the other on the trailing edge. A layout of the suction side array panel is shown in Figure 4-21, where the panel boundaries are the solid black lines. The pressure side array is a mirror image of the suction side array. The spanwise line of the array is

located approximately 0.64" from the start of the fillet of the rounded trailing edge. The chordwise line of the array is located 3.84" from 50% span of the airfoil. This offset necessary due to the center-span chord profile of pressure taps. The center-to-center spacing of the transducers at their densest-spaced location, the part closest to 50% span and closest to the trailing edge, is the minimum possible spacing of 0.16". The next sensors in each direction are located 0.32" away from their neighbors, and those after them 0.64" away. This array design leads to a non-redundant population of sensor spacings, maximizing the number of spatial lags available in a cross-correlation comparison. The spacings in each direction are 0.16", 0.32", 0.48", 0.64", 0.96", and 1.12". A plot of these spacings is shown in Figure 4-22. Essentially, these spacings, or lag distances, are the available cross-correlation spacings for computing turbulent spatial correlation scales in a homogeneous turbulence field, without making the Taylor frozen-field hypothesis [Tennekes & Lumley 1972]. In other words, the cross-correlation of the turbulence as a function of space is only available at discrete lag vectors. These discrete coordinates are the data points plotted in the figure.

A signal-conditioning board is necessary for use with the Kulite sensors, to provide appropriate power and amplification. This board is located outside of the airfoil model. For minimum additional noise, the wires from the Kulites are run through a grounded shielding tube before exiting the model. Additionally, a three-axis PCB accelerometer was mounted inside the model near the trailing edge Kulites, for future analysis of any vibrational coupling into surface pressure fluctuations. Note that only the component normal to the surface of the model was measured, due to data acquisition system channel count considerations.

A National Instruments PXI-1045 chassis is used for all dynamic data acquisition (DAQ). The first slot of the chassis is dedicated to a MXI-4 card, which is connected via a fiber-optic

cable to a workstation running LabVIEW. The remaining card slots in the chassis contain NI PXI-4462 DAQ cards, for a total of 68 channels. Each channel has 24-bit resolution with 118 dB effective dynamic range. The maximum sampling rate available per-channel is 204,800 samples per second. All measurements of linear instrumentation, such as surface pressure transducers and microphones, are ac coupled with a -3 dB cut-on of 3.4 Hz. Nonlinear measurement schemes such as hotwire data acquisition are not ac coupled. The DAQ cards automatically select the appropriate anti-aliasing filter characteristics for the operation of their sigma-delta A/D converters.

Hotwire Anemometry

Constant-temperature hotwire anemometry (CTA) was selected for in-flow velocity measurements in the vicinity of the trailing edge. While the technique suffers from directional ambiguity for single-wire probes, it provides high spatial and temporal resolution. The resulting mean and fluctuating velocity data can be used in conjunction with steady and/or unsteady pressure measurements to characterize the model behavior in a given facility, and allow for cross-facility comparison of results.

A hotwire works on the principle of forced convection, using a heat transfer model to determine flow velocity. For constant-temperature anemometry, a closed-loop controller is used to hold the wire at a constant resistance, and thus a constant temperature T_w [Bruun 1995].

$$Q = (T_w - T_0)(A + BU^n) \quad (4-5)$$

Equation (4-5), known as King's Law, relates the total heat flux, Q , to the difference in temperature between the hotwire and the flow, $T_w - T_0$, and the local flow velocity normal to the axis of the wire, nominally the local streamwise flow speed U in a shear flow. A , B and n are calibration constants. By assuming that heat flux is related to the square of bridge voltage E , a

directly measureable quantity, a calibration relation can be constructed, as shown in Equation (4-6).

$$\frac{E^2}{(T_w - T_0)} = A + BU^n \quad (4-6)$$

A Dantec 55P15 boundary layer hotwire probe is attached to a 55H21 probe holder, connected to a 90N10 streamline CTA controller frame. The probe holder is enclosed in a NACA 0012 airfoil extrusion with a 4" chord, to minimize vibration and probe arm drag for center-test-section measurements. This airfoil extrusion is connected to a traverse above the wind tunnel test section. A 2-axis Velmex stepper traverse was used for vertical and axial movement of probes. A schematic of a single-wire installation with the 2-axis traverse is shown in Figure 4-23. Photographs of a similar installation in UFAFF featuring a DU 96-W-180 airfoil are shown in Figure 4-24 and Figure 4-25 from below and above the model, respectively.

The hotwire system is calibrated in the tunnel free stream using a pitot-static probe. Calibration is conducted relative to a Heise HQS -1 0-15" H₂O module installed in an ST-2H chassis. Both the pitot-static probe and the hotwire anemometer are placed in the core flow of the wind tunnel test section, and the wind tunnel operated at many discrete test section velocities. Test section fluid temperature is also measured using a Heise system. Wire temperature is output from the hotwire bridge controller, and dc-coupled voltage fluctuations are measured using a PXI-4462 card. These data are fit to Equation (4-6) using a least-squares method in MATLAB, to determine the appropriate calibration constants. For preliminary hotwire measurements, the DAQ system was set to acquire data at a rate of 32,768 samples per second. The range was set for zero to five volts. An example calibration curve is given in Figure 4-26. The coefficients determined through the least-squares fit can then be used, in conjunction with the mean temperature and fluctuating voltage measurements, to determine the fluctuating velocity

magnitude observed by the wire. It should be noted that the effective sensitivity of the hotwire is driven by the temperature difference between the ambient fluid and the wire, so operating at a large temperature difference is preferable. In these cases the wire temperature was approximately 1.8 times the absolute mean temperature of the fluid.

A single hotwire boundary layer survey was conducted at the centerline of the trailing edge of the NACA 63-215 mod-B model, for a Mach number of $M = 0.17$. This was done right off of the beginning of the trailing edge fillet of the model. The steady and fluctuating components of the measurement were separated and evaluated. The survey was conducted by bringing the hotwire to just off the surface of the airfoil (< 0.001 m), and traversing upwards towards the freestream. The mean and fluctuating profiles for the trailing edge boundary layer are shown in Figure 4-27. The coordinate system shown is not wall-normal, but the trailing edge angle at the rear end of the airfoil is very small, so the plot should approximately match a wall-normal profile.

This experiment was repeated just behind the airfoil (< 0.001 m behind the trailing edge), and the full wake profile was measured. Results are shown in Figure 4-28. Comparing the two profiles reveals potential wake thinning as the shear layer leaves the trailing edge of the airfoil. Integral parameters for the boundary layer profile were computed using a least-squares fit to Musker's boundary layer velocity profile [Musker 1979], as at the time of measurement probe vibration was such that the near-wall region of the boundary layer could not be measured. The boundary layer thickness δ was estimated with this method to be 0.018 m, with a displacement thickness δ^* of 0.0036 m and a momentum thickness θ of 0.0024, leading to a shape factor of 1.5. As an aside, since the data were collected a new traversing system and hotwire installation hardware were purchased for use in the facility to reduce this vibration problem.

Acoustic Measurements

To determine the acoustic character of an airfoil, far-field microphone measurements must also be performed. Unfortunately, the noise source of interest in this case, the airfoil's trailing edge, is only one of many sources a single microphone may measure. A brief, non-comprehensive list of other potential contributors to a single microphone is presented.

- Leading edge noise
- Edge noise from the lip of the front of the test section
- Shear layer noise
- Shear layer-collector interaction noise from the rear of the test section
- Scrubbing noise from the test section acoustic walls
- Noise from unsteady model-wall interactions
- Local hydrodynamic pressure fluctuations over the microphone face
- Electronic noise

Due to the potential presence of all these contaminants, multiple microphone measurements must be made within a single experiment set. The data from these microphones can be processed in numerous ways. Both coherence-based techniques and basic array techniques will be considered.

Coherence-Based Techniques

Coherence-based techniques make few assumptions on the nature of the source, aside from the linearity of signal behavior between one or multiple sources. However, implicit within the use of such techniques is the assumption that there is either a single, dominant, coherent source; or that the multiple coherent, incoherent or partially coherent sources generating the measured field can be spatially lumped relative to the measurement domain. In essence, this means that the characteristic source dimensions are significantly smaller than the length scales of the measurement. A schematic of this situation showing a line source which would meet this criterion is given in Figure 4-29, where the length scale of the source, l , is much smaller than the distance D from the source to the observers, shown as microphones. The consequences of this

assumption are discussed in more detail in Appendix C. Coherence-based techniques rely primarily on statistical analysis and averaging to remove any noise sources which are incoherent between multiple measurement microphones, and focus on a coherent field which may be generated by multiple coherent or incoherent sources. Such techniques should be very effective at removing line noise and local hydrodynamic contamination, but will have difficulty separating the effects of multiple acoustic sources which are correlated and common to all microphones.

Coherent output power

The simplest coherence technique to utilize involves a two-microphone measurement. This technique has been used extensively in previous research [Brooks & Hodgson 1981; Hutcheson & Brooks 2002]. While the technique can be used in conjunction with a dipole source model for trailing edge noise, as demonstrated by Hutcheson and Brooks, the basic coherent power method can be derived without one.

To start, some simple spectral relations will be defined [Bendat & Piersol 2000].

$$G_{yy}(f) = 2 \lim_{T \rightarrow \infty} \frac{1}{T} E [Y_k^*(f, T) Y_k(f, T)] \quad (4-7)$$

$$G_{xy}(f) = 2 \lim_{T \rightarrow \infty} \frac{1}{T} E [X_k^*(f, T) Y_k(f, T)] \quad (4-8)$$

$$\gamma_{xy}^2(f) = \frac{|G_{xy}(f)|^2}{G_{xx}(f)G_{yy}(f)} = \frac{G_{xy}^*(f)G_{xy}(f)}{G_{xx}(f)G_{yy}(f)} \quad (4-9)$$

Equation (4-7) defines the one-sided autospectral density function of a signal. Here, Y is the Fourier Transform of a block of acquired time series y . Y^* is the complex conjugate of the original transformed signal, T is the length of the data block in units of time, k is the individual block number, and f is the frequency of interest. This equation is valid for all frequencies aside from the zero-frequency and Nyquist frequency. For those data points, the coefficient of 2

becomes unity. Equation (4-8) defines the cross spectral density of a pair of signals, which gives a relationship between signals x and y . This relationship is normalized to a zero-to-unity coefficient in Equation (4-9), where γ^2 is defined as the ordinary coherence function relating signals x and y . Note that for subsequent equations, frequency dependence is implied but not stated.

Figure 4-30 shows a Single-Input/Two-Output (SITO) system. Here, X is the source, and is treated as unmeasurable. U is the source signal after it has propagated from the source to a microphone, and is considered the signal of interest. N is uncorrelated measurement noise, either due to electronic line noise, or a physical mechanism exciting a sensor. Y is the sensor output. Equations (4-10) through (4-13) provide the mathematical identities associated with a SITO system.

$$Y_i = H_i X + N_i = U_i + N_i, i = 1, 2 \quad (4-10)$$

$$G_{y_i y_i} = |H_i|^2 G_{xx} + G_{n_i n_i} = H_i^* H_i G_{xx} + G_{n_i n_i} = G_{u_i u_i} + G_{n_i n_i} \quad (4-11)$$

$$G_{y_1 y_2} = G_{u_1 u_2} \quad (4-12)$$

$$\gamma_{u_1 u_2}^2 = \frac{|G_{u_1 u_2}|^2}{G_{u_1 u_1} G_{u_2 u_2}} = \frac{H_1^* H_2 G_{xx} H_1 H_2^* G_{xx}}{H_1^* H_1 G_{xx} H_2^* H_2 G_{xx}} = 1 \quad (4-13)$$

By assuming that the noise terms N_i between the two channels are perfectly incoherent, the cross-spectrum of the measurement collapses to the autospectrum of the source passing through two unique transfer functions, as shown in Equation (4-12). This allows for the definition of the source coherence between the two channels as unity in Equation (4-13). This can be leveraged to define the Coherent Output Power (COP) for a given channel in Equation (4-14).

$$COP_1 = \gamma_{y_1 y_2}^2 G_{y_1 y_1} = \frac{|G_{y_1 y_2}|^2}{G_{y_2 y_2}} = \frac{|G_{u_1 u_2}|^2}{G_{u_2 u_2} + G_{n_2 n_2}} = \frac{|G_{u_1 u_2}|^2 / G_{u_2 u_2}}{1 + G_{n_2 n_2} / G_{u_2 u_2}} = \frac{|H_1|^2 G_{xx}}{1 + 1/SNR_2} = \frac{G_{u_1 u_1}}{1 + 1/SNR_2} \quad (4-14)$$

Here, it is shown that the Coherent Output Power at microphone 1 is proportional to the coherent source strength measured by the channel, but is biased low by the signal-to-noise ratio (SNR) of the second microphone. A similar equation can be constructed for microphone 2. Thus, if both microphones have significant noise contamination, the Coherent Output Power method will underpredict the true source levels at each microphone [Bahr *et al.* 2008].

If the two microphones are placed at equal but opposite locations above and below a trailing edge, then some additional simplifications can be made [Brooks & Hodgson 1981]. The transfer function for the trailing edge noise propagation can be treated as having a distance-based attenuation factor and a distance-based time lag, of the form shown in Equation (4-15). Here the sign of the pi term in the phase angle is dependent on whether the microphone is referenced as located above or below the model trailing edge.

$$H_i = H(r_i) e^{-j(\pm\pi/2 + kr_i)} \quad (4-15)$$

For two microphones placed at equal and opposite sides of a trailing edge, then Equation (4-16) holds.

$$\begin{aligned} G_{y_1 y_2} &= \frac{2}{T} E \left[(H_1 X + N_1)^* (H_2 X + N_2) \right] \\ G_{y_1 y_2} &= \frac{2}{T} E \left[H_1^* H_2 X^* X + H_1^* X^* N_2 + H_2 X N_1^* + N_1^* N_2 \right] \\ G_{y_1 y_2} &= \frac{2}{T} H_1^* H_2 E \left[X^* X \right] + \frac{2}{T} H_1^* E \left[X^* N_2 \right] + \frac{2}{T} H_2 E \left[X N_1^* \right] + \frac{2}{T} E \left[N_1^* N_2 \right] \\ G_{y_1 y_2} &= H_1^* H_2 G_{xx} = H(r_m) e^{j(\pi/2 + kr_m)} H(r_m) e^{-j(-\pi/2 + kr_m)} = |H(r_m)|^2 G_{xx} e^{j\pi} \end{aligned} \quad (4-16)$$

Therefore, if the true trailing edge noise signal is simply considered to be the magnitude of the source signal at a given distance from the trailing edge, then Equation (4-17) provides a direct solution.

$$\left|G_{y_1 y_2}\right| = \left|H\left(r_m\right)\right|^2 G_{xx} = G_{u_1 u_1} = G_{u_2 u_2} \quad (4-17)$$

This formulation ideally provides a noiseless estimate of trailing edge noise without bias, but, unlike the generalized coherent output power previously defined, is sensitive to any positional uncertainties in microphone placement, and requires a shear layer correction to account for refraction effects on the signal propagation path. Note that if the shear layer corrections are identical for the upper and lower microphones, e.g. if open-jet test section flow about the model was behaving in a symmetric manner due to negligible lift, then the shear layer correction will cancel between the two microphones.

The first acoustic measurements performed on the UF NACA 63-215 Mod-B involved a coherent power analysis. For these experiments, a pair of Brüel & Kjær Model 4939-A-011 ¼” microphones with Type 2670 preamplifiers and a Type 2829 power supply was used. These were connected to a PXI-4462 DAQ board, and installed in the facility at opposing sides of the model trailing edge, as shown in Figure 4-31. Note that the displayed coordinate system is that used for constructing trailing edge noise directivity plots, and is similar to that shown in previous chapters, Figure 2-1, as the upper or lower side of the model in the previous discussion was arbitrary. This coordinate system, however, is different from the one used in beamforming analysis. The microphones were covered with foam windscreens to reduce local hydrodynamic pressure fluctuations, and calibrated with a B&K Pistonphone Type 4228 at a single frequency. It was assumed that, given the measurement bandwidth of the microphones used (~100 kHz) the instrumentation would have near-flat magnitude and phase response for the majority of the

measured acoustic bandwidth (10 kHz), so only a single-tone calibration was necessary. Data were acquired at 65,536 samples per second. Spectral blocks were 4096 points long, resulting in 16 Hz binwidth FFTs, with 3000 blocks collected and averaged. Results were compared to a data set provided by Dr. F. V. Hutcheson of NASA LaRC. Dr. Hutcheson kindly provided the cross-spectral matrix (CSM) for a data set most closely matching UF's trailing edge configuration, operated at a -1.2° AoA and a Mach number of 0.17. The UF data were collected using a 0° AoA at a Mach number of 0.17. The comparison, plotted in Figure 4-32, shows agreement for frequencies with moderate coherence, shown in Figure 4-33. Note the slight offset in peak location is due to a small difference in trailing edge thicknesses t between models, as Figure 4-8 shows the UF model's trailing edge is slightly undersized from design. This can be accounted for as approximately a 10% difference, and the data collapse with thickness-based Strouhal scaling, shown in Figure 4-34. Level comparisons are also approximate, as the NASA data binwidth is 17.45 Hz. No shear layer corrections have been applied to this data.

Of key interest in this comparison is the phase relationship between the two microphones. In an ideal measurement, the coherent output power method should see a phase offset of π radians from the first microphone to the second. If the microphones are not quite equally spaced, there should be a linear phase shift as a function of frequency, as shown above in the cross-spectral magnitude formulation. The cross-channel phase relationship between the first and second microphones in the UF and NASA data set is plotted in Figure 4-35. As shown here, there is a linear phase relationship between the two microphones in both cases below 5 kHz, indicating that the source assumptions may be correct at these frequencies. However, above 5 kHz there is a total breakdown of the phase relationship, corresponding to the previously seen breakdown in coherence. This appears to be indicative that either the trailing edge noise source

is not strong above this frequency, or the nature of the contaminating noise is such that the coherent power method cannot separate it from the trailing edge noise source.

All experiments for this body of work were organized such that a coherent output power solution could be calculated as a reference value while other data were collected. The aeroacoustic array plate used, discussed subsequently, was designed such that a B&K 4138 1/8” pressure field microphone could be installed at the array center for comparison between array output and direct microphone measurement. A second microphone, a G.R.A.S. 1/4” 40BE, was present on the opposing side of the airfoil for reference, along with several other microphones. Both microphones were placed a nominal 1 m distance from the trailing edge of the array. A schematic of this setup is shown in Figure 4-36. For comparison, experiments were repeated with a 1/4” B&K 4939 free field microphone in place of the array plate, located where the 4138 microphone was located when the plate was present, as shown in Figure 4-37. A third configuration involved offsetting the phased array downstream of the airfoil by 0.25 m, as shown in Figure 4-38. For all of these experiments, 30 seconds of data were acquired continuously at 102,400 samples per second to allow for maximum flexibility in post-processing. All time series data were stored as 32-bit floating point binary files (little-endian).

Uncertainty calculations with this method are straightforward. Both are available from Bendat & Piersol [Bendat & Piersol 2000]. For the generalized coherent output power, the normalized standard deviation is given by Equation (4-18).

$$\varepsilon[COP_1] = \frac{\sqrt{\text{var}[\hat{G}_w]}}{G_w} = \frac{\sqrt{2 - \gamma_{y_1 y_2}^2}}{|\gamma_{y_1 y_2}| \sqrt{n_d}} \quad (4-18)$$

Here, n_d is the effective number of spectral block averages. This is computed by finding the total number of spectral averages from overlap analysis and correcting for the selected window

function, as computed from Equation (4-19), where N_{blocks} is the total number of non-overlapped blocks available, r is the overlap fraction, here 0.75, and 0.52 is a data-dependency correction factor computed for a hanning window at 75% overlap [Cattafesta 2010].

$$n_d = 0.52 \text{ floor} \left(1 + \frac{N_{blocks} - 1}{1 - r} \right) \quad (4-19)$$

Note that while the true probability density function follows a Chi-squared distribution, for a large number of degrees of freedom (spectral block averages in this case) this converges to a Gaussian function and computing a 95% confidence interval is thus straightforward. For the case with modeled, ideal microphone locations, the normalized standard deviation is given by Equation (4-20). For coherent power methods, bias error in the narrowband spectral estimates will not be considered, but should be negligible for these situations based on scaling [Bendat & Piersol 2000].

$$\varepsilon \left[\left| G_{y_1 y_2} \right| \right] = \frac{1}{\sqrt{n_d \gamma_{y_1 y_2}^2}} \quad (4-20)$$

Three-microphone method

The SITO system developed in the previous section can be extended to a generalized Single-Input/Multiple-Output system with a minimum of three-microphones. The solution for this three-microphone system is developed and cast into a readily solvable set of equations [Bendat & Piersol 2000].

$$\begin{aligned}
G_{u_1u_1} &= \frac{|G_{y_1y_2}| |G_{y_1y_3}|}{|G_{y_2y_3}|} \\
G_{u_2u_2} &= \frac{|G_{y_1y_2}| |G_{y_2y_3}|}{|G_{y_1y_3}|} \\
G_{u_3u_3} &= \frac{|G_{y_1y_3}| |G_{y_2y_3}|}{|G_{y_1y_2}|}
\end{aligned} \tag{4-21}$$

Equation Set (4-21) provides a basic statement of the results, but suffers dramatically when the cross-spectral magnitude in the denominator of an equation is small. This formulation is recast into a more stable solution in the first part of Appendix B, where positive power for the predictions is enforced. This is summarized starting with Equation (4-22) and continuing through Equation (4-24).

$$G_{y_iy_i} = G_{u_iu_i} + G_{n_in_i} = G_{u_iu_i} \left(1 + \frac{1}{SNR_i} \right), i = 1, 2, 3 \tag{4-22}$$

$$\begin{aligned}
\frac{1}{SNR_1} &= \left| \sqrt{\frac{\gamma_{y_2y_3}^2}{\gamma_{y_1y_2}^2 \gamma_{y_1y_3}^2}} - 1 \right| \\
\frac{1}{SNR_2} &= \left| \sqrt{\frac{\gamma_{y_1y_3}^2}{\gamma_{y_1y_2}^2 \gamma_{y_2y_3}^2}} - 1 \right| \\
\frac{1}{SNR_3} &= \left| \sqrt{\frac{\gamma_{y_1y_2}^2}{\gamma_{y_1y_3}^2 \gamma_{y_2y_3}^2}} - 1 \right|
\end{aligned} \tag{4-23}$$

$$G_{u_iu_i} = \frac{G_{y_iy_i}}{\left(1 + \frac{1}{SNR_i} \right)}, i = 1, 2, 3 \tag{4-24}$$

The three-microphone method has the advantage of completely removing incoherent noise contamination, regardless of differences in modeled propagation paths between the different channels, as was required for the coherent output power method, although the source must still be spatially lumped. This is done by modeling each channel's observed noise in addition to the

desired signal, as shown in Equation (4-23) where the signal-to-noise ratios, SNR , are evaluated. As with all other coherence-based techniques, the method may have difficulties resolving true physical noise sources when the sources become spatially distributed with partial coherence, as is so often the case in real measurements. This is addressed in more detail in Appendix C.

The three-microphone method can be applied when more than three-microphones are present in a measurement setup by selecting subsets of microphone triads. However, ambiguities exist regarding which microphone combinations provide the “best” results. This is pertinent to trailing edge noise in that a skewed local prediction of acoustic levels may lead to erroneous directivity results, in addition to providing false overall sound pressure level information. One approach, discussed in Appendix B, involves building a statistical table of all possible three-microphone predictions. An alternative is to move to a technique which uses more than three-microphones in each individual solution.

As discussed in Appendix B, the number of equations quickly outpaces the number of unknowns when more than three-microphones are used in a single solution, as the number of unknowns scales linearly with the number of microphones while the number of equations scales quadratically. This scaling is shown in Table B-1 with both formulae and examples. One method for dealing with this is a least-squares solution [Bahr *et al.* 2008]. This method performs a minimization fit for signal and noise estimates of each channel. This is done by re-scaling Equations (4-11) and (4-13), while leveraging Equation (4-12). The resulting functions for minimization are given in Equations (4-25) and (4-26), where v is used in place of u .

$$e_{1i} = \frac{G_{y_i y_i}}{G_{v_i v_i} + G_{n_i n_i}} - 1 \quad (4-25)$$

$$e_{2ij} = \frac{|G_{y_i y_j}|^2}{G_{v_i v_i} G_{v_j v_j}} - 1 \quad (4-26)$$

While preliminary results using this technique are included, the computation cost is sufficiently high that it will not be applied to the main body of this research. As a by-product of this work, more efficient techniques have been conceived using covariance-based approaches based upon a single source assumption [Du *et al.* 2010]. The first of these methods minimizes the Frobenius Norm of the difference between the cross-spectral matrix (CSM) of the microphone signals and the modeled signal and noise matrices. The second method leverages the Rank-1 behavior of the signal matrix to model the difference between the CSM and the noise data as Rank-1. The third method, a Maximum Likelihood method, assumes independent and identically distributed random Gaussian processes and minimizes a log-likelihood function. These codes are applied to the data collected in this body of research.

Preliminary experiments involving the three-microphone method and least-squares method were conducted using a line array of microphones in UFAFF. A schematic of this installation is shown in Figure 4-39. These runs used a single Brüel & Kjær Type 4939 ¼ inch microphone located at -90° from the trailing edge of the airfoil, opposite an 11-element linear array composed of Panasonic WM-61A omnidirectional electret microphones. Note that the microphones are powered from the PXI-4462 cards through a constant-current 4 mA output. As shown, the linear array was placed 1.13 m below the model chord line, with microphone 5 located directly below the model trailing edge at 90°. The array element spacing was 0.178 m, covering the physical angles between 58° and 133°. This setup was subsequently inverted, and directivity measurements were also conducted on the suction side of the airfoil. During the preliminary experiment phase, the electret microphones were calibrated in a plane-wave tube referenced to a

B&K 4939 microphone up to 6 kHz. While this calibration did not cover their remaining bandwidth of interest, 6 kHz to 20 kHz as audio microphones, the calibration does cover the frequency range where trailing edge noise is observed to be dominant, below 5 kHz.

Linear array measurements were collected as contiguous time series for each channel. The sampling rate was set to 32,768 samples per second, and 30 seconds of data were collected for each channel. For spectral estimation, block lengths were designated as 2048 samples, resulting in a 16 Hz narrowband bin width. The data blocks were processed with 75% overlap and a Hanning window, resulting in 996 effective averages and 3.2% normalized autospectral random uncertainty.

In these preliminary experiments, the methods were applied to linear array measurements to estimate the trailing-edge noise source directivity pattern, after application of a shear layer correction to compute the correct source-microphone angle relation [Amiet 1978a; Sanford 2008]. Table 4-4 lists the geometric microphone installation angles relative to the trailing edge downstream ray, and their corresponding corrected angles in a freestream of infinite extent with Mach number M . For the computation, the shear layer was located 0.42 m from the microphones, with a test section Mach number of 0.17. The spectra, processed with varying techniques, were integrated, normalized by the corrected 90° measurement, converted to (unweighted) overall levels (dB), and compared to Howe's solution [Howe 1978]. Normalization divides Equation (2-21) by all terms held constant in the experimental set, leaving the directivity function given in Equation (4-27).

$$\frac{\overline{p^2}}{p_{90\text{deg}}^2}, dB = 10 \log_{10} \left(\frac{2 \sin^2 \theta_r / 2}{(1 + M \cos \theta_r)^3 [1 + (M - M_V) \cos \theta_r]^2} \right) \quad (4-27)$$

Here, θ_r is the shear layer corrected angle and M_V is the eddy convection Mach number, assumed to be approximately 60% of the mean-flow Mach number [Brooks & Hodgson 1981].

The spectral integration is performed using the scaling provided by Blake [Blake 1986] for the appropriate cut-on frequencies of trailing edge noise. The lower bounds of the overall sound pressure level integration of each microphone's power spectral density can be established using the trailing edge boundary layer thickness via Equation (4-28).

$$\frac{\omega\delta}{U_\infty} \geq 0.6 \quad (4-28)$$

This gives the lowest frequency of interest for trailing edge noise, while the upper bounds are dictated by the facility background noise. Equation (4-28) gives a characteristic frequency estimate from a boundary layer parameter such that fluctuations of wavelength on the order of or larger than the boundary layer thickness in length scale will not be noticeably scattered from the trailing edge. This is actually only one of three presented by Blake, the others being stated in Equations (4-29) and (4-30). These two are an airfoil compactness statement based on the airfoil chord C and an argument of leading edge independence from trailing edge noise radiation. The leading edge independence condition is computed to be approximately 250 Hz for $M = 0.17$. Of The boundary layer condition is approximately 310 Hz, while the compactness condition is about 465 Hz. The leading edge independence condition is selected as it provides the largest bandwidth (and thus the greatest possible error) in the analysis.

$$\frac{\omega C}{c_0} \geq 2\pi \quad (4-29)$$

$$\frac{\omega C}{2U_\infty} \geq 10 \quad (4-30)$$

For multiple-microphone measurements, the phase between each microphone in the linear array and the Brüel & Kjær microphone placed opposite the model is extracted from the cross-spectral matrix. Then the deviation of the phase, adjusted by the shear layer correction, from that of a dipole at the trailing edge is computed. The upper integration bound is determined by the frequency where this phase relationship degrades to random behavior, which coincides with the frequency where the ordinary coherence function trends to zero.

The results from these preliminary experiments compare the differing coherent power methods and allow for planning of the main experimental body of the research. The COP, three-microphone and least-squares methods are applied to the microphone 5 data in Figure 4-40. Note that microphone 12 is the opposing B&K 4939 from Figure 4-39, and is the reference microphone used for coherent power. This microphone, along with microphone 4 in the linear array, is included in the processing for the 3-microphone method. The least squares method is computed using all of the microphones except microphones 1 and 2 closest to the collector. These microphones are neglected because when the linear array was placed on the pressure side of the model, microphones 1 and 2 were in a downwash region generated by the model's lift. This downwash region generated an excessive amount of hydrodynamic fluctuation contamination in the microphone measurements. These microphones were not influenced when the linear array was positioned on the suction side of the model.

Figure 4-41 shows a comparison of the corrected, measured phase angle between microphones 5 and 12 compared to a theoretical prediction for a dipole located at the trailing edge (without a scattering correction). This presentation shows that for low frequencies, the corrected data possess the expected dipole-like behavior. The near zero coherence at high frequencies results in random phase angle behavior. Note the necessity of the shear layer

correction in this analysis due to the unequal spacing of the microphone locations from the trailing edge.

The deviations of the linear array phase plots from dipole behavior are shown in Figure 4-42 and Figure 4-43, with Blake's cut-on criteria. The plotted data are the difference, in radians, between the corrected cross-spectral phase and that predicted by theory, with Blake's predicted cut-on frequency for trailing edge noise plotted [Blake 1986]. As shown, aside from microphones 1 and 2, the phase behavior is in good agreement from the computed lower bounds up to 4 kHz. Note that the data points near the maximum and minimum phase values Figure 4-43 actually phase-wrap back onto the main band of the plot.

The directivity plots are shown in Figure 4-44 for integrated levels from 250 to 4000 Hz. For most cases, as long as the measurement was well away from the model downwash, even the raw autospectral integration provided good agreement with the theory, although without cross-spectral information an upper integration bound could not be set. All of the coherent power methods are in good agreement with theory. With the exception of 75°, all of the methods differ from each other by no more than ~1 dB, while the maximum deviation from theory is ~2 dB.

This preliminary data set serves several purposes in the layout of subsequent experiments for the research. One of the first is that it shows that integrated directivity levels, while in good agreement between the different analysis techniques, do a poor job at highlighting the detailed differences of each method. As such, directivity, in the two-dimensional sense, will not be a parameter of interest in the final research. Second, the data show that all of these methods predict different levels. Above a certain threshold, when the predicted dipole-like phase behavior breaks down, all of the methods have significant disagreement. As such, uncertainties

are necessary to see if, when accounted for, they can demonstrate agreement between different methods.

Also, it should be noted that so far none of these experiments have addressed three-dimensional and multi-source field effects in terms of coherent power analysis. Based on the discussion in Appendix C, when a distributed source region composed of incoherent sources is observed by a set of microphones, the coherence measurements between microphones can trend to zero, even though each microphone could be observing an identical set of sources with no incoherent noise contamination. This behavior is observed to be a function of experimental geometry, and is associated with a near field measurement effect. In essence, if the source field is not spatially lumped, an average cancellation effect can occur depending on source and observer orientation. The conclusion of the appendix is that this effect can be mitigated, at least in the case of a source like trailing edge noise where the geometry is known to be symmetric, but placing the microphones such that they are located on the source line's plane of symmetry. For the nominal three-microphone analysis in this body of work, the G.R.A.S. 40BE downstream of the one used for two-microphone solutions is used for all experimental configurations. For additional analysis options in future work, G.R.A.S. 40BE microphones are placed along the airfoil's upper span in addition to those placed chordwise in Figure 4-36, Figure 4-37 and Figure 4-38. Figure 4-45 expands upon the previous experimental configuration figures by showing the orientation of this upper array of microphones. Note that by assuming equivalent shear layer behavior above and below the model, as the upper and lower microphones are located equidistant from the model trailing edge in Figure 4-37, as previously discussed no shear layer correction should be necessary for the coherent power method from Equation (4-17). This assumption can be considered valid for low-lift conditions, as this will lead to minimal test section jet deflection.

Given the equivalent-lift AoA formulation from Equation (4-3), this assumption should be valid for the planned angles of attack.

The additional upper array microphones are placed based on overall test section dimensions and data acquisition constraints. 7 G.R.A.S. microphones are the maximum allowable with a 68-channel data acquisition system. The phased array requires 45 channels for the array electrets plus an additional channel for the center reference microphone. Surface-mounted Kulites require another 14 channels. The model accelerometer requires a single channel, leaving 7 channels for the upper array.

Uncertainty estimates are necessary for comparison between techniques, as just discussed. While they were relatively simple for two-microphone methods, with three or more microphones they are not as straightforward. The absolute value operating on the square root terms in Equation (4-23) makes a simple classic uncertainty propagation difficult without expanding approximate derivatives. Since the uncertainty will be large for the predicted low-coherence frequency bins, such linear expansions may be in error [Yardibi *et al.* 2010a]. As such, the simplest solution is to conduct a set of Monte Carlo simulations for the multi-microphone solution, where the inputs to the code are perturbed by a Gaussian random input of standard deviation determined by the random uncertainty of each input component. For example, with the three-microphone methods the inputs consist of the raw autospectra and ordinary coherence functions. Bendat & Piersol [Bendat & Piersol 2000] give the normalized autospectral random error repeated in Equation (4-31).

$$\varepsilon \left[G_{y_i, v_i} \right] = \frac{1}{\sqrt{n_d}} \quad (4-31)$$

The uncertainty of the ordinary coherence function is given in Equation (4-32), where frequency dependence is implied and suppressed.

$$\varepsilon \left[\gamma_{y_i y_j}^2 \right] = \frac{\sqrt{2} \left[1 - \gamma_{y_i y_j}^2 \right]}{\left| \gamma_{y_i y_j} \right| \sqrt{n_d}}, i \neq j \quad (4-32)$$

More advanced coherent power techniques may leverage the full complex-valued cross spectral matrix (CSM). For these methods, the diagonal of the cross spectral matrix is perturbed using Equation (4-31). The off-diagonal terms must be separated into their real and imaginary, or co- and quad-spectral, components, as in Equation (4-33).

$$G_{y_i y_j} = C_{y_i y_j} + \sqrt{-1} * Q_{y_i y_j}, i \neq j \quad (4-33)$$

The co-spectrum normalized standard deviation is given in Equation (4-34), and the quad-spectrum normalized standard deviation in Equation (4-35), again from Bendat & Piersol [Bendat & Piersol 2000].

$$\varepsilon \left[C_{y_i y_j} \right] = \frac{\sqrt{G_{y_i y_i} G_{y_j y_j} + C_{y_i y_j}^2 - Q_{y_i y_j}^2}}{C_{y_i y_j} \sqrt{2n_d}}, i \neq j \quad (4-34)$$

$$\varepsilon \left[Q_{y_i y_j} \right] = \frac{\sqrt{G_{y_i y_i} G_{y_j y_j} + Q_{y_i y_j}^2 - C_{y_i y_j}^2}}{Q_{y_i y_j} \sqrt{2n_d}}, i \neq j \quad (4-35)$$

Beamforming Techniques

Traditional beamforming techniques involve the assumption of a source field consisting of a sum of incoherent monopoles. When this assumption is made, beamforming can be used to estimate the locations of acoustic sources, as well as the field level at the array center due to each source. This technique has been applied often to analysis of trailing edge noise experimental data with various modifications [Brooks & Humphreys 2006a; Hutcheson & Brooks 2002; Shannon *et al.* 2005]. For an open-jet facility, shear layer corrections are applied to each microphone's signal prior to the application of beamforming algorithms [Amiet 1978a]. This is done using a pre-computed array of data for known microphone and scanning grid [Sanford 2008]. Classic

delay-and-sum (DAS) methods can be used to construct source maps, but these are sensitive to contamination from local flow noise [Humphreys *et al.* 1998; Mosher 1996]. When these methods are cast in the frequency domain, one commonly-used method for dealing with contamination is diagonal removal (DR) from the CSM. By setting all autospectral diagonal terms to zero, the system noise as listed in Equation (4-11) goes to zero. However, the coherent source contribution to the diagonal is also eliminated. This approach can significantly improve the resulting source maps but can cause erroneous, negative level calculations over distributed source regions [Hutcheson & Brooks 2004]. These negative power levels can be dealt with in an integrated level code by setting them equal to zero in the power summation [Oerlemans *et al.* 2007a]. Diagonal removal also assumes that noise sources are uncorrelated between microphone channels, such that contamination is constrained to the cross spectral matrix diagonal. However, if non-acoustic correlated noise is introduced, such as coherent flow structures passing over the array surface, significant errors may still be present in the results.

To further reduce contamination, the cross spectral matrix element, Equation (4-12), can be modified to Equation (4-36).

$$G_{y_i y_j} = G_{u_i u_j} + G_{n_i n_j} \quad (4-36)$$

Here, it is no longer assumed that noise contamination sources are incoherent with each other, although it is still assumed that the noise sources are not coherent with the acoustic sources of interest. One method employed in previous literature [Humphreys *et al.* 1998] uses background noise subtraction. With background noise subtraction, the measured cross-spectral matrix of an empty test section with flow is measured and assumed to be the coherent noise term in Equation (4-36). Then, the test is repeated with the model in place and is measured. The difference is assumed to be the desired coherent acoustic sources of interest with the model present. In other

words, the coherent noise term is assumed to be the same with and without the model installed. However, this approach can lead to unexpected results because the installed model can significantly change the flow patterns in the chamber, leading to new noise sources. Based on previous research in UFAFF, diagonal removal will be used, but background subtraction will not be used, as background subtraction has been observed to induce clearly erroneous behavior in beam maps from the facility [Bahr *et al.* 2008].

The power at a grid point in a scanning plane for the standard delay and sum beamformer in the frequency domain is given in Equation (4-37) [Dougherty 2002; Yardibi *et al.* 2010a; Yardibi *et al.* 2010c].

$$P_l = \frac{1}{M^2} \vec{a}_l^H \vec{G} \vec{a}_l \quad (4-37)$$

Here, l is the index of the scanning point, M is the number of microphones in the array, \vec{G} is the CSM, \vec{a} is the steering vector, defined in Equation (4-38), and \vec{a}^H is the conjugate transpose of the steering vector.

$$\vec{a}_l = \frac{1}{r_{l,0}} \left[r_{l,1} e^{-jk r_{l,1}}, \dots, r_{l,M} e^{-jk r_{l,M}} \right]^T \quad (4-38)$$

The distance $r_{l,0}$ is from the array center to the l th scanning point, $r_{l,m}$ from each microphone to the scanning point, $[\]^T$ the non-conjugate transpose, k the acoustic wavenumber for the frequency of interest as defined in Equation (2-13), and $j = \sqrt{-1}$ (as opposed to an index as used earlier in this chapter). If diagonal removal is used, the denominator in Equation (4-37) is changed to $M^2 - M$ to account for the reduced number of microphones in the final summation. Integrated levels are computed using Equation (4-39) [Oerlemans *et al.* 2007a; Yardibi *et al.* 2010c].

$$P_L = \frac{\sum_{l \in L} P_l}{\sum_{l \in L} PSF(l)} \quad (4-39)$$

L is the integration region of interest, and $PSF(l)$ is the array response, or point-spread function, to an ideal centered source at scanning location l . Essentially, the summed DAS prediction within the integration region is normalized by the summed point spread function. This is a dramatically simplified expression of a true deconvolution, and suffers from several pitfalls depending on the behavior of the point-spread function in the integration region [Oerlemans *et al.* 2007a]. Array aperture effects can still be important even with this integration normalization. However, the computational expense of this method is much less than more advanced algorithms, and the method has a recent formulation for overall uncertainty [Yardibi *et al.* 2010a]. Due to computational expense and the interest in uncertainty, the experiments presented in this work will be formulated and analyzed only in the context of the standard DAS beamformer, with acknowledgement of the method's inherent weaknesses.

A zero-redundancy spiral aperture array was designed using the tools designed by Underbrink [Underbrink 1995], and fabricated for use in the UFAFF. The physical array consists of a 0.5 m diameter, ½" thick aluminum plate with 45 flush-mounted Panasonic WM-61A microphones. The disk edges are treated with acoustic foam to minimize scattering effects. A photograph of this array is shown in Figure 4-46. A solid plate is selected over free field installation of the microphones on rods due to microphone packaging, installation and traversing simplicity. This array was selected over a previously-designed, 1.82 m diameter 63 element array for two reasons. First, the nature of the free jet test section flow field is such that having a larger array located only 1 m from the model would induce significant flow over the array surface. Second, a smaller array provides the opportunity to offset the array from its baseline location, and study how small or moderate shifts in array position can affect the relationship

between an integrated array level and a coherence-based method. Additionally, previous internal research has shown that large arrays will under-predict acoustic levels from directional sources such as dipoles. The 3 dB beamwidth of the array is plotted in Figure 4-47. Note that part of the cost of a smaller, more flexible array arises in its complete inability to discern source direction below approximately 650 Hz. Coordinates for this medium aperture array are listed in Table 4-5. The installation uncertainty of the microphone locations in the plate is on the order of 0.001". A selection of individual-frequency point-spread functions of the array with contours of -5 dB, -10 dB and -15 dB are shown in Figure 4-48 through Figure 4-53. The selected frequencies correspond to frequencies analyzed in detail in Chapter 5. Note that at 20,000 Hz, the array's sidelobes grow beyond the -10 dB level.

For phased array measurements, the phase response of individual microphones within the array is important, and can play a significant role in the uncertainty of output spectra [Yardibi *et al.* 2010a]. As such, array calibration is extremely important over the entire bandwidth of interest of the array. Unfortunately, experience has shown the basic group array calibration technique [Dougherty 2002] to be very sensitive to imperfections in the anechoic environment, as well as partial scattering off of the array edges, even with acoustic edge treatment. Group array calibration can correct for errors in steering vectors due to microphone response, as well as those due to microphone positional uncertainties. As mentioned previously, the microphone positional uncertainties in a plate-based array are minimal. Therefore, if the microphones have proper frequency response calibrations over their entire range of operation, the group calibration procedure should no longer be necessary. This assumes small differences in temperature and ambient pressure between individual calibration and experimental conditions play a small role in microphone responses, but such an assumption is always inherent in an experiment unless

calibration occurs immediately before or after data acquisition. An in-situ method of individual array microphone calibration referenced to the array-centered B&K 4138 microphone is given in detail in Appendix D. The summary of this calibration result is that the array microphones have been calibrated for use from 512 Hz to 20 kHz, assuming that the B&K microphone has flat response within this bandwidth.

Array measurements were collected simultaneously with all other channels, as previously discussed, at a sampling rate of 102,400 samples per second for 30 seconds. CSMs were built using 6400-point discrete Fourier transforms (DFTs) for a 16 Hz binwidth. The data blocks were processed with 75% overlap using a Hanning window function, leading to 996 effective averages n_d with a normalized autospectral random uncertainty of 3.2%. Diagonal removal is used in all processing. The integration region is set to a 0.4 m x 1.06 m box centered on the trailing edge of the model in the $z = 1$ plane of the array coordinate system shown in Figure 4-45. The x-dimension of the region is chosen to balance computational costs with capturing the trailing edge noise lobe at as low of a frequency as possible, while still attempting to reject noise from the front and back of the test section (setting a maximum dimension of 0.5 m). The y-dimension of the integration region is chosen to encompass almost the entire model wetted span, aside from a small region on each side of the model to reject some of the possible sidewall noise. Note that this means the entire point spread function 3 dB lobe isn't contained within the y-dimensions of the integration region below 1,392 Hz, and within the x-dimensions until 3,312 Hz. Shear layer corrections are computed for the entire region in a 0.02 m x 0.02 m dense grid. This same grid density is used in the integration procedure.

The existing uncertainty code for a delay-and-sum beamformer conducts Monte Carlo trials based on uncertainties in the beamformer input [Yardibi *et al.* 2010a]. Simple mechanical

uncertainties include the microphone locations in the array plate, already estimated at 0.001", as well as uncertainty in the distance from the array to the source scan plane, which is considered as the measurement uncertainty of distances in the wind tunnel facility, 1/16", as well as the thickness of the model trailing edge, 0.13", to account for the ambiguity of the reference location on the trailing edge for measurement relative to the true noise source plane. These inputs to the code are all drawn from Gaussian random number generators, with the aforementioned values used as the input standard deviation. Temperature uncertainty is computed based on in-situ measurements during testing, and again is treated as an independent Gaussian random variable. The final input uncertainties are due to the microphone frequency response functions. Rather than attempt to compute individual response uncertainties for each microphone, this is treated as a batch problem, where the magnitude and phase responses of all of the microphones in the array, computed in Appendix D, are used to compute the overall system variance, and the subsequent standard deviations are used to perturb microphone behavior again using a Gaussian random number generator.

Test Matrix

The final test matrix for the dissertation experiment set can include significant tunnel speed variations, minor angle of attack changes, and some minor instrumentation offsets. The goal of these perturbations on a baseline case isn't to exhaustively quantify the trailing edge noise signature of this particular model, but to provide enough variation to the signal to cover a large spread of potential inputs to the analysis techniques. The overall test matrix is given in Table 4-6. The test section Mach number is swept from the tunnel minimum of 0.05, to the maximum with the NACA 63-215 mod-B installed of 0.19. The angle of attack is perturbed to $\pm 1.5^\circ$. The array is offset 0.25 m behind the model from its baseline location. This moderate offset is selected for a minor directivity change, without moving the array too close to the known

contamination region of the test section jet collector. This offset also maintains a microphone directly opposite the array center. Finally, the array is removed and replaced with a single B&K 4939 microphone to study the plate installation effects. These conditions should provide sufficient data to make some statements regarding the agreement of different trailing edge noise measurement techniques.

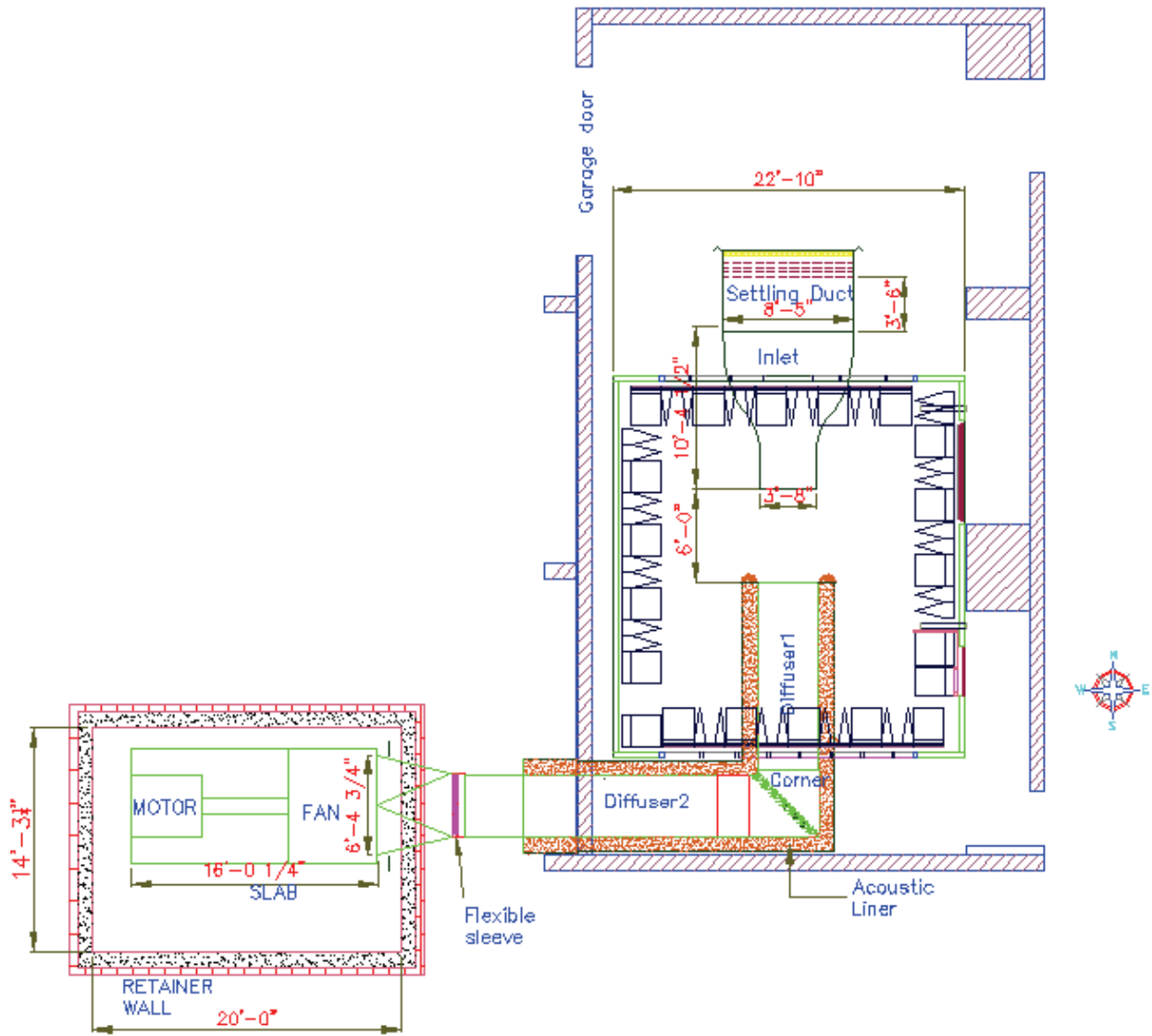


Figure 4-1. Planform schematic of UFAFF showing the flow path from the garage entrance (top), through the open-jet test section and out through the fan section.

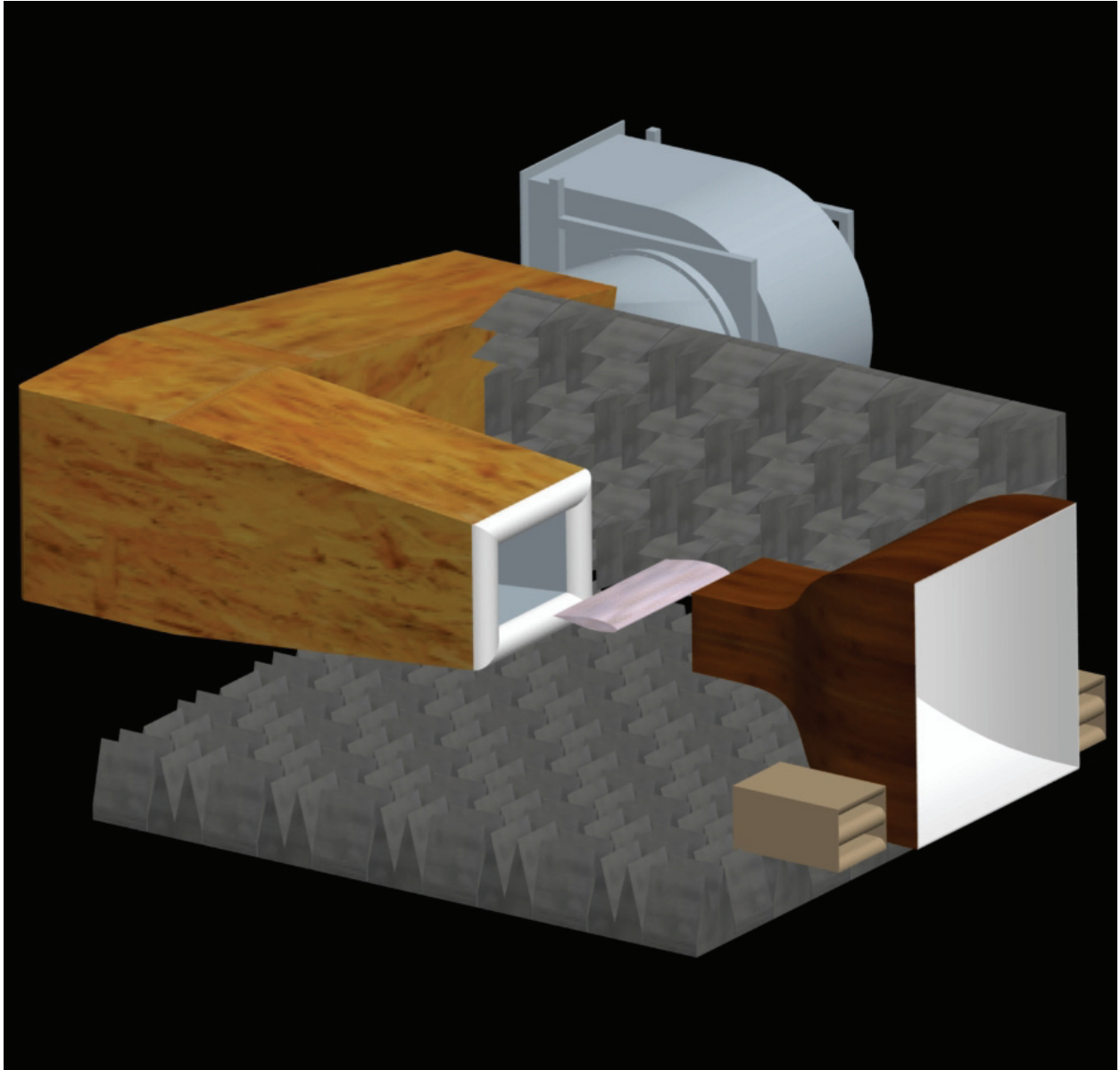


Figure 4-2. Isometric schematic of UFAFF. Note that the silencer boxes next to the contraction have been removed and blocked off with sealed panels and acoustic wedges for all experiments conducted for the main body of this research.

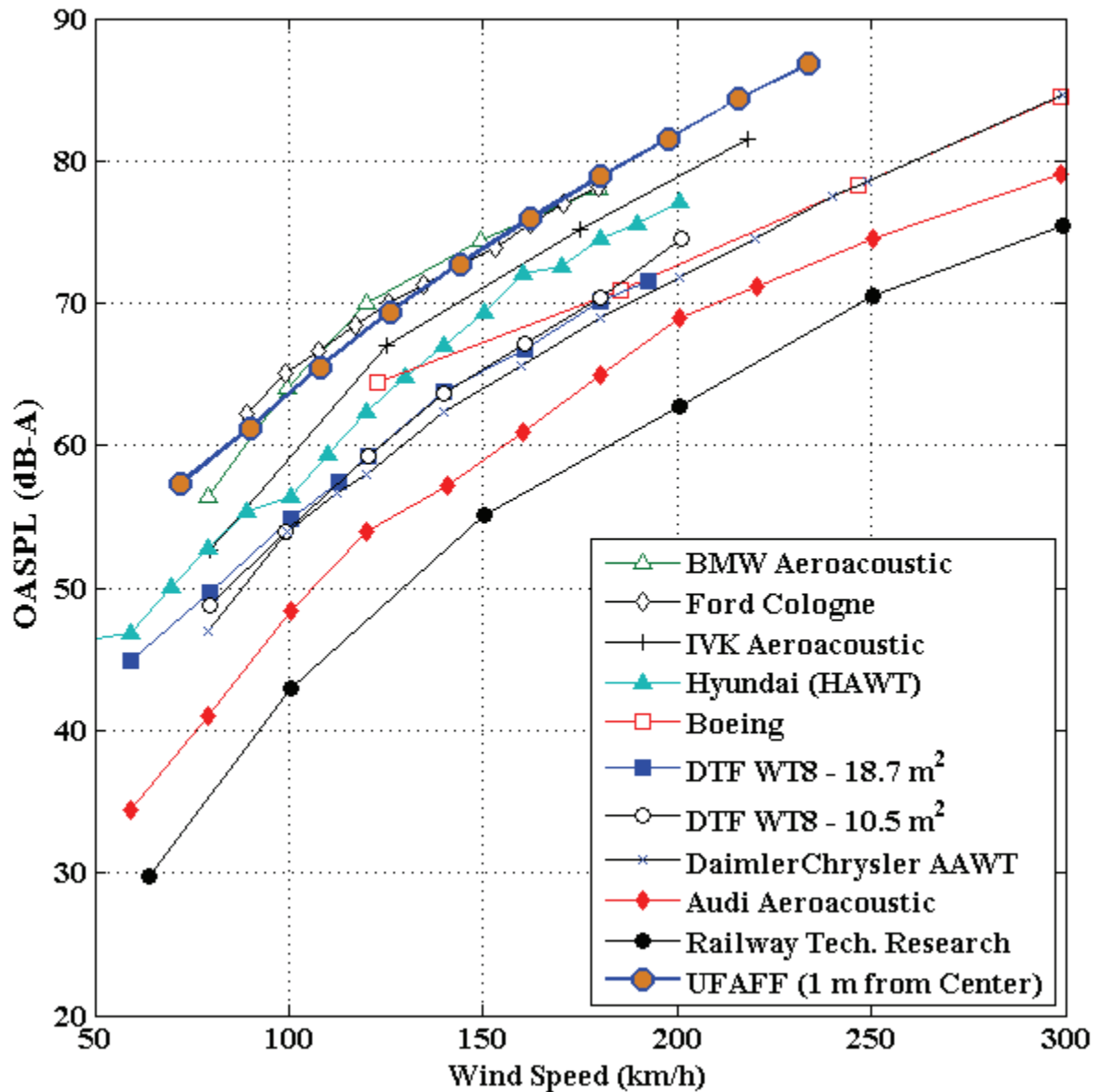


Figure 4-3. A-Weighted out-of-flow background noise comparison between different aeroacoustic flow facilities. Non-UF data are adapted from Duell et al. [Duell *et al.* 2002]. Note that the UF data were collected only 1 m from the test section centerline. Most other facilities' measurements occurred much further away, leading to lower acoustic levels from models in addition to lower background noise levels.

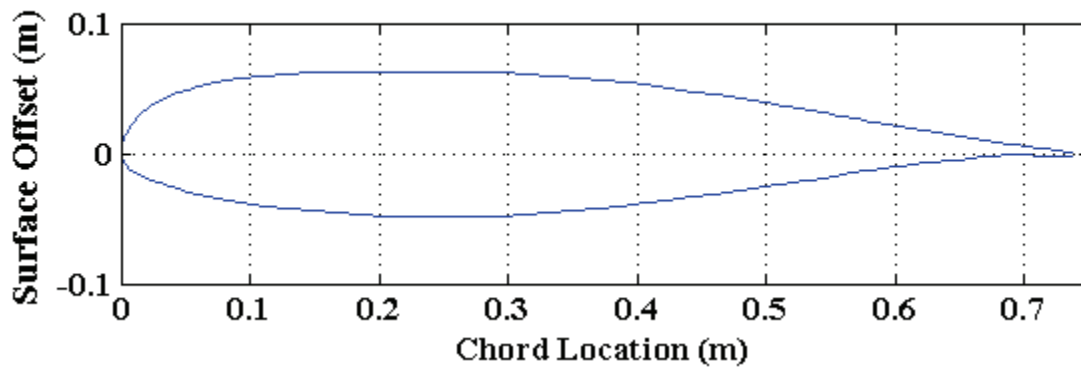


Figure 4-4. Cross section of UF NACA 63-215 Mod-B airfoil.

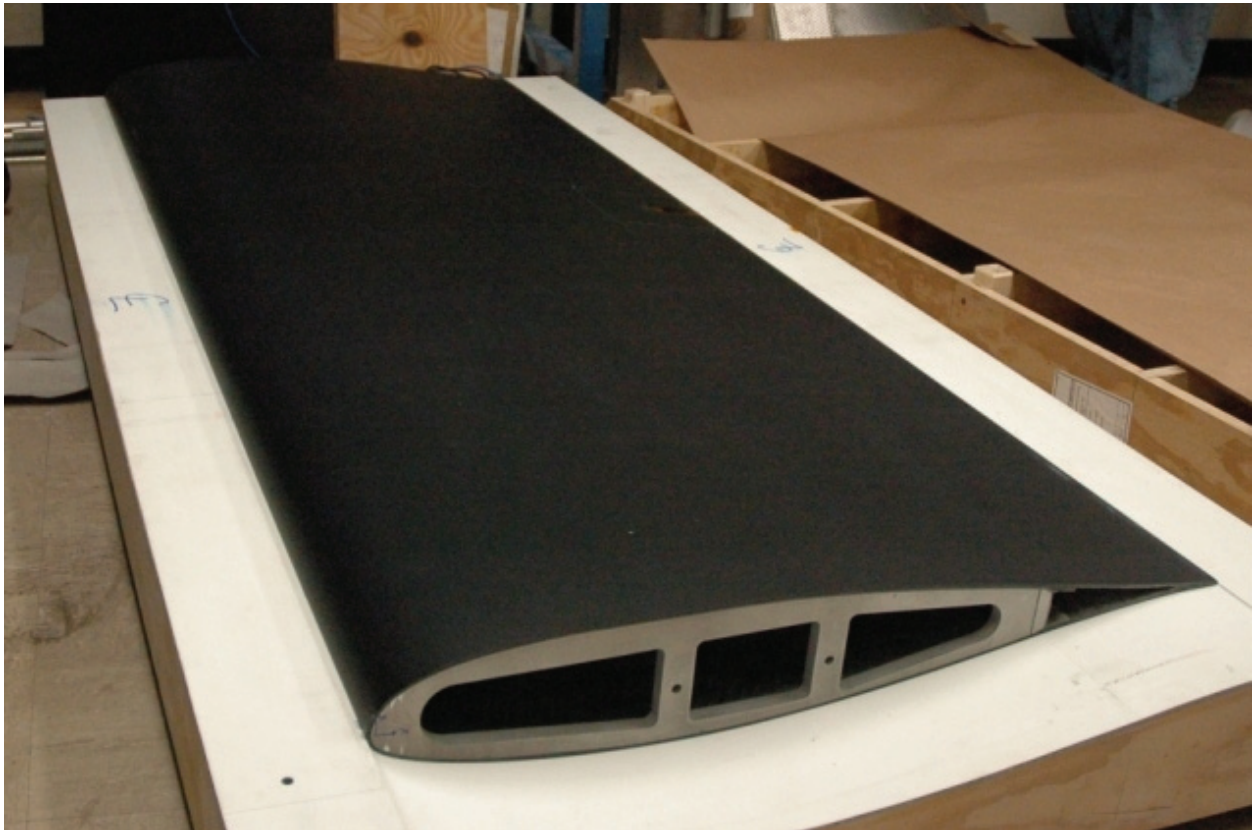


Figure 4-5. Photograph of UF NACA 63-215 Mod-B airfoil.



Figure 4-6. Photograph of UF NACA 63-215 installed in UFAFF, from below. Trip tape is visible on the model leading edge. Note the large access panel in the center of the model, and the smaller dynamic pressure transducer panel near the trailing edge.

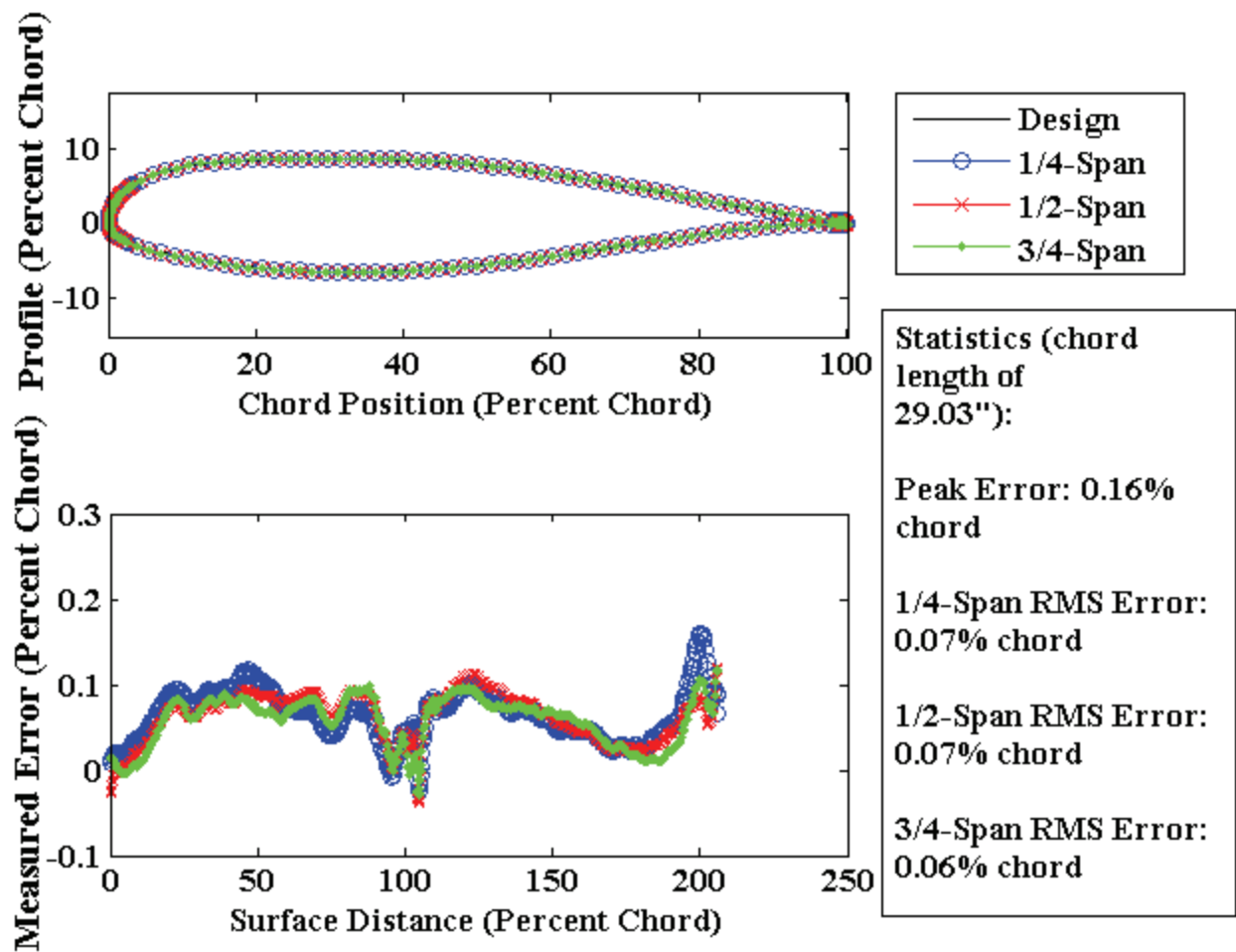


Figure 4-7. UF NACA 63-215 Mod-B profile deviation between design and measured coordinates.

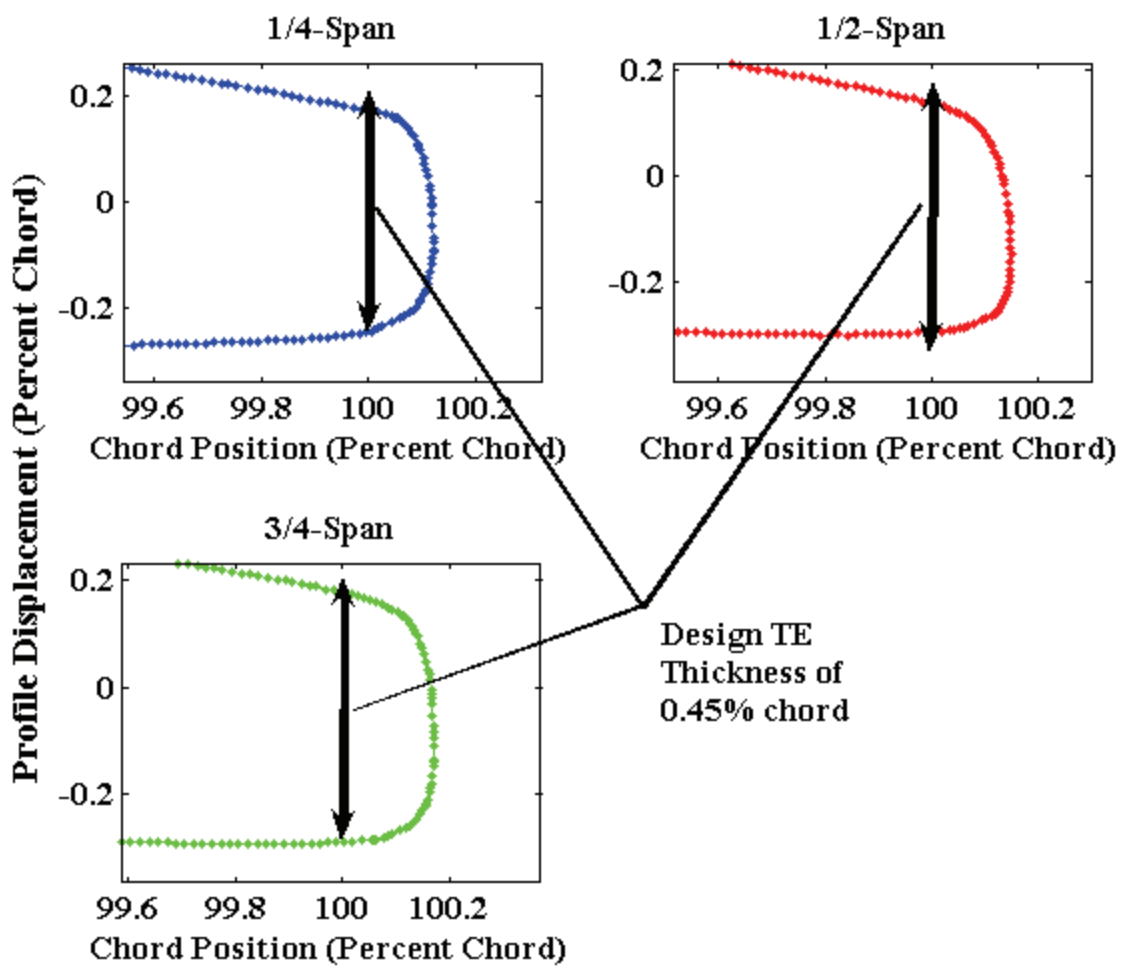


Figure 4-8. Trailing edge profiles at varying spanwise locations.

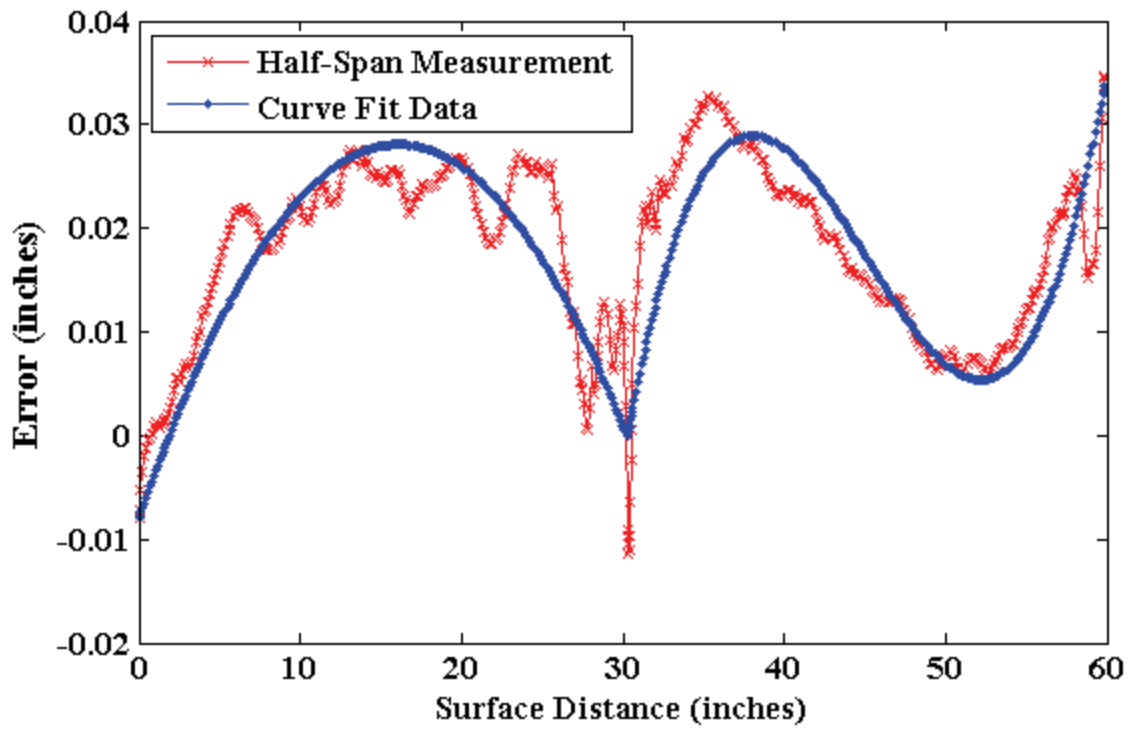


Figure 4-9. Surface error curve fits for UF NACA 63-215 Mod-B.

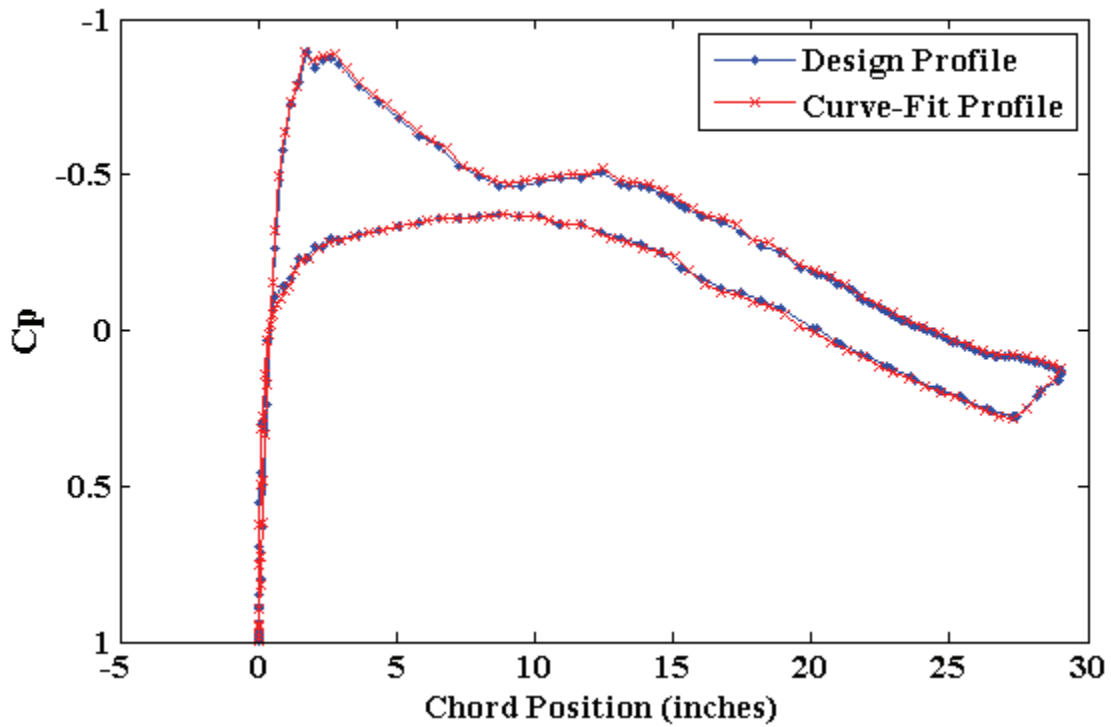


Figure 4-10. X-Foil predicted Cp distributions for design and modified profiles, $M = 0.17$.

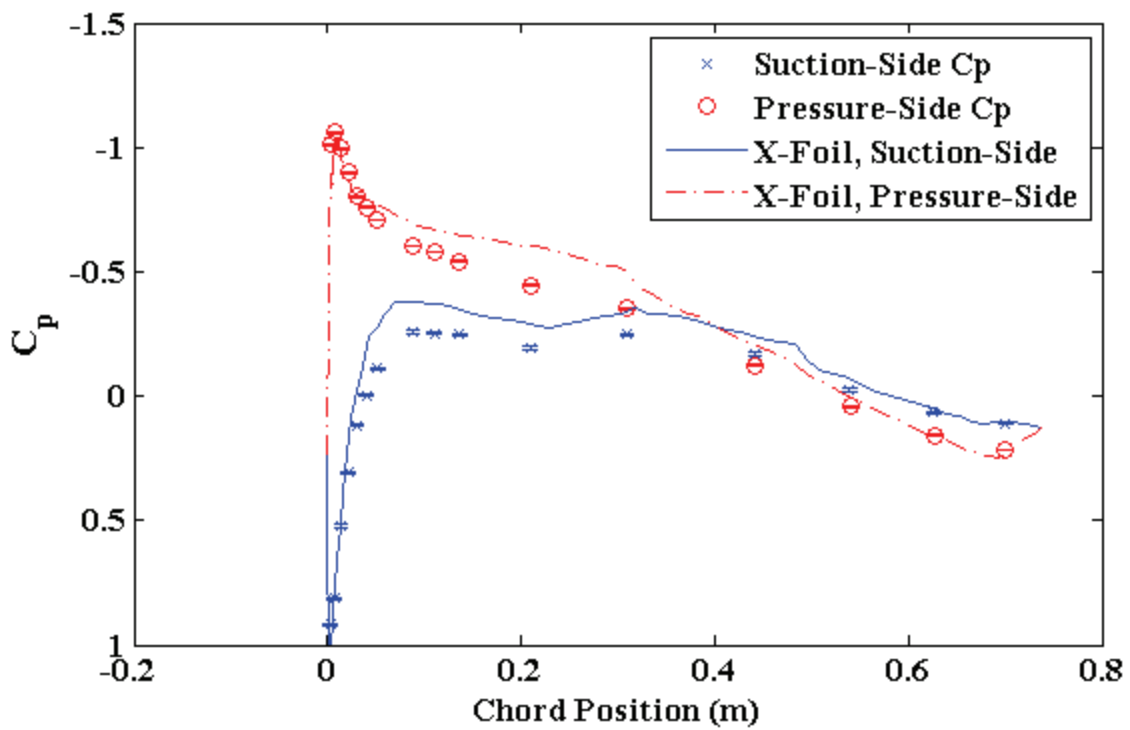


Figure 4-11. C_p for -7.5° geometric AoA (-3.14° equivalent lift freestream).

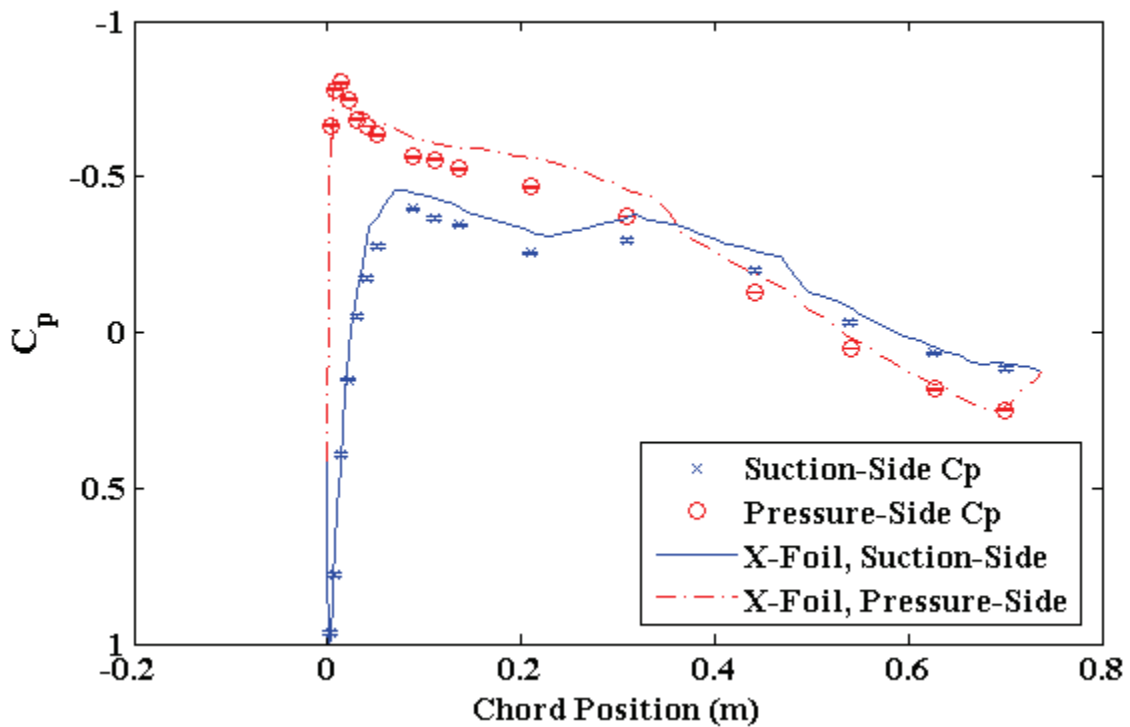


Figure 4-12. C_p for -5° geometric AoA (-2.63° equivalent lift freestream).

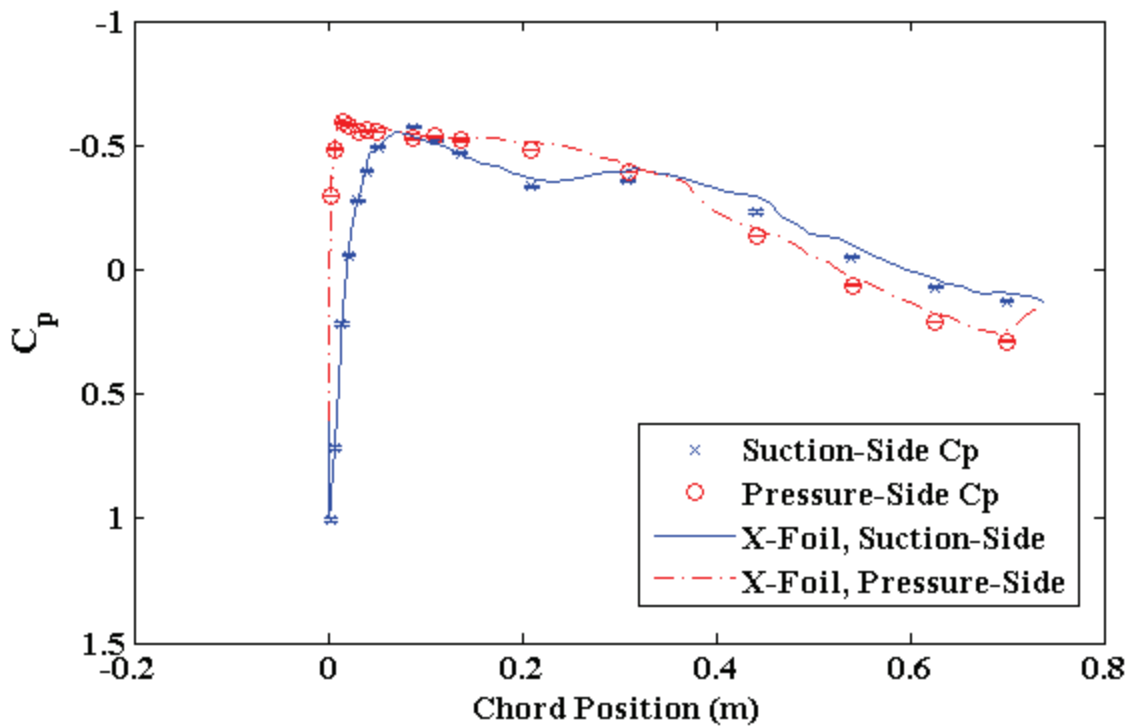


Figure 4-13. C_p for -2.5° geometric AoA (-1.98° equivalent lift freestream).

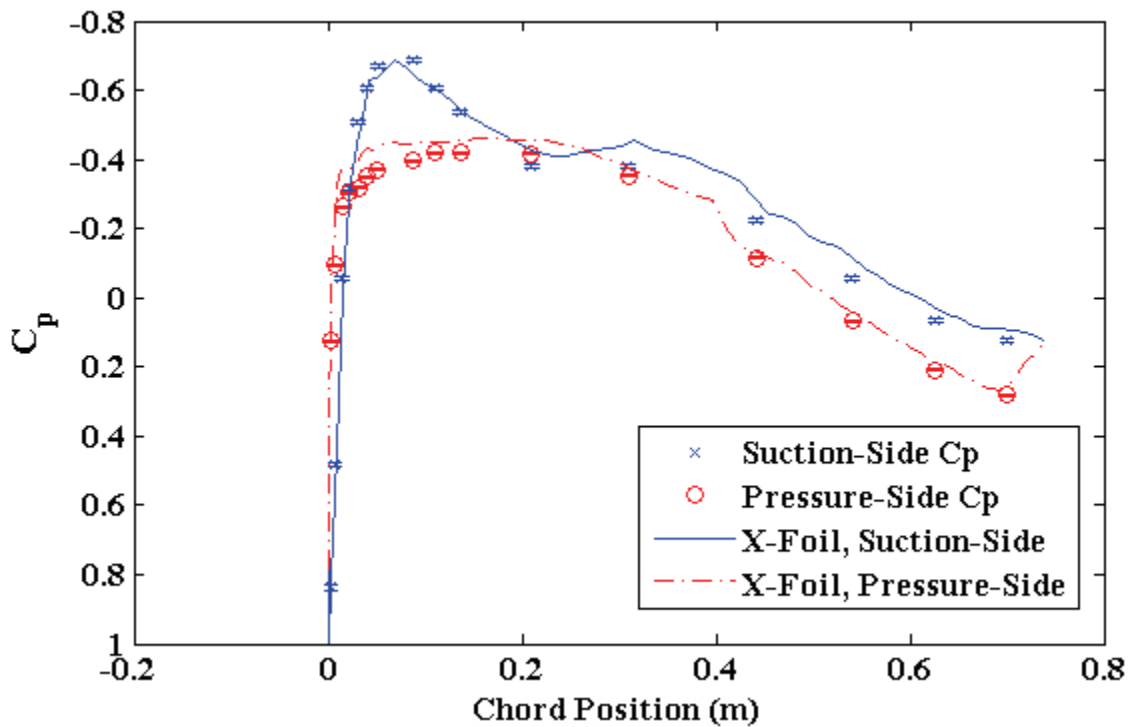


Figure 4-14. C_p for 0° geometric AoA (-1.19° equivalent lift freestream).

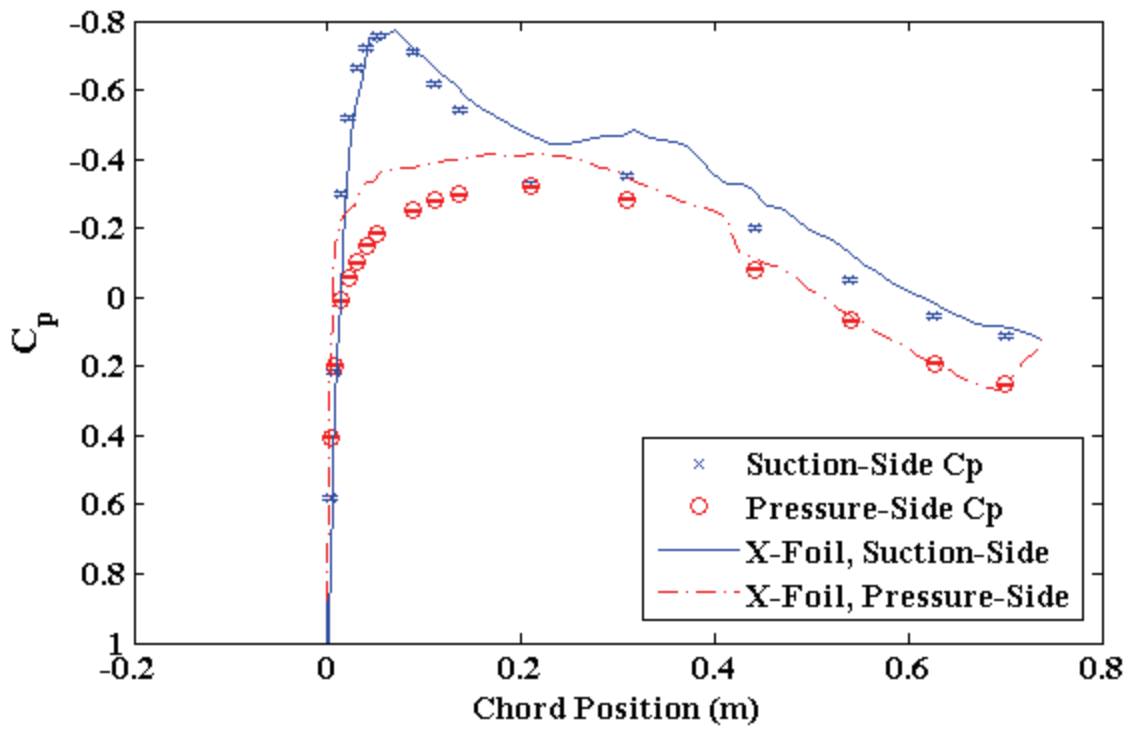


Figure 4-15. C_p for 2.5° geometric AoA (-0.65° equivalent lift freestream).

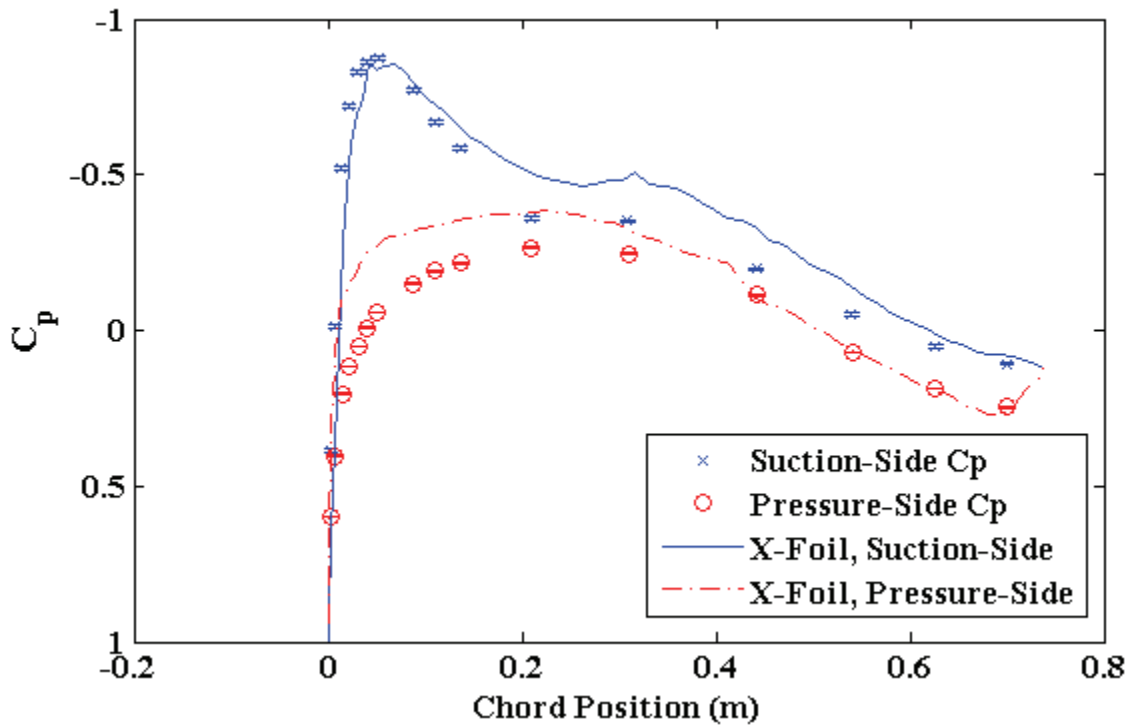


Figure 4-16. C_p for 5° geometric AoA (-0.15° equivalent lift freestream).

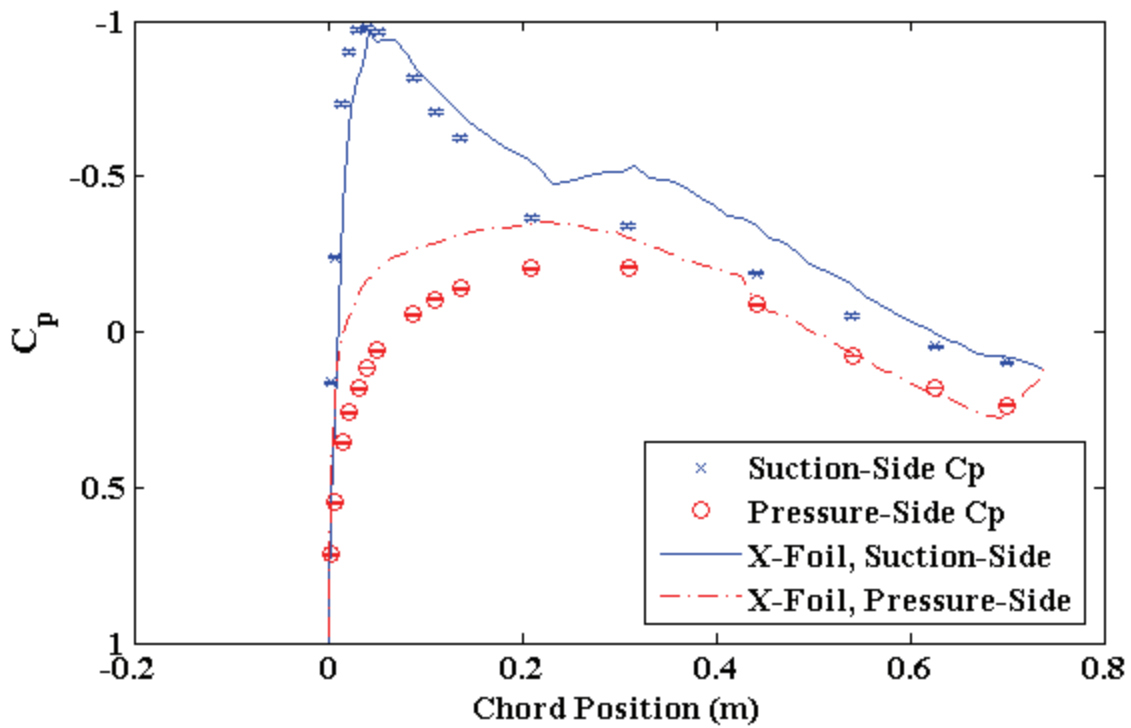


Figure 4-17. C_p for 7.5° geometric AoA (0.33° equivalent lift freestream).

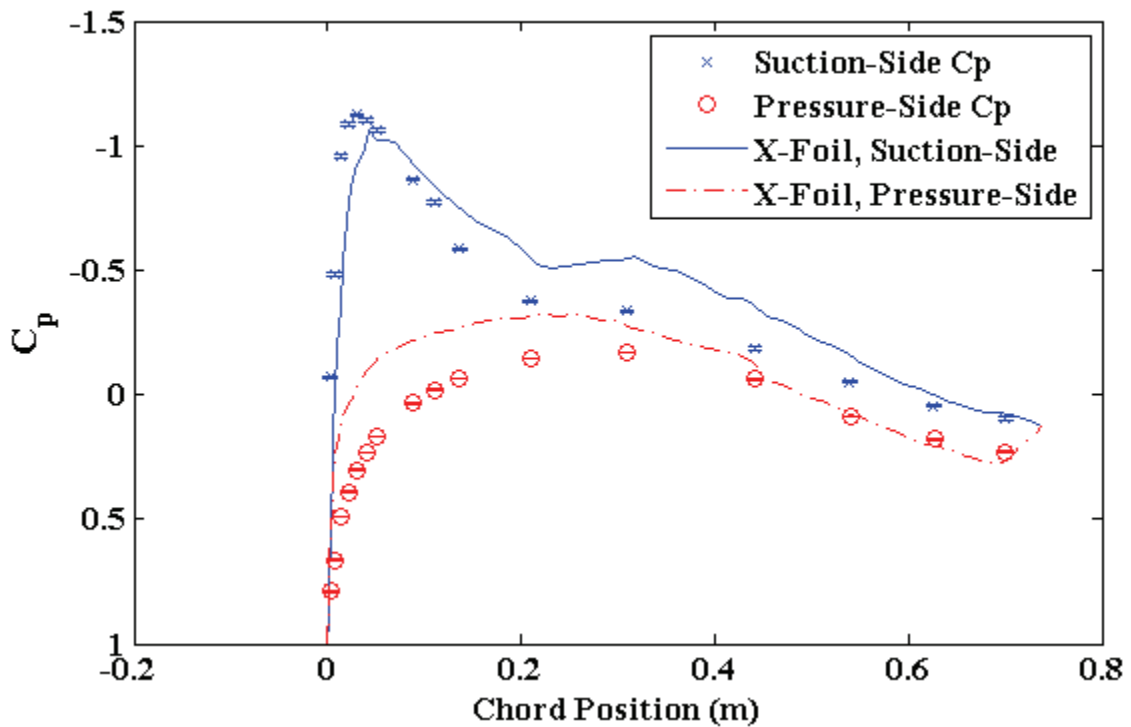


Figure 4-18. C_p for 10° geometric AoA (0.76° equivalent lift freestream).

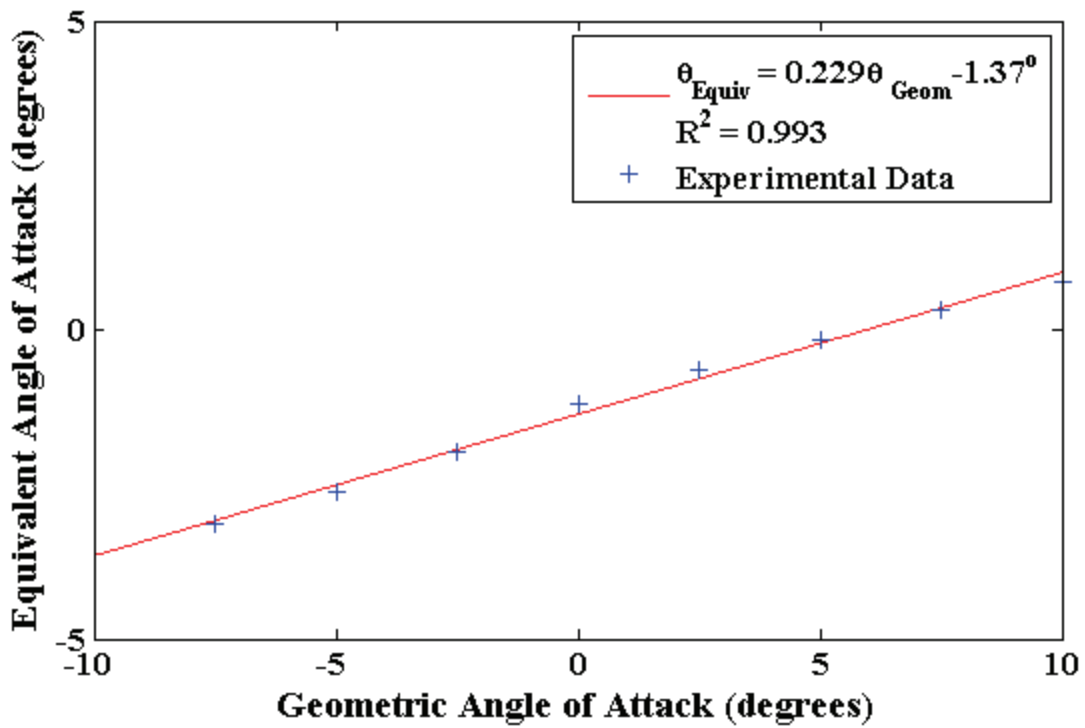


Figure 4-19. Installed, equivalent-lift AoA scaling with geometric AoA for UF NACA 63-215.

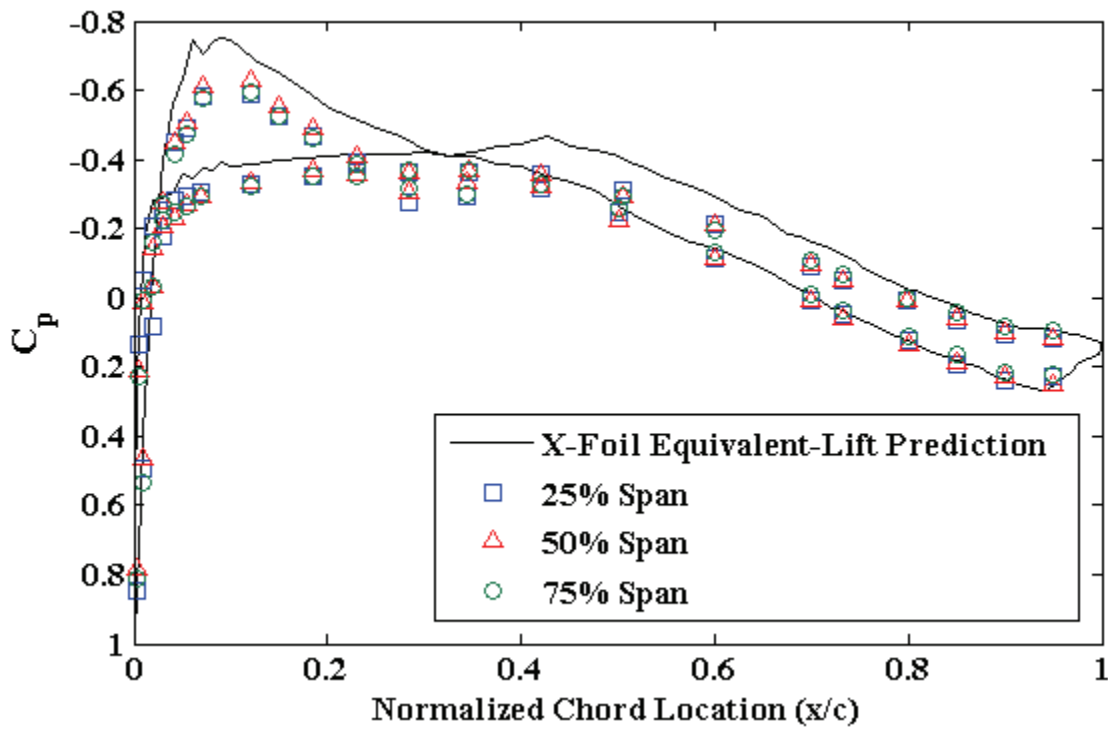


Figure 4-20. Evaluation of spanwise uniformity at zero-degree geometric AoA.

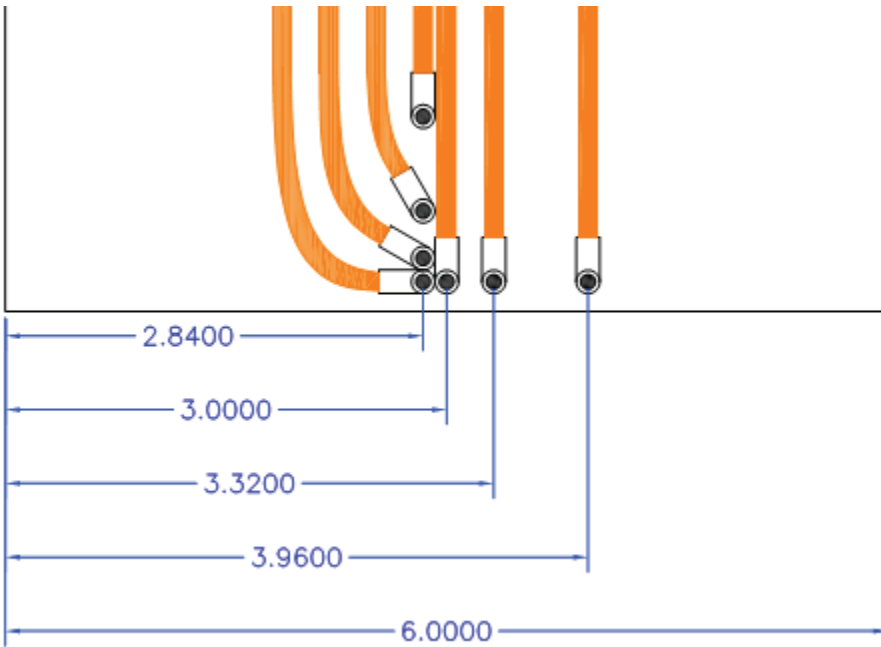


Figure 4-21. Trailing edge sensor layout for the NACA 63-215 Mod-B, with orange lines representing ribbon cabling, and all dimensions in inches. Note the vertical spacings are equal to horizontal ones. Distance from the trailing edge is given in the text.

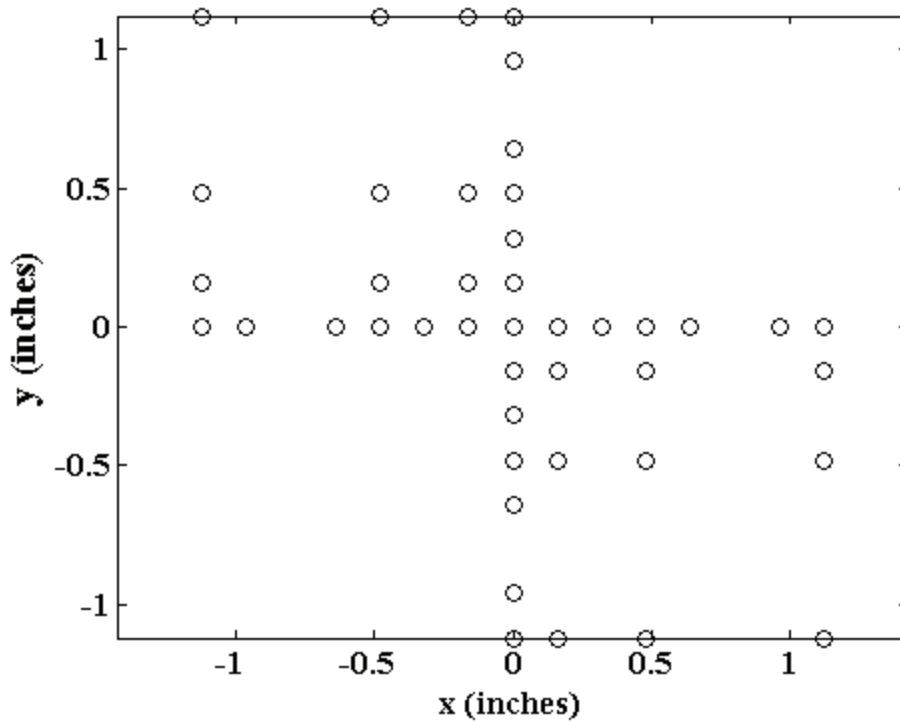


Figure 4-22. Map of trailing edge array spacings.

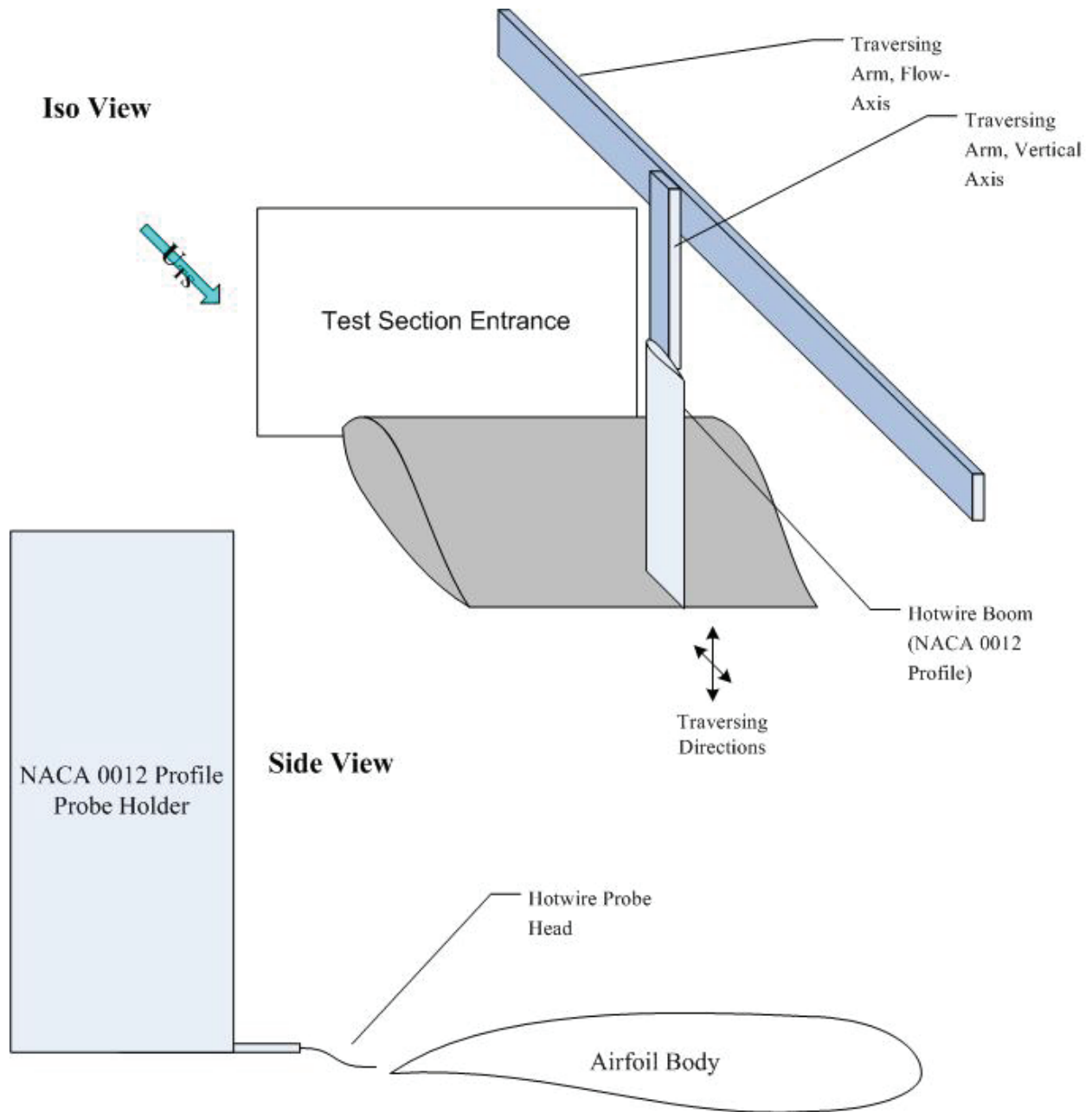


Figure 4-23. Schematic of a single-wire, 2-axis traverse experiment.



Figure 4-24. Photograph of hotwire installation for a DU 96-W-180 airfoil, from below the model, viewing the trailing edge.

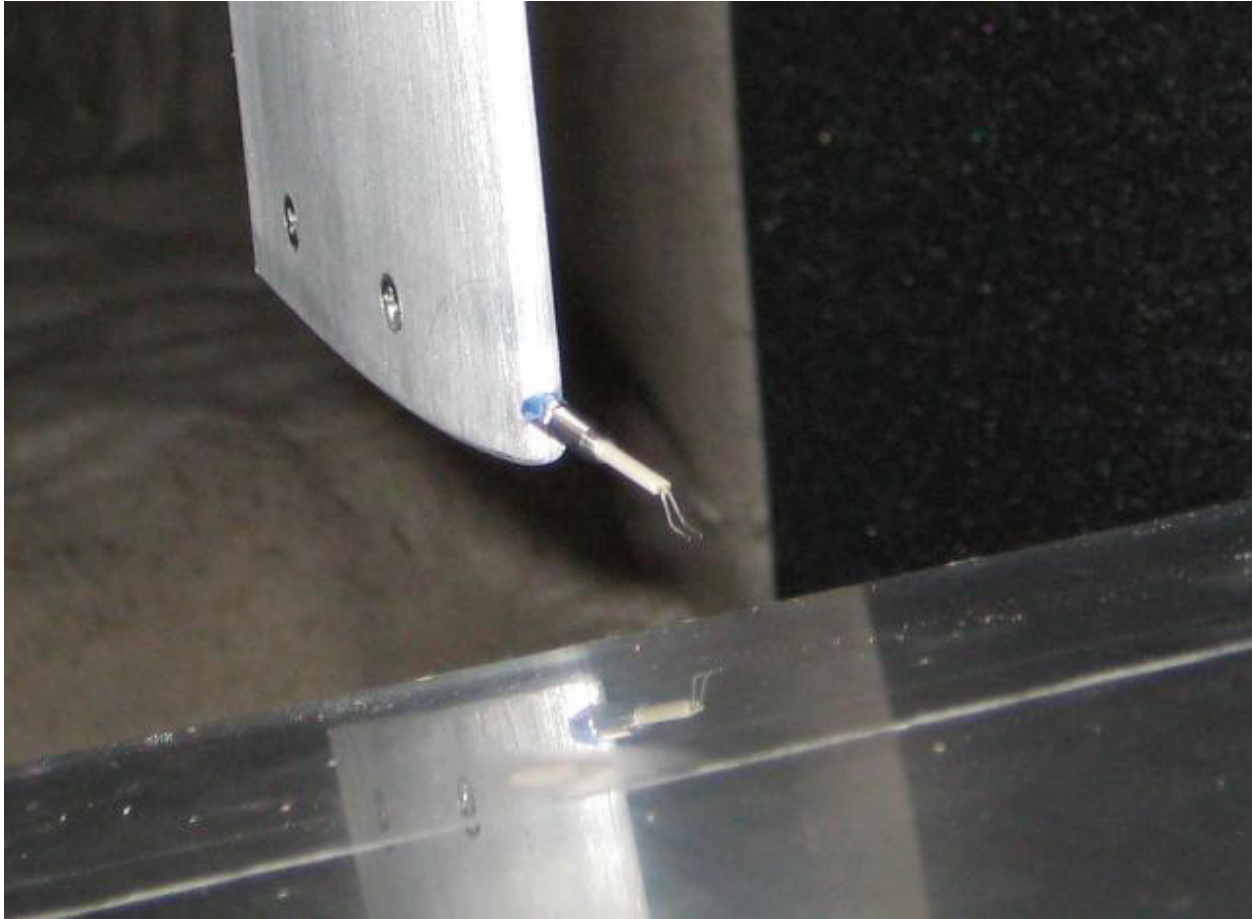


Figure 4-25. Photograph of hotwire installation for a DU 96-W-180 airfoil from above the model, viewing the trailing edge.

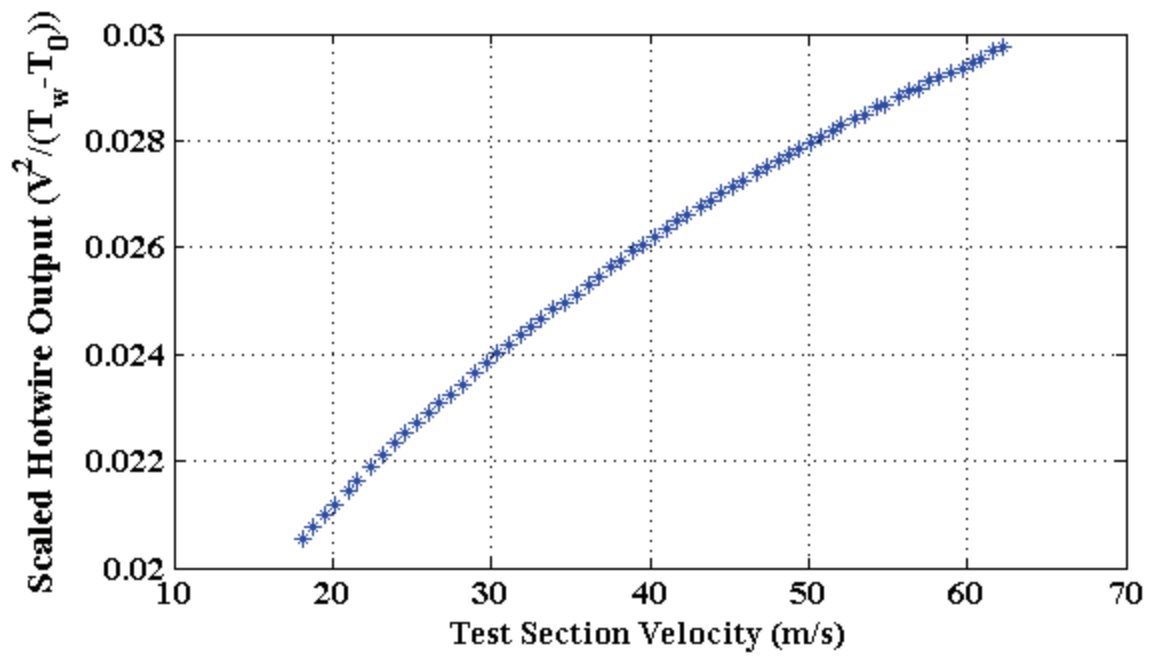


Figure 4-26. Example hotwire calibration data to be used with King's Law.

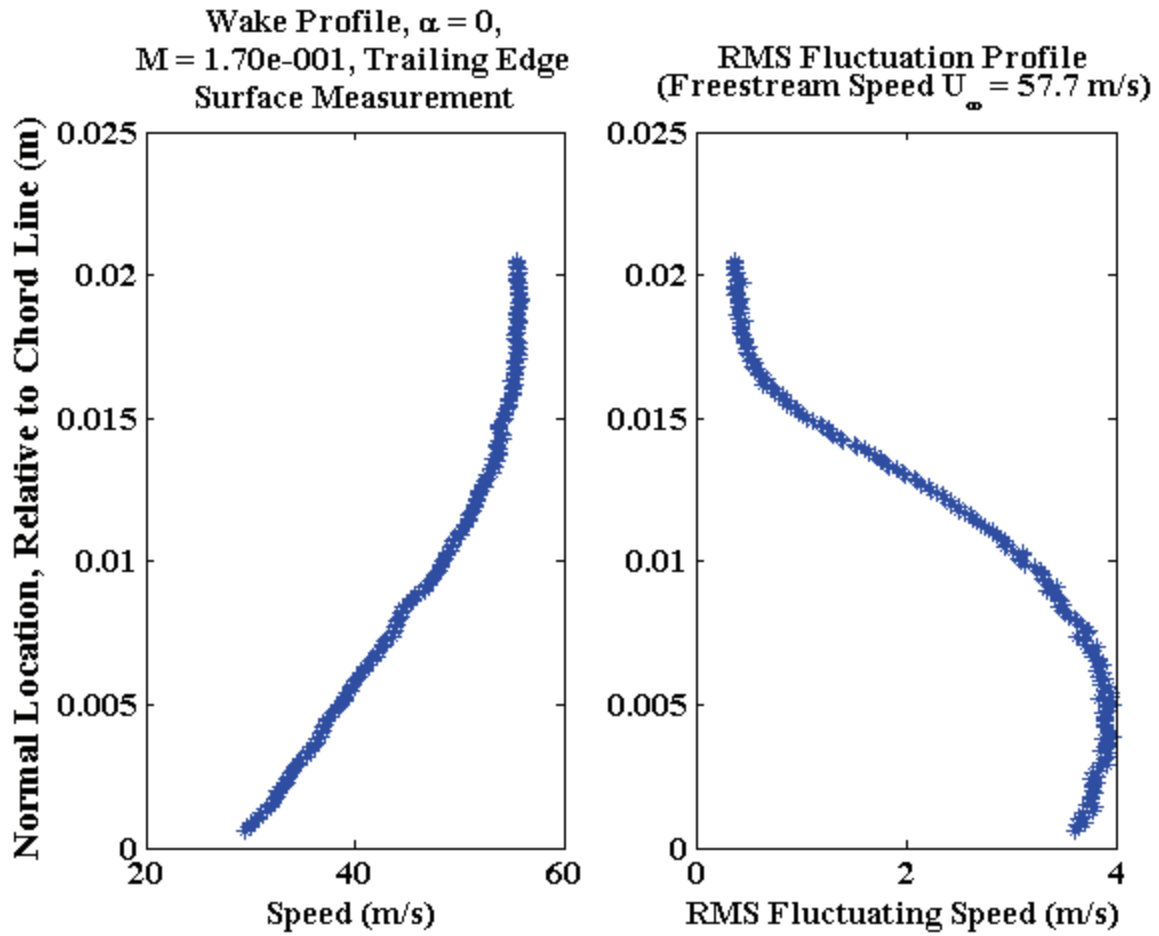


Figure 4-27. Plot of mean and fluctuating boundary layer velocity profile in the trailing edge vicinity. Note that the y-axis does not originate on the airfoil surface. An offset of approximately 5×10^{-4} m is present.

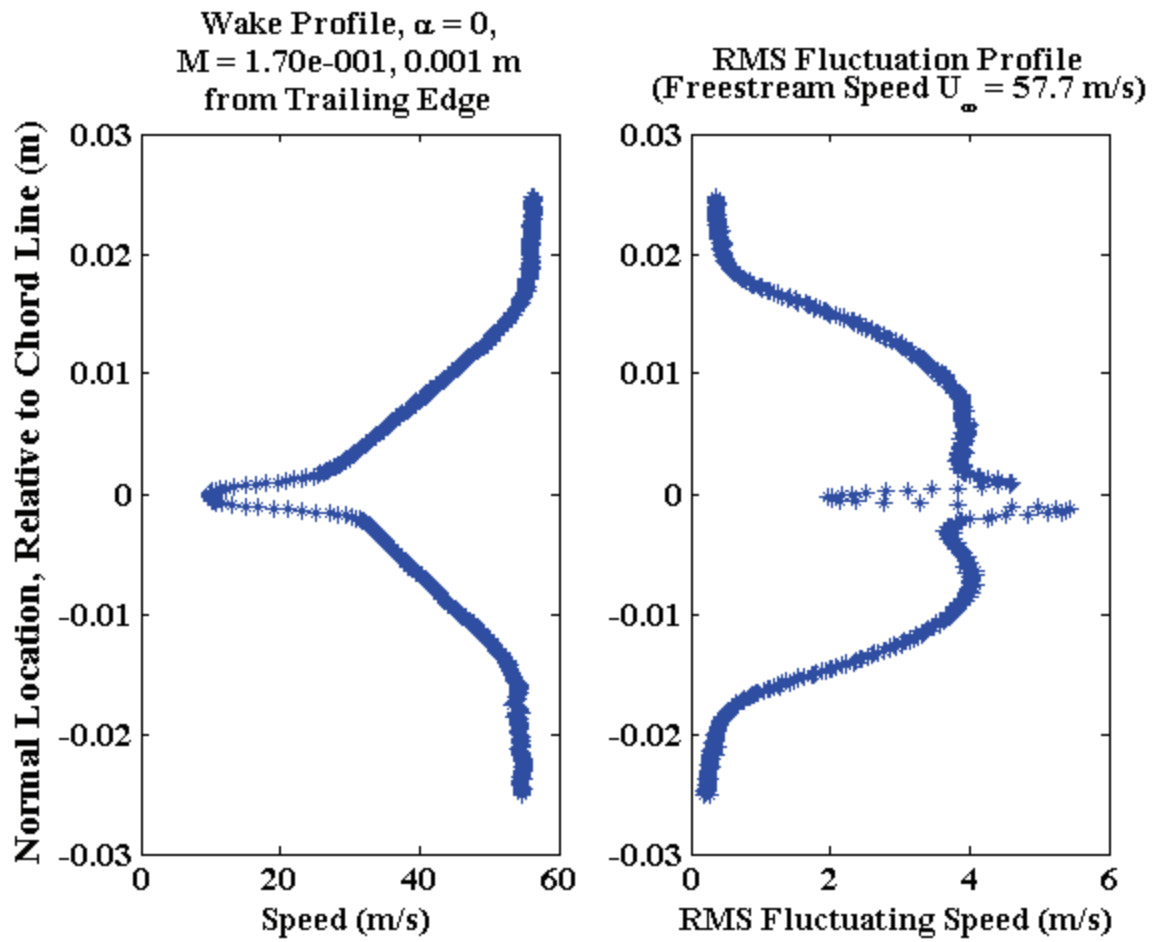


Figure 4-28. Plot of mean and fluctuating wake profile in the trailing edge vicinity.

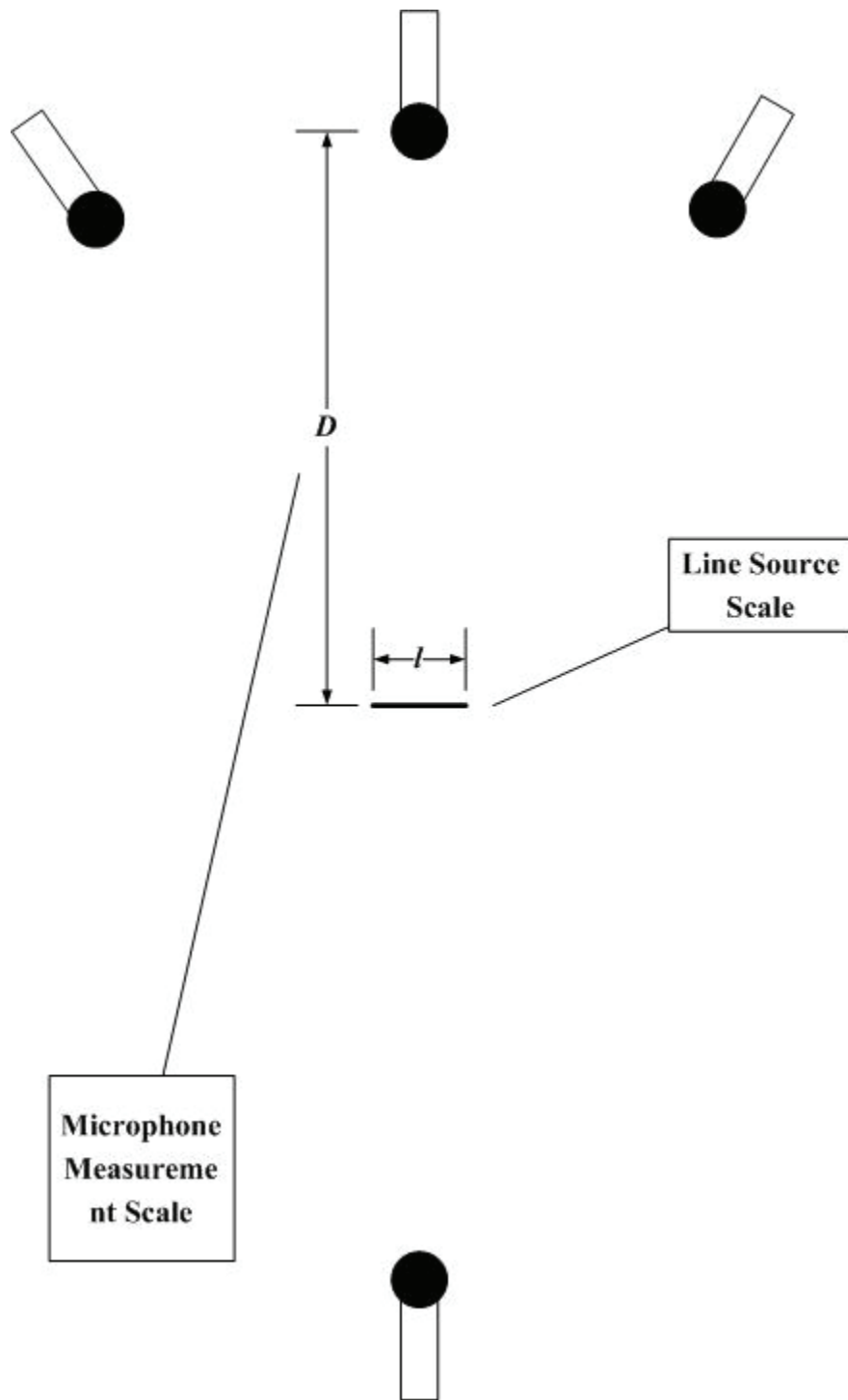


Figure 4-29. Schematic of an ideal, spatially lumped line source in a coherent power-based analysis.

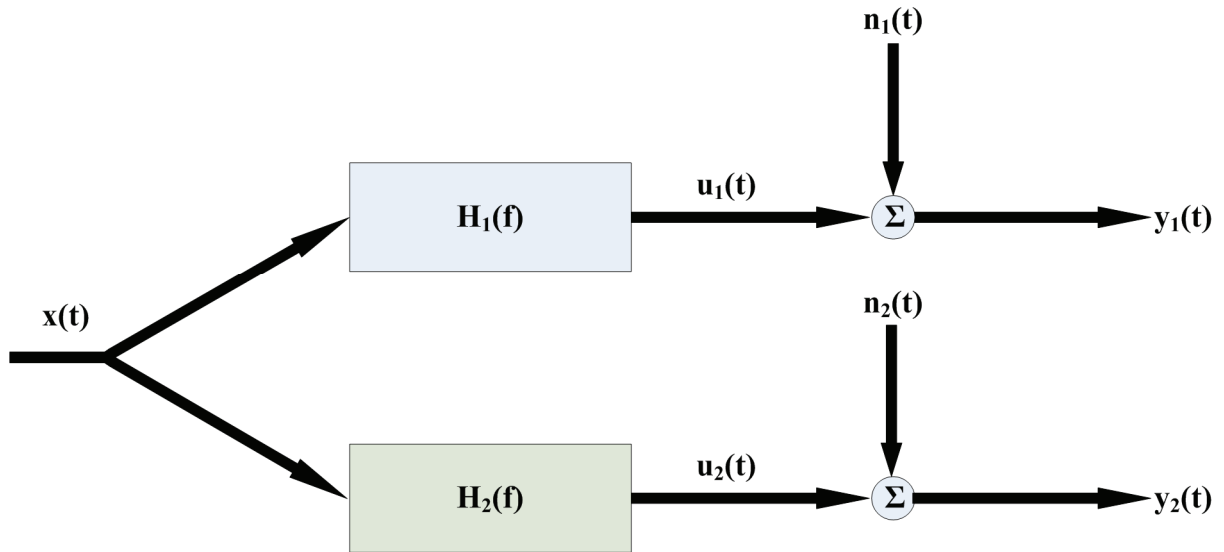


Figure 4-30. Block diagram for a Single-Input-Two-Output (SITO) system.

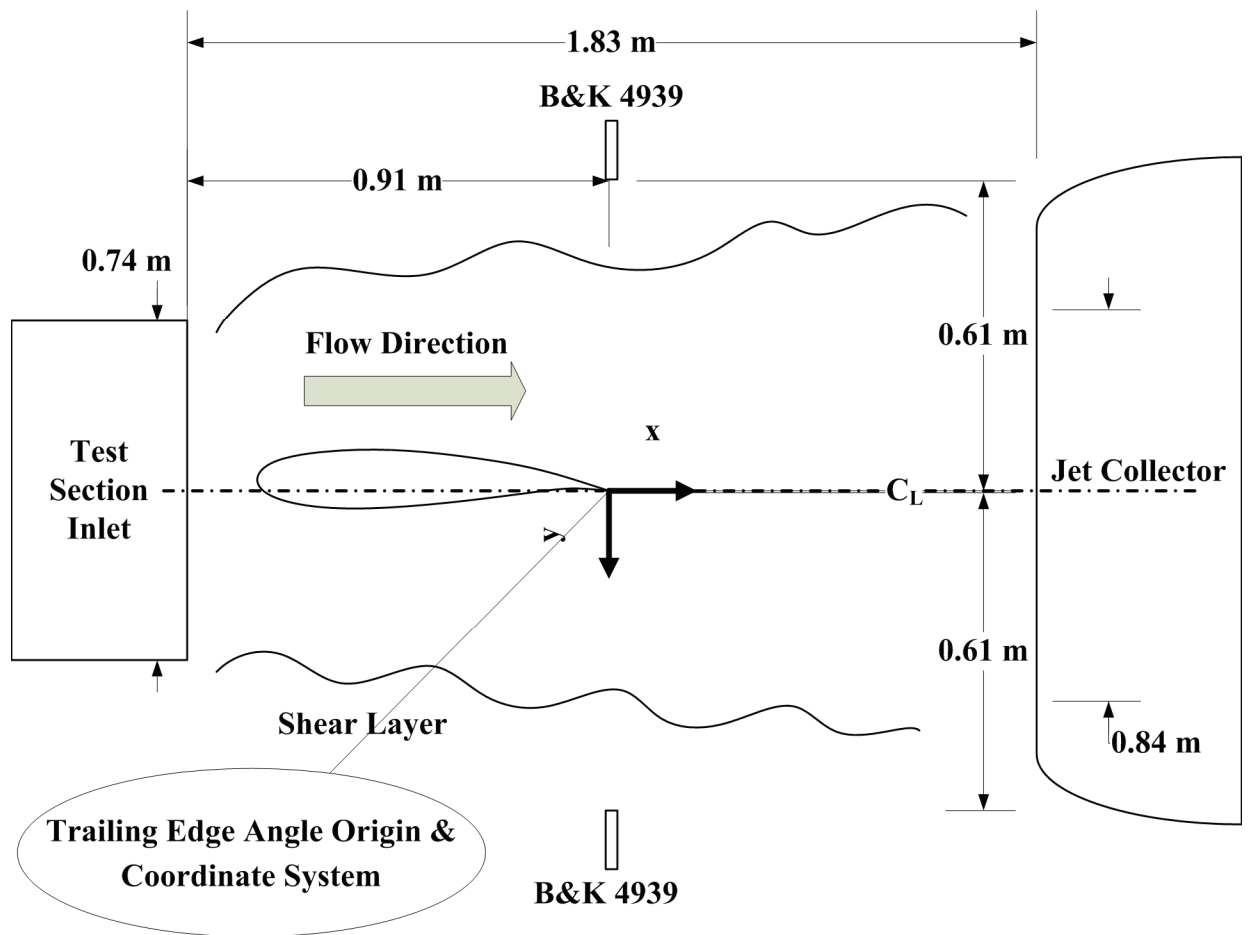


Figure 4-31. Installation schematic for coherent output power measurements.

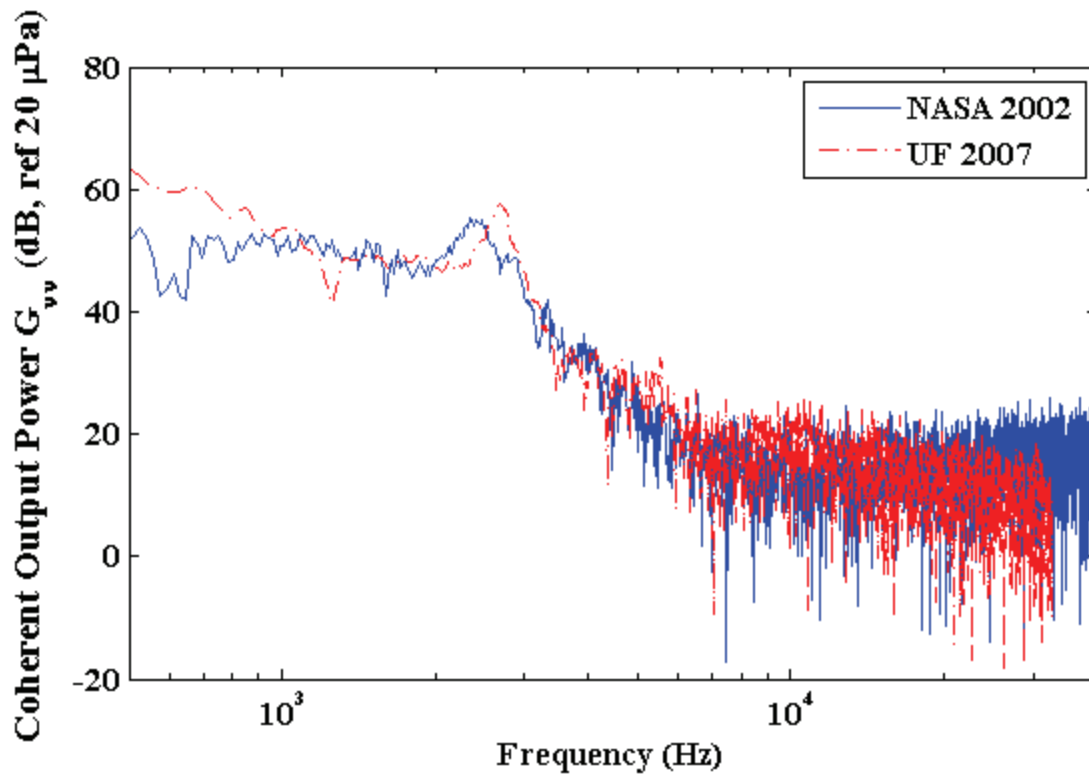


Figure 4-32. Coherent Output Power compared between two experiment sets.

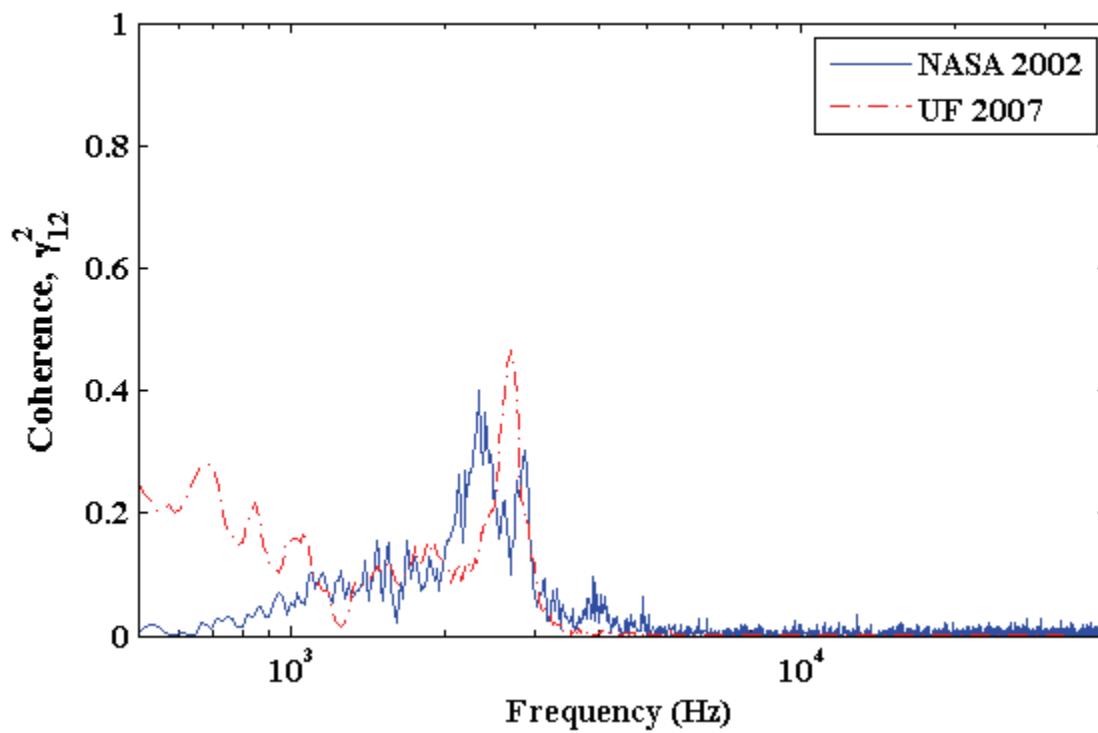


Figure 4-33. Cross-channel coherence compared between two experiment sets.

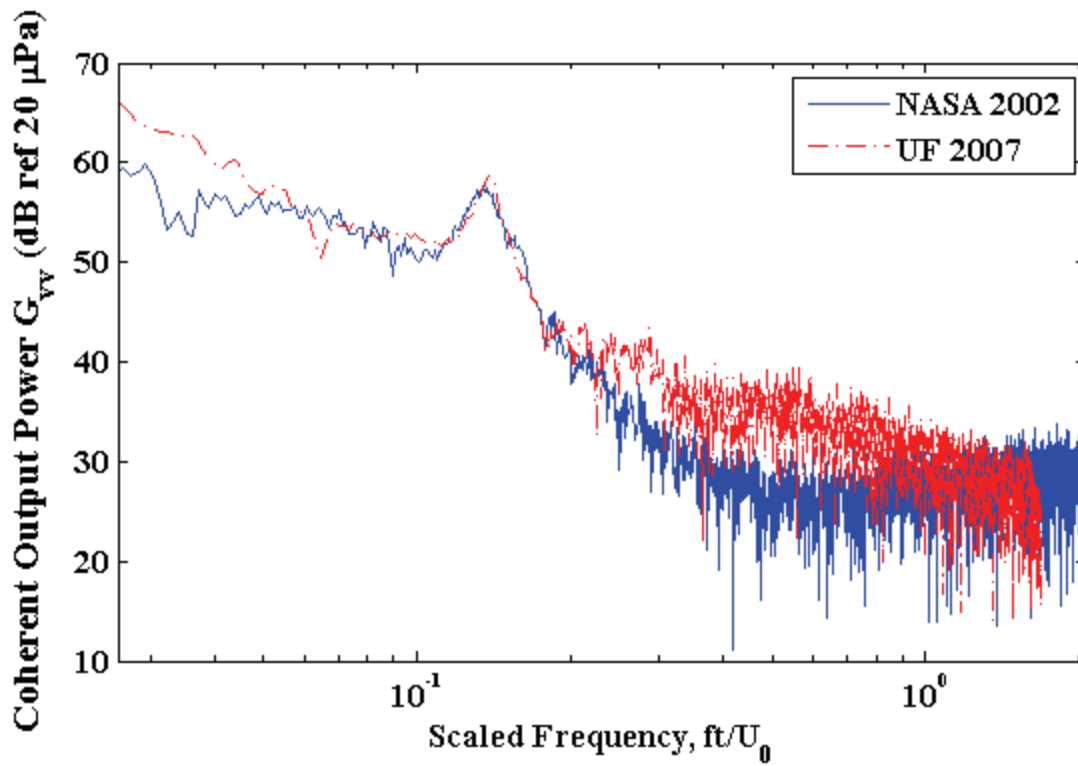


Figure 4-34. Coherent Output Power plotted as a function of scaled frequency.

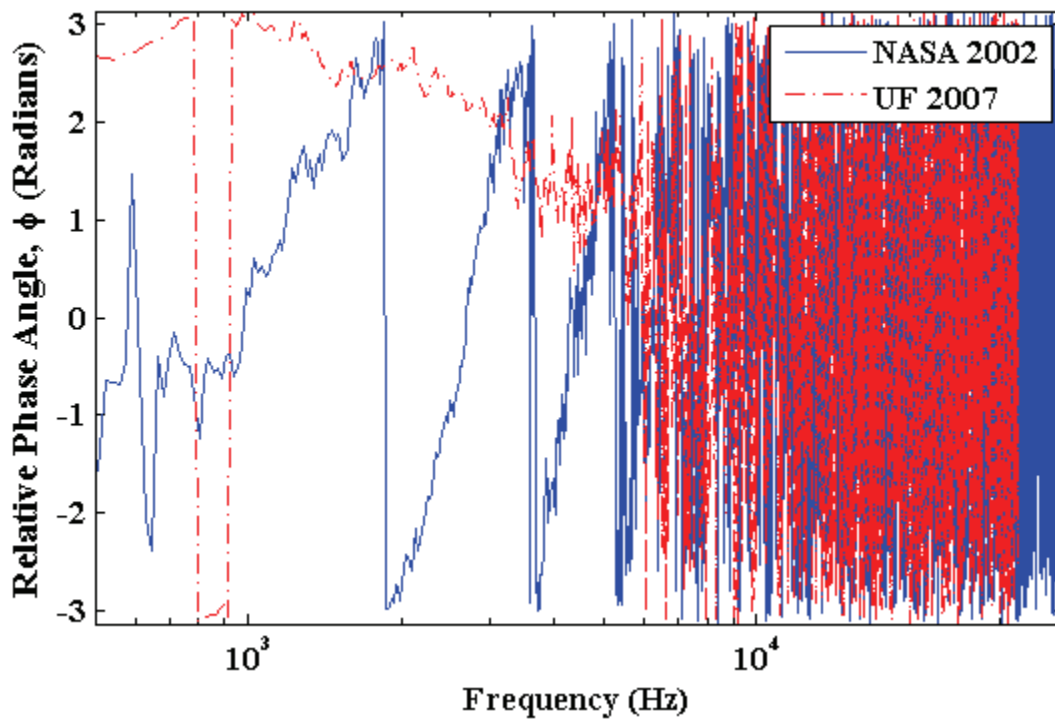


Figure 4-35. Cross-channel phase angle compared between two experiment sets.

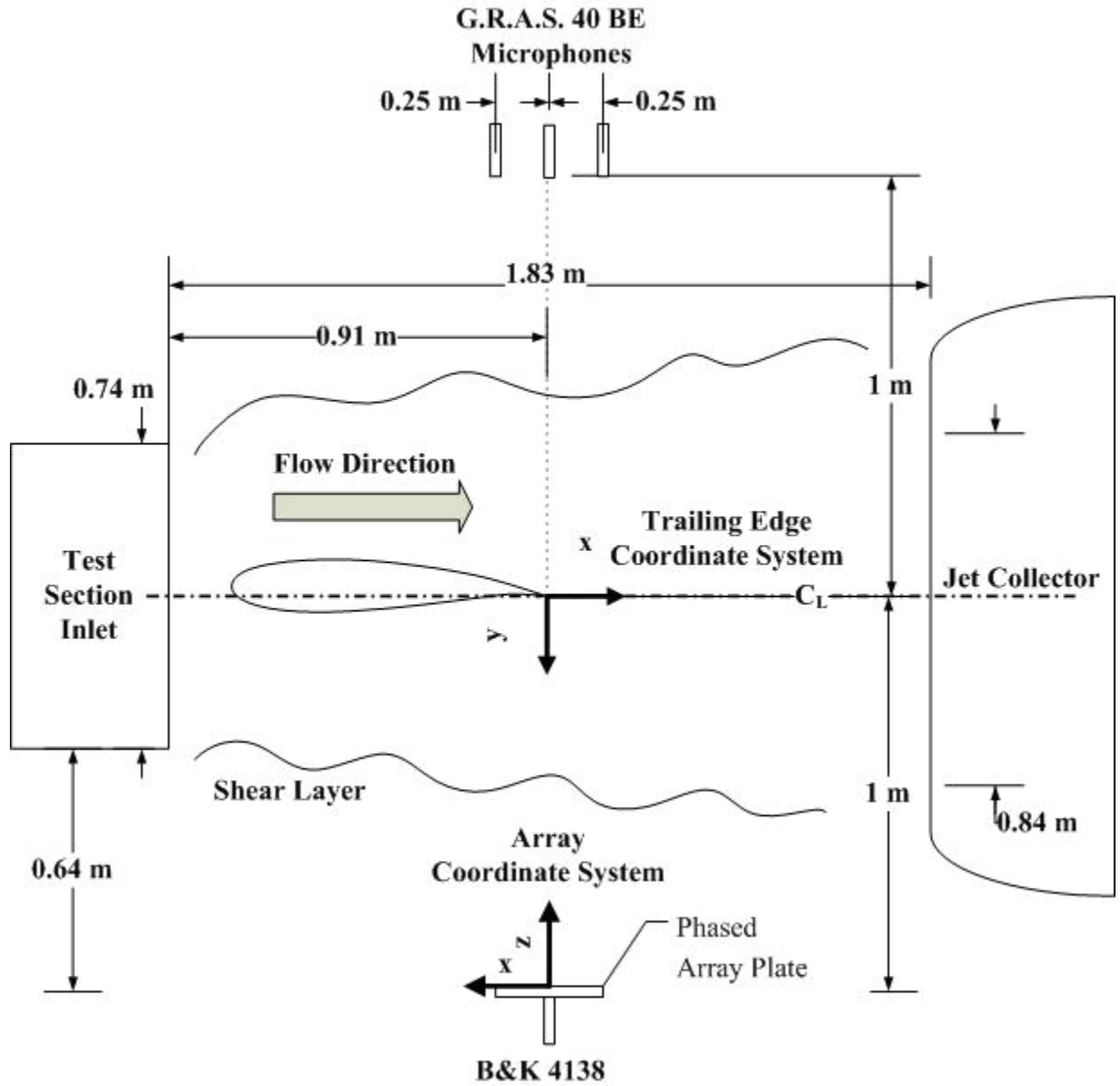


Figure 4-36. Baseline experimental configuration with phased array.

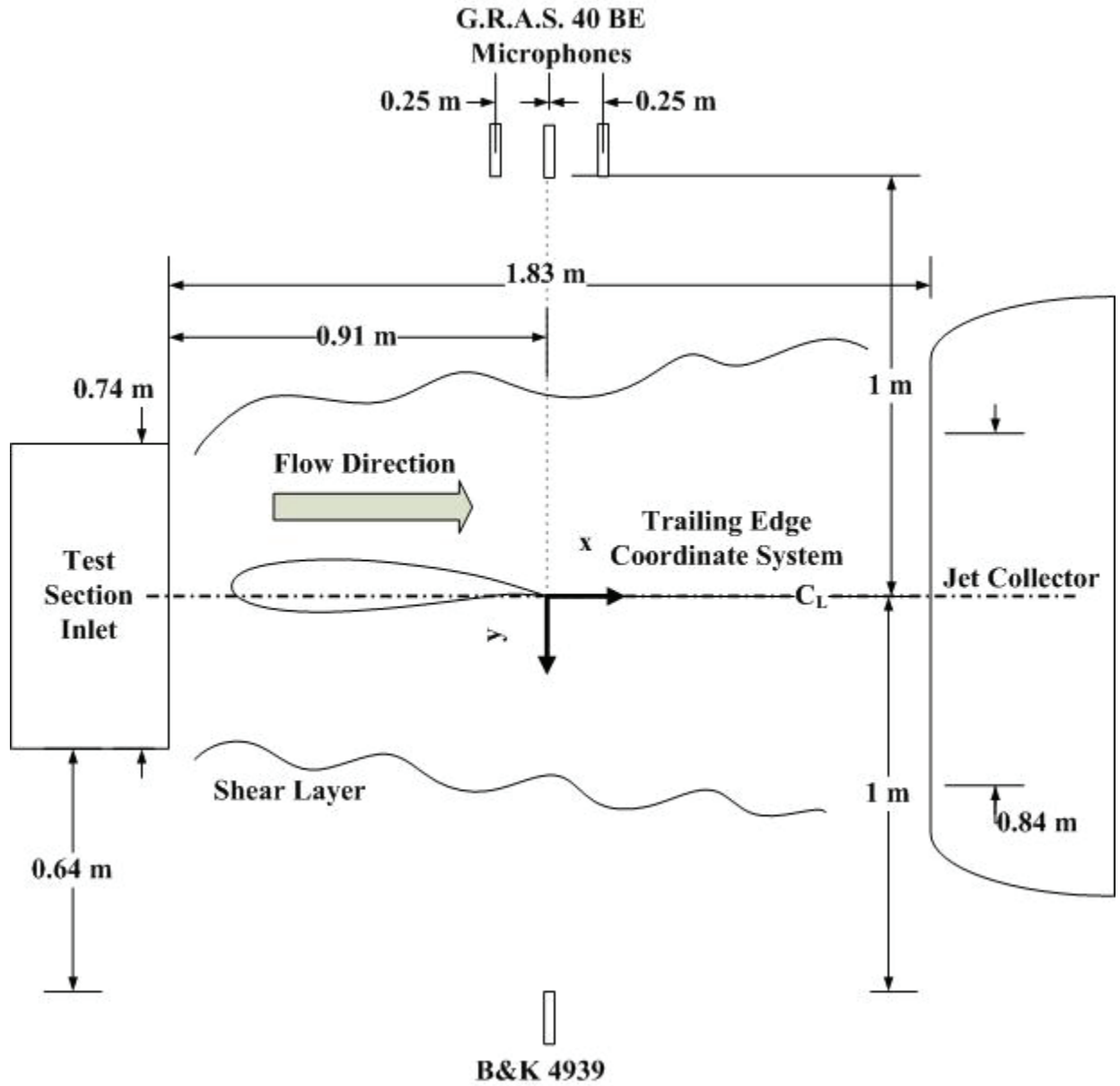


Figure 4-37. Experimental configuration with free field microphone located at equivalent array location in free space.

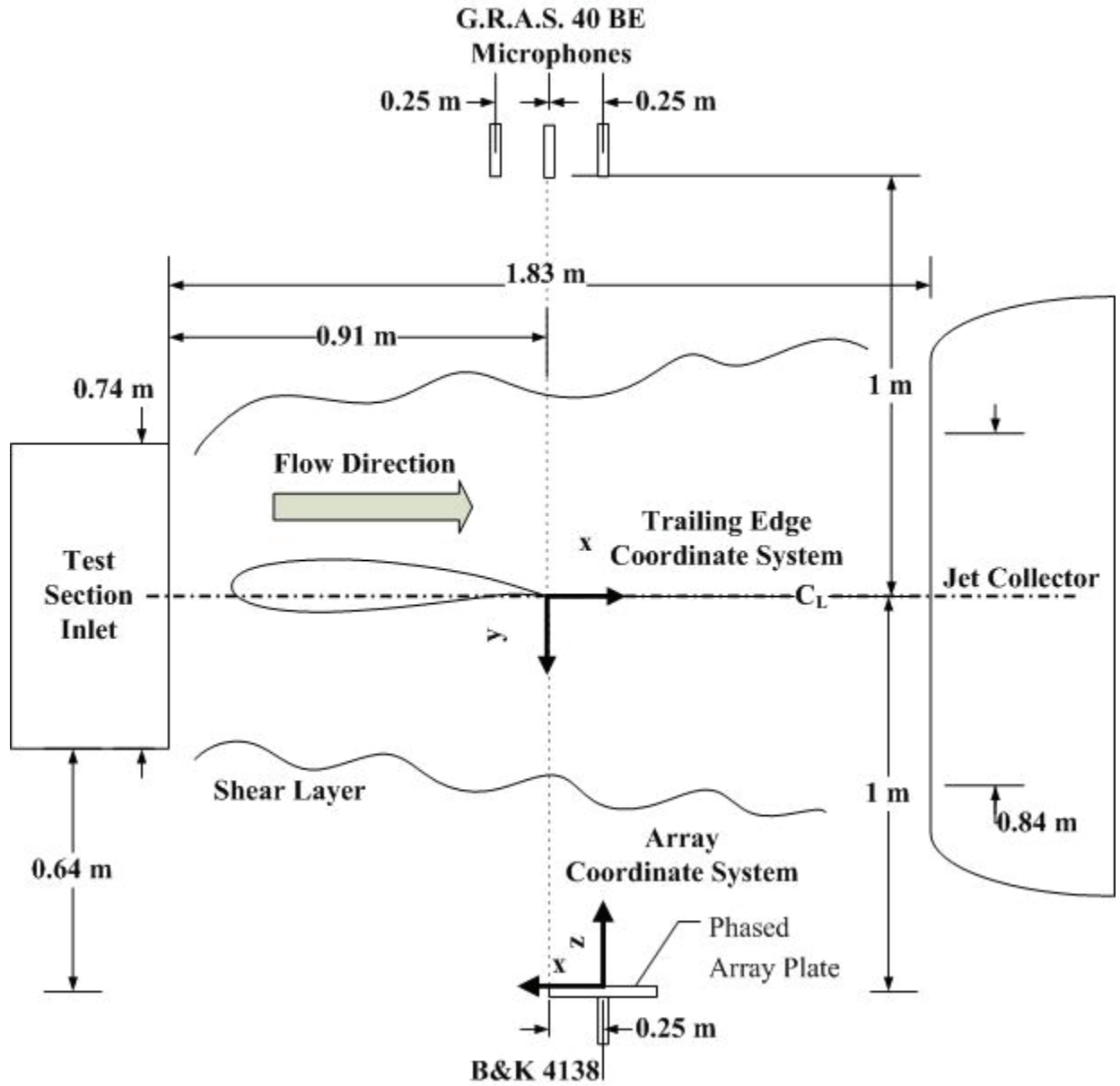


Figure 4-38. Experimental configuration with array horizontally offset from trailing edge by 0.25 m.

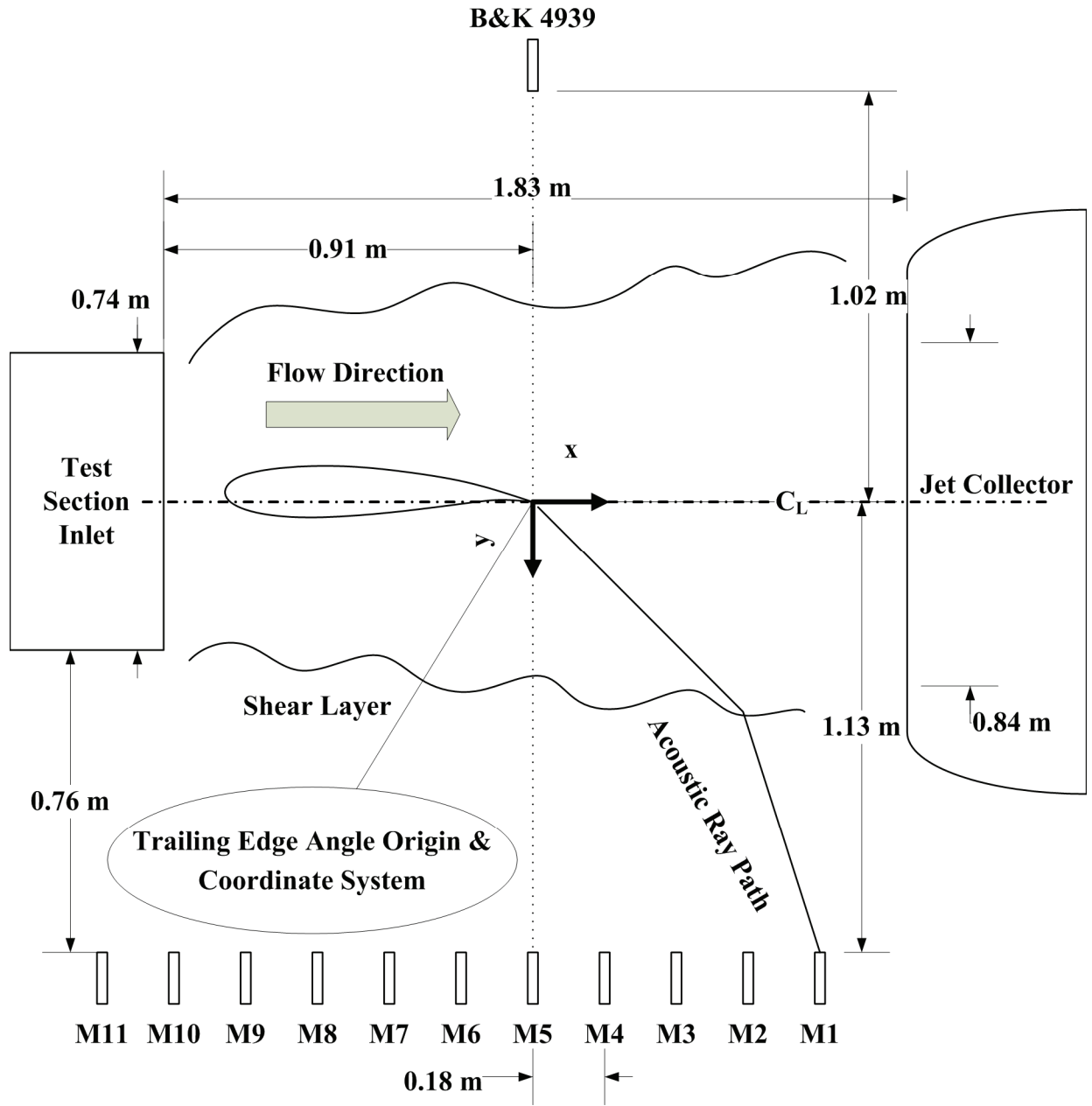


Figure 4-39. Experimental configuration for linear array measurements conducted prior to current body of research.

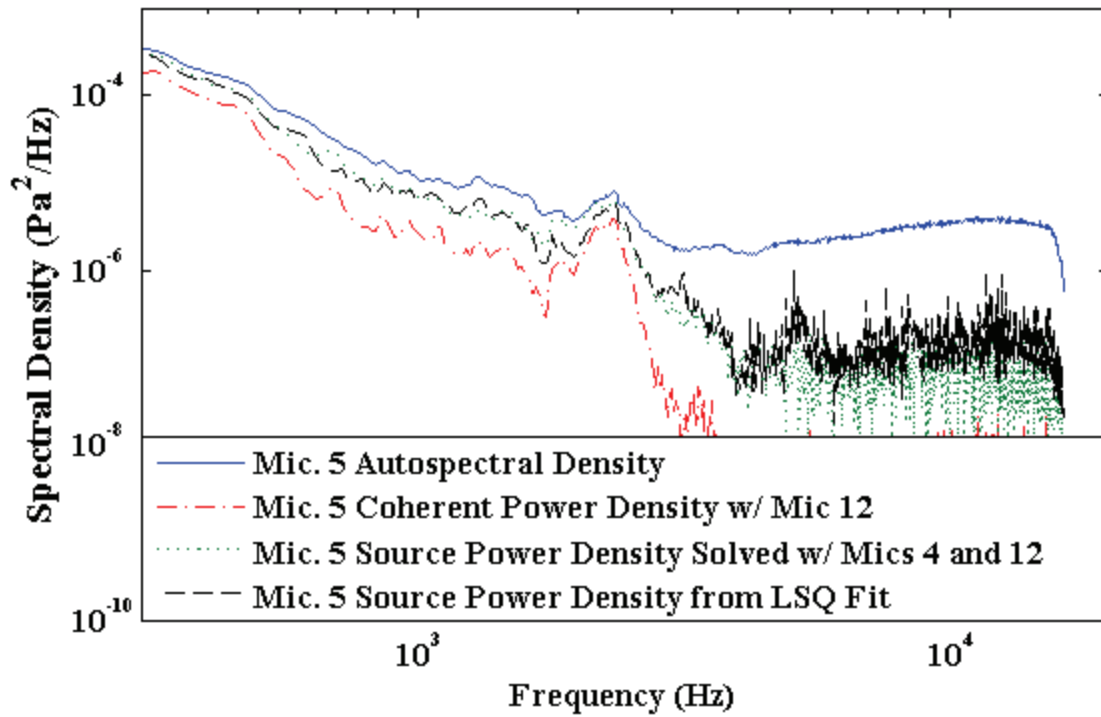


Figure 4-40. Comparison of differing coherence-based noise reduction techniques.

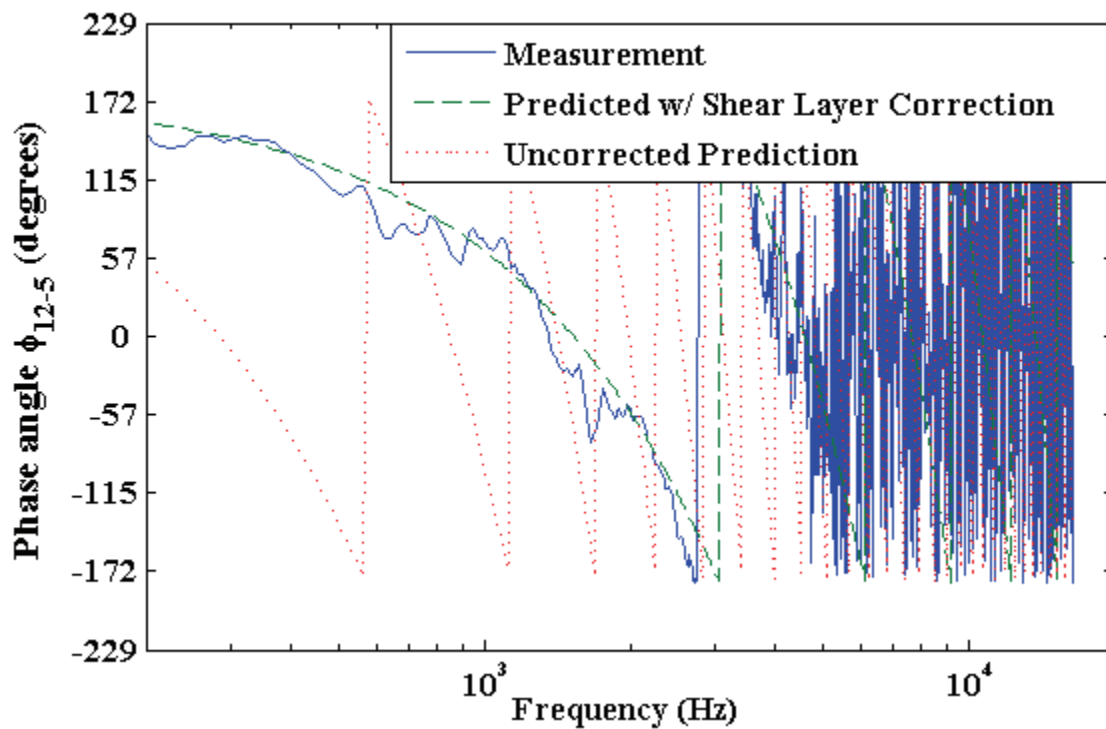


Figure 4-41. Effect of shear layer correction on reliability of dipole-like assumption.

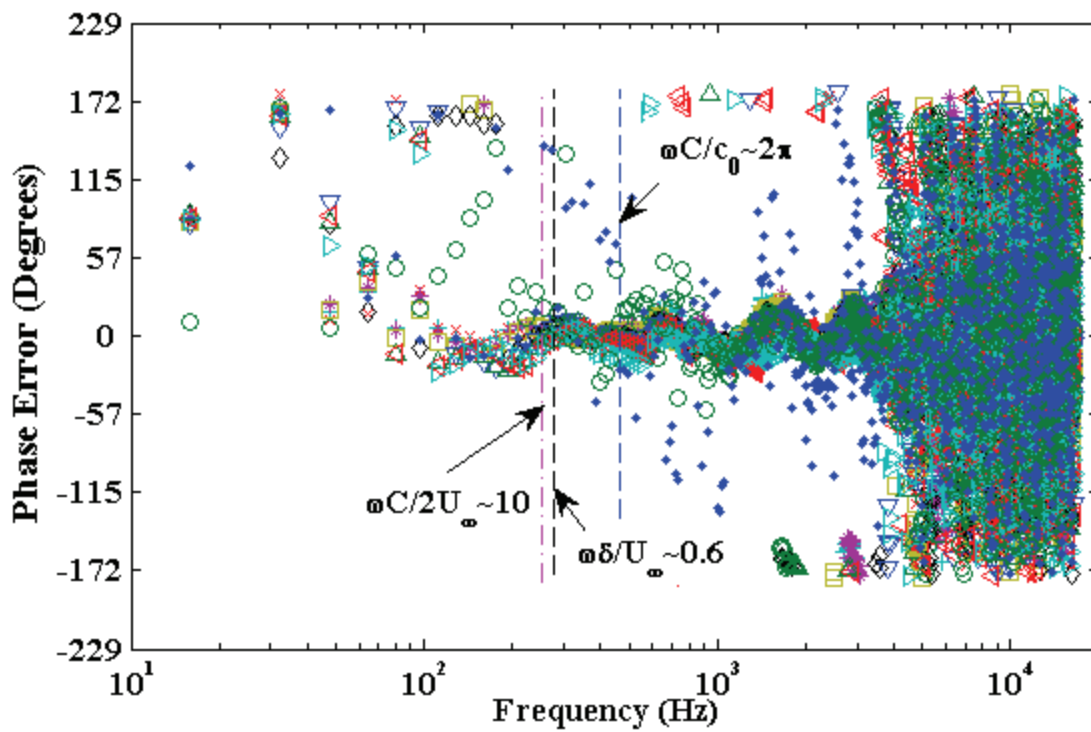


Figure 4-42. Phase error comparison for linear array microphones, referenced to microphone 12.

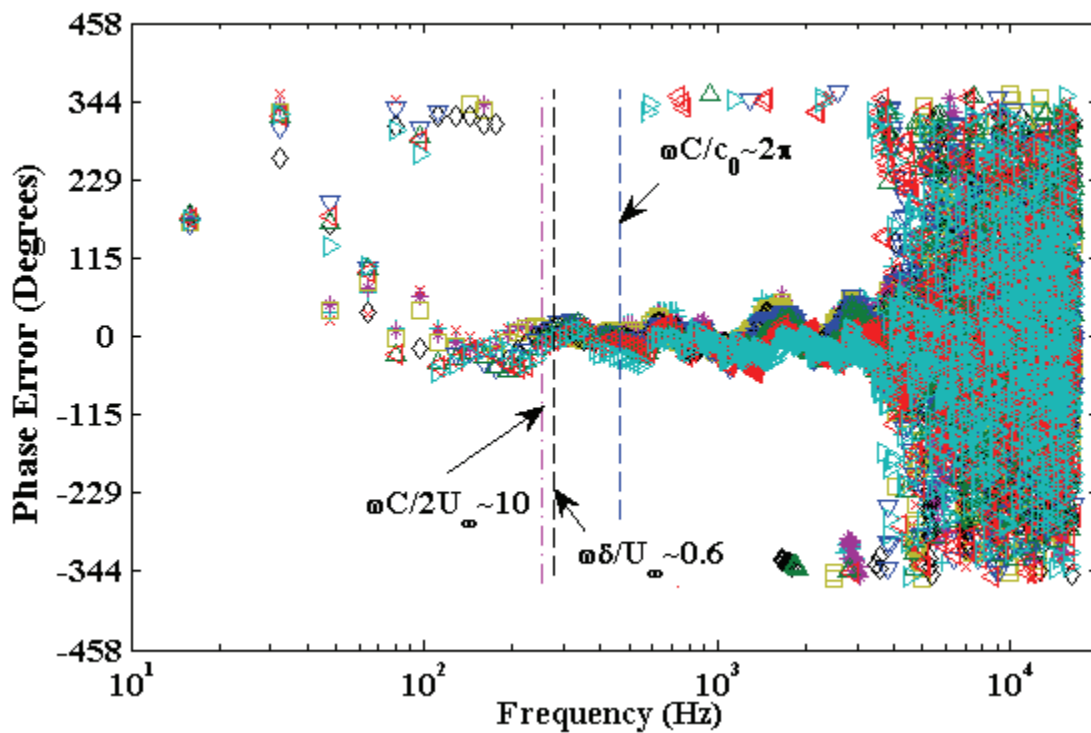


Figure 4-43. Phase error comparison for non-contaminated linear array microphones,

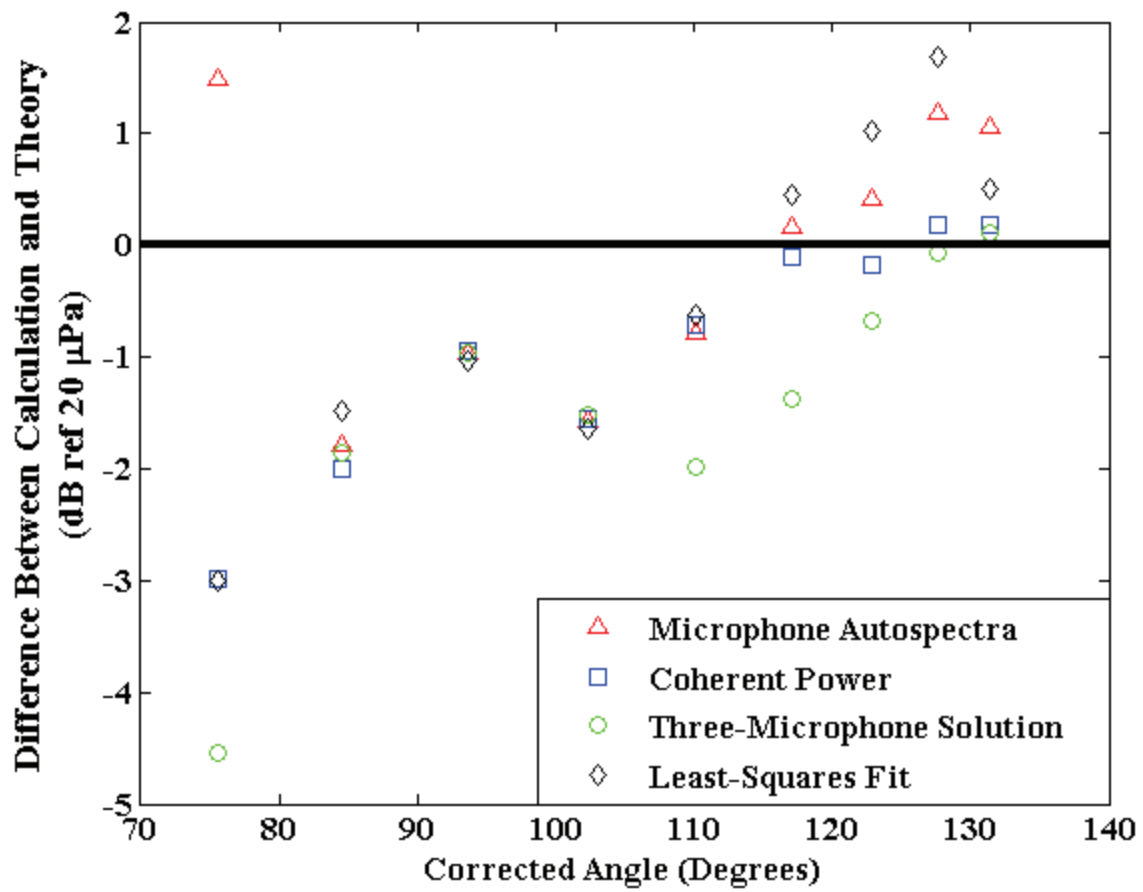


Figure 4-44. Comparison of power predictions from different methodologies.

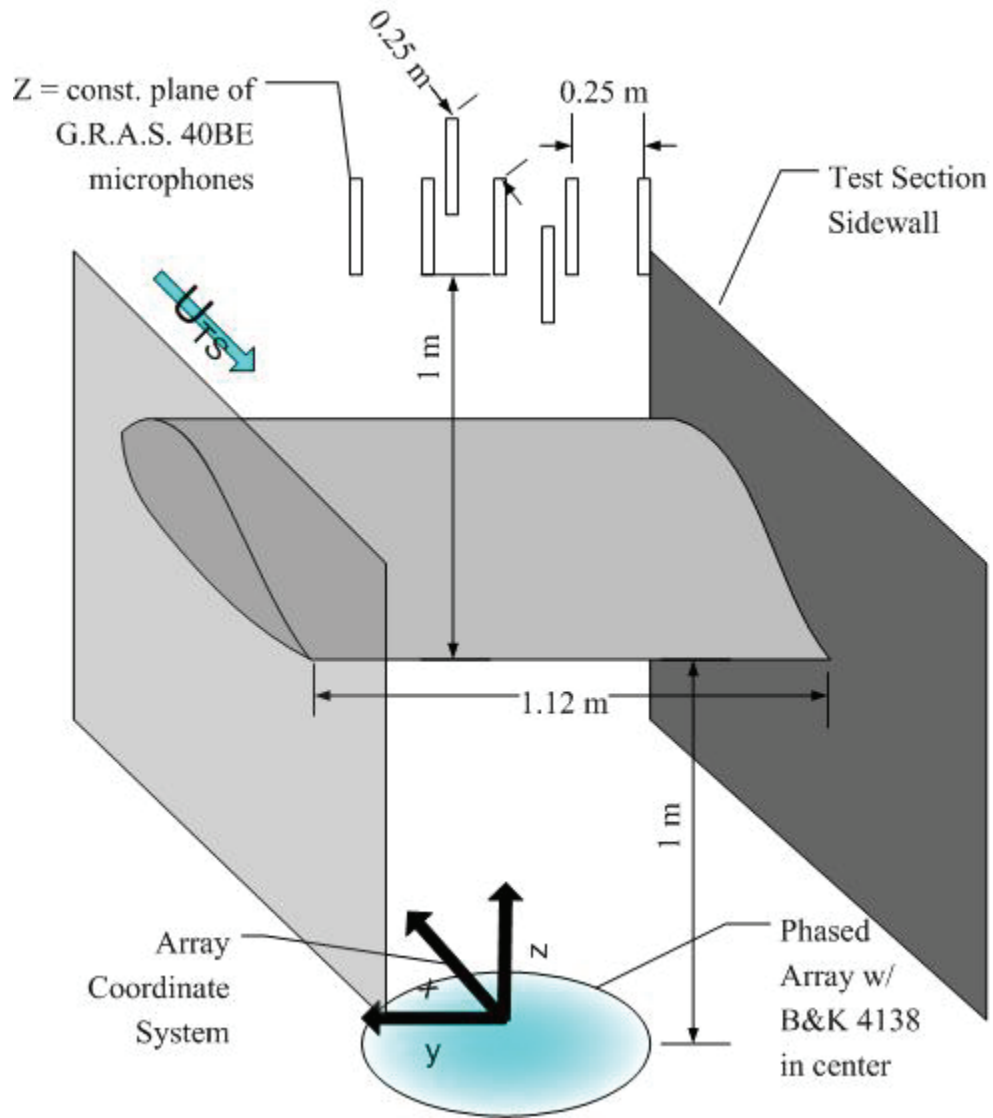


Figure 4-45. Isometric schematic of baseline experimental configuration.

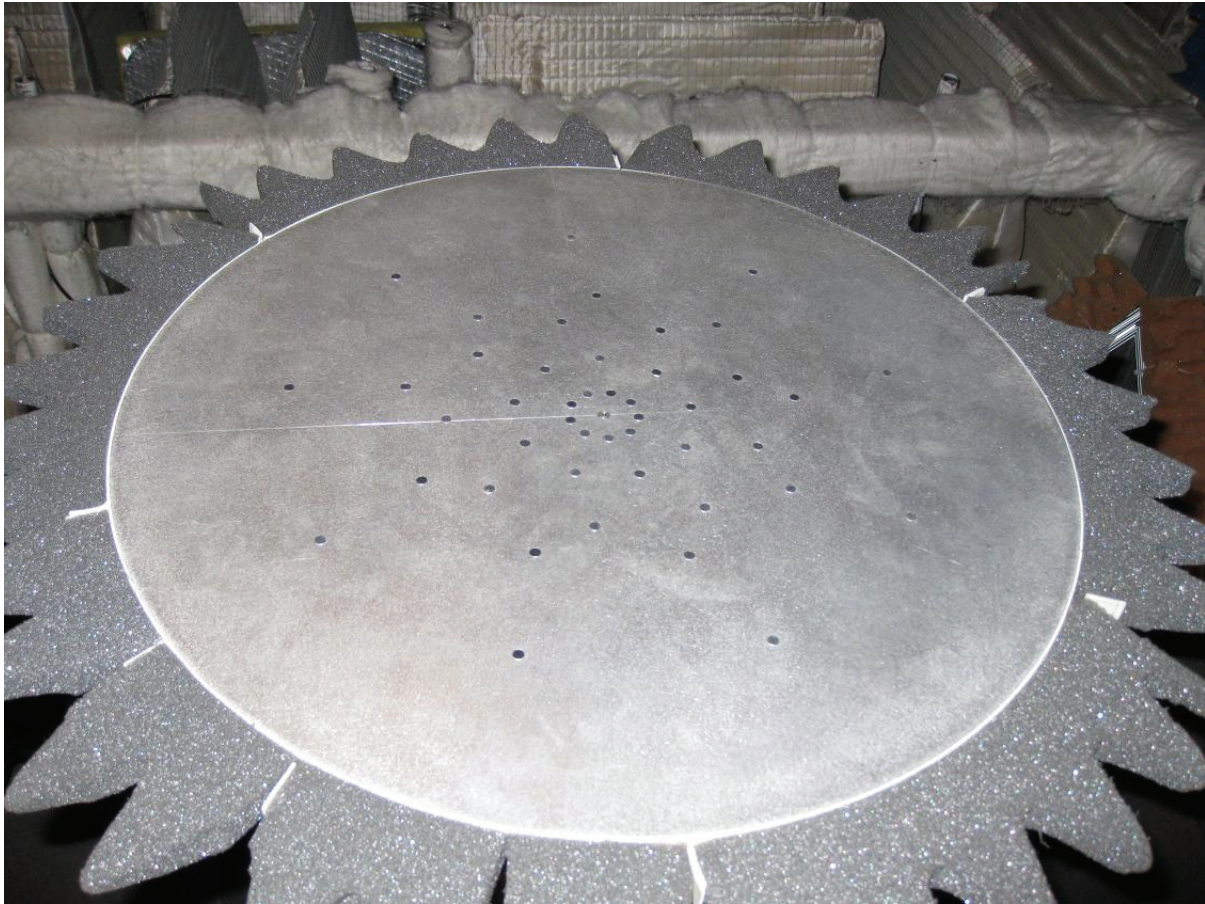


Figure 4-46. Layout of the UFAFF medium aperture array with acoustic treatment.

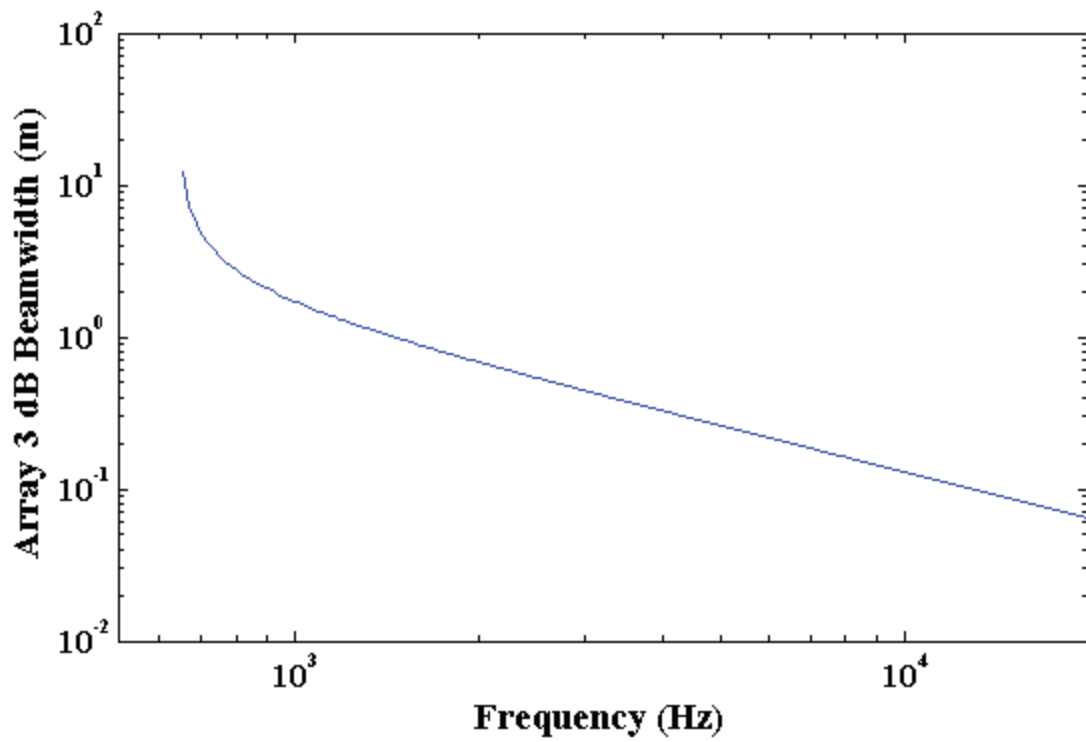


Figure 4-47. 3 dB beamwidth of the UFAFF medium aperture array as a function of frequency.

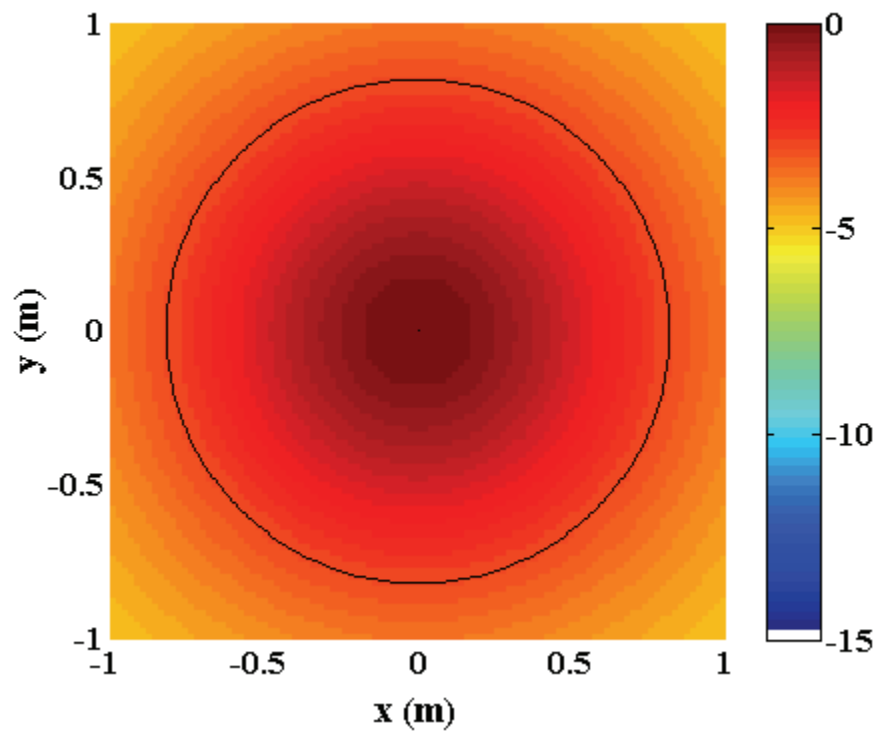


Figure 4-48. PSF for medium-aperture array at 1,024 Hz.

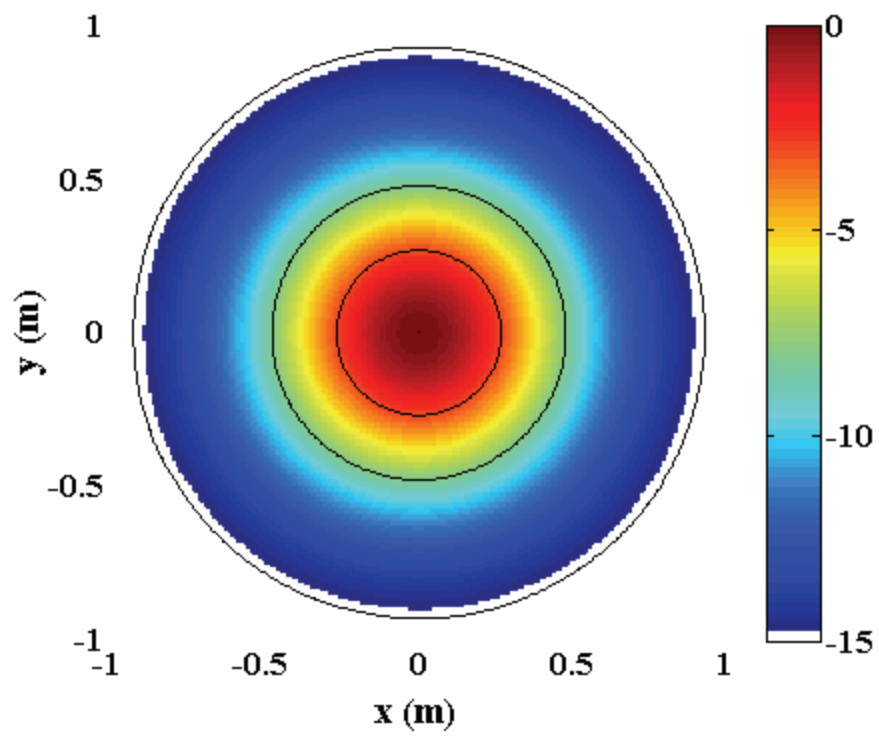


Figure 4-49. PSF for medium-aperture array at 2,512 Hz.

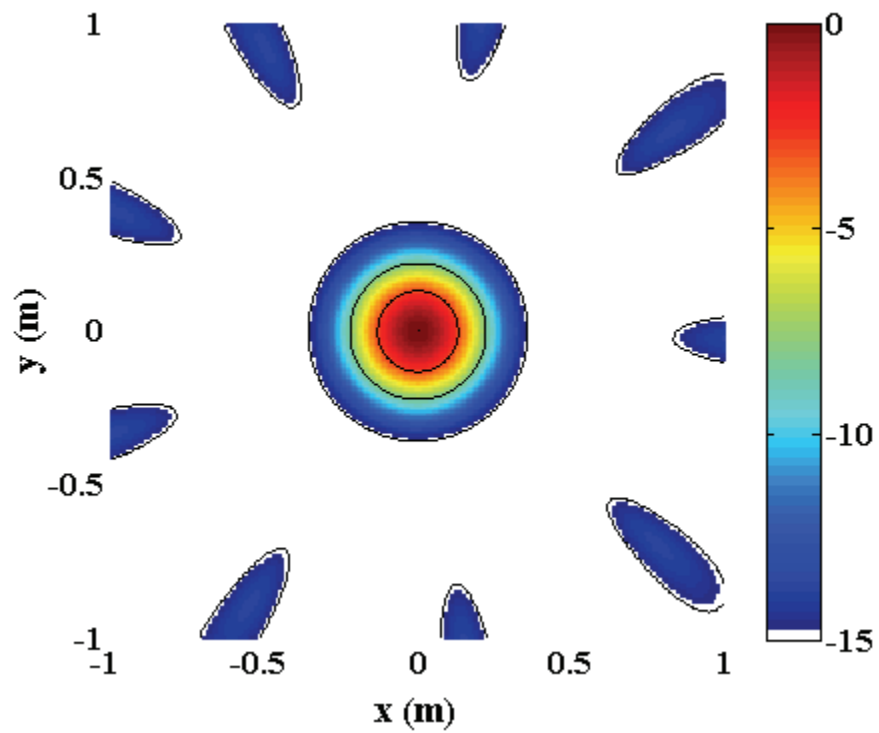


Figure 4-50. PSF for medium-aperture array at 5,008 Hz.

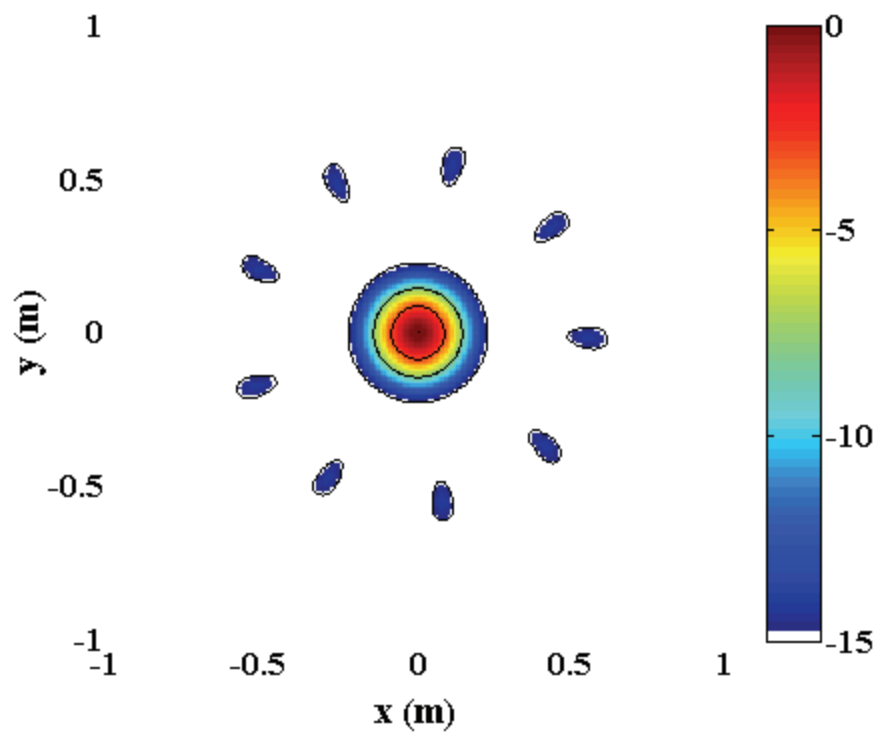


Figure 4-51. PSF for medium-aperture array at 7,600 Hz.

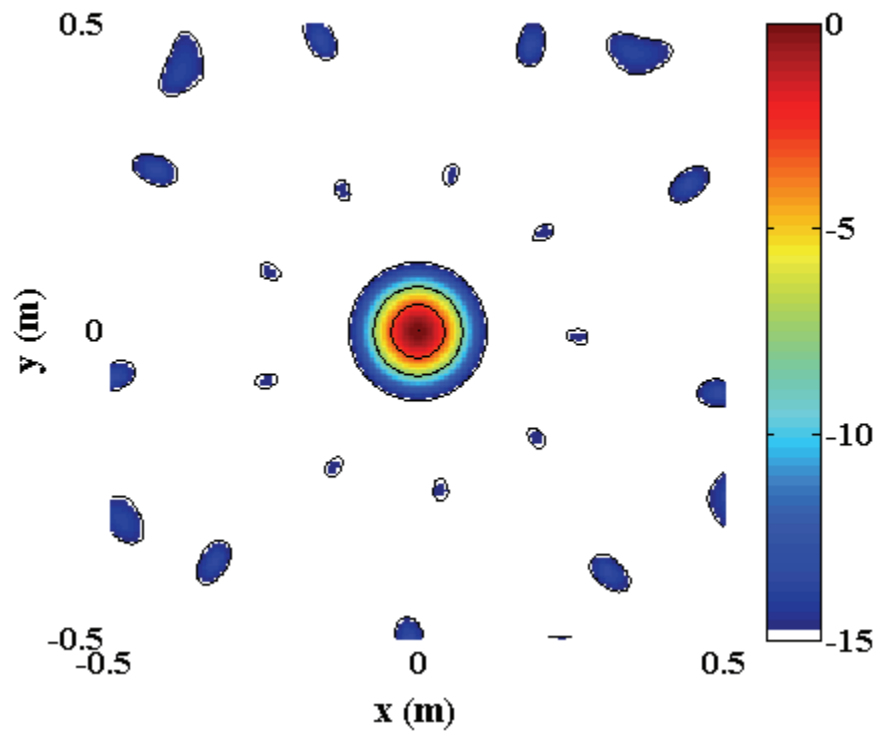


Figure 4-52. PSF for medium-aperture array at 15,008 Hz.

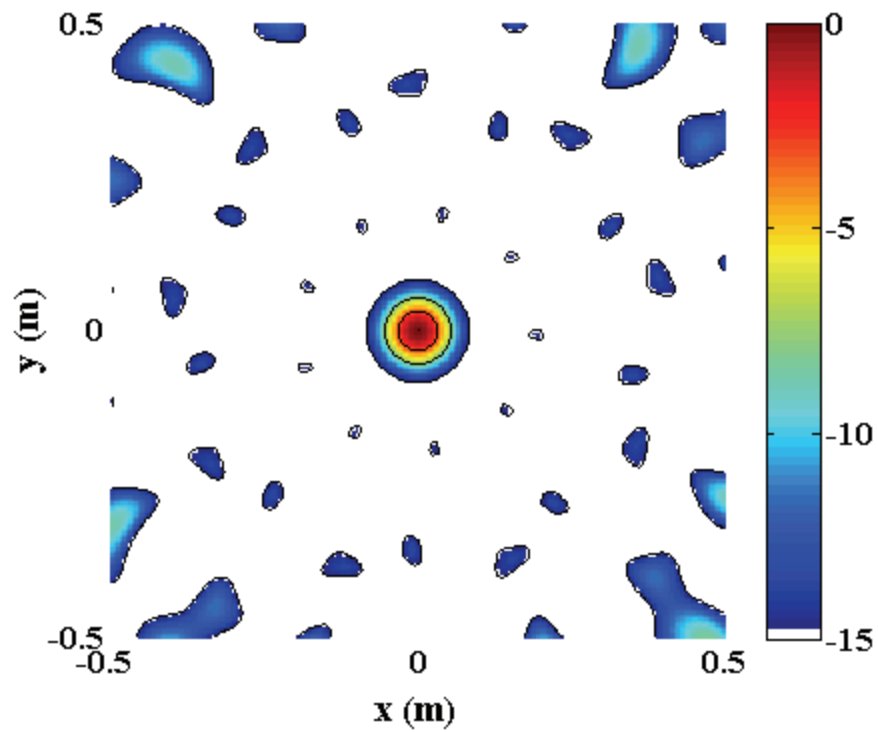


Figure 4-53. PSF for medium-aperture array at 20,000 Hz.

Table 4-1. Key UFAFF design characteristics.

Facility Characteristic	Design Value
Maximum test section velocity	76 m/s
Test section height	0.74 m
Test section width	1.12 m
Test section length	1.83 m
Maximum Reynolds number (based on model chord of 2/3 rd test section width, or 0.75 m)	3.7×10^6
Measured turbulence intensity	<0.05%

Table 4-2. UF NACA 63-215 Mod-B airfoil profile design coordinates.

x, m	y, m	x, m	y, m	x, m	y, m	x, m	y, m	x, m	y, m
0.7374	0.0013	0.5845	0.0247	0.2784	0.0634	0.0005	-0.0025	0.3876	-0.0399
0.7364	0.0015	0.5808	0.0254	0.2583	0.0638	0.0006	-0.0030	0.4060	-0.0378
0.7322	0.0021	0.5747	0.0265	0.2404	0.0639	0.0008	-0.0034	0.4244	-0.0355
0.7265	0.0029	0.5711	0.0271	0.2218	0.0640	0.0016	-0.0050	0.4428	-0.0332
0.7230	0.0033	0.5650	0.0282	0.2034	0.0641	0.0023	-0.0063	0.4613	-0.0307
0.7172	0.0041	0.5614	0.0289	0.1850	0.0640	0.0031	-0.0073	0.4797	-0.0280
0.7137	0.0046	0.5552	0.0300	0.1665	0.0637	0.0039	-0.0082	0.5086	-0.0236
0.7081	0.0054	0.5516	0.0307	0.1481	0.0631	0.0077	-0.0117	0.5124	-0.0230
0.7045	0.0059	0.5455	0.0318	0.1297	0.0623	0.0151	-0.0162	0.5315	-0.0200
0.6997	0.0065	0.5419	0.0324	0.1112	0.0609	0.0226	-0.0196	0.5352	-0.0194
0.6954	0.0071	0.5358	0.0335	0.0928	0.0588	0.0300	-0.0224	0.5543	-0.0165
0.6897	0.0078	0.5322	0.0342	0.0743	0.0559	0.0374	-0.0249	0.5582	-0.0160
0.6862	0.0083	0.5261	0.0352	0.0669	0.0543	0.0448	-0.0271	0.5772	-0.0131
0.6791	0.0092	0.5226	0.0359	0.0595	0.0525	0.0522	-0.0291	0.5811	-0.0126
0.6768	0.0095	0.5165	0.0369	0.0521	0.0503	0.0595	-0.0308	0.6002	-0.0099
0.6696	0.0106	0.5129	0.0375	0.0447	0.0479	0.0669	-0.0325	0.6040	-0.0094
0.6674	0.0109	0.5069	0.0385	0.0373	0.0448	0.0743	-0.0339	0.6231	-0.0069
0.6615	0.0118	0.4981	0.0400	0.0299	0.0412	0.0927	-0.0372	0.6270	-0.0065
0.6579	0.0123	0.4797	0.0431	0.0224	0.0367	0.1112	-0.0399	0.6461	-0.0043
0.6520	0.0133	0.4613	0.0460	0.0150	0.0306	0.1296	-0.0422	0.6494	-0.0040
0.6484	0.0138	0.4429	0.0488	0.0075	0.0221	0.1480	-0.0441	0.6499	-0.0039
0.6425	0.0148	0.4245	0.0513	0.0038	0.0155	0.1665	-0.0457	0.6691	-0.0021
0.6388	0.0154	0.4060	0.0537	0.0030	0.0137	0.1849	-0.0469	0.6724	-0.0019
0.6329	0.0164	0.3920	0.0554	0.0023	0.0118	0.2033	-0.0478	0.6729	-0.0018
0.6292	0.0170	0.3866	0.0560	0.0015	0.0094	0.2217	-0.0484	0.6922	-0.0008
0.6233	0.0180	0.3778	0.0570	0.0008	0.0064	0.2402	-0.0486	0.6955	-0.0007
0.6197	0.0186	0.3692	0.0579	0.0006	0.0057	0.2586	-0.0485	0.6960	-0.0007
0.6136	0.0196	0.3590	0.0589	0.0005	0.0048	0.2770	-0.0481	0.7154	-0.0010
0.6100	0.0203	0.3508	0.0596	0.0003	0.0039	0.2955	-0.0474	0.7187	-0.0011
0.6039	0.0213	0.3412	0.0604	0.0002	0.0026	0.3139	-0.0464	0.7193	-0.0011
0.6003	0.0219	0.3323	0.0610	0.0000	0.0000	0.3323	-0.0452	0.7347	-0.0013
0.5943	0.0230	0.3139	0.0622	0.0002	-0.0010	0.3507	-0.0436	0.7352	-0.0013
0.5906	0.0236	0.2955	0.0630	0.0003	-0.0018	0.3692	-0.0418	0.7374	-0.0013

Table 4-3. UF NACA 63-215 Mod-B chord wise pressure tap locations.

Tap number	Tap distance from leading edge, m
1	0.0000
2	0.0037
3	0.0074
4	0.0147
5	0.0221
6	0.0313
7	0.0405
8	0.0516
9	0.0663
10	0.0884
11	0.1105
12	0.1363
13	0.1694
14	0.2099
15	0.2541
16	0.3094
17	0.3683
18	0.4420
19	0.5156
20	0.5525
21	0.5893
22	0.6261
23	0.6629
24	0.6998

Table 4-4. Geometric and corrected microphone angles.

Microphone number	Geometric angle from trailing edge, degrees	Corrected angle from trailing edge ($M = 0.17$), degrees	Geometric distance from trailing edge, m	Corrected distance from trailing edge ($M = 0.17$), m
1	57.7	59.2	1.34	1.34
2	64.7	67.1	1.25	1.25
3	72.5	75.6	1.19	1.19
4	81.0	84.6	1.14	1.15
5	90.0	93.6	1.13	1.13
6	99.0	102.3	1.14	1.15
7	107.5	110.1	1.19	1.19
8	115.3	117.0	1.25	1.25
9	122.3	122.8	1.34	1.34
10	128.3	127.6	1.44	1.44
11	133.4	131.5	1.56	1.56

Table 4-5. UFAFF medium-aperture array microphone design coordinates.

x, in.	y, in.	x, in.	y, in.	x, in.	y, in.
0.7310	0.0000	1.7023	-0.8207	1.7268	-3.8568
0.5600	0.4699	1.8316	0.4655	3.802	-1.8445
0.1269	0.7199	1.1039	1.5339	4.0981	1.0309
-0.3655	0.6331	-2.7990	1.6970	2.4767	3.4239
-0.6869	0.2500	-3.2350	-0.4992	-0.3036	4.2149
-0.6969	-0.2500	-2.1572	-2.4618	-2.9418	3.0336
-0.3655	-0.6331	-0.0701	-3.2725	-5.1648	-4.1624
0.1269	-0.7199	2.0498	-2.5520	-1.2809	-6.5084
0.5600	-0.4699	3.2106	-0.6373	3.2023	-5.8091
-0.1404	1.8846	2.8691	1.5755	6.1871	-2.3916
-1.3189	1.3535	1.1852	3.0512	6.2769	2.1449
-1.8803	0.1890	-1.0534	3.0991	3.4297	5.6778
-1.5619	-1.0639	-4.2035	0.4329	-1.0223	6.5540
-0.5127	-1.8190	-3.4984	-2.3703	-4.9960	4.3635
0.7765	-1.7229	-1.1563	-4.0645	-6.6319	0.1313

Table 4-6. Test matrix of experiments to study measurement techniques.

Array Location	Mach number range	Geometric Angles of Attack
1 m below trailing edge	0.05 to 0.19 in 0.01 increments	-1.5°, 0°, 1.5°
1 m below trailing edge and 0.25 m downstream	0.05 to 0.19 in 0.01 increments	0°
Removed, B&K 4939 1 m below trailing edge	0.05 to 0.19 in 0.01 increments	0°

CHAPTER 5 RESULTS & DISCUSSION

This chapter will discuss the results of the experiments from the test matrix proposed in Table 4-6. First, the data will be evaluated and compared between experimental conditions to check for installation effects of the microphone phased array. This is followed by evaluation of the two- and three-microphone methods available. Analysis will focus on the comparison of results between different installation techniques, and the different ways the two-microphone solution can be computed. Uncertainties will be used to show where different methods agree. Preliminary results from covariance-based approaches will be shown and discussed. Beamforming results will then be computed and compared to previous techniques. Finally, 1/3rd-octave band result scaling will be shown for different Mach numbers and angles of attack, and compared to existing empirical solution codes [Moriarty 2005].

Installation Effects

The first data to be analyzed are autospectral data. The necessity of various processing techniques can be quickly verified by comparing the raw measurement autospectra to background noise measurements, collected in previous work using G.R.A.S. 40BE microphones. Four cases are selected for this evaluation. Two cases are for the phased array installation, Figure 4-36, and two for the free-field microphone installation, Figure 4-37. The zero-degree AoA case will be considered, as the free-field microphone data were not collected for any other angles of attack. Mach numbers of 0.10 and 0.17 are selected for comparison. These data are plotted in Figure 5-1 and Figure 5-2. Background noise data for the facility at a near-equivalent microphone location are only available from previous work in 5 m/s increments, so the background noise data plotted are at a slightly higher speed of 35 m/s for the airfoil experiments' 34.4 m/s at Mach 0.10. For the Mach 0.17 data, which was equivalent to 58.5 m/s, the two

closest background noise data sets are 55 m/s and 60 m/s. Since the experimental data fall between these two values, both noise curves are plotted. The background noise measured is also from a microphone 5" closer to the test section than the data collected with the model installed. Background noise measurements were conducted using G.R.A.S. 40BE 1/4" free field microphones in free space.

Two things are immediately evident from these plots. First, the model's noise is only above the facility background noise for a portion of the audible spectrum. Second, there is a dramatic difference in observed signal from the free-field microphone to the array-installed microphone. In an attempt to separate the local effects of the array installation, such as acoustic scattering and/or flow over the array face, from any global installation effects, these same plots are generated in Figure 5-3 and Figure 5-4 for the upper central microphone from Figure 4-36 and Figure 4-37. Here, background noise measurements are available at the same speeds, but 7" closer to the test section, so background noise comparisons are again qualitative. It is clear from these comparisons that the offset in the array microphone measurement is a local effect, while some of the ripple may be global, at least at the lower Mach number of $M = 0.10$. The term "global" is applied here as installing the phased array on one side of the model affects a free field microphone measurement on the opposing side.

The ripple in the microphone spectra must be addressed next. Ripple in an acoustic spectrum is a characteristic of a reflected acoustic signal. A reflection, as derived in detail in Appendix D, can appear as a ripple in autospectral levels. One way to identify the time scales of a reflection is to look at the cepstrum magnitude of a signal [Randall & Hee 1981]. While the details of this analysis are again shown in Appendix D, in essence an inverse Fourier transform

of the logarithm of a power spectrum's magnitude will accentuate the time scales associated with any ripple in an autospectrum.

The cepstrum magnitudes, or gamnitudes, of the array and free-field microphone autospectra are plotted in Figure 5-5 and Figure 5-6, as a function of quefrequency. Quefrequency can be thought of as lag time, like in correlation analysis, and has dimensions of time. The ripple in the array data manifests as a fluctuation in gamnitude at around a quefrequency of 5.5 – 6.5 milliseconds. This feature appears to be Mach number independent. Multiplying quefrequency by the speed of sound and re-plotting the data for a Mach number of 0.17 can give an indication of the propagation distance of this reflective feature. In this case, the reflected signal appears to have travelled an additional distance of approximately two meters, beyond the initial one meter transit from the airfoil trailing edge, as shown in Figure 5-7. The most likely candidate for a 2 m reflection based on the geometry illustrated in Figure 4-36 would be an acoustic signal which reflects off of the array face and back up to the model (1 m), and then reflects off of the model and back down to the array (1 m).

The ripple in the G.R.A.S. 40BE signal in Figure 5-3 can be analyzed in a similar manner. The cepstrum plots for the array- and free field comparison signals are shown in Figure 5-8. Again, there is a significant difference between the signals at a quefrequency of 6 ms, although the comparison is not as clean as in the previous plots. As these data were acquired simultaneously with the data from the B&K cepstrum analysis, again this corresponds to an additional distance traveled of approximately 2 m. Again Figure 4-36 can be used to illustrate the situation. Here, a wave can be pictured leaving the trailing edge and traveling one meter before arriving at both the array plate and the upper center free field microphone. A reflection then occurs off of the array plate, and travels two additional meters before arriving at the upper microphone. Again, the

array plate is the source of the observed reflection, which would explain why the ripple isn't present in the free field autospectrum plotted in Figure 5-3 for the experimental configuration from Figure 4-37. Note that the ripple is not noticeably present in the G.R.A.S. autospectra in Figure 5-4. One potential hypothesis as to why this is the case could be due to shear layer refraction and convective effects. These are significantly stronger at $M = 0.17$ as compared to $M = 0.10$, and would contribute to the reflected signal from the array being convected downstream of the upper microphone. Also, multiple transitions of the acoustic signal through multiple shear layers could break down the correlation of the reflection with the original signal. Such correlation is required for reflections to cause ripple in autospectra.

Having tentatively identified the ripple feature in the spectra, several things can now be said about it. First, this feature is likely due to a model noise source, and is independent from tunnel background noise. Second, this feature should be expected for all frequencies for which the trailing edge is the source and may be a good indicator that the airfoil trailing edge is significantly contributing to a given bandwidth. The only frequencies which would be unaffected by this effect would be those which are too low (i.e. wavelength too large) to interact with the 20" diameter aluminum disk used for the phased array, and such frequencies are well below the scope of interest of this study, due to the limitations of the acoustic array's calibration bandwidth. Such frequencies also fall below the upper values of Blake's criteria for trailing edge noise [Blake 1986]. Also, as a coherent reflection of the airfoil noise source, this ripple feature should be preserved for all analysis techniques, since none of the present techniques considered can isolate a signal which is an image of a base signal at a specific time delay. Finally, the difference in propagation behavior between the upper and lower microphones when the array is present will invalidate the second, noiseless model of the coherent output power method. This

can be said because Equation (4-17) is dependent on the assumption from Equation (4-15) that the propagation path model from the trailing edge to each microphone is of equal magnitude but opposite phase above and below the model. If one of the microphones is experiencing a reflection which the other does not observe, or observes in a reduced fashion, this assumption cannot hold. Equation (4-14) can still be used as it makes no such assumption, but as shown the results will suffer a bias from SNR issues.

Comparison of Two-Microphone Methods

The two-microphone techniques from Equation (4-14) and Equation (4-17) are now evaluated for the two experimental conditions from Figure 4-36 and Figure 4-37. As just discussed, the cross-spectral magnitude expression of the coherent power, Equation (4-17), is expected to be invalid for measurements with the array plate installed in the tunnel. Nonetheless, this method is compared to the appropriate coherent power method for that installation, Equation (4-14), to evaluate any significant differences. Both techniques are valid for the free field microphone installation. However, they should not give the same results for acoustic signals except under conditions where the measurement is noiseless, as the general coherence method is biased low by the line noise of the opposing microphone, while the cross-spectral magnitude is not. Finally, the noise-contaminated coherent power technique must be evaluated between the cases with the phased array plate, Figure 4-36, and those with the equivalently-located free field microphone, Figure 4-37, to see how if this method is approximately installation-independent. In all subsequent figures, the general coherent power case from Equation (4-14) will be labeled as “COP, General” while the trailing edge noise-specific coherent power case from Equation (4-17) will be labeled as “COP, Dipole Assumption.”

Coherent power results for Mach 0.10 and Mach 0.17 are plotted in Figure 5-9 and Figure 5-10 for the array-based microphone case of Figure 4-36. As plotted, both cases appear to agree

within the frequency range of the shedding peak, which is clearly visible in each plot. However, upon further consideration it is clear that this cannot be the case, as in an ideal measurement the general COP method should underpredict the dipole-specific COP method by the noise power in the measurement. For the two techniques to agree, there would be negligible measurement noise in the second microphone. However, the offset in the raw autospectrum indicates a significant amount of incoherent noise in the first microphone's autospectrum, and as Figure 5-11 shows, the difference between the second microphone's autospectrum and general COP solution would indicate a significant amount of incoherent noise in that microphone's measurement as well. Notably the dipole-assumption COP predicts higher levels than the autospectrum for the second microphone in this case. As the microphone autospectrum should be a sum of signal and noise powers, both of which are non-negative terms, it should not be possible for a signal prediction to be higher than the microphone's autospectrum. This is indicative of a breakdown in the assumptions in this method. As such, the agreement of the two methods in the B&K 4138 prediction for a limited bandwidth is suspect, and may be coincidental.

Coherent power results for Mach 0.10 and Mach 0.17 are plotted in Figure 5-12 and Figure 5-13 for the free field microphone case of Figure 4-37. These appear to be more in-line with the mathematics of each method, where the coherence multiplication method should appear similar to the cross-spectral magnitude method, but with lower levels due to the noise level bias. Note that no shear layer correction has been applied to the dipole-assumption COP case, as for these low lift conditions, with these specific microphone locations, the shear layer corrections should cancel for this method, as previously discussed. The predictions for the opposing G.R.A.S. 40BE microphone are shown in Figure 5-14, and show a more appropriate expected behavior for both methods in regards to the microphone autospectrum. The two methods have very similar

spectral shape up to a frequency of about 3 kHz for the Mach 0.10 case and 5 kHz for the Mach 0.17 case, before degrading to what appears to be noise. In an attempt to determine if the character of the methods changes at these frequencies, the 95% confidence bounds of the methods, computed from Equation (4-18) and Equation (4-20), will be plotted and checked for overlap, shown in Figure 5-15 and Figure 5-16. It is clear from these plots that above the aforementioned frequencies, the measurements are the same within the shown confidence intervals as the blue and red regions overlap to a purple shade, whereas at lower frequencies they are distinct. Also at higher frequencies the size of the confidence intervals grows dramatically, quickly scaling from being one or two dB wide to on the order of tens of decibels. As these techniques are coherence-based, the ordinary coherence between the upper and lower microphones is an obvious culprit, appearing in the denominator of the corresponding equations, Equation (4-18) and Equation (4-20). Figure 5-17 is a plot of the coherence between the two microphones for these two cases, and confirms this behavior.

Finally, the two-microphone prediction between the array case and free field case must be compared. This is only done for the general COP formulation, as the dipole assumption formulation has just been shown to be erroneous for the array case. Figure 5-18 and Figure 5-19 plot the results for Mach numbers of 0.10 and 0.17. As shown, the results of the array installation and free field installation are distinctly different at frequencies of non-zero coherence. The measured coherent field is dramatically different, as would be expected for an installation which generates additional scattering and reflection. These data illustrate that care must be taken when comparing results using different experimental setups, as significantly different physical effects can be observed.

Three-Microphone Method

Two microphone methods have been shown to be affected by the installation of the phased array. The dipole-based coherent power method provides erroneous results when the array plate is present. The general coherent power method should function properly in both cases, but insufficient information is present in the solution to validate the output, since the method is affected by SNR. The behavior of both methods appears consistent for the free field microphone case, but again insufficient information is present to validate the relative behavior, since a noise power estimate is required to check the offset from the one method to the next. The three-microphone method provides an estimate of the SNR, so it is the next method analyzed. Figure 5-20 and Figure 5-21 show the nominal three-microphone signal estimate as compared to the general coherent power results for the installed array cases from Figure 4-36, at Mach numbers of 0.10 and 0.17. Figure 5-22 and Figure 5-23 show the same plots, as well as dipole assumption-based coherent power result, for the free field installation from Figure 4-37 for Mach numbers of 0.10 and 0.17.

As expected, for the array-based cases of Figure 4-36, the three-microphone method falls somewhere between the raw microphone autospectrum and two microphone prediction. Plotting the uncertainties for these two Mach numbers in Figure 5-24 and Figure 5-25 shows that, at least for the non-zero coherence frequency region, the three-microphone method is truly distinct from the coherent power method. For the free field microphone cases, the three-microphone method should match the cross-spectral magnitude method for an ideal source. However, as Figure 5-26 shows, the results are close but distinct for almost the entire coherent measurement region. Specifically, the coherent power method finds a solution between 1-3 dB below the three-microphone method below 1 kHz. Above 1.3 kHz, the coherent power method is off from the three-microphone method by about a decibel until the uncertainty regions become large near 2

kHz. Based on Equation (4-17) and Equation (4-24), both methods provide a noiseless estimate of the coherent acoustic strength. For them to differ, the assumptions inherent in one or both methods must be faulty. For instance, if the dominant source for a given frequency is not located at the trailing edge of the model, such a field could generate misleading results with the dipole assumption-based coherent power method. Alternatively, as discussed in Appendix C, the source field could be sufficiently distributed such that both the three-microphone method and the dipole assumption-based coherent power method both fail. The agreement between both methods when the airfoil trailing edge is the dominant source is reinforced in Figure 5-27, where the two methods completely match in the vicinity of the shedding peak of the airfoil trailing edge. Such a comparison could be a good indicator of the dominance of trailing edge noise within a given bandwidth. If the cross-spectral magnitude and three-microphone methods agree within uncertainty bounds, a dominant acoustic source is likely located in the vicinity of the airfoil trailing edge.

As discussed in Chapter 4, Monte Carlo analysis was used to compute uncertainties for the three-microphone method. This was done using a Gaussian random number generator to perturb the coherence of each microphone combination, using Equation (4-32) to determine the appropriate variance and subsequent standard deviation of the Gaussian random variable. A positivity constraint was assigned in the loop such that when low coherence levels with large variance were perturbed, the resultant coherence could not be negative. Instead it was set to an infinitesimally-small positive value. The behavior of these Monte Carlo simulations must be evaluated. The uncertainty bounds plotted so far have been for 1,000 iterations of the Monte Carlo simulation. To check convergence, 10,000 iterations were run and the confidence interval compared to the 1,000 iteration case. This is shown in Figure 5-28 and Figure 5-29 for the free

field cases. For almost every frequency bin the data appear converged. The cumulative distribution function (cdf) of the data is evaluated at several frequencies in the overall spectrum of the free field Mach number 0.17 case. The frequency 2,512 Hz is selected in Figure 5-30, as this appears to be the shedding peak of the airfoil. Here, the data appear Gaussian in nature with a skewness of 0.168 and a kurtosis of 2.95. The frequency 3,392 Hz is selected in Figure 5-31 as this frequency is where the spread in the uncertainty region becomes large. The data appear nominally Gaussian at first glance, but the non-zero offset at zero power present at the beginning of the cdf is non-physical. This is due to the non-negative zero constraint placed on coherence perturbations in the Monte Carlo analysis. Indeed non-Gaussian behavior is identified via the skewness of 0.492 and a kurtosis of 3.69. Next, the frequency 6,000 Hz is shown in Figure 5-32, and 12,000 Hz in Figure 5-33. These two frequencies are fully into the large uncertainty region. Both show that a significant number of the predictions are forced to zero power. Also, a bimodal shape appears in the data, more pronounced in the 6,000 Hz data than the 12,000 Hz data. Both conditions are dramatically far from Gaussian data behavior, with 6,000 Hz having a skewness of 3.37 and a kurtosis of 12.6, and 12,000 Hz having a skewness of 5.80 and a kurtosis of 36.2.

Finally, the 95% confidence interval is plotted under both the nominal solution and the mean of the Monte Carlo trials in Figure 5-34 and Figure 5-35. It appears that the nominal and mean value diverge as the Monte Carlo trial distribution becomes bimodal, with the mean solution predicting higher than the nominal. This could be an additional breakpoint beyond which the results are considered unreliable. Previous methods of checking for near-zero coherence and a breakdown in regular phase behavior showed similar break frequencies.

Additional Linear Array Analysis

The techniques described by Du et al. [Du *et al.* 2010] are also applied to the data collected, using the data set of the upper array of G.R.A.S. 40BE microphones and the in-plate

B&K 4138 microphone as shown in Figure 4-36. The nominal results for the methods for the default condition of 20 internal iterations are plotted in Figure 5-36, and compared to three-microphone uncertainty levels for the array plate experimental setup. The three-microphone method is used for comparison as it also solves for both signal and noise powers. These methods estimate the same parameters for higher channel counts. As shown in the plot, the methods all come extremely close to the 95% confidence interval of the three-microphone method near the shedding peak of the airfoil, such that within their confidence intervals they may match.

However, discrepancies are seen in most of the rest of the signal bandwidth. This may indicate that the 20 internal iterations to each algorithm are insufficient for this data set, so a brief convergence study was conducted for each method, such that 50 and 100 iterations were also allowed. This becomes important for the uncertainty analysis, as a 1000-iteration Monte Carlo analysis with 20 internal iterations is manageable, and has been conducted for the single case shown in Figure 5-36. The solution time scaled to unmanageable levels for the scope of this research with internal iteration counts of 50 and 100.

Figure 5-37 shows the solution variation with increasing internal iteration count for the Frobenius Norm Method. As shown, for the entire range for which the solution appears well-behaved, the solution output is independent of iteration count. This solution could be considered converged. However, in the upper frequency range of this case, the solution is dependent on iteration count. Figure 5-38 shows the convergence behavior of the Rank-1 Method. Aside from the shedding peak, these data within the expected model acoustic range may not be converged at 20 iterations, or even 50 or 100 iterations. Interestingly, the data for higher frequencies, where most of the coherent power methods discussed so far appear to fail and have severe uncertainty issues, appears converged and well-behaved. However, the physical meaning of this result,

which is in disagreement with all previous methods, is not fully understood, and thus quantitative uncertainty comparison will be avoided for the time being. Finally, Figure 5-39 shows the convergence behavior for the Maximum Likelihood Method. This method again shows convergence in the vicinity of the trailing edge shedding peak, but nowhere else. As none of the methods appear fully converged, the single available Monte Carlo trial will not be presented in this work. It should be noted that all of these methods assume a single coherent source between all of the microphones, as is assumed for two- and three-microphone methods. The number of iterations for convergence could be an indicator of the nature of the acoustic field, and again if the trailing edge is acting as a single, dominant source within a given bandwidth. For frequencies where a given method has difficulty with convergence, there may be an indication that the source field strongly violates the method's assumptions.

Beamforming Results

Phased array data were collected for the entire test matrix and analyzed using a frequency-domain Delay-and-Sum (DAS) beamformer, as discussed previously. However, due to computational expense, only one Monte Carlo analysis of an integrated spectrum was conducted. The zero-degree angle of attack case at a Mach number of 0.17 was selected. Figure 5-40 shows the results of the nominal beamformer inputs and three-microphone data in comparison to the B&K autospectrum from the array installation of Figure 4-36. The two methods are in closest agreement near the model's shedding peak, and have predictions within 1 dB of each other. They have the greatest difference in prediction at approximately 5 kHz, where they differ by over 10 dB. Based on the behavior of the predictions in relation to the microphone autospectrum, this is the region where the coherent acoustic source becomes weak in relation to the incoherent noise. Figure 5-41 shows the uncertainty bounds from the Monte Carlo trials in comparison to the three-microphone method uncertainty bounds. Aside from the shedding peak, the data are

not in agreement for the lower frequencies of the measurement bounds. This could be due to the aperture effects of this smaller array at lower frequencies, the presence of sources which violate the assumptions of the three-microphone method, and even the incoherent source assumption of the beamformer. Based on the uncertainty bounds of the analysis methods, there is overlap and thus agreement at higher frequencies. However, this is due in large part to the uncertainty bounds on the three-microphone method results spanning such a great range of power predictions.

Several features of the uncertainty bounds in the beamformer output are striking and warrant further evaluation. The hump structure in the uncertainty bounds at higher frequencies is one such feature. Also, the trend of the beamformer at frequencies slightly above the shedding peak warrants investigation, as it is significantly different from the three-microphone behavior. Another, as shown in Figure 5-42, is the trending of the nominal integrated level with the Monte Carlo mean. With beamforming, spatial information is available, so at each investigation frequency selected a full test section beam map will be generated, in addition to cumulative distribution function estimates.

The first frequency to be evaluated is 1,024 Hz. This is a frequency where the array has a large main lobe, approximately 1.6 m based on Figure 4-47, so the majority of noise reduction will occur from the diagonal removal operation on the CSM. In effect, because the weighting of the steering vectors from Equation (4-38) will be small at very low frequencies for a small array, at this frequency the DAS output could be considered the mean of the sum of the off-diagonal powers of the CSM. The beam map of these data, with appropriate shear layer corrections applied, is shown in Figure 5-43, and the Monte Carlo cdf in Figure 5-44. In this beam map, as in all subsequent ones, the space occupied by the model is indicated with a shaded rectangle. A

black-bordered box is drawn as the boundary of the integration region. Flow through the test section is from right to left, so the integration box is drawn around the model trailing edge. For this case, allowing for the large array response region, it would appear that the dominant noise source is coming from behind the model. Given the size of the array's main response lobe at this frequency, it would be difficult to blindly state whether the dominant acoustic source is due to the model's wake region or UFAFF's jet collector leading to the diffuser. However, based on the comparison of autospectra in Figure 5-2 between experimental configurations and facility background noise, it is evident that this acoustic source is not solely due to background jet collector effects. The skewness of the Monte Carlo trial data is 0.237, and the kurtosis 3.33.

The second frequency evaluated is the shedding peak as noted in the free microphone cases previously at 2,512 Hz. The beam map is shown in Figure 5-45, and the cdf in Figure 5-46. As expected, the airfoil trailing edge is the dominant noise source in the beam map. The jet collector appears to have some slight contribution to the overall measured noise at this frequency, and very little leading edge or inlet contribution is noticeable. The data skewness is 0.186, and its kurtosis 3.19, showing Gaussian-like behavior as at the previous frequency.

The third frequency, 5,008 Hz is evaluated next, with its beam map shown in Figure 5-47 and cdf in Figure 5-48. This frequency was selected as it is near the point on the integrated spectra where the mean and nominal level predictions begin to diverge, and the uncertainty bounds increase. From the beam map, it is clear that at this frequency sidewall boundary layer noise and jet collector noise are the two dominant sources. Also, while in the previous two frequencies the nominal power prediction fell below the median and mean predictions, here it is nearly the same. With a skewness of 0.338 and kurtosis of 3.59, the data begin to diverge more from expected Gaussian behavior. Also notable is the fact that at this frequency the results are

very different from those predicted by the three-microphone method, even when accounting for uncertainty bounds. This would be consistent with the lack of dominance of the trailing edge noise source.

At 7,600 Hz, the uncertainty bounds span nearly 25 dB, and the nominal integrated value is dramatically higher than the Monte Carlo mean. The beam map of this frequency is shown in Figure 5-49, and its cdf in Figure 5-50. The sidewall noise appears to be the dominant noise source, and collector noise has reduced below the plotted threshold for much of the collector area. A strong noise source is noticeable on the upper leading edge of the airfoil. This may be due to a leak in the sidewalls, which is highly possible given the installation methodology. While it could also be related to the sidewall boundary layer rolling up as a horseshoe vortex around the airfoil leading edge, similar behavior should be seen on the lower leading edge in the plot if that can be a strong noise source. Statistically, the data show a strong bimodal behavior, where the nominal integrated level falls near the peak of the second, smaller mode, while the mean falls towards the end of the first, larger peak. The skewness and kurtosis of the data are of course significantly off from Gaussian values, at 0.904 and 2.18, respectively.

At 8,800 Hz, the spread of the uncertainty region has decreased dramatically from 7,600 Hz. The beam map and cdf of this frequency are shown in Figure 5-51 and Figure 5-52. Again, the sidewalls appear as the dominant noise source. Again, the distribution appears bimodal, with the nominal integrated level falling on the second, smaller peak. The spread between the peaks is reduced from the previous frequency. The data skewness is 0.692, and its kurtosis is 2.38.

At 15,008 Hz, the data spread is again large. The beam map is shown in Figure 5-53, and the cdf in Figure 5-54. The sidewall boundary layers no longer appear to be dominant noise sources. The leading edge source is still strong here, as are some other, unidentifiable noise

sources near the rear of the test section. Within the integration region, little is visible. The data spread behaves similarly to the previous bimodal cases, with a skewness of 0.946 and kurtosis of 2.78.

Finally, at 20,000 Hz, the Monte Carlo mean surpasses the nominal integration by a significant amount. The beam map is plotted in Figure 5-55, and the cdf in Figure 5-56. The same noise sources are visible here as were visible in the 15,008 Hz map, although additional sources appear within the field. These may be sidelobe images of true noise sources. The data spread appears to have returned to single-mode behavior, but with a skewness of -0.482 and kurtosis of 2.50 is significantly deviated from Gaussian. The nominal condition falls on the lower tail of the distribution.

Based on the Monte Carlo trials of the data, it appears that the behavior of the Monte Carlo results appear as tight, near-Gaussian distributions for frequencies where the airfoil trailing edge is dominant. This also appears to be the case for frequencies where airfoil trailing edge noise is a significant contributor, as in the frequencies below the airfoil shedding peak. When the sidewall noise is dominant, the distribution has strong bimodal behavior. This could be inherent in the noise mechanism of the sidewall boundary layers, or it could be due to the sidewall noise passing in or out of the integration region in a manner that is dependent on the Monte Carlo parameters. It would appear that when the sidewalls are no longer a significant contribution, either aperture effects or the beamforming noise floor are the dominant sources within the integration region. At these frequencies, the distribution of the Monte Carlo data again changes character. In future work, detailed uncertainty analysis of the entire beamforming region at all of these frequencies is warranted. Due to computational expense, such analysis is beyond the scope of the current work.

In evaluating DAS integrated levels, a brief discussion should be dedicated to the effect of varying integration bounds. The nominal bounds, 0.4 m x 1.06 m centered on the airfoil trailing edge, are selected to provide some rejection of sidewall noise while capturing the majority of the trailing edge shedding peak behavior. Computational expense is also a consideration. Several frequencies of a single case, Mach number of 0.17 at 0 degree angle of attack, are evaluated with varying integration regions to see what role this effect may play in computing power levels.

The first frequency evaluated is the airfoil shedding peak at 2,512 Hz. The integrated results for different integration bounds are presented in Table 5-1. It is evident from these data that varying the integration region in the x-direction has little effect on computed acoustic levels. Varying the y-dimensions shifts the power by approximately 2.4 to 2.5 dB. A solution on this order of magnitude might be expected if the trailing edge consisted of a line of incoherent dipoles. Including the edges of the span will have a noticeable power contribution. However, doubling the number of sources in the integration region, by doubling the length of trailing edge included in the region, will not double the predicted power as the additional sources may be further from the array.

The next frequency evaluated is 7,600 Hz. This frequency is selected as it has little observable trailing edge noise in its nominal beam map in Figure 5-49, and appears dominated by sidewall noise and the model's leading edge source. The different power predictions are listed in Table 5-2. The results show that DAS is predicting zero power for the airfoil center-span region, as every integration region which completely excludes the sidewall noise by having a small y-dimension is computed as negatively-infinite on a decibel scale. As the integration region begins to include sidewall sources the power prediction climbs dramatically. Similarly, increasing the x-dimension of the integration region substantially increases the power prediction.

This behavior may contribute to the large uncertainty bounds of this frequency. In the Monte Carlo simulation, perturbing the DAS inputs will alter the amount of sidewall noise in the integration region. Varying the integration region, similarly, alters the amount of sidewall noise contributing to the overall integrated level.

The final frequency considered is 20,000 Hz. This frequency is selected as the only major observable noise sources are due to the leading edge and some rear-test section sources, shown in the nominal beam map in Figure 5-55. The results of this analysis are listed in Table 5-3.

Trends in these data are more difficult to evaluate. For most cases, a small increase in predicted power occurs by increasing the overall y-dimension of the integration region. The x-dimension slightly increases the prediction when going from a small to medium size, but has no effect when going from medium to large. Notably, for an x-dimension of 1.2 m, when the y-dimension increases from 0.4 m to 0.8 m a power decrease occurs. Intuitively this may make little sense as integration is a summation of source power within a region, but recall from Equation (4-39) that the integration is normalized by the array's PSF within the integration region. If additional sources are not introduced, but the PSF's summation increases due to the inclusion of additional sidewalls, the predicted power within a region will decrease. If a true source is present within an integration region, the inclusion of the PSF's sidelobe should be accompanied by the inclusion of the source's sidelobe such that the summation is ideally balanced and no additional power is predicted. A power reduction may indicate that the integrated source power is actually due to sidelobes of sources outside of the integration region. This reinforces the suspicion regarding the visible acoustic sources at this frequency as mentioned previously.

1/3rd Octave Scaling

Mach Number Scaling

Spectral scaling for the coherent power, three-microphone, and beamforming methods is now shown for various Mach numbers. These are shown in 1/3rd octave levels, to allow direct comparison with one of the free software tools for airfoil noise analysis, NAFNoise [Moriarty 2005]. The NAFNoise inputs are computed using the equivalent-lift AoA of the airfoil, X-Foil for boundary layer properties, and the BPM method for turbulent boundary layer noise calculations, which were measured using the dipole assumption-based coherent power method applied to data from uncambered airfoils [Brooks *et al.* 1989]. Based on the beam maps from the previous section, it appears that leading edge noise can be neglected for these computations. This would make sense given the low test section turbulence intensity of the facility.

1/3rd octave plots are synthesized for the coherent power and three-microphone methods by summing the appropriate bins of the narrowband spectra. The plotted data are all for the array-installed cases, not for the free field microphone cases. 1/3rd octave plots for the beam forming data are computed both this way, and by summing the appropriate bandwidth of CSMs prior to beamforming, and then beamforming at the center frequency of each band.

While data for Mach numbers of 0.05 through 0.19 in 0.01 increments were collected, for the sake of conciseness and due to computational time limitations a subset of the data is presented for Mach numbers of 0.05, 0.07, 0.10, 0.12, 0.15 and 0.17. The data are shown in Figure 5-57 through Figure 5-62. The lower frequency bounds of trailing edge noise based on the previously-discussed criteria defined by Blake [Blake 1986] in general fall below the minimum frequency bound of the plots. An upper frequency bound is drawn as a black dashed line over the data, and is located by determining the frequency breakdown of the coherence between the upper and lower microphones, specifically where the ordinary coherence function

drops below 1%. Essentially this is the upper bound of the valid region of coherent power methods. Immediately evident is the fact that for the most part, all methods are in agreement with NAFNoise regarding the location of the shedding peak of the airfoil for higher Mach numbers. For lower Mach numbers, the coherence-based methods appear to capture the roll-off after the shedding peak, but both beamforming methods miss it. This is sensible, as the shedding peak is sufficiently low frequency at lower Mach numbers that the array has no ability to reject extraneous acoustic sources. For the most part, the two different array computation methods are the same aside from end effects of the summing process in the first and last frequency bins. However, at the condition of 0.12 Mach number, they are dramatically different at higher frequencies. It is not immediately clear why this might occur only for this case, but as this is the bandwidth where sidewall noise would appear to dominate it may be that some self-relationship of the sidewall noise within the CSM is the culprit.

Also noticeable is that at Mach numbers of 0.05, 0.07 and 0.17 all of the methods except the coherent power method come extremely close to matching the NAFNoise output, and even coherent power is close at Mach 0.17. This is puzzling, as it should not be the case. NAFNoise uses prediction codes formulated by Brooks et al. in 1989 [Brooks *et al.* 1989], using the dipole assumption-based coherent power technique. The measurements conducted in QFF were performed using free-field microphones, so the observed airfoil behavior, as shown previously, should be dramatically different. Specifically, all of the phased array data shown here are from the experimental configuration shown in Figure 4-36, but the BPM data are from a configuration similar to that in Figure 4-37. Comparing array-installed to free field data in narrowband spectra was shown to have up to a 10 dB difference at the shedding peak earlier in this chapter, as shown in Figure 5-1 Figure 5-2. Such results would indicate that NAFNoise tends to overpredict

shedding noise strength. This conclusion is consistent with the rest of the 1/3rd octave bands presented in this chapter.

While at the highest Mach number most of the analysis techniques catch the shape of the airfoil shedding peak, none of them match the low or high frequency behavior of the prediction code. Based on the beam maps, this can be explained by considering the facility background noise sources. UFAFF background noise appears to have significant contributions from the jet collector at low frequencies. QFF, on the other hand, has no jet collector as the wind tunnel exhausts into a large room, thus the calibration data collected for the BPM study did not have to deal with lower frequency contamination. A cross-correlation editing technique was used in the BPM data for the reduction of facility background noise. This could also play a significant role in the behavior of the code at high frequencies, although the levels are in sufficient agreement with the coherent power analysis that low-coherence uncertainties could account for the behavior. As an additional consideration, the QFF data were collected using rigid sideplates to constrain the flow to a nominally two-dimensional field, instead of acoustic foam as used in UFAFF. This could cause standing wave patterns across the test section and lead to altered acoustic measurements [Oerlemans & Sijtsma 2000]. Additionally, the boundary layer behavior over the flat plates could be dramatically different over these solid sidewalls as compared to the behavior over porous acoustic foam, which would have an undetermined effect on the sidewall noise source's behavior.

Angle of Attack Behavior

The data for AoA variation are shown in Figure 5-63 through Figure 5-66. The data are for geometric AoAs of -1.5° and 1.5°, which correspond to X-Foil predicted equivalent-lift AoAs of -1.715° and -1.025°. 0° geometric AoA corresponds to -1.37° equivalent lift. Again for brevity's sake and due to computational expense, only data for Mach numbers of 0.10 and 0.17

are reduced and plotted. As shown, the coherence-based methods show slight variation above the shedding peak as a function of AoA, as compared to the NAFNoise prediction. However, little other difference exists for this small perturbation in AoA.

Instrumentation Offset

The results for traversing the array 0.25 m further downstream along the test section axis, as illustrated in Figure 4-38, are shown in Figure 5-67 and Figure 5-68. The data are in much poorer agreement with the NAFNoise output, and actually appears to fail at detecting the shedding peak. It was suspected that there was sufficient flow over the face of the array that even the gain from beamforming with diagonal removal was insufficient to overcome flow noise contamination. This suspicion is reinforced by the behavior of the coherence between the B&K 4138 microphone and the opposing G.R.A.S. 40BE, which was sufficiently low, $< 1\%$ through the entire bandwidth of interest, that no upper bound could be determined for the acoustic field at a Mach number of 0.10. As such, no upper bound is drawn on the plot. For the data at $M = 0.17$, only one frequency bin, 2688 Hz, is above 1% coherence. This bin has a coherence of 1.2%. Because of this behavior no upper bound is applied to the $M = 0.17$ data either.

The array data are examined at several conditions to confirm suspicions regarding flow contamination. One condition, the airfoil shedding peak of 2,512 Hz at a Mach number of 0.17, is shown in Figure 5-69, with the appropriate $1/3^{\text{rd}}$ octave plot at 2,500 Hz is shown in Figure 5-70. In both of the cases, some noise is visible in the vicinity of the airfoil, but the appropriately positioned integration region fails to capture it, and the overlay of the model position shows that this noise source doesn't really appear to be trailing edge as it was with the centered array. This mass of apparent noise may be due to flow over the array, or it could be caused by invalidation of the shear layer correction method. Depending exactly on how the test section shear layer interacts with the jet collector, which is now much closer to the array, the planar shear layer

assumption likely breaks down as the flow field becomes a complicated, viscous region. If this is the case, beamforming would no longer be capable of extracting usable model information, and the dramatically higher microphone self-noise would make acoustic extraction through coherent power methods extremely difficult.

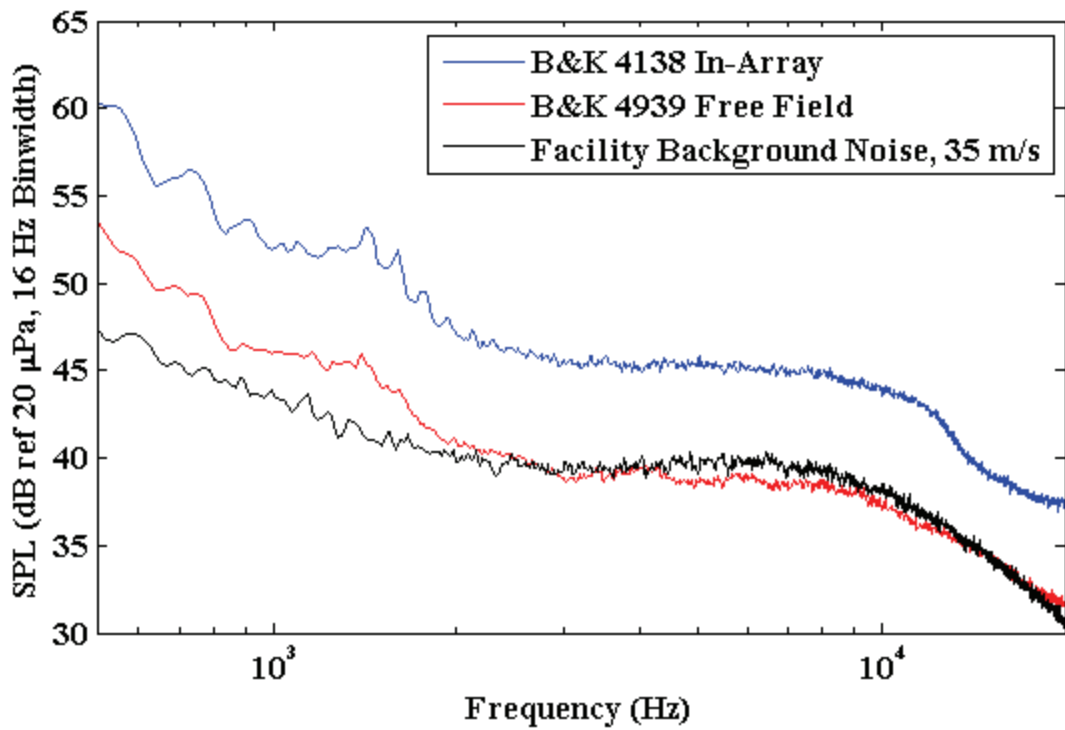


Figure 5-1. Model installation effects and background noise for a Mach number of 0.10.

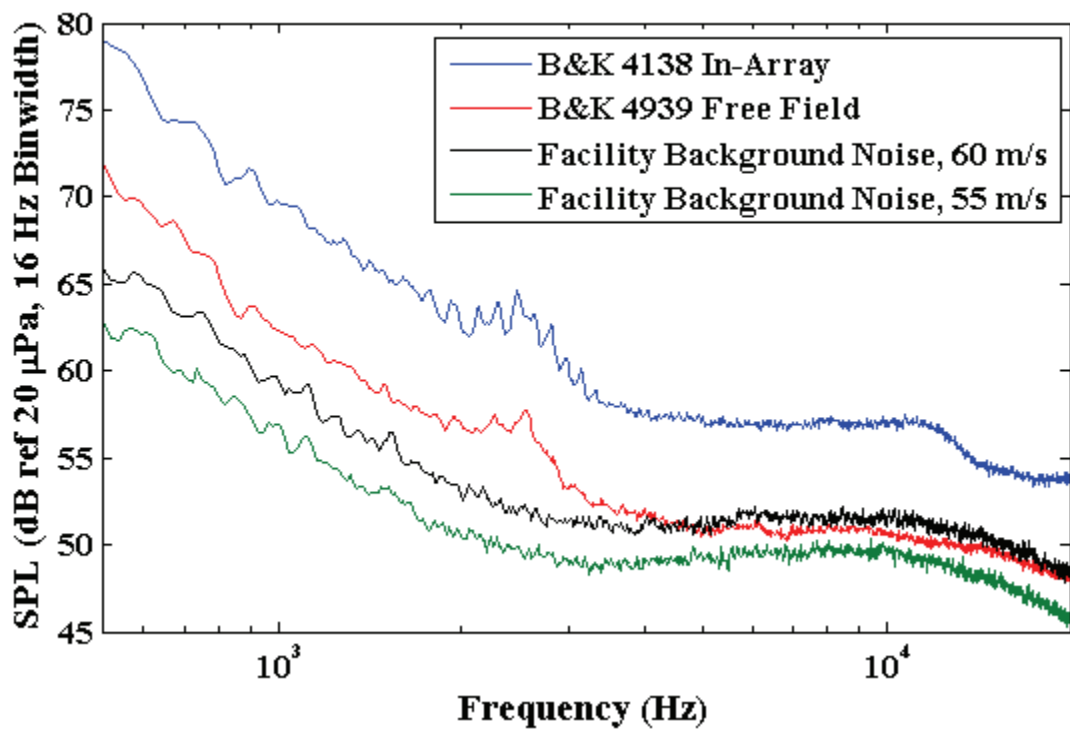


Figure 5-2. Model installation effects and background noise for a Mach number of 0.17.

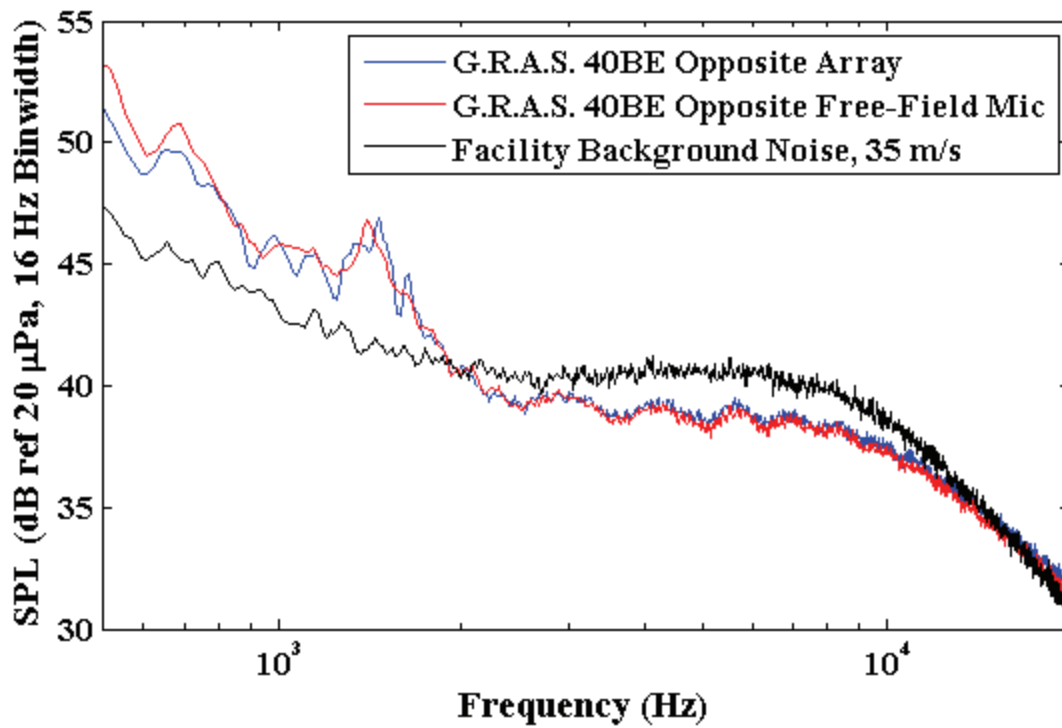


Figure 5-3. Installation effects and background noise for upper mic, Mach number of 0.10.

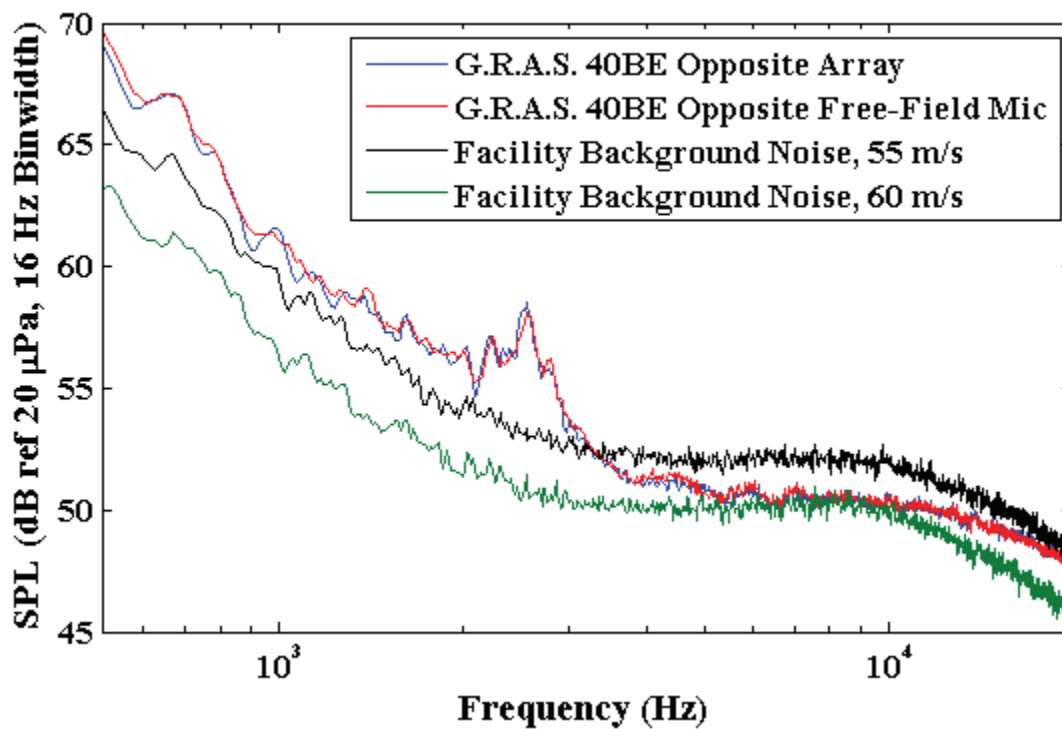


Figure 5-4. Installation effects and background noise for upper mic, Mach number of 0.17.

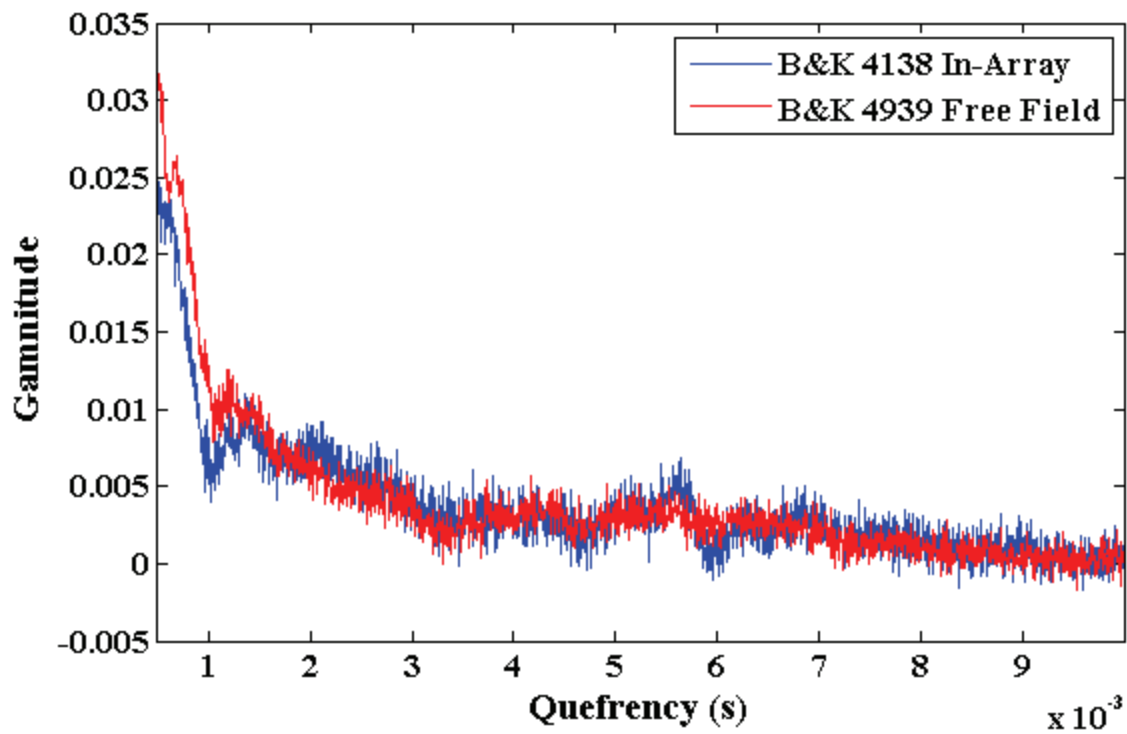


Figure 5-5. Cepstrum comparison of installation effects for a Mach number of 0.10.

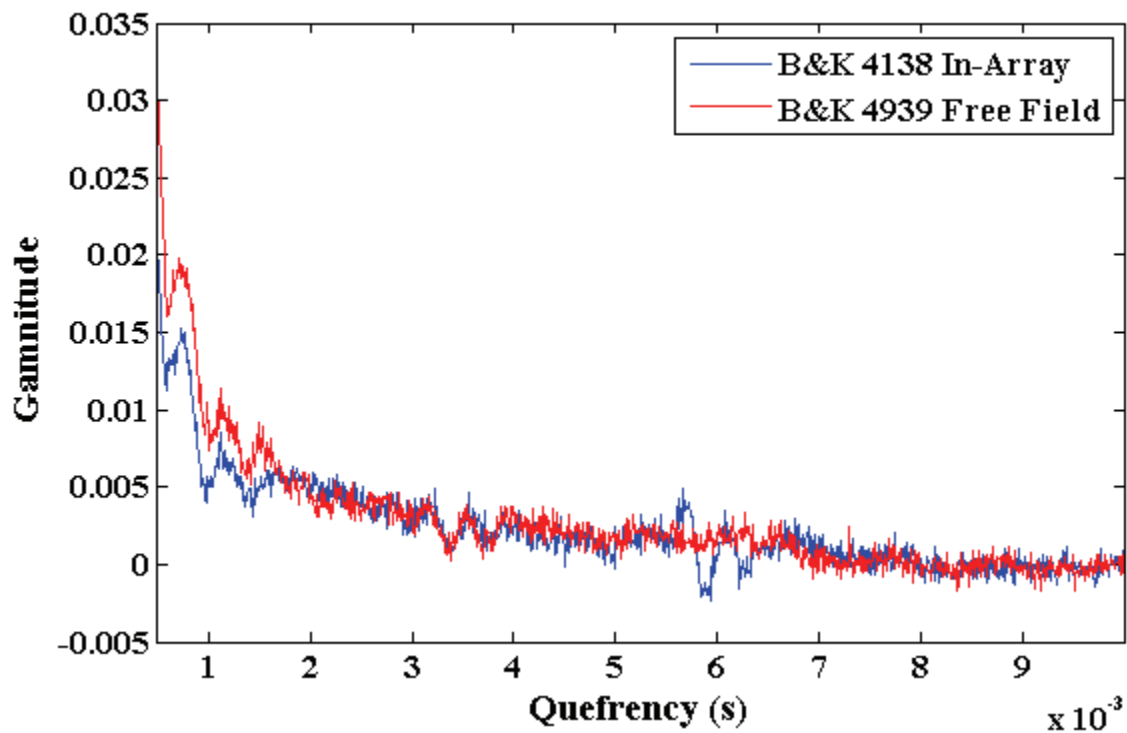


Figure 5-6. Cepstrum comparison of installation effects for a Mach number of 0.17.

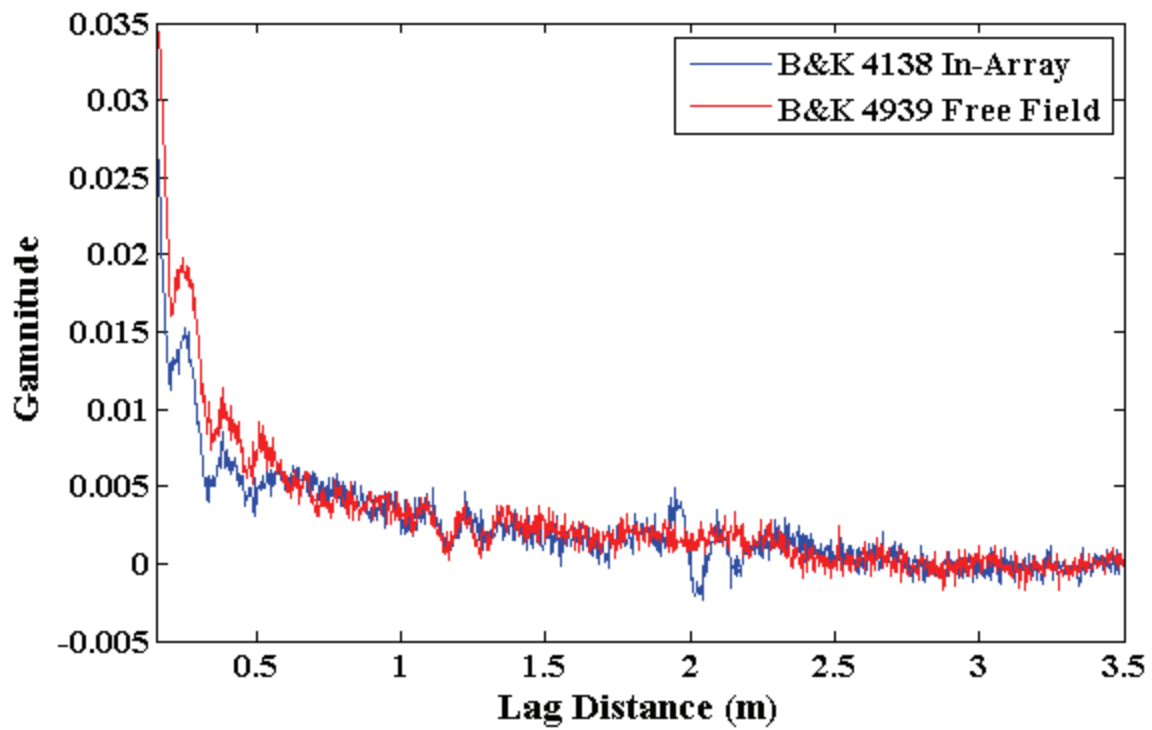


Figure 5-7. Cepstrum comparison of installation effects for a Mach number of 0.17, where quefrency has been converted to an equivalent lag distance using the measured speed of sound.

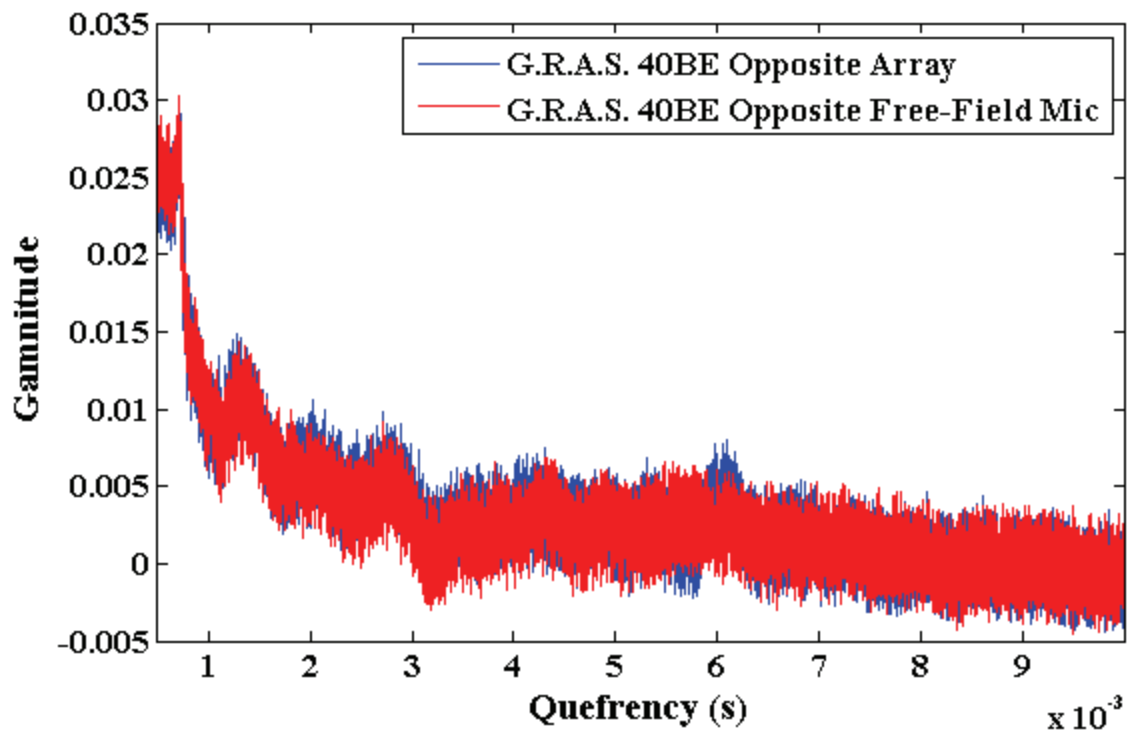


Figure 5-8. Cepstrum comparison of installation effects for a Mach number of $M = 0.10$, for free field microphones mounted above the model trailing edge.

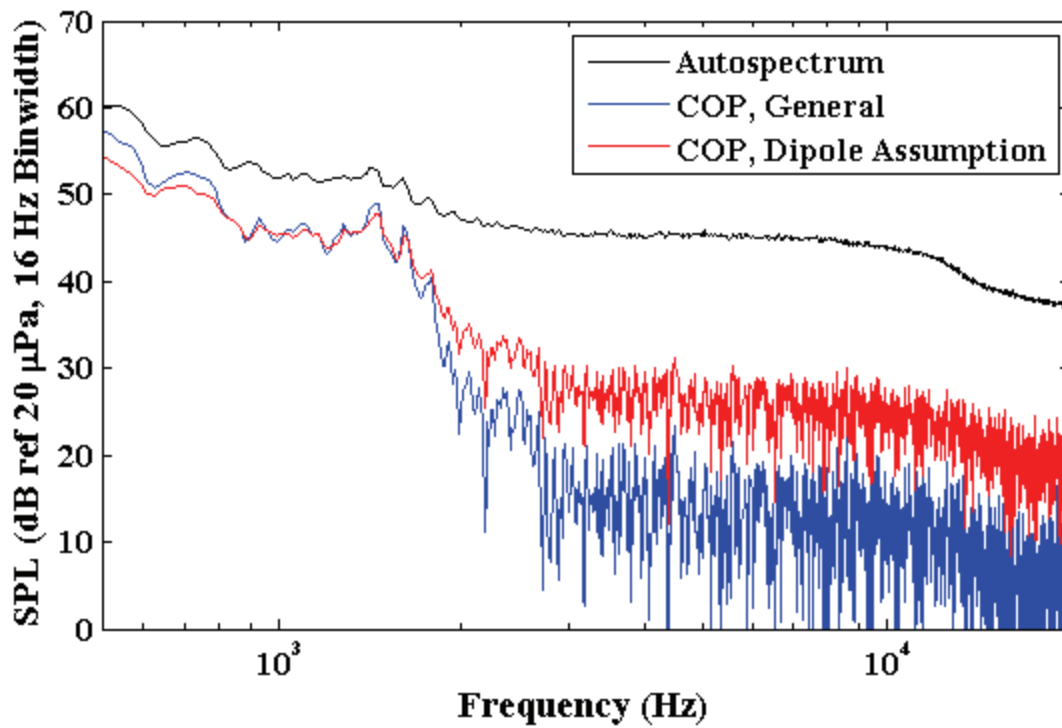


Figure 5-9. Coherent power analysis of in-array B&K 4138 for a Mach number of 0.10.

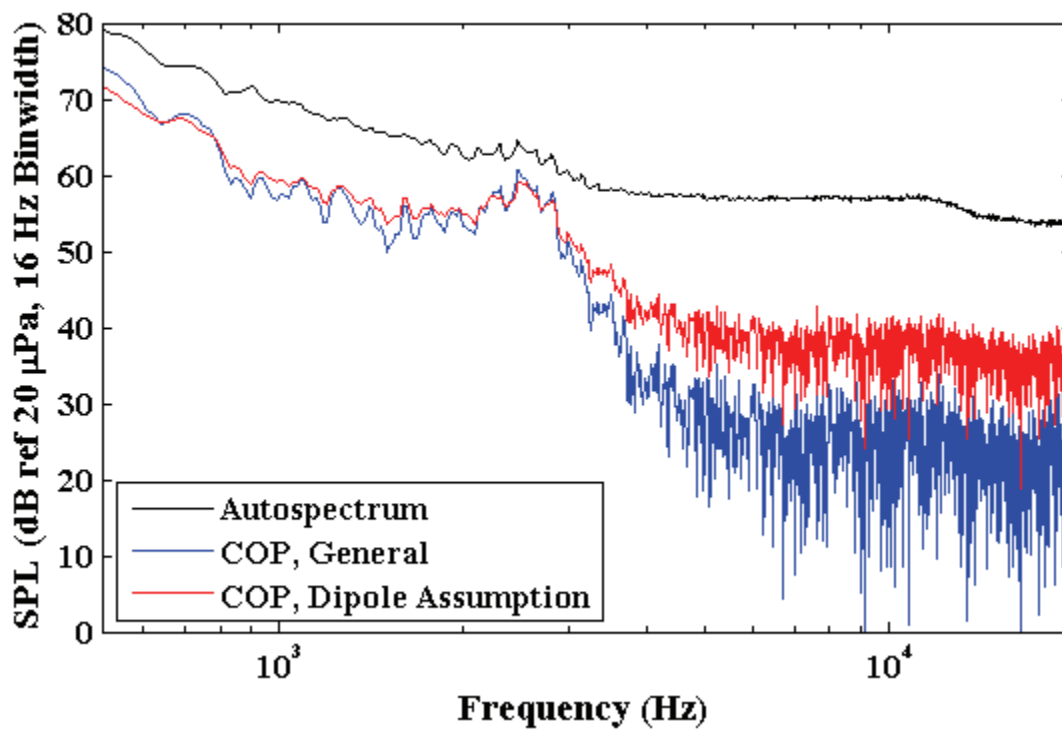


Figure 5-10. Coherent power analysis of in-array B&K 4138 for a Mach number of 0.17.

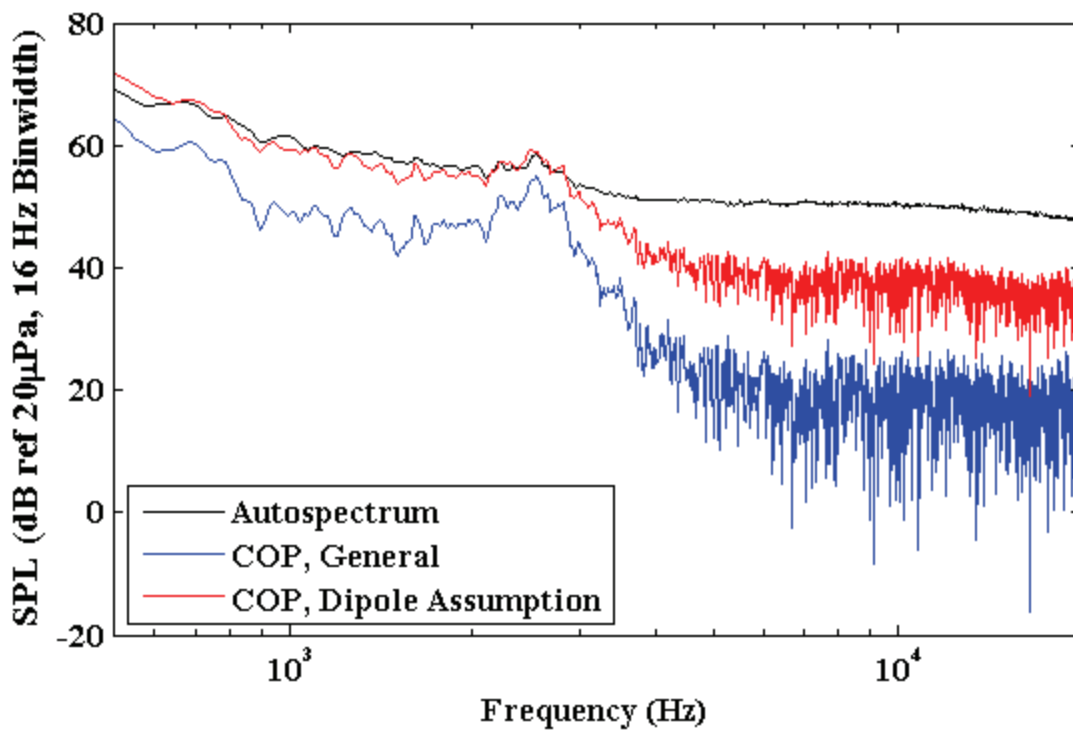


Figure 5-11. Coherent power analysis of opposite-array G.R.A.S. 40BE for $M = 0.17$.

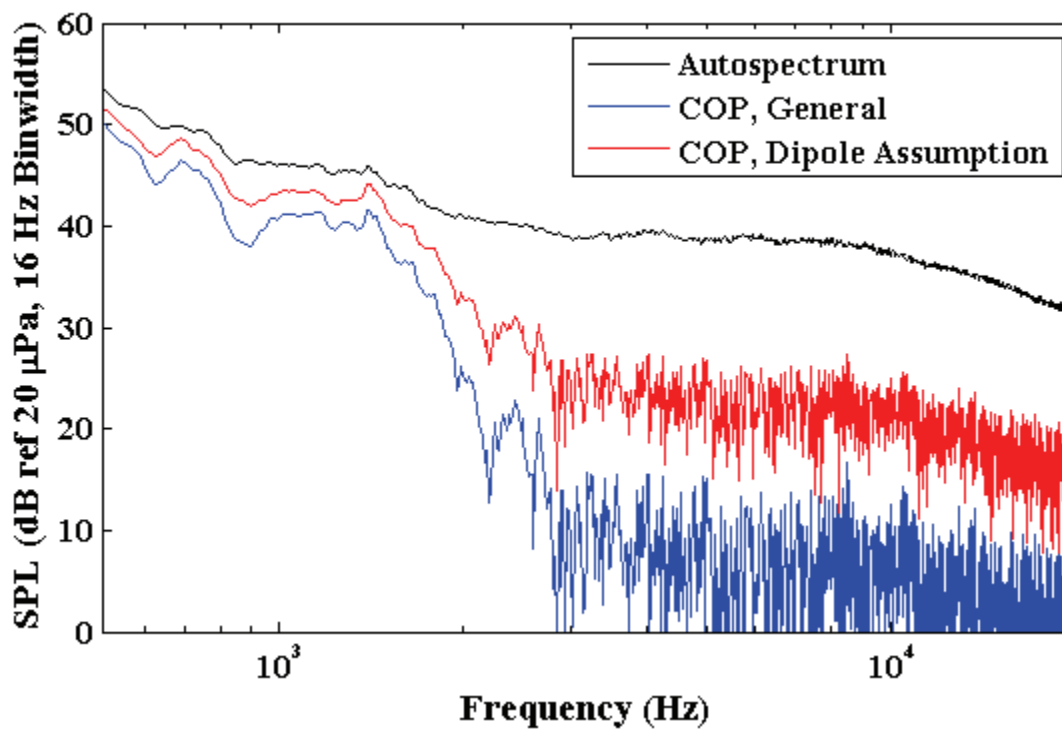


Figure 5-12. Coherent power analysis of free field B&K 4939 for a Mach number of 0.10.

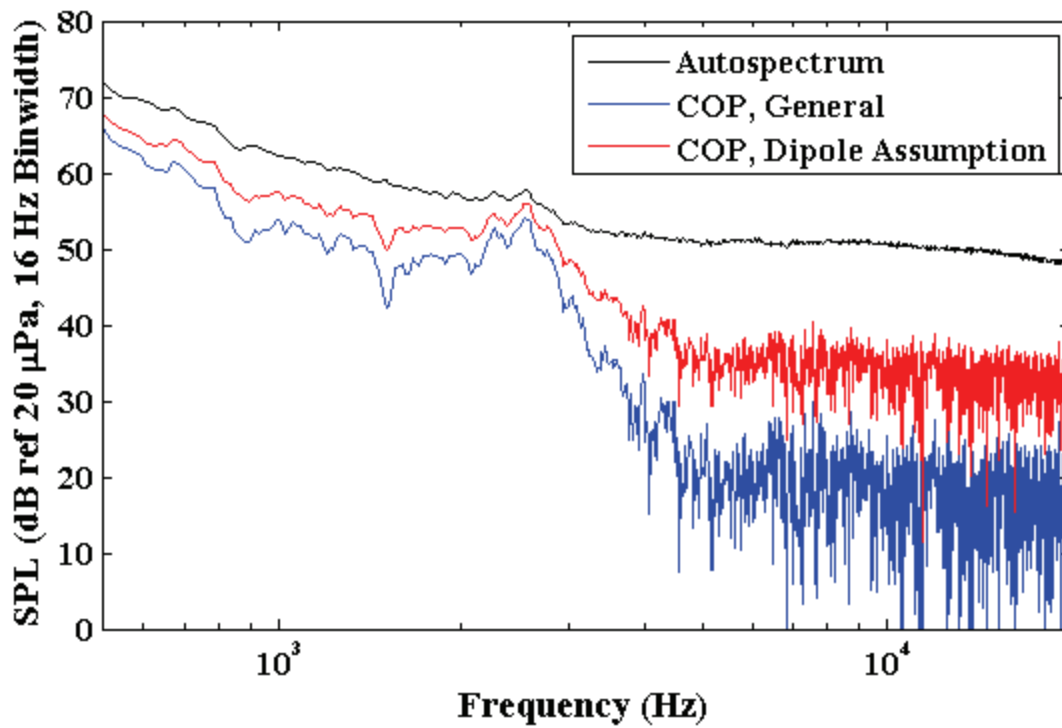


Figure 5-13. Coherent power analysis of free field B&K 4939 for a Mach number of 0.17.

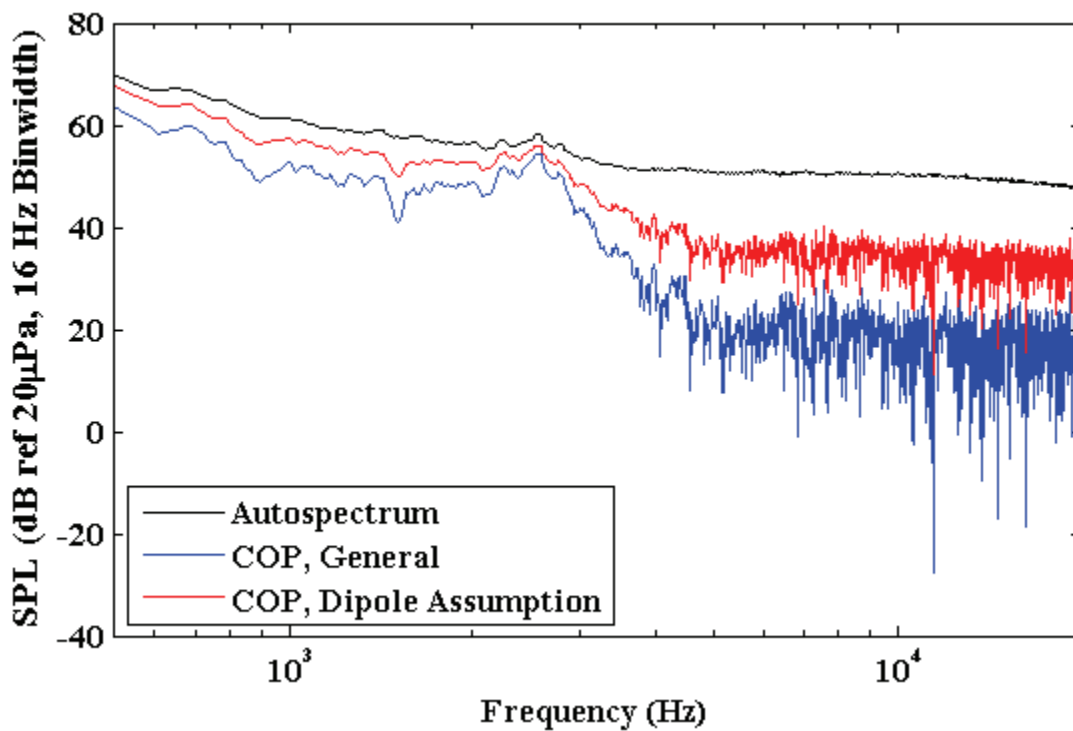


Figure 5-14. Coherent power analysis of free-field opposing G.R.A.S. 40BE for M = 0.17.

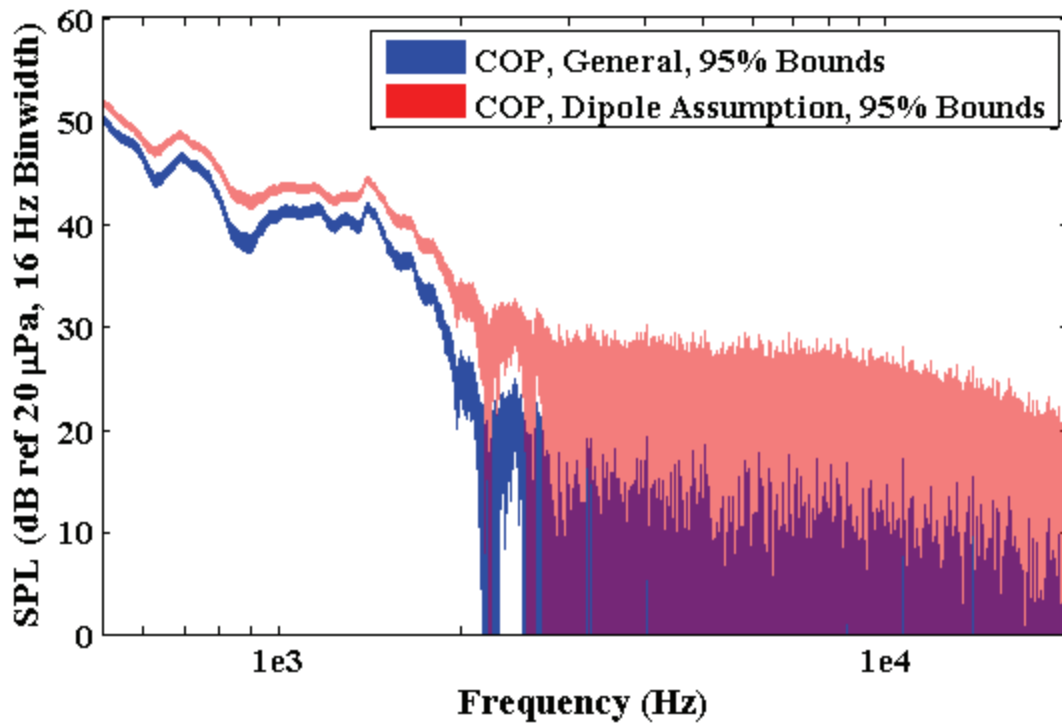


Figure 5-15. COP confidence intervals for the free field case for a Mach number of 0.10.

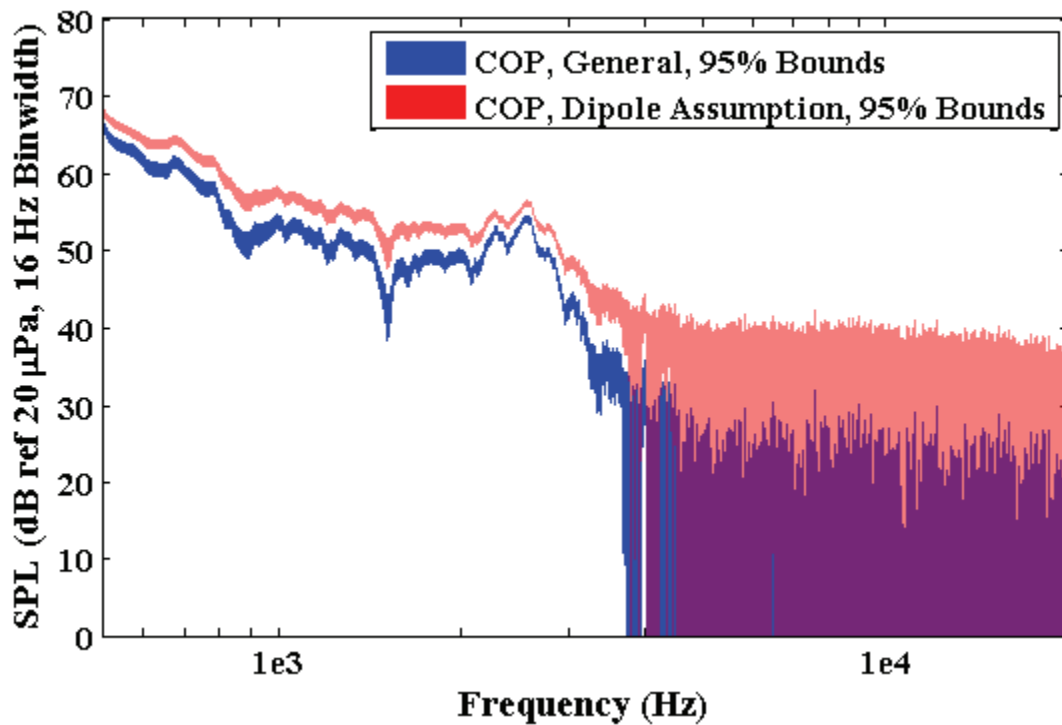


Figure 5-16. COP confidence intervals for the free field case for a Mach number of 0.17.

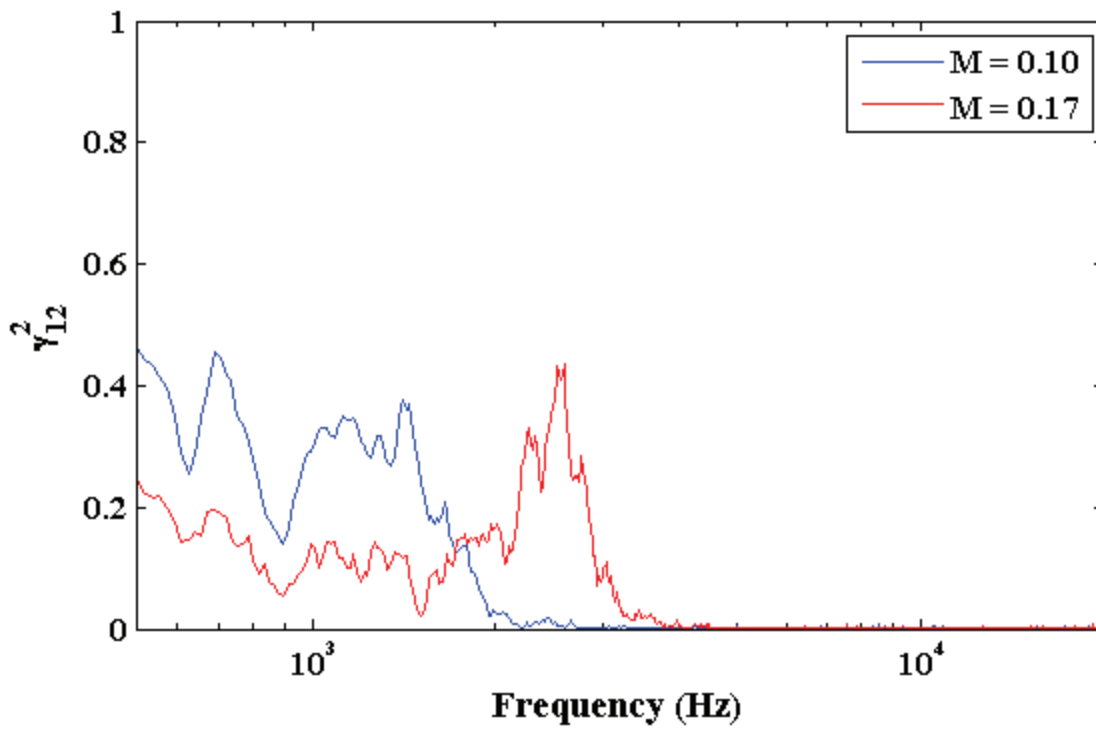


Figure 5-17. Ordinary coherence function computed between the upper G.R.A.S. 40BE and lower B&K 4939 trailing edge microphones for the free-field case, for two different Mach numbers.

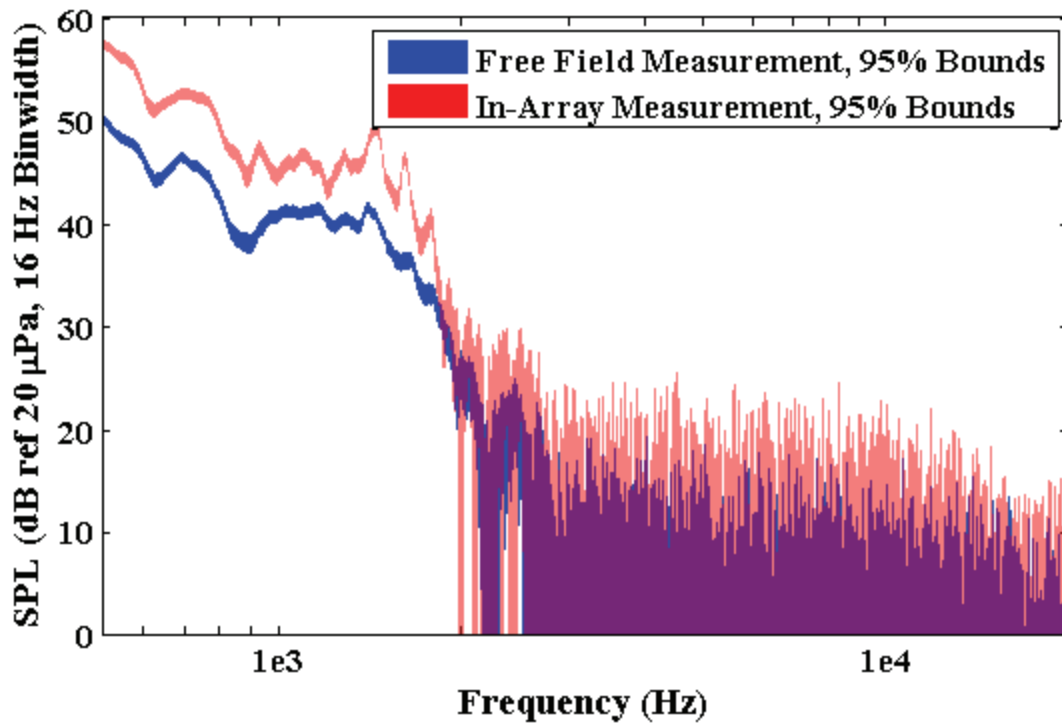


Figure 5-18. Uncertainty bounds on installation effects for COP analysis, Mach number of 0.10.

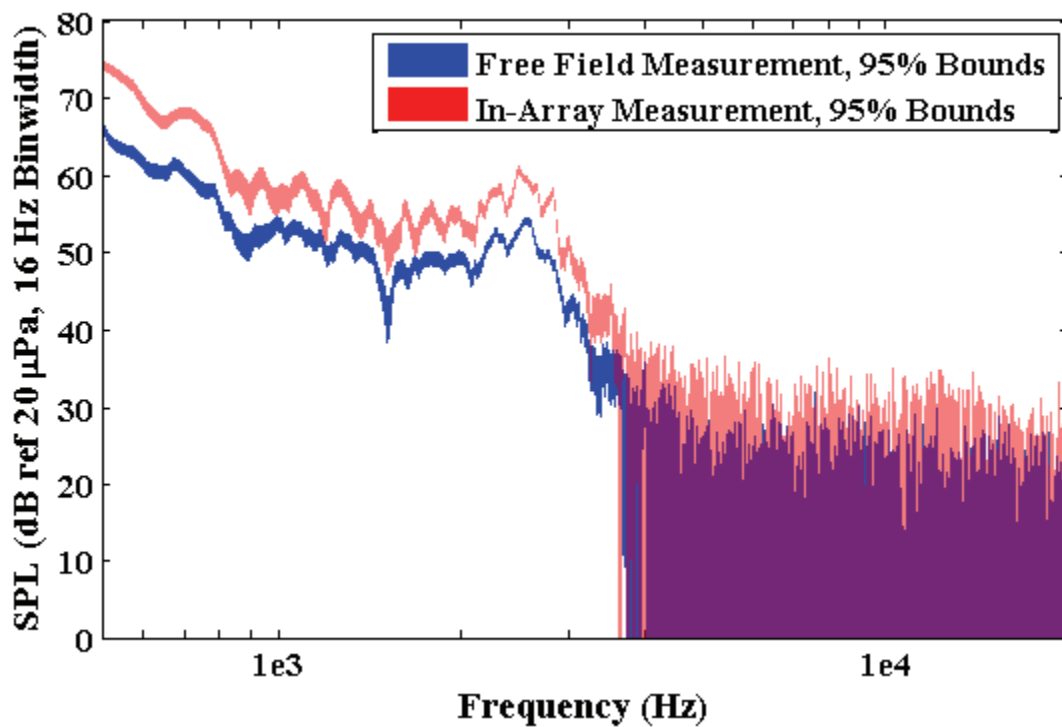


Figure 5-19. Uncertainty bounds on installation effects for COP analysis, Mach number of 0.17.

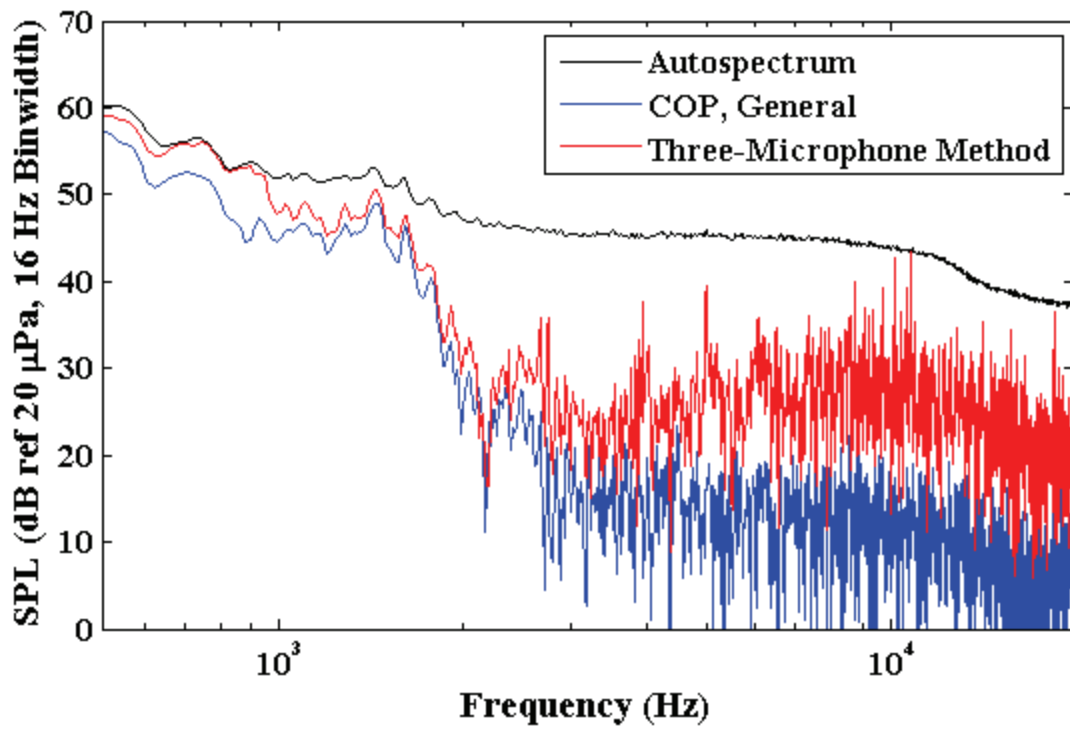


Figure 5-20. Comparison of two- and three-microphone methods for array case at $M = 0.10$.

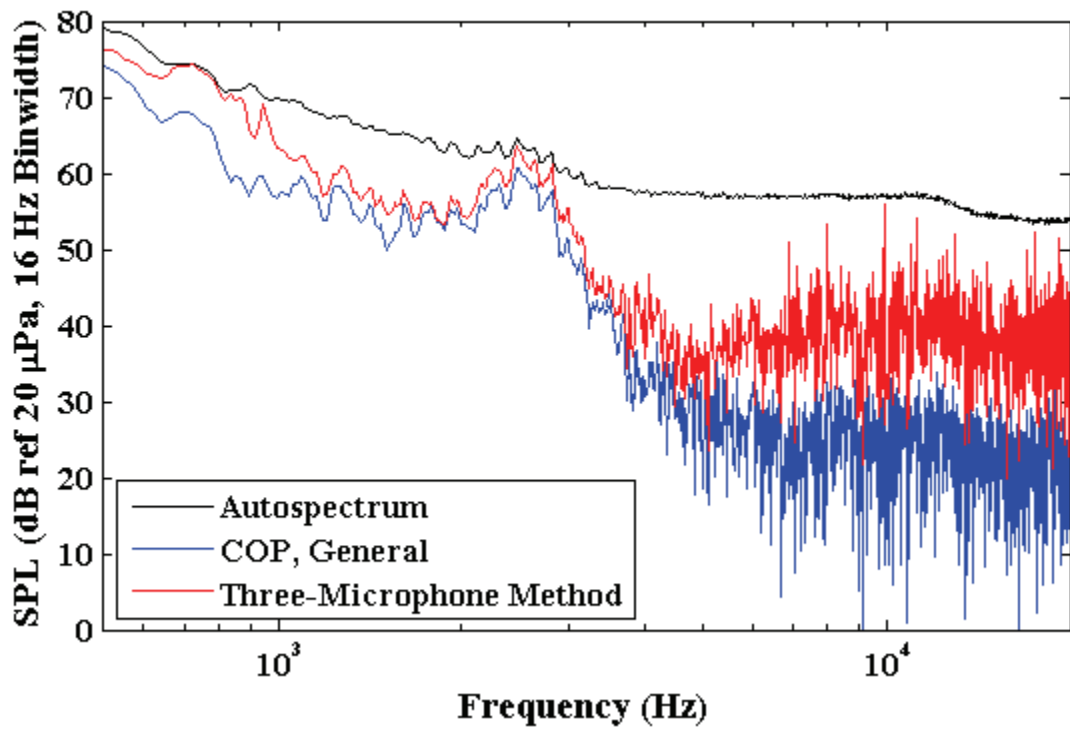


Figure 5-21. Comparison of two- and three-microphone methods for array case at $M = 0.17$.

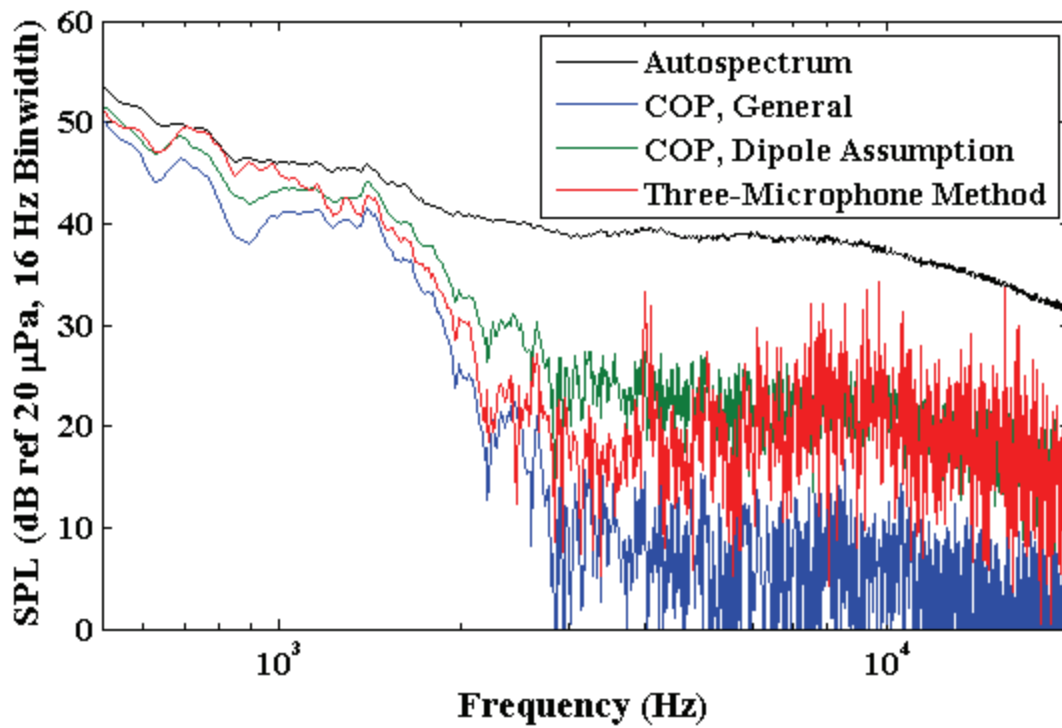


Figure 5-22. Comparison of two- and three-microphone methods for free case at $M = 0.10$.

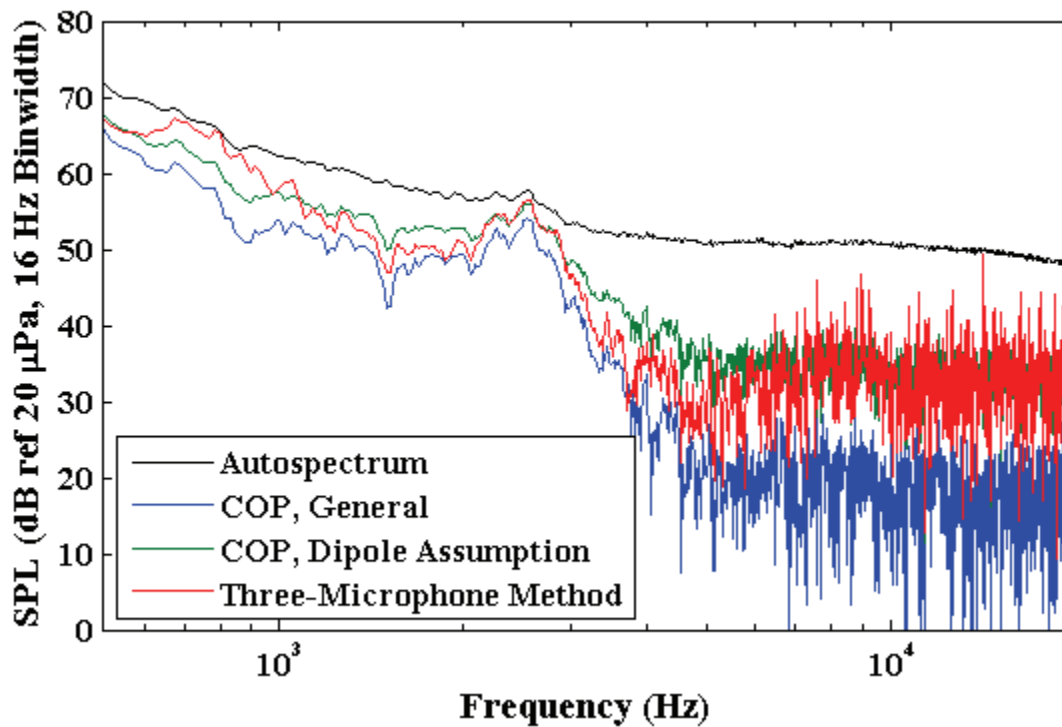


Figure 5-23. Comparison of two- and three-microphone methods for free case at $M = 0.17$.

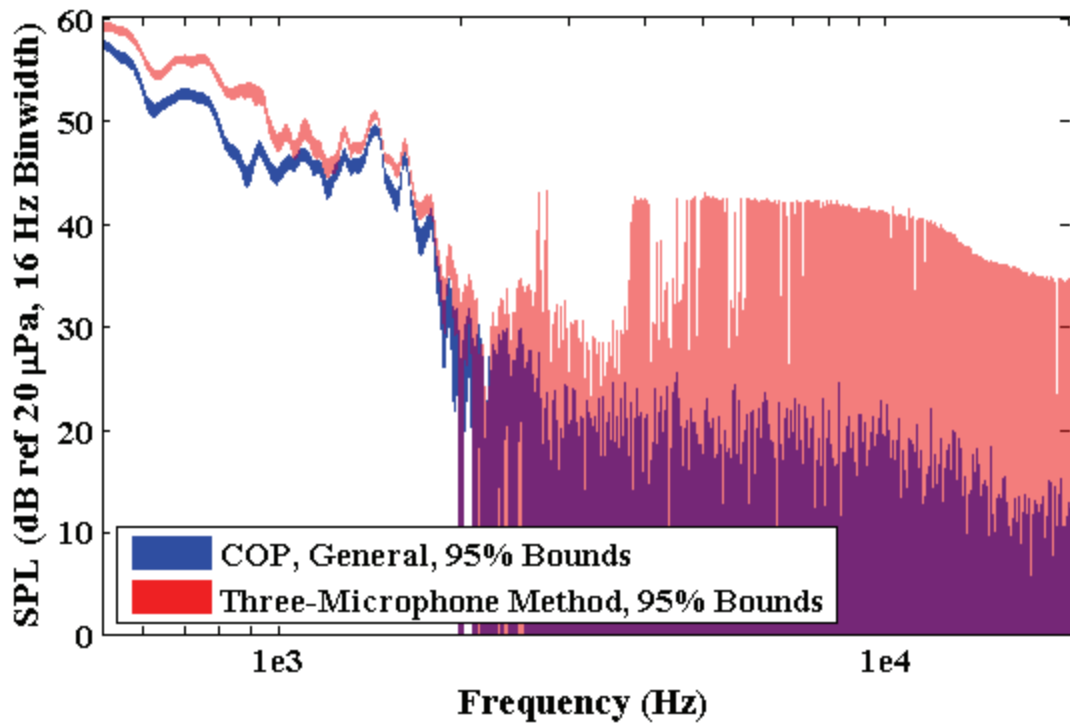


Figure 5-24. Uncertainty bounds for differing methods for array case at $M = 0.10$.

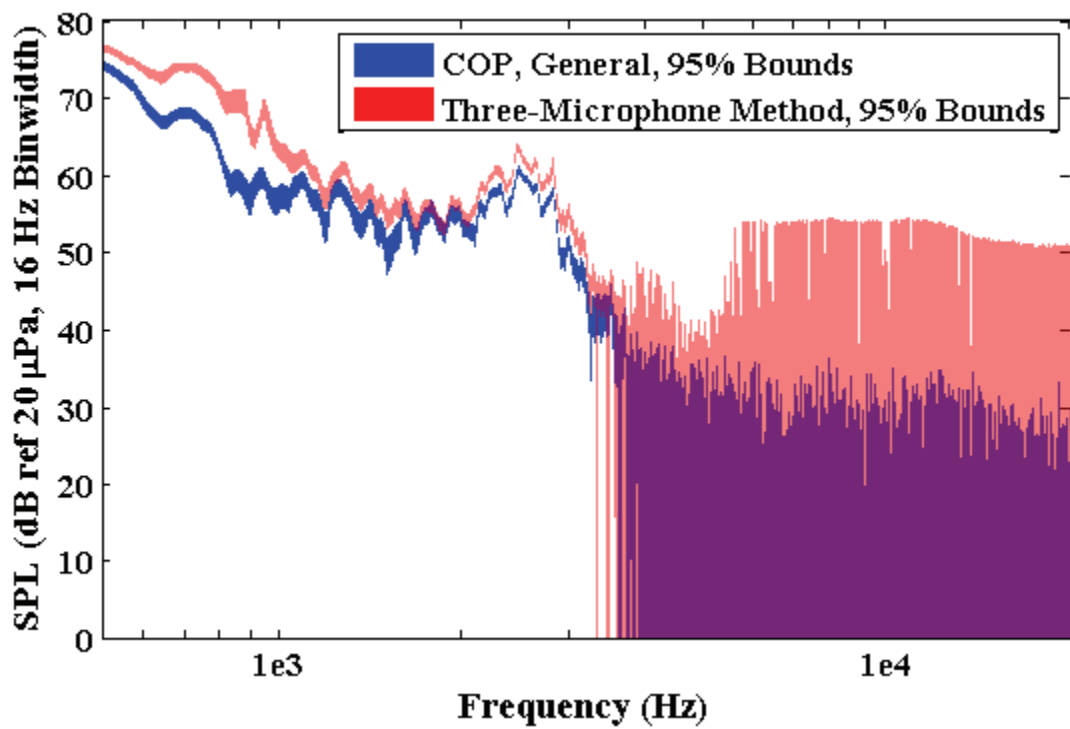


Figure 5-25. Uncertainty bounds for differing methods for array case at $M = 0.17$.

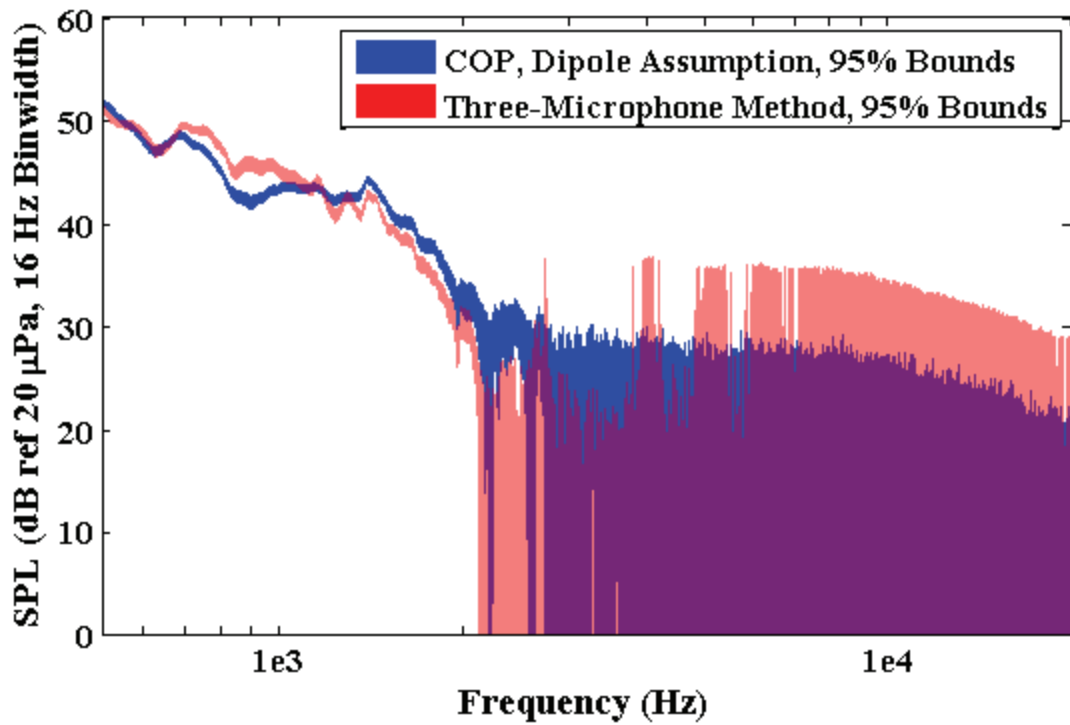


Figure 5-26. Uncertainty bounds for differing methods for free field case at $M = 0.10$.

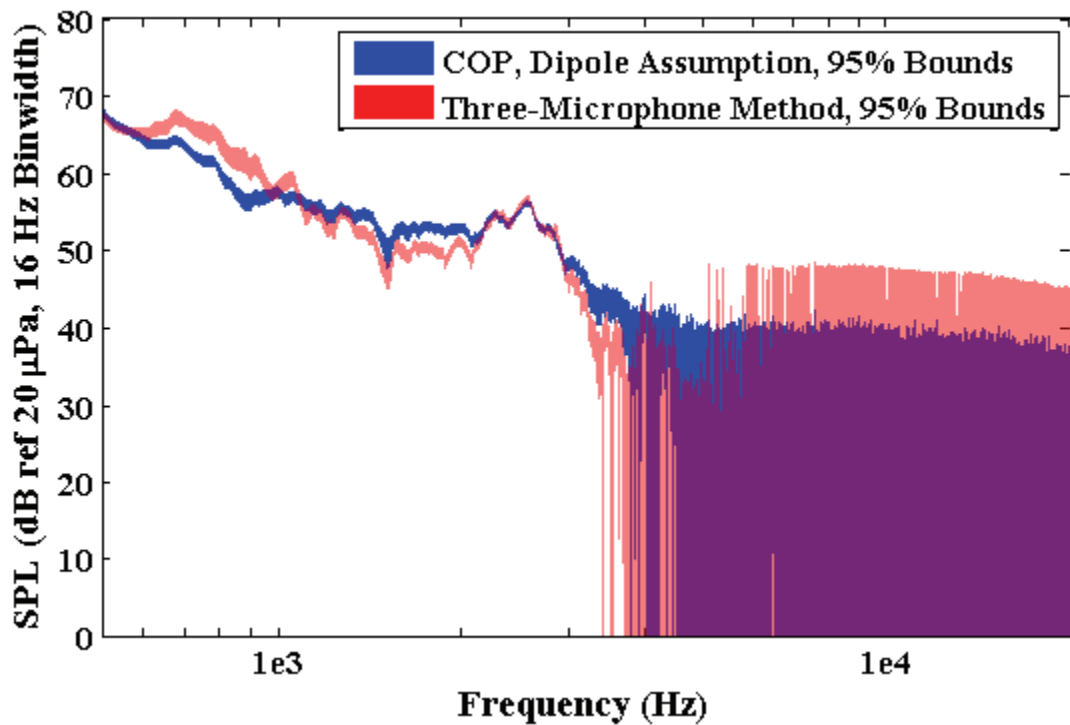


Figure 5-27. Uncertainty bounds for differing methods for free field case at $M = 0.17$.

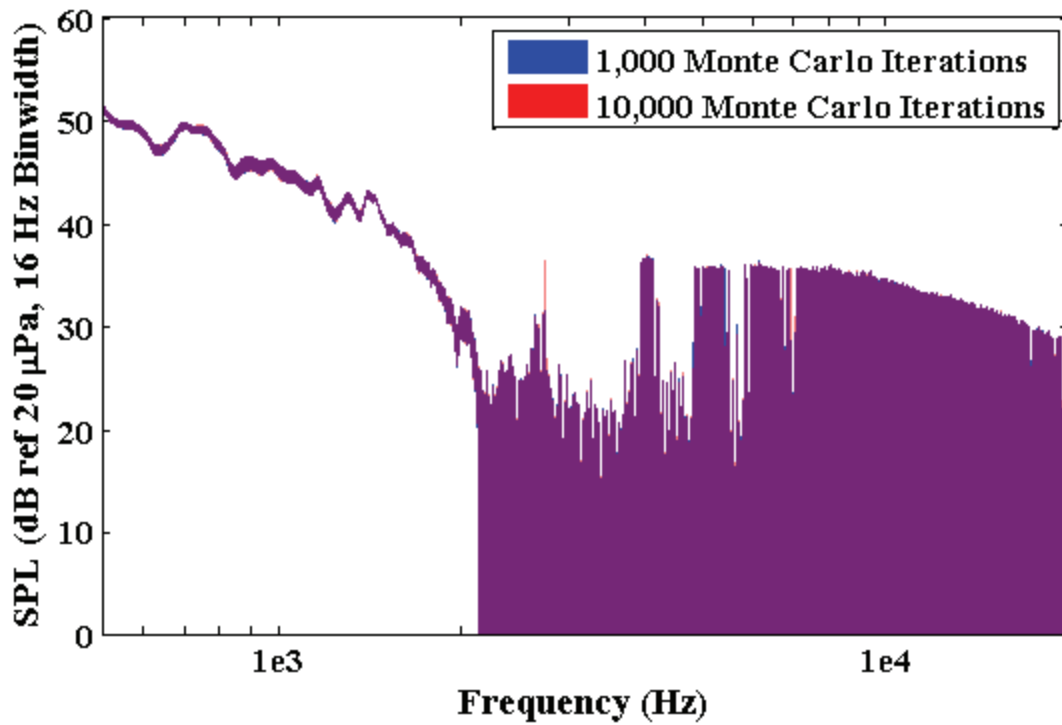


Figure 5-28. Convergence analysis of Monte Carlo uncertainties for free field case of $M = 0.10$.

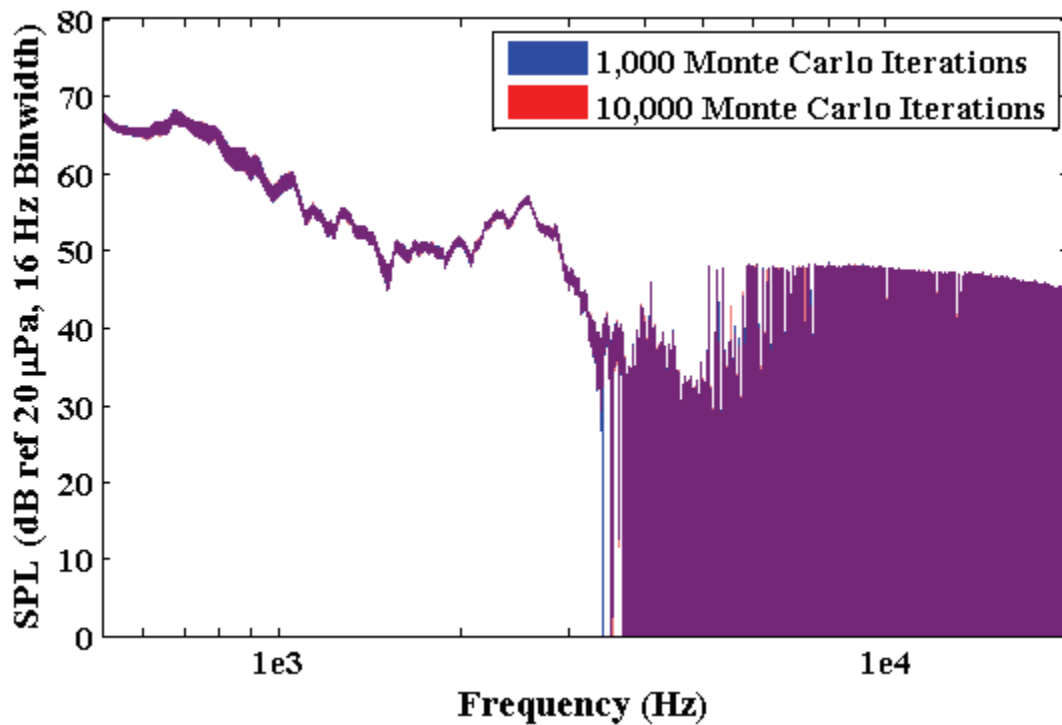


Figure 5-29. Convergence analysis of Monte Carlo uncertainties for free field case of $M = 0.17$.

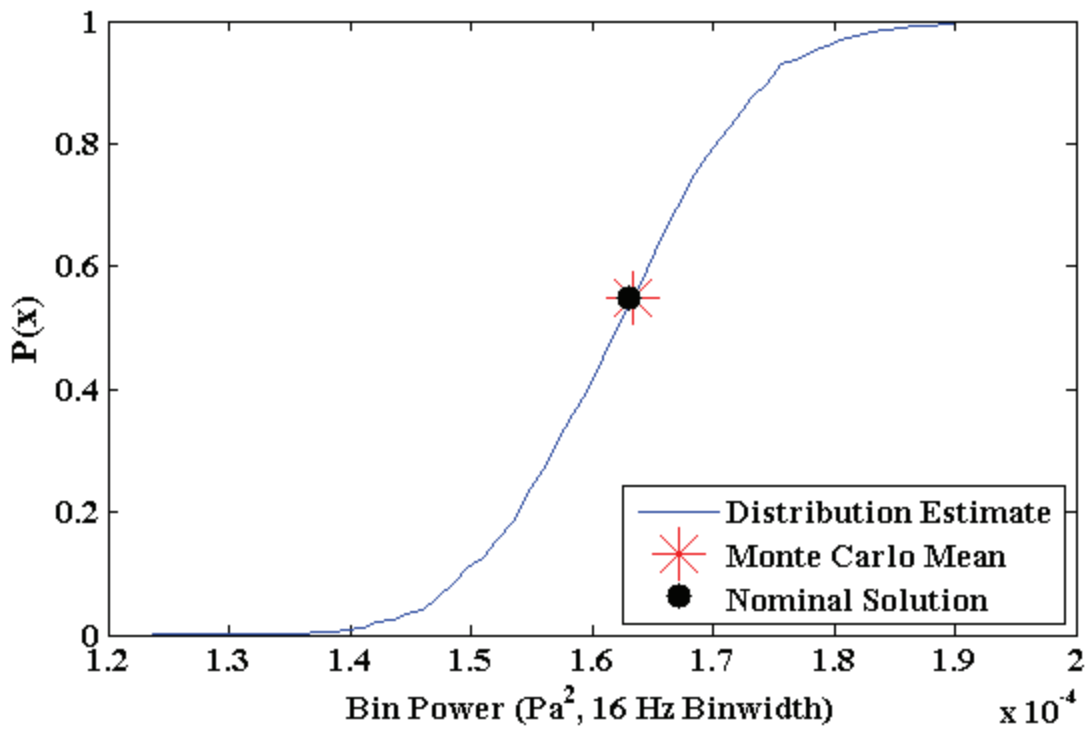


Figure 5-30. Cdf of Monte Carlo results for free field case of $M = 0.17$ at 2,512 Hz.

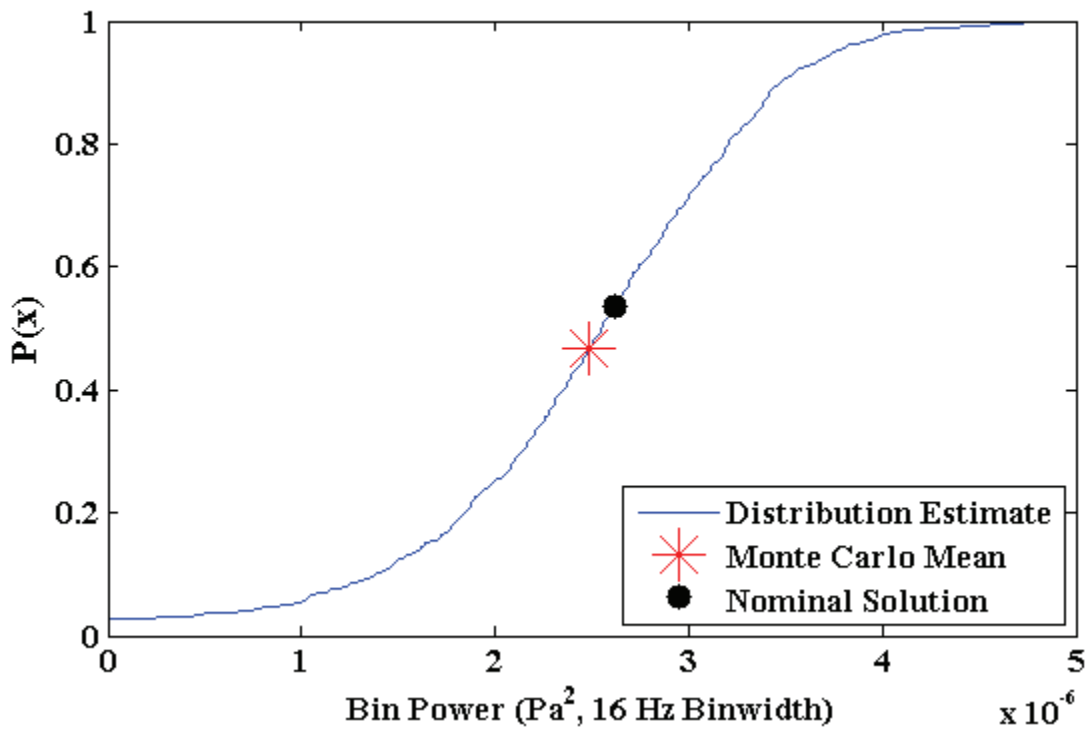


Figure 5-31. Cdf of Monte Carlo results for free field case of $M = 0.17$ at 3,392 Hz.

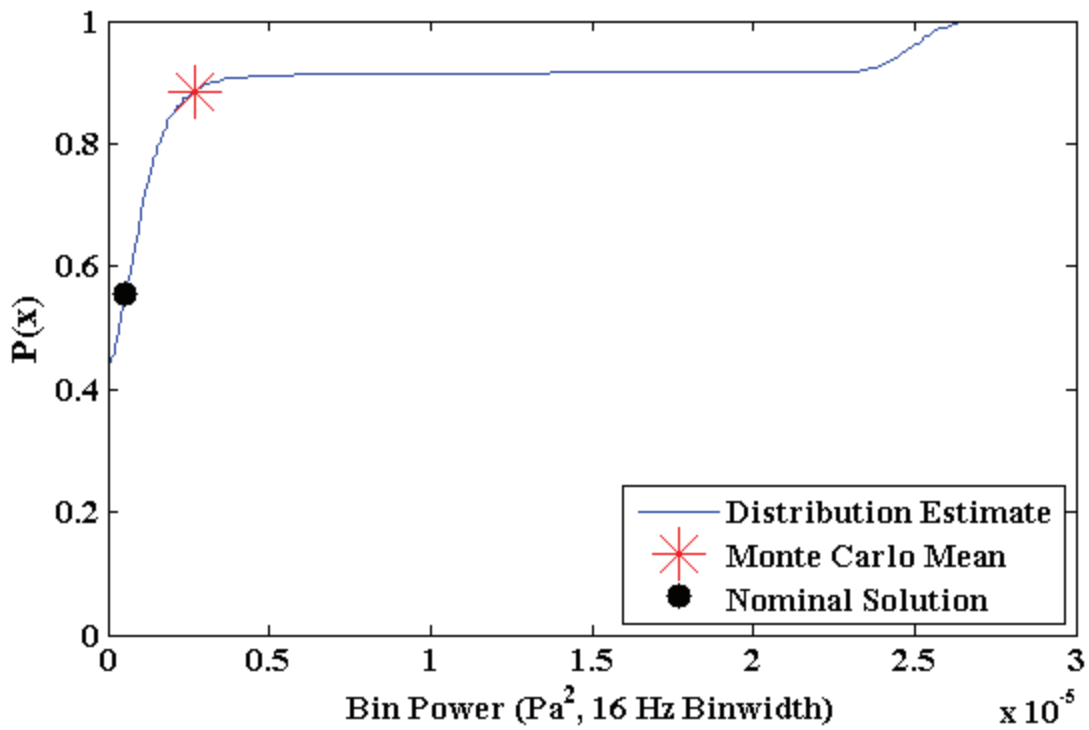


Figure 5-32. Cdf of Monte Carlo results for free field case of $M = 0.17$ at $6,000$ Hz.

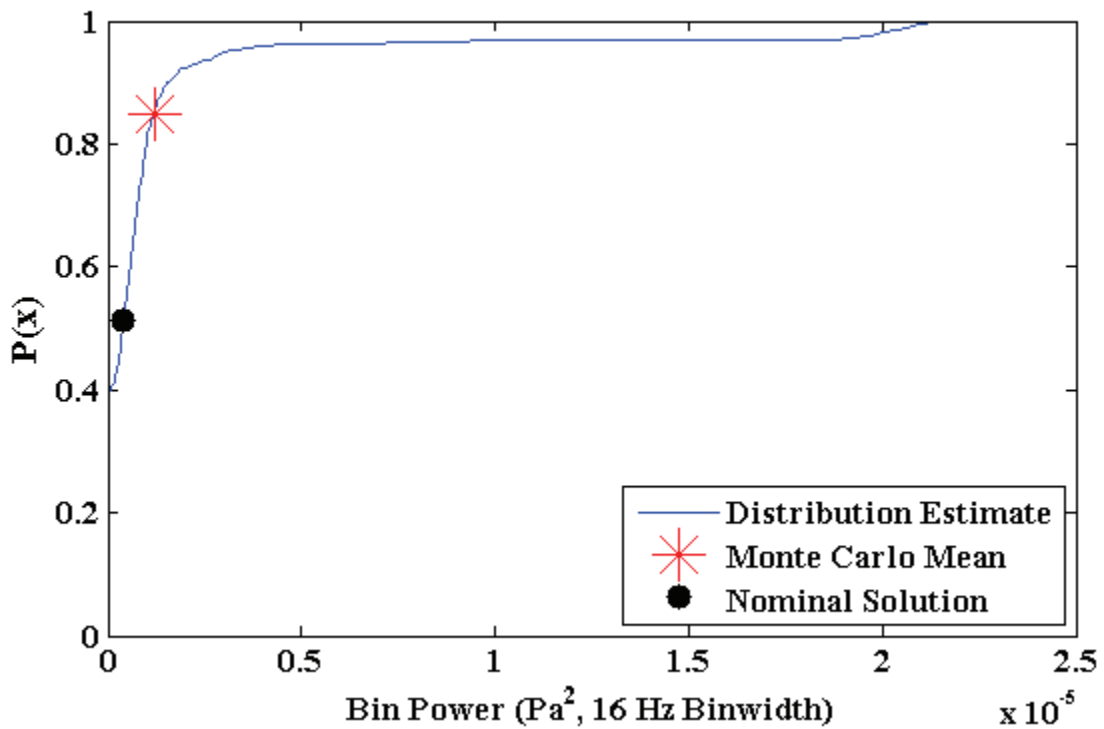


Figure 5-33. Cdf of Monte Carlo results for free field case of $M = 0.17$ at $12,000$ Hz.

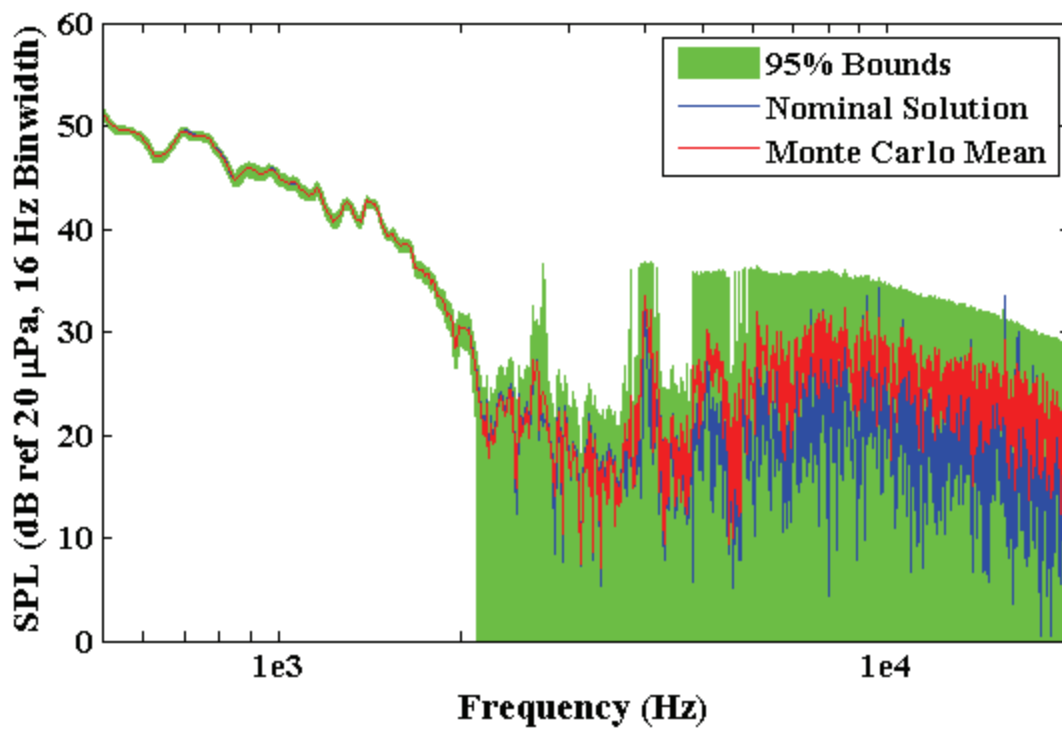


Figure 5-34. Nominal and mean three-microphone methods with confidence intervals, $M = 0.10$.

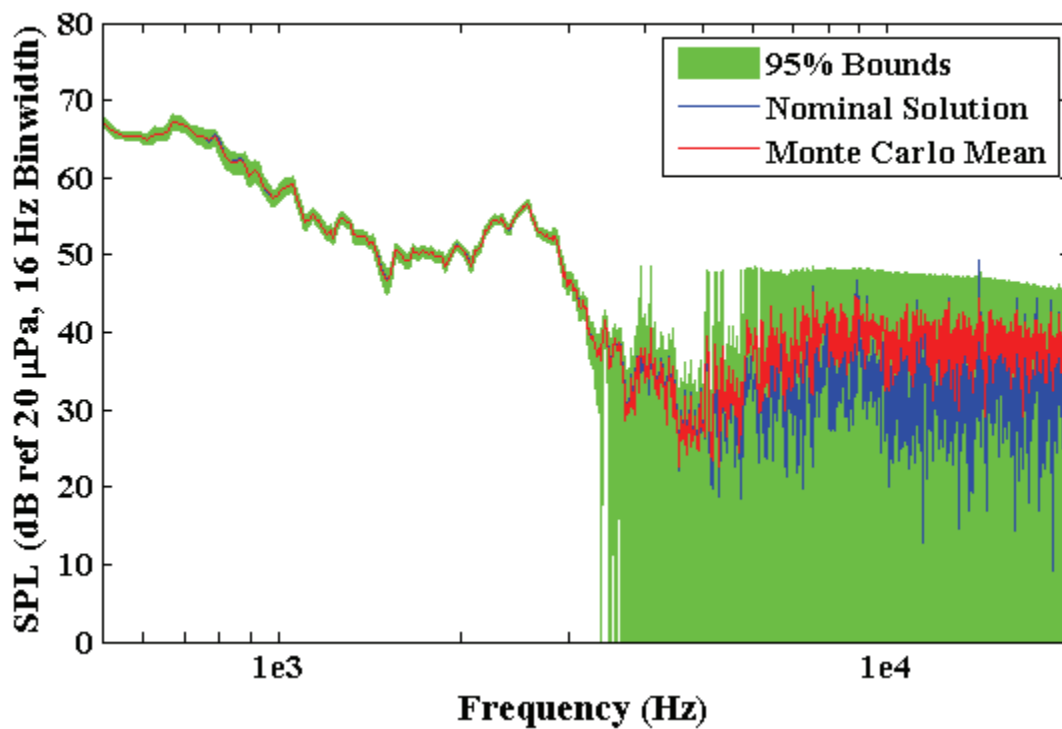


Figure 5-35. Nominal and mean three-microphone methods with confidence intervals, $M = 0.17$.

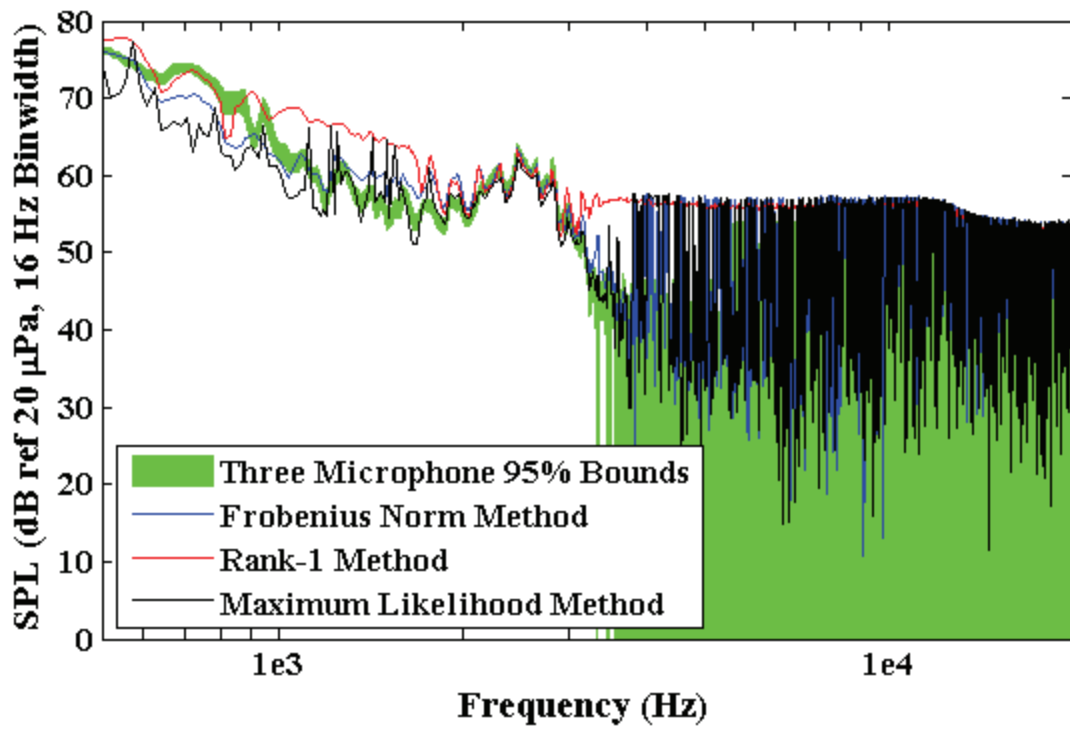


Figure 5-36. Comparison of covariance-based fitting approaches for free field, $M = 0.17$.

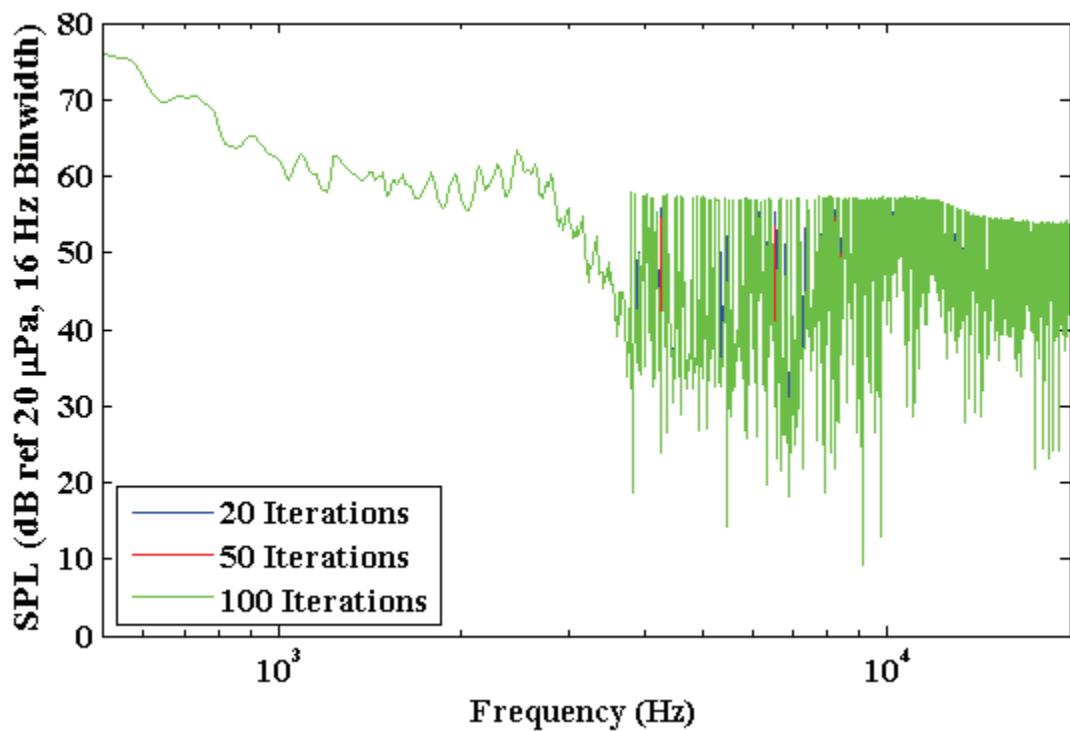


Figure 5-37. Variation of Frobenius Norm Method solution for varying internal iterations.

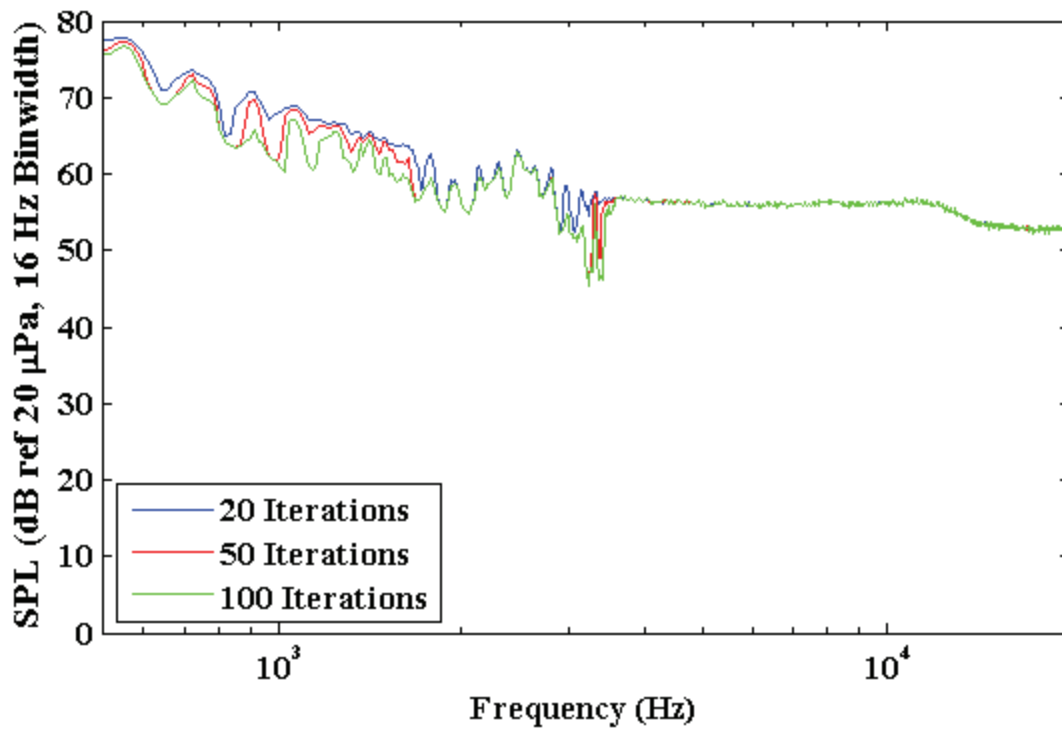


Figure 5-38. Variation of Rank-1 Method solution for varying internal iterations.

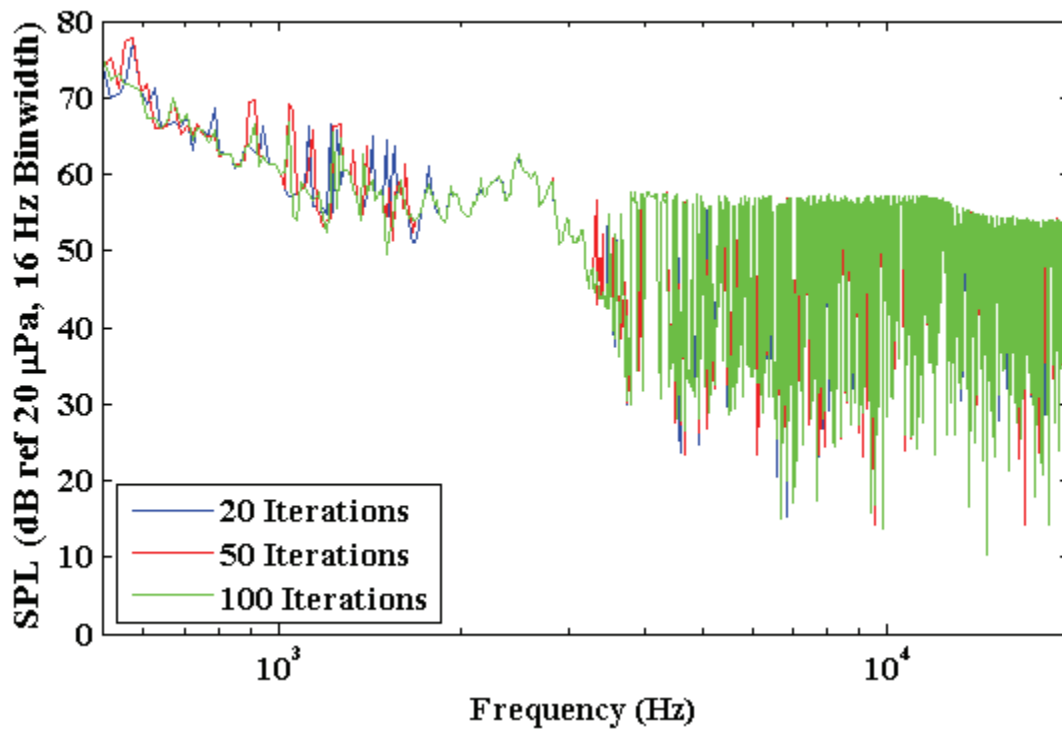


Figure 5-39. Variation of Maximum Likelihood Method solution for varying internal iterations.

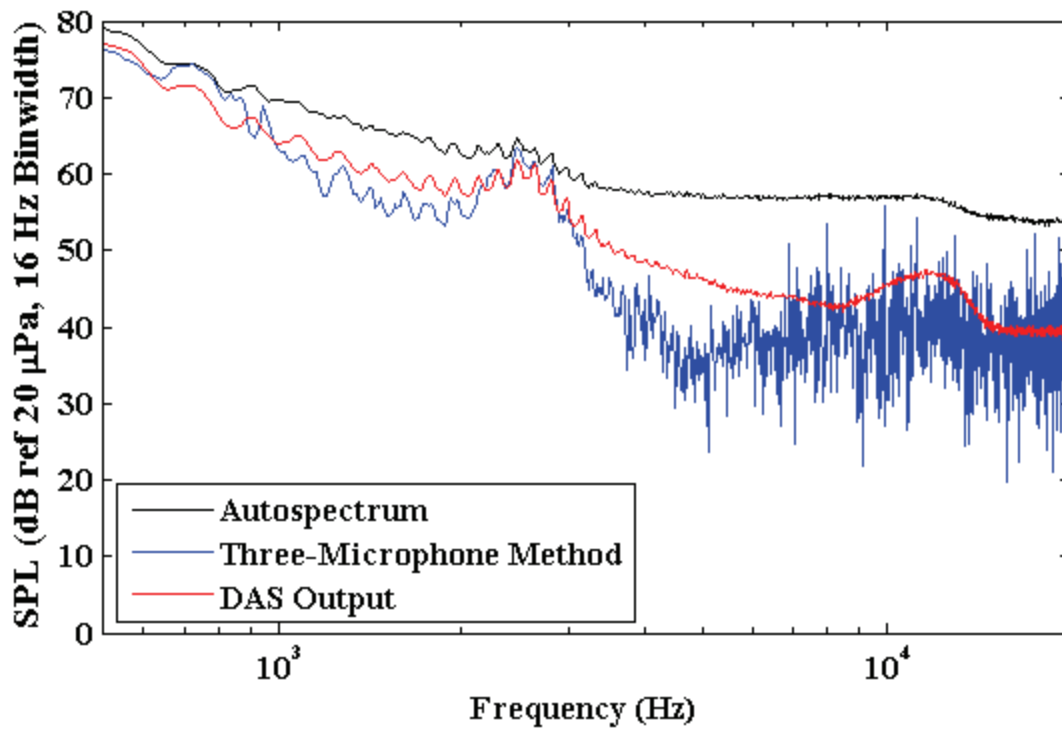


Figure 5-40. Comparison of three-microphone method and DAS for $M = 0.17$.

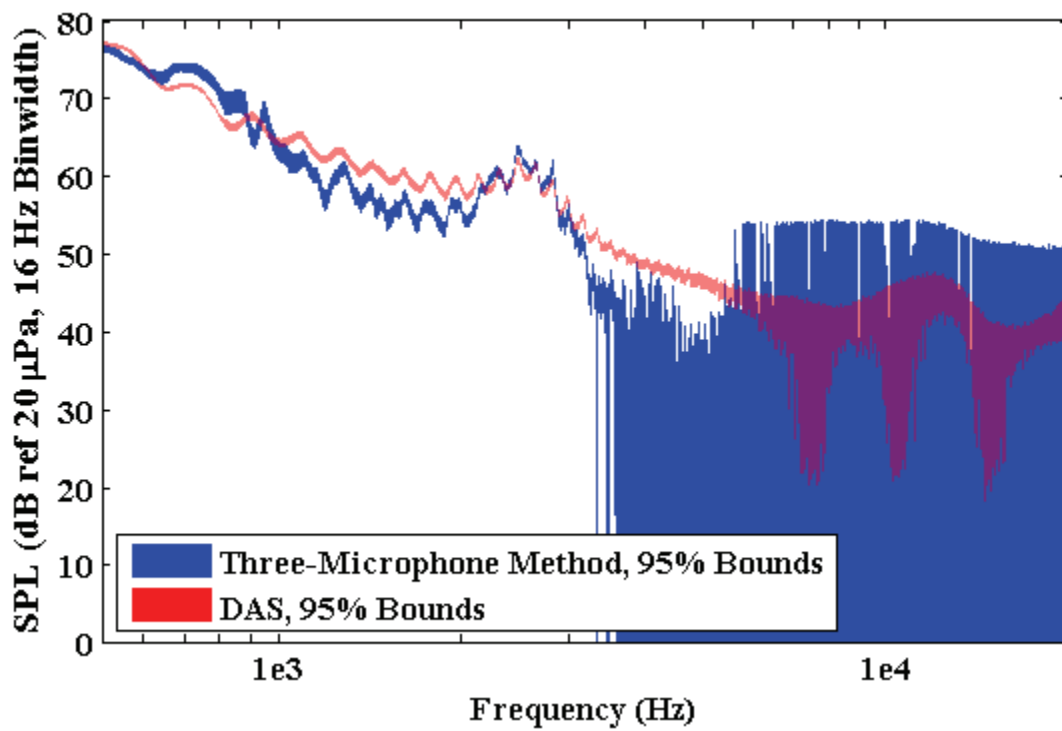


Figure 5-41. Comparison of confidence interval bounds for $M = 0.17$.

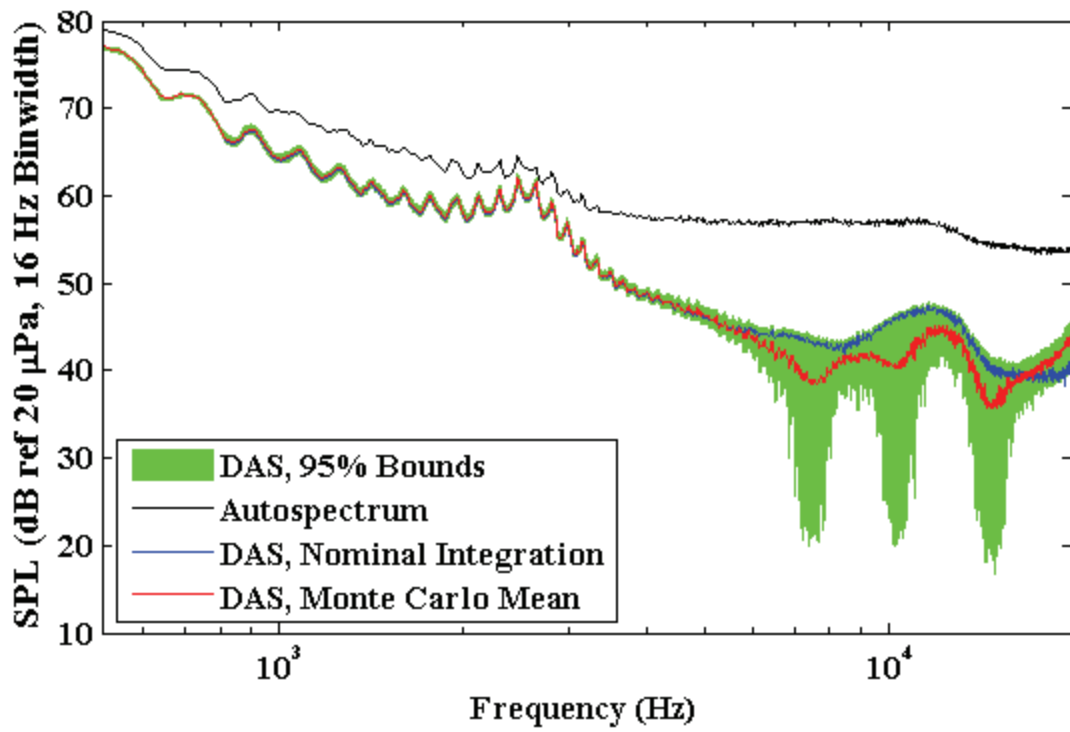


Figure 5-42. Comparison of nominal and Monte Carlo mean solutions for $M = 0.17$.

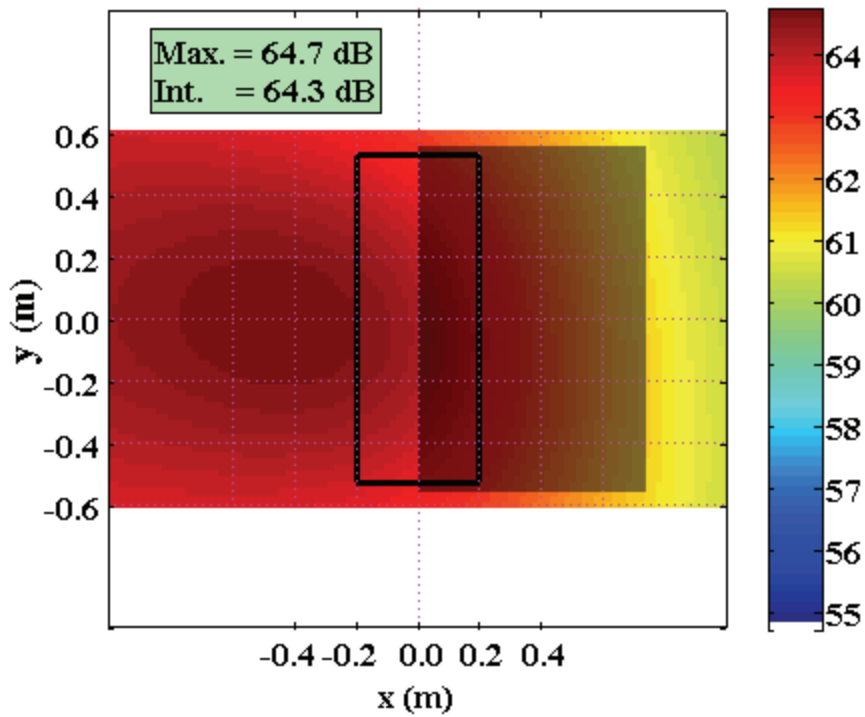


Figure 5-43. Beam map of test section at 1,024 Hz, $M = 0.17$, 0 degree AoA.

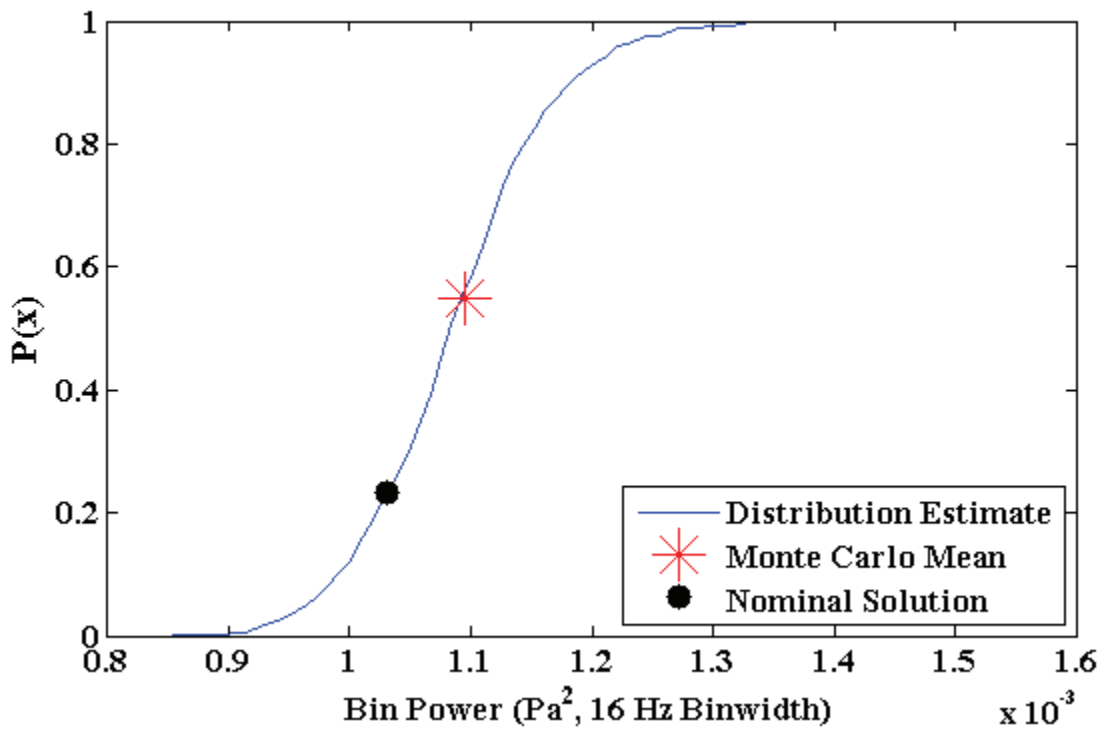


Figure 5-44. Cdf of integrated Monte Carlo data at 1,024 Hz, $M = 0.17$, 0 degree AoA.

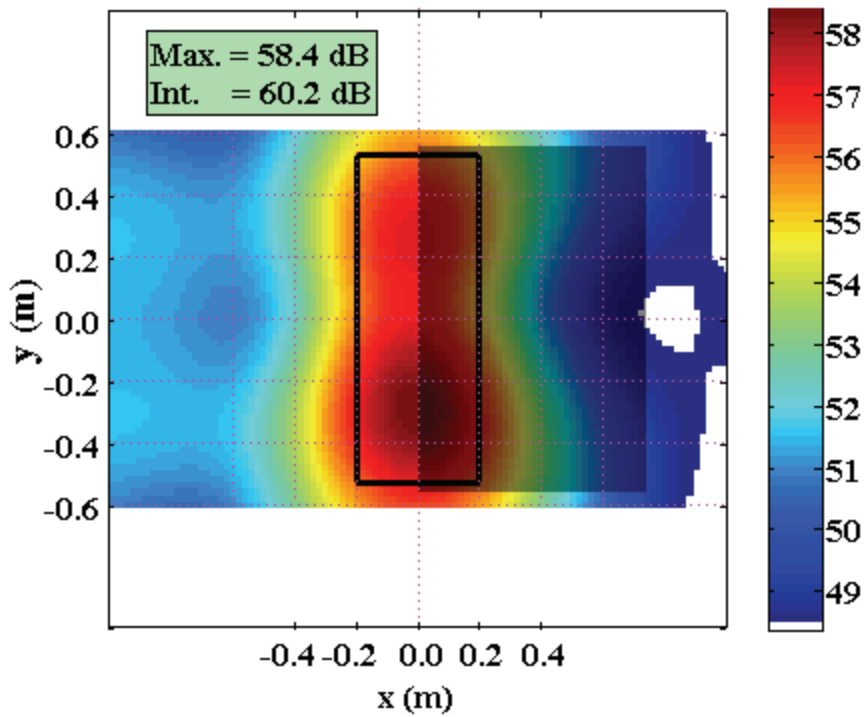


Figure 5-45. Beam map of test section at 2,512 Hz, $M = 0.17$, 0 degree AoA.

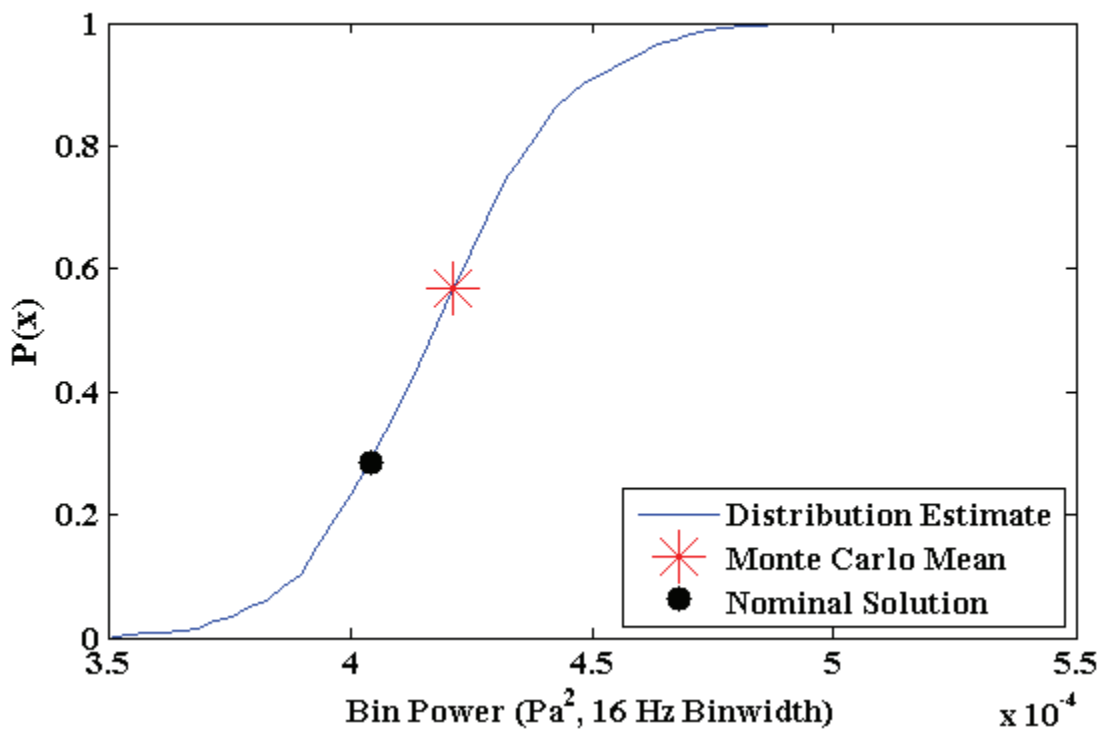


Figure 5-46. Cdf of integrated Monte Carlo data at 2,512 Hz, $M = 0.17$, 0 degree AoA.

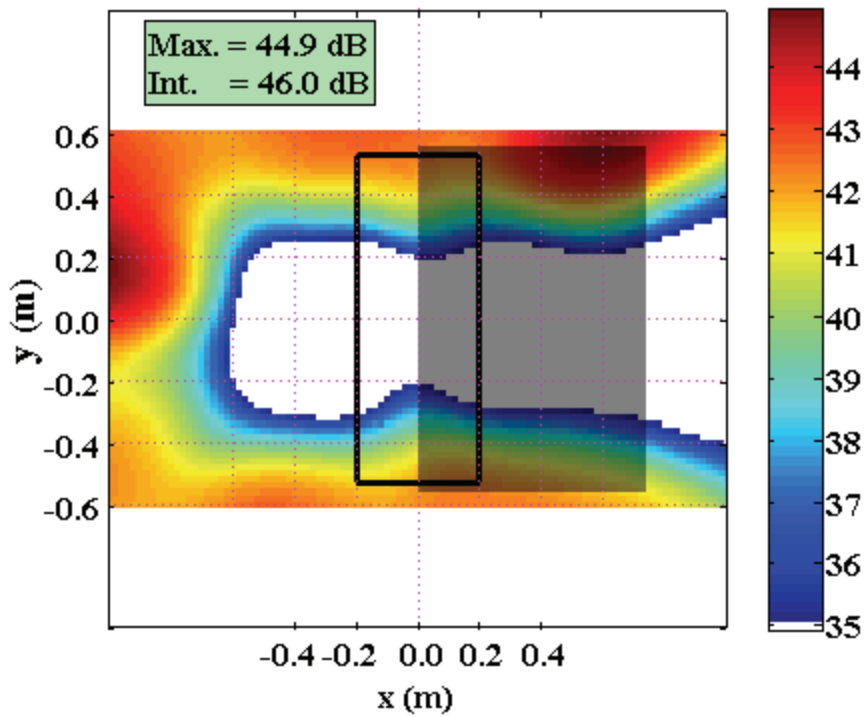


Figure 5-47. Beam map of test section at 5,008 Hz, $M = 0.17$, 0 degree AoA.

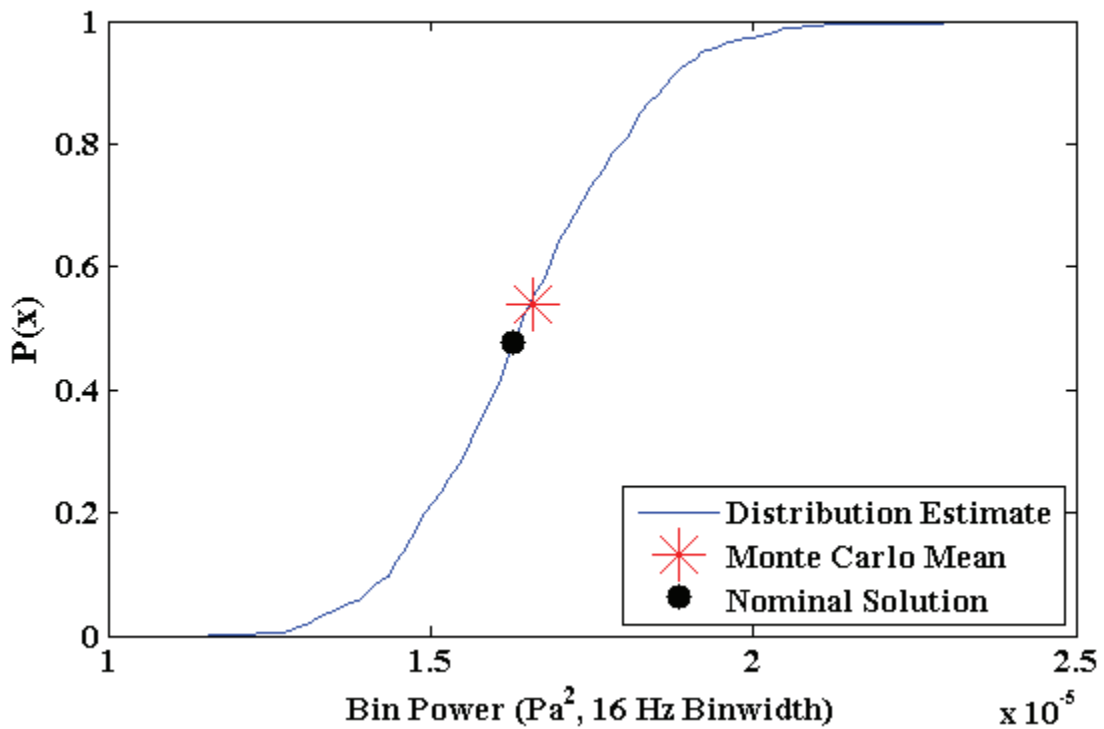


Figure 5-48. Cdf of integrated Monte Carlo data at 5,008 Hz, $M = 0.17$, 0 degree AoA.

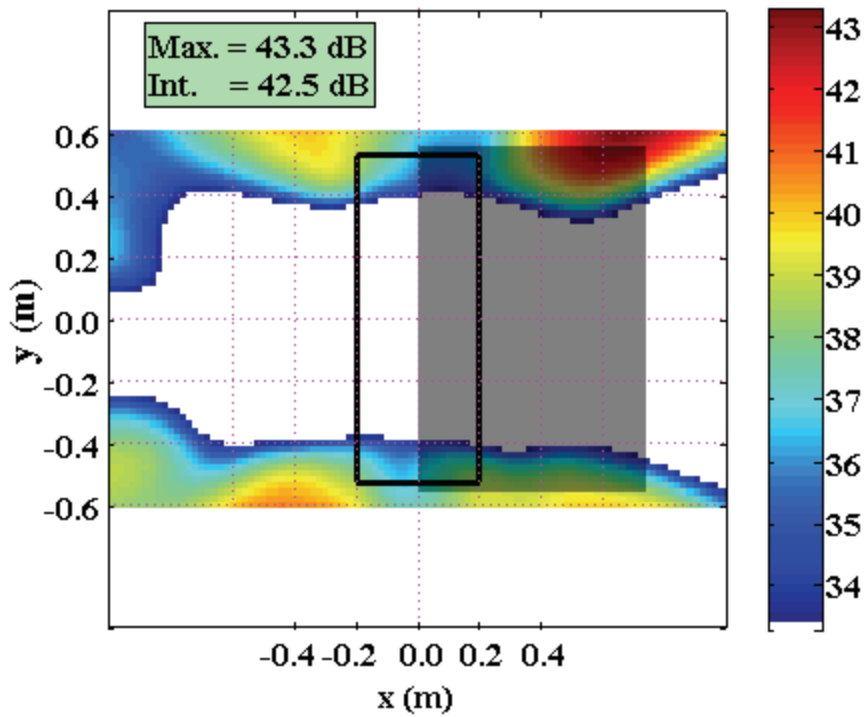


Figure 5-49. Beam map of test section at 7,600 Hz, $M = 0.17$, 0 degree AoA.

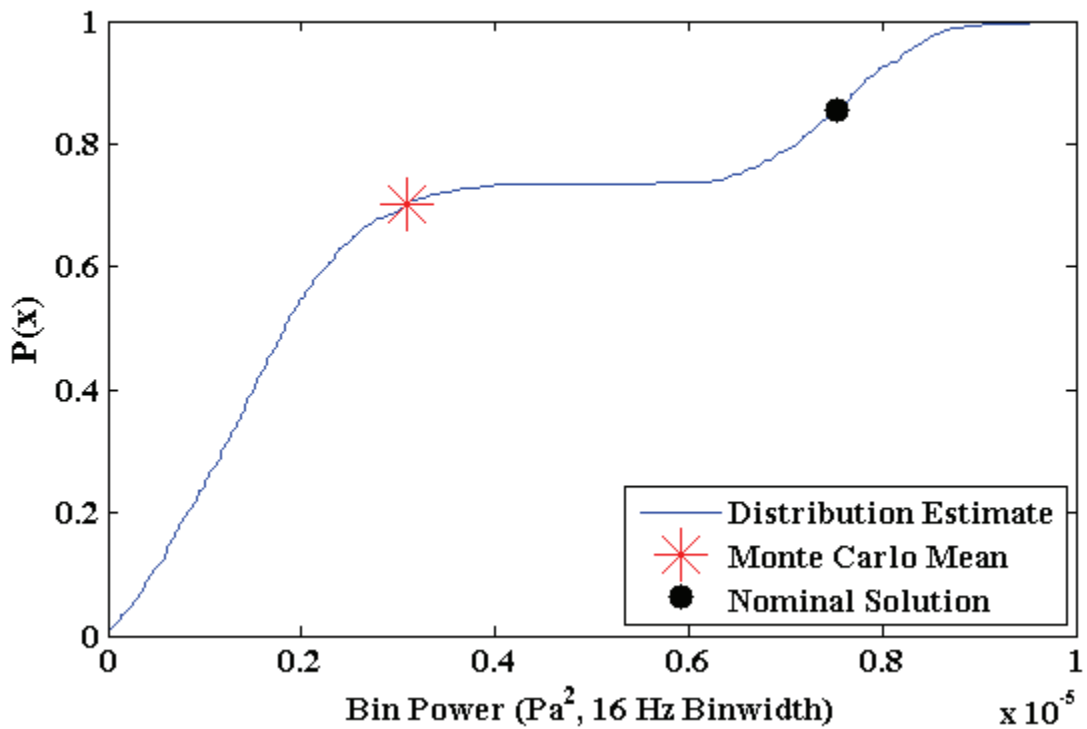


Figure 5-50. Cdf of integrated Monte Carlo data at 7,600 Hz, $M = 0.17$, 0 degree AoA.

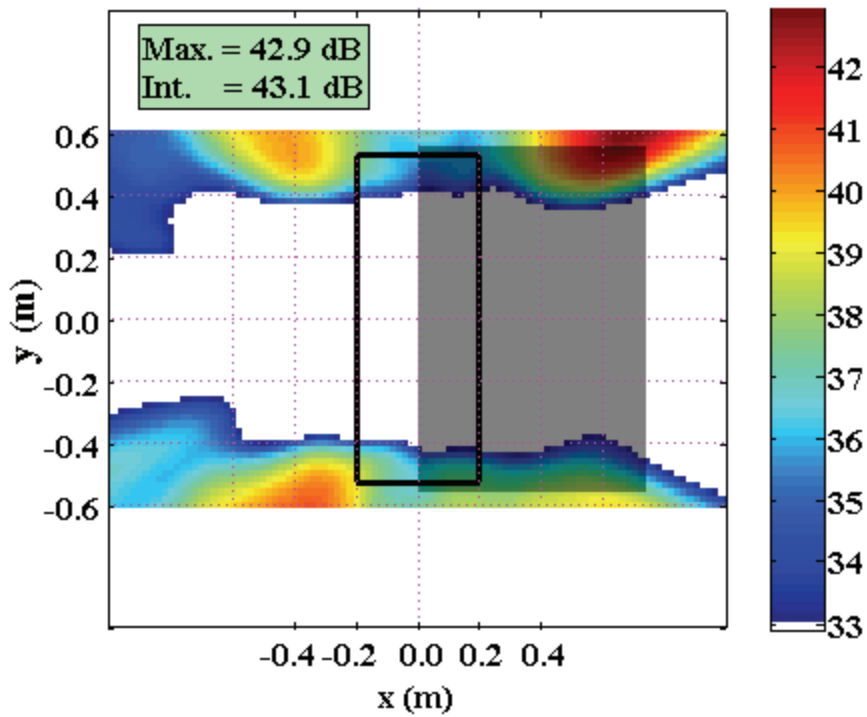


Figure 5-51. Beam map of test section at 8,800 Hz, $M = 0.17$, 0 degree AoA.

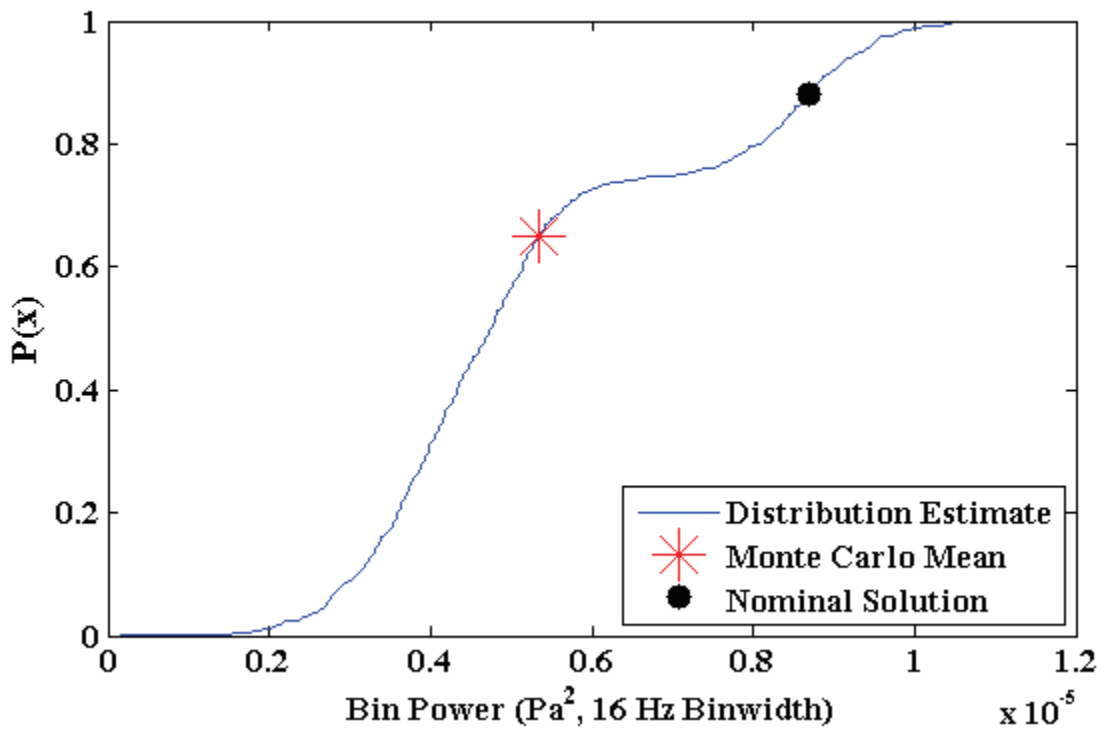


Figure 5-52. Cdf of integrated Monte Carlo data at 8,800 Hz, $M = 0.17$, 0 degree AoA.

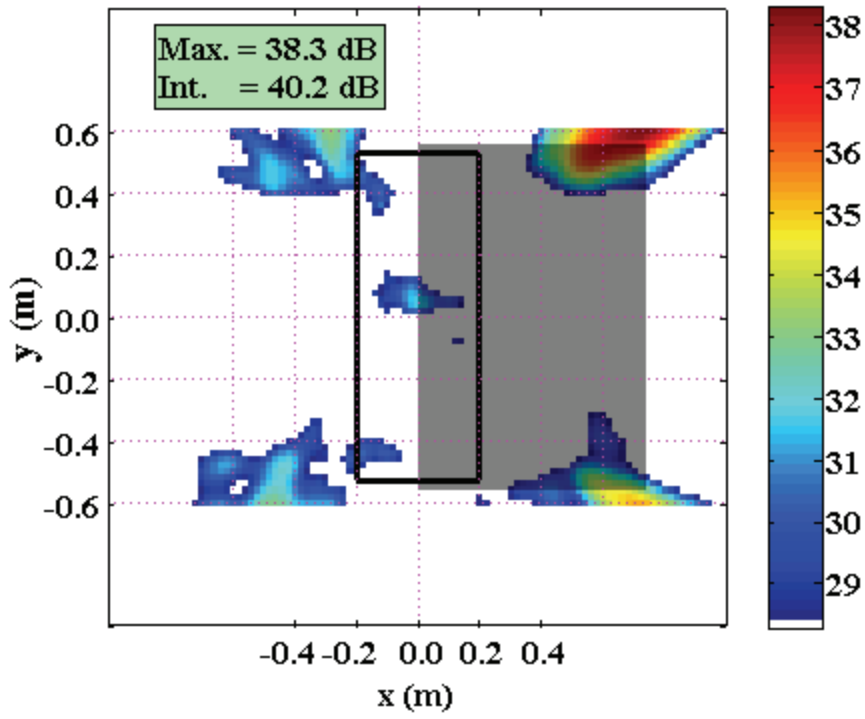


Figure 5-53. Beam map of test section at 15,008 Hz, M = 0.17, 0 degree AoA.

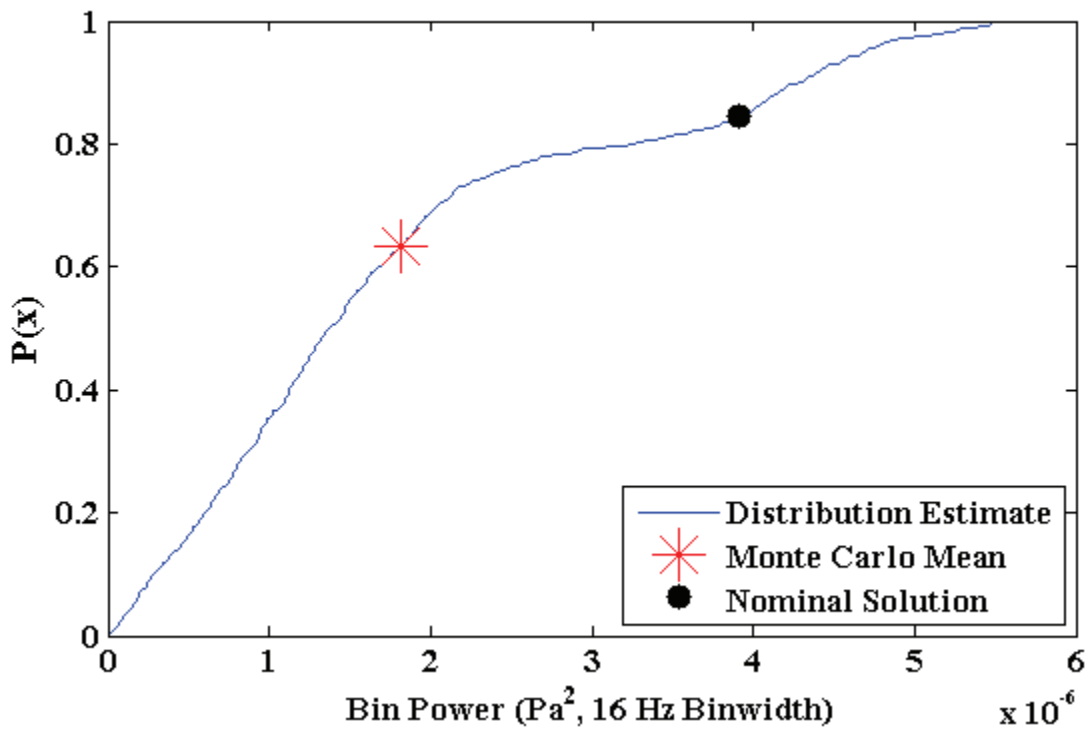


Figure 5-54. Cdf of integrated Monte Carlo data at 15,008 Hz, M = 0.17, 0 degree AoA.

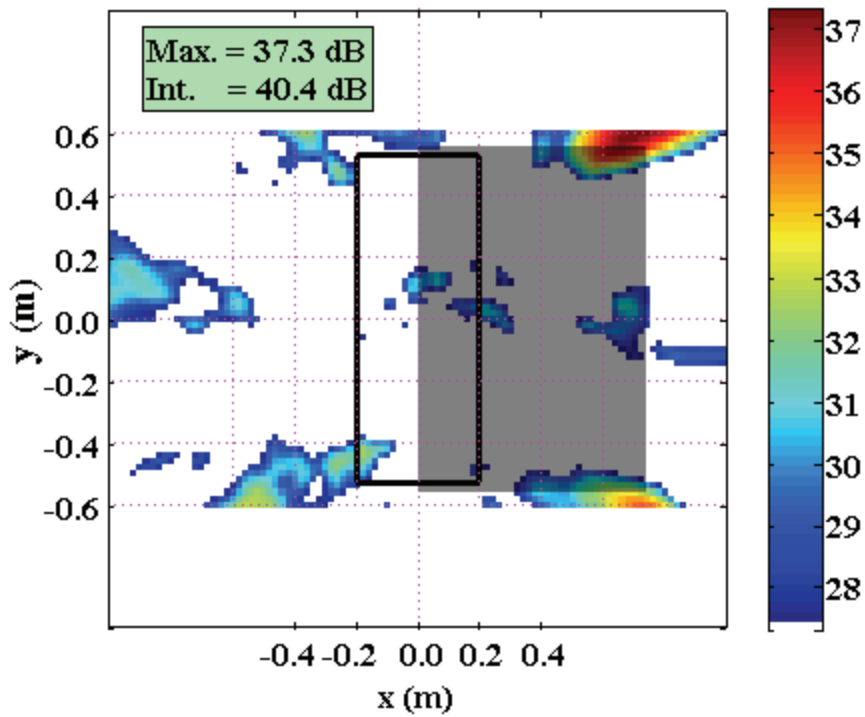


Figure 5-55. Beam map of test section at 20,000 Hz, $M = 0.17$, 0 degree AoA.

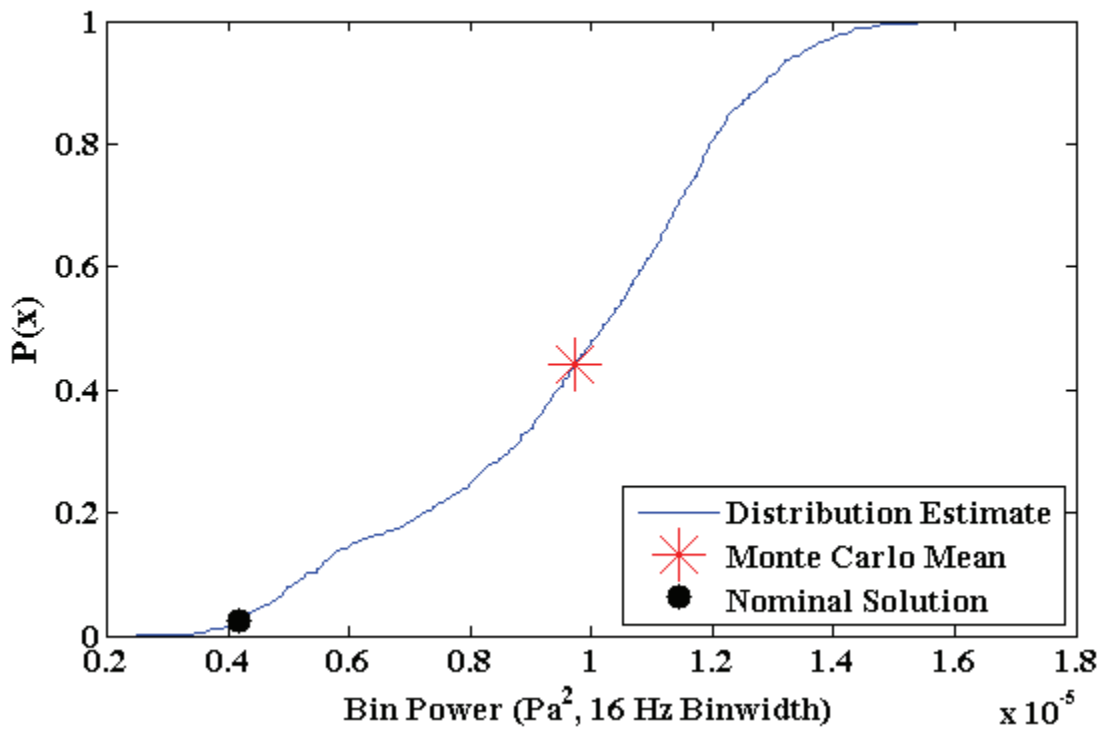


Figure 5-56. Cdf of integrated Monte Carlo data at 20,000 Hz, $M = 0.17$, 0 degree AoA.

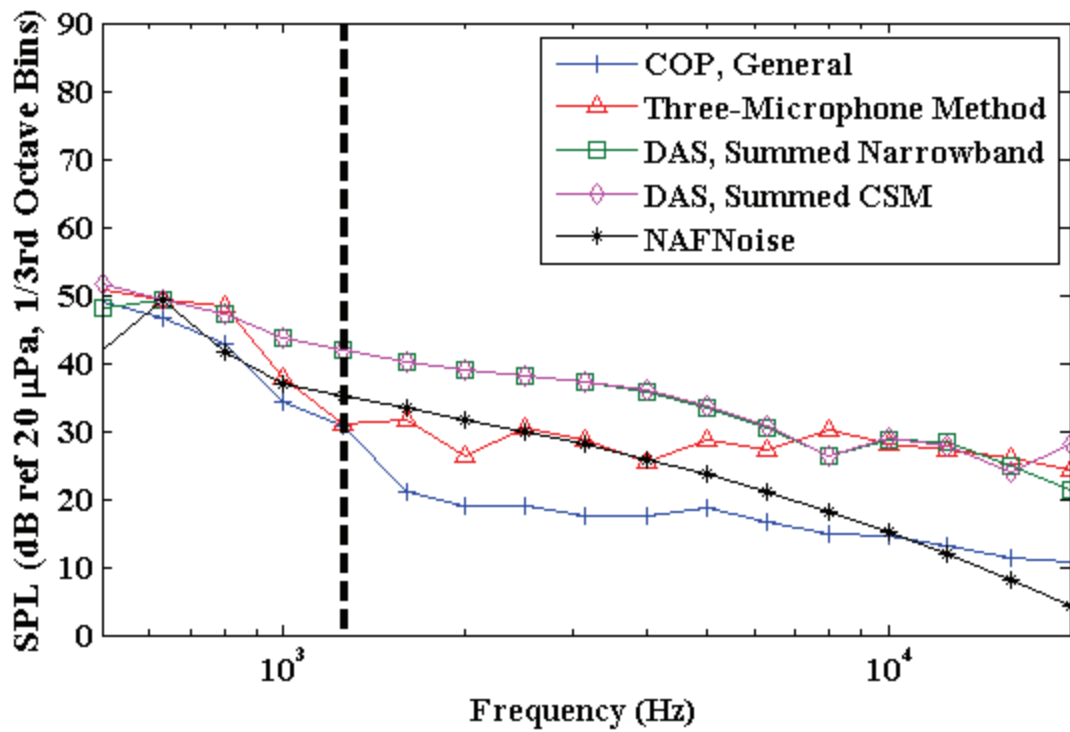


Figure 5-57. 1/3rd octave method comparisons for a Mach number of 0.05 and 0 degree AoA.

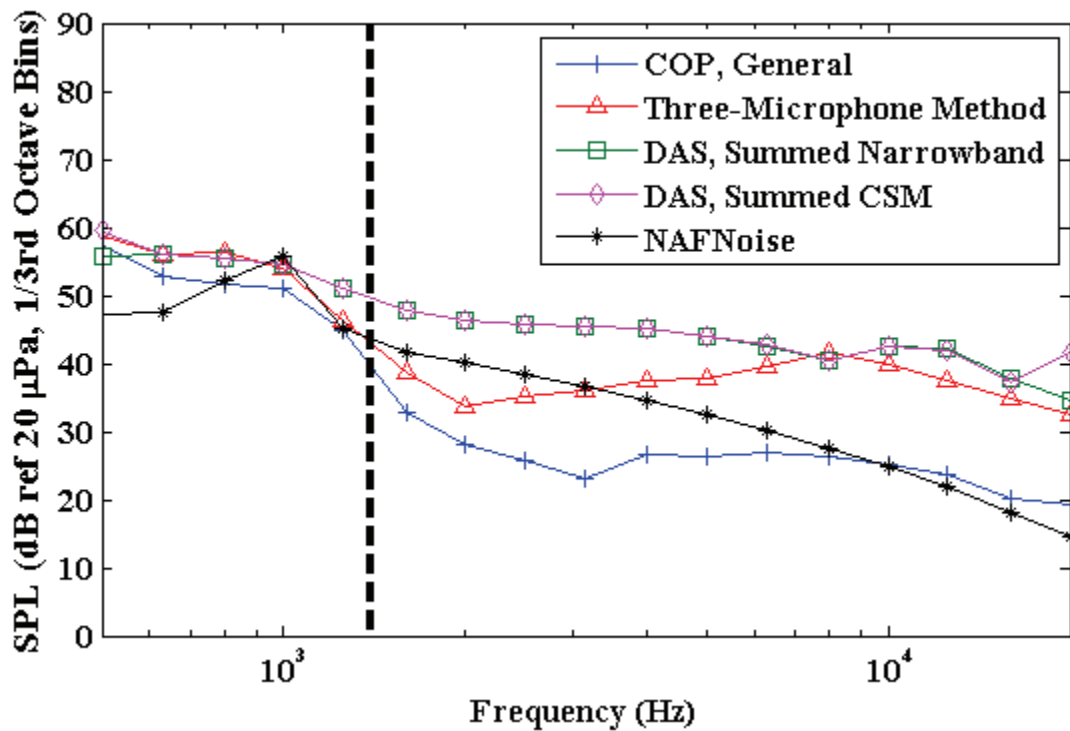


Figure 5-58. 1/3rd octave method comparisons for a Mach number of 0.07 and 0 degree AoA.

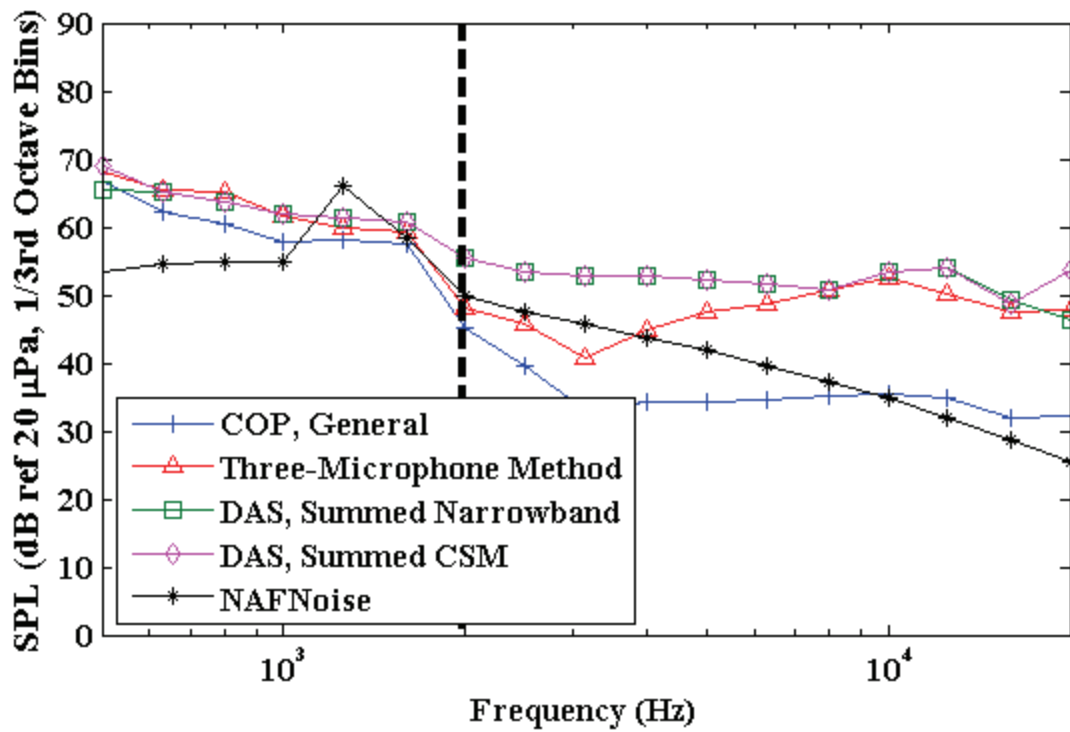


Figure 5-59. 1/3rd octave method comparisons for a Mach number of 0.10 and 0 degree AoA.

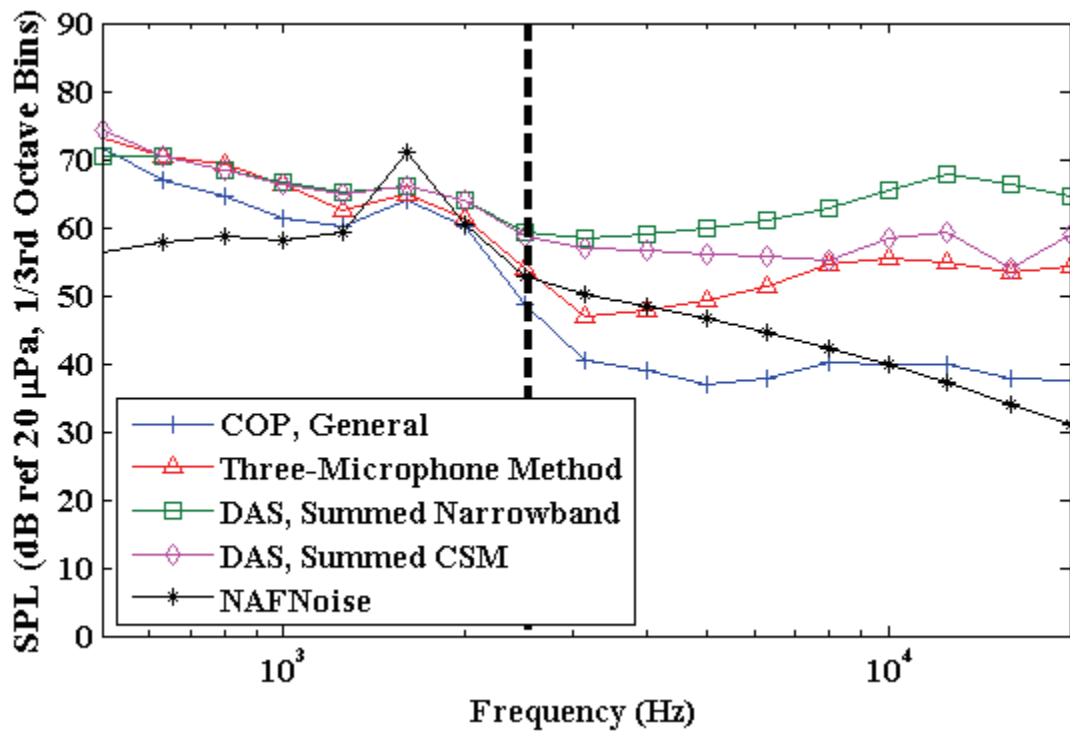


Figure 5-60. 1/3rd octave method comparisons for a Mach number of 0.12 and 0 degree AoA.

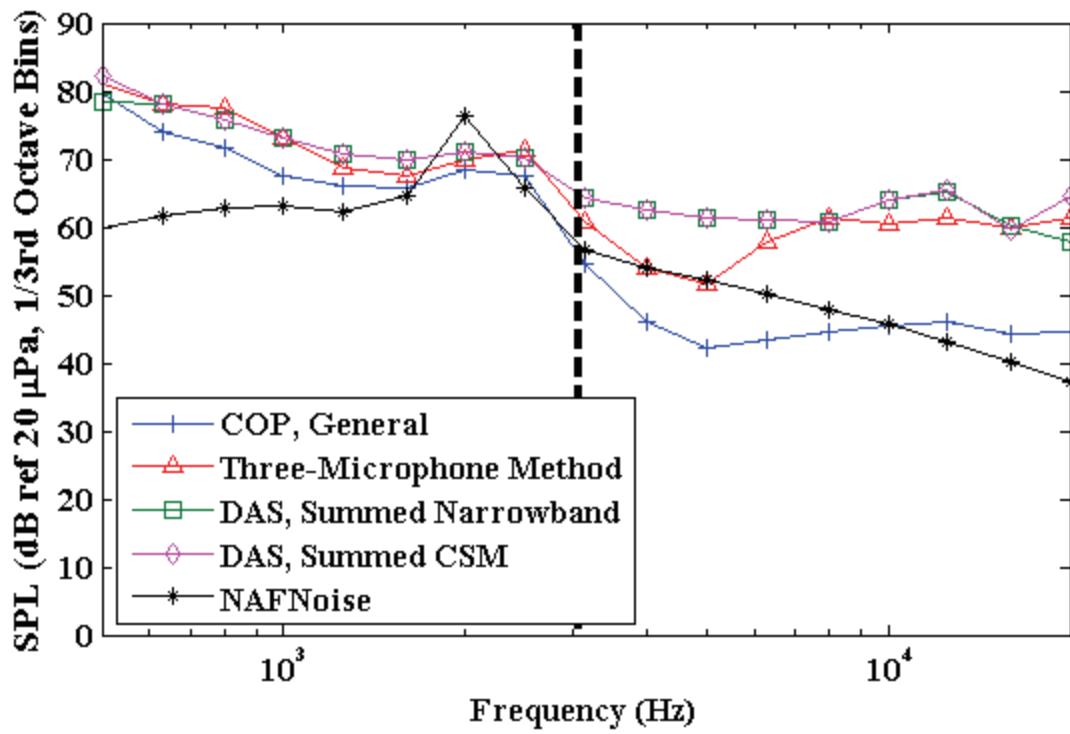


Figure 5-61. 1/3rd octave method comparisons for a Mach number of 0.15 and 0 degree AoA.

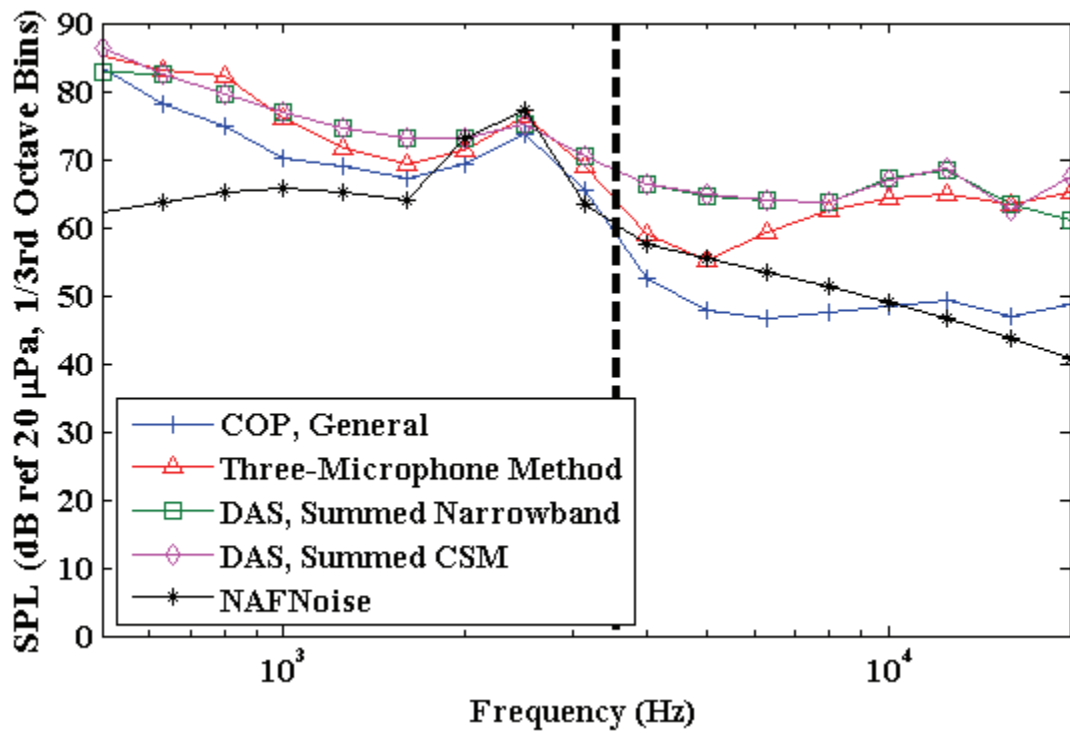


Figure 5-62. 1/3rd octave method comparisons for a Mach number of 0.17 and 0 degree AoA.

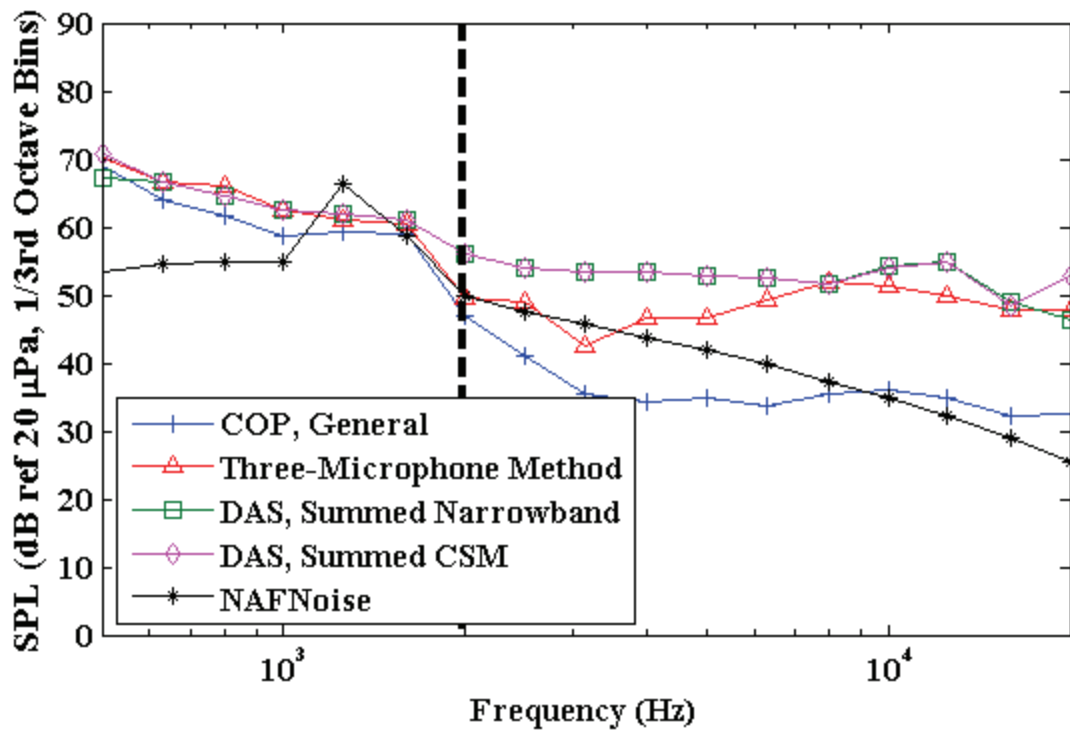


Figure 5-63. 1/3rd octave method comparisons for a Mach number of 0.10 at -1.5 degree AoA.

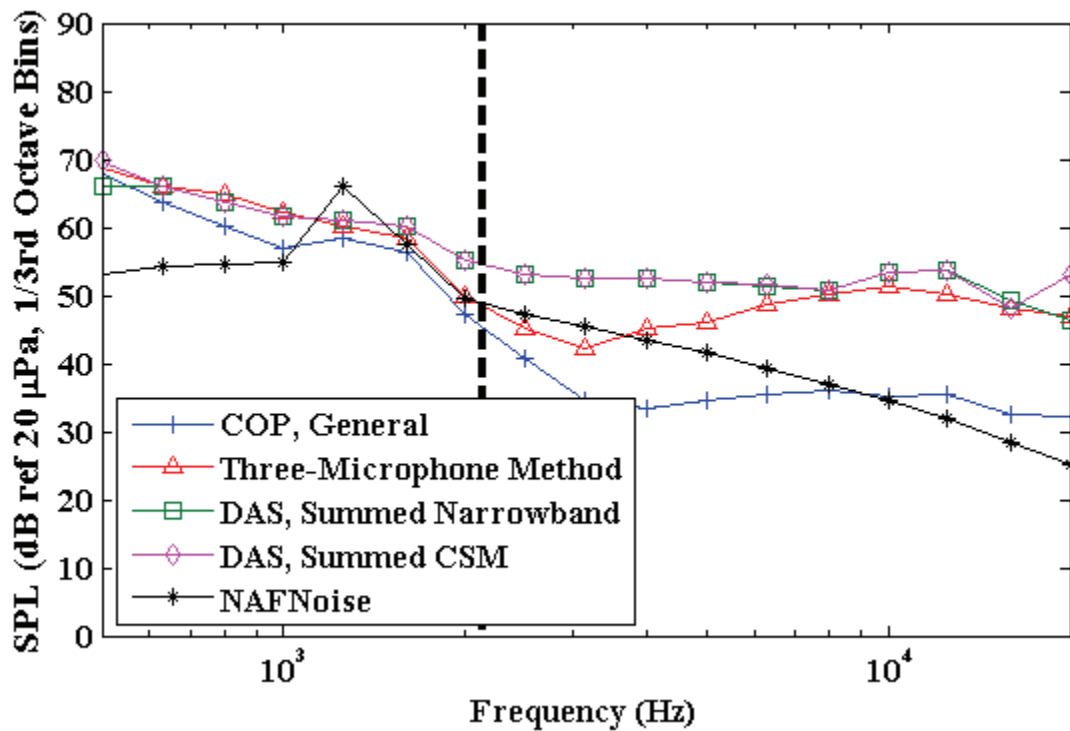


Figure 5-64. 1/3rd octave method comparisons for a Mach number of 0.10 at 1.5 degree AoA.

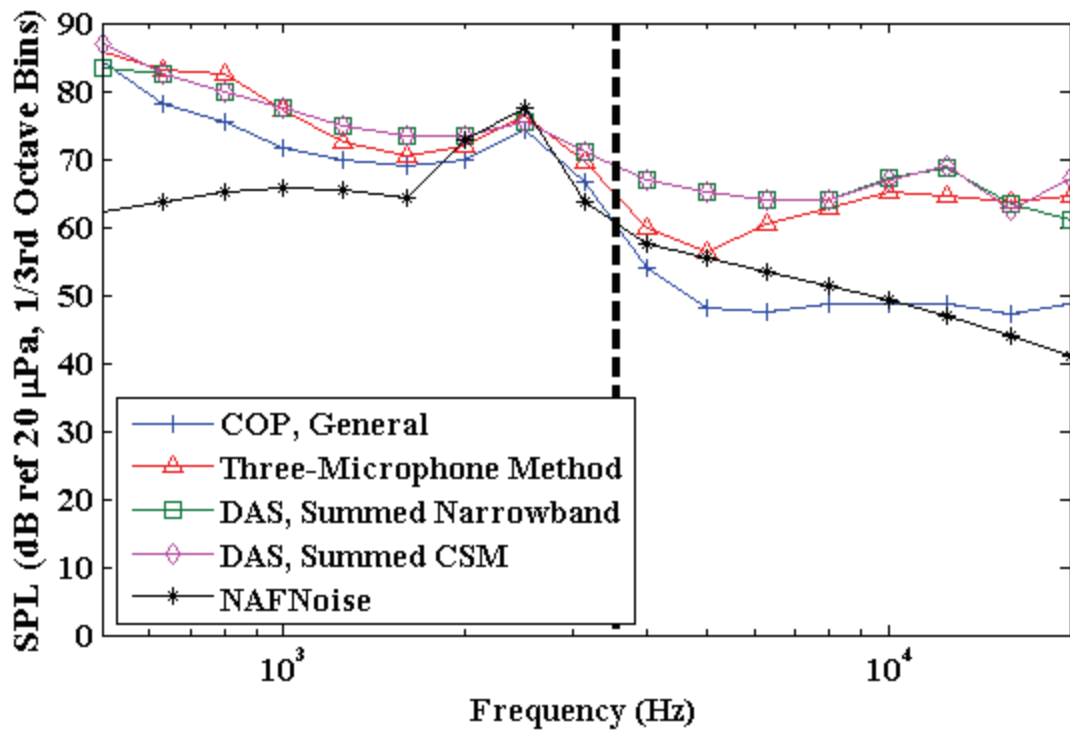


Figure 5-65. 1/3rd octave method comparisons for a Mach number of 0.17 at -1.5 degree AoA.

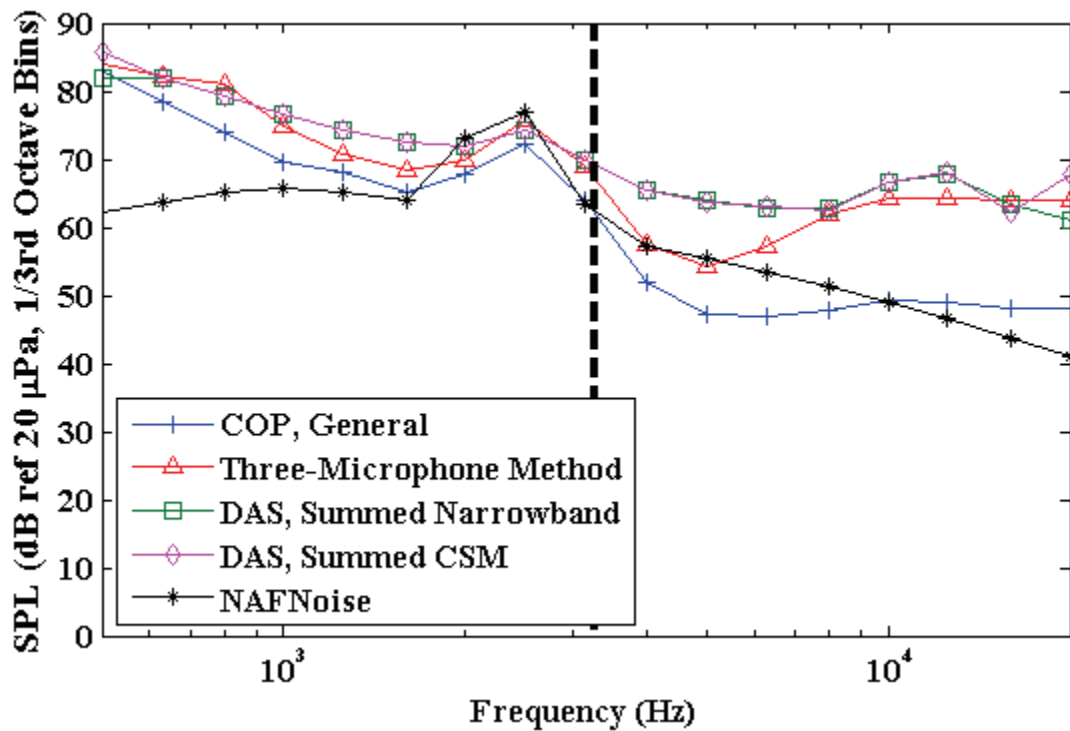


Figure 5-66. 1/3rd octave method comparisons for a Mach number of 0.17 at 1.5 degree AoA.

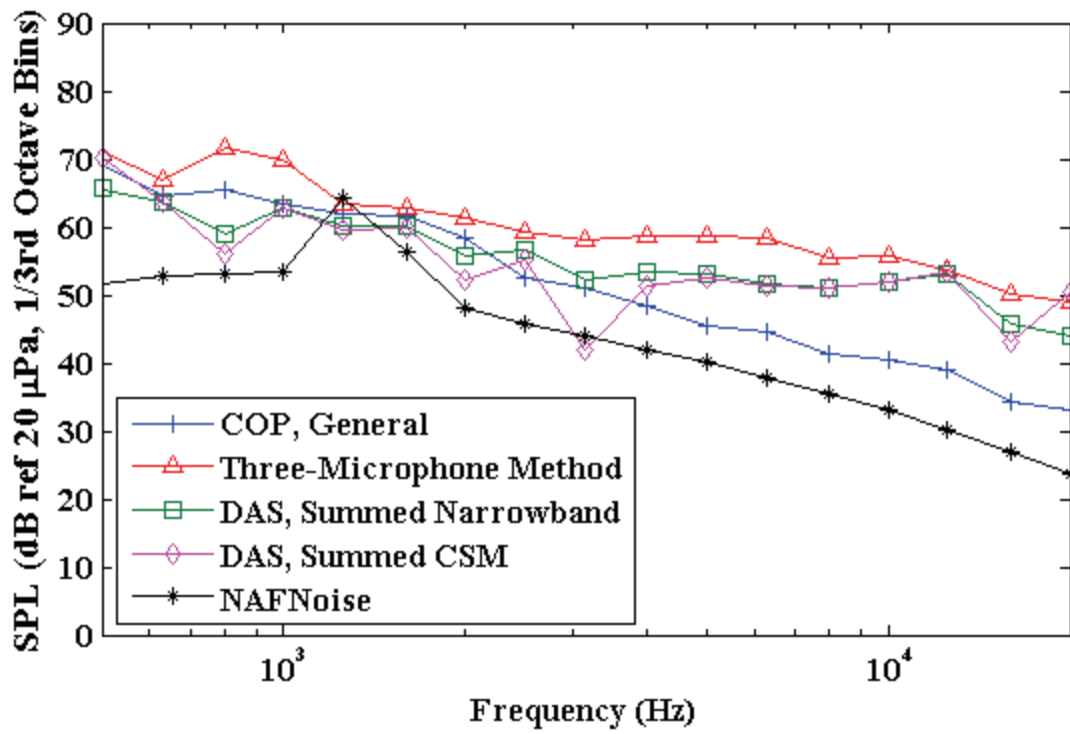


Figure 5-67. 1/3rd octave method comparisons for M = 0.10, 0 degree AoA with offset array.

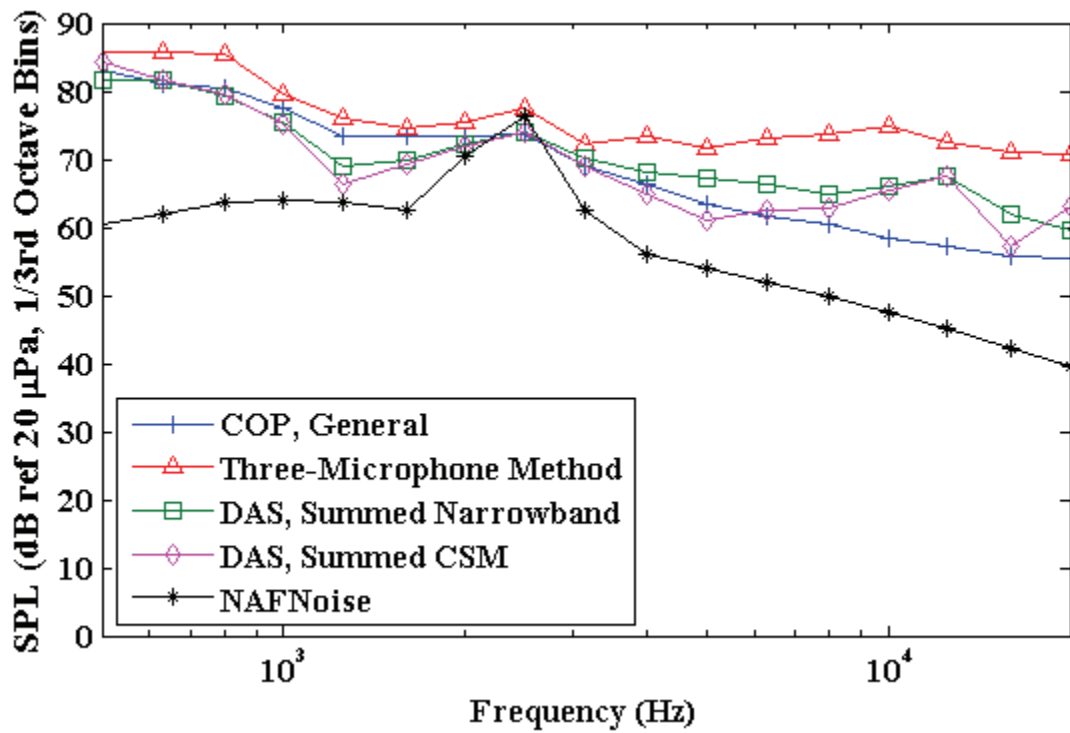


Figure 5-68. 1/3rd octave method comparisons for M = 0.17, 0 degree AoA with offset array.

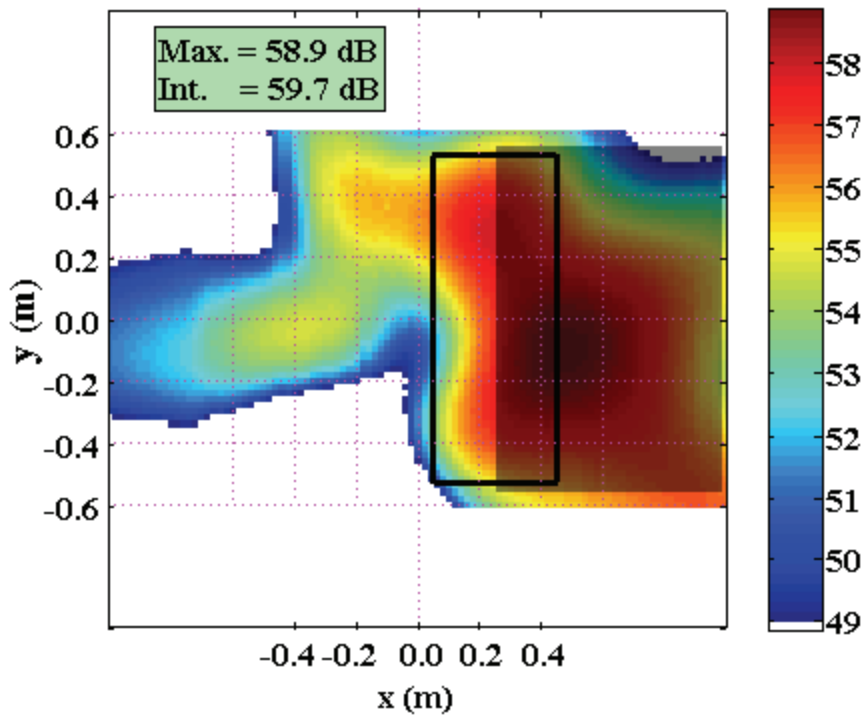


Figure 5-69. Beam map of narrowband CSM at 2,512 Hz for offset array at $M = 0.17$, $AoA = 0$.

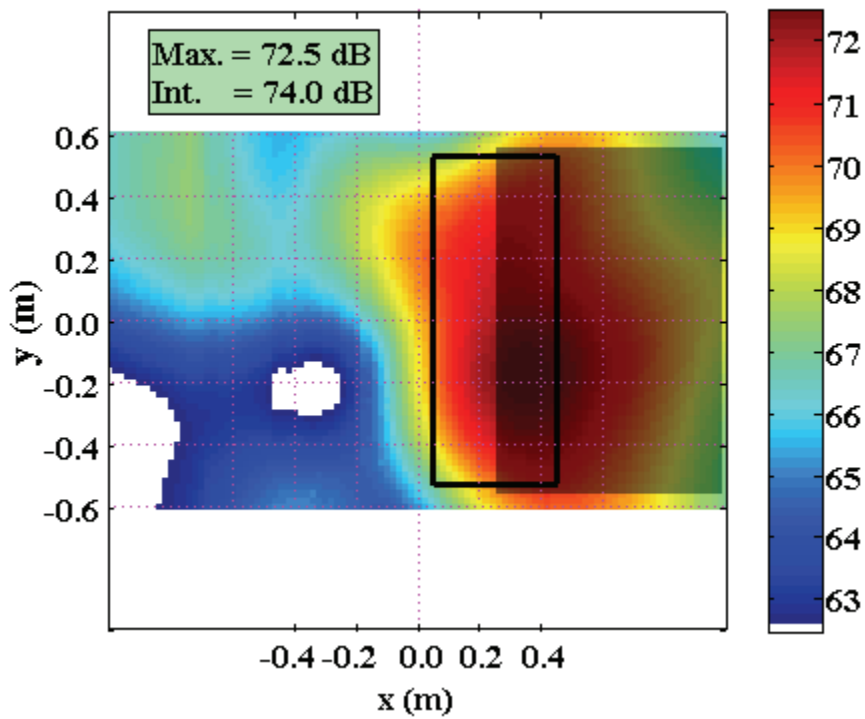


Figure 5-70. Beam map of $1/3^{\text{rd}}$ octave CSM at 2,500 Hz for offset array at $M = 0.17$, $AoA = 0$.

Table 5-1. Integrated array levels at 2,512 Hz for $M = 0.17$, 0 degree AoA for varying integration region dimensions. The nominal integration region, spanning from $x = -0.2$ m to 0.2 m and $y = -0.53$ m to 0.53 m and shown in Figure 5-45 with the frequency's beam map, is listed first.

x-boundary, min (m)	x-boundary, max (m)	y-boundary, min (m)	y-boundary, max (m)	SPL (dB ref 20 μ Pa, 16 Hz binwidth)
-0.2	0.2	-0.53	0.53	60.2
-0.2	0.2	-0.2	0.2	58.1
-0.2	0.2	-0.4	0.4	59.5
-0.2	0.2	-0.6	0.6	60.5
-0.4	0.4	-0.2	0.2	57.9
-0.4	0.4	-0.4	0.4	59.3
-0.4	0.4	-0.6	0.6	60.4
-0.6	0.6	-0.2	0.2	58.1
-0.6	0.6	-0.4	0.4	59.5
-0.6	0.6	-0.6	0.6	60.5

Table 5-2. Integrated array levels at 7,600 Hz for $M = 0.17$, 0 degree AoA for varying integration region dimensions. The nominal integration region, spanning from $x = -0.2$ to 0.2 m and $y = -0.53$ m to 0.53 m and shown in Figure 5-49 with the frequency's beam map, is listed first.

x-boundary, min (m)	x-boundary, max (m)	y-boundary, min (m)	y-boundary, max (m)	SPL (dB ref 20 μ Pa, 16 Hz binwidth)
-0.2	0.2	-0.53	0.53	42.5
-0.2	0.2	-0.2	0.2	-Inf
-0.2	0.2	-0.4	0.4	34.7
-0.2	0.2	-0.6	0.6	44.4
-0.4	0.4	-0.2	0.2	-Inf
-0.4	0.4	-0.4	0.4	38.0
-0.4	0.4	-0.6	0.6	48.0
-0.6	0.6	-0.2	0.2	-Inf
-0.6	0.6	-0.4	0.4	40.2
-0.6	0.6	-0.6	0.6	50.1

Table 5-3. Integrated array levels at 20,000 Hz for $M = 0.17$, 0 degree AoA for varying integration region dimensions. The nominal integration region, spanning from $x = -0.2$ to 0.2 m and $y = -0.53$ m to 0.53 m and shown in Figure 5-55 with the frequency's beam map, is listed first.

x-boundary, min (m)	x-boundary, max (m)	y-boundary, min (m)	y-boundary, max (m)	SPL (dB ref 20 μ Pa, 16 Hz binwidth)
-0.2	0.2	-0.53	0.53	40.4
-0.2	0.2	-0.2	0.2	38.4
-0.2	0.2	-0.4	0.4	38.9
-0.2	0.2	-0.6	0.6	40.6
-0.4	0.4	-0.2	0.2	40.0
-0.4	0.4	-0.4	0.4	40.1
-0.4	0.4	-0.6	0.6	42.0
-0.6	0.6	-0.2	0.2	40.0
-0.6	0.6	-0.4	0.4	38.4
-0.6	0.6	-0.6	0.6	41.9

CHAPTER 6 CONCLUSIONS & FUTURE WORK

The measurement of acoustic sources in wind tunnel testing is a common task, and one in which many tools are available. Autospectral analysis is of course the simplest but has no mechanism for decoupling the acoustic field of interest from measurement noise. Basic analysis tools, such as coherent power analysis formulated in two different ways in Equation (4-14) and Equation (4-17), provide an estimate of the coherent signal field, but are either biased in power by measurement noise in the first case, or highly specific in their assumptions and application in the second. A slight increase in measurement complexity yields the three-microphone method, Equation (4-24), which provides estimates of both signal and noise strength. However, the assumptions inherent in this method limit its applicability in multi-source measurements, as discussed in Appendix C. Generalized analysis techniques such as covariance-based fitting methods may provide more robust estimates for a single dominant noise source when more than three microphones are used in an experimental configuration, but additional research is required to determine convergence parameters for the methods when sources are distributed, as well as how to best leverage the methods in experimental setup. Beamforming methods, such as the frequency-domain DAS beamformer in Equation (4-37), provide the most information, but at the cost of experimental and processing complexity. Also, different algorithms can yield different results. The data shown in the previous chapter make one thing abundantly clear: measurement of trailing edge noise is not a straightforward task. The methods which are so often blindly used in acoustic analysis can have tremendous systematic uncertainties in their output, and only through careful consideration of these uncertainties and the physical setup can results be compared.

In regards to the specifics of trailing edge noise measurement, coherence-based techniques appear to operate well on the actual airfoil trailing edge noise source, within their limiting assumptions given the number of microphones used, but suffer severe penalties in frequency ranges where noise appears to come from distributed background sources. Unfortunately, beamforming is required to assess the presence of other potential noise sources. Beamforming methods can provide more information and improved results, but even they suffer from large uncertainty in output depending on measurement conditions. Standard beamforming methods also have no way of removing low frequency noise, as the array resolution becomes poor. Also, high frequency aperture effects may be an issue. It is only through a combined effort of examining all the possible analysis methods that some understanding of the noise source behavior can be gained.

The overall data acquired in this body of work appear to be in qualitative agreement with previous work. This is not necessarily due to the quality of the current or previous results, but to the large measurement uncertainties over so much of the bandwidth of interest. At the airfoil shedding peak and below, most uncertainty bounds are distinct and conclusions can be drawn about when and why some methods differ, for instance generalized coherent power underpredicting acoustic levels from beamforming or the three-microphone method due to limitations in its formulation. However, at higher frequencies where the background noise is not well behaved, uncertainties become large and all methods overlap solely because the confidence intervals occupy such a large logarithmic power domain. Based on the levels seen, it would appear that the airfoil is not generating appreciable noise within this higher bandwidth. However, the background noise could just be loud enough to mask an interesting noise feature of the airfoil.

From the present work, it appears that array-based measurements provide the best, most well-behaved results in determining trailing edge noise. The lower frequency bound on the array-based methods is unfortunately a strong limitation given the predicted bandwidth of trailing edge noise. To properly reject contaminating noise at low frequencies, a larger array is necessary. Unfortunately the cost of using a larger array is that sidelobe contamination becomes a concern at lower frequencies. While existing deconvolution approaches appear and warrant further investigation, as shown in Appendix E, the computational expense involved makes them prohibitive for routine use. As a preliminary recommendation, it appears that a hybrid approach could be used. Here, for frequencies where the array spatial resolution is poor relative to the size of the wind tunnel test section, Appendix C would suggest that the three-microphone method would perform well at extracting the acoustic field of the measurement, although it would not provide information regarding the nature of the acoustic source. Array output could be considered once the array beamwidth becomes small enough to start rejecting acoustic energy from extraneous sources in the facility.

It should be noted that, based on Appendix C, the validity of coherent power methods is strongly dependent on the spanwise behavior of the trailing edge. For a large number of incoherent sources along the trailing edge span, which based on the discussion in Chapter 2 could physically model the turbulent flow field in the vicinity of the trailing edge, spanwise microphone coherence breaks down more quickly as a function of reduced source-to-source spacing. This indicates that a reduction in spanwise correlation scales, for example due to the introduction of trailing edge serrations [Howe 1991], would have an adverse effect on any spanwise coherence measurements. As the trailing edge noise source no longer exists along a single, centered line with respect to the measurement microphones, even a center-span coherence

measurement may under-estimate acoustic levels at higher frequencies as long as the measurement microphones are near the model. Specifically, a degradation in ordinary coherence levels could occur which would cause coherent power-based prediction methods to provide underestimates of the true acoustic field.

For an ideal trailing edge noise measurement with these techniques, a facility should have noise sources far removed from the airfoil noise source, and measurement microphones far removed from the model. The coherence-reduction effects of Appendix C would be for the most part negated under these conditions. While UF AFF is limited in the overall measurement domain, it may be useful to consider removing the jet collector and forward part of the facility diffuser. This acoustic source appears to contaminate a large portion of the lower frequency spectra, but moving the collector to the rear of UF AFF's anechoic chamber will reduce the maximum flow speed. Nonetheless, the noise reduction benefits may be worthwhile. Regarding sidewall noise, some additional investigation of the sidewalls is warranted as beam maps indicate they are a major noise source from near 5 kHz to somewhere below 15 kHz. The acoustic absorption coefficient of the sidewalls used in the facility is plotted in Figure 6-1. Clearly, the absorption is non-ideal at frequencies well within the predicted bandwidth of this model's trailing edge. In addition, the porous nature of the sidewalls may allow for flow through the surface, introducing additional noise. A hybrid sidewall fabrication should be examined, where an acoustically treated thin surface is used, backed with a bulk acoustic absorber with better absorption properties. This wall should be bounded with impermeable material to prevent large scale flow through the wall, and the facility background noise re-examined.

Regarding instrumentation for this idealized setup, it has clearly been shown that a medium-sized plate-based array contaminates the test section acoustic field beyond acceptable

levels. This array design was selected based on convenience of installation for the WM-61a microphones, as previous work with them in on free-field rod installations proved difficult. Also, the plate-based array minimized the need for steering vector corrections, based on positional uncertainty of microphones. However, additional edge-scattering issues were introduced and complicated the group microphone calibration process, as discussed in Appendix D. For an ideal measurement, individually-calibrated free-field microphones would be used, installed on acoustically treated rods. Unfortunately, these will suffer self-scattering issues at higher frequencies which are directivity dependent, but for a model with a predicted bandwidth below 5 kHz such scattering would not be an issue. As long as these microphones could be accurately located in free space relative to the model, beamforming could be conducted without contaminating the model noise spectra with reflections. Additionally, larger arrays with nested sub-array designs should be used. The larger array will localize noise sources and specify overall integration bounds, while the smaller array will conduct the true source integration without suffering from source directivity effects. Currently such a design is infeasible in UFAFF due to DAQ system channel count limitations, but should be evaluated for future work.

Future work must leverage source behavior in the analysis of these measurement techniques. The data acquired here were collected in conjunction with surface pressure fluctuations in the vicinity of the trailing edge, on both sides of the model. These pressure fluctuations, once processed appropriately, can be used with source model techniques to attempt to match far field noise predictions with measurements. Also, the surface pressure data must be collected in conjunction with in-flow interrogation techniques such as two-point hotwire correlations, PIV, and/or LDV to gain a better understanding of how the overall flow field in the vicinity of the airfoil trailing edge relates to the surface pressure fluctuations. This current body

of research demonstrated that trailing edge noise is a difficult measurement, and there can be tremendous ambiguity in acoustic results. The next step in trailing edge noise analysis will require more source information to leverage in processing results. The next step in acoustic analysis is less clear. Fast deconvolution approaches must be investigated. A preliminary comparison between DAS and DAMAS is provided in Appendix E. SC-DAMAS [Yardibi *et al.* 2008] should also be investigated and compared to baseline DAMAS results. DAMAS is still limited by the source assumptions used in DAS, but a more generalized, semi-coherent source model for beamforming, such as DAMAS-C or MACS [Yardibi *et al.* 2010b] could be applied to the data to determine if any coherent source fields are present, or if the results are driven by incoherent trailing edge (or sidewall, diffuser etc.) sources. These methods could be used in conjunction with surface pressure and flow correlation data to determine over what bandwidth an aeroacoustic noise source is largely correlated, lending itself to coherent power analysis, and over what bandwidth it is largely uncorrelated, lending itself to conventional beamforming approaches. It is only with this combination of source and field information that some of the measurement ambiguity present in aeroacoustic wind tunnel testing can be reduced.

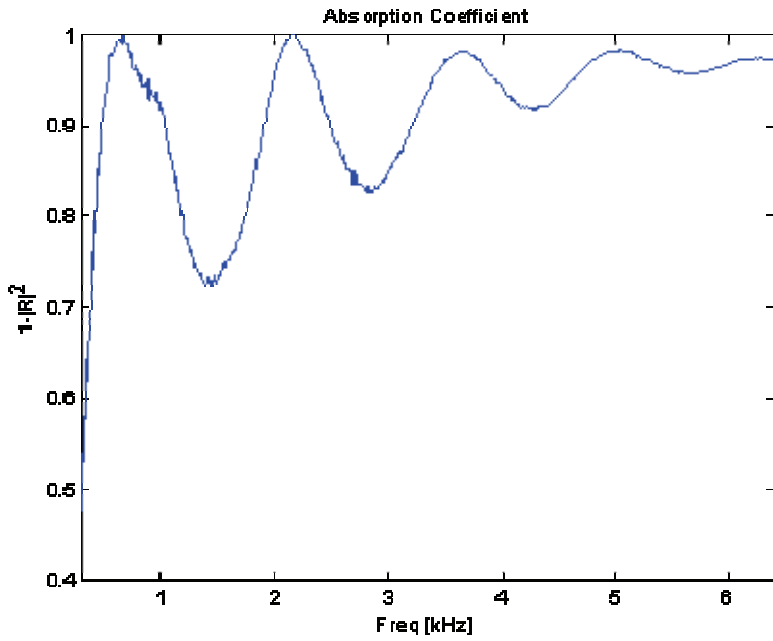


Figure 6-1. Acoustic absorption coefficient of sidewalls used in UFAFF.

APPENDIX A
AIRFOIL COORDINATE DESIGN AND MEASUREMENT COMPARISON CODE

```
function [s,e,MSE,t1n] = AFSNE(X,XM,x0,y0,theta)

% AFE is a function to compute the surface-normal error of a final,
% fabricated airfoil to its initial design coordinates.
% This function is of the form
%
% [s,e,MSE,t1n] = AFSNE(X,XM,x0,y0,theta)
%
% Where X is a two-column matrix of the design airfoil coordinates, and XM
% is the measured coordinates of the final airfoil, in the same format.
% These matrices should be formatted as X-Foil coordinates, where they
% begin at the suction-side trailing edge, wrap around the airfoil suction
% side, around the leading edge, and back to the pressure-side trailing
% edge. Files output from FoilXPort.m are of the correct format. t1n has
% been added as an exported quantity to allow for foil design
% modifications based on curve-fitted offset tables. t1n is the local
% normal slope to the surface (in radians).
%
% x0 and y0 are x and y offsets to apply to the measured coordinates, in
% case there is a coordinate system offset from the design values.
% Similarly, theta is a rotation applied to the measured coordinates, to
% correct for rotational disparities, in radians.
%
% The output s is the surface distance along the airfoil from the
% suction-side trailing edge, based on a linear approximation. e is the
% error at each s location, e(s). MSE is the mean-square of e.
%
% Note that this code will assume that both the airfoil design coordinates
% and the measured surface profile are reasonably smooth, and that they
% are already positioned close to the final overlay. This only works
% for a 2-D case. If the trailing edge is significantly different between
% the two profiles, the calculated error will be erroneous. Also, an
% alternate form of this code, AFMSE, is written which only outputs the
% mean-square error, MSE, for use with fmincon and other optimizing
% software.
%
% Example: Given a design airfoil coordinate set specified by the matrix
% UF_Design, and measured coordinates of the final airfoil, UF_QA, both in
% inches, a known offset of .05 inches in the x-direction, .07 inches in
% the y-direction and 1/60th of a radian (3 degrees) is applied. The
% usage would be
%
% [s,e,MSE] = AFSNE(UF_Design,UF_QA,.05,.07,1/60)
%
```

```

% to get the normal error around the airfoil.

%% This cell block implements the desired offsets to XM.

% Implement offsets
XMo(:,1) = XM(:,1) - x0;
XMo(:,2) = XM(:,2) - y0;

% Implement rotation matrix
G = [cos(theta) sin(theta); -sin(theta) cos(theta)];
XMq = XMo*G;

%% Calculate the slope of the design profile at all supplied coordinates
% Central difference is used for all points except the beginning and end,
% which use respective forward and backward differences.

M = length(X(:,1));

t1a = zeros(1,M);
t1a(1) = atan2(X(2,2)-X(1,2),X(2,1)-X(1,1));
for i = 2:(M-1);
    t1a(i) = atan2(X(i+1,2)-X(i-1,2),X(i+1,1)-X(i-1,1));
end;
t1a(M) = atan2(X(M,2)-X(M-1,2),X(M,1)-X(M-1,1));
t1 = unwrap(t1a);

% Calculate the slope of the line normal to the design airfoil surface at
% each point.

t1n = t1 - pi/2;

% Trim the trailing edge of the measured profile, if necessary. Apply a
% rotation to the surface using the surface normal angle to find which
% points are beyond the surface profile. Retain the points just before
% and after the profile for interpolation.

[Ytemp,Imin] = min(XMq(:,1));
XTtemp(:,1) = XMq(:,1) - X(1,1);
XTtemp(:,2) = XMq(:,2) - X(1,2);
RTtemp = [cos(-t1n(1)) sin(-t1n(1)); -sin(-t1n(1)) cos(-t1n(1))];
XTR = XTtemp*RTtemp;
jj = 1;
for i = 2:Imin;
    if XTR(i-1,2) < 0;
        if XTR(i,2) > 0;
            jj = i-1;
        end
    end
end

```

```

    end;
end;
end;
XTtemp2(:,1) = XMq(:,1) - X(M,1);
XTtemp2(:,2) = XMq(:,2) - X(M,2);
RTtemp2 = [cos(-t1n(M)) sin(-t1n(M)); -sin(-t1n(M)) cos(-t1n(M))];
XTR2 = XTtemp2*RTtemp2;
kk = length(XMq(:,1));
for i = (Imin+1):length(XMq(:,1));
    if XTR2(i,2) > 0;
        if XTR2(i-1,2) < 0;
            kk = i;
        end;
    end;
end;
end;

j = 0;
for i = jj:kk;
    j = j + 1;
    XMp(j,:) = XMq(i,:);
end;
N = length(XMp(:,1));

% Calculate the streamwise distance
s = zeros(1,M);
smp = zeros(1,N);
s(1) = 0;
smp(1) = 0;
for i = 2:M;
    s(i) = s(i-1) + sqrt((X(i,2)-X(i-1,2))^2 + (X(i,1)-X(i-1,1))^2);
end;
for i = 2:N;
    smp(i) = smp(i-1) + sqrt((XMp(i,2)-XMp(i-1,2))^2 ...
        + (XMp(i,1)-XMp(i-1,1))^2);
end;
%% Locate the two QA points closest to each design point, calculate the
% line between those two points, and then the intersection point between
% the line and the normal of the design point. Use this point to
% calculate the local normal error. Note that for debugging, A and B are
% indexed. If need arises, these values could be loop-only. Once B is
% determined as the closest point, angles are used to enforce A and B
% occurring on opposite sides of the surface normal vector.

A = zeros(M,2);
B = zeros(M,2);
As = zeros(1,M);

```

```

Bs = zeros(1,M);
J = zeros(1,M);
for i = 1:M;
    A(i,:) = XMp(1,:);
    As(i) = smp(1);
    B(i,:) = XMp(2,:);
    Bs(i) = smp(2);
    for j = 2:N;
        if (sqrt((X(i,1)-XMp(j,1))^2+(X(i,2)-XMp(j,2))^2) < ...
            sqrt((X(i,1)-B(i,1))^2+(X(i,2)-B(i,2))^2));
            B(i,:) = XMp(j,:);
            Bs(i) = smp(j);
            A(i,:) = XMp(j-1,:);
            As(i) = smp(j-1);
            J(i) = j;
        end;
    end;
end
end

% To catch the points in error, apply a translation to each
% local set, and then a rotation to set the surface normal to an angle of
% zero. The OXB angle should have an opposite sign from the OXA angle.
% If not, shift A and B forward by one point each.

```

```

At = zeros(M,2);
Bt = zeros(M,2);
Ats = zeros(M,2);
Bts = zeros(M,2);
OXA = zeros(1,M);
OXB = zeros(1,M);
for i = 2:M-1;
    At(i,:) = A(i,:) - X(i,:);
    Bt(i,:) = B(i,:) - X(i,:);
    rt = [cos(-t1n(i)) sin(-t1n(i)); -sin(-t1n(i)) cos(-t1n(i))];
    Ats(i,:) = At(i,:)*rt;
    Bts(i,:) = Bt(i,:)*rt;
    OXA(i) = atan2(Ats(i,2),Ats(i,1));
    OXB(i) = atan2(Bts(i,2),Bts(i,1));
    if J(i) < N-1;
        if sign(OXA(i)) == sign(OXB(i));
            A(i,:) = B(i,:);
            As(i) = Bs(i);
            B(i,:) = XMp(J(i)+1,:);
            Bs(i) = smp(J(i)+1);
        end;
    end;
end;
end;

```

```

end;

tb = zeros(1,M);
theta2 = zeros(1,M);
dl = zeros(1,M);
for i = 1:M;
    tb(i) = atan2(B(i,2)-A(i,2),B(i,1)-A(i,1));
    theta2(i) = atan2(A(i,2)-X(i,2),A(i,1)-X(i,1));
    dl(i) = sqrt((X(i,1)-A(i,1))^2+(X(i,2)-A(i,2))^2);
end;
tb = unwrap(tb);
theta2 = unwrap(theta2);
phi = 2*pi - tb - (pi - theta2);
theta3 = t1n - theta2;
psi = pi - theta3 - phi;
e = dl.*sin(phi)./sin(psi);
MSE = mean(e.*e);

```

APPENDIX B
ANALYSIS OF THE THREE-MICROPHONE METHOD

Formulation

The system shown in Figure 4-30 is extended to more coherent outputs from a single source, contaminated by extraneous, incoherent line noise. The autospectral density of a signal is defined in Equation (4-11), but it should be noted that this is strictly only true when source and noise are incoherent, as the cross terms between the two shown in Equation (B-1) cancel out through averaging.

$$G_{y_i y_i} = 2 \lim_{T \rightarrow \infty} \frac{1}{T} E \left[U_i^* U_i + U_i^* N_i + N_i^* U_i + N_i^* N_i \right] \quad (\text{B-1})$$

Similarly, the relation shown for the cross-spectral density given in Equation (4-12) only holds if the noise inputs are incoherent both with the source signal and with each other, cancelling the additional terms shown in Equation (B-2).

$$G_{y_i y_j} = 2 \lim_{T \rightarrow \infty} \frac{1}{T} E \left[U_i^* U_j + U_i^* N_j + N_i^* U_j + N_i^* N_j \right] \quad (\text{B-2})$$

For m microphones, the autospectral density of microphone i is reformulated in Equation (B-3).

$$G_{y_i y_i} = G_{u_i u_i} + G_{n_i n_i} = G_{u_i u_i} \left(1 + \frac{1}{SNR_i} \right) \quad (\text{B-3})$$

This, in conjunction with Equation (4-12) and Equation (4-13), allows for a restructuring of the problem in terms of measured coherence and channel SNRs.

$$\gamma_{u_i u_j}^2 = 1 = \frac{\frac{|G_{y_i y_j}|^2}{G_{y_i y_i} G_{y_j y_j}}}{\left(1 + \frac{1}{SNR_i} \right) \left(1 + \frac{1}{SNR_j} \right)} = \frac{|G_{y_i y_j}|^2}{G_{y_i y_i} G_{y_j y_j}} \left(1 + \frac{1}{SNR_i} \right) \left(1 + \frac{1}{SNR_j} \right) \quad (\text{B-4})$$

$$\frac{1}{\gamma_{y_i y_j}^2} = \left(1 + \frac{1}{SNR_i} \right) \left(1 + \frac{1}{SNR_j} \right) \quad (\text{B-5})$$

Equation (B-3) and Equation (B-5) comprise a system with $m + (m-1)/2$ equations for $2m$ unknowns (m autospectral densities and m SNRs). As summarized in Table B-1, for two microphones, the number of unknowns (4) exceeds the number of equations, so the COP method must be used. When three-microphones are used, an exact solution is possible. For $m > 3$ microphones, the number of equations exceeds the number of unknowns, and other options, such as a least-squares constrained solution or covariance-based approaches, must be considered. Alternatively, the three-microphone method can still be applied, by evaluating different combinations of microphones within the data set.

Simulation & Analysis

A piston in an infinite baffle is simulated with a ka of 3, for non-uniform directivity pattern without true nulls [Blackstock 2000]. This model is selected due to its simple, analytic nature. The overall situation is similar to trailing edge noise measurements conducted in UFAFF, where microphones are not expected to be present in directivity nulls, but significant power variation may occur over a line array of transducers. The baseline pattern is shown in Figure B-1, along with 19 sampling points selected to simulate microphone measurements.

The piston is sized such that the frequency of interest is 2048 Hz. The Sampling rate is set to 65,536 samples per second for 60 seconds, and individual block length set to 4096, for a total of 3837 blocks, or 1995 effective averages with a hanning window and 75% overlap. Note that in subsequent analyses, even the zero-noise case was processed using a hanning window, despite the fact that the blocks were sized correctly for no leakage in processing a pure sinusoid. This was done to preserve peak behavior between the zero noise case and the finite SNR cases. The microphones are placed in 10 degree increments from -90 degrees to 90 degrees around the field. Noise power was generated by using a Gaussian random generator with unity standard deviation to simulate a microphone measurement at each channel. A cross-spectral matrix was generated

for the noise signal, and then the autospectral noise powers were used to determine the baseline signal-to-noise ratio. The cross-spectral matrix (CSM) was then scaled to generate a desired signal-to-noise ratio, and added to the clean simulation of the acoustic CSM.

Figure B-2, Figure B-3, and Figure B-4 show the predicted directivity pattern using the three-microphone method for several signal-to-noise ratios (SNRs). The predicted directivity is compared to the true directivity pattern, the directivity computed by a processed, clean signal autospectrum, and the directivity computed using the pure autospectral power. The two nearest microphones to the microphone of interest are selected for the coherent power prediction. The plots show that with a sufficient number of averages, the nearest-microphone method successfully recovers the directivity for a Signal-to-Noise Ratio (SNR) of 10, and gets the overall shape correct for an SNR of 1. The method fails for an SNR of 0.1. It should be noted that simulations were run for shorter periods of time and with fewer averages, and resulted in output directivity patterns that were unresolvable for an SNR of 1. The SNR is defined for the frequency bin of interest only as this is a tonal simulation, as opposed to band-integration for broad-band noise as in true measurements in the chamber. This was done to reduce the overall simulation complexity, since the three-microphone method is formulated for frequency-by-frequency analysis, so if the three-microphone method can fail in a tonal situation, it can fail in a broadband one.

Multiple references [Bendat & Piersol 2000; Chung 1977] discuss the three-microphone method and derive it, showing that the solution is exact for incoherent noise, regardless of input signal-to-noise ratio. One of the assumptions of the solution must be violated for it to fail in predicting the true signal power. The first, and easiest to evaluate with this simulation, is that of uncorrelated noise contamination.

The noise added with Matlab's random number generator is not completely uncorrelated between channels. Even a small value of noise coherence can contaminate the method. It would appear that the contamination becomes a true problem when the coherence of the overall measured signal approaches the magnitude of the coherence of the contaminating noise. Figure B-5, Figure B-6, and Figure B-7 show color maps of the cross-spectral matrix coherence at the input frequency of interest, as compared to color maps of the simulated noise CSM. As the diagonal of the coherence matrix would be identically equal to unity, it is set to zero to increase the resolution of the color map for the rest of the matrix. Not shown is the cross-spectral matrix of the input signal without noise, which was verified to be universally unity.

Given that the three-microphone method begins to break down at lower signal-to-noise ratios when selecting the nearest two microphones for each reference microphone, the next step in evaluating the method is to determine if any combination of microphones successfully recover the true power. To do this, a histogram is constructed of the power prediction of all possible microphone combinations for the mid-array microphone, and compared to the true signal power. Figure B-8, Figure B-9, and Figure B-10 show these histograms for varying SNRs. The data spread gets large as the SNR becomes low, so the likelihood of an individual microphone combination being in error becomes high. However, for the most part, the data are still clustered around the true power value.

A modified approach is taken to the computation of the three-microphone power estimate. All possible combinations of microphones are used, and then the average power from all the estimates is computed for each microphone. The directivity pattern for this technique is shown in Figure B-11, Figure B-12, and Figure B-13. The data for an SNR of 1 have improved, but SNR = 0.1 still shows poor results.

Based on the histograms, it is evident that the low SNR conditions have significant outliers present in the power predictions. An outlier rejection method based on the modified Thompson-Tau technique [Wheeler & Ganji 1996] can be applied to the power predictions, and the mean power for each microphone re-calculated. These modified directivity predictions are shown in Figure B-14, Figure B-15, and Figure B-16. An SNR of 1 is clearly resolved, and even in the case of SNR of 0.1, the overall directivity shape begins to emerge, at least enough to allow for qualitative discussion.

A technique is required to determine when the mean three-microphone method is trustworthy when the true noise data are unknown. The predicted SNR ratio for the simulation can be plotted with respect to the true input SNR for microphone 10, and evaluated both without and with outlier rejection. This is shown in Figure B-17. Without outlier rejection, significant estimate spread and breakdown is seen below true SNR values of 1. Once outlier rejection is applied, the mean value does not deviate significantly from the true power on a log scale until approaching an SNR of 0.25. Two data characteristics are evident in this regime. First, the prediction spread becomes greater than an order of magnitude. Second, the low-power tail of the prediction cluster spreads further and further from the central cluster. These can be used as warning indications as to when mean three-microphone method predictions become suspect.

For the entirety of the previous discussion, the microphone on the main lobe has been used as the reference microphone. This microphone's statistics would be considered the best case for the simulation, as it received the strongest output from the sound source. One of the worst-case microphones, microphone 1 located at -90° , is briefly analyzed as another example case of outlier rejection. As shown in Figure B-18, this method again begins to falter from the true power at SNRs below 0.5. However, for the most part the data trend holds near the true power

until below SNRs of 0.05. Here, the data spread again passes an order of magnitude, and tails in the log-scale SNR prediction become significant even after outlier rejection.

It should be noted that this SNR of 0.05 corresponds to the same case where microphone 10 has an SNR of 1, so a conservative application of this technique may involve generating logarithmic tables of SNR predictions for every microphone in the measurement system, and checking to see if any of them fail the potential criteria discussed above. If so, that microphone should be discarded from directivity analysis. Regarding the difference in SNR reliability of Microphone 1 vs. Microphone 10, it can be hypothesized that this is due to the availability of other high-SNR microphones in the measurement. Microphone 10 may only be reliable down to an SNR of 0.5 to 0.3 because it has the highest true signal available within the directivity lobe, and therefore has no other stronger reference microphones for de-noising. Microphone 1 may be reliable down to 0.05 because it can reference to the stronger microphones on the main body of the lobe.

As the data rejection scheme is shown on a log scale, it may be helpful to evaluate the histograms of rejected data linearly to get a sense of the computed distribution both with and without an outlier rejection scheme. Figure B-19 and Figure B-20 show histograms of the data without and with point rejection, to assess the behavior of the scheme. As shown, the rejection methodology does little to eliminate low-end power estimates, but handles over-estimated powers well.

Finally, the three-microphone method is compared against itself, using the nearest neighbor selection vs. using the mean power technique with outlier rejection, as well as a two-microphone coherent output power method, where the coherent power is just taken as the cross-channel coherence multiplied by the autospectrum of the channel of interest. For the two-

microphone method, the nearest adjacent microphone channel is used and the coherent output power is computed using the general formulation of Equation (4-14). Figure B-21, Figure B-22, and Figure B-23 show the directivity comparison for varying true SNR values.

As is shown on the plots, the mean-method with outlier rejection for three-microphones has the best performance, in theory coming with greater computational cost. However, the three-microphone method still runs in a trivial amount of time, especially when compared to beamforming algorithms, on a modern workstation using Matlab. As such, when a large number of source observation locations are available for a simple source under noisy conditions, the mean three-microphone method with outlier rejection should be considered. As sources become more complicated, however, this method will fall victim to the same effects as other coherence-based techniques. Appendix C goes into more detail regarding the effect of more complicated source fields on coherence-based analysis.

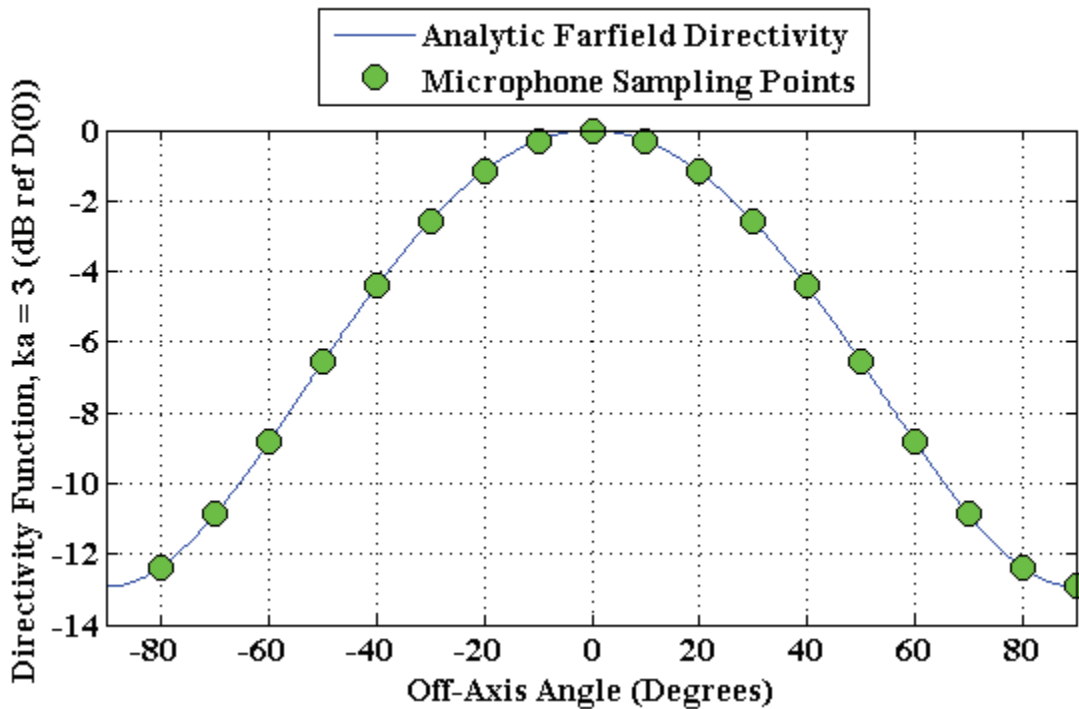


Figure B-1. Piston in an infinite baffle, directivity pattern for $ka = 3$.

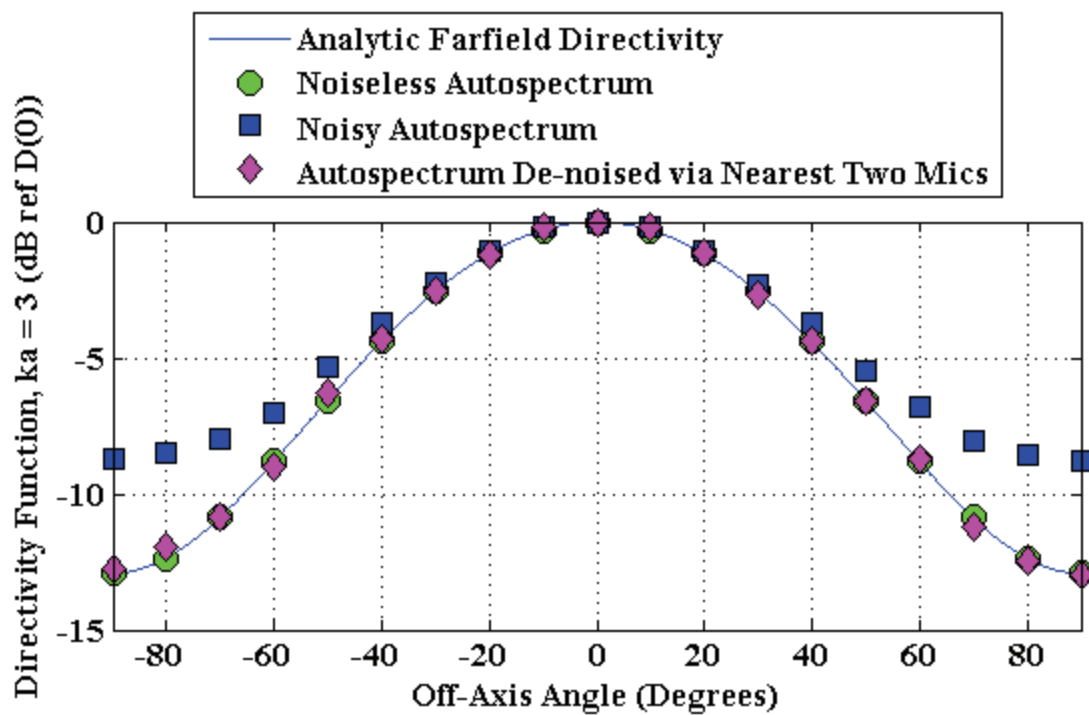


Figure B-2. Directivity pattern for $SNR = 10$, using nearest-two microphone selection.

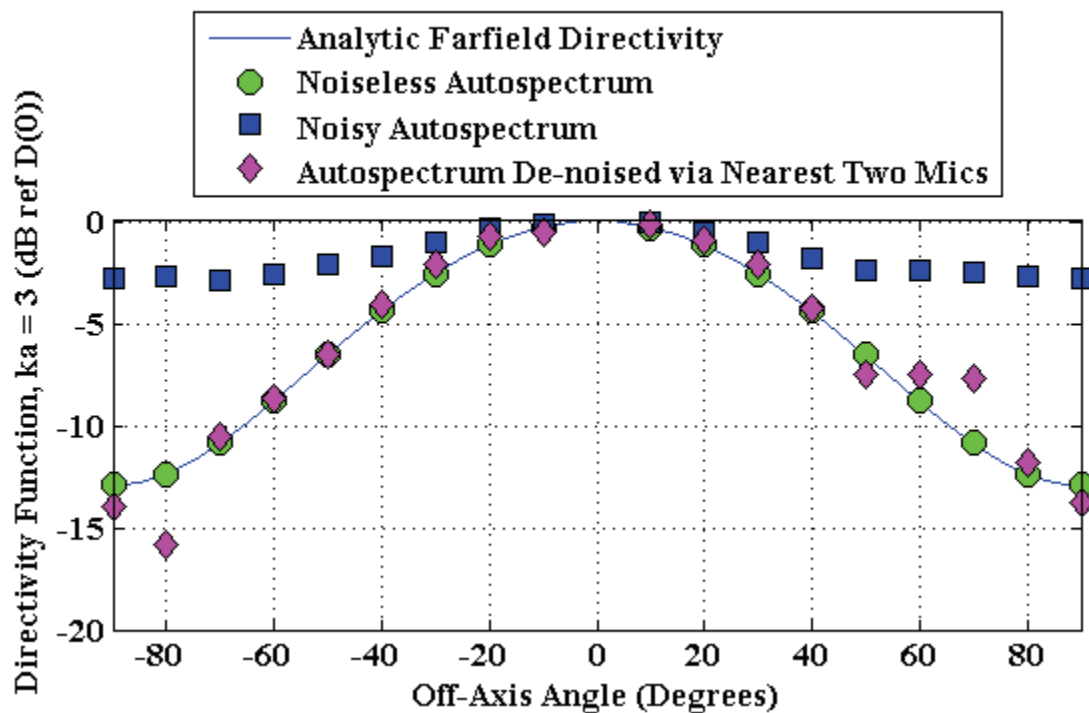


Figure B-3. Directivity pattern for $SNR = 1$, using nearest-two microphone selection.

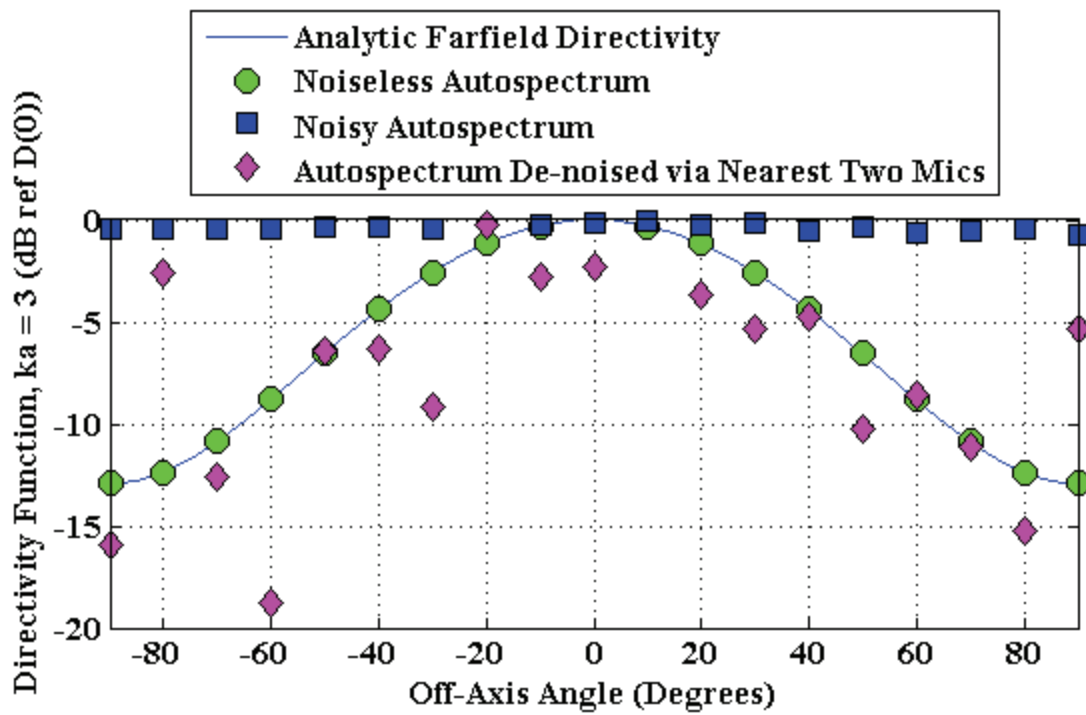


Figure B-4. Directivity pattern for SNR = 0.1, using nearest-two microphone selection.

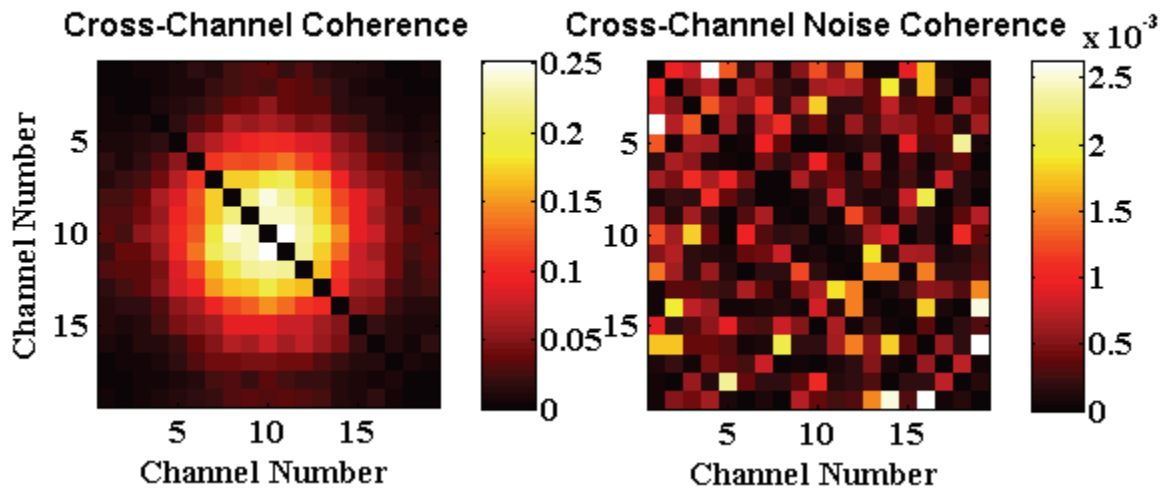


Figure B-5. Color maps of cross-channel coherence, SNR = 10.

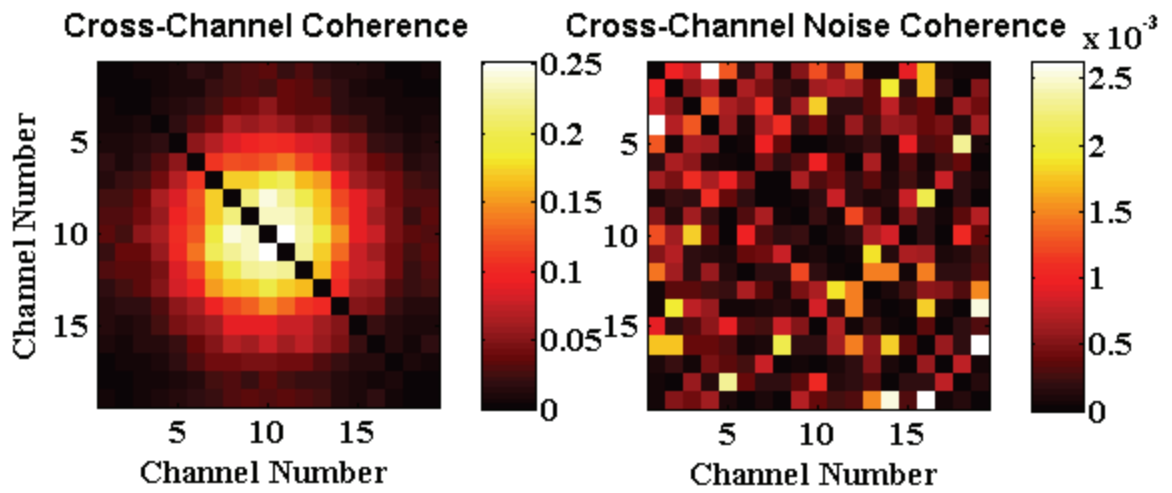


Figure B-6. Color maps of cross-channel coherence, SNR = 1.

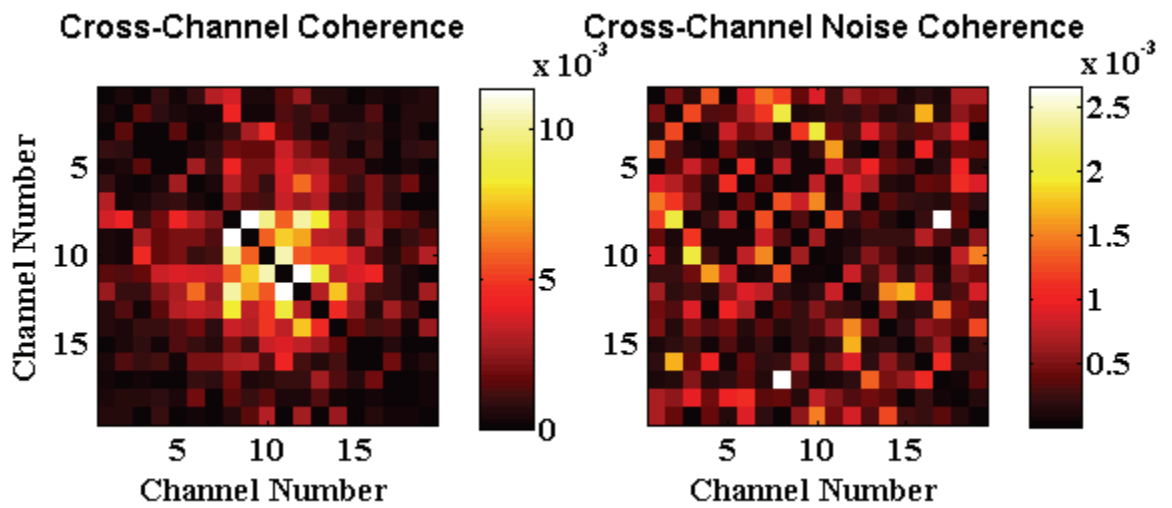


Figure B-7. Color maps of cross-channel coherence, SNR = 0.1.

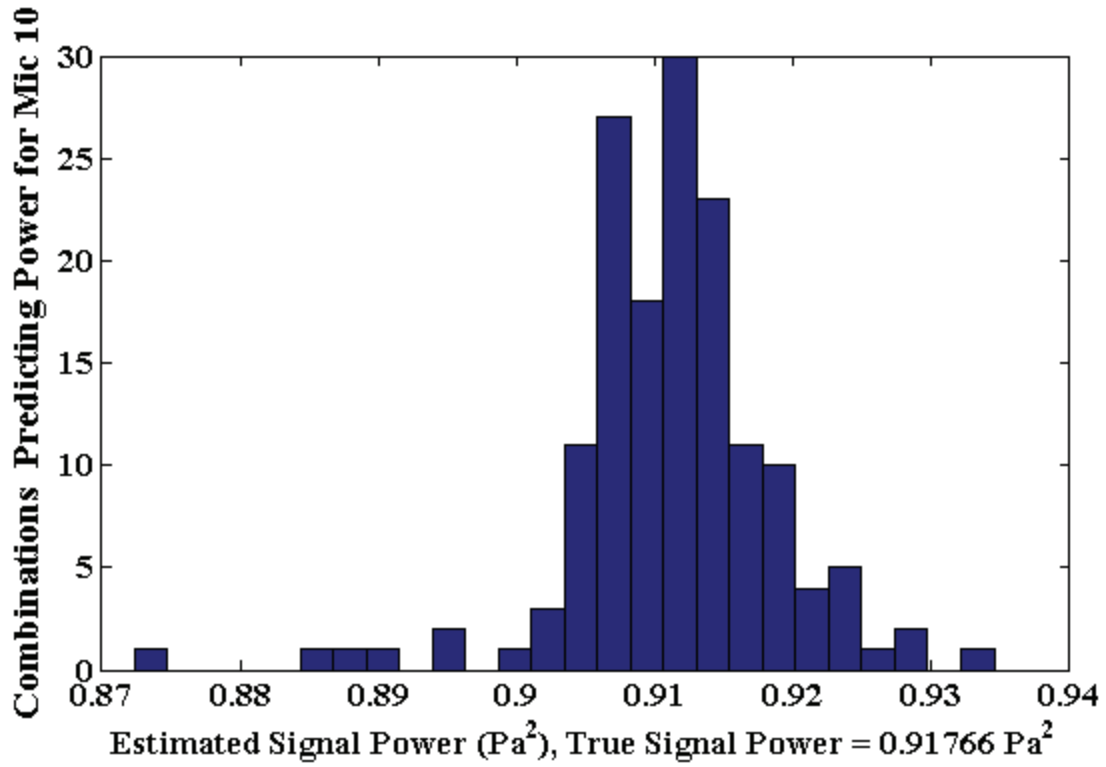


Figure B-8. Histogram of power predictions for SNR = 10.

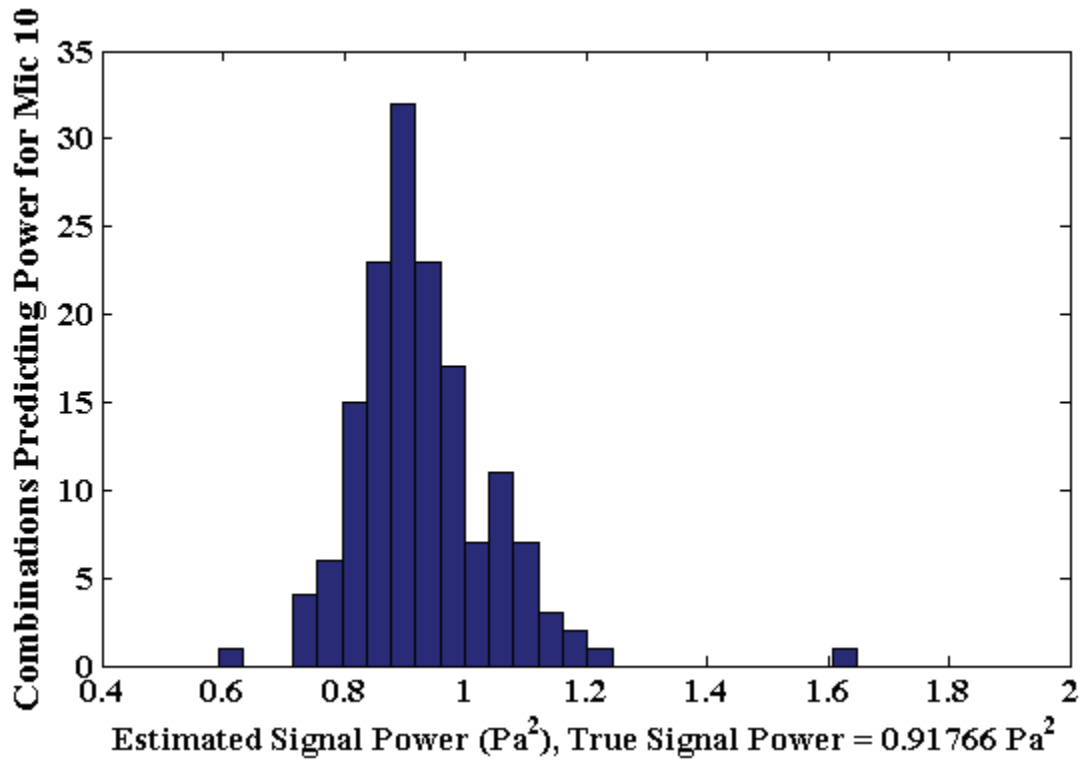


Figure B-9. Histogram of power predictions for SNR = 1.

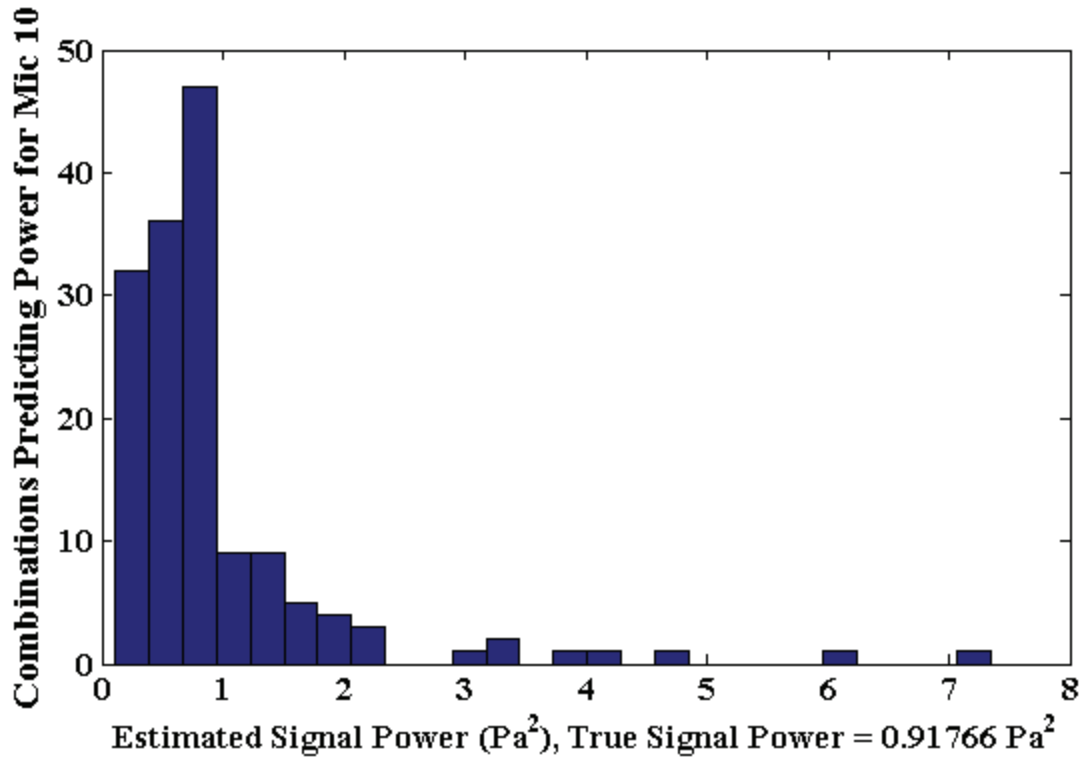


Figure B-10. Histogram of power predictions for SNR = 0.1.

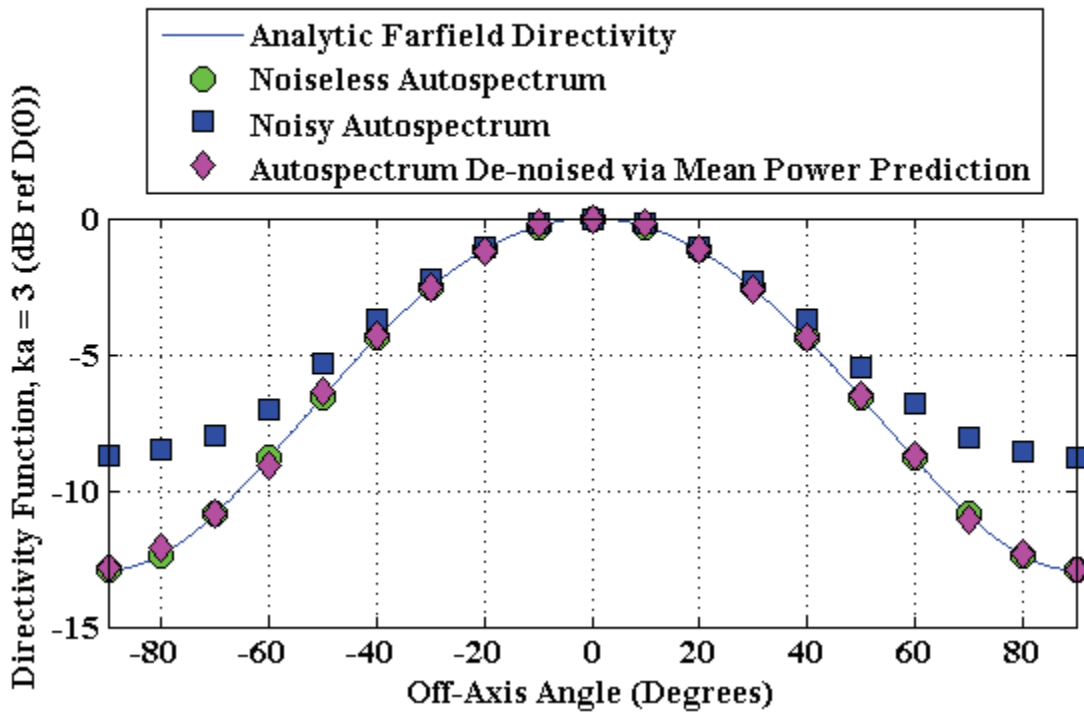


Figure B-11. Directivity from mean power prediction method for SNR = 10.

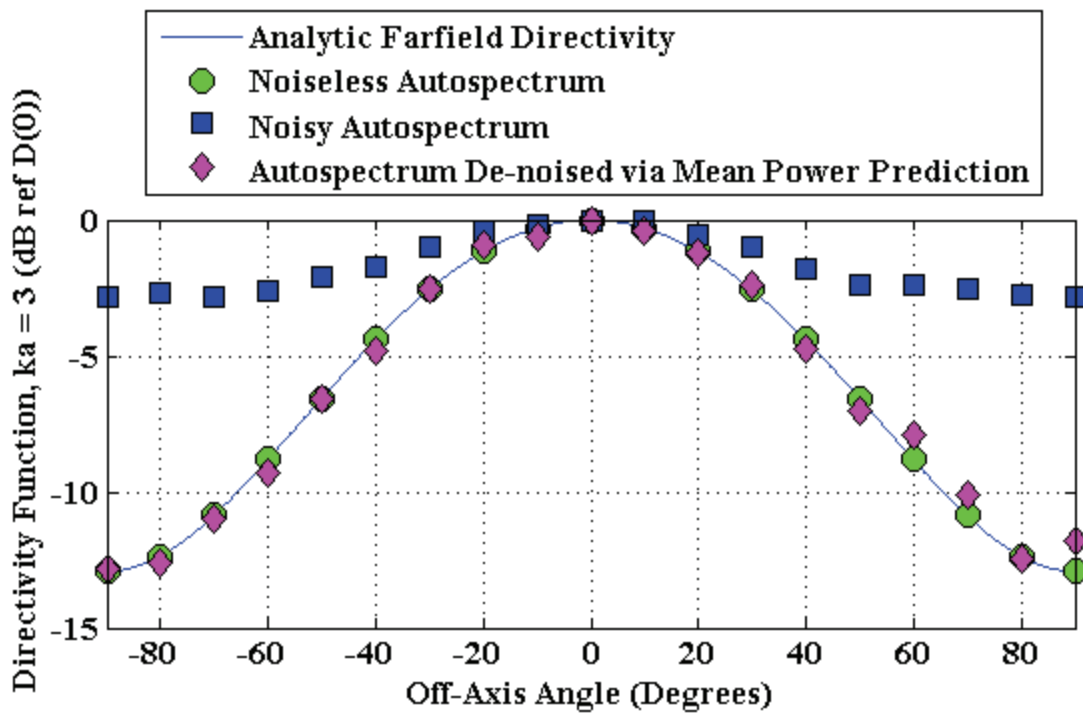


Figure B-12. Directivity from mean power prediction method for SNR = 1.

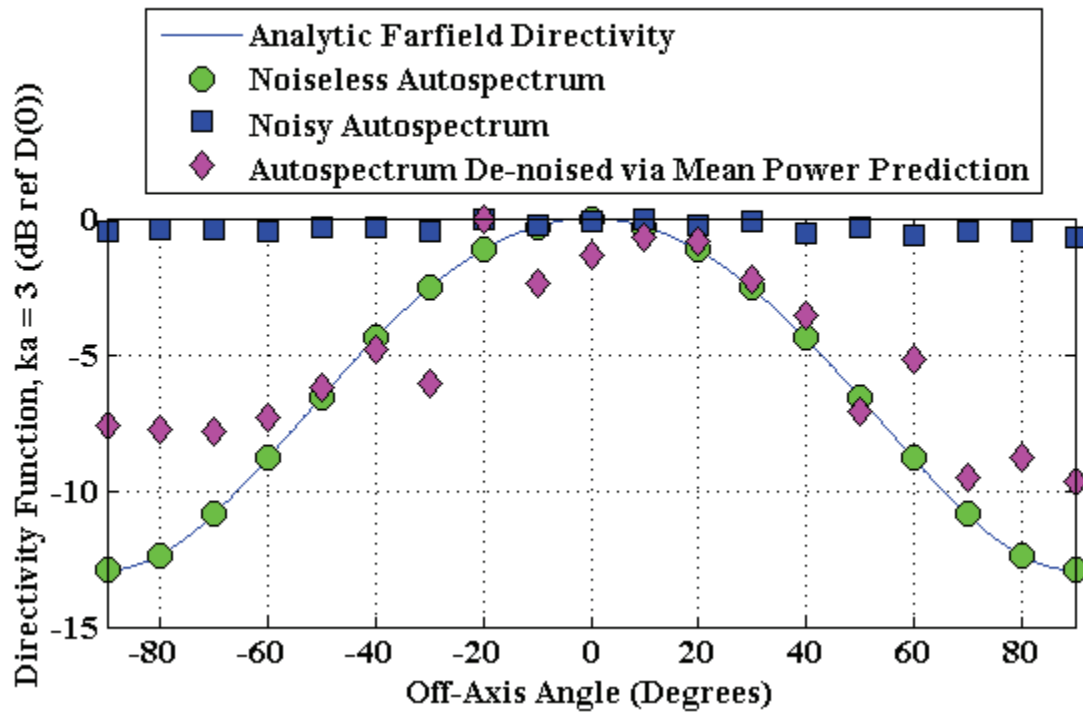


Figure B-13. Directivity from mean power prediction method for SNR = 0.1.

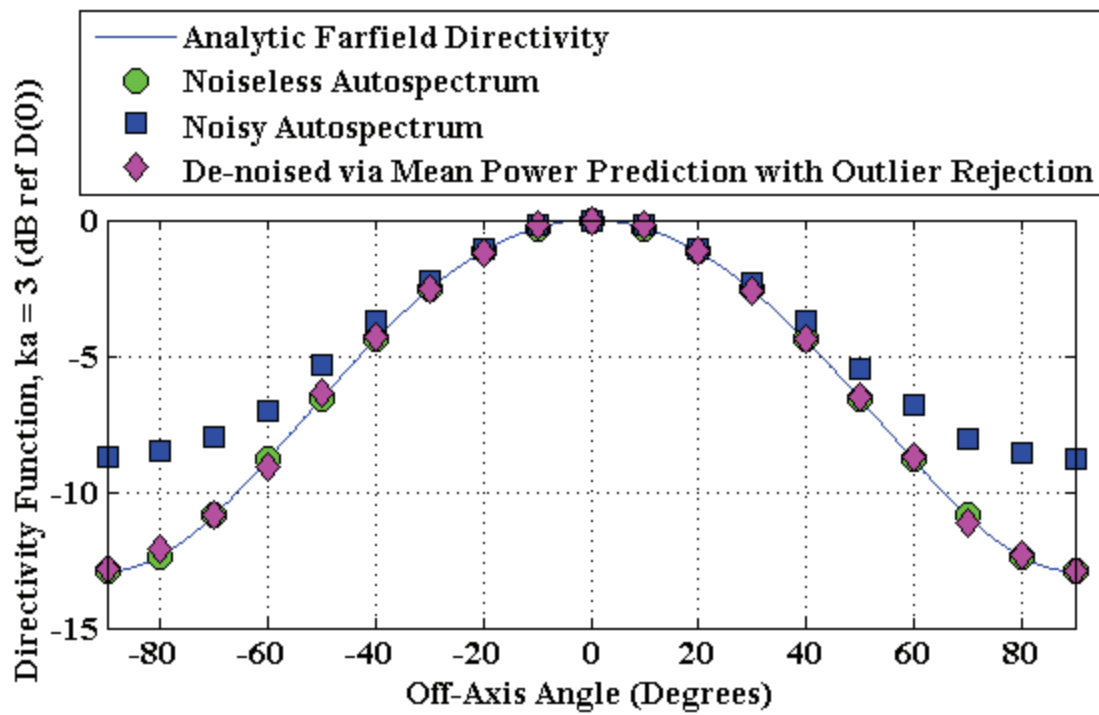


Figure B-14. Directivity for mean power prediction method with outlier rejection, SNR = 10.

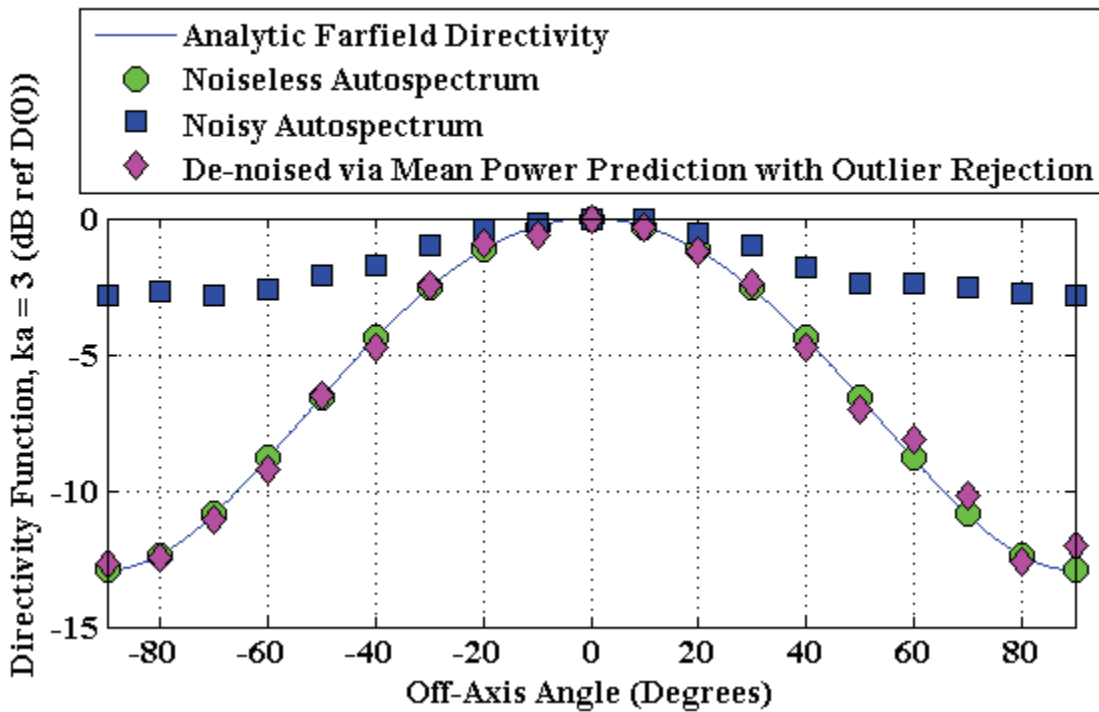


Figure B-15. Directivity for mean power prediction method with outlier rejection, SNR = 1.

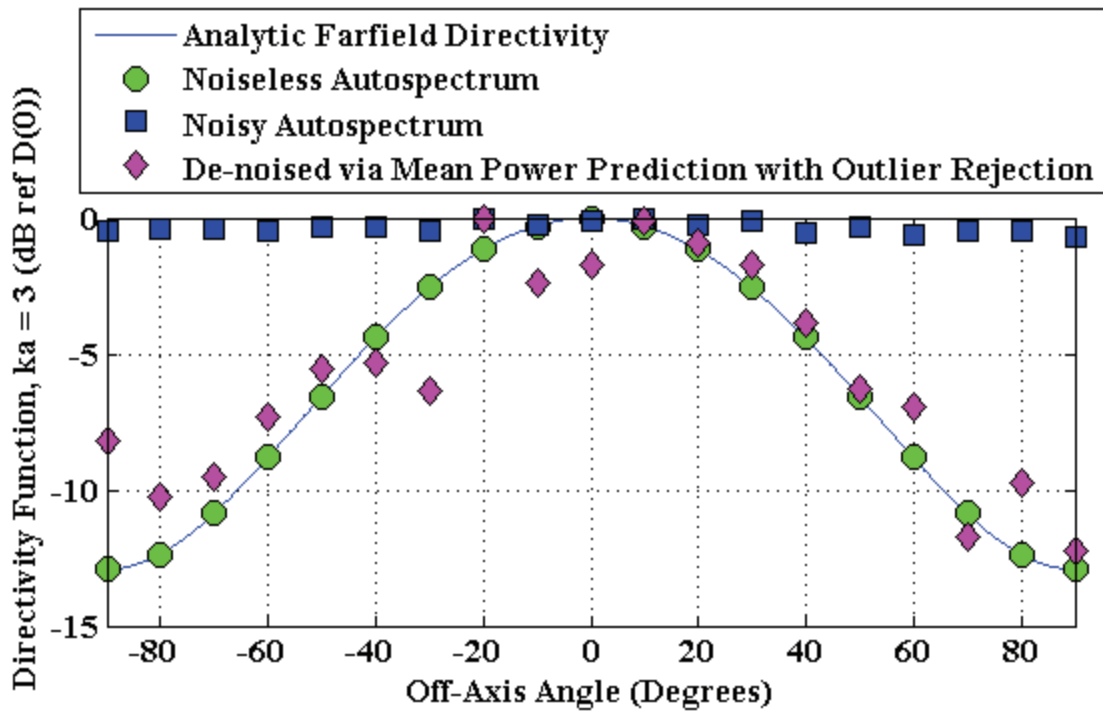


Figure B-16. Directivity for mean power prediction method with outlier rejection, SNR = 0.1.

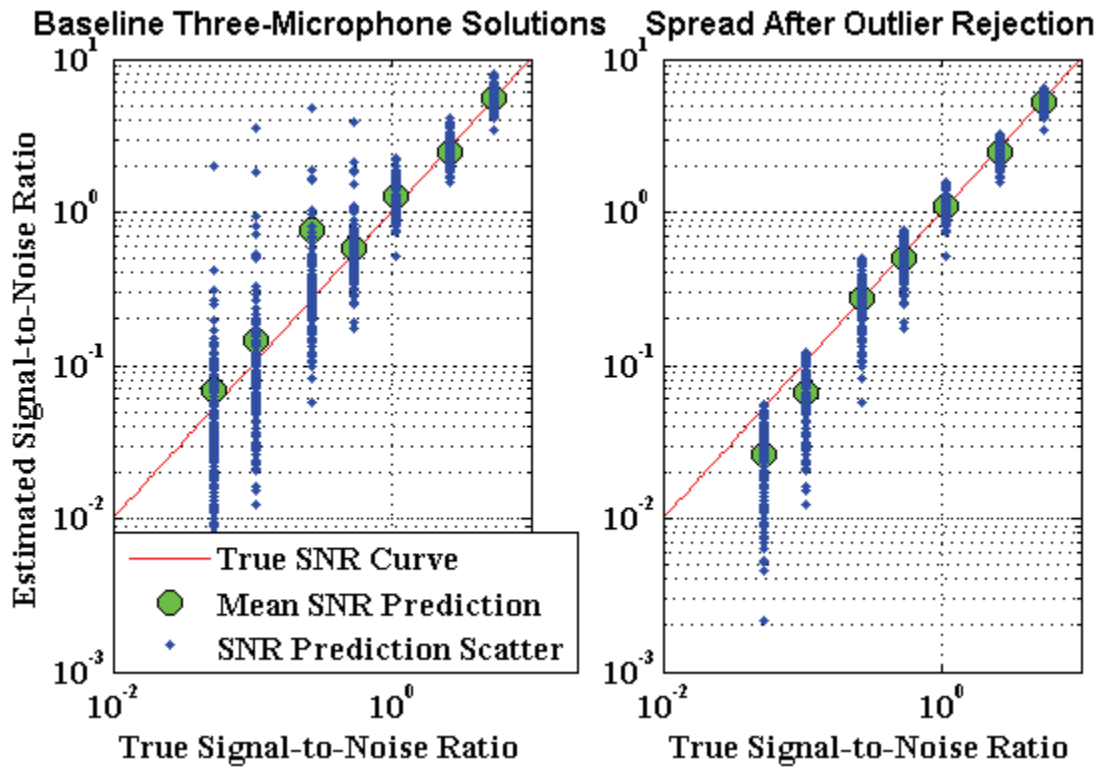


Figure B-17. SNR data spread for microphone 10.

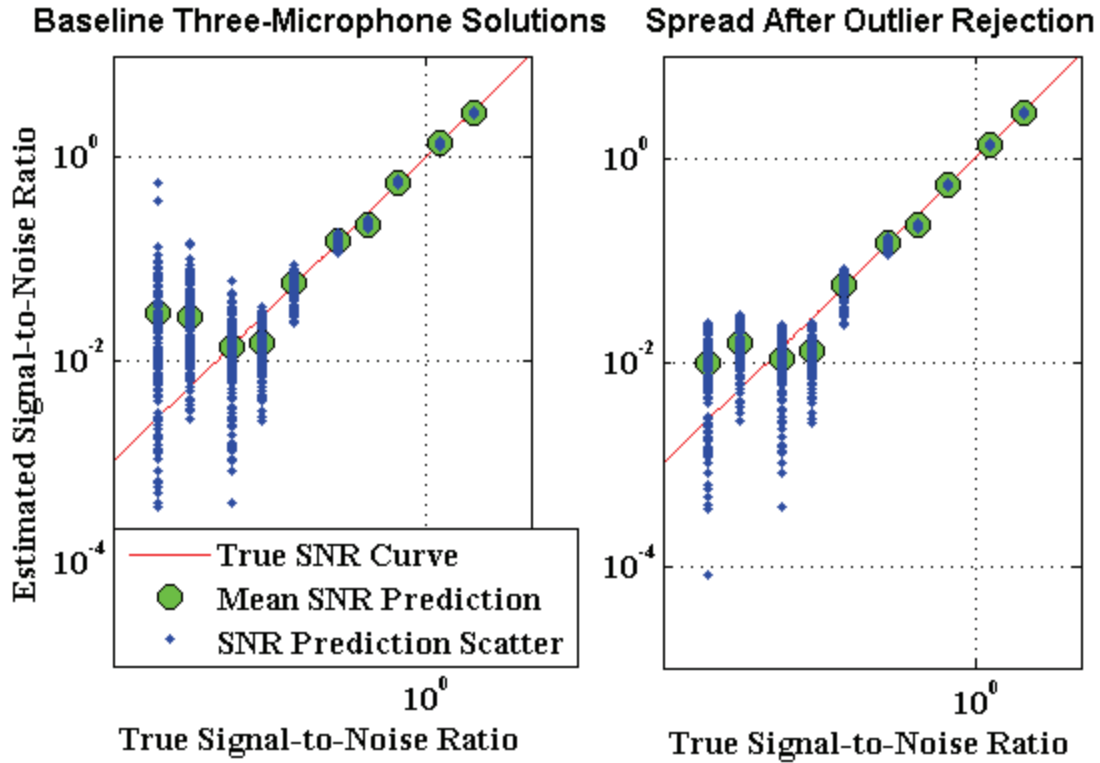


Figure B-18. SNR data spread for microphone 1.

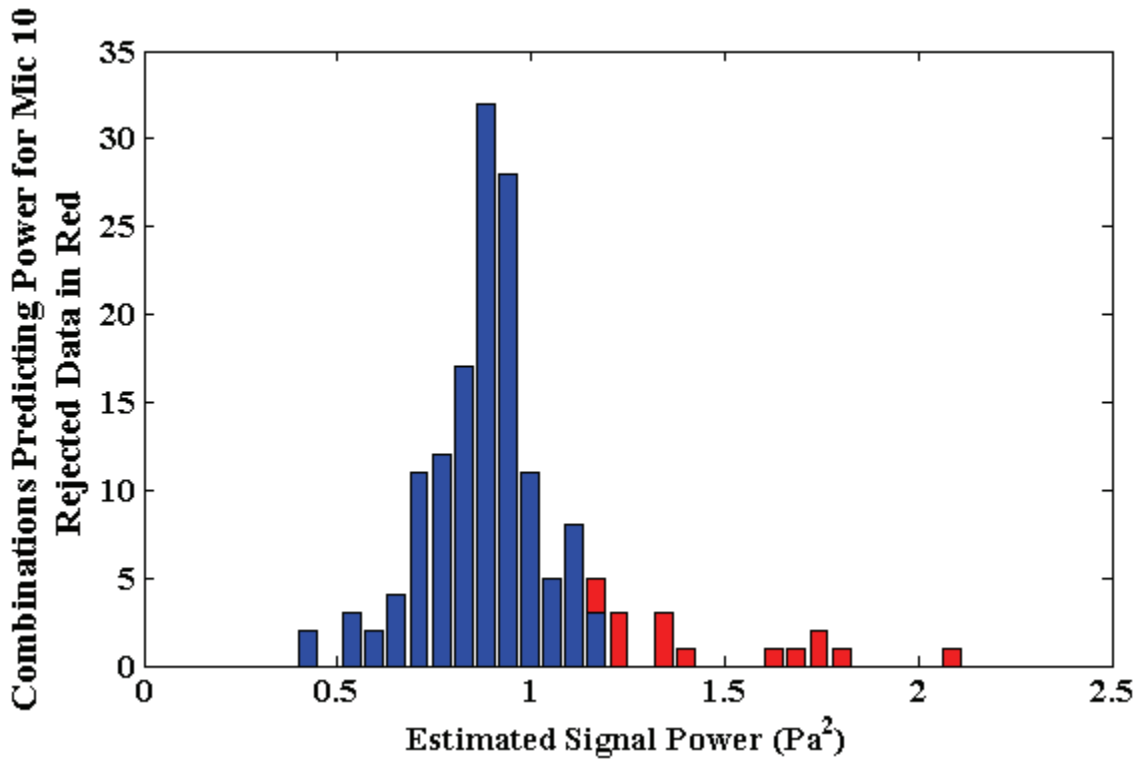


Figure B-19. Histogram of estimated powers for microphone 10 and a true SNR of 0.5.

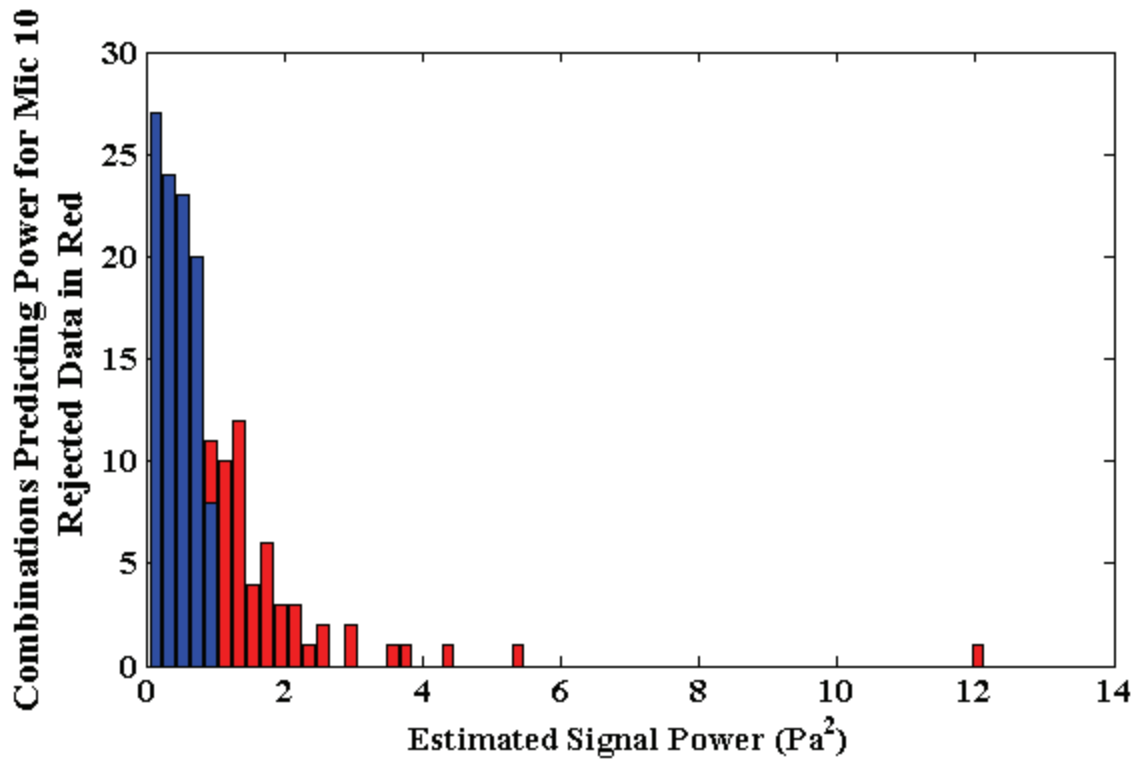


Figure B-20. Histogram of estimated powers for microphone 10 and a true SNR of 0.05.

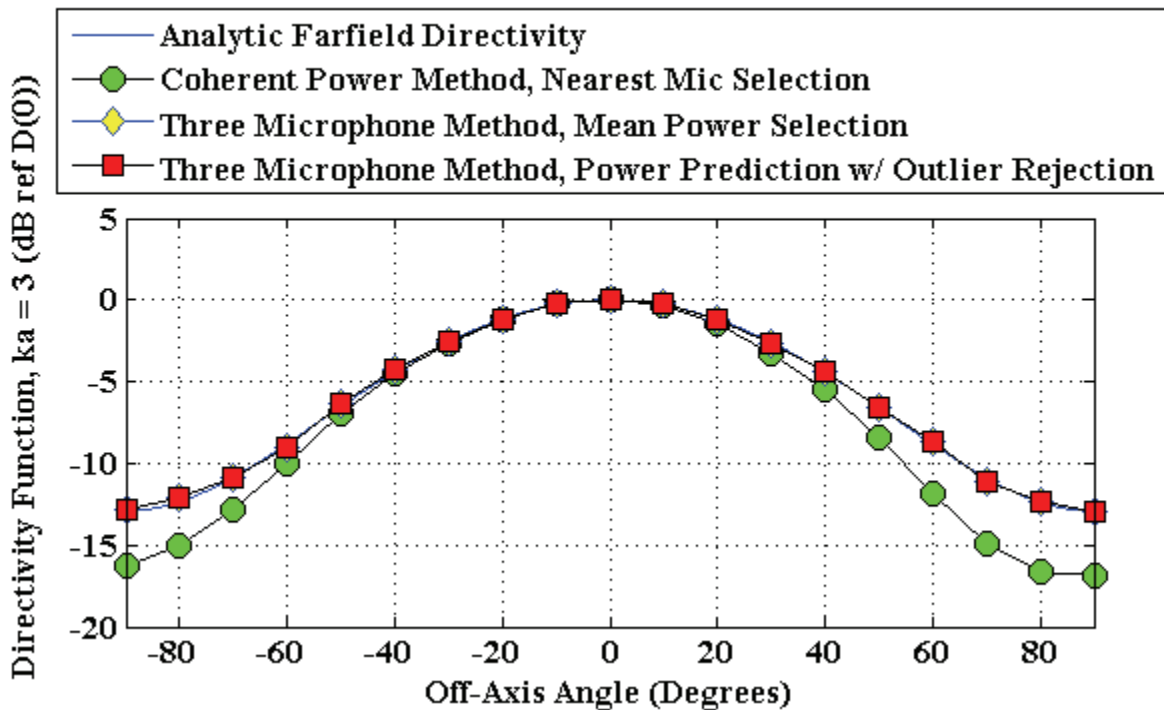


Figure B-21. Directivity comparison for SNR = 10.

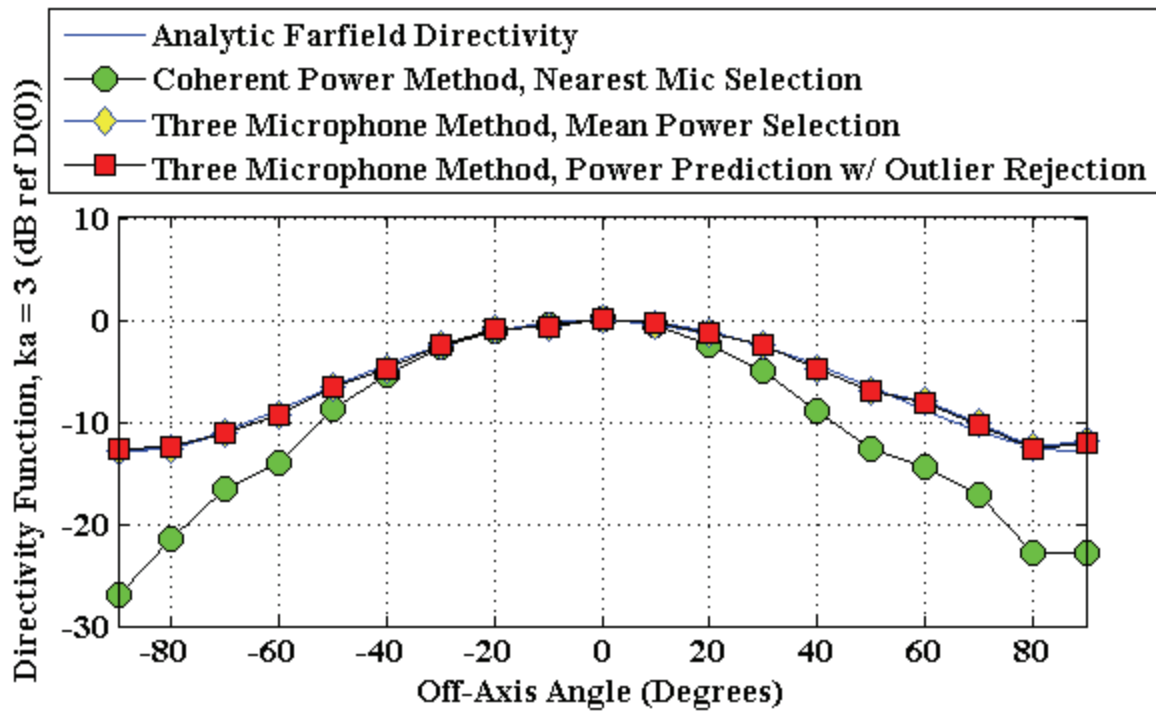


Figure B-22. Directivity comparison for SNR = 1.

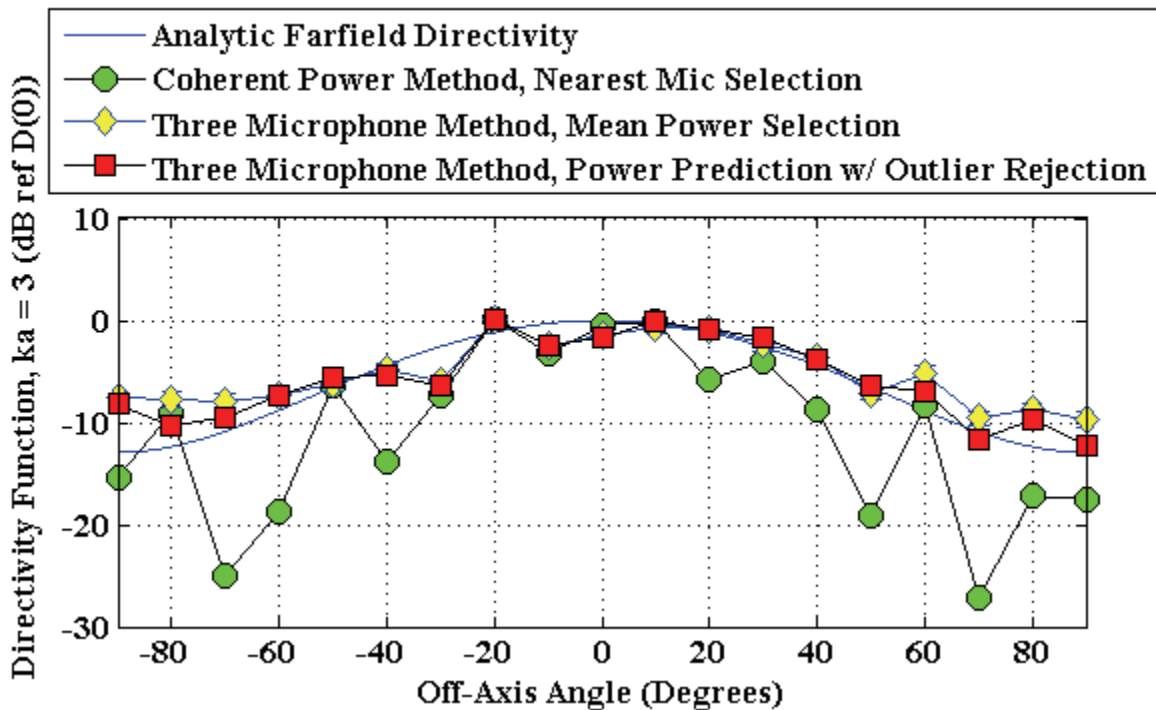


Figure B-23. Directivity comparison for SNR = 0.1.

Table B-1. Equation-unknown scaling for varying channel count

Number of Microphones, m	Number of Unknowns, $2m$	Number of Equations, $(m^2+m)/2$	Solution Method
2	4	3	COP
3	6	6	Exact
4	8	10	Least-Squares Constrained, Microphone Subsets
22	44	253	Least-Squares Constrained, Microphone Subsets

APPENDIX C
EFFECT OF MULTIPLE SOURCES ON COHERENCE-BASED ANALYSIS

For the most part in this body of work, the mathematics of coherence-based analysis have been discussed in terms of a single coherent source, as shown schematically in Figure 4-30 for two output observations. As aeroacoustic sources can have complicated natures and distributed behavior, it is of interest to see how multiple coherent sources affect the output of these methods.

Two-Input/Two-Output Analysis

A block diagram for a two-input, two output (TITO) system with no additive incoherent noise is shown in Figure C-1. In this figure, the input acoustic sources as functions of time are denoted by $x_1(t)$ and $x_2(t)$. The propagation path from the first source to the first observer is denoted as a function of frequency by $H_{11}(f)$. The path from the first source to the second observer is denoted by $H_{12}(f)$. This convention is maintained throughout this work, where the path from the i th source to the j th observer will be $H_{ij}(f)$. Similarly, the signal at the first observer due to the first source is denoted as a function of time by ${}^1u_1(t)$, and the signal at the first observer due to the second source is denoted as ${}^2u_1(t)$. In general, the signal at the j th observer due to the i th source will be ${}^i u_j(t)$. Finally, the total measured signal at the first observer is $y_1(t)$ and that at the second observer is $y_2(t)$. The only data which would be experimentally available is the measured data at the observers.

All analysis in this discussion will be conducted in the frequency domain. The Fourier transform of each source and observer signal can be defined using Equation (C-1), where T is used consistently as in Chapter 4 as the data block length.

$$X(f) = \mathfrak{F}[x(t)] = \int_0^T x(t) e^{-j2\pi ft} dt \quad (\text{C-1})$$

Discretization effects will not be considered. Auto- and cross-spectral densities are computed using the expressions in Equation (4-7) and Equation (4-8), and the ordinary coherence function is computed from Equation (4-9). At this stage of analysis, the coherence between the sources, $\gamma_{x_1 x_2}^2(f)$, is undetermined. From systems analysis [Bendat & Piersol 2000], the propagation path or impulse response function would be convolved in the time domain, so the frequency-response function, the Fourier transform of the impulse response function, is multiplied in the frequency domain as in Equation (C-2).

$${}^i U_j(f) = H_{ij}(f) X_i(f) \quad (\text{C-2})$$

For all subsequent equations, frequency-dependence is suppressed.

Autospectral Scaling

The autospectral density of the signal at observer 1, suppressing the block length limit to show the estimate instead of the true value, is shown in Equation (C-3).

$$\begin{aligned} G_{y_1 y_1} &= \frac{2}{T} E[Y_1^* Y_1] = \frac{2}{T} E\left[({}^1 U_1 + {}^2 U_1)^* ({}^1 U_1 + {}^2 U_1)\right] \\ G_{y_1 y_1} &= \frac{2}{T} E\left[{}^1 U_1^* {}^1 U_1 + {}^1 U_1^* {}^2 U_1 + {}^2 U_1^* {}^1 U_1 + {}^2 U_1^* {}^2 U_1\right] \\ G_{y_1 y_1} &= \frac{2}{T} E[{}^1 U_1^* {}^1 U_1] + \frac{2}{T} E[{}^1 U_1^* {}^2 U_1] + \frac{2}{T} E[{}^2 U_1^* {}^1 U_1] + \frac{2}{T} E[{}^2 U_1^* {}^2 U_1] \\ G_{y_1 y_1} &= G_{1_{u_1^2 u_1}} + G_{2_{u_1^2 u_1}} + G_{1_{u_1^1 u_1}} + G_{2_{u_1^1 u_1}} \end{aligned} \quad (\text{C-3})$$

The observed autospectral density is the sum of autospectral densities of the sources and their cross-spectral densities. These cross-spectral densities can be re-expressed as phasors, shown in Equation (C-4), where $\theta_{1_{u_1^2 u_1}}$ would be the phase angle between sources 1 and 2 observed at observer 1.

$$\begin{aligned} G_{1_{u_1^2 u_1}} &= \left| G_{1_{u_1^2 u_1}} \right| e^{j\theta_{1_{u_1^2 u_1}}} \\ G_{2_{u_1^1 u_1}} &= \left| G_{2_{u_1^1 u_1}} \right| e^{j\theta_{2_{u_1^1 u_1}}} \end{aligned} \quad (\text{C-4})$$

For real signals $x_i(t)$ and $y_j(t)$, the identities in Equation (C-5) and Equation (C-6) hold.

$$\left| G_{1_{u_1^2 u_1}} \right| = \left| G_{2_{u_1^1 u_1}} \right| \quad (\text{C-5})$$

$$\theta_{1_{u_1^2 u_1}} = -\theta_{2_{u_1^1 u_1}} \quad (\text{C-6})$$

The coherence between the two observed signals can be expressed as the coherence between the two sources.

$$\gamma_{1_{u_1^2 u_1}}^2 = \frac{\left| G_{1_{u_1^2 u_1}} \right|^2}{G_{1_{u_1^1 u_1}} G_{2_{u_1^2 u_1}}} = \frac{G_{1_{u_1^2 u_1}}^* G_{1_{u_1^2 u_1}}}{G_{1_{u_1^1 u_1}} G_{2_{u_1^2 u_1}}} = \frac{G_{2_{u_1^1 u_1}} G_{1_{u_1^2 u_1}}}{G_{1_{u_1^1 u_1}} G_{2_{u_1^2 u_1}}} \quad (\text{C-7})$$

$$G_{1_{u_1^1 u_1}} = \frac{2}{T} E \left[{}^1 U_1^* {}^1 U_1 \right] = \frac{2}{T} E \left[H_{11}^* X_1^* H_{11} X_1 \right] = H_{11}^* H_{11} G_{x_1 x_1} = |H_{11}|^2 G_{x_1 x_1} \quad (\text{C-8})$$

$$G_{2_{u_1^2 u_1}} = \frac{2}{T} E \left[{}^2 U_1^* {}^2 U_1 \right] = \frac{2}{T} E \left[H_{21}^* X_2^* H_{21} X_2 \right] = H_{21}^* H_{21} G_{x_2 x_2} = |H_{21}|^2 G_{x_2 x_2}$$

$$G_{1_{u_1^2 u_1}} = \frac{2}{T} E \left[{}^1 U_1^* {}^2 U_1 \right] = \frac{2}{T} E \left[H_{11}^* X_1^* H_{21} X_2 \right] = H_{11}^* H_{21} G_{x_1 x_2} \quad (\text{C-9})$$

$$G_{2_{u_1^1 u_1}} = \frac{2}{T} E \left[{}^2 U_1^* {}^1 U_1 \right] = \frac{2}{T} E \left[H_{21}^* X_2^* H_{11} X_1 \right] = H_{21}^* H_{11} G_{x_2 x_1}$$

$$\gamma_{1_{u_1^2 u_1}}^2 = \frac{\cancel{H_{21}^*} \cancel{H_{21}} \cancel{H_{11}^*} \cancel{H_{11}} G_{x_2 x_1} G_{x_1 x_2}}{\cancel{H_{11}^*} \cancel{H_{11}} \cancel{H_{21}^*} \cancel{H_{21}} G_{x_1 x_1} G_{x_2 x_2}} = \frac{\left| G_{x_1 x_2} \right|^2}{G_{x_1 x_1} G_{x_2 x_2}} = \gamma_{x_1 x_2}^2 \quad (\text{C-10})$$

This in turn can be used to re-express the cross-spectral density magnitude in Equation (C-11).

$$\left| G_{1_{u_1^2 u_1}} \right| = \sqrt{\gamma_{x_1 x_2}^2 G_{1_{u_1^1 u_1}} G_{2_{u_1^2 u_1}}} \quad (\text{C-11})$$

Substituting Equation (C-11) into Equation (C-5), while substituting Equation (C-5) and Equation (C-6) into Equation (C-4), and finally substituting Equation (C-4) into Equation (C-3) yields Equation (C-12).

$$G_{y_1 y_1} = G_{1_{u_1^1 u_1}} + G_{2_{u_1^2 u_1}} + \left(e^{j\theta_{1_{u_1^2 u_1}}} - e^{-j\theta_{1_{u_1^2 u_1}}} \right) \sqrt{\gamma_{x_1 x_2}^2 G_{1_{u_1^1 u_1}} G_{2_{u_1^2 u_1}}} \quad (\text{C-12})$$

This equation can be modified using Euler's Formula in Equation (C-13), yielding a final form shown in Equation (C-14).

$$\begin{aligned} e^{j\theta_{u_1^2 u_1}} &= \cos \theta_{u_1^2 u_1} + j \sin \theta_{u_1^2 u_1} \\ e^{-j\theta_{u_1^2 u_1}} &= \cos \theta_{u_1^2 u_1} - j \sin \theta_{u_1^2 u_1} \end{aligned} \quad (\text{C-13})$$

$$\begin{aligned} G_{y_1 y_1} &= G_{u_1^1 u_1} + G_{u_1^2 u_1} + \\ &\quad \left(\cancel{\cos \theta_{u_1^2 u_1}} + \cancel{j \sin \theta_{u_1^2 u_1}} + \cancel{\cos \theta_{u_1^2 u_1}} - \cancel{j \sin \theta_{u_1^2 u_1}} \right) \sqrt{\gamma_{x_1 x_2}^2 G_{u_1^1 u_1} G_{u_1^2 u_1}} \\ G_{y_1 y_1} &= G_{u_1^1 u_1} + G_{u_1^2 u_1} + 2 \cos \theta_{u_1^2 u_1} \sqrt{\gamma_{x_1 x_2}^2 G_{u_1^1 u_1} G_{u_1^2 u_1}} \end{aligned} \quad (\text{C-14})$$

In essence, the power measured by observer 1 is equal to the sum of the individual source contributions and the coherent power between the two sources.

Limiting cases of behavior can be evaluated. If the sources are perfectly coherent, with $\gamma_{x_1 x_2}^2 = 1$, and in phase, meaning that the phase angle $\theta_{u_1^2 u_1} = 0$, Equation (C-14) limits to Equation (C-15).

$$G_{y_1 y_1} = G_{u_1^1 u_1} + G_{u_1^2 u_1} + 2\sqrt{G_{u_1^1 u_1} G_{u_1^2 u_1}} \quad (\text{C-15})$$

This can be further simplified by assuming the sources have equal power contribution at the observer location, as in Equation (C-16).

$$G_{y_1 y_1} = G_{u_1 u_1} + G_{u_1 u_1} + 2\sqrt{G_{u_1 u_1}^2} = 4G_{u_1 u_1} \quad (\text{C-16})$$

Here, the coherence reinforces the signal, such that two equal inputs quadruple the measured power of a single source. This is sensible, since a doubling of signal level would yield a quadrupling of power for a single self-coherent signal. If instead the sources are assumed to be perfectly coherent, equal power and out of phase with a phase angle of $\theta_{u_1^2 u_1} = \pm\pi$, Equation (C-14) reduces to Equation (C-17).

$$G_{y_1 y_1} = G_{u_1 u_1} + G_{u_1 u_1} - 2\sqrt{G_{u_1 u_1}^2} = 0 \quad (\text{C-17})$$

Coherent, out of phase sources (where the phase angle between the sources is $\pm\pi$) of equal power cancel perfectly. Finally, if the sources are assumed to be incoherent such that $\gamma_{x_1 x_2}^2 = 0$ then Equation (C-14) simplifies to Equation (C-18).

$$G_{y_1 y_1} = G_{u_1^1 u_1} + G_{u_1^2 u_1} \quad (\text{C-18})$$

The autospectral density measured at observer 1 is simply the sum of the individual source power spectral densities propagated to the observer.

Cross-Spectral Scaling

The cross-spectral density between measurements at observers 1 and 2 from Figure C-1 is given in Equation (C-19).

$$\begin{aligned} G_{y_1 y_2} &= \frac{2}{T} E[Y_1^* Y_2] = \frac{2}{T} E\left[\left({}^1U_1 + {}^2U_1\right)^* \left({}^1U_2 + {}^2U_2\right)\right] \\ G_{y_1 y_2} &= \frac{2}{T} E\left[{}^1U_1^* {}^1U_2 + {}^1U_1^* {}^2U_2 + {}^2U_1^* {}^1U_2 + {}^2U_1^* {}^2U_2\right] \\ G_{y_1 y_2} &= \frac{2}{T} E\left[{}^1U_1^* {}^1U_2\right] + \frac{2}{T} E\left[{}^1U_1^* {}^2U_2\right] + \frac{2}{T} E\left[{}^2U_1^* {}^1U_2\right] + \frac{2}{T} E\left[{}^2U_1^* {}^2U_2\right] \\ G_{y_1 y_2} &= G_{u_1^1 u_2} + G_{u_1^2 u_2} + G_{u_1^1 u_2} + G_{u_1^2 u_2} \\ G_{y_1 y_2} &= \left|G_{u_1^1 u_2}\right| e^{j\theta_{u_1^1 u_2}} + \left|G_{u_1^2 u_2}\right| e^{j\theta_{u_1^2 u_2}} + \left|G_{u_1^1 u_2}\right| e^{j\theta_{u_1^1 u_2}} + \left|G_{u_1^2 u_2}\right| e^{j\theta_{u_1^2 u_2}} \end{aligned} \quad (\text{C-19})$$

Leveraging similar techniques as those used in the autospectral scaling allows for the use of the coherence between the sources to simplify the cross-source terms.

$$\left|G_{u_1^2 u_2}\right| = \sqrt{\gamma_{x_1 x_2}^2 G_{u_1^1 u_1} G_{u_2^2 u_2}} \quad (\text{C-20})$$

$$\left|G_{u_1^1 u_2}\right| = \sqrt{\gamma_{x_1 x_2}^2 G_{u_1^2 u_1} G_{u_2^1 u_2}} \quad (\text{C-21})$$

Equation (4-13) can be used for the remaining two terms.

$$\left|G_{u_1^1 u_2}\right| = \sqrt{G_{u_1^1 u_1} G_{u_2^1 u_2}} \quad (\text{C-22})$$

$$\left| G_{2_{u_1^2 u_2}} \right| = \sqrt{G_{2_{u_1^2 u_1}} G_{2_{u_2^2 u_2}}} \quad (\text{C-23})$$

Without knowledge of the propagation path behavior and the relative phases of the sources, the phase angles within Equation (C-19) cannot be simplified. The overall expression for the cross-spectral density is re-stated in terms of individual autospectral densities and phase angles in Equation (C-24).

$$G_{y_1 y_2} = \sqrt{G_{1_{u_1^1 u_1}} G_{1_{u_2^1 u_2}}} e^{j\theta_{1_{u_1^1 u_2}}} + \sqrt{G_{2_{u_1^2 u_1}} G_{2_{u_2^2 u_2}}} e^{j\theta_{2_{u_1^2 u_2}}} + \sqrt{\gamma^2 G_{1_{u_1^1 u_1}} G_{2_{u_2^2 u_2}}} e^{j\theta_{1_{u_1^2 u_2}}} + \sqrt{\gamma^2 G_{2_{u_1^2 u_1}} G_{1_{u_2^1 u_2}}} e^{j\theta_{2_{u_1^1 u_2}}} \quad (\text{C-24})$$

The first and second terms can be interpreted as the individual source contributions to the cross spectrum, while the third and fourth terms are based on source coherence, and can behave similarly to the cross-source terms in the autospectral analysis for limiting cases of unity and zero coherence.

Coherent Output Power Behavior

The fundamental contributions of each source to the overall, noiseless measured values have just been discussed. Now the effects of these contributions to an analysis on a noisy signal must be evaluated. Figure C-2 shows the modified setup. Without additional source information or more advanced analysis methods, there is no way to decouple the two sources using a coherent output power analysis. The method is simply used to remove the individual channel noise terms, $n_1(t)$ and $n_2(t)$, and analyze the acoustic field which is coherent between the two microphones, denoted as $w_1(t)$ and $w_2(t)$. In the pressure domain these add linearly such that the resultant desired parameters of interest are given in Equation (C-25) and Equation (C-26).

$$w_1(t) = u_1(t) + n_1(t) \quad (\text{C-25})$$

$$w_2(t) = u_2(t) + n_2(t) \quad (\text{C-26})$$

Unfortunately, analysis must occur in terms of power in the frequency domain, so the additive behavior is coherence-dependent, as demonstrated in previous sections. The acoustic autospectral density is thus given in Equation (C-27) and Equation (C-28), and is the key parameter desired using coherence-based analysis.

$$G_{w_1 w_1} = G_{1_{u_1^1 u_1}} + G_{2_{u_1^2 u_1}} + 2 \cos \theta_{1_{u_1^2 u_1}} \sqrt{\gamma_{x_1 x_2}^2 G_{1_{u_1^1 u_1}} G_{2_{u_1^2 u_1}}} \quad (\text{C-27})$$

$$G_{w_2 w_2} = G_{1_{u_2^1 u_2}} + G_{2_{u_2^2 u_2}} + 2 \cos \theta_{1_{u_2^2 u_2}} \sqrt{\gamma_{x_1 x_2}^2 G_{1_{u_2^1 u_2}} G_{2_{u_2^2 u_2}}} \quad (\text{C-28})$$

As the noise terms are uncorrelated, the measured autospectral densities are simply the acoustic autospectral densities plus the individual noise autospectral densities, shown in Equation (C-29) and Equation (C-30).

$$G_{y_1 y_1} = G_{w_1 w_1} + G_{n_1 n_1} \quad (\text{C-29})$$

$$G_{y_2 y_2} = G_{w_2 w_2} + G_{n_2 n_2} \quad (\text{C-30})$$

Based on Equation (4-12), the cross-spectral density can be expressed in Equation (C-31), where $G_{w_1 w_2}$ is simply equivalent to Equation (C-24).

$$G_{y_1 y_2} = G_{w_1 w_2} \quad (\text{C-31})$$

It must now be determined if Equation (4-14) and Equation (4-17) behave as expected under two-source conditions.

To analyze Equation (4-14), the behavior of the ordinary coherence function between observers $\gamma_{y_1 y_2}^2$ must be evaluated. As it is evident that this will contain a significant number of terms, the general coherent output power can be re-expressed in Equation (C-32), using Equation (C-30) and Equation (C-31).

$$COP_1 = \gamma_{y_1 y_2}^2 G_{y_1 y_1} = \frac{|G_{y_1 y_2}|^2}{G_{y_2 y_2}} = \frac{|G_{w_1 w_2}|^2}{G_{w_2 w_2} + G_{n_2 n_2}} \quad (\text{C-32})$$

This equation must then be evaluated to see if the identity in Equation (C-33), which would yield the coherent power at observer 1, biased low by the opposing observer's SNR as shown in Equation (4-14), holds. Note that for equations where the statement is to be validated, = is replaced with = ? to indicate an equivalency check is necessary.

$$\frac{|G_{w_1 w_2}|^2}{G_{w_2 w_2} + G_{n_2 n_2}} = ? \frac{G_{w_1 w_1}}{1 + \frac{G_{n_2 n_2}}{G_{w_2 w_2}}} = \frac{G_{w_1 w_1}}{1 + \frac{1}{SNR_2}} \quad (C-33)$$

This can be evaluated by substituting from Equation (C-24) and Equation (C-30).

$$\frac{|G_{w_1 w_2}|^2}{G_{w_2 w_2} + G_{n_2 n_2}} = \frac{1}{1 + \frac{1}{SNR_2}} \frac{|G_{w_1 w_2}|^2}{G_{w_2 w_2}} \Rightarrow \frac{|G_{w_1 w_2}|^2}{G_{w_2 w_2}} = ? G_{w_1 w_1} \Rightarrow \frac{|G_{w_1 w_2}|^2}{G_{w_2 w_2} G_{w_1 w_1}} = \gamma^2 = ? 1 \quad (C-34)$$

The formulation becomes a test of the coherence function when two sources are present.

$$\begin{aligned} \gamma_{w_1 w_2}^2 &= \frac{|G_{w_1 w_2}|^2}{G_{w_1 w_1} G_{w_2 w_2}} = \frac{G_{w_1 w_2}^* G_{w_1 w_2}}{G_{w_1 w_1} G_{w_2 w_2}} = \\ &= \frac{\sqrt{G_{1u_1^1 u_1^1} G_{1u_2^1 u_2^1}} e^{-j\theta_{1u_1^1 u_2^1}} + \sqrt{G_{2u_1^2 u_1^2} G_{2u_2^2 u_2^2}} e^{-j\theta_{2u_1^2 u_2^2}} + \sqrt{\gamma_{x_1 x_2}^2 G_{1u_1^1 u_1^1} G_{2u_2^2 u_2^2}} e^{-j\theta_{1u_1^1 u_2^2}} + \sqrt{\gamma_{x_1 x_2}^2 G_{2u_1^2 u_1^2} G_{1u_2^1 u_2^1}} e^{-j\theta_{2u_1^2 u_2^1}}}{G_{1u_1^1 u_1^1} + G_{2u_1^2 u_1^2} + 2 \cos \theta_{1u_1^1 u_1^2} \sqrt{\gamma_{x_1 x_2}^2 G_{1u_1^1 u_1^1} G_{2u_1^2 u_1^2}}} \\ &\times \frac{\sqrt{G_{1u_1^1 u_1^1} G_{1u_2^1 u_2^1}} e^{j\theta_{1u_1^1 u_2^1}} + \sqrt{G_{2u_1^2 u_1^2} G_{2u_2^2 u_2^2}} e^{j\theta_{2u_1^2 u_2^2}} + \sqrt{\gamma_{x_1 x_2}^2 G_{1u_1^1 u_1^1} G_{2u_2^2 u_2^2}} e^{j\theta_{1u_1^1 u_2^2}} + \sqrt{\gamma_{x_1 x_2}^2 G_{2u_1^2 u_1^2} G_{1u_2^1 u_2^1}} e^{j\theta_{2u_1^2 u_2^1}}}{G_{1u_2^1 u_2^1} + G_{2u_2^2 u_2^2} + 2 \cos \theta_{1u_2^1 u_2^2} \sqrt{\gamma_{x_1 x_2}^2 G_{1u_2^1 u_2^1} G_{2u_2^2 u_2^2}}} \end{aligned} \quad (C-35)$$

In general, this is intractable without making simplifying assumptions. For the simplest case, the sources can be treated as perfectly incoherent. In such a case, Equation (C-35) can be simplified to Equation (C-36).

$$\begin{aligned} \gamma_{w_1 w_2}^2 &= \frac{\left(\sqrt{G_{1u_1^1 u_1^1} G_{1u_2^1 u_2^1}} e^{-j\theta_{1u_1^1 u_2^1}} + \sqrt{G_{2u_1^2 u_1^2} G_{2u_2^2 u_2^2}} e^{-j\theta_{2u_1^2 u_2^2}} \right) \left(\sqrt{G_{1u_1^1 u_1^1} G_{1u_2^1 u_2^1}} e^{j\theta_{1u_1^1 u_2^1}} + \sqrt{G_{2u_1^2 u_1^2} G_{2u_2^2 u_2^2}} e^{j\theta_{2u_1^2 u_2^2}} \right)}{\left(G_{1u_1^1 u_1^1} + G_{2u_1^2 u_1^2} \right) \left(G_{1u_2^1 u_2^1} + G_{2u_2^2 u_2^2} \right)} \\ &= \frac{G_{1u_1^1 u_1^1} G_{1u_2^1 u_2^1} + G_{2u_1^2 u_1^2} G_{2u_2^2 u_2^2} + 2 \cos(\theta_{1u_1^1 u_2^1} - \theta_{2u_1^2 u_2^2}) \sqrt{G_{1u_1^1 u_1^1} G_{1u_2^1 u_2^1} G_{2u_1^2 u_1^2} G_{2u_2^2 u_2^2}}}{G_{1u_1^1 u_1^1} G_{1u_2^1 u_2^1} + G_{2u_1^2 u_1^2} G_{2u_2^2 u_2^2} + G_{1u_1^1 u_1^1} G_{2u_2^2 u_2^2} + G_{2u_1^2 u_1^2} G_{1u_2^1 u_2^1}} \end{aligned} \quad (C-36)$$

In general, the cosine term in the numerator of this equation will reduce the coherence of the signal. Therefore, for incoherent sources, the general COP method will not hold. However, for

further simplification, the cosine term can be evaluated at unity. This is equivalent to the schematic in Figure C-3, where the phase angle between observers for source 1 is equal to the phase angle between observers for source 2.

$$\gamma_{w_1 w_2}^2 = \frac{G_{1u_1^1 u_1} G_{1u_2^1 u_2} + G_{2u_1^2 u_1} G_{2u_2^2 u_2} + 2\sqrt{G_{1u_1^1 u_1} G_{1u_2^1 u_2} G_{2u_1^2 u_1} G_{2u_2^2 u_2}}}{G_{1u_1^1 u_1} G_{1u_2^1 u_2} + G_{2u_1^2 u_1} G_{2u_2^2 u_2} + G_{1u_1^1 u_1} G_{2u_2^2 u_2} + G_{2u_1^2 u_1} G_{1u_2^1 u_2}} \quad (\text{C-37})$$

Finally, if all of the source powers at the observer locations are equal, the coherence function in Equation (C-37) can be reduced one last time.

$$\gamma_{w_1 w_2}^2 = \frac{G_{uu} G_{uu} + G_{uu} G_{uu} + 2\sqrt{G_{uu} G_{uu} G_{uu} G_{uu}}}{G_{uu} G_{uu} + G_{uu} G_{uu} + G_{uu} G_{uu} + G_{uu} G_{uu}} = \frac{4(G_{uu})^2}{4(G_{uu})^2} = 1 \quad (\text{C-38})$$

This shows that for perfectly incoherent sources of equal power with equal distance to observer locations, the general coherent power method will behave as expected. Specifically, with proper microphone placement, if trailing edge noise were considered a line of incoherent sources, the general coherent power method would still function as expected. However, if the geometry of the source arrangement becomes more complicated such that the phase angle difference term returns, the coherence function will underpredict from what is expected. Also, when source coherence is introduced, additional complications occur. This would indicate that the method would handle distributed source fields with complicated coherence, such as boundary layer noise on the sidewalls, poorly.

This procedure can also be applied to the dipole-assumption based coherent power method of Equation (4-17), as shown in Equation (C-39).

$$\left| G_{w_1 w_2} \right| = ? G_{w_1 w_1} \quad (\text{C-39})$$

$$\begin{aligned}
|G_{w_1 w_2}| &= \\
& \left| \sqrt{G_{1u_1^1 u_1} G_{1u_2^1 u_2}} e^{j\theta_{1u_1^1 u_2}} + \sqrt{G_{2u_1^2 u_1} G_{2u_2^2 u_2}} e^{j\theta_{2u_1^2 u_2}} \right. \\
& \left. + \sqrt{\gamma_{x_1 x_2}^2 G_{1u_1^1 u_1} G_{2u_2^2 u_2}} e^{j\theta_{1u_1^1 u_2}} + \sqrt{\gamma_{x_1 x_2}^2 G_{2u_1^2 u_1} G_{1u_2^1 u_2}} e^{j\theta_{2u_1^2 u_2}} \right| \\
& = ? G_{1u_1^1 u_1} + G_{2u_1^2 u_1} + 2 \cos \theta_{1u_1^2 u_1} \sqrt{\gamma_{x_1 x_2}^2 G_{1u_1^1 u_1} G_{2u_1^2 u_1}}
\end{aligned} \tag{C-40}$$

Again, the solution to this is complicated. Again, it can be simplified by assuming incoherent sources.

$$|G_{w_1 w_2}| = \left| \sqrt{G_{1u_1^1 u_1} G_{1u_2^1 u_2}} e^{j\theta_{1u_1^1 u_2}} + \sqrt{G_{2u_1^2 u_1} G_{2u_2^2 u_2}} e^{j\theta_{2u_1^2 u_2}} \right| = ? G_{1u_1^1 u_1} + G_{2u_1^2 u_1} \tag{C-41}$$

As a dipole assumption is already applied to the data, the phase angles in Equation (C-41) can be evaluated.

$$\theta_{1u_1^1 u_2} = \theta_{2u_1^2 u_2} = \pi \tag{C-42}$$

$$e^{j\theta_{1u_1^1 u_2}} = e^{j\theta_{2u_1^2 u_2}} = -1 \tag{C-43}$$

Again, if equal source powers are assumed, the equation properly reduces to the assumed behavior, as shown in Equation (C-44).

$$|G_{w_1 w_2}| = \left| -\sqrt{G_{uu} G_{uu}} - \sqrt{G_{uu} G_{uu}} \right| = G_{uu} + G_{uu} = 2G_{uu} \tag{C-44}$$

As with the general coherent power method, the dipole assumption-based coherent power method should behave as expected under the same conditions set for the general coherent power method, in addition to the assumption that the sources are incoherent dipoles, again schematically shown in Figure C-3 if the sources are considered as dipoles instead of monopoles. It will be shown in subsequent discussion that incoherent dipole sources will behave similarly to incoherent monopoles regarding coherent power analysis. For general distributed, partially-coherent source fields, the cross-spectral magnitude will not properly predict the microphone autospectra due to the phasor summation.

General Monopole Multiple-Input/Multiple-Output Behavior

The TITO analysis presented previously shows that depending on the source nature and arrangement with respect to a measurement, a coherence-based analysis method may predict incorrect levels due to source coherence under-prediction. Under certain limiting circumstances, however, the methods may predict the correct acoustic levels. Validation of these methods under a more generalized condition is necessary to determine if under-prediction is likely in trailing edge noise measurements.

Problem Formulation

Generalized equation scaling as conducted in the previous section would be difficult and is beyond the scope of the discussion in this appendix. Instead, a specific physical problem will be formulated in terms of a multiple-input/multiple-output (MIMO) system and then analyzed.

Trailing edge noise is a function of, among other things, the spanwise coherence of the boundary layer turbulence as shown in Equation (2-19) and Equation (2-21). If it is assumed that this correlation length scale is small relative to the wetted span of an airfoil, the trailing edge noise source can be simplified, for the purposes of this discussion, to be a line of uncorrelated sources with a spacing of this correlation length scale. A schematic of this idealized source setup is shown in Figure C-4, while the associated block diagram is shown in Figure C-5. For this stage of discussion, all sources are treated as monopoles. Observers are considered to be idealized microphones. This three-microphone setup is analogous to the spanwise microphone setup shown in Figure 4-45. The equation for the pressure field generated by a harmonic monopole operating at a single frequency, adapted from Blackstock [Blackstock 2000], is given in Equation (C-45).

$$p'(r, t, q) = \text{Re} \left\{ \frac{A}{4\pi r} e^{j(\omega_0 t - k_0 r - \phi_q)} \right\} = \frac{A}{4\pi r} \cos(\omega_0 t - k_0 r - \phi_q) \quad (\text{C-45})$$

Here, p' denotes the acoustic pressure fluctuation at location r from the source at time t . The source is fluctuating at ω_0 radians per second, with an associated wavenumber k_0 defined via Equation (2-13) with c_0 as the acoustic speed of sound in meters per second. A is the acoustic source strength, here treated as an arbitrary constant set to unity. ϕ_q is the randomized source phase. To construct a set of incoherent sources, a random variable is necessary such that the average cross-power between the sources is zero. This phase randomization is introduced for such a purpose. The mathematics of this will be evident in the subsequent discussion. This phase angle in reality would likely be some function of the turbulent correlation time scale, but for this discussion will be treated as a function of data block number q . The analysis is treated such that a continuous data set is available which is broken up into Q total blocks of data, each T seconds long.

The time-domain expression from Equation (C-45) can be converted into a frequency-domain expression of the monopole sound field through a finite Fourier transform in Equation (C-46).

$$\begin{aligned}
\Im(p') &= P'(r, \omega, q) = \int_0^T p'(r, t, q) e^{-j\omega t} dt \\
P'(r, \omega, q) &= \int_0^T \frac{A}{4\pi r} \cos(\omega_0 t - k_0 r - \phi_q) e^{-j\omega t} dt \\
&= \frac{A}{4\pi r} \int_0^T \left[\cos(\omega_0 t) \cos(k_0 r + \phi_q) + \sin(\omega_0 t) \sin(k_0 r + \phi_q) \right] e^{-j\omega t} dt \\
&= \frac{A}{4\pi r} \int_0^T \left[\cos(\omega_0 t) \cos(k_0 r + \phi_q) + \sin(\omega_0 t) \sin(k_0 r + \phi_q) \right] [\cos(\omega t) - j \sin(\omega t)] dt \\
&= \frac{A}{4\pi r} \left[\cos(k_0 r + \phi_q) \int_0^T \cos(\omega_0 t) \cos(\omega t) dt - j \cos(k_0 r + \phi_q) \int_0^T \cos(\omega_0 t) \sin(\omega t) dt \right. \\
&\quad \left. + \sin(k_0 r + \phi_q) \int_0^T \sin(\omega_0 t) \cos(\omega t) dt - j \sin(k_0 r + \phi_q) \int_0^T \sin(\omega_0 t) \sin(\omega t) dt \right]
\end{aligned} \tag{C-46}$$

Orthogonality can be applied such that the function is zero for all ω except ω_0 (and $-\omega_0$, but this analysis only deals with single-sided spectra, so only positive frequencies will be discussed, and power will be doubled where appropriate).

$$P'(r, \omega_0, q) = \frac{A}{4\pi r} \left[\cos(k_0 r + \phi_q) \int_0^T \cos^2(\omega_0 t) dt - j \sin(k_0 r + \phi_q) \int_0^T \sin^2(\omega_0 t) dt \right]$$

$$= \frac{A}{4\pi r} \left\{ \cos(k_0 r + \phi_q) \left[\frac{t}{2} + \frac{1}{4\omega_0} \sin(2\omega_0 t) \right] \Big|_0^T - j \sin(k_0 r + \phi_q) \left[\frac{t}{2} - \frac{1}{4\omega_0} \sin(2\omega_0 t) \right] \Big|_0^T \right\} \quad (\text{C-47})$$

As periodicity is assumed over the block length T , Equation (C-47) reduces to Equation (C-48).

$$P'(r, \omega_0, q) = \frac{A}{4\pi r} \left[\frac{T}{2} \cos(k_0 r + \phi_q) - j \frac{T}{2} \sin(k_0 r + \phi_q) \right] = \frac{AT}{8\pi r} e^{-j(k_0 r + \phi_q)} \quad (\text{C-48})$$

From this equation, the output at microphone 1 due to source m is expressed in Equation (C-49).

Microphone 2's output is expressed in Equation (C-50), and Microphone 3's in Equation (C-51).

Note that here the subscript of ϕ has been updated to reflect its dependence on source as well as block number.

$${}^m U_1(\omega_0, q) = \frac{AT}{8\pi \sqrt{(m\Delta x)^2 + (\Delta h)^2}} e^{-j(k_0 \sqrt{(m\Delta x)^2 + (\Delta h)^2} + \phi_{mq})} \quad (\text{C-49})$$

$${}^m U_2(\omega_0, q) = \frac{AT}{8\pi \sqrt{(m\Delta x)^2 + (\Delta h)^2}} e^{-j(k_0 \sqrt{(m\Delta x)^2 + (\Delta h)^2} + \phi_{mq})} \quad (\text{C-50})$$

$${}^m U_3(\omega_0, q) = \frac{AT}{8\pi \sqrt{(\Delta y + m\Delta x)^2 + (\Delta h)^2}} e^{-j(k_0 \sqrt{(\Delta y + m\Delta x)^2 + (\Delta h)^2} + \phi_{mq})} \quad (\text{C-51})$$

The total pressure field for each microphone is thus expressed in Equation (C-52), Equation (C-53) and Equation (C-54).

$$Y_1(\omega_0, q) = \frac{AT}{8\pi} \sum_{m=-M}^M \frac{e^{-j(k_0 \sqrt{(m\Delta x)^2 + (\Delta h)^2} + \phi_{mq})}}{\sqrt{(m\Delta x)^2 + (\Delta h)^2}} + N_1(\omega_0, q) \quad (\text{C-52})$$

$$Y_2(\omega_0, q) = \frac{AT}{8\pi} \sum_{m=-M}^M \frac{e^{-j(k_0 \sqrt{(m\Delta x)^2 + (\Delta h)^2} + \phi_{mq})}}{\sqrt{(m\Delta x)^2 + (\Delta h)^2}} + N_2(\omega_0, q) \quad (\text{C-53})$$

$$Y_3(\omega_0, q) = \frac{AT}{8\pi} \sum_{m=-M}^M \frac{e^{-j(k_0 \sqrt{(\Delta y + m\Delta x)^2 + (\Delta h)^2} + \phi_{mq})}}{\sqrt{(\Delta y + m\Delta x)^2 + (\Delta h)^2}} + N_3(\omega_0, q) \quad (\text{C-54})$$

Auto- and cross-spectral densities will now be considered. The autospectral density of source m at microphone 1 is expressed in Equation (C-55). Here, each block's phase angle term identically cancels.

$$\begin{aligned} G_{m_{u_1}^m u_1}(\omega_0) &= \frac{2}{T} E[{}^m U_1^* {}^m U_1] \\ &= \frac{2}{QT} \sum_{q=1}^Q \left\{ \left[\frac{AT}{8\pi \sqrt{(m\Delta x)^2 + (\Delta h)^2}} e^{j(k_0 \sqrt{(m\Delta x)^2 + (\Delta h)^2} + \phi_{mq})} \right] \right. \\ &\quad \times \left. \left[\frac{AT}{8\pi \sqrt{(m\Delta x)^2 + (\Delta h)^2}} e^{-j(k_0 \sqrt{(m\Delta x)^2 + (\Delta h)^2} + \phi_{mq})} \right] \right\} \\ &= \frac{A^2 T}{32\pi^2 [(m\Delta x)^2 + (\Delta h)^2]} \end{aligned} \quad (\text{C-55})$$

Microphones 2 and 3 are constructed similarly in Equation (C-56) and Equation (C-57).

$$G_{m_{u_2}^m u_2}(\omega_0) = \frac{A^2 T}{32\pi^2 [(m\Delta x)^2 + (\Delta h)^2]} \quad (\text{C-56})$$

$$G_{m_{u_3}^m u_3}(\omega_0) = \frac{A^2 T}{32\pi^2 [(\Delta y + m\Delta x)^2 + (\Delta h)^2]} \quad (\text{C-57})$$

The cross-spectral density between two sources at a given microphone is expressed by Equation (C-58).

$$\begin{aligned}
G_{m_{u_1}^n u_1}(\omega_0) &= \frac{2}{T} E \left[{}^m U_1^* {}^n U_1 \right] \\
&= \frac{2}{QT} \sum_{q=1}^Q \left\{ \left[\frac{AT}{8\pi \sqrt{(m\Delta x)^2 + (\Delta h)^2}} e^{j \left(k \sqrt{(m\Delta x)^2 + (\Delta h)^2} + \phi_{mq} \right)} \right] \right. \\
&\quad \times \left. \left[\frac{AT}{8\pi \sqrt{(n\Delta x)^2 + (\Delta h)^2}} e^{-j \left(k \sqrt{(n\Delta x)^2 + (\Delta h)^2} + \phi_{nq} \right)} \right] \right\} \\
&= \frac{A^2 T e^{jk \left(\sqrt{(m\Delta x)^2 + (\Delta h)^2} - \sqrt{(n\Delta x)^2 + (\Delta h)^2} \right)}}{32Q\pi^2 \sqrt{(m\Delta x)^2 + (\Delta h)^2} \sqrt{(n\Delta x)^2 + (\Delta h)^2}} \sum_{q=1}^Q e^{j(\phi_{mq} - \phi_{nq})}
\end{aligned} \tag{C-58}$$

The variables ϕ_{mq} and ϕ_{nq} are defined as uncorrelated random variables, so the phasor term $e^{j(\phi_{mq} - \phi_{nq})}$ should vary randomly between -1 and 1 on the real axis, and $-j$ and j on the imaginary axis. For a sufficiently large number of blocks Q , the summation term should approach zero, validating this method of defining incoherent monopole sources, which should have cross-spectra which are identically zero, as given in Equation (C-59). The same holds for the cross-spectra between individual sources at microphones 2 and 3.

$$G_{m_{u_1}^n u_1}(\omega_0) = G_{m_{u_2}^n u_2}(\omega_0) = G_{m_{u_3}^n u_3}(\omega_0) = 0 \tag{C-59}$$

The autospectral density of each microphone signal can now be constructed (assuming noise is uncorrelated with input).

$$\begin{aligned}
G_{y_1 y_1}(\omega_0) &= \frac{2}{QT} \sum_{q=1}^Q \left\{ \sum_{m=-M}^M \sum_{n=-M}^M \left[\frac{AT}{8\pi \sqrt{(m\Delta x)^2 + (\Delta h)^2}} e^{j \left(k_0 \sqrt{(m\Delta x)^2 + (\Delta h)^2} + \phi_{mq} \right)} \right] \right. \\
&\quad \times \left. \left[\frac{AT}{8\pi \sqrt{(n\Delta x)^2 + (\Delta h)^2}} e^{-j \left(k_0 \sqrt{(n\Delta x)^2 + (\Delta h)^2} + \phi_{nq} \right)} \right] + N_1^* N_1 \right\} \\
&= \frac{A^2 T}{32\pi^2} \sum_{m=-M}^M \frac{1}{(m\Delta x)^2 + (\Delta h)^2} + G_{n_1 n_1} = \sum_{m=-M}^M G_{m_{u_1}^m u_1} + G_{n_1 n_1} = G_{w_1 w_1} + G_{n_1 n_1}
\end{aligned} \tag{C-60}$$

Equation (C-60) simplifies as such because it was shown in Equation (C-58) and Equation (C-59) that summation terms are zero for $m \neq n$. The autospectral densities for microphones 2 and 3 are given in Equation (C-61) and Equation (C-62).

$$G_{y_2 y_2}(\omega_0) = \frac{A^2 T}{32\pi^2} \sum_{m=-M}^M \frac{1}{(m\Delta x)^2 + (\Delta h)^2} + G_{n_2 n_2} = \sum_{m=-M}^M G_{u_2^m u_2^m} + G_{n_2 n_2} = G_{w_2 w_2} + G_{n_2 n_2} \quad (\text{C-61})$$

$$\begin{aligned} G_{y_3 y_3}(\omega_0) &= \frac{A^2 T}{32\pi^2} \sum_{m=-M}^M \frac{1}{(\Delta y + m\Delta x)^2 + (\Delta h)^2} + G_{n_3 n_3} = \sum_{m=-M}^M G_{u_3^m u_3^m} + G_{n_3 n_3} \\ &= G_{w_3 w_3} + G_{n_3 n_3} \end{aligned} \quad (\text{C-62})$$

As expected for incoherent sources, the overall source power field is equivalent to the sum of the individual power contributions of each source.

Cross-spectral densities must now be considered. The cross-spectral density between the contribution of source m at microphone 1 and source m at microphone 2 is derived in Equation (C-63).

$$\begin{aligned} G_{m_{u_1^m u_2^m}}(\omega_0) &= \frac{2}{T} E \left[{}^m U_1^* {}^m U_2 \right] \\ &= \frac{2}{QT} \sum_{q=1}^Q \left\{ \left[\frac{AT}{8\pi\sqrt{(m\Delta x)^2 + (\Delta h)^2}} e^{j(k_0\sqrt{(m\Delta x)^2 + (\Delta h)^2} + \phi_{mq})} \right] \right. \\ &\quad \times \left. \left[\frac{AT}{8\pi\sqrt{(m\Delta x)^2 + (\Delta h)^2}} e^{-j(k_0\sqrt{(m\Delta x)^2 + (\Delta h)^2} + \phi_{mq})} \right] \right\} \\ &= \frac{A^2 T}{32\pi^2 [(m\Delta x)^2 + (\Delta h)^2]} \end{aligned} \quad (\text{C-63})$$

As shown previously, for equal-power monopoles with equidistant observers, the cross-spectral density will reduce to the autospectral density. However, microphones 1 and 3 and microphones 2 and 3 do not form equidistant pairs. The formulation for these cross-spectral densities, computed the same way as that between microphones 1 and 2, is more complicated.

$$G_{m_{u_1}^m u_3}(\omega_0) = \frac{A^2 T e^{jk_0(\sqrt{(m\Delta x)^2 + (\Delta h)^2} - \sqrt{(\Delta y + m\Delta x)^2 + (\Delta h)^2})}}{32\pi^2 \sqrt{(m\Delta x)^2 + (\Delta h)^2} \sqrt{(\Delta y + m\Delta x)^2 + (\Delta h)^2}} \quad (\text{C-64})$$

$$G_{m_{u_2}^m u_3}(\omega_0) = \frac{A^2 T e^{jk_0(\sqrt{(m\Delta x)^2 + (\Delta h)^2} - \sqrt{(\Delta y + m\Delta x)^2 + (\Delta h)^2})}}{32\pi^2 \sqrt{(m\Delta x)^2 + (\Delta h)^2} \sqrt{(\Delta y + m\Delta x)^2 + (\Delta h)^2}} \quad (\text{C-65})$$

In Equation (C-64) and Equation (C-65), a phase offset can exist in each of the cross-spectral density terms. As with the autospectral density computations, any cross-source/cross-observer cross-spectral densities will be equal to zero. As such, the overall cross-spectral density between each observer pair is computed in Equation (C-66), Equation (C-67) and Equation (C-68).

$$G_{y_1 y_2}(\omega_0) = \frac{A^2 T}{32\pi^2} \sum_{m=-M}^M \frac{1}{(m\Delta x)^2 + (\Delta h)^2} = \sum_{m=-M}^M G_{m_{u_1}^m u_2} = G_{w_1 w_2} \quad (\text{C-66})$$

$$G_{y_1 y_3}(\omega_0) = \frac{A^2 T}{32\pi^2} \sum_{m=-M}^M \frac{e^{jk_0(\sqrt{(m\Delta x)^2 + (\Delta h)^2} - \sqrt{(\Delta y + m\Delta x)^2 + (\Delta h)^2})}}{\sqrt{(m\Delta x)^2 + (\Delta h)^2} \sqrt{(\Delta y + m\Delta x)^2 + (\Delta h)^2}} = \sum_{m=-M}^M G_{m_{u_1}^m u_3} = G_{w_1 w_3} \quad (\text{C-67})$$

$$G_{y_2 y_3}(\omega_0) = \frac{A^2 T}{32\pi^2} \sum_{m=-M}^M \frac{e^{jk_0(\sqrt{(m\Delta x)^2 + (\Delta h)^2} - \sqrt{(\Delta y + m\Delta x)^2 + (\Delta h)^2})}}{\sqrt{(m\Delta x)^2 + (\Delta h)^2} \sqrt{(\Delta y + m\Delta x)^2 + (\Delta h)^2}} = \sum_{m=-M}^M G_{m_{u_2}^m u_3} = G_{w_2 w_3} \quad (\text{C-68})$$

As has been demonstrated for a single source in Equation (4-13), the coherence of a single source's signal across two microphones is unity.

$$\gamma_{m_{u_1}^m u_2}^2(\omega_0) = \gamma_{m_{u_1}^m u_3}^2(\omega_0) = \gamma_{m_{u_2}^m u_3}^2(\omega_0) = 1 \quad (\text{C-69})$$

The total cross-channel coherence between microphones 1 and 2 is given in Equation (C-70).

$$\begin{aligned}
\gamma_{y_1 y_2}^2(\omega_0) &= \frac{\left| \frac{A^2 T}{32\pi^2} \sum_{m=-M}^M G_{u_1^m u_2} \right|^2}{\left(\frac{A^2 T}{32\pi^2} \sum_{n=-M}^M G_{u_1^n u_1} + G_{n_1 n_1} \right) \left(\frac{A^2 T}{32\pi^2} \sum_{p=-M}^M G_{u_2^p u_2} + G_{n_2 n_2} \right)} \\
&= \frac{\left(\frac{A^2 T}{32\pi^2} \sum_{m=-M}^M G_{u_1^m u_2} \right)^* \left(\frac{A^2 T}{32\pi^2} \sum_{r=-M}^M G_{u_1^r u_2} \right)}{\left(\frac{A^2 T}{32\pi^2} \sum_{n=-M}^M G_{u_1^n u_1} + G_{n_1 n_1} \right) \left(\frac{A^2 T}{32\pi^2} \sum_{p=-M}^M G_{u_2^p u_2} + G_{n_2 n_2} \right)}
\end{aligned} \tag{C-70}$$

In the limiting condition of no incoherent line noise, this reduces to Equation (C-71).

$$\gamma_{y_1 y_2}^2(\omega_0) = \frac{\left(\frac{A^2 T}{32\pi^2} \sum_{m=-M}^M \frac{1}{(m\Delta x)^2 + (\Delta h)^2} \right) \left(\frac{A^2 T}{32\pi^2} \sum_{r=-M}^M \frac{1}{(r\Delta x)^2 + (\Delta h)^2} \right)}{\left(\frac{A^2 T}{32\pi^2} \sum_{n=-M}^M \frac{1}{(n\Delta x)^2 + (\Delta h)^2} \right) \left(\frac{A^2 T}{32\pi^2} \sum_{p=-M}^M \frac{1}{(p\Delta x)^2 + (\Delta h)^2} \right)} = 1 \tag{C-71}$$

The coherence between microphones 1 and 2 in the absence of incoherent line noise reduces to unity, indicating that these two microphones will properly predict local coherent source power when using coherence-based analysis methods. This is consistent with the TITO system shown in the previous section. However, when one of the microphones, microphone 3, is offset, the scaling is more difficult. For noiseless conditions, the coherence is given in Equation (C-72).

$$\gamma_{y_1 y_3}^2(\omega_0) = \gamma_{w_1 w_3}^2 = \frac{|G_{w_1 w_3}|^2}{G_{w_1 w_1} G_{w_3 w_3}} = \frac{\left(\sum_{m=-M}^M G_{u_1^m u_3} \right)^* \left(\sum_{r=-M}^M G_{u_1^r u_3} \right)}{\left(\sum_{n=-M}^M G_{u_1^n u_1} \right) \left(\sum_{p=-M}^M G_{u_3^p u_3} \right)} \tag{C-72}$$

The numerator term can be expanded as in Equation (C-73).

$$\begin{aligned}
|G_{y_1, y_3}|^2 &= \frac{A^4 T^2}{1024 \pi^4} \left(\sum_{m=-M}^M \frac{e^{jk(\sqrt{(m\Delta x)^2 + (\Delta h)^2} - \sqrt{(\Delta y + m\Delta x)^2 + (\Delta h)^2})}}{\sqrt{(m\Delta x)^2 + (\Delta h)^2} \sqrt{(\Delta y + m\Delta x)^2 + (\Delta h)^2}} \right) \\
&\quad \times \left(\sum_{r=-M}^M \frac{e^{jk_0(\sqrt{(r\Delta x)^2 + (\Delta h)^2} - \sqrt{(\Delta y + r\Delta x)^2 + (\Delta h)^2})}}{\sqrt{(r\Delta x)^2 + (\Delta h)^2} \sqrt{(\Delta y + r\Delta x)^2 + (\Delta h)^2}} \right) \\
&= \frac{A^4 T^2}{1024 \pi^4} \sum_{m=-M}^M \sum_{r=-M}^M \left\{ \frac{e^{jk_0(\sqrt{(m\Delta x)^2 + (\Delta h)^2} - \sqrt{(\Delta y + m\Delta x)^2 + (\Delta h)^2})}}{\sqrt{(m\Delta x)^2 + (\Delta h)^2} \sqrt{(\Delta y + m\Delta x)^2 + (\Delta h)^2}} \right. \\
&\quad \left. \times \frac{e^{jk_0(\sqrt{(r\Delta x)^2 + (\Delta h)^2} + \sqrt{(\Delta y + r\Delta x)^2 + (\Delta h)^2})}}{\sqrt{(r\Delta x)^2 + (\Delta h)^2} \sqrt{(\Delta y + r\Delta x)^2 + (\Delta h)^2}} \right\}
\end{aligned} \tag{C-73}$$

Given the nature of the problem, no assumption can be made with regard to the scaling of $m\Delta x$ or Δy to Δh , so no further simplification may be possible.

Simulation

Instead, an example will be used similar to an experimental setup in UFAFF (neglecting flow and shear layer effects). Here, the microphone distance from the trailing edge will be $\Delta h = 1$ m, and the microphone spacing will be $\Delta y = 0.178$ m. This horizontal spacing is slightly less than that shown in Figure 4-45, but has been used in previous work. As the correlation scales for the model are currently unknown, a correlation length scale/source spacing will be selected as $\Delta x = 0.02$ m, as this is the grid density used in beamforming analysis. The model wetted span of 44" gives a value for M of 28 (rounding up) for a total of 57 sources. The source strength A will be taken as unity, and the block length will be $T = 0.0625$ sec as is often used in UFAFF spectral processing.

Solving for the coherence between microphones 1 and 3 as a function of frequency yields the curve shown in Figure C-6. As previously-discussed, coherent power methods are dependent on the noiseless source field of interest having a coherence of unity. This plotted coherence

function shows that if microphones are oriented along the span of a line of sources, and one of those microphones, microphone 3, is not centered along that line, a dramatic reduction in the coherence function occurs as frequency increases. This is due to the phasor summation in the cross-spectral magnitude term of Equation (C-73). As such, both two-microphone coherent power methods, Equation (4-14) depending on the coherence function and Equation (4-17) depending on the cross-spectral magnitude, would dramatically underpredict the true autospectral levels at higher frequencies, as based on Equation (C-55) and Equation (C-60) the autospectral density levels of the sources are frequency-independent.

Based on Equation (4-23), the effect this would have on three-microphone predictions is less straightforward. If microphones 1 and 2 are observing the same field, which would be true for being positioned on equal, opposite sides of a line of incoherent monopoles as in Figure C-4, their coherence in a noiseless measurement will be unity as shown in Equation (C-71). Also, as both microphones are observing the same signal, the coherence between microphones 1 and 3 will be the same as that between microphones 2 and 3. This would indicate that when computing the *SNR* values for microphones 1 and 2, the error from the coherence underprediction would ideally divide out, although realistically the nulls in the visible hump structure could lead to divide-by-zero issues. Only microphone 3's *SNR* prediction would suffer, as is shown in Figure C-7, where microphone 3's true autospectral density is compared to its three-microphone prediction. This means that under ideal conditions, as long as the first two microphones are placed carefully with respect to a known source field, a third microphone can have sub-optimal source location and still allow for good *SNR* estimates of the first two. In the case of trailing edge noise, the third microphone can have some offset as long as the first two are centered on opposite sides of the trailing edge. The dipole-like behavior of the trailing edge source is not

expected to have a significant effect on this behavior beyond what is seen with the monopoles, as these computations are dependent on the cross-spectral magnitude, so the π phase difference between the upper and lower surfaces should not contribute.

Having analyzed the effects of offsetting an observer along the source line span, the observer can now be offset depth-wise. This is analogous to the actual three-microphone method used in this dissertation, where the third microphone is slightly downstream from the upper microphone, as shown in Figure 4-37. The source schematic for this setup is shown in Figure C-8. The autospectral and cross-spectral densities for each source's contribution to the third microphone must be slightly updated based on the new geometry.

$$G_{m_{u_3}m_{u_3}}(\omega_0) = \frac{A^2 T}{32\pi^2 \left[(m\Delta x)^2 + (\Delta z)^2 + (\Delta h)^2 \right]} \quad (\text{C-74})$$

$$G_{m_{u_1}m_{u_3}}(\omega_0) = G_{m_{u_2}m_{u_3}}(\omega_0) = \frac{A^2 T e^{jk \left(\sqrt{(m\Delta x)^2 + (\Delta h)^2} - \sqrt{(m\Delta x)^2 + (\Delta z)^2 + (\Delta h)^2} \right)}}{32\pi^2 \sqrt{(m\Delta x)^2 + (\Delta h)^2} \sqrt{(m\Delta x)^2 + (\Delta z)^2 + (\Delta h)^2}} \quad (\text{C-75})$$

The updated source contributions from Equation (C-74) and Equation (C-75) can be substituted into Equation (C-72), and the coherence function recomputed using the same values as previously selected, except with $\Delta y = \Delta z$. The resultant coherence plot is shown in Figure C-9. This case shows far improved behavior, with less than 5% coherence loss by 20 kHz. Centering the third microphone along the span of sources and locating it slightly offset in the z -direction has dramatically improved the performance of the coherence prediction, and in this case a divide-by-zero condition is no longer of concern in the three-microphone method. The corresponding power prediction for microphone 3 is shown in Figure C-10. This result would also indicate that small positional errors in microphone 1 and microphone 2 placement would

have a small effect on coherence breakdown based on multiple sources, as long as the microphones remain in the plane which bisects the line of incoherent sources.

In an effort to evaluate the severity of this spanwise effect, an additional simulation is conducted using a set of eight microphones, as shown in Figure C-11. This spanwise arrangement of microphones, with the same spacing of 0.178 m as used previously, mirrors a previously-acquired data set in UFAFF involving a DU 96-W-180 airfoil. All previous formulations for the monopole field are used, with the appropriate substitutions of $2\Delta y$ and $3\Delta y$ for Δy depending on the microphone location. The resultant coherence plots for several of the microphones are shown in Figure C-12. The local autospectral density predictions are shown in Figure C-13, as computed using the three-microphone method referencing microphones 1 and 5. As shown, for typical length scales within UFAFF, increasing spanwise offset of a measurement microphone causes increased coherence breakdown due to phasor cancellation in the cross-spectral magnitude. An increase is noted at high frequencies for γ_{y_1, y_2}^2 with a corresponding increase in predicted power $G_{u_2 u_2}$. The behavior may be part of some large-scale spectral periodicity, but this cannot be known without further investigation, which is not conducted at this time.

Dipole Analysis and Comparison with Experimental Data

While it was previously assumed that a line of incoherent dipoles would behave similarly to a line of incoherent monopoles, this assumption should be verified. The time-domain expression for a harmonic dipole [Dowling & Ffowcs Williams 1983] is adapted in Equation (C-76).

$$p'(r, \theta, t, q) = \text{Re} \left\{ \frac{f \cos \theta}{4\pi} \left(\frac{jk_0}{r} + \frac{1}{r^2} \right) e^{j(\omega_0 t - k_0 r - \phi_q)} \right\} \quad (\text{C-76})$$

Note the additional angular dependence θ . Also note that this angle is $\pi/2$ offset from that used in Figure 2-1, distinguishing these idealized dipoles from the true trailing edge coordinate system. The dipole strength is f . The time-domain expression can be expanded, as in Equation (C-77).

$$\begin{aligned}
p'(r, \theta, t, q) &= \text{Re} \left\{ \frac{f \cos \theta}{4\pi} \left(\frac{jk_0}{r} + \frac{1}{r^2} \right) \left[\cos(\omega_0 t - k_0 r - \phi_q) + j \sin(\omega_0 t - k_0 r - \phi_q) \right] \right\} \\
&= \text{Re} \left\{ \frac{f \cos \theta}{4\pi} \left[\frac{jk_0 \cos(\omega_0 t - k_0 r - \phi_q)}{r} - \frac{k_0 \sin(\omega_0 t - k_0 r - \phi_q)}{r} \right. \right. \\
&\quad \left. \left. + \frac{\cos(\omega_0 t - k_0 r - \phi_q)}{r^2} + \frac{j \sin(\omega_0 t - k_0 r - \phi_q)}{r^2} \right] \right\} \\
&= \frac{f \cos \theta \cos(\omega_0 t - k_0 r - \phi_q)}{4\pi r^2} - \frac{fk_0 \cos \theta \sin(\omega_0 t - k_0 r - \phi_q)}{4\pi r}
\end{aligned} \tag{C-77}$$

As with the monopole analysis, this expression can be converted to the frequency domain through a finite Fourier transform in Equation (C-78).

$$\begin{aligned}
P'(r, \theta, \omega, q) &= \frac{f \cos \theta}{4\pi r} \left[\int_0^T \frac{\cos(\omega_0 t - k_0 r - \phi_q)}{r} e^{-j\omega t} dt \right. \\
&\quad \left. - \int_0^T k_0 \sin(\omega_0 t - k_0 r - \phi_q) e^{-j\omega t} dt \right] \\
&= \frac{f \cos \theta}{4\pi r} \left\{ \frac{1}{r} \int_0^T \left[\cos(\omega_0 t) \cos(k_0 r + \phi_q) + \sin(\omega_0 t) \sin(k_0 r + \phi_q) \right] e^{-j\omega t} dt \right. \\
&\quad \left. - k_0 \int_0^T \left[\sin(\omega_0 t) \cos(k_0 r + \phi_q) - \cos(\omega_0 t) \sin(k_0 r + \phi_q) \right] e^{-j\omega t} dt \right\} \\
&= \frac{f \cos \theta}{4\pi r} \left\{ \frac{1}{r} \int_0^T \left[\cos(\omega_0 t) \cos(k_0 r + \phi_q) + \sin(\omega_0 t) \sin(k_0 r + \phi_q) \right] \right. \\
&\quad \times \left[\cos(\omega t) - j \sin(\omega t) \right] dt \\
&\quad - k_0 \int_0^T \left[\sin(\omega_0 t) \cos(k_0 r + \phi_q) - \cos(\omega_0 t) \sin(k_0 r + \phi_q) \right] \\
&\quad \left. \left[\cos(\omega t) - j \sin(\omega t) \right] dt \right\}
\end{aligned} \tag{C-78}$$

Again, orthogonality cancels the integrals between sines and cosines, as well as those where $\omega \neq \omega_0$ frequency mismatches, leaving Equation (C-79).

$$\begin{aligned}
P'(r, \theta, \omega_0, q) &= \frac{f \cos \theta}{4\pi r} \left\{ \frac{\cos(k_0 r + \phi_q)}{r} \int_0^T \cos^2(\omega_0 t) dt \right. \\
&\quad - \frac{j \sin(k_0 r + \phi_q)}{r} \int_0^T \sin^2(\omega_0 t) dt + j k_0 \cos(k_0 r + \phi_q) \int_0^T \sin^2(\omega_0 t) dt \\
&\quad \left. + k_0 \sin(k_0 r + \phi_q) \int_0^T \cos^2(\omega_0 t) dt \right\} \\
&= \frac{f \cos \theta}{4\pi r} \left\{ \frac{\cos(k_0 r + \phi_q)}{r} \left[\frac{t}{2} + \frac{1}{4\omega_0} \sin(2\omega_0 t) \right] \right\}_0^T \\
&\quad - \frac{j \sin(k_0 r + \phi_q)}{r} \left[\frac{t}{2} - \frac{1}{4\omega_0} \sin(2\omega_0 t) \right] \Big|_0^T \\
&\quad + j k_0 \cos(k_0 r + \phi_q) \left[\frac{t}{2} - \frac{1}{4\omega_0} \sin(2\omega_0 t) \right] \Big|_0^T \\
&\quad + k_0 \sin(k_0 r + \phi_q) \left[\frac{t}{2} + \frac{1}{4\omega_0} \sin(2\omega_0 t) \right] \Big|_0^T \Big\} \\
&= \frac{f \cos \theta}{4\pi r} \left\{ \frac{T \cos(k_0 r + \phi_q)}{2r} - \frac{jT \sin(k_0 r + \phi_q)}{2r} \right. \\
&\quad \left. + \frac{j k_0 T \cos(k_0 r + \phi_q)}{2} + \frac{k_0 T \sin(k_0 r + \phi_q)}{2} \right\} \tag{C-79} \\
&= \frac{f \cos \theta}{4\pi r} \left\{ \left[\frac{T}{2r} + \frac{j k_0 T}{2} \right] \left[\cos(k_0 r + \phi_q) - j \sin(k_0 r + \phi_q) \right] \right\} \\
&= \frac{fT \cos \theta}{8\pi r^2} (1 + j k_0 r) e^{-j(k_0 r + \phi_q)}
\end{aligned}$$

The output at microphone 1 due to source m can thus be defined in Equation (C-80), by substituting Equation (C-81).

$$\begin{aligned}
{}^m U_1(\omega_0, q) &= \frac{fT \frac{\Delta h}{\sqrt{(m\Delta x)^2 + (\Delta h)^2}}}{8\pi [(m\Delta x)^2 + (\Delta h)^2]} \left[1 + jk_0 \sqrt{(m\Delta x)^2 + (\Delta h)^2} \right] e^{-j[k_0 \sqrt{(m\Delta x)^2 + (\Delta h)^2} + \phi_{mq}]} \\
&= \frac{fT \Delta h}{8\pi [(m\Delta x)^2 + (\Delta h)^2]^{\frac{3}{2}}} \left[1 + jk_0 \sqrt{(m\Delta x)^2 + (\Delta h)^2} \right] e^{-j[k_0 \sqrt{(m\Delta x)^2 + (\Delta h)^2} + \phi_{mq}]}
\end{aligned} \tag{C-80}$$

$$\cos \theta = \frac{\Delta h}{\sqrt{(m\Delta x)^2 + (\Delta h)^2}} \tag{C-81}$$

The autospectral density contribution of each source is thus given in Equation (C-82).

$$\begin{aligned}
G_{m_{u_1} m_{u_1}}(\omega_0) &= \frac{2}{T} E[{}^m U_1^* {}^m U_1] \\
&= \frac{2}{QT} \sum_{q=1}^Q \left\{ \frac{fT \Delta h \left[1 + jk_0 \sqrt{(m\Delta x)^2 + (\Delta h)^2} \right]}{8\pi [(m\Delta x)^2 + (\Delta h)^2]^{\frac{3}{2}}} e^{-j[k_0 \sqrt{(m\Delta x)^2 + (\Delta h)^2} + \phi_{mq}]} \right\}^* \\
&\quad \times \left\{ \frac{fT \Delta h \left[1 + jk_0 \sqrt{(m\Delta x)^2 + (\Delta h)^2} \right]}{8\pi [(m\Delta x)^2 + (\Delta h)^2]^{\frac{3}{2}}} e^{-j[k_0 \sqrt{(m\Delta x)^2 + (\Delta h)^2} + \phi_{mq}]} \right\} \\
&= \frac{f^2 T \Delta h^2}{32Q\pi^2 [(m\Delta x)^2 + (\Delta h)^2]^3} \\
&\quad \times \sum_{q=1}^Q \left\{ \left[1 + jk_0 \sqrt{(m\Delta x)^2 + (\Delta h)^2} \right] e^{-j[k_0 \sqrt{(m\Delta x)^2 + (\Delta h)^2} + \phi_{mq}]} \right\}^* \\
&\quad \times \left\{ \left[1 + jk_0 \sqrt{(m\Delta x)^2 + (\Delta h)^2} \right] e^{-j[k_0 \sqrt{(m\Delta x)^2 + (\Delta h)^2} + \phi_{mq}]} \right\} \\
&= \frac{f^2 T \Delta h^2 \left\{ 1 + k_0^2 [(m\Delta x)^2 + (\Delta h)^2] \right\}}{32\pi^2 [(m\Delta x)^2 + (\Delta h)^2]^3}
\end{aligned} \tag{C-82}$$

If the original, more generalized coordinate system is desired, the output at microphone i due to source m can instead be stated in Equation (C-83).

$${}^m U_i(\omega_0, q) = \frac{fT \cos({}^m \theta_i)}{8\pi ({}^m r_i)^2} [1 + jk_0 ({}^m r_i)] e^{-j[k_0 ({}^m r_i) + \phi_{mq}]} \quad (\text{C-83})$$

Here, ${}^m \theta_i$ is the angle from source m to the i th microphone, and ${}^m r_i$ is the distance from source m to the i th microphone. The corresponding autospectral density contribution is given in Equation (C-84), using the same methodology as shown in Equation (C-82).

$$G_{m u_i m u_i}(\omega_0) = \frac{f^2 T \cos^2({}^m \theta_i) [1 + k_0^2 ({}^m r_i)^2]}{32\pi^2 ({}^m r_i)^4} \quad (\text{C-84})$$

Similarly, the cross-spectral density between microphones i and j due to source m is given in Equation (C-85).

$$\begin{aligned} G_{m u_i m u_j}(\omega_0) &= \frac{2}{QT} \sum_{q=1}^Q \left\{ \frac{fT \cos({}^m \theta_i)}{8\pi ({}^m r_i)^2} [1 - jk_0 ({}^m r_i)] e^{j[k_0 ({}^m r_i) + \phi_{mq}]} \right\} \\ &\quad \times \left\{ \frac{fT \cos({}^m \theta_j)}{8\pi ({}^m r_j)^2} [1 + jk_0 ({}^m r_j)] e^{-j[k_0 ({}^m r_j) + \phi_{mq}]} \right\} \\ &= \frac{f^2 T \cos({}^m \theta_i) \cos({}^m \theta_j)}{32\pi^2 ({}^m r_i)^2 ({}^m r_j)^2} \\ &\quad \times [1 - jk_0 ({}^m r_i) + jk_0 ({}^m r_j) + k_0^2 ({}^m r_i) ({}^m r_j)] e^{j[k_0 ({}^m r_i - {}^m r_j)]} \\ &= \frac{f^2 T [\cos({}^m \theta_i - {}^m \theta_j) + \cos({}^m \theta_i + {}^m \theta_j)]}{64\pi^2 ({}^m r_i)^2 ({}^m r_j)^2} \\ &\quad \times [1 - jk_0 ({}^m r_i) + jk_0 ({}^m r_j) + k_0^2 ({}^m r_i) ({}^m r_j)] e^{j[k_0 ({}^m r_i - {}^m r_j)]} \end{aligned} \quad (\text{C-85})$$

Equation (C-84) and Equation (C-85) can be substituted into noiseless, generalized forms of Equation (C-60) and Equation (C-66) to construct the total autospectral and cross-spectral density at the i th microphone and between the i th and j th microphones, given respectively in Equation (C-86) and Equation (C-87).

$$G_{y_i y_i}(\omega_0) = \sum_{m=-M}^M G_{u_i^m u_i^m} = G_{w_i w_i} \quad (\text{C-86})$$

$$G_{y_i y_j}(\omega_0) = \sum_{m=-M}^M G_{u_i^m u_j^m} = G_{w_i w_j} \quad (\text{C-87})$$

With these formulae, identical analysis can be conducted as with the monopole sources for a constant dipole strength f of unity, with the source and microphone locations defined in Figure C-11. The resulting coherence functions are shown in Figure C-14, and look similar to the monopole behavior. The corresponding three-microphone power predictions are shown in Figure C-15. Note that the power-law based increase shown for the true autospectral densities of the microphone measurements is due to the $(k_0 r)^2$ term in the numerator of the autospectral and cross-spectral density solutions. Note that as the true autospectral density scales with the square of frequency, the bounds of the oscillatory behavior in the three-microphone prediction appear reasonably flat. A comparison of the ratio of the predicted power to the true power, shown in Figure C-16, appears similar to the monopole behavior. The roll-off follows a roughly 6 dB per octave line. The high-frequency increase in predicted power for microphone 2 is present with the dipole sources, as well.

Finally, a comparison is made between monopole simulations, dipole simulations, and real experimental data for a DU 96-W-180 airfoil at 0 degree AoA and a Reynolds number of $1e6$. The microphone locations for the DU 96 match those from Figure C-11, where the trailing edge of the airfoil is co-located with the line running through the acoustic source centers. The microphone spacing is 0.178 m. The DU-96 airfoil is oriented and installed similarly to the NACA 63-215 model shown in Figure 4-37, but the spanwise microphone array is below the model in the test section instead of above it. The real data were acquired at 65,536 samples per second using UFAFF's PXI chassis and processed with a Hanning window. The coherence

between microphones 1 and 4 is shown in Figure C-17. While the data do not overlap perfectly, the shape and behavior of the experimental data is very close to the simulated data, indicating that the mechanisms driving the experimental results could definitely be those derived in this appendix. One open question for future work from this plot is whether an inverse problem formulation can be applied to experimental data in an attempt to determine the source field's correlation length scale. Such a discussion is beyond the scope of this appendix.

Summary

Derivations of coherence-based analysis have been conducted for generalized sources in a TITO system. These derivations showed that under specific conditions, which match the idealized installation conditions for two-microphone measurements in previous work [Brooks & Hodgson 1981; Hutcheson & Brooks 2002], the coherent power methods behave as expected. These ideal installation conditions are defined such that the microphones are at a model's center span and directly above and below the model's trailing edge. Similarly, the three-microphone method is shown to, under ideal installation conditions, properly extract the coherent power field for centered microphones. Simulations for incoherent lines of sources agree with derivations.

However, when microphones are no longer ideally centered or equally-spaced with respect to source fields, it appears cancellation effects in cross-spectral density source summations force coherent power methods, both two- and three-microphone, to dramatically underpredict true coherent field levels. This cancellation structure is observed in both simulated and experimental data. Such results make even measurements conducted with ideal installation conditions suspect, as while the installation locations are ideal with respect to the airfoil trailing edge noise source, they are not ideal with respect to other background noise sources. Cancellation effects may be present when the facility background noise is similar to or greater than trailing edge noise in level, leading to unreliable power estimates from coherence-based techniques for distributed

source regions. The structure of this coherence breakdown is observed to be highly dependent on both the source and observer locations, and may be related to compactness conditions where the acoustic wavenumber k is small with respect to the measurement dimensions. This compactness condition would induce an effective upper frequency limit on coherence-based measurement techniques.

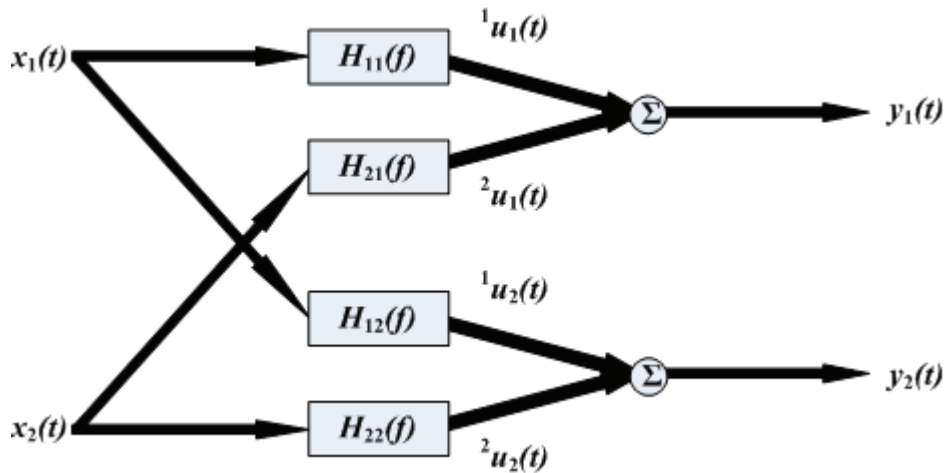


Figure C-1. Schematic of Two-Input/Two-Output system with no additive noise.

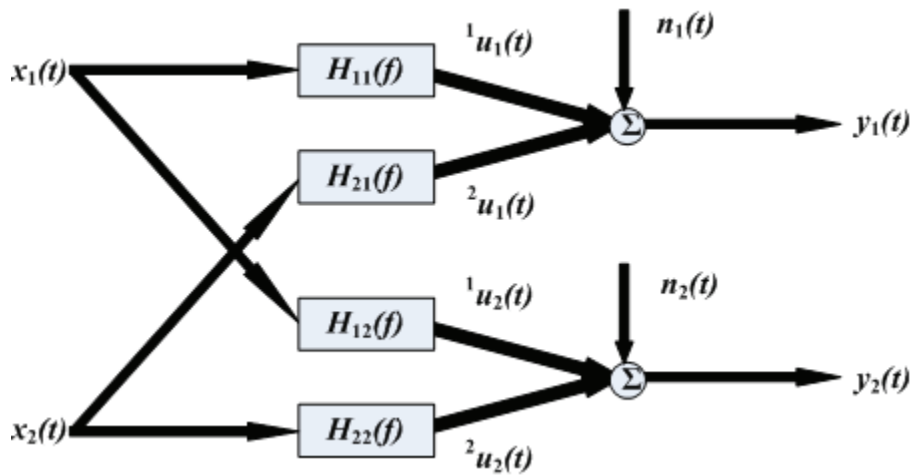


Figure C-2. Schematic of Two-Input/Two-Output system with incoherent measurement noise.

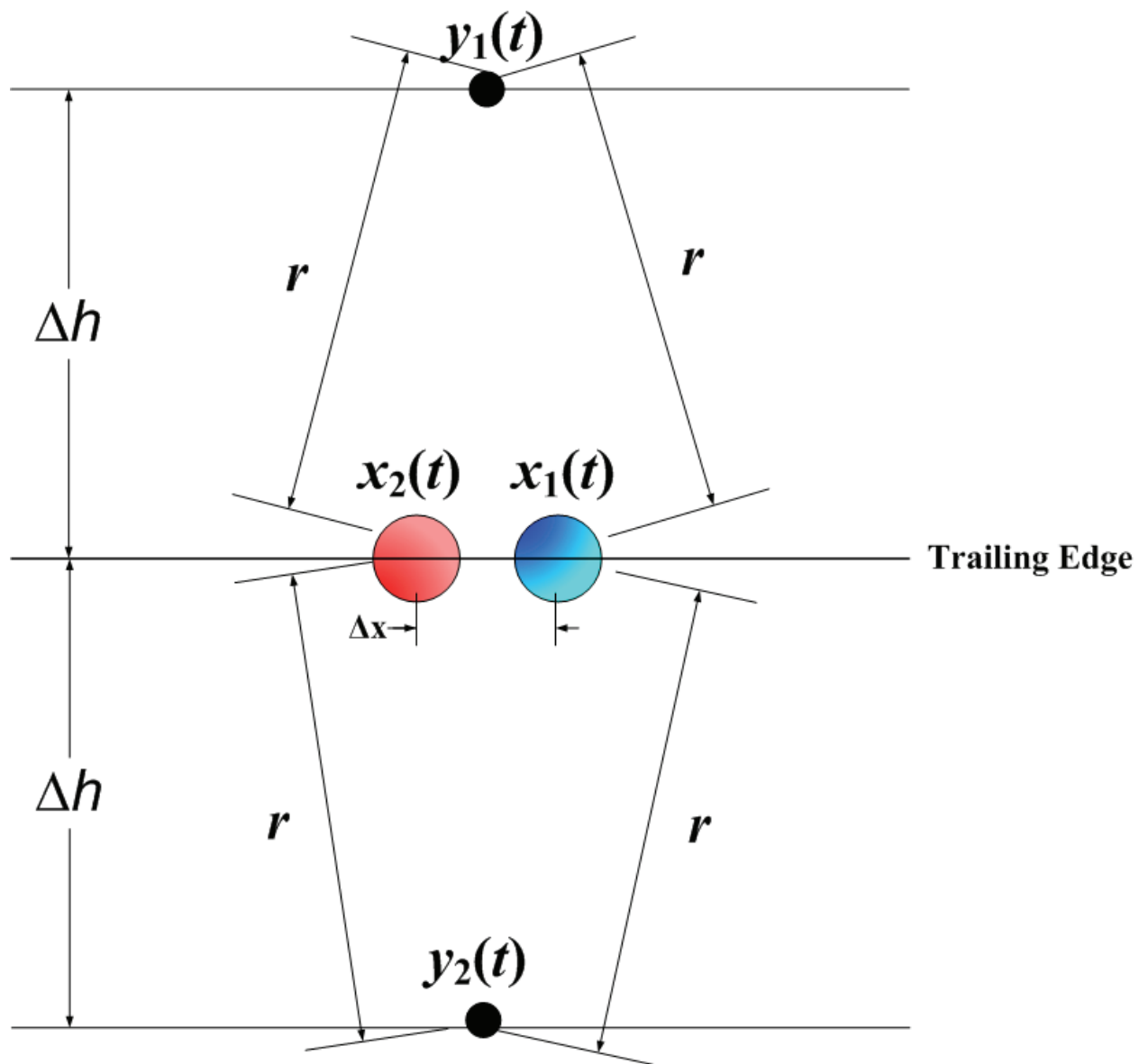


Figure C-3. TITO situation where, for monopole sources, all phase angle differences cancel.

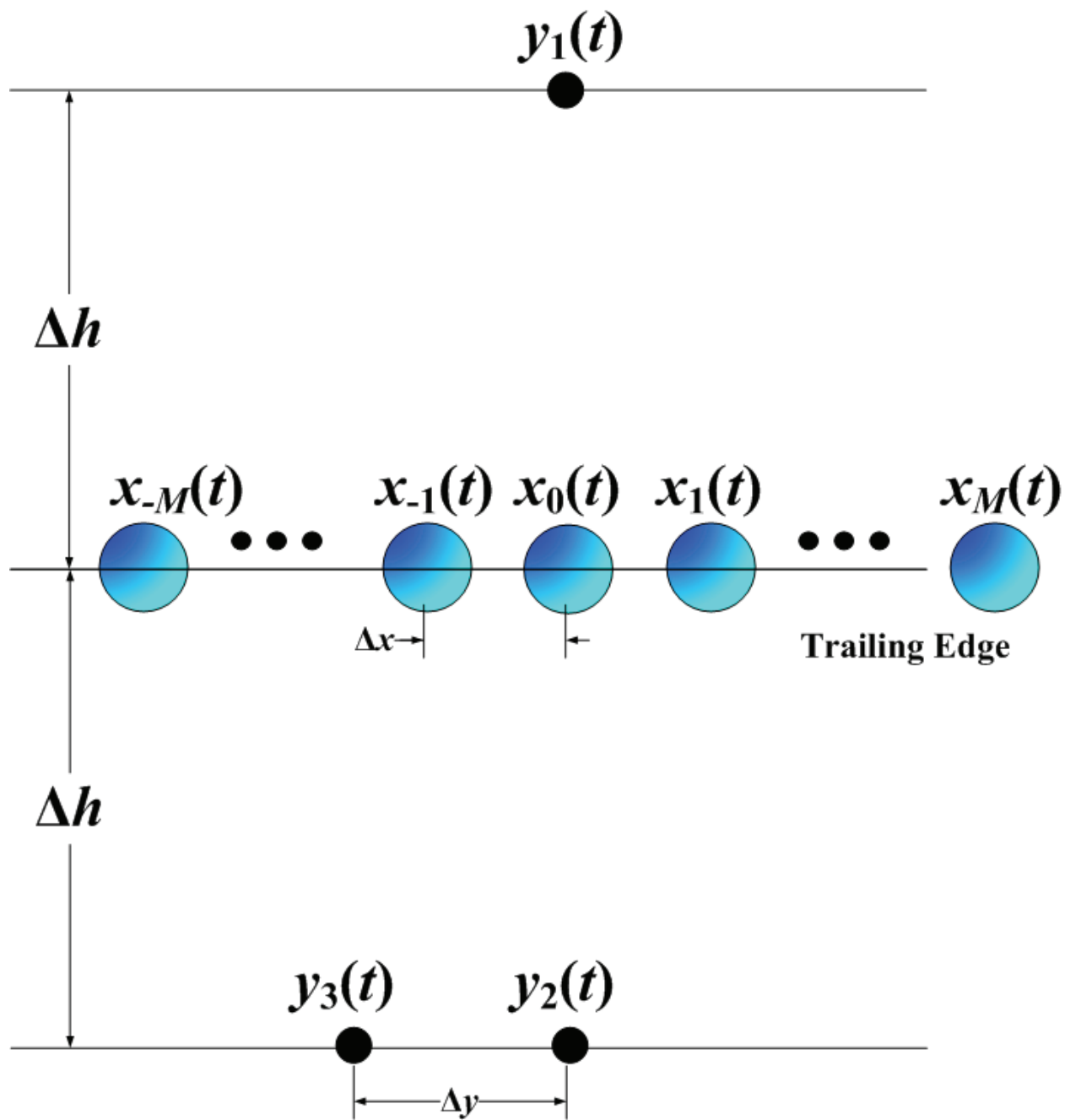


Figure C-4. Three-observer MIMO system modeling a trailing edge of incoherent sources. Here, the third observer is offset spanwise along the simulated trailing edge.

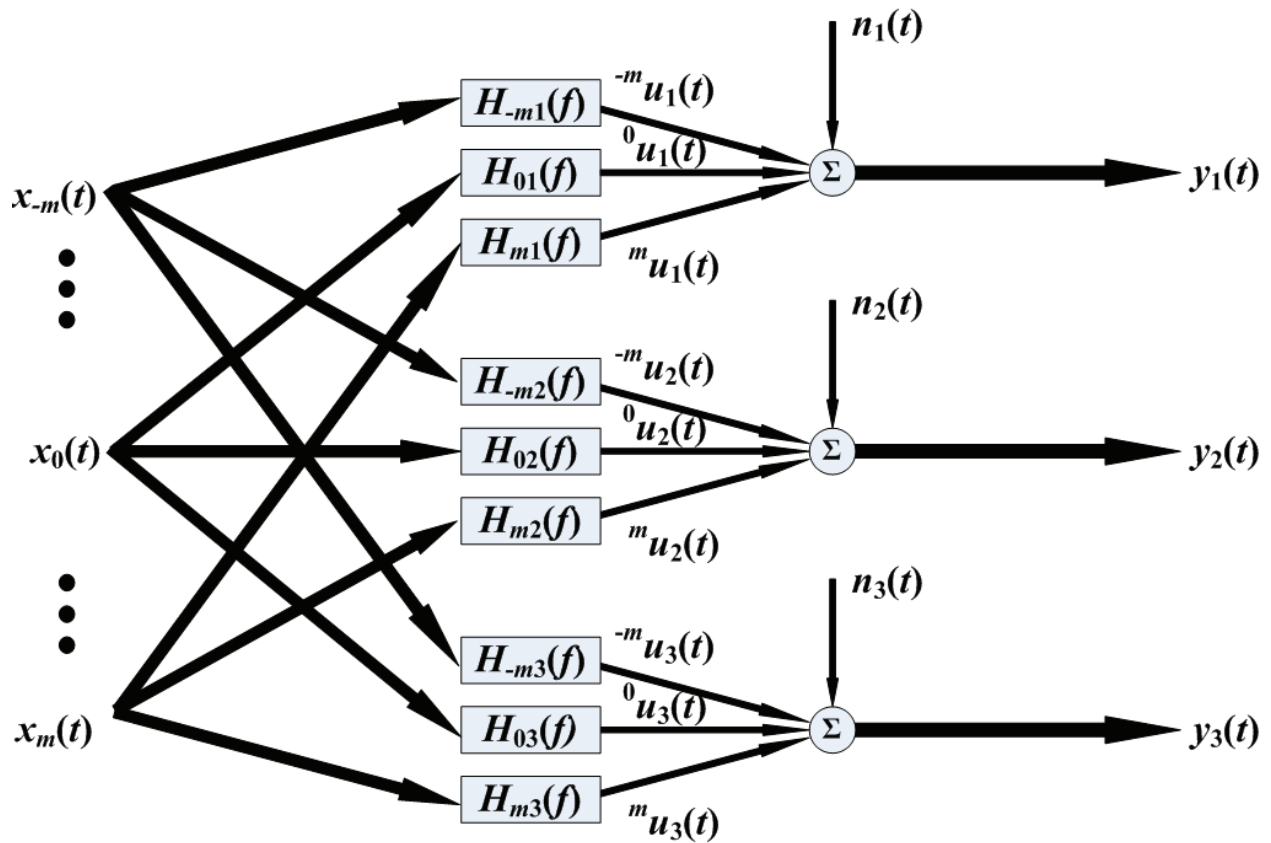


Figure C-5. Three-observer MIMO block diagram for the analysis of the system shown in Figure C-4.

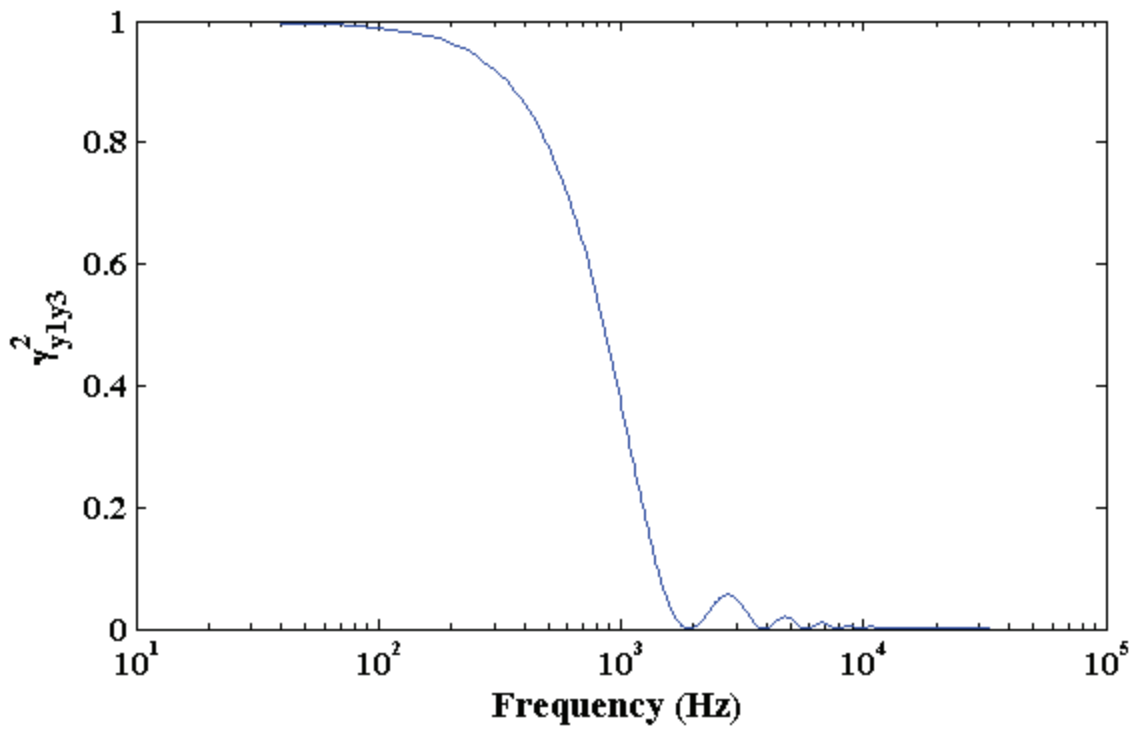


Figure C-6. Coherence between microphones 1 and 3 based on the schematic in Figure C-4.

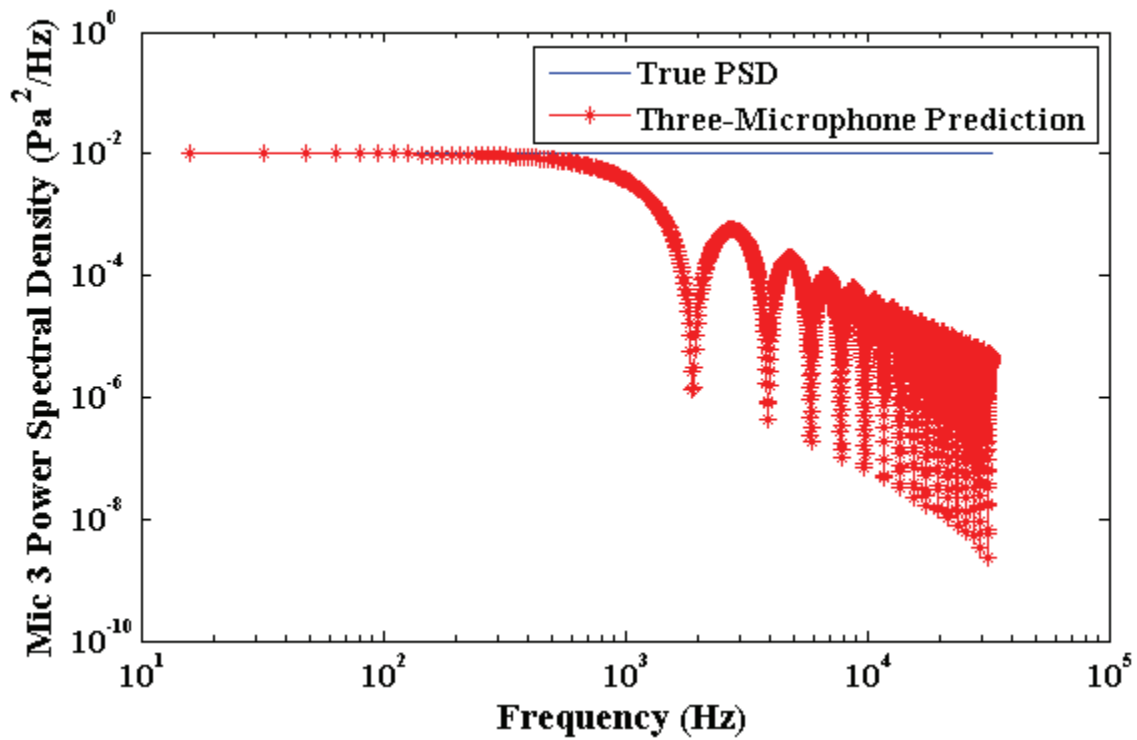


Figure C-7. Three-microphone prediction for microphone 3 from Figure C-4.

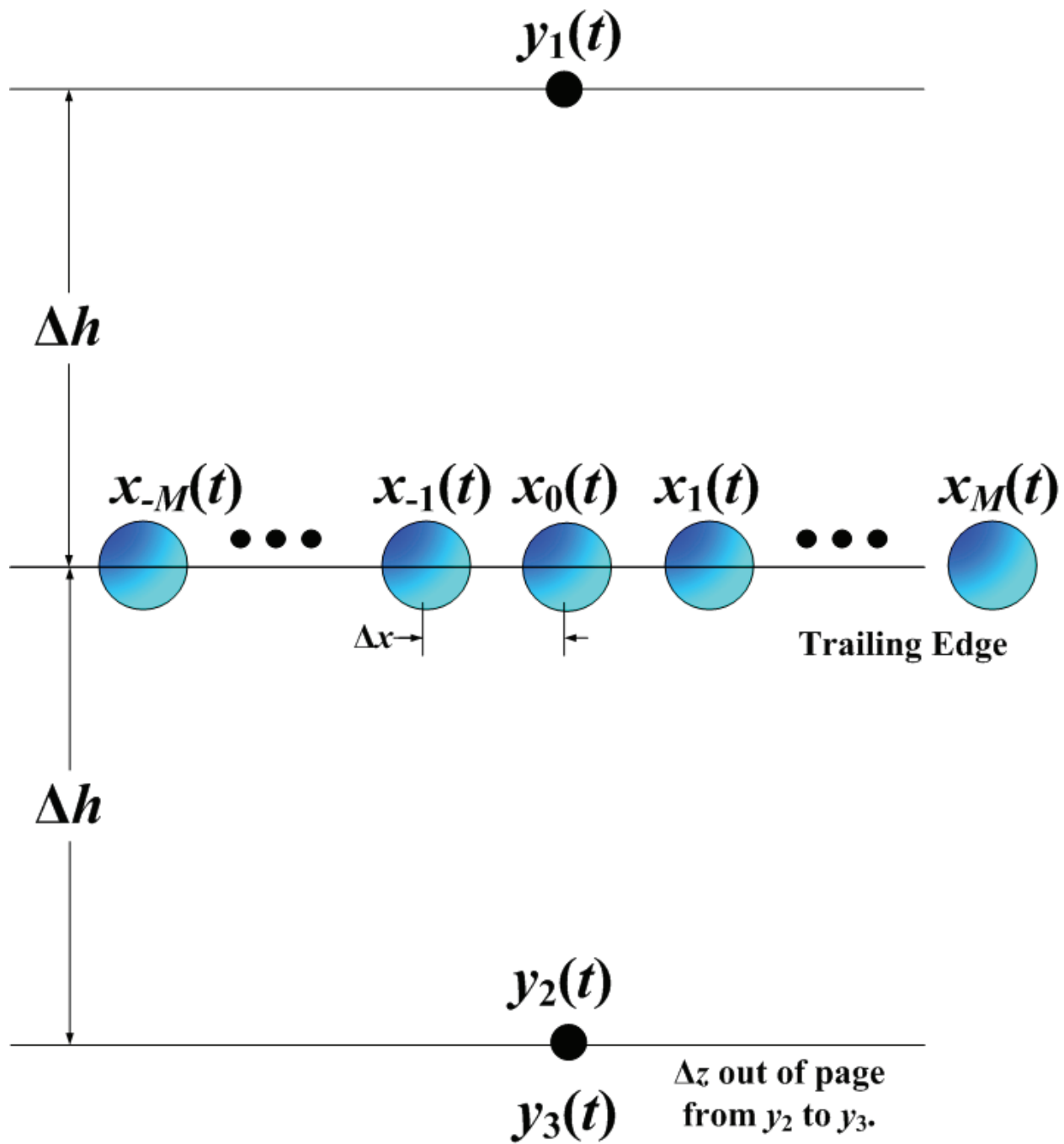


Figure C-8. Three-observer MIMO system modeling a trailing edge of incoherent sources. Here, the third observer is offset depth-wise into the page.

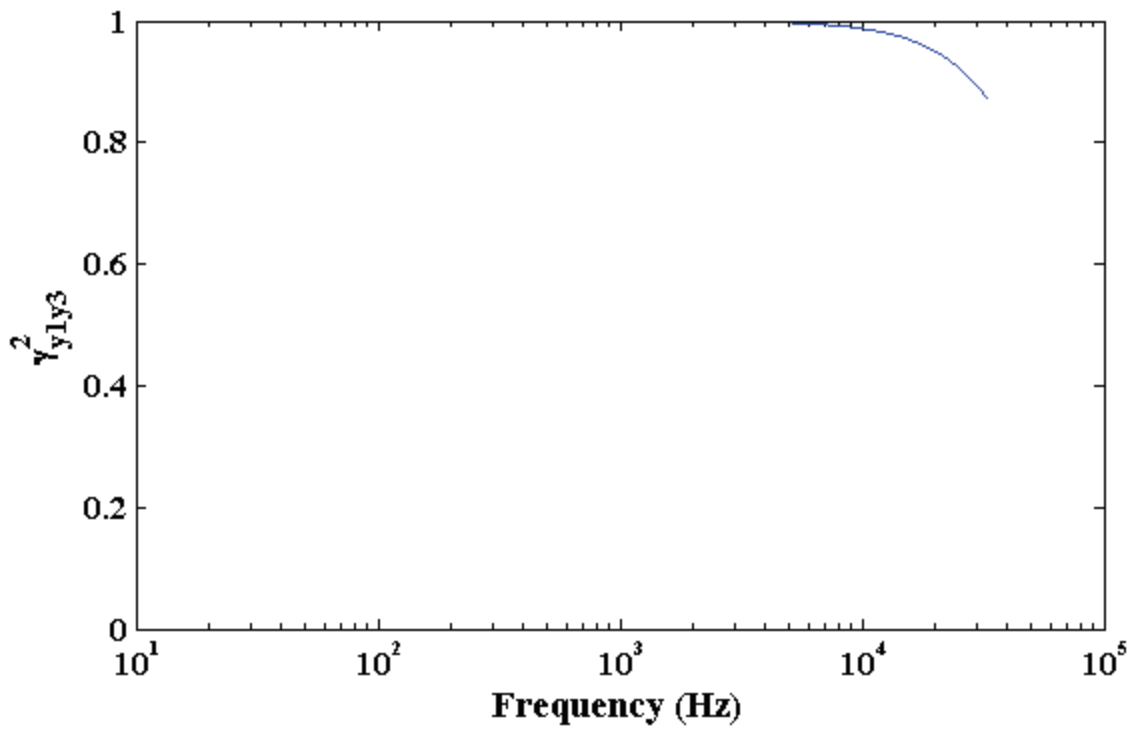


Figure C-9. Coherence between microphones 1 and 3 based the schematic in Figure C-8.

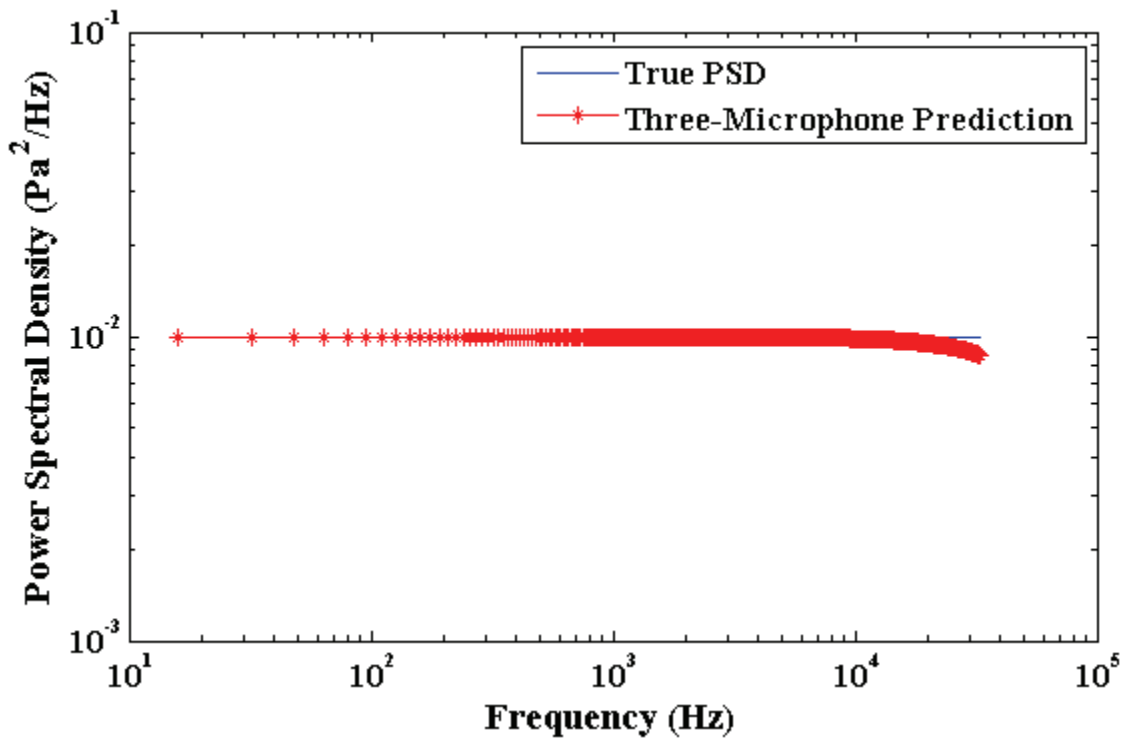


Figure C-10. Three-microphone prediction for microphone 3 from Figure C-8.

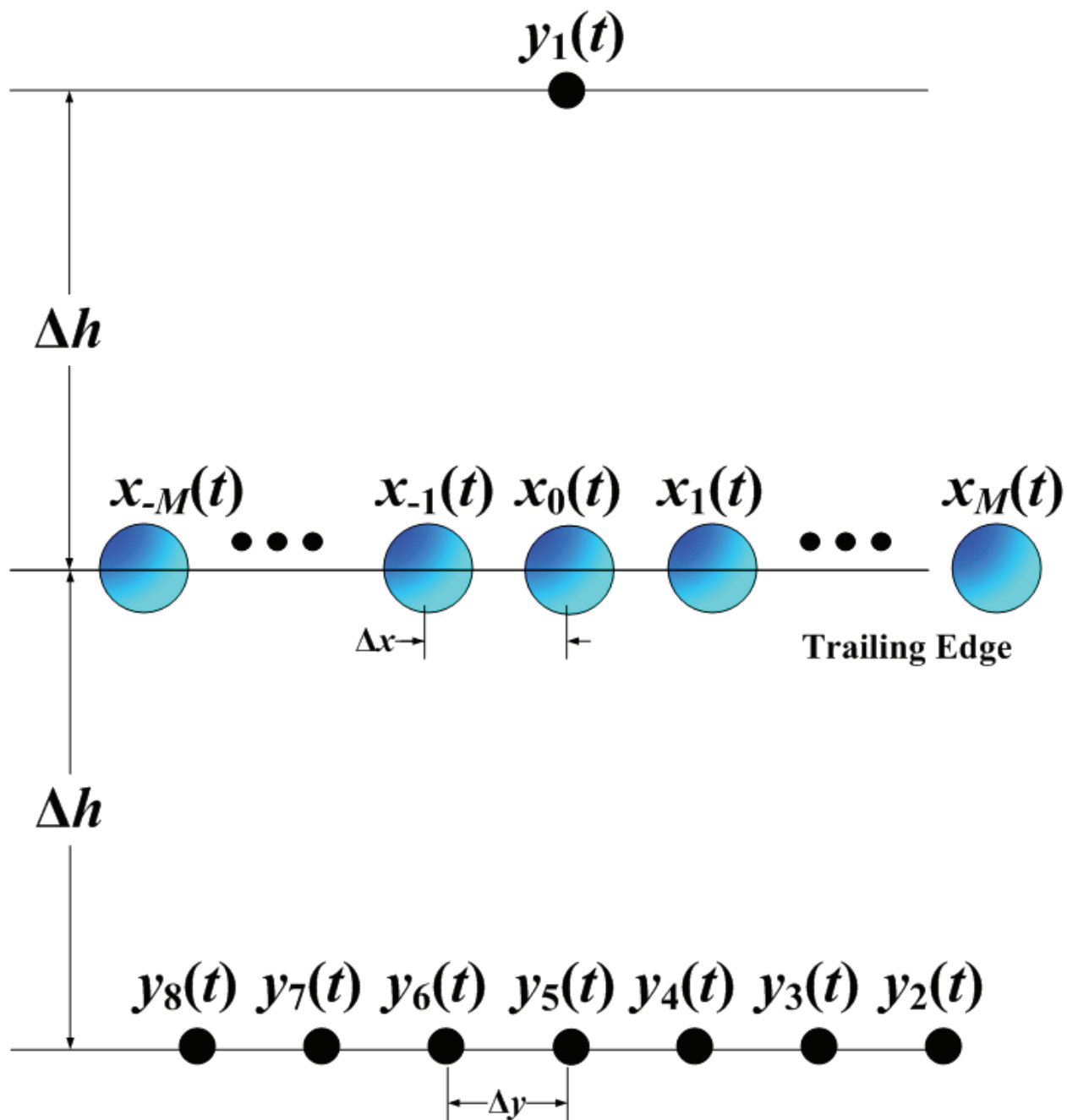


Figure C-11. Eight-observer MIMO system modeling a trailing edge of incoherent sources. Here, the lower observers are offset spanwise along the simulated trailing edge from the central, fifth observer.

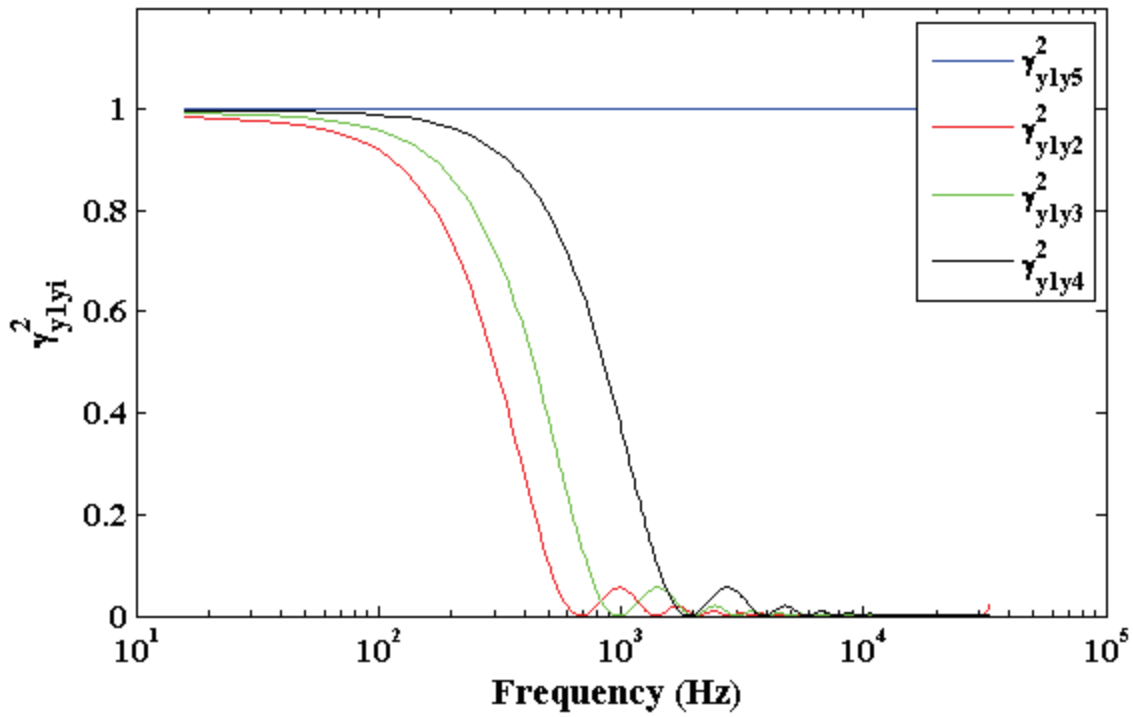


Figure C-12. Coherence function for spanwise microphones based on schematic in Figure C-11.

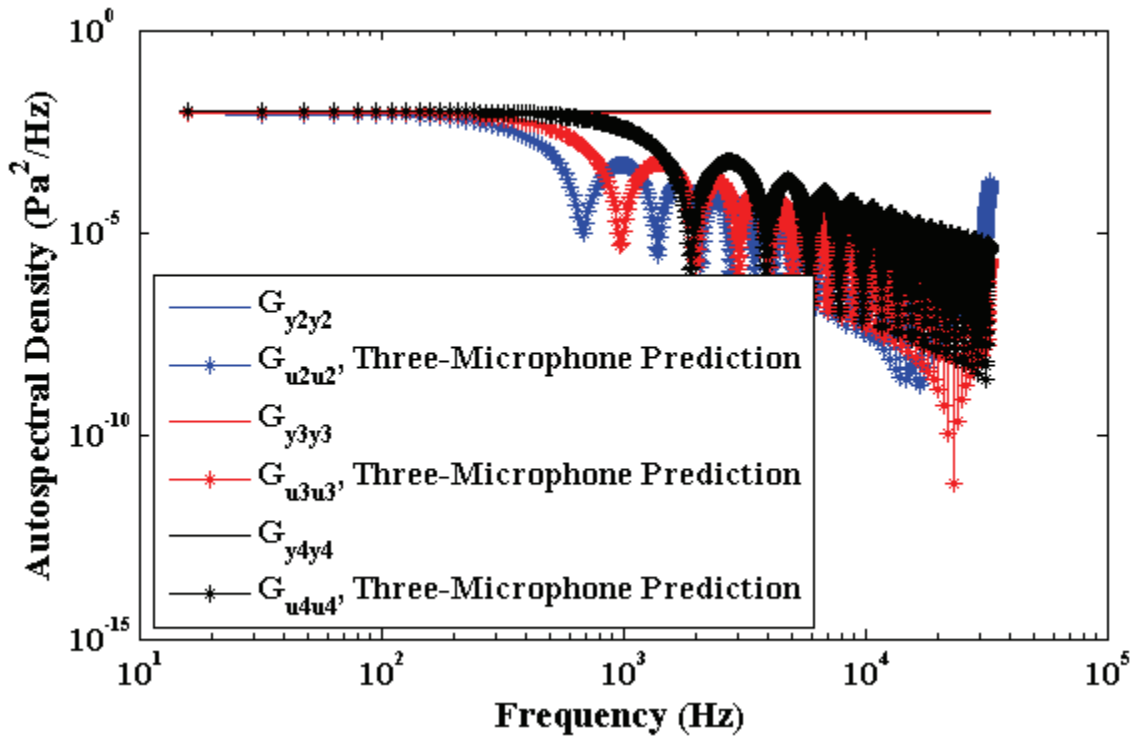


Figure C-13. Three-microphone predictions for microphones 2 through 4 in Figure C-11.

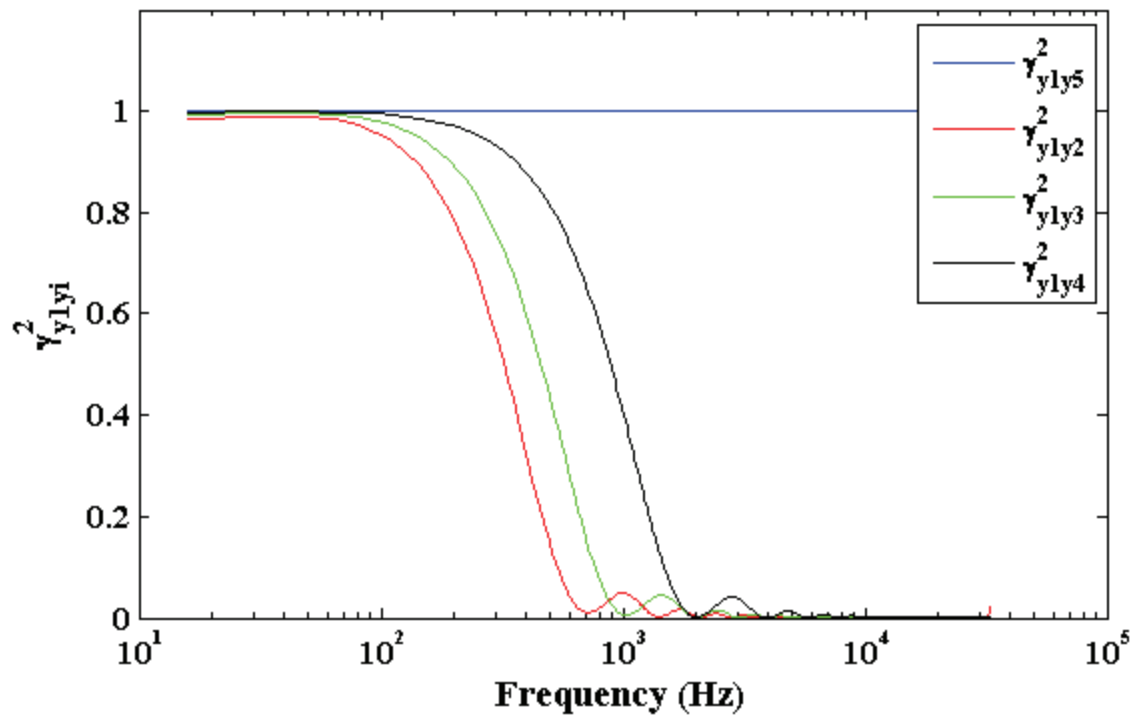


Figure C-14. Coherence for spanwise microphones, dipole sources located in Figure C-11.

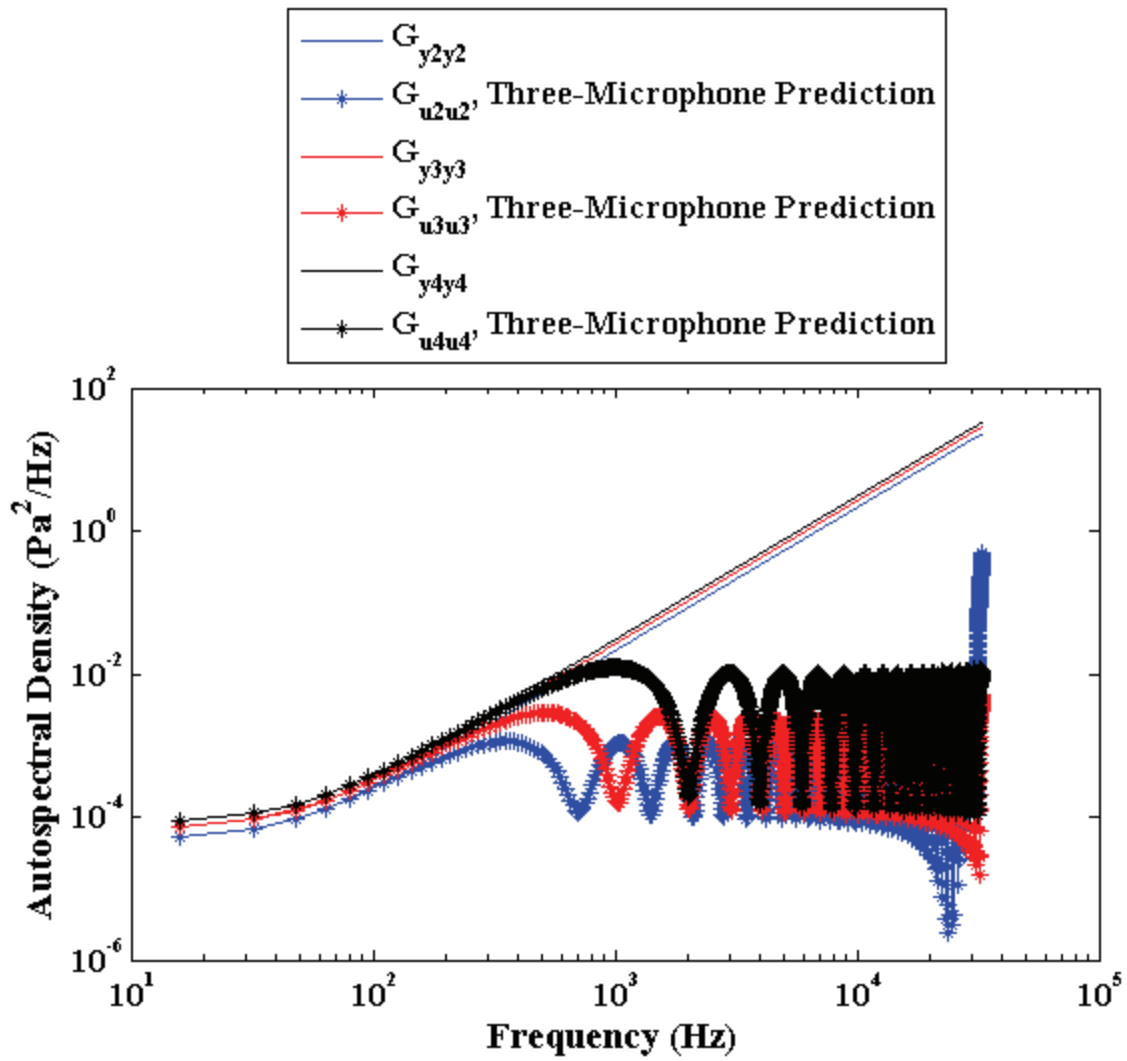


Figure C-15. Three-microphone solution, microphones 2 through 4 in Figure C-11 for dipoles.

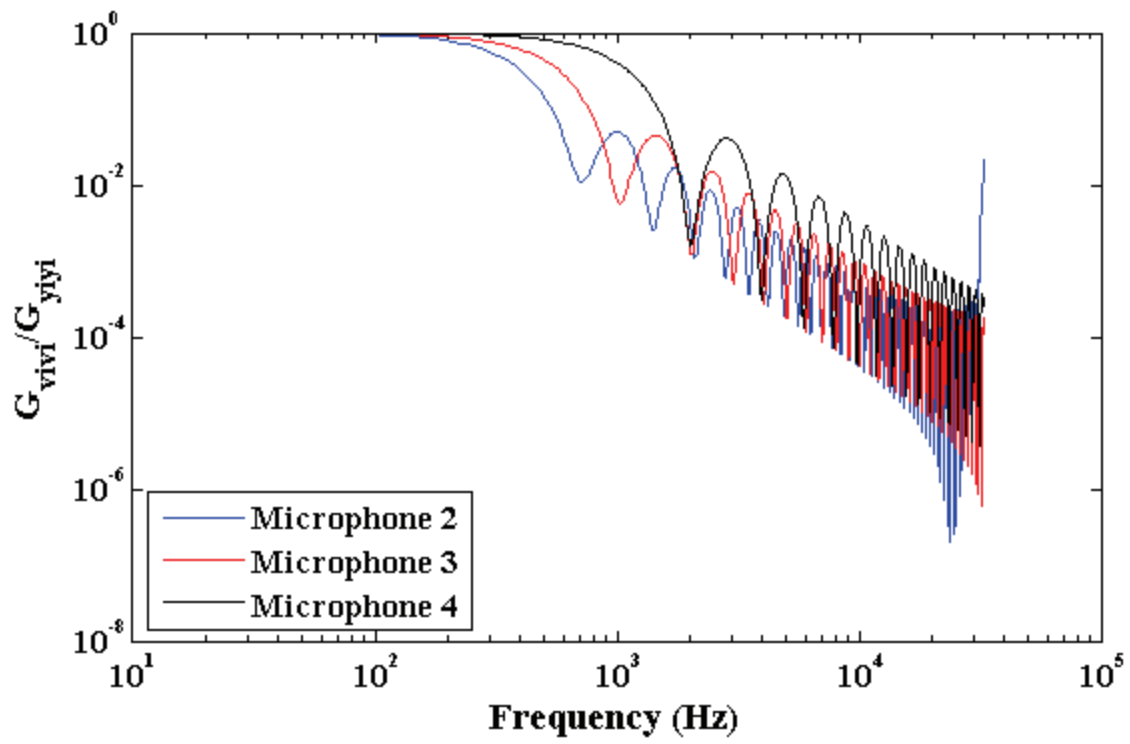


Figure C-16. Ratio of predicted power to true power for microphones in Figure C-11 for dipoles.

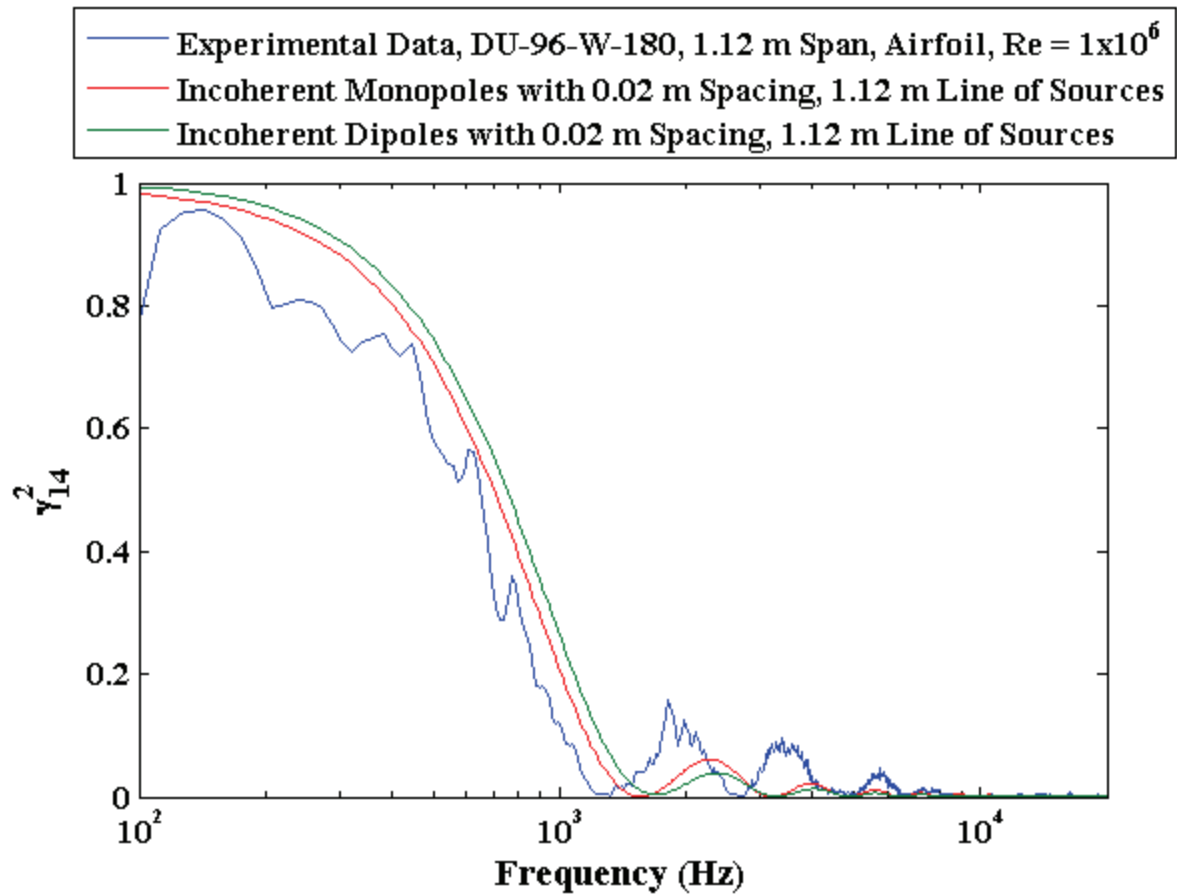


Figure C-17. Comparison of experimental coherence with simulated source coherence between microphones 1 and 4 from Figure C-11.

APPENDIX D ARRAY CALIBRATION IN THE PRESENCE OF ECHOES

In the use of aeroacoustic arrays, array calibration is a necessity if one desires to extract quantified information from beam maps. This calibration may compensate for steering vector errors due to positional uncertainty of the microphones, and it may substitute for individual magnitude and phase calibration of each array microphone when an appropriate reference microphone is provided [Dougherty 2002]. However, all microphones in the array are required to see the same calibration signal. If they see an additional source which is incoherent with the calibration signal, the beamforming algorithms may still correct the phase angles of the steering vectors, but the magnitude of the reference microphone will be in error. If the additional sources are coherent, e.g. from reflections of the calibration signal, the magnitude and phase calibrations will be in error. Due to the difficulty of in-situ, reflection-free calibration in some aeroacoustic facilities, an analysis technique which allows for the detection and filtering of these contaminating signals would be helpful, at least for post-processing calibration data which are found to be in error, when re-running calibration experiments is infeasible or impossible.

Ideal Case Problem Statement

For initial discussion, an array will be treated as a simple two-microphone measurement, rather than a large channel count multi-arm logarithmic spiral array, as addressed later. In an ideal case, these two microphones are at known locations from a monopole source, in an environment with a precisely-measured speed of sound. The first microphone is treated as a reference microphone with an ideal response. The second microphone has an unknown response function. The objective of this idealized experiment is to determine the second microphone's frequency response function. A schematic of this experiment is shown in Figure D-1. A block diagram of the signal path is shown in Figure D-2, where $x(t)$ is the ideal source output, $H_1(f)$

and $H_2(f)$ are the ideal propagation frequency response functions as subsequently defined, $H_m(f)$ is the unknown microphone response, and $y_1(t)$ and $y_2(t)$ are the final measured signals from microphones 1 and 2. Once the second microphone's response function is known, data collected could be corrected by dividing by the response function's magnitude, and subtracting its phase shift.

Ideal Case Analysis

Assuming ideal far-field monopole behavior, the observed ideal acoustic pressure field can be defined in Equation (D-1) [Blackstock 2000], a generalized version of that defined in Equation (C-45).

$$p(r, t) = \frac{x\left(t - r/c_0\right)}{4\pi r} \quad (\text{D-1})$$

As in prior analysis, c_0 is the isentropic speed of sound. The equivalent frequency-domain expression for a harmonic source is adapted from Equation (C-48) in Equation (D-2).

$$P(r, f) = \frac{X(f)e^{-jkr}}{4\pi r} \quad (\text{D-2})$$

The wavenumber k is defined in Equation (2-13). The pressure field at each microphone can thus be formulated in Equation (D-3) and Equation (D-4).

$$Y_1(f) = \frac{X(f)e^{-jkr_1}}{4\pi r_1} \quad (\text{D-3})$$

$$Y_2(f) = \frac{H_m(f)X(f)e^{-jkr_2}}{4\pi r_2} \quad (\text{D-4})$$

Although the measurement is noiseless and so a direct calculation would work, formulation for an optimal Wiener filter is still used for consistency in discussion. All power spectral

densities are given as two-sided, as subsequent spectral analysis and modification are computed on two-sided functions. However, the factor of two in the denominator due to the two-sided nature of Fourier transforms of sines and cosines is omitted.

For ideal functions, the auto- and cross-spectral densities can be expressed in Equation (D-5) through Equation (D-8).

$$S_{xx}(f) = \frac{1}{T} X^* X \quad (D-5)$$

$$S_{y_1 y_1}(f) = \frac{1}{T} Y_1^* Y_1 = \frac{X^* X e^{jkr_1} e^{-jkr_1}}{T(4\pi r_1)^2} = \frac{S_{xx}}{16\pi^2 r_1^2} \quad (D-6)$$

$$S_{y_2 y_2}(f) = \frac{1}{T} Y_2^* Y_2 = \frac{H_m^* H_m X^* X e^{jkr_2} e^{-jkr_2}}{T(4\pi r_2)^2} = \frac{|H_m|^2 S_{xx}}{16\pi^2 r_2^2} \quad (D-7)$$

$$S_{y_1 y_2}(f) = \frac{1}{T} Y_1^* Y_2 = \frac{H_m X^* X e^{jkr_1} e^{-jkr_2}}{T(4\pi r_1)(4\pi r_2)} = \frac{H_m S_{xx} e^{jk(r_1-r_2)}}{16\pi^2 r_1 r_2} \quad (D-8)$$

The relationship between the two microphone signals can be leveraged to calculate the frequency response function of microphone 2, as shown in Equation (D-9) and Equation (D-10).

$$\begin{aligned} H_{y_1 y_2}(f) &= \frac{S_{y_1 y_2}}{S_{y_1 y_1}} = \frac{H_m \cancel{S_{xx}} e^{jk(r_1-r_2)}}{16\pi^2 \cancel{r_1} r_2} \times \frac{\cancel{16\pi^2} r_1^2}{\cancel{S_{xx}}} \\ &= H_m \frac{r_1}{r_2} e^{jk(r_1-r_2)} \end{aligned} \quad (D-9)$$

$$H_m(f) = H_{y_1 y_2} \frac{r_2}{r_1} e^{jk(r_2-r_1)} \quad (D-10)$$

Single Ideal Reflection

Figure D-3 and Figure D-4 schematically show the effect of adding an ideal reflective surface to the calibration experiment. The autocorrelation of microphone 1 will be computed and transformed into its autospectral density to demonstrate the effect of adding a reflection to a

general signal. Then, assuming broadband, time-harmonic monopole behavior, the remaining power spectral densities will be computed.

The signal at microphone 1 can now be expressed as the sum of the two signals, where the ideal reflecting surface is treated as creating an image source of the monopole, such that the reflected wave is treated as travelling a total distance (and undergoing spherical spreading) of r_{21} . This is given in Equation (D-11).

$$y_1(t) = \frac{x\left(t - r_{11}/c_0\right)}{4\pi r_{11}} + \frac{x\left(t - r_{21}/c_0\right)}{4\pi r_{21}} \quad (\text{D-11})$$

The autocorrelation of a stationary signal is defined in Equation (D-12) [Bendat & Piersol 2000].

$$R_{xx}(\tau) = \lim_{T \rightarrow \infty} \frac{1}{T} \int_0^T x(t)x(t+\tau) dt = E[x(t)x(t+\tau)] \quad (\text{D-12})$$

Here, the expected value operator occurs as a time average of the product of the delayed signal to the baseline signal. The autocorrelation of the first microphone is computed in Equation (D-13).

$$R_{y_1 y_1}(\tau) = E \left\{ \left[\frac{x\left(t - r_{11}/c_0\right)}{4\pi r_{11}} + \frac{x\left(t - r_{21}/c_0\right)}{4\pi r_{21}} \right] \left[\frac{x\left(t - r_{11}/c_0 + \tau\right)}{4\pi r_{11}} + \frac{x\left(t - r_{21}/c_0 + \tau\right)}{4\pi r_{21}} \right] \right\} \quad (\text{D-13})$$

Assuming a sufficiently long record, a change of variables can be applied, defining $t' = t - r_{11}/c_0$.

$$\begin{aligned}
R_{y_1 y_1}(\tau) &= E \left\{ \left[\frac{x(t')}{4\pi r_{11}} + \frac{x\left(t' - \frac{r_{21} - r_{11}}{c_0}\right)}{4\pi r_{21}} \right] \left[\frac{x(t'+\tau)}{4\pi r_{11}} + \frac{x\left(t' - \frac{r_{21} - r_{11}}{c_0} + \tau\right)}{4\pi r_{21}} \right] \right\} \\
&= E \left[\frac{x(t')x(t'+\tau)}{16\pi^2 r_{11}^2} \right] + E \left[\frac{x(t')x\left(t' - \frac{r_{21} - r_{11}}{c_0} + \tau\right)}{16\pi^2 r_{11} r_{21}} \right] + \\
&\quad E \left[\frac{x\left(t' - \frac{r_{21} - r_{11}}{c_0}\right)x(t'+\tau)}{16\pi^2 r_{21} r_{11}} \right] + E \left[\frac{x\left(t' - \frac{r_{21} - r_{11}}{c_0}\right)x\left(t' - \frac{r_{21} - r_{11}}{c_0} + \tau\right)}{16\pi^2 r_{21}^2} \right]
\end{aligned} \tag{D-14}$$

Again applying a change of variables within individual expected value operations and solving, the final form of the autocorrelation is constructed in Equation (D-15).

$$R_{y_1 y_1}(\tau) = \frac{1}{16\pi^2} \left\{ \left(\frac{1}{r_{11}^2} + \frac{1}{r_{21}^2} \right) R_{xx}(\tau) + \frac{1}{r_{11} r_{21}} \left[R_{xx}\left(\tau + \frac{r_{21} - r_{11}}{c_0}\right) + R_{xx}\left(\tau - \frac{r_{21} - r_{11}}{c_0}\right) \right] \right\} \tag{D-15}$$

The autospectral density of a signal is the Fourier transform of its autocorrelation, shown in Equation (D-16) [Bendat & Piersol 2000].

$$S_{xx}(f) = \int_{-\infty}^{\infty} R_{xx}(\tau) e^{-j2\pi f\tau} d\tau \tag{D-16}$$

Using this identity, the autospectral density of the first microphone is constructed in Equation (D-17).

$$\begin{aligned}
S_{y_1 y_1}(f) &= \frac{1}{16\pi^2} \left\{ \left(\frac{1}{r_{11}^2} + \frac{1}{r_{21}^2} \right) \int_{-\infty}^{\infty} R_{xx}(\tau) e^{-j2\pi f\tau} d\tau + \right. \\
&\quad \left. \frac{1}{r_{11} r_{21}} \left[\int_{-\infty}^{\infty} R_{xx}\left(\tau + \frac{r_{21} - r_{11}}{c_0}\right) e^{-j2\pi f\tau} d\tau + \int_{-\infty}^{\infty} R_{xx}\left(\tau - \frac{r_{21} - r_{11}}{c_0}\right) e^{-j2\pi f\tau} d\tau \right] \right\}
\end{aligned} \tag{D-17}$$

The integration variable in the second and third terms can be changed, giving Equation (D-18).

$$\begin{aligned}
S_{y_1 y_1}(f) &= \frac{1}{16\pi^2} \left\{ \left(\frac{1}{r_{11}^2} + \frac{1}{r_{21}^2} \right) \int_{-\infty}^{\infty} R_{xx}(\tau) e^{-j2\pi f \tau} d\tau + \right. \\
&\quad \left. \frac{1}{r_{11} r_{21}} \left[\int_{-\infty}^{\infty} R_{xx}(\tau') e^{-j2\pi f \left(\tau' - \frac{r_{21} - r_{11}}{c_0} \right)} d\tau' + \int_{-\infty}^{\infty} R_{xx}(\tau'') e^{-j2\pi f \left(\tau'' + \frac{r_{21} - r_{11}}{c_0} \right)} d\tau'' \right] \right\} \\
&= \frac{1}{16\pi^2} \left\{ \left(\frac{1}{r_{11}^2} + \frac{1}{r_{21}^2} \right) S_{xx}(f) + \frac{1}{r_{11} r_{21}} \left[e^{j2\pi f \frac{r_{21} - r_{11}}{c_0}} + e^{-j2\pi f \frac{r_{21} - r_{11}}{c_0}} \right] S_{xx}(f) \right\} \\
&= \frac{1}{16\pi^2} \left[\frac{1}{r_{11}^2} + \frac{1}{r_{21}^2} + \frac{2}{r_{11} r_{21}} \cos \left(2\pi f \frac{r_{21} - r_{11}}{c_0} \right) \right] S_{xx}(f)
\end{aligned} \tag{D-18}$$

In addition to the magnitude offset from the reflection, the autospectral density shows an oscillatory behavior in the magnitude response with a period dependent on the speed of sound and difference in ray lengths, regardless of the nature of the stationary waveform. If a harmonic source waveform is assumed, this can also be shown through frequency-domain construction of the power spectral densities in Equation (D-19) through Equation (D-22).

$$Y_1(f) = \left[\frac{e^{-jkr_{11}}}{4\pi r_{11}} + \frac{e^{-jkr_{21}}}{4\pi r_{21}} \right] X(f) \tag{D-19}$$

$$Y_2(f) = H_m(f) \left[\frac{e^{-jkr_{12}}}{4\pi r_{12}} + \frac{e^{-jkr_{22}}}{4\pi r_{22}} \right] X(f) \tag{D-20}$$

$$\begin{aligned}
S_{y_2 y_2}(f) &= \frac{1}{T} Y_2^* Y_2 = |H_m|^2 \left[\left(\frac{e^{jkr_{12}}}{4\pi r_{12}} + \frac{e^{jkr_{22}}}{4\pi r_{22}} \right) \left(\frac{e^{-jkr_{12}}}{4\pi r_{12}} + \frac{e^{-jkr_{22}}}{4\pi r_{22}} \right) \right] S_{xx} \\
&= \frac{|H_m|^2}{16\pi^2} \left[\frac{1}{r_{12}^2} + \frac{1}{r_{22}^2} + \frac{2}{r_{12} r_{22}} \cos(kr_{22} - kr_{12}) \right] S_{xx}
\end{aligned} \tag{D-21}$$

$$\begin{aligned}
S_{y_1 y_2}(f) &= \frac{1}{T} Y_1^* Y_2 = \frac{H_m}{16\pi^2} \left[\left(\frac{e^{jkr_{11}}}{r_{11}} + \frac{e^{jkr_{21}}}{r_{21}} \right) \left(\frac{e^{-jkr_{12}}}{r_{12}} + \frac{e^{-jkr_{22}}}{r_{22}} \right) \right] S_{xx} \\
&= \frac{H_m}{16\pi^2} \left(\frac{e^{jk(r_{11} - r_{12})}}{r_{11} r_{12}} + \frac{e^{jk(r_{11} - r_{22})}}{r_{11} r_{22}} + \frac{e^{jk(r_{21} - r_{12})}}{r_{21} r_{12}} + \frac{e^{jk(r_{21} - r_{22})}}{r_{21} r_{22}} \right) S_{xx}
\end{aligned} \tag{D-22}$$

As shown, autospectra and cross-spectra are contaminated by real and complex oscillatory behavior, dependent on lag times. While r_{11} and r_{12} (the direct path lengths) are well known for this calibration problem, the reflected path lengths may not be. Equation (D-23) and Equation (D-24) show the results of attempting to solve for the second microphone's response function.

$$H_{y_1 y_2}(f) = \frac{S_{y_1 y_2}}{S_{y_1 y_1}} = \frac{H_m \left[\frac{e^{jk(r_{11}-r_{12})}}{r_{11}r_{12}} + \frac{e^{jk(r_{11}-r_{22})}}{r_{11}r_{22}} + \frac{e^{jk(r_{21}-r_{12})}}{r_{21}r_{12}} + \frac{e^{jk(r_{21}-r_{22})}}{r_{21}r_{22}} \right]}{\left[\frac{1}{r_{11}^2} + \frac{1}{r_{21}^2} + \frac{2}{r_{11}r_{21}} \cos(kr_{21} - kr_{11}) \right]} \quad (\text{D-23})$$

$$H_m(f) = H_{y_1 y_2} \frac{\left[\frac{1}{r_{11}^2} + \frac{1}{r_{21}^2} + \frac{2}{r_{11}r_{21}} \cos(kr_{21} - kr_{11}) \right]}{\left[\frac{e^{jk(r_{11}-r_{12})}}{r_{11}r_{12}} + \frac{e^{jk(r_{11}-r_{22})}}{r_{11}r_{22}} + \frac{e^{jk(r_{21}-r_{12})}}{r_{21}r_{12}} + \frac{e^{jk(r_{21}-r_{22})}}{r_{21}r_{22}} \right]} \quad (\text{D-24})$$

Without the reflected path lengths, the microphone response cannot be determined, as the reflection adds terms to both the magnitude and phase of the computed frequency response function. Attempting to solve for the microphone response using the known direct distances will yield the erroneous estimate of the response in Equation (D-25).

$$\begin{aligned} \widehat{H}_m(f) &= H_{y_1 y_2} \frac{r_{12}}{r_{11}} e^{jk(r_{12}-r_{11})} \\ &= \frac{H_m \left[\frac{e^{jk(r_{11}-r_{12})}}{r_{11}r_{12}} + \frac{e^{jk(r_{11}-r_{22})}}{r_{11}r_{22}} + \frac{e^{jk(r_{21}-r_{12})}}{r_{21}r_{12}} + \frac{e^{jk(r_{21}-r_{22})}}{r_{21}r_{22}} \right]}{\left[\frac{1}{r_{11}^2} + \frac{1}{r_{21}^2} + \frac{2}{r_{11}r_{21}} \cos(kr_{21} - kr_{11}) \right]} \frac{r_{12}}{r_{11}} e^{jk(r_{12}-r_{11})} \\ &= H_m \frac{\left[1 + \frac{r_{12}e^{jk(r_{12}-r_{22})}}{r_{22}} + \frac{r_{11}e^{jk(r_{21}-r_{11})}}{r_{21}} + \frac{r_{11}r_{12}e^{jk(r_{12}-r_{11})}e^{jk(r_{21}-r_{22})}}{r_{21}r_{22}} \right]}{\left[1 + \frac{r_{11}^2}{r_{21}^2} + 2\frac{r_{11}}{r_{21}} \cos(kr_{21} - kr_{11}) \right]} \end{aligned} \quad (\text{D-25})$$

Analysis Options

Filtering in the frequency domain cannot solve this problem, as the contaminating terms occupy the same bandwidth as the function of interest. One potential option is to window the autocorrelation function and cross-correlation function, as the reflections occur at different time delays from the original function occurrence. If the original function is approximately white noise, its autocorrelation is a delta function, so correlation windowing should be straightforward. However, in many situations the signal is band-limited, so the autocorrelation has a finite duration. If this duration overlaps the time delay of the reflection, the reflection cannot be windowed without significantly altering the baseline function's correlation functions, and subsequently its spectral density functions. One option is to inverse transform the computed frequency response, edit the reflections out of it, and forward transform. Another is cepstral analysis (or alansys, following cepstral nomenclature) [Randall & Hee 1981].

Impulse Response Analysis

The second microphone's impulse response function referenced to the first microphone can be constructed by computing the inverse Fourier transform of the frequency response function from Equation (D-23), as shown in Equation (D-26).

$$\begin{aligned}
 h_{y_1 y_2}(t) &= \mathfrak{F}^{-1} \left[H_{y_1 y_2}(f) \right] \\
 &= \int_0^{\infty} h_m(t - \tau) \times \\
 &\quad \left[\frac{e^{j2\pi f(r_{11} - r_{12})/c_0}}{r_{11} r_{12}} + \frac{e^{j2\pi f(r_{11} - r_{22})/c_0}}{r_{11} r_{22}} + \frac{e^{j2\pi f(r_{21} - r_{12})/c_0}}{r_{21} r_{12}} + \frac{e^{j2\pi f(r_{21} - r_{22})/c_0}}{r_{21} r_{22}} \right. \\
 &\quad \left. \int_{-\infty}^{\infty} \frac{1}{\frac{1}{r_{11}^2} + \frac{1}{r_{21}^2} + \frac{2}{r_{11} r_{21}} \cos 2\pi f (r_{21} - r_{11})/c_0} \times \right. \\
 &\quad \left. e^{j2\pi f \tau} df \right] d\tau
 \end{aligned} \tag{D-26}$$

This effective impulse response function is simply a convolution of the microphone's impulse response with a series of delta functions at each combination of lag times due to the contaminating reflections. Assuming the microphone's frequency response function is broad, its impulse response function should be sharp, allowing for a boxcar window to be placed around the primary peak in the impulse response function, corresponding to the time given in Equation (D-27).

$$t = \frac{(r_{12} - r_{11})}{c_0} \quad (\text{D-27})$$

This windowed impulse response function can be forward-transformed into the frequency domain. It can then be analyzed as in the ideal, no-reflection case to solve for the second microphone's frequency response function.

Cepstrum Analysis

Computing a cepstrum of a signal is a form of homomorphic analysis where signals which are convolved or multiplied in some domains are transformed to be additive in another [Randall & Hee 1981]. For example, a signal which is convolved in the time domain is shown in Equation (D-28).

$$y(t) = \int_0^t h(\tau) x(t - \tau) d\tau \quad (\text{D-28})$$

This convolution becomes multiplication in the frequency domain, shown in Equation (D-29).

$$Y(f) = \mathfrak{F}\{y(t)\} = \mathfrak{F}\left\{\int_0^t h(\tau) x(t - \tau) d\tau\right\} = H(f) X(f) \quad (\text{D-29})$$

If the logarithm of each side is taken, the product of the input and frequency response function becomes a sum. While these two signals may still overlap in the frequency domain, the inverse Fourier transform of this logarithm can be taken. Depending on the nature of these functions,

they may be easily separable in this new “quefreny” domain. This is demonstrated in Equation (D-30) and Equation (D-31).

$$\log(Y) = \log(HX) = \log(H) + \log(X) \quad (\text{D-30})$$

$$\mathfrak{T}^{-1}\{\log(Y)\} = \mathfrak{T}^{-1}\{\log(H)\} + \mathfrak{T}^{-1}\{\log(X)\} \quad (\text{D-31})$$

Note that strictly speaking, there are two types of cepstral analysis. In the first, the auto-power spectrum is converted to a logarithmic scale and inverse-transformed. This can be edited and transformed back into the frequency domain, but as it only operates on real power spectra, no cross-power spectra can be evaluated, preventing its use in this study. A second method exists where the complex logarithm of each term is computed, given in Equation (D-32) [Randall & Hee 1981].

$$\ln(X) = \ln(|X|e^{j\phi}) = \ln|X| + j\phi \quad (\text{D-32})$$

When a function is analytically known, this is straightforward. However, when dealing with discrete data, a phase-unwrapping method is required, else the inverse transform of this function will be nonsense. A phase-unwrapping/wrapping scheme is implemented in the MATLAB function `cceps` and its inverse `icceps`.

Note also that when computing an inverse Fourier transform of a finite, discrete data set, aliasing occurs in the cepstral computation. This is due to the nonlinearity introduced by the logarithmic operation generating harmonics of the base spectral content of the signal, well beyond the Nyquist sampling requirements of the inverse transform. This can lead to erratic behavior of the signal in the quefreny domain, and must be kept in mind when filtering (or “liftering”). This can be avoided through a pole-zero factorization method of a well-behaved spectrum, also available in MATLAB, but the factorization method is dramatically more expensive from a computational perspective.

The second ideal case, with a single reflection, is restated in logarithmic form in Equation (D-33).

$$\ln(S_{y_1 y_1}) = \ln(S_{xx}) + \ln \left[\frac{1}{r_{11}^2} + \frac{1}{r_{21}^2} + \frac{2}{r_{11} r_{21}} \cos \left(2\pi f \frac{r_{21} - r_{11}}{c_0} \right) \right] - 2 \ln(4\pi) \quad (\text{D-33})$$

This equation consists of three terms. The first is the logarithmic autospectral density of the input function, and the last is a constant. The central term is the natural logarithm of an offset cosine function. The cepstrum of the spectrum can then be computed in Equation (D-34).

$$\begin{aligned} \mathfrak{S}^{-1} \left\{ \ln(S_{y_1 y_1}) \right\} &= \int_{-\infty}^{\infty} \ln(S_{y_1 y_1}) e^{j2\pi f \tau} df = \int_{-\infty}^{\infty} \ln(S_{xx}) e^{j2\pi f \tau} df + \\ &\int_{-\infty}^{\infty} \ln \left[\frac{1}{r_{11}^2} + \frac{1}{r_{21}^2} + \frac{2}{r_{11} r_{21}} \cos \left(2\pi f \frac{r_{21} - r_{11}}{c_0} \right) \right] e^{j2\pi f \tau} df - \\ &2 \ln(4\pi) \int_{-\infty}^{\infty} e^{j2\pi f \tau} df \end{aligned} \quad (\text{D-34})$$

The last term in the cepstrum is the inverse Fourier transform of a constant.

$$2 \ln(4\pi) \int_{-\infty}^{\infty} e^{j2\pi f \tau} df = 2 \ln(4\pi) \delta(\tau) \quad (\text{D-35})$$

If it is assumed that the input autospectral density is true white noise, its cepstrum also becomes the inverse transform of a constant, as given in Equation (D-36).

$$\int_{-\infty}^{\infty} \ln(S_{xx}) e^{j2\pi f \tau} df = \ln|S_{xx}| \delta(\tau) \quad (\text{D-36})$$

The remaining term can be expressed as the series expansion of the natural logarithm [Abramowitz & Stegun 1965].

$$\ln z = (z-1) - \frac{1}{2}(z-1)^2 + \frac{1}{3}(z-1)^3 - \dots \quad (\text{D-37})$$

The expansion in Equation (D-37) assumes that $|z-1| \leq 1$ and $z \neq 0$, which for illustrative purposes can be assumed to be satisfied with appropriate choice of ray lengths. This expansion can then be shown in Equation (D-38).

$$\begin{aligned}
\ln \left[\frac{1}{r_{11}^2} + \frac{1}{r_{21}^2} + \frac{2}{r_{11}r_{21}} \cos \left(2\pi f \frac{r_{21}-r_{11}}{c_0} \right) \right] &= \left[\frac{1}{r_{11}^2} + \frac{1}{r_{21}^2} + \frac{2}{r_{11}r_{21}} \cos \left(2\pi f \frac{r_{21}-r_{11}}{c_0} \right) - 1 \right] - \\
&\frac{1}{2} \left[\frac{1}{r_{11}^2} + \frac{1}{r_{21}^2} + \frac{2}{r_{11}r_{21}} \cos \left(2\pi f \frac{r_{21}-r_{11}}{c_0} \right) - 1 \right]^2 + \\
&\frac{1}{3} \left[\frac{1}{r_{11}^2} + \frac{1}{r_{21}^2} + \frac{2}{r_{11}r_{21}} \cos \left(2\pi f \frac{r_{21}-r_{11}}{c_0} \right) - 1 \right]^3 - \dots
\end{aligned} \tag{D-38}$$

This expansion acts as a constant offset summed with an infinite set of harmonics. These harmonics share a fundamental periodicity in the frequency domain, given in Equation (D-39).

$$f_0 = \frac{c_0}{r_{21} - r_{11}} \tag{D-39}$$

When the inverse transform of this term is computed, it will manifest as a series of delta functions. One will occur at a quefrequency of zero, corresponding to the constant offset. The remaining delta functions will occur at quefrequencies which are harmonics (or “rahmonics”), given in Equation (D-40).

$$\tau_0 = \frac{r_{21} - r_{11}}{c_0} \tag{D-40}$$

Therefore, the influence of the reflection, aside from the offset at zero quefrequency, can be removed by multiplying the power cepstrum by zero for quefrequencies above a certain cut-off of interest. The cepstrum computation has effectively separated the envelope of the input power spectrum from the influence of the reflections.

The current discussion holds for a white noise input, but if the input were white noise a correlation window would also prove satisfactory. This application must again involve the frequency response function, where the input power spectral term has been removed, shown in Equation (D-41).

$$\ln[H_{y_1y_2}] = \ln[H_m] + \ln\left[\frac{e^{jk(r_{11}-r_{12})}}{r_{11}r_{12}} + \frac{e^{jk(r_{11}-r_{22})}}{r_{11}r_{22}} + \frac{e^{jk(r_{21}-r_{12})}}{r_{21}r_{12}} + \frac{e^{jk(r_{21}-r_{22})}}{r_{21}r_{22}}\right] - \ln\left[\frac{1}{r_{11}^2} + \frac{1}{r_{21}^2} + \frac{2}{r_{11}r_{21}}\cos(kr_{21} - kr_{11})\right] \quad (\text{D-41})$$

Here, the cepstrum of the function will consist of the cepstrum of the reflections and the cepstrum of the second microphone's response. The cepstrum of the reflection terms will again consist of delta functions (or in the case of the imaginary terms, delta distributions) located mostly at higher quefrequencies for the dimensions of a typical aeroacoustic facility. The cepstrum of the second microphone's response function should be concentrated at lower quefrequencies for a given measurement bandwidth, modeling it as a canonical second-order system, for example. For such a case, most of the influence of the reflections should be removable through liftering, where certain quefrequency values are set to zero by multiplying the cepstrum by a window function, and inverse-transforming the frequency response function. Using the alternative of the frequency response between the source and second microphone, this can be expressed in Equation (D-42).

$$\ln[H_{xy_2}] = \ln[H_m] + \ln\left[\frac{e^{-jkr_{12}}}{r_{12}} + \frac{e^{-jkr_{22}}}{r_{22}}\right] - \ln[4\pi] \quad (\text{D-42})$$

Note that in subsequent usage, the complex cepstrum will be used whenever cross-spectral or cross-correlation terms are of interest.

Single Ideal Reflection: Simulation

A simple simulation is now performed, using an input typical of that used in the University of Florida Aeroacoustic Flow Facility (UFAFF) for calibration, and typical reflection length scales and speeds of sound. The second microphone is simulated as an underdamped, canonical second order system with a corner frequency of 16,000 Hz and a passband magnitude of unity.

The damping ratio is set to 0.5 for a moderate resonance peak. While this is not necessarily how a good measurement microphone would perform, it adds an interesting feature to the frequency response function (or FRF) which the filtering techniques must resolve. The total response and phase angle of the microphone frequency response are given in Equation (D-43) and Equation (D-44), respectively [Cattafesta 2010]. The magnitude response is shown in Figure D-5. The phase angle is shown in Figure D-6.

$$H_m(f) = \frac{1}{\sqrt{\left[1 - \left(\frac{f}{f_c}\right)^2\right]^2 + \left[2\zeta\left(\frac{f}{f_c}\right)\right]^2}} e^{j\theta} \quad (\text{D-43})$$

$$\theta(f) = -\tan^{-1} \left[\frac{2\zeta\left(\frac{f}{f_c}\right)}{1 - \left(\frac{f}{f_c}\right)^2} \right] \quad (\text{D-44})$$

The input waveform is a Schroeder multisine, which is a periodic broadband signal defined in Equation (D-45) through Equation (D-47) [Simon & Schoukens 2000].

$$x(t) = \sum_{k=1}^F A_k \cos(2\pi f_k t + \phi_k) \quad (\text{D-45})$$

$$f_k = kf_0 \quad (\text{D-46})$$

$$\phi_k = \frac{-k(k-1)\pi}{F} \quad (\text{D-47})$$

Here, the fundamental frequency is selected as 16 Hz. The waveform is designed to have uniform spectral content from 304 Hz ($k = 19$) to 24,304 Hz ($k = 1519$), simulating the passband of the speaker system used in UFAFF for systems calibration. Waveform magnitude is normalized to a peak-to-peak level of unity. The waveform is plotted in Figure D-7. Residual noise with a power magnitude of 10^{-12} below the passband signal is added to the remaining

signal bandwidth to improve performance of the cepstral computations, as problems were noted when zeros occurred on the unit circle of a data sequence's Z-transform. The power spectral density of the multisine is plotted in Figure D-8.

The distance from the first microphone to the source is set to 1 m, simulating a typical array distance from a source in the facility test section. The distance from the first microphone to the second is 0.559 m, to match the distance from the center microphone to the outermost microphone in the facility's large aperture phased array. The remaining distances are given in Equation (D-48) through Equation (D-50), when the reflecting plane is treated as a test section sidewall, 0.559 m horizontally from the source (opposite the second microphone).

$$r_{12} = \sqrt{1^2 + .559^2} = 1.146 \text{ m} \quad (\text{D-48})$$

$$r_{21} = 2\sqrt{.5^2 + .559^2} = 1.500 \text{ m} \quad (\text{D-49})$$

$$r_{22} = 1.952 \text{ m} \quad (\text{D-50})$$

The speed of sound is set to 345 m/s. Data are simulated as acquired at 102,400 samples per second. A single block of data spanning 1/16th of a second (6400 points) is analyzed. To simulate an ideal delay of the periodic input, the records are circularly shifted by an appropriate amount at each microphone. The resultant power spectral densities (or PSDs) of microphones 1 and 2 are shown in Figure D-9 and Figure D-10. The corresponding frequency response function magnitude and phase estimates for the microphone are shown in Figure D-11 and Figure D-12 compared to their true values.

As seen in Figure D-13 and Figure D-14, in both forms of analysis the reflections are easily separable from the initial signal. Here, magnitude is simply the cepstral term for magnitude, and is a dimensionless logarithmic quantity. Note that in the impulse-response function, reflections appear as offset and scaled forms of the initial peak, as would be expected

when the microphone impulse response is convolved with a delta sequence at the reflection times. However, in the cepstral plot, while the initial peak resembles the impulse response function, the secondary reflection peaks are delta functions, since the cepstrum of the microphone impulse response is added to the reflection delta sequence instead of convolved with it.

For both methods, a boxcar window is applied to the primary peak of the plot. Several sizes of boxcar window are applied, although all are sufficiently small to cut out any reflection terms. Note that while the impulse response is one-sided, and thus only the beginning of the sequence need be passed, the cepstrum has some two-sided characteristics. As such, the cepstral window must be shifted to pass the end of the cepstral sequence, as shown in Figure D-15. For simplicity in these simulations, the same shifted window will be applied to both the cepstrum and the impulse response function. In true analysis applications a more optimum method may be desired. Window sizes of 1.2 ms, 1.6 ms, 2.0 ms, 2.3 ms and 2.7 ms are used.

Both methods come sufficiently close to predicting the frequency response function that plotting direct overlays will not give a sense of their accuracy. The relative magnitude error of the two methods for different window sizes is plotted in Figure D-16 and Figure D-17. The phase error is plotted in Figure D-18 and Figure D-19. Overall, the impulse response windowing appears to perform better than the cepstrum windowing, although for the small window case the tail of the base impulse response function was clipped, leading to worse performance. It would appear that more care is necessary in applying the window to impulse response functions than to cepstral functions. Instead of centering the window at zero time, a boxcar with some small sample lead should be applied near the peak of the primary impulse response peak.

Real Experimental Conditions

The simulated data show that both impulse response windowing and cepstrum windowing/liftering have the capacity to remove echoes from a signal and solve for an unknown frequency response function. This study must now be extended to real experimental conditions. First, the major components of a real experiment will be shown schematically, and the problem formulated. Then, acquired data will be analyzed.

Figure D-20 shows a schematic of the experimental setup used in array calibration. A Schroeder multisine is generated by a function generator, run through an amplifier to a speaker. The speaker is mounted to an exponential horn, which is designed to minimize internal reflections while reducing the effective source area, such that a compact monopole behavior can be expected over the frequency range of operation of the speaker [Blackstock 2000]. Note that this horn still has some internal reflections which will manifest in the output signal. Also, some small non-linearities may exist in the amplifier and speaker output when the power is set high enough for desired signal strength.

The effective acoustic source at the exit of the horn-speaker assembly has three displayed paths to a given microphone. If the microphone is not centered, it may experience up to five paths. The direct path is assumed to follow simple spherical spreading, as discussed in previous sections. However, the sidewall reflections and edge scatter are non-ideal, and undergo a frequency dependent magnitude and phase shift. Depending on the setup, these may be attenuated by additional sidewall padding and an acoustic foam edge treatment applied to the edges of the array disk, as shown in Figure 4-46. Note that the shown array is a 45-element array. The array used in this section's analysis is UFAFF's LAMDA array, a larger 63-element array [Bahr *et al.* 2008]. The sidewall padding, for the most part, removes the sidewall reflections, but the array edge treatment does not completely mitigate edge scattering.

A B&K 4939 1/8" condenser microphone is located at the center of the array plate as the ideal microphone reference to the array microphones, which are uncalibrated Panasonic WM-61a microphones. The signal at the B&K microphone is given in Equation (D-51).

$$Y_1(f) = \left[\frac{e^{-jkr_{11}}}{4\pi r_{11}} + H_{wall} \frac{e^{-jkr_{21}}}{4\pi r_{21}} + H_{edge} e^{-jkr_{31}} \right] H_s G_{xx} \quad (D-51)$$

The second term in the brackets is simply the FRF of the wall material for a given oblique incidence multiplied by the spherical spreading function for the reflected image source. The third term cannot be treated as a spherical image source due to the more complex nature of edge scattering, but it should have a dominant component due to propagation from the speaker to the edge to the microphone, r_{31} . The amplifier-speaker-horn response H_s accounts for both the direct frequency response of the system, as well as any internal reflections from the horn end to the speaker and back to free space. Non-linearities in this term as mentioned above would make quantitative analysis of it questionable, but the cross-correlations and impulse response estimates involving it can still give a good idea of the system time delays. Similarly, for any electret microphone in the system, the signal measured is given in Equation (D-52).

$$Y_m(f) = H_m \times \left[\frac{e^{-jkr_{1m}}}{4\pi r_{1m}} + H_{wall1m} \frac{e^{-jkr_{21m}}}{4\pi r_{21m}} + H_{wall2m} \frac{e^{-jkr_{22m}}}{4\pi r_{21m}} + H_{edge1m} e^{-jkr_{31m}} + H_{edge2m} e^{-jkr_{32m}} \right] \times H_s G_{xx} \quad (D-52)$$

As mentioned previously, in the more general case separate reflections will pass by the microphone from each sidewall and each surface wave.

The signal used in this particular case is a modified Schroeder multisine with a bandwidth from 7,248 Hz to 14,480 Hz, in 16 Hz steps. As this is slightly less than an octave band, any non-linearities in the system will be evident from harmonics, sum frequencies and different

frequencies outside of the signal passband. The measured output from the function generator (before amplification) is shown in Figure D-21, with its power spectral density in Figure D-22. While some frequency content is present outside of the measurement bandwidth, due to the D/A of the arbitrary waveform editor, it is over four orders of magnitude below the band of interest and so can be safely neglected. Note that the plotted PSDs are segments of two-sided spectra, and are thus offset by a factor of two from a true one-sided PSD.

The power spectral density of the reference B&K microphone is plotted in Figure D-23. Some small system nonlinearity is present, as the next octave band above the function generator output octave has a relatively flat-band shape, approximately two orders of magnitude reduced in level. At such a reduced level this may not play much of a roll in frequency response estimates of the amplifier-speaker-horn system, so after finding the microphone response functions it would be possible to go back and solve for the amplifier-speaker-horn FRF. However, such a task is beyond the scope of this work.

Previously, it was mentioned that when sufficient bandwidth is present in a signal, its autocorrelation function could be directly edited to remove reflections. Figure D-24 presents the autocorrelation function of the B&K reference microphone. While the multipath peaks are visible in the signal for the appropriate delays (1.4 ms for the first sidewall, 3 ms for the first internal horn reflection and 3.7 ms for the edge reflection), there is no distinct zero region between the primary autocorrelation peak and these reflections. Editing the autocorrelations would likely remove important parts of the direct-incidence signal. Note that this data are for the worst-case scenario, with untreated sidewalls and untreated array plate edges.

Figure D-25 and Figure D-26 show the magnitude and phase estimates for an electret close to the center of the array (0.107 m), denoted here as electret 1. Figure D-27 and Figure D-28

show the magnitude and phase estimates for an electret far from the center of the array (0.559 m), labeled as electret 63. These numbers are assigned based on the microphone's array index. Both sets of data show strong contamination from reflections. The impulse response and cepstrum of the impulse response between the reference microphone and each of the electret microphones must be examined to see if filtering or liftering is possible.

The functions are computed for both microphones 1 and 63. Reflection time scales are clearly evident in the impulse response plots of Figure D-29 and Figure D-30, while by inspection there are only small ripples present in the cepstral plots of Figure D-31 and Figure D-32. However, the as cepstrum is logarithmic in scale, it may contain more information in a small ripple than is directly evident.

A .window is applied to the data which passes all data 1 ms after and 1 ms circularly before the peak of each function. The data are then reverse transformed and analyzed. The magnitude and phase estimates of microphone 1 are shown in Figure D-33 and Figure D-34 respectively. Microphone 63's estimates are shown in Figure D-35 and Figure D-36. For both microphones, the magnitude response is significantly smoothed while trending along a line of expected behavior. However, cepstral liftering appears to do a worse job of restoring the phase behavior for microphone 63 than impulse response filtering.

Window length is evaluated by filtering/liftering again with a 0.25 ms window ahead and behind the peak of the impulse response and cepstra sequences. The results for electret 1 are plotted in Figure D-37 and Figure D-38. The results for electret 63 are plotted in Figure D-39 and Figure D-40. For the smaller window, the magnitude response again looks reasonable. However, the cepstrum liftering performs very poorly with phase estimate. At first glance it would appear that impulse response filtering is the best option. However, it should be noted that

as the filtering window is decreased in size, the impulse response function approaches a delta function, which would have a frequency response magnitude of one and phase shift of zero. Since the bandwidth of interest appears to be reasonably flat for the microphone, an over-filtered impulse response could still appear to be capturing the system dynamics. Furthermore, the algorithm used to compute the signal cepstrum utilizes a phase-unwrapping technique. Since the signal bandwidth is undefined below 7,248 Hz, the phase-unwrap will be unwrapping random noise phase angles, dramatically altering the behavior of the cepstrum computation.

To get a better sense of the behavior of impulse response filtering, a larger bandwidth measurement is necessary so the roll-off region of the electret microphones can be captured. For cepstrum analysis, a larger bandwidth signal is also required to fill in the lower frequencies and check if phase unwrapping is the dominant problem. Two options are available for broadband analysis. The first experiment conducted used a signal with multisine components ranging from 304 Hz to 28,816 Hz. This measurement is the easiest to analyze, but may suffer signal-to-noise issues related to the maximum system output, as well as non-linear contamination of upper frequencies from lower ones. The second option is to patch together the seven octave bands run in separate experiments. This overlap process would not be entirely accurate when evaluating the autospectra of a given microphone, since the speaker output may not be the same from run to run due to amplifier instability or ambient conditions. However, as the physical setup was completely unaltered as the bands were shifted, the mic-to-mic frequency response functions should be the same. If they are the same, then a hybrid, broadband FRF can be patched together from the seven runs spanning 304 Hz to 28,816 Hz. This should capture the entire range of operation of the BMS speaker, and provide enough bandwidth to check both the cepstral phase

issues, by filling out the lower frequencies of the measurement, and the reliability of impulse response filtering, by measuring beyond the cut-off frequency of the electret microphones.

For brevity's sake, the broadband analysis, conducted identically to the octave band above, is not presented. The results showed similar behavior to the octave band analysis. Based on the questions raised above, a more reliable processing technique is necessary. For large arrays, visual inspection of each microphone frequency response function and manual editing of the appropriate filters will prove infeasible, and automation requires a consistently reliable processing technique.

Downsampling

For cepstra, one of the easiest things to evaluate is the contribution of individual components of the FRF to the cepstrum. Recalling that the complex cepstrum of a frequency response function is the sum of the magnitude and phase components of the FRF, the inverse transform of the two components are additive and thus can be evaluated individually. In this analysis, the broadband data are used. Note that unless otherwise stated, logarithms are base e .

As Figure D-41 shows, when signal levels are low, the estimate of the frequency response function breaks down. This observation is reinforced in Figure D-43, with the sudden breakdown of a clear phase relationship at frequencies below and above the speaker output band. The second plot in the phase figures is the minimum-delay-shift signal, which is simply the unwrapped phase angle with a constant integer delay applied. This minimizes the imaginary contribution to the zero-frequency bin, which can interfere with signal reconstruction if only the real component of cepstra is taken, as it would be since a true cepstrum should be nominally real. These plots also show that the phase data have the largest contribution to low-frequencies from Figure D-44, while the magnitude cepstrum is best used for identification of reflections, which are visible as ripples in Figure D-42.

Figure D-45 is a schematic of the existing data situation. While the desired region does not actually extend to the dc component of the FRF curve, the very-low frequency behavior is necessary to avoid fluctuations in the phase of the calibration curve in the lower bands of interest. Removal of high-frequency components is more straightforward, and will be discussed first.

The most obvious solution is to apply an ideal low-pass filter to the data. While this may also lead to irregular behavior in the impulse response function of the filter, as the time-domain representation of an ideal low-pass filter is non-causal, the data may still be usable from a reflection-removal standpoint and will thus be evaluated in subsequent discussion. More troubling is the effect this will have on cepstral analysis. Zeroing out the higher-frequency data will result in negatively infinite data when the logarithm is taken, leading to singular behavior in the inverse Fourier transform applied to construct a cepstrum. While the magnitude can be filtered after the logarithm is taken and the phase filtered separately, a more direct solution would be to downsample the data. If the frequency response curves are band-pass filtered at $\pm\pi/2$ on the unit circle, and then the resulting data expanded to encompass the entire unit circle, the data have effectively been downsampled by a factor of two. In essence, the time-domain sampling rate has been cut from 102,400 samples per second to 51,200 samples per second. The unit circle schematic of this is shown in Figure D-46.

Figure D-47 through Figure D-50 show the magnitude and phase results for the downsampled data. Downsampling the data has removed sufficient fluctuation from the cepstral plots that reflections are far more evident in both the magnitude and phase components of the cepstrum. From here, the data can be boxcar windowed as previously, and transformed back into the frequency domain. Comparisons between the full dataset liftering and downsampled liftering

are shown in Figure D-51 through Figure D-54. While the magnitude response in both the original data and the downsampled data appears to trend reasonably well with the original estimate, with some mild low-frequency undershoot, downsampling clearly improves the data fit for phase angle estimates. However, the ripple in the phase angle is still sufficient to yield questionable calibration results.

Low Frequency Treatment

To improve the performance of the data fit, the lower frequencies for which no data were collected will now be modeled. The base frequency used in lowband signals was 304 Hz, but judging from the plotted phase response, the speaker output may have been insufficient for calibration below 512 Hz. By fitting magnitude and phase data to these frequencies, it may be possible to reduce the ripple in the phase estimate and improve the low-frequency magnitude estimate.

Fitting data to the magnitude response is simple. As data are only missing for the 0 Hz to 496 Hz bins, it can be assumed that the microphone passes these signals with little difficulty. While in reality the microphone likely has a low-frequency cut-on, this frequency should be sufficiently low that the first non-zero bin, 16 Hz, will be unaffected. For the sake of data fitting, 0 Hz will be treated as part of the pass band. Qualitatively, a value can be assigned by assigning these low frequency bins a magnitude response equal to the average magnitude of the 304 Hz to 10 kHz bins, which should be reasonably close to the true microphone response for a measurement microphone with 20 kHz bandwidth. Phase fitting can be a bit more difficult. As a first attempt, a regression line will be drawn through the unwrapped phase angle from -10 kHz to 10 kHz, neglecting the -496 Hz to 496 Hz bins. This should project a rough estimate of the phase behavior for these low frequency bins, while maintaining an identically zero phase offset at 0 Hz.

The lifiered signals with the curve fit low frequencies are plotted in Figure D-55 through Figure D-58. The plots show an improvement in the passband response trend of the magnitude estimate, but little change for the phase. Note the jump at high frequencies in the phase behavior is due to phase angle wrap, which was unwrapped in previous plots. Downsampling the signal improves phase angle estimates. Fitting the low frequency data improves the magnitude estimate. However, the ripple in phase angle prediction is still a problem.

As this could be a microphone-specific issue, another microphone is selected for evaluation. The downsampled phase estimate for electret 43 is shown in Figure D-59. Here, a severe error in the phase angle is present. It appears that the reflection contribution to phase angle fluctuations is sufficiently large that it causes a phase shift of greater than 180 degrees, which “tricks” phase unwrapping algorithms. While a larger unwrap tolerance could be applied, this would have implications at other locations in the phase spectrum. This observation leads to questioning how many microphones suffer from this issue. Figure D-60 shows the unwrapped angles for all 63 electret microphones, before lag time correction from the B&K microphone is applied. As shown, most of the microphones undergo huge phase shifts in the 1000 Hz to 1200 Hz band, which are on the order of 360 degrees. That is, the jump is sufficiently large that there is actually no jump at all when wrapped phases are plotted. This evidently causes severe issues with cepstrum-based methods when predicting phase response.

The phase angles for a case where there is edge treatment on the array and the test section sidewalls have additional, wedge based absorption are shown in Figure D-61. As is evident, the phase angle shift is not as severe. Upon further inspection, however, an attempt at a phase angle estimate proves fruitless, as seen in Figure D-62. While manual tweaking of windows and phase shifts may allow for cepstral liftering, for blind calibration it appears that impulse response

windowing may prove to be both the simpler and safer choice. The impulse-response-windowed signals for the case of untreated edges and untreated sidewalls for electret 43 is shown in Figure D-63 through Figure D-66. Clearly, impulse response windowing does not suffer from the same problems as cepstral methods, as no phase wrapping is required. Correct window size selection is still important for minimum ripple in the frequency response estimates. Also, downsampling appears to reduce the performance of an impulse response window method. In an effort to improve performance and reduce the sensitivity to window size selection, a 50 %Tukey window is applied with the results plotted in Figure D-67 and Figure D-68. The Tukey window, which consists of a flat pass region which transitions to a flat stop region through a blended, raised cosine section, is selected to perfectly pass the main portion of the impulse response. It appears to allow longer segments of the impulse response to be used, as shown, before significant ripple is introduced into the FRF estimate.

After some minor experimentation, a Tukey window of 0.4 ms (± 0.2 ms around the peak of the impulse response function), is selected. This is used for both treated and untreated experiments. The treated results for electret 43 are shown in Figure D-69 and Figure D-70, and show far less dependence on window size than the untreated case. A comparison between 0.4 ms window cases with treated and untreated conditions is shown in Figure D-71 and Figure D-72. While there is some variation in magnitude estimates, the phase estimates match remarkably well.

Application to Beamforming Results

The need for this calibration technique is now demonstrated. Figure D-73 shows the standard delay-and-sum beam map of a calibration experiment with the medium-aperture array from Figure 4-46 at 1120 Hz. Figure D-74 is the same data set after application of an eigenvalue-based group calibration technique, designed to compensate for steering vector errors

[Dougherty 2002]. In both figures, the acoustic source is located at the center of the region plot, centered within the black integration box. The data are contaminated by non-ideal reflections located in the upper and lower portions of the scan region, as no other acoustic sources were present in this experiment. While inspection of the original beam map may obviously indicate these data are unsuitable for a group calibration technique, if only a few frequencies are contaminated like this and a broad-frequency-range, narrowband calibration is desired, this calibration method could easily be applied without knowing it is in error.

When the source is offset by 0.5 m in the positive x-direction, the uncalibrated data appear to locate the source, although the source is highly skew, in Figure D-75. However, when the calibration which corrected Figure D-73 to Figure D-74 is applied, Figure D-76 is the result. As expected by applying a grossly inaccurate calibration, the new beam map is nonsense as it completely misses the true source and predicts a large source region in empty space. In contrast, when the new calibration technique is applied to the data, the result in Figure D-77 indicates that the true source behavior is preserved although the distribution is still smeared.

The calibration technique is now evaluated at frequencies where the data do not appear corrupted by coherent reflection effects. 10 kHz and 20 kHz are well beyond the absorption cut-offs for sidewall foam used in UFAFF, so both should show reasonable behavior even for uncalibrated cases assuming the microphones do not require dramatic calibration corrections. The uncalibrated beam maps are shown in Figure D-78 and Figure D-80. The source field appears well-behaved. The source shape is not perfectly circular like a true monopole, but it is close. The center of the beam map's predicted source is slightly offset from the nominal source location, but this offset is within experimental uncertainty of the horn's location in free space. The associated calibrated beam maps are shown in Figure D-79 and Figure D-81. The shape of

the higher-power beam contours in these plots may be slightly more circular, but such judgment is mainly qualitative in nature. The physical acoustic source may be slightly skew due to irregularities in the horn or speaker, so there is no proof that the calibration has improved or worsened the shape of the acoustic field. What is evident is the dramatic increase in predicted power at 20 kHz. Throughout this appendix it has been clear that the magnitude and phase roll-off of the electret microphones begin well below 20 kHz. The calibration procedure has, upon initial investigation, compensated for the individual sensor responses in the beam map power estimate. While this is not proof that the calibration technique is truly quantitatively correct, it does provide evidence that it is behaving as intended.

Conclusion

Impulse response filtering appears to be a viable method for calibrating array microphones in a semi-echoic environment. Under certain conditions, cepstral methods may work. However, one of the primary strengths of cepstral methods, the ability to algebraically separate a spectrum's envelope from reflections and other convolved phenomena, appears to be wasted when dealing with frequency-response functions, since the time-domain equivalent of these are sharply separated from their reflections. If spectral filtering were of interest, where the autocorrelation of a signal overlaps with its reflection, a cepstral filtering method would likely be a better alternative to time-domain windowing of a signal.

Impulse response filtering has been applied to an array measurement contaminated with coherent reflections, and has demonstrated the ability to preserve source location from a reflective calibration data set, in which a standard array calibration fails. It also appears to appropriately compensate for sensor response roll-off at higher frequencies.

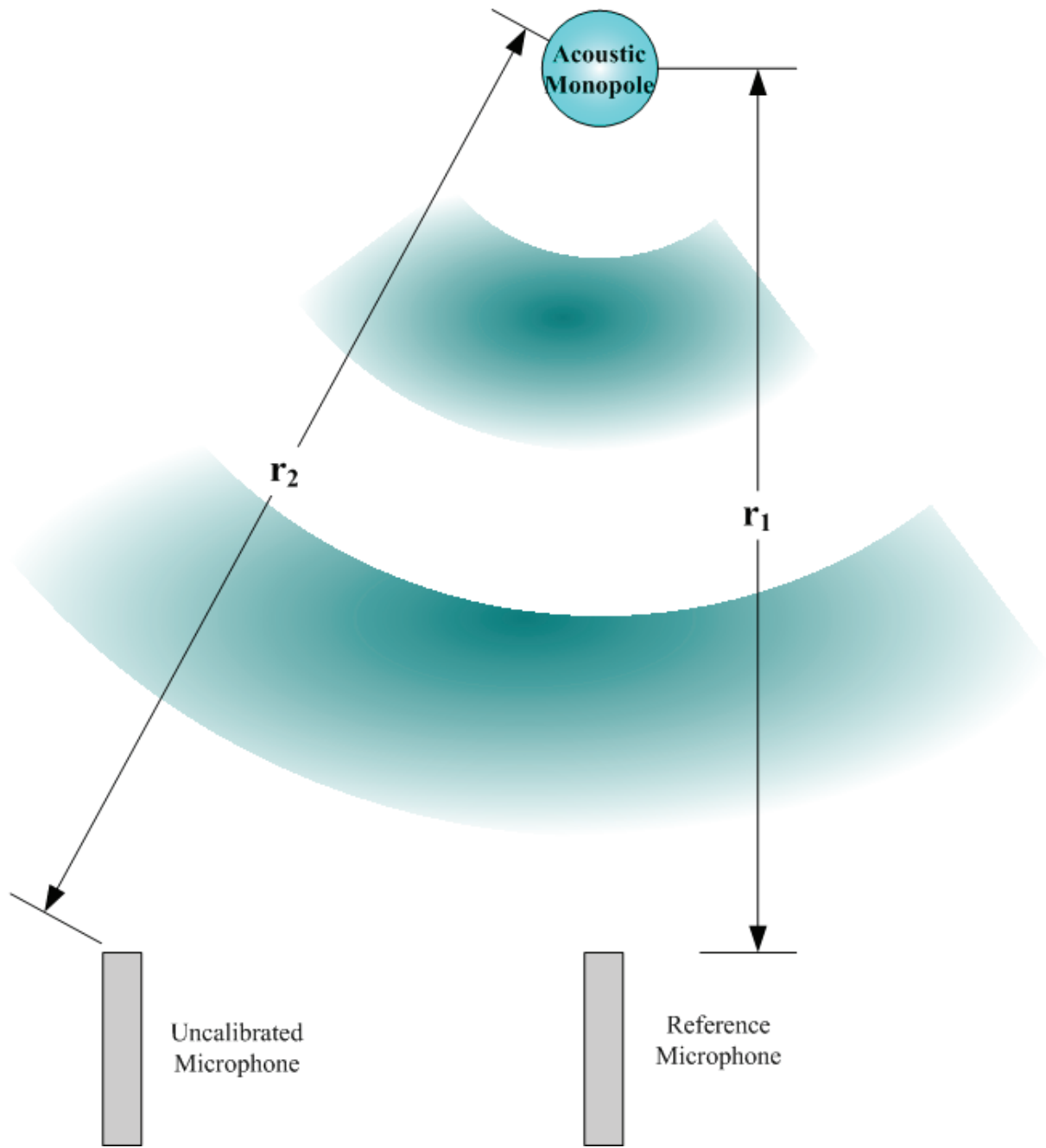


Figure D-1. Simplified acoustic calibration experiment with an ideal source field.

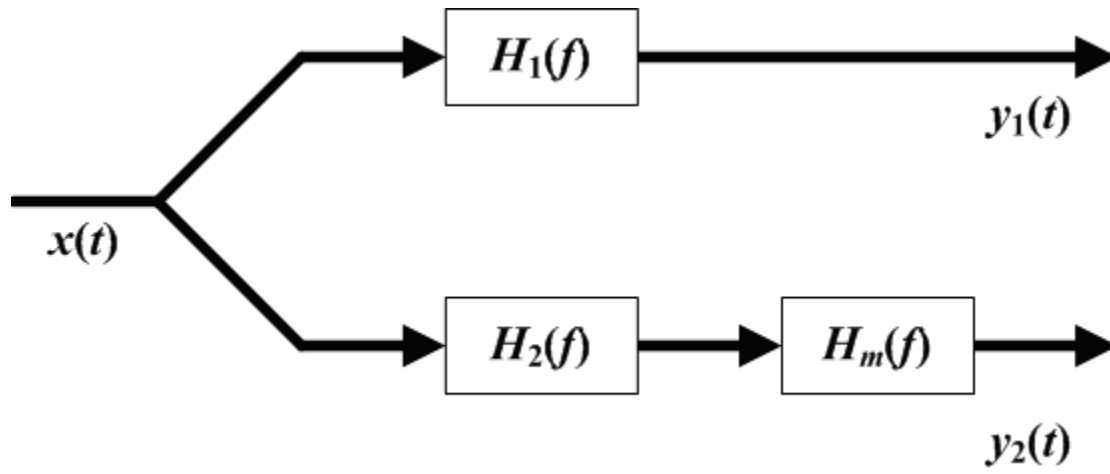


Figure D-2. Block diagram of ideal acoustic calibration.

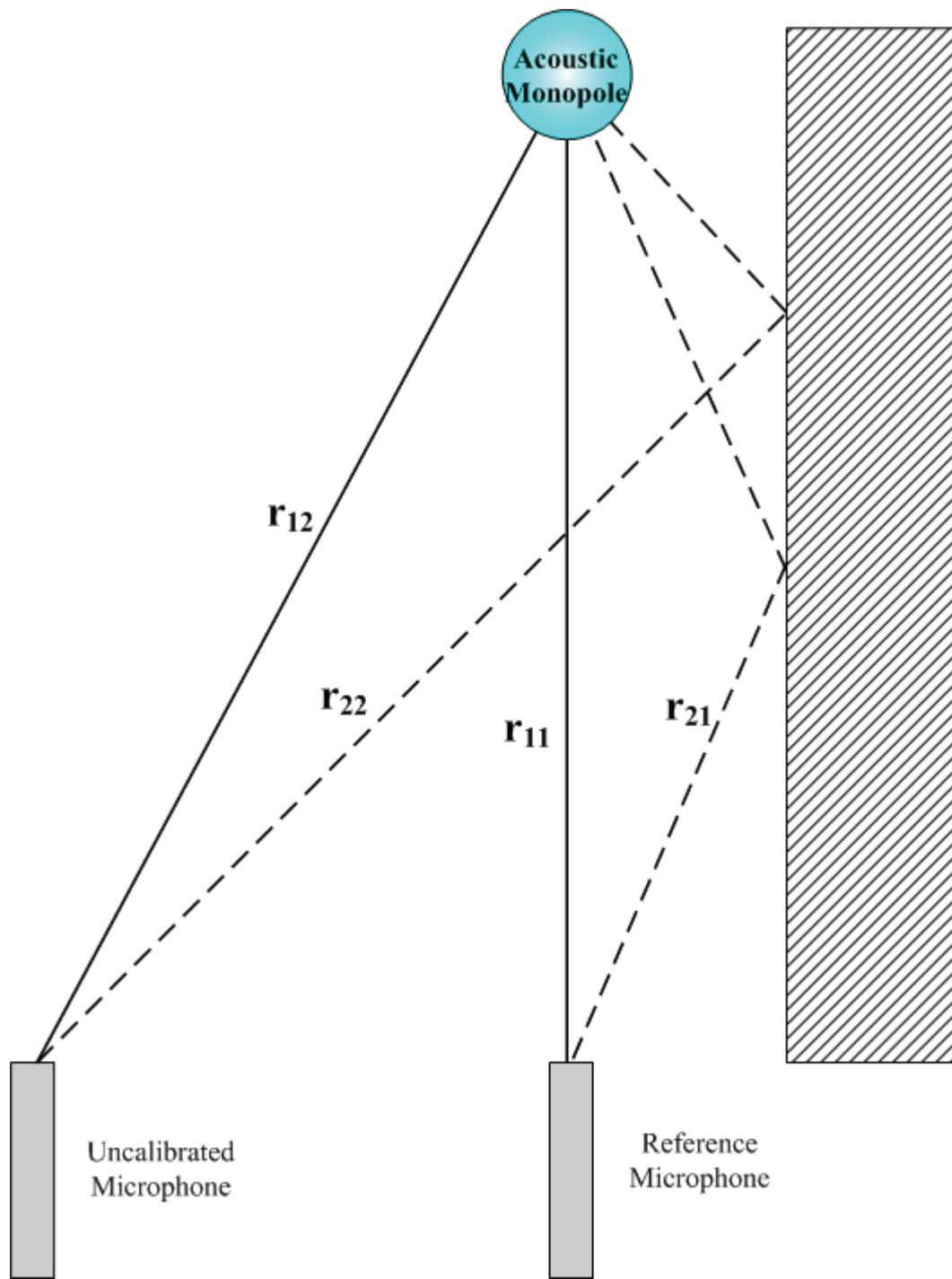


Figure D-3. Acoustic calibration experiment with a single reflection.

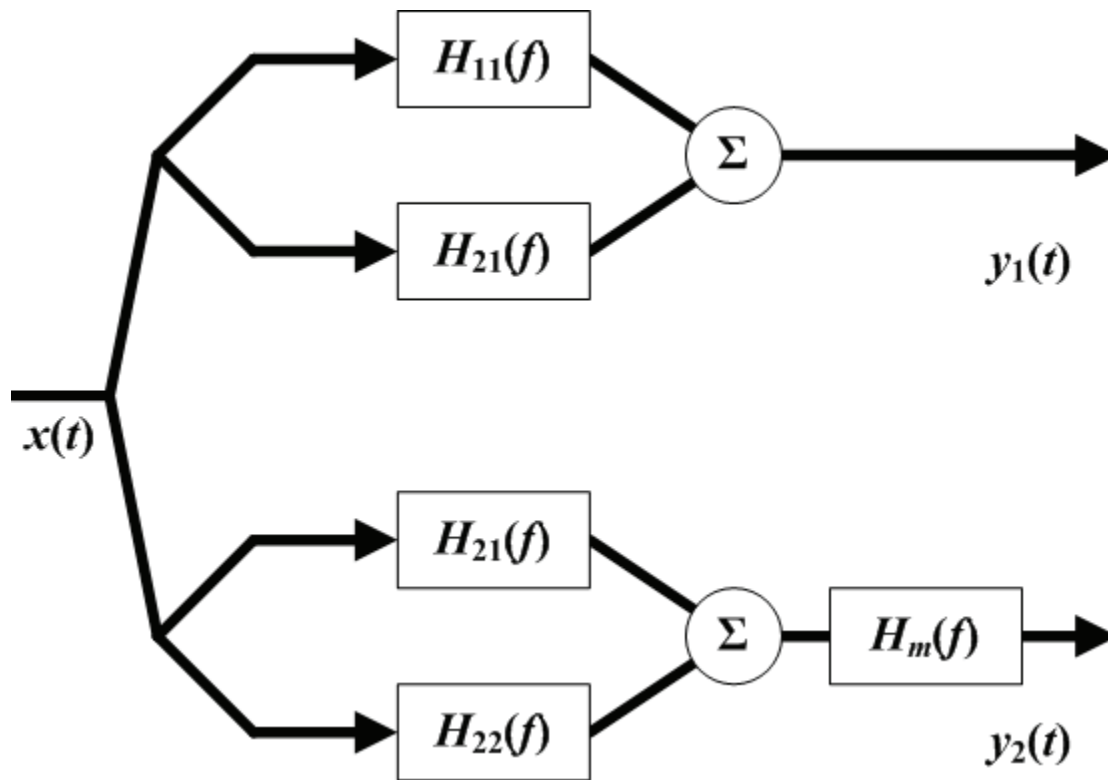


Figure D-4. Block diagram of acoustic calibration with a single reflection.

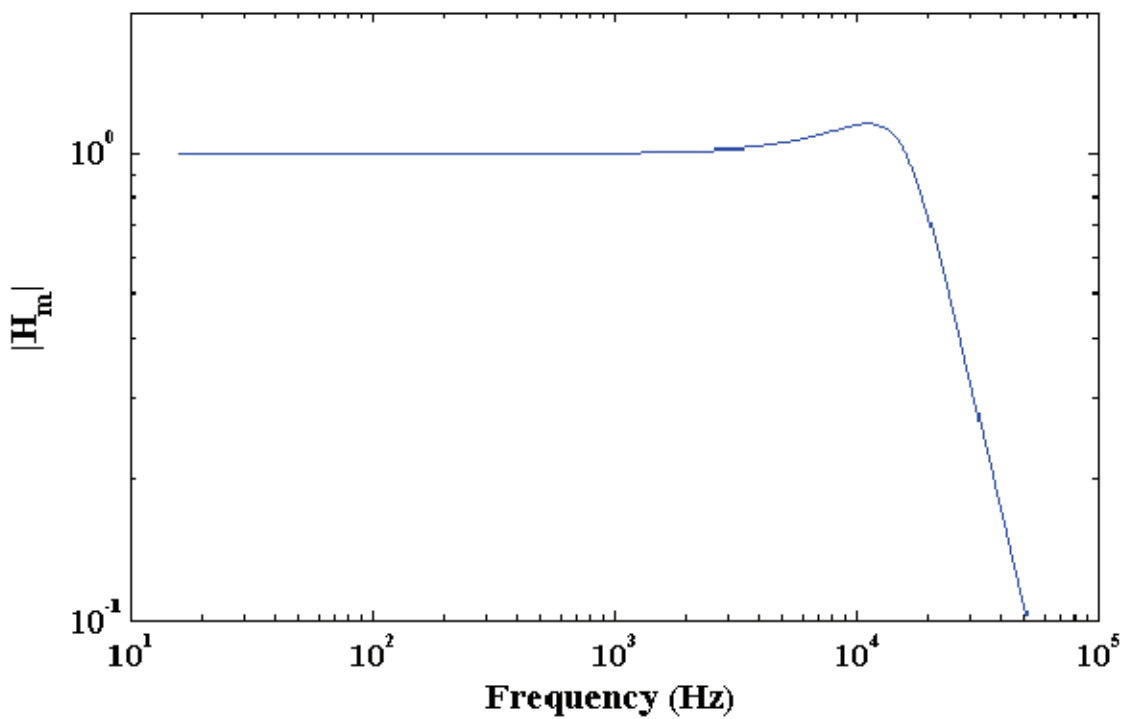


Figure D-5. True frequency response magnitude of the second microphone.

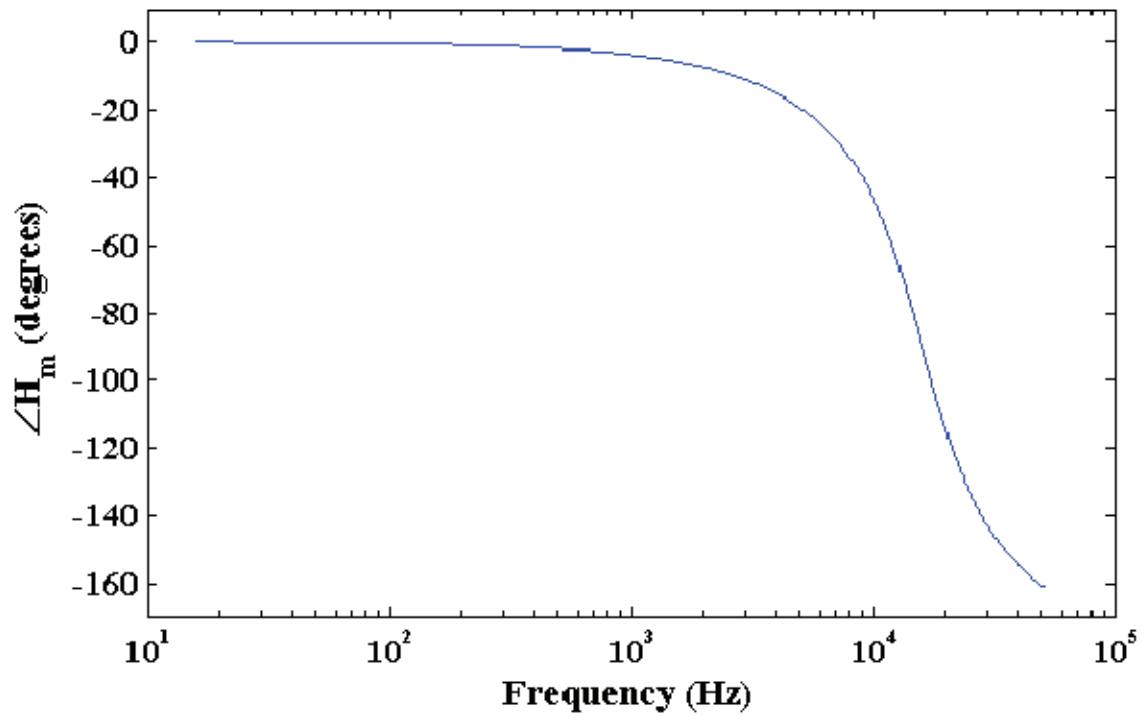


Figure D-6. True frequency response phase angle of the second microphone.

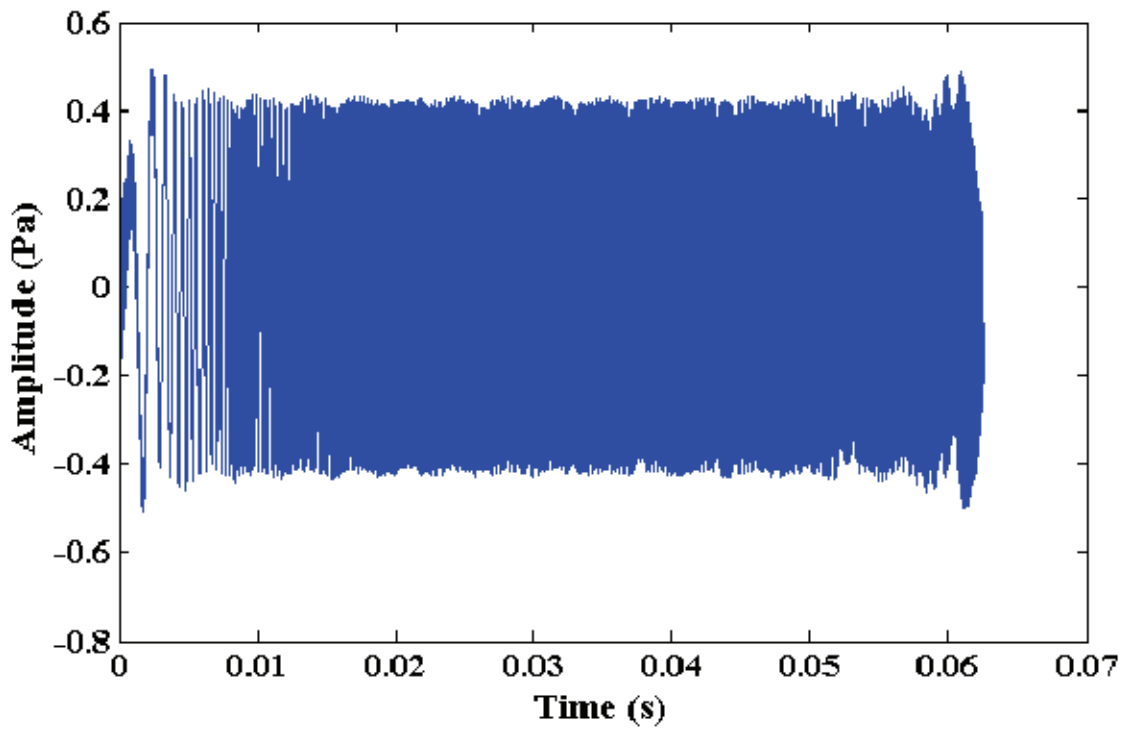


Figure D-7. Schroeder Multisine input waveform.

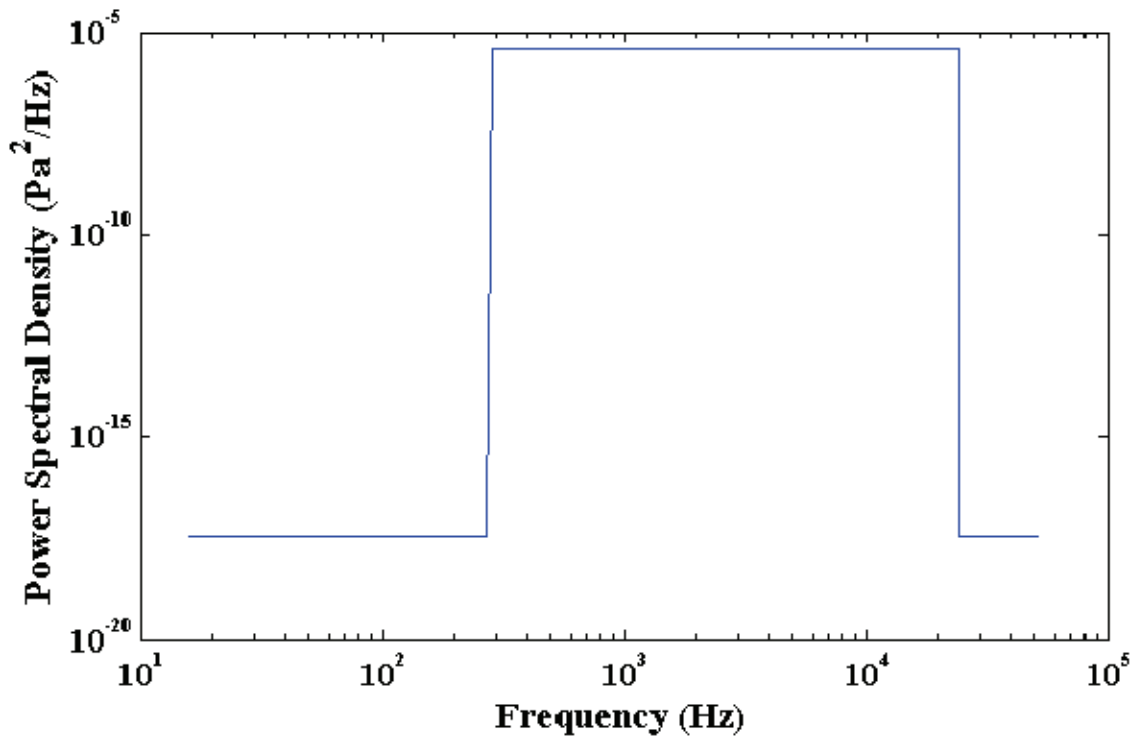


Figure D-8. Schroeder Multisine input power spectral density.

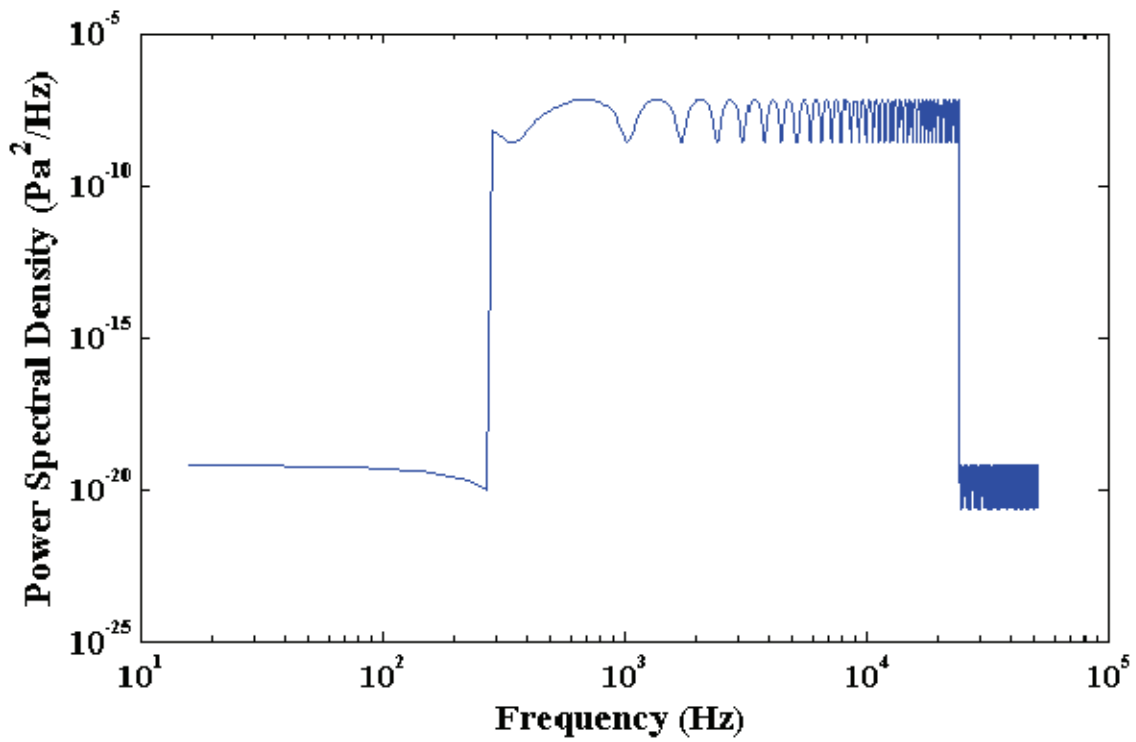


Figure D-9. Microphone 1 power spectral density.

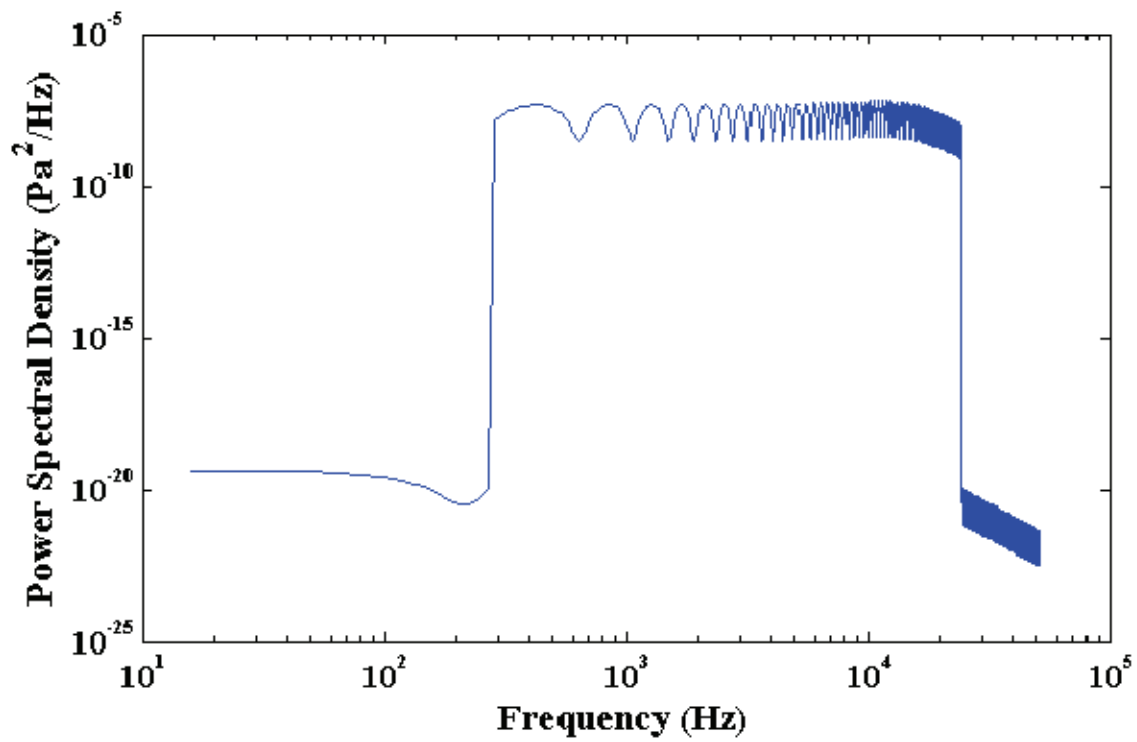


Figure D-10. Microphone 2 power spectral density.

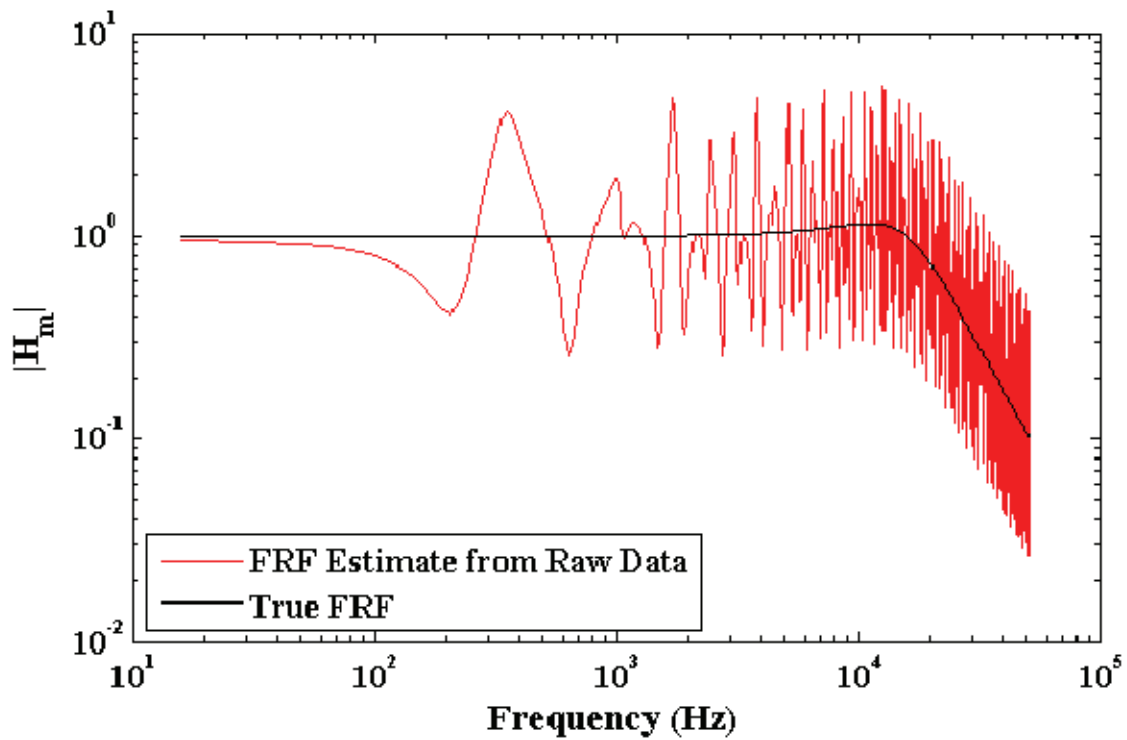


Figure D-11. Comparison of frequency response estimate magnitudes.

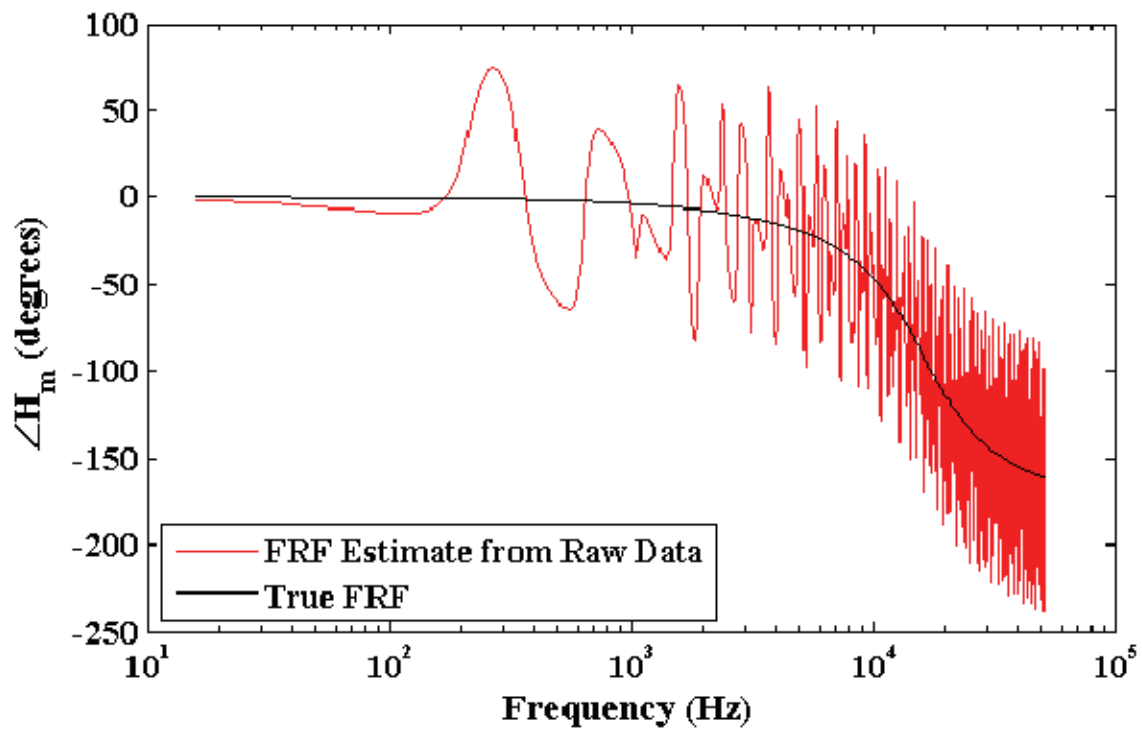


Figure D-12. Comparison of frequency response estimate phase angles.

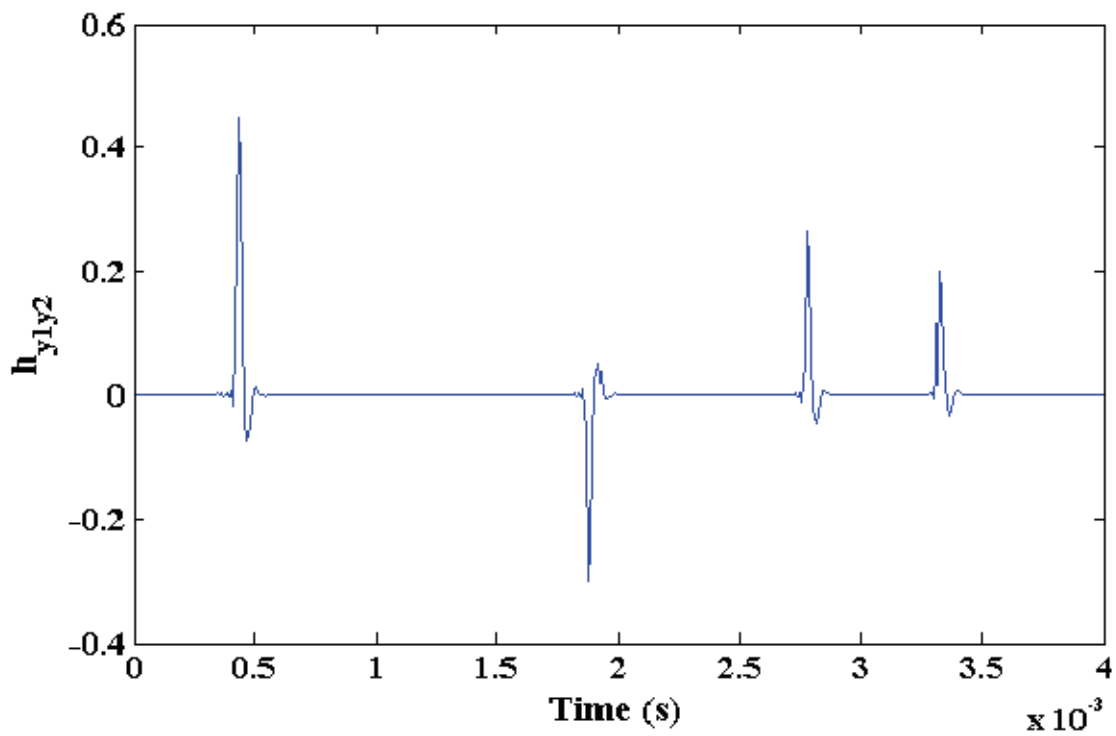


Figure D-13. Impulse response estimate, inverse-transformed from FRF estimate.

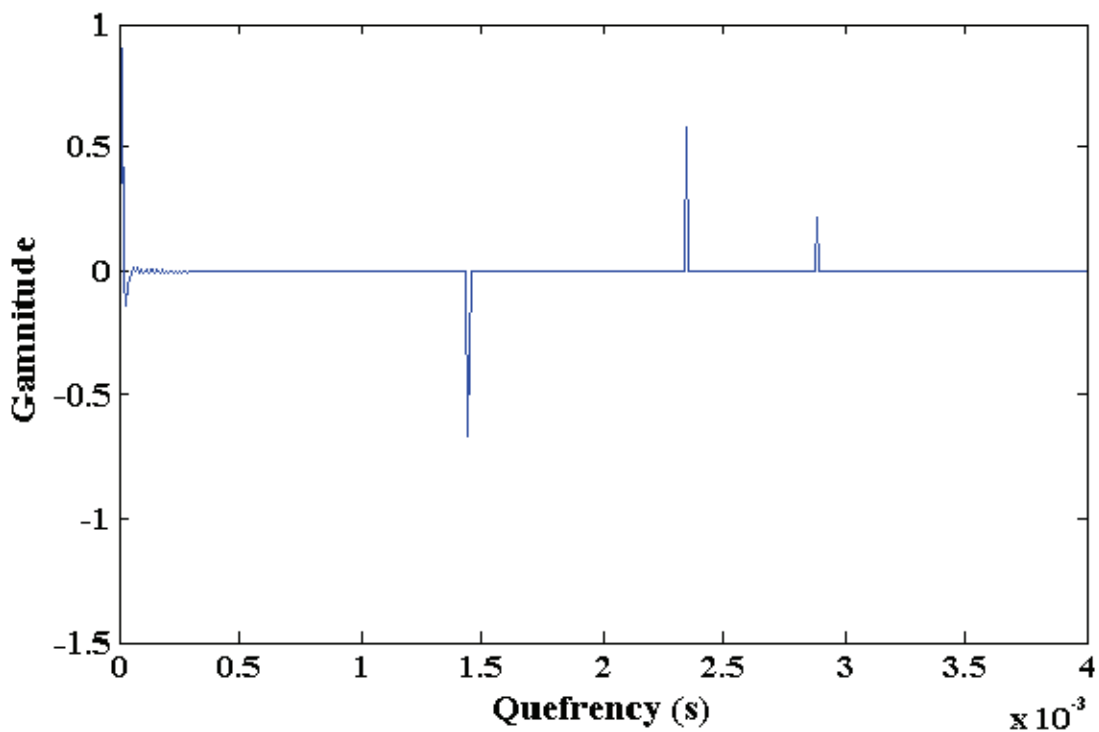


Figure D-14. Cepstrum of impulse response estimate.

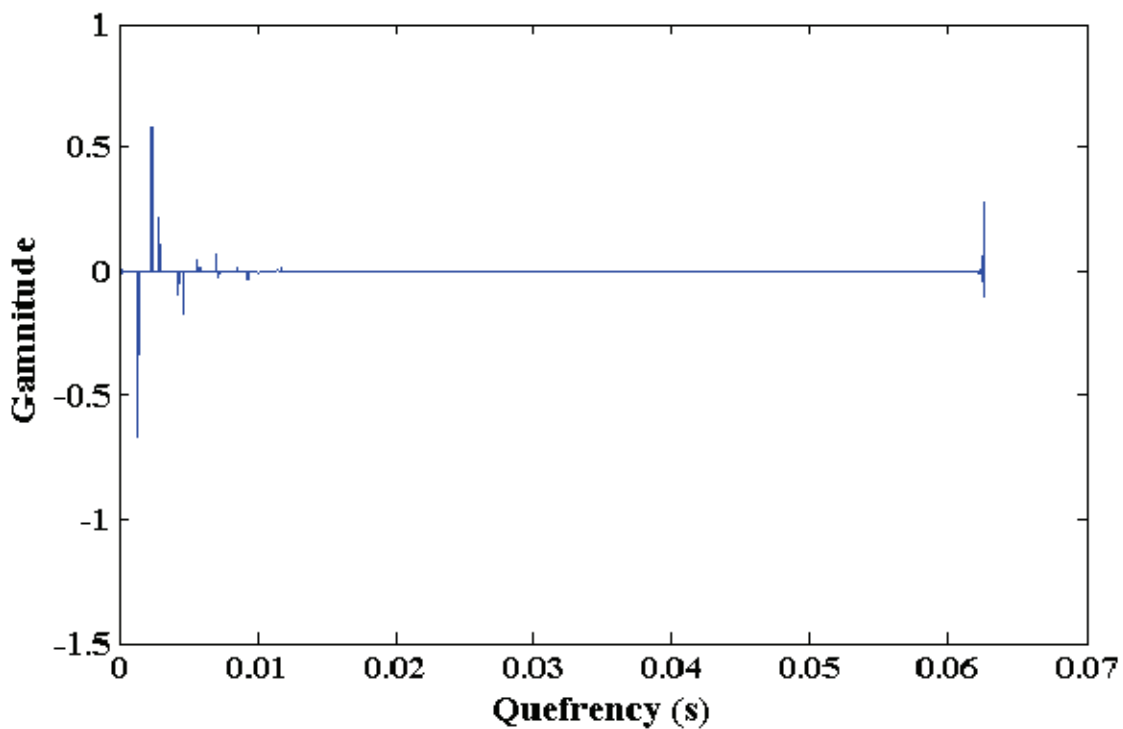


Figure D-15. Cepstrum of impulse response estimate, showing the full computed record.

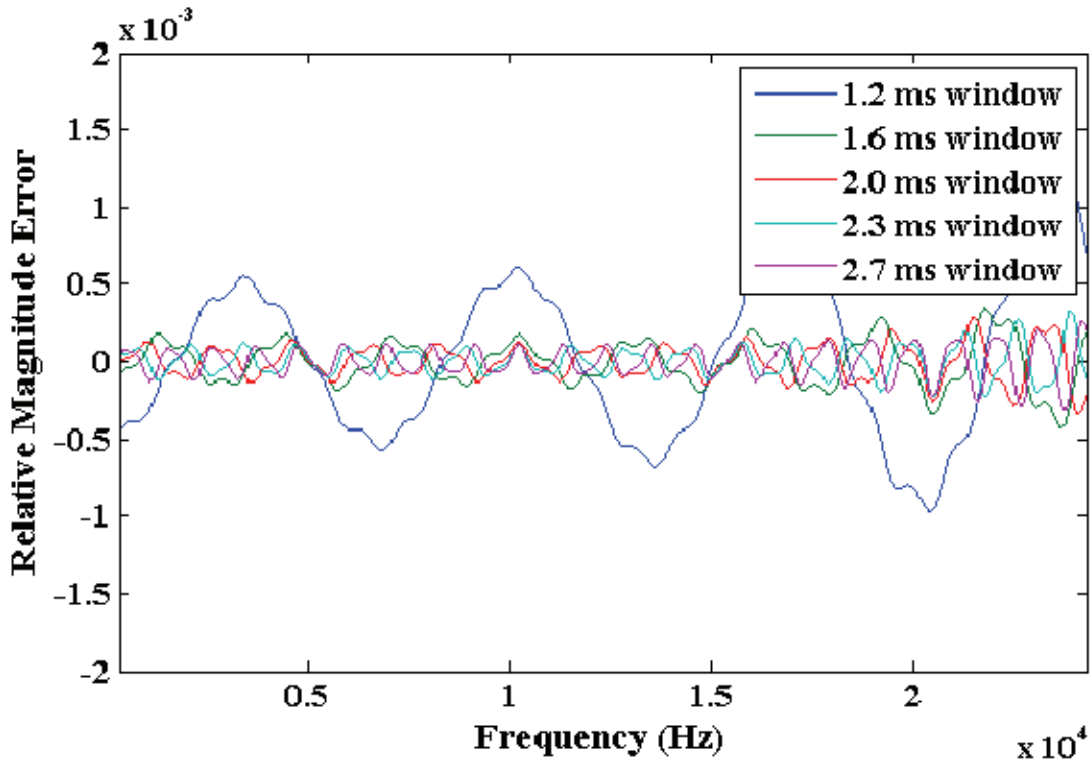


Figure D-16. Relative FRF magnitude error for impulse response windowing.

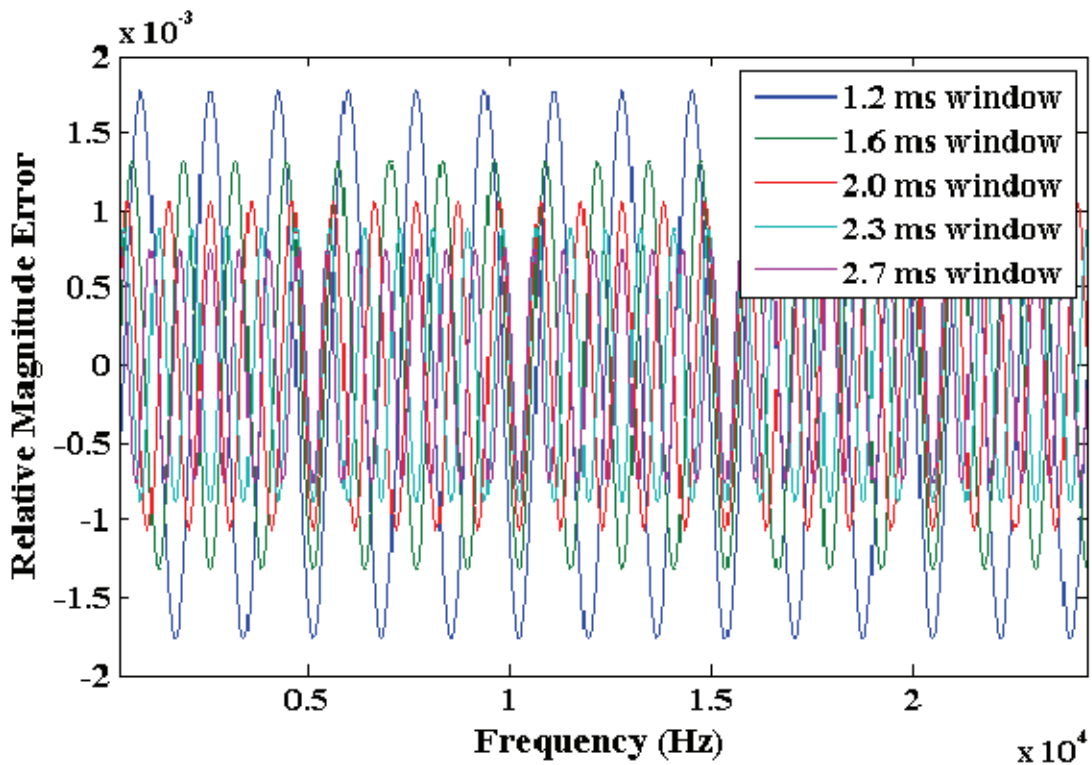


Figure D-17. Relative FRF magnitude error for cepstrum windowing.

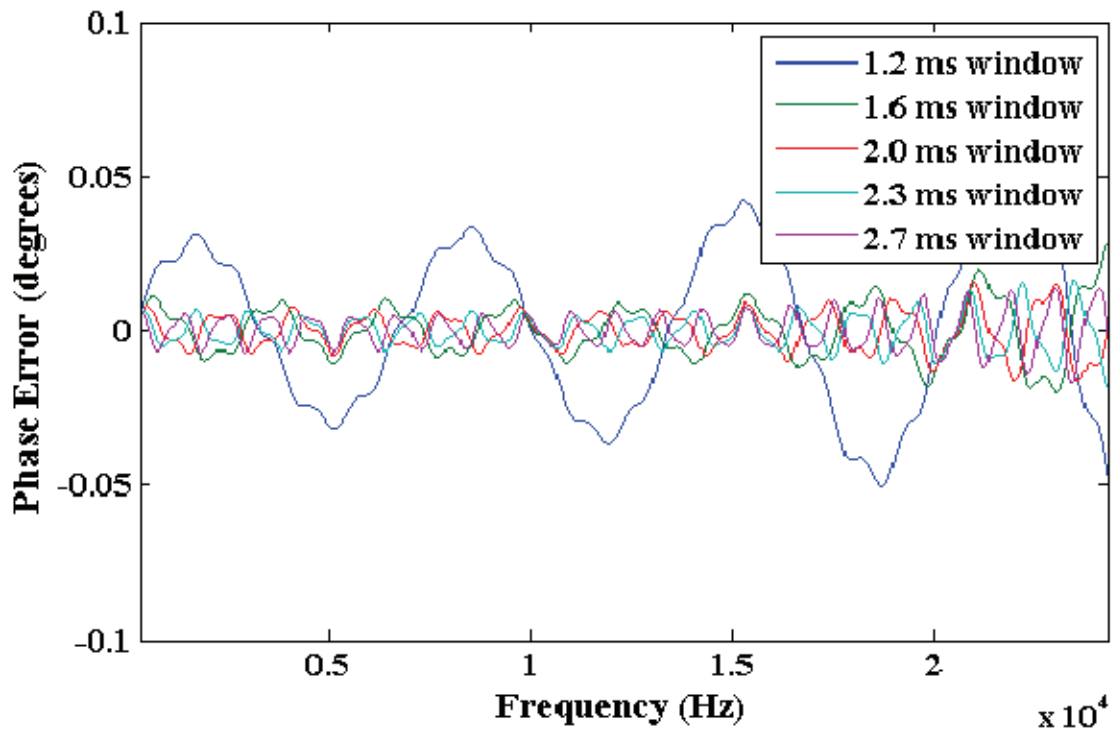


Figure D-18. FRF phase error for impulse response windowing.

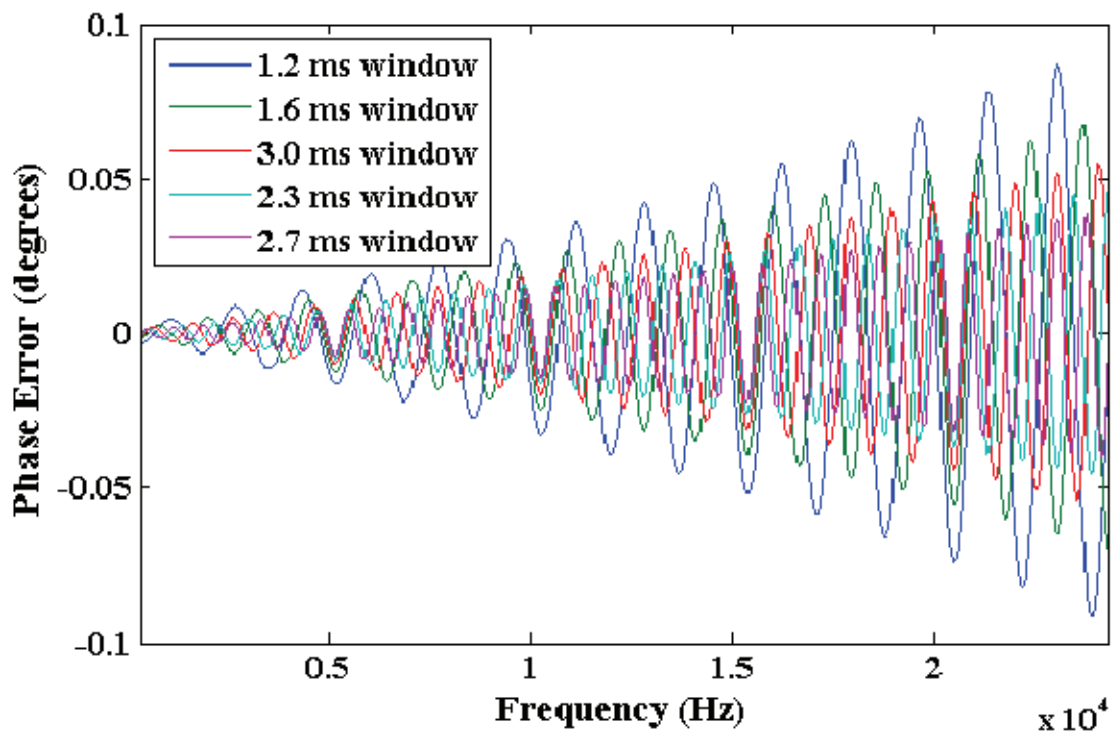


Figure D-19. FRF phase error for cepstrum windowing.

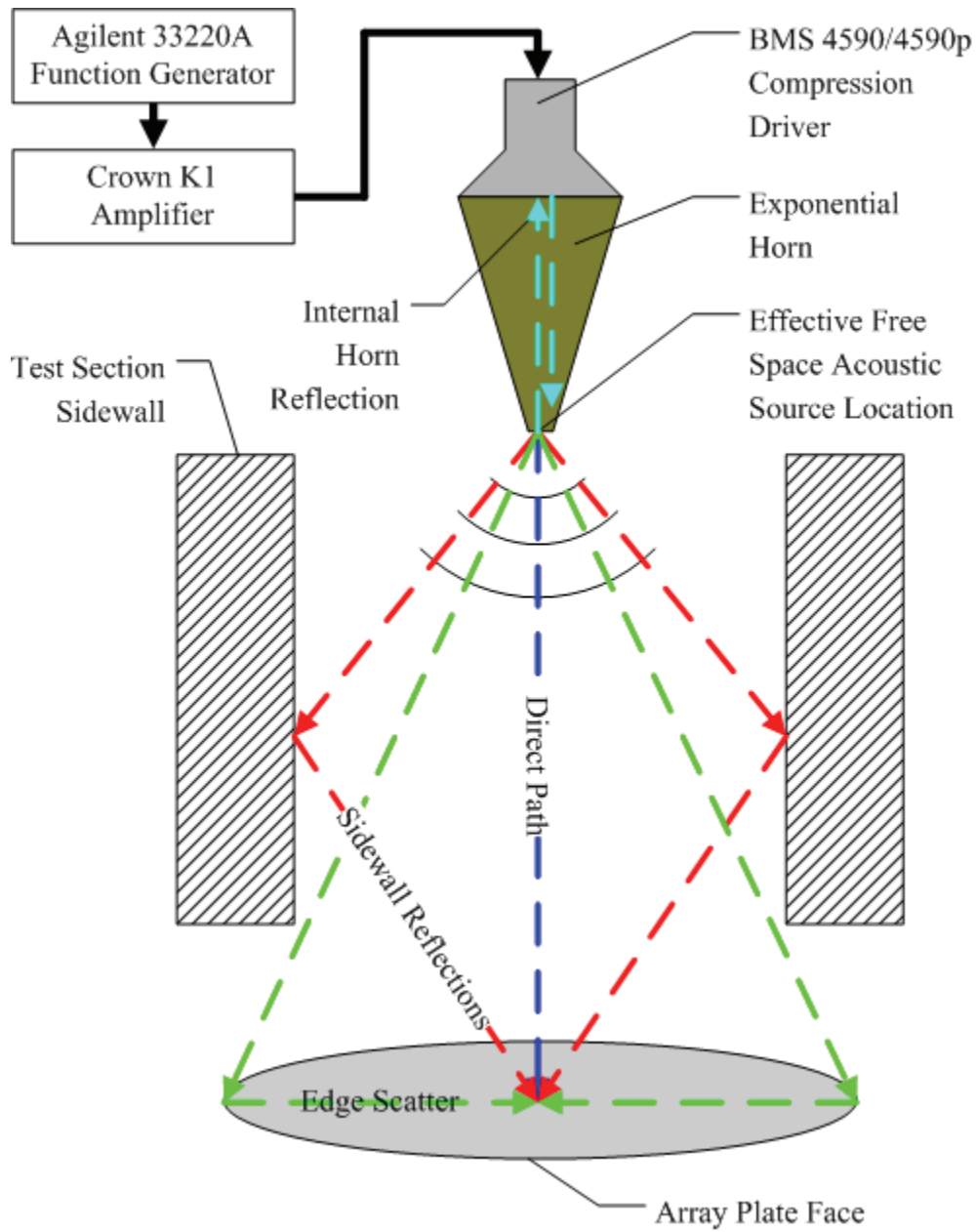


Figure D-20. Schematic of array calibration experimental setup.

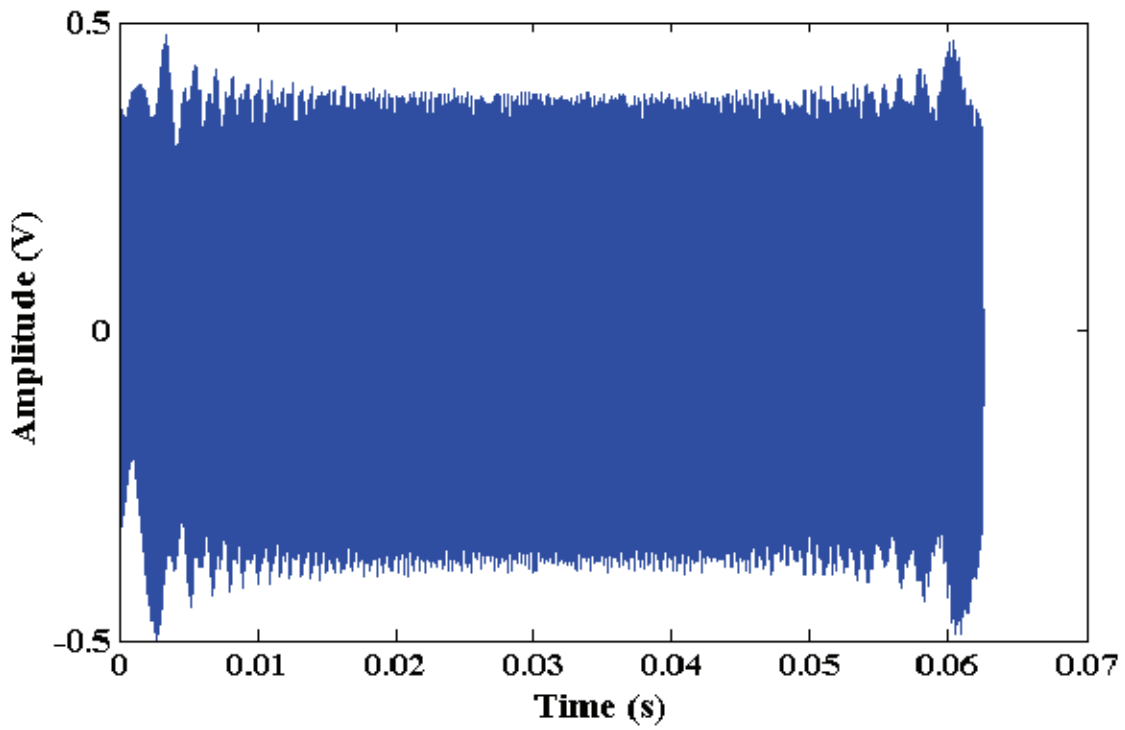


Figure D-21. Multisine used in experiment, measured from function generator output.

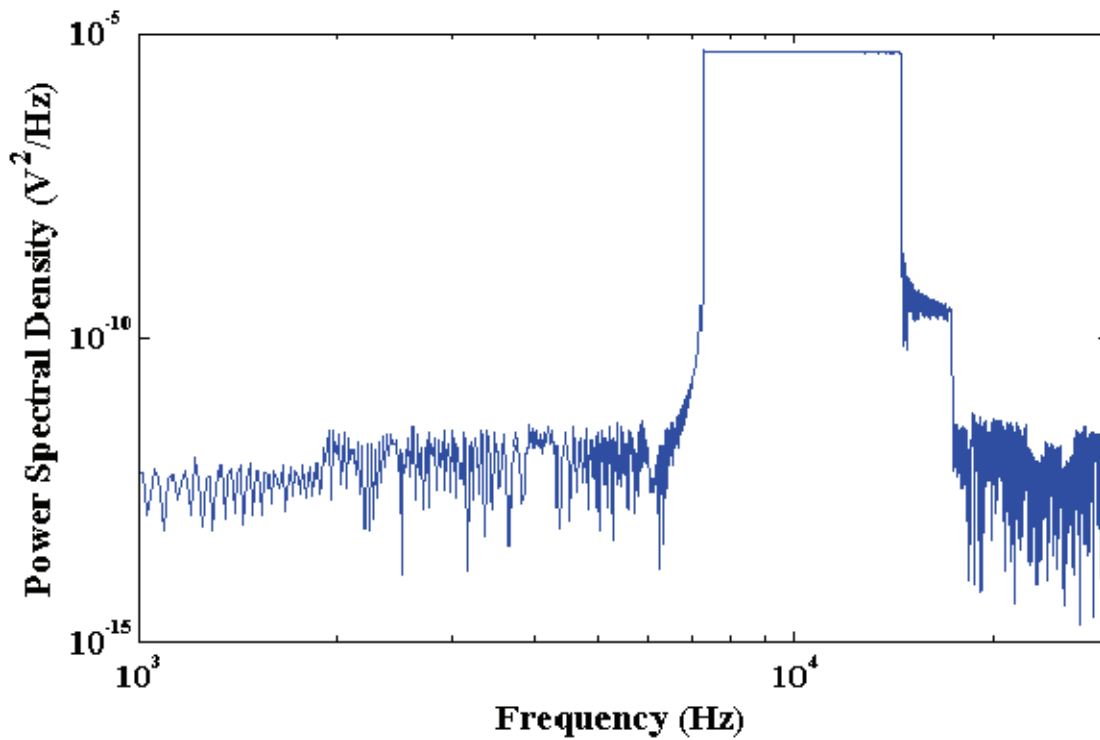


Figure D-22. Power spectral density of function generator output.

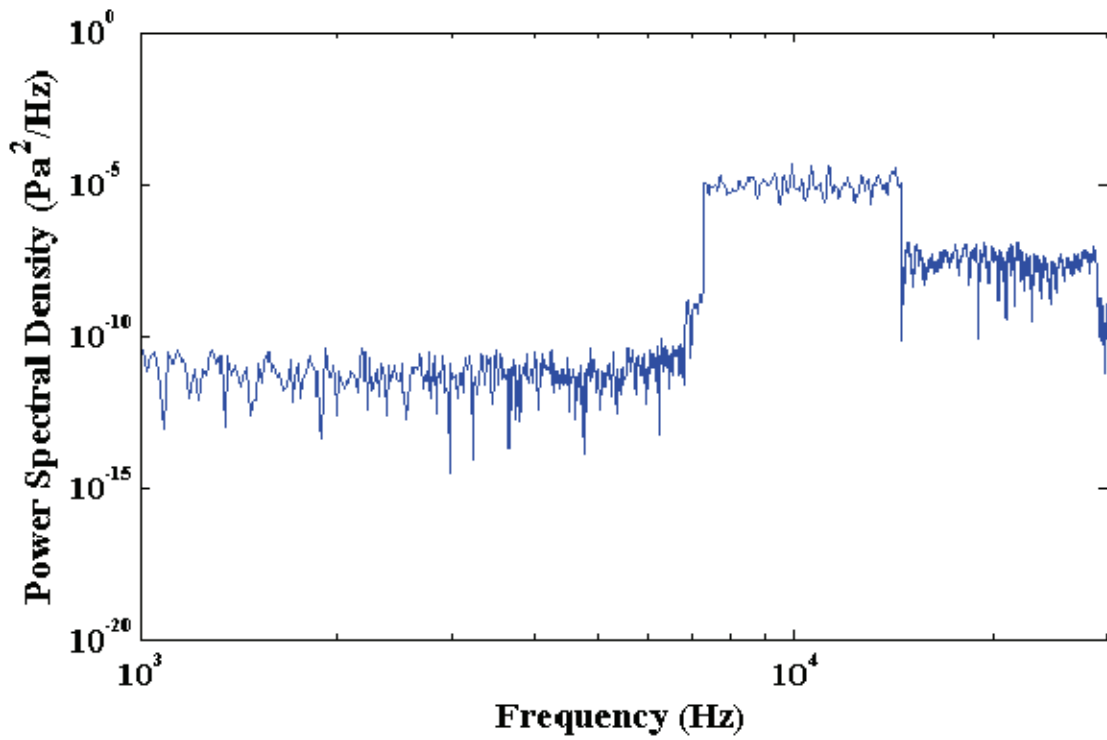


Figure D-23. Power spectral density of reference B&K microphone located at array center.

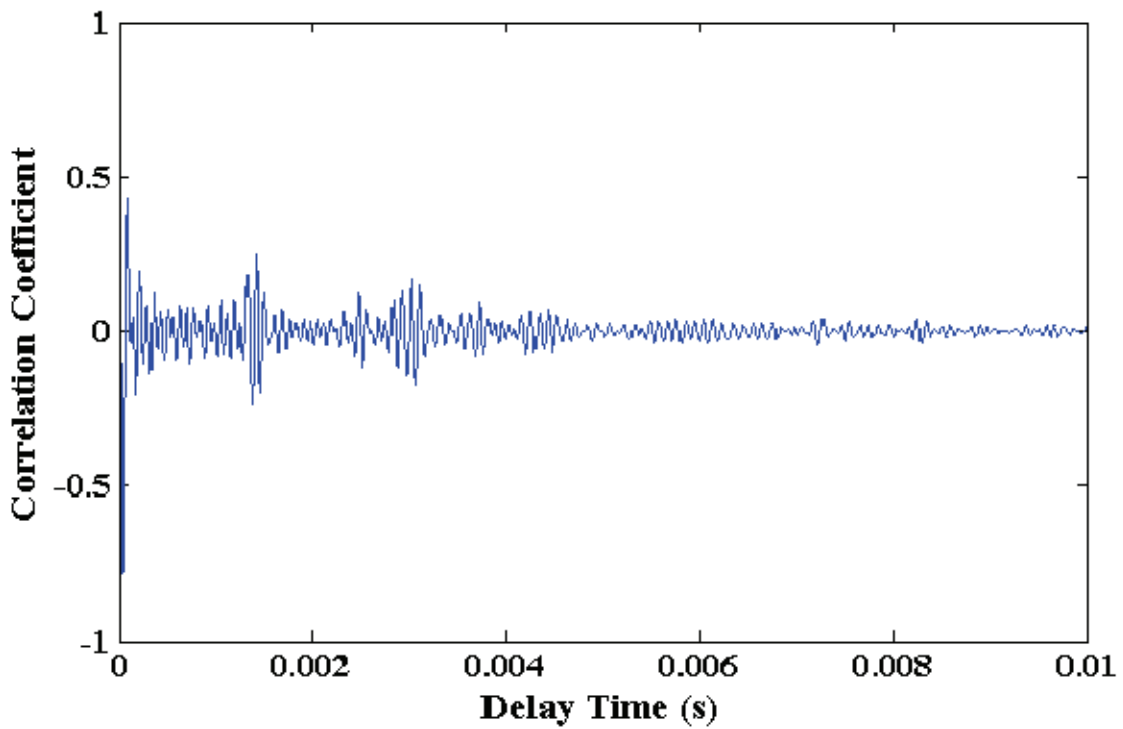


Figure D-24. B&K measurement autocorrelation function, normalized to correlation coefficient.

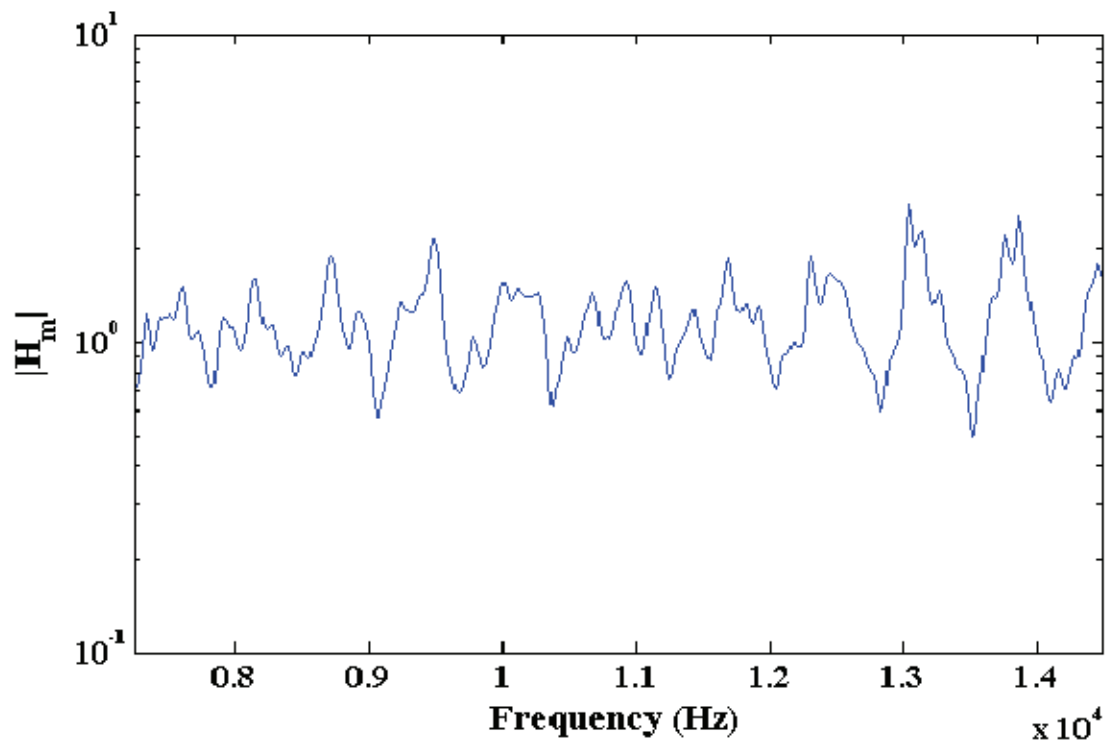


Figure D-25. Frequency response magnitude estimate for electret 1.

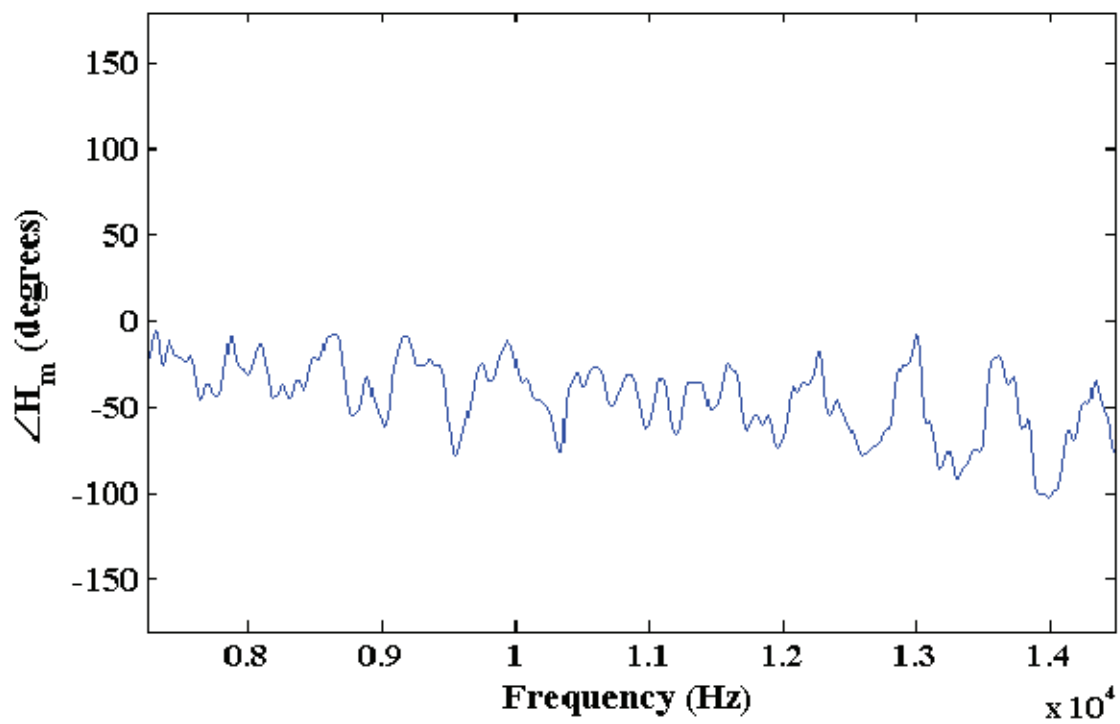


Figure D-26. Frequency response phase angle estimate for electret 1.

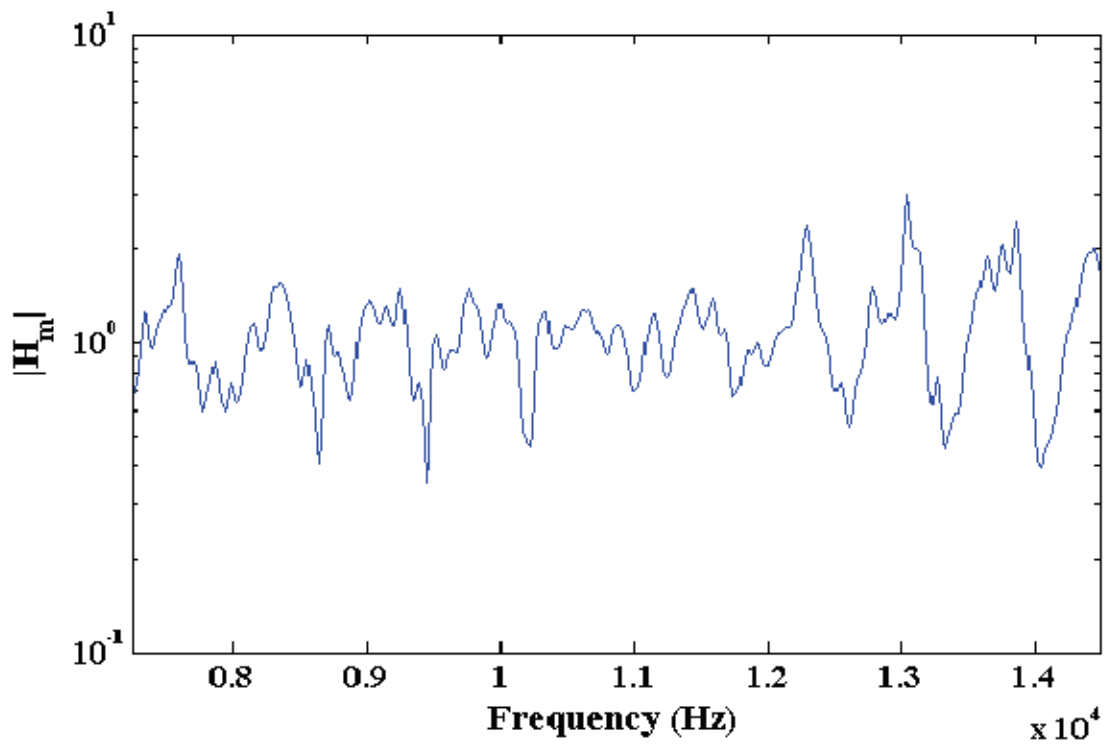


Figure D-27. Frequency response magnitude estimate for electret 63.

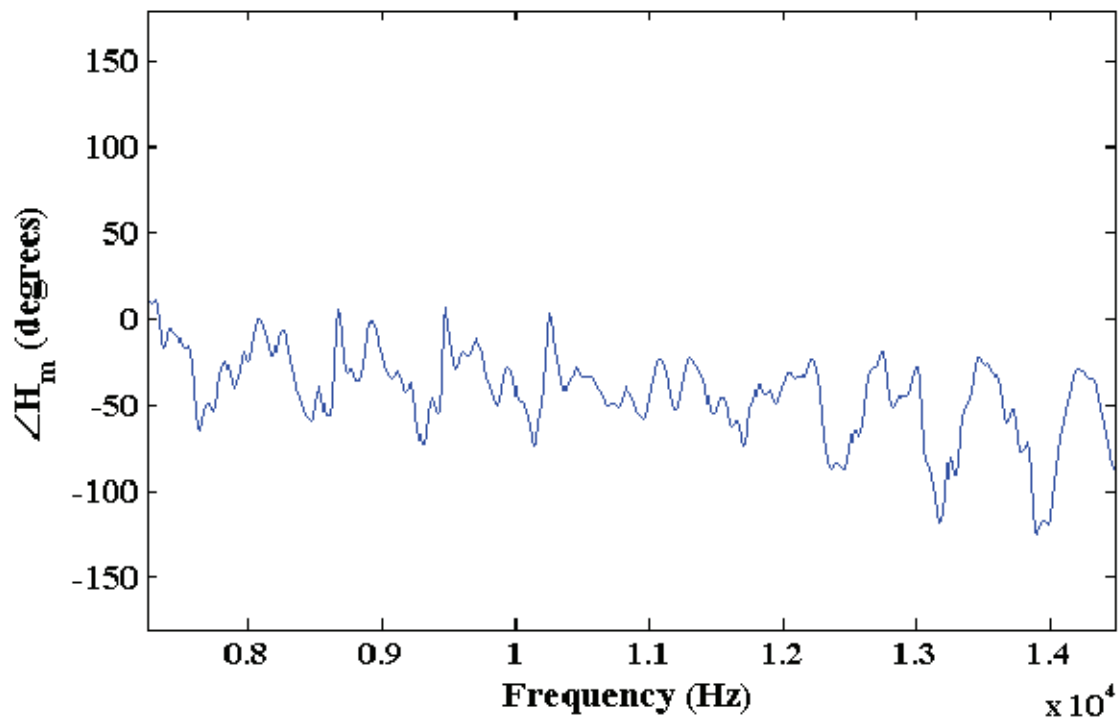


Figure D-28. Frequency response phase angle estimate for electret 63.

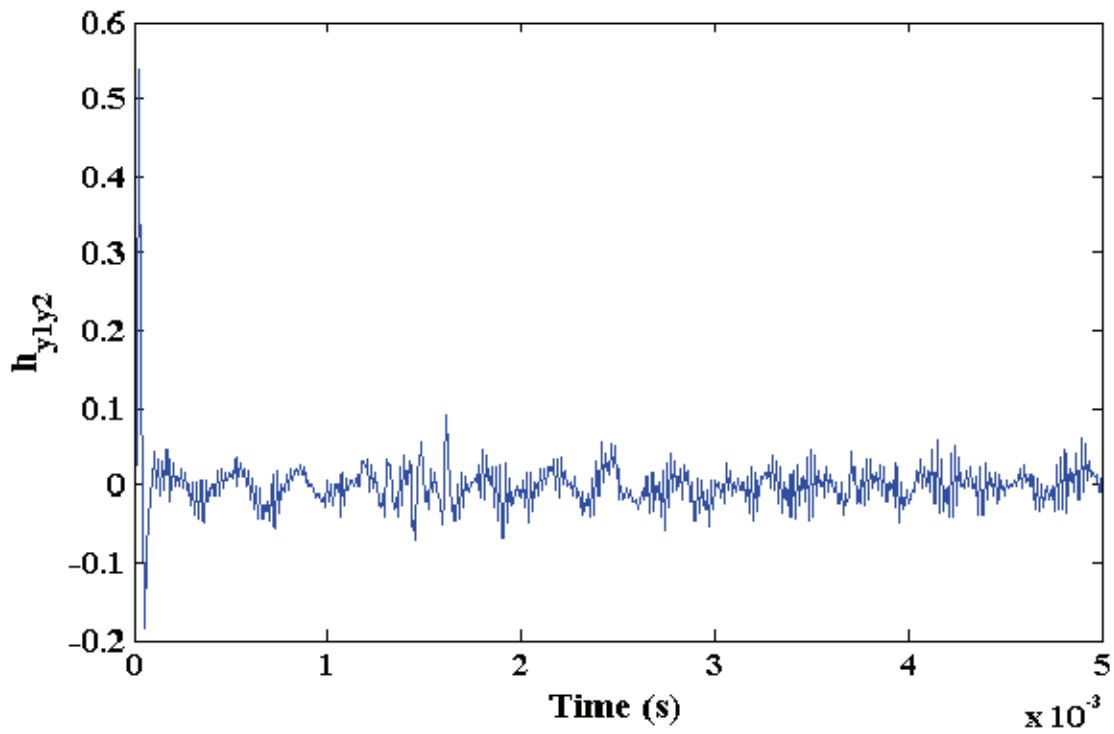


Figure D-29. Impulse response estimate between reference microphone and electret 1.

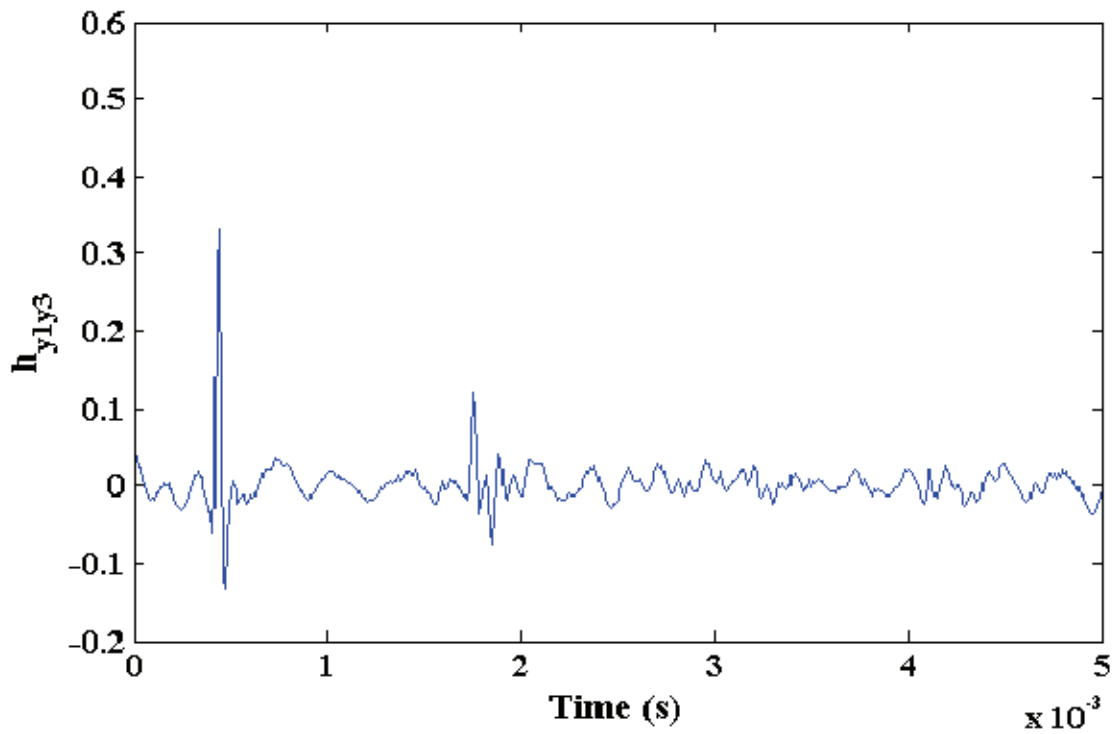


Figure D-30. Impulse response estimate between reference microphone and electret 63.

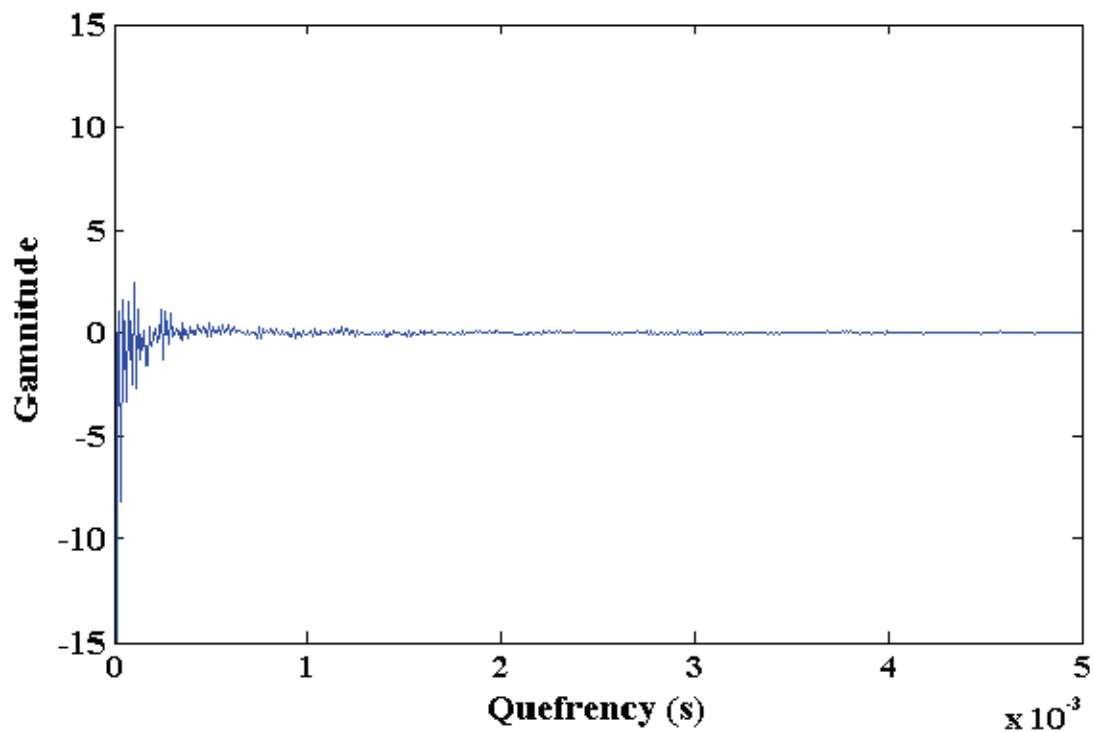


Figure D-31. Cepstrum estimate between reference microphone and electret 1.

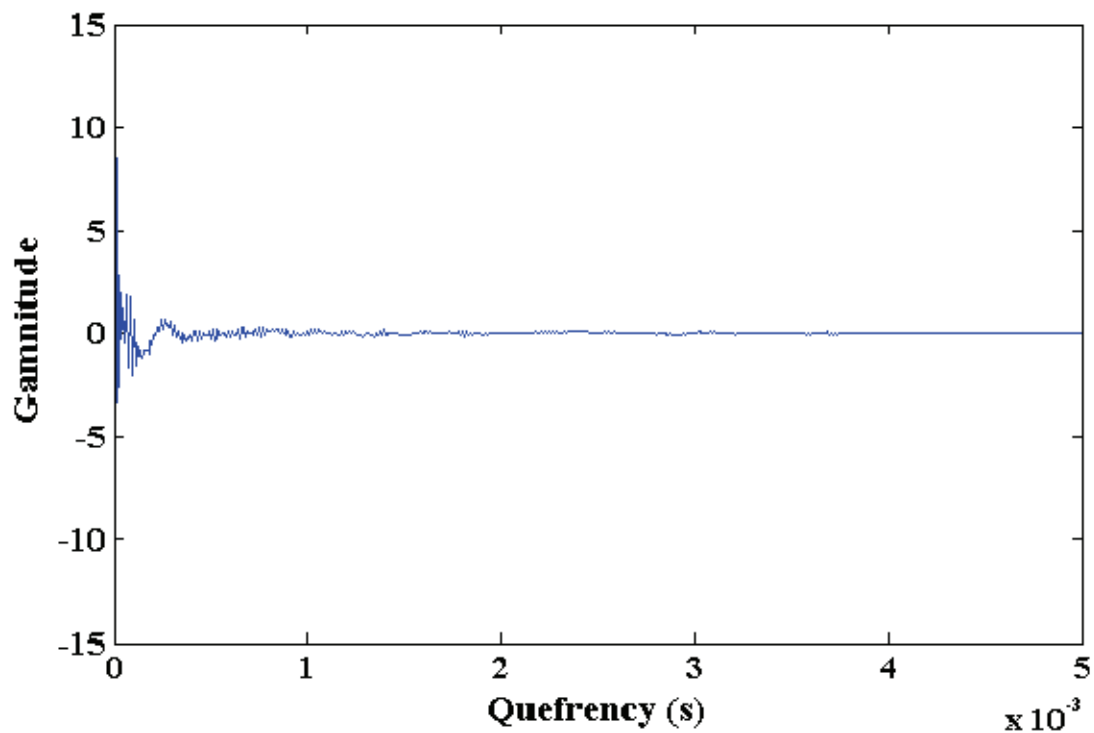


Figure D-32. Cepstrum estimate between reference microphone and electret 63.

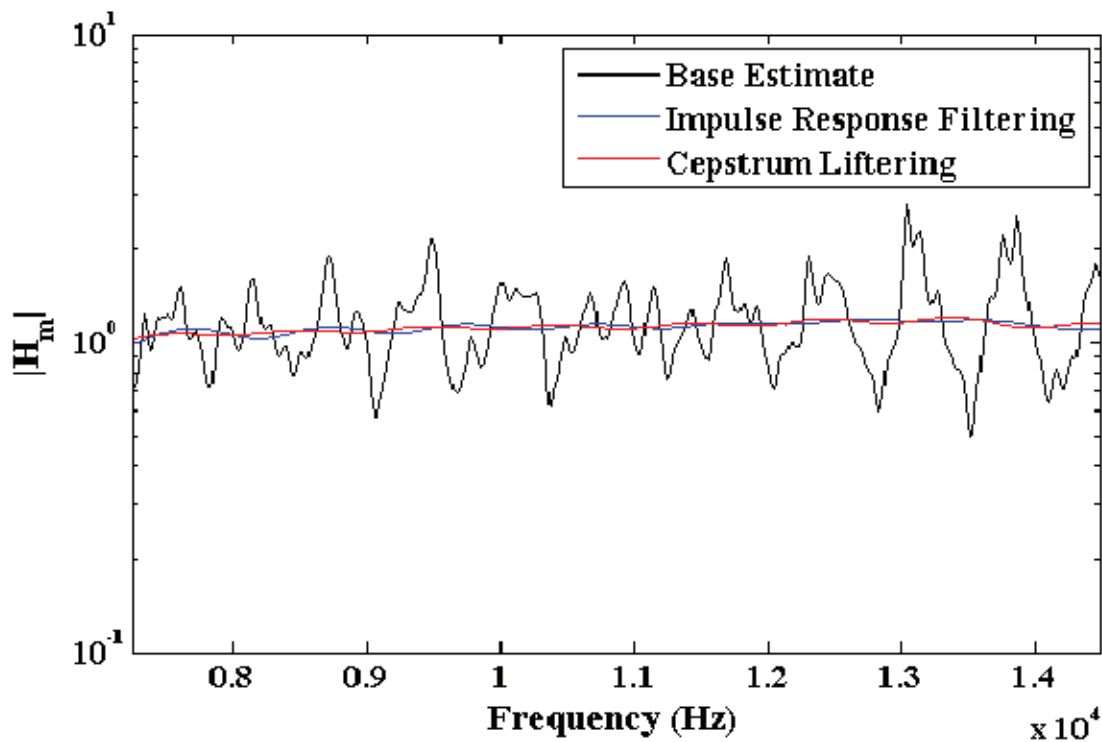


Figure D-33. FRF magnitude estimates for electret 1 comparing different methods.

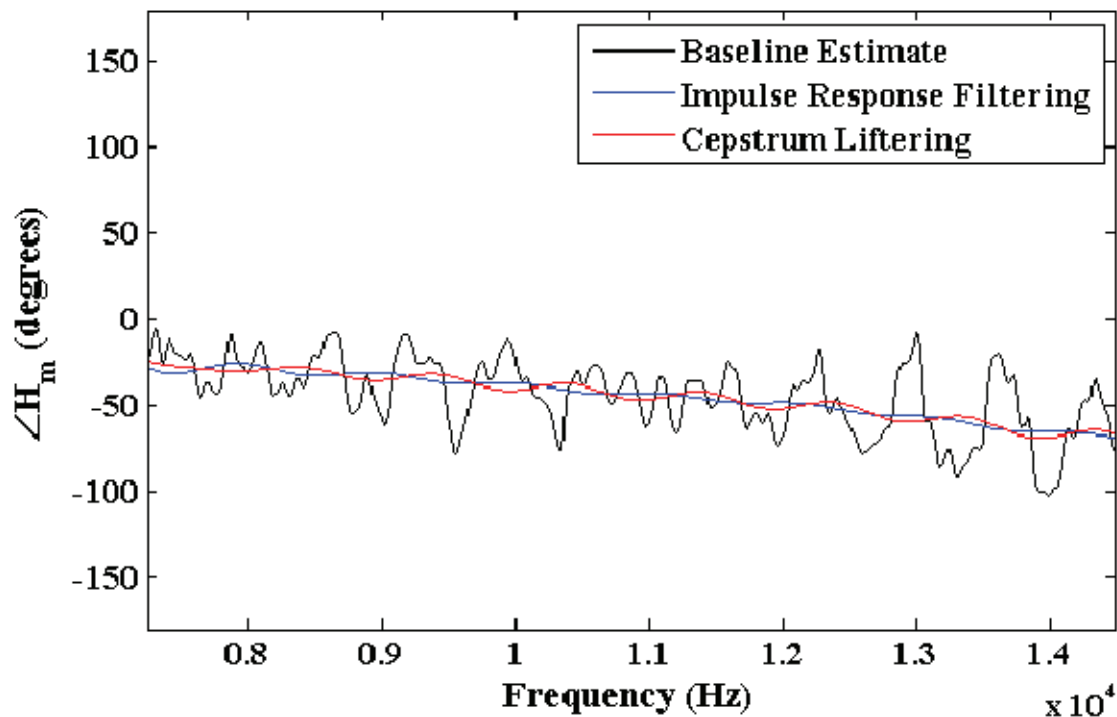


Figure D-34. FRF phase estimates for electret 1 comparing different methods.

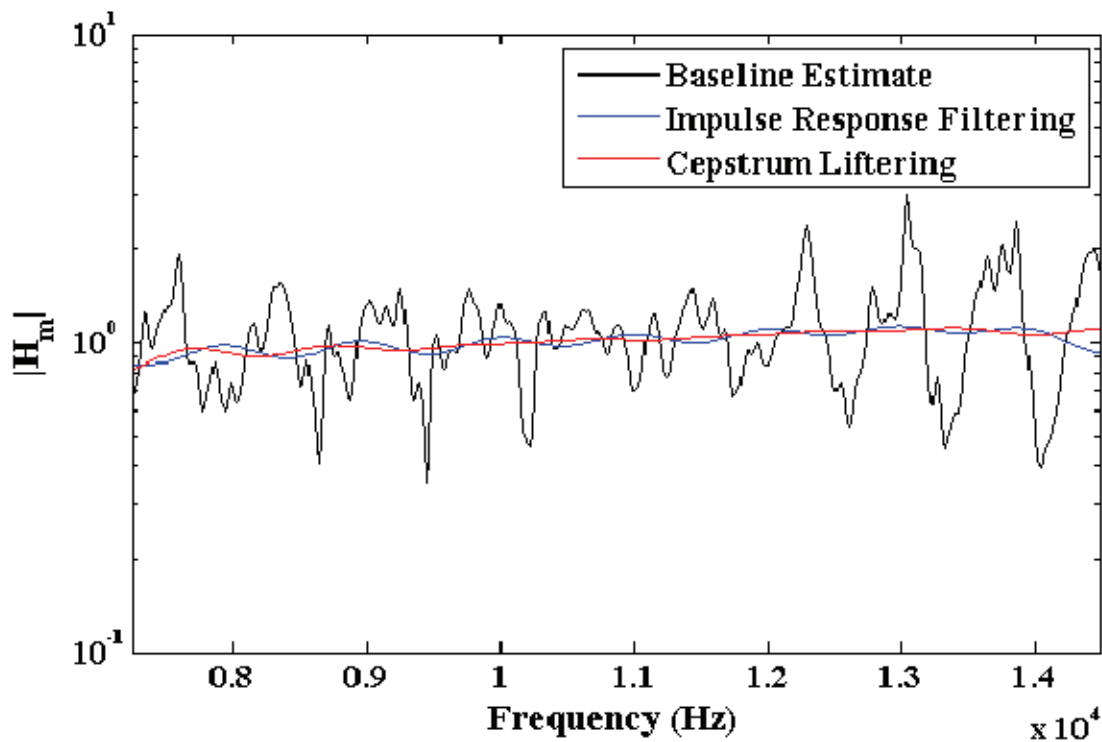


Figure D-35. FRF magnitude estimates for electret 63 comparing different methods.

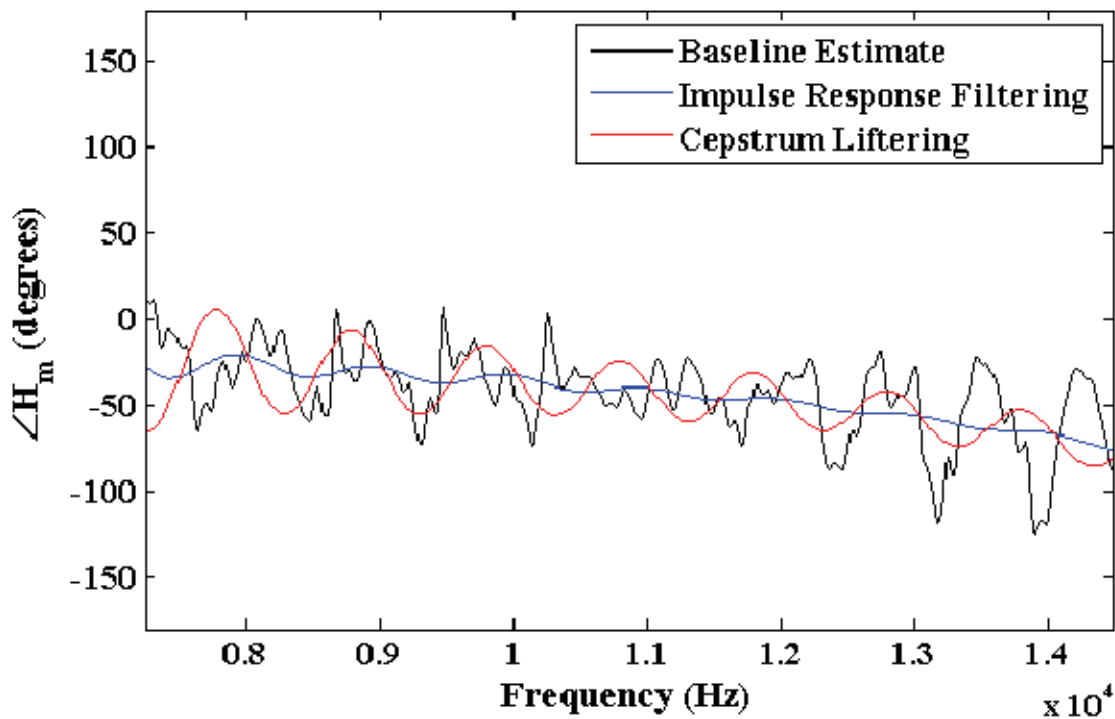


Figure D-36. FRF phase estimates for electret 63 comparing different methods.

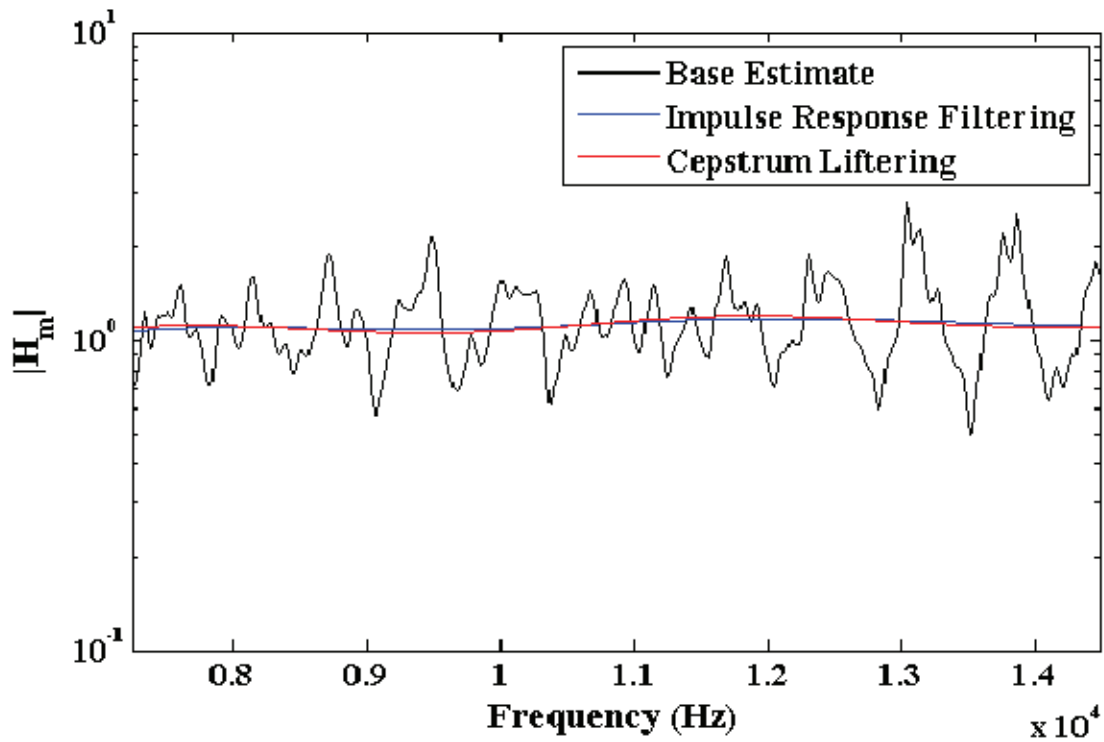


Figure D-37. FRF magnitude estimates for electret 1, 0.25 ms window.

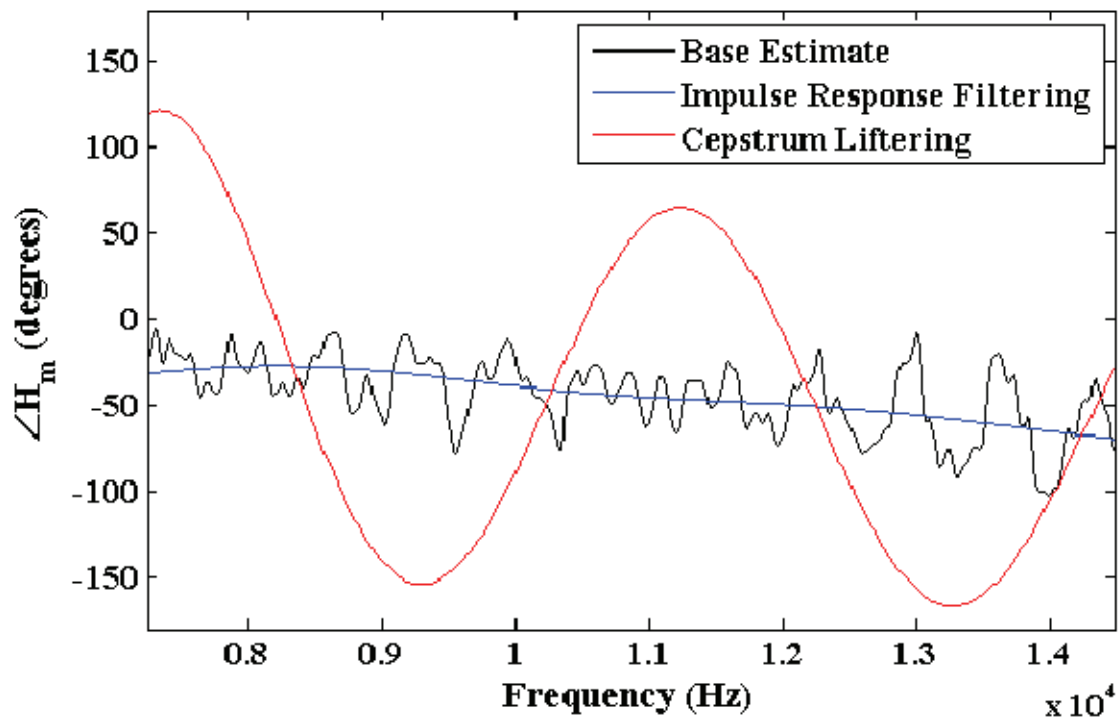


Figure D-38. FRF phase estimates for electret 1, 0.25 ms window.

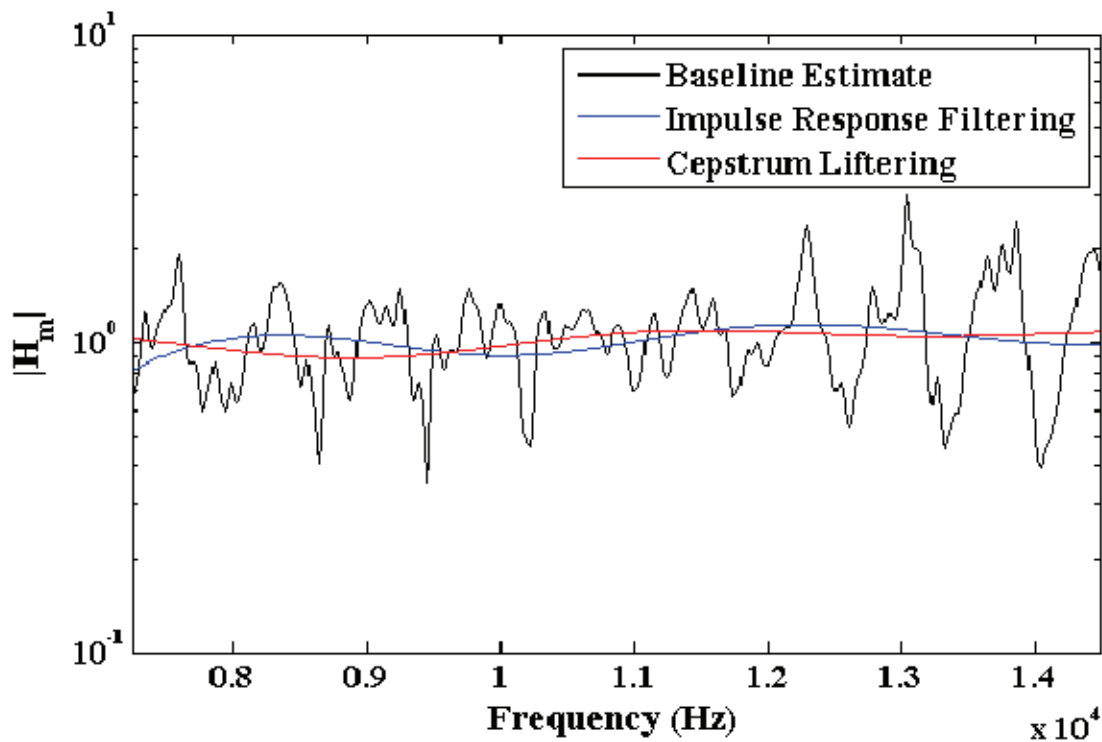


Figure D-39. FRF magnitude estimates for electret 63, 0.25 ms window.

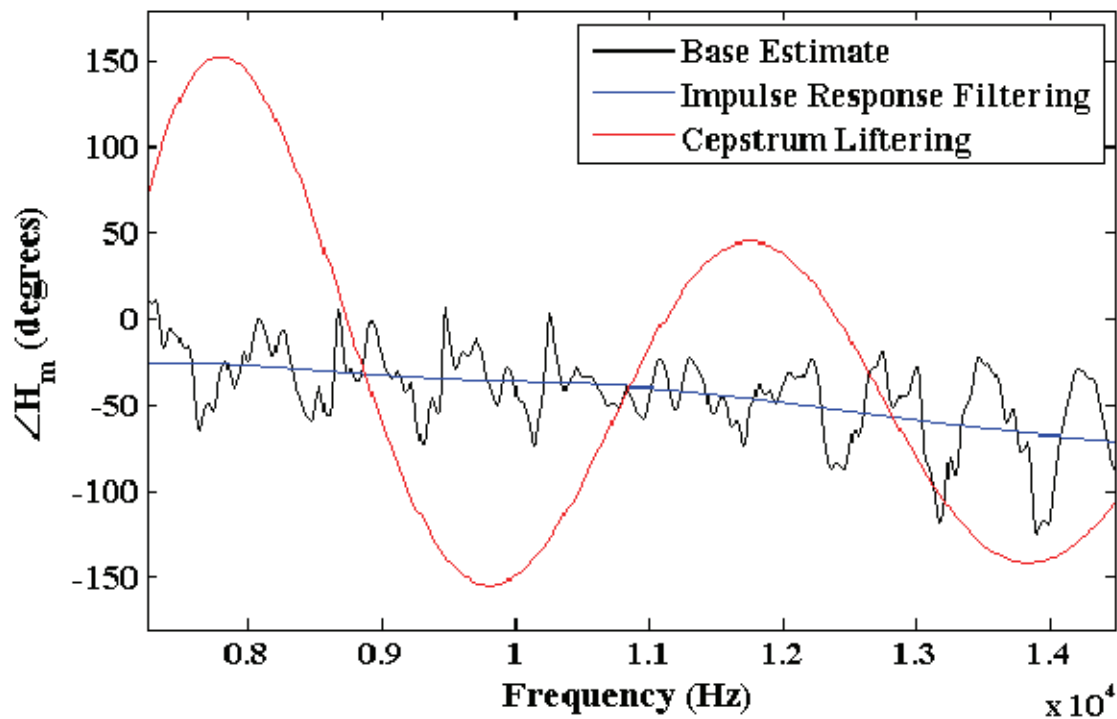


Figure D-40. FRF phase estimates for electret 63, 0.25 ms window.

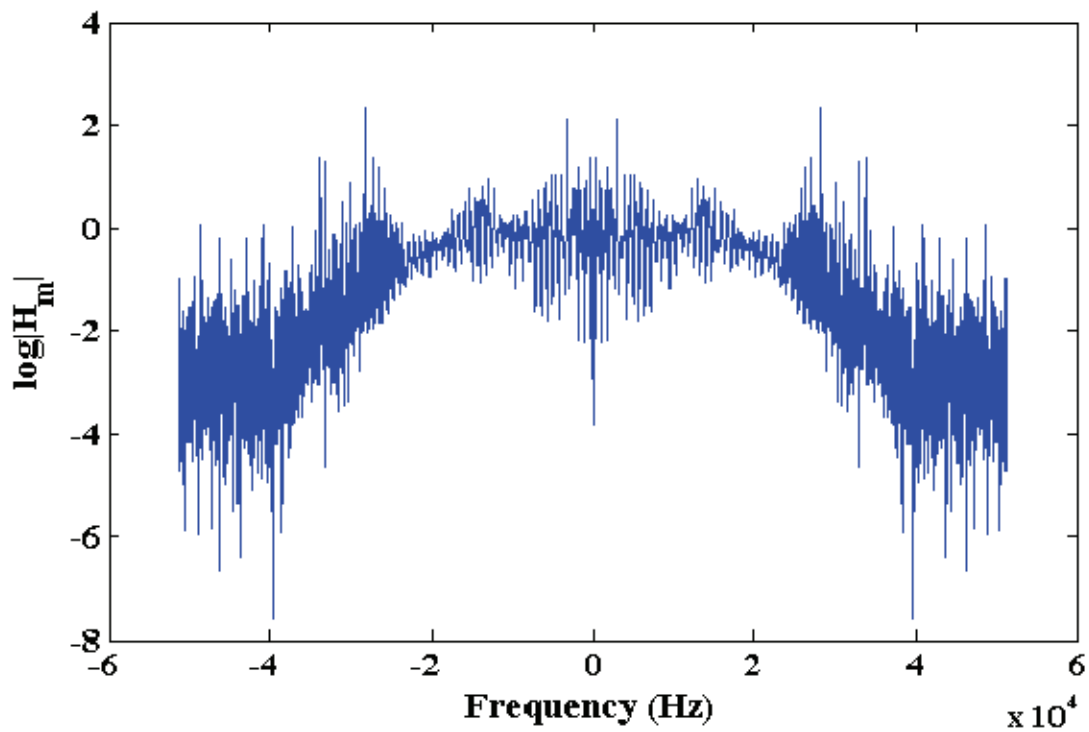


Figure D-41. Logarithm of the two-sided FRF magnitude between B&K and electret 63.

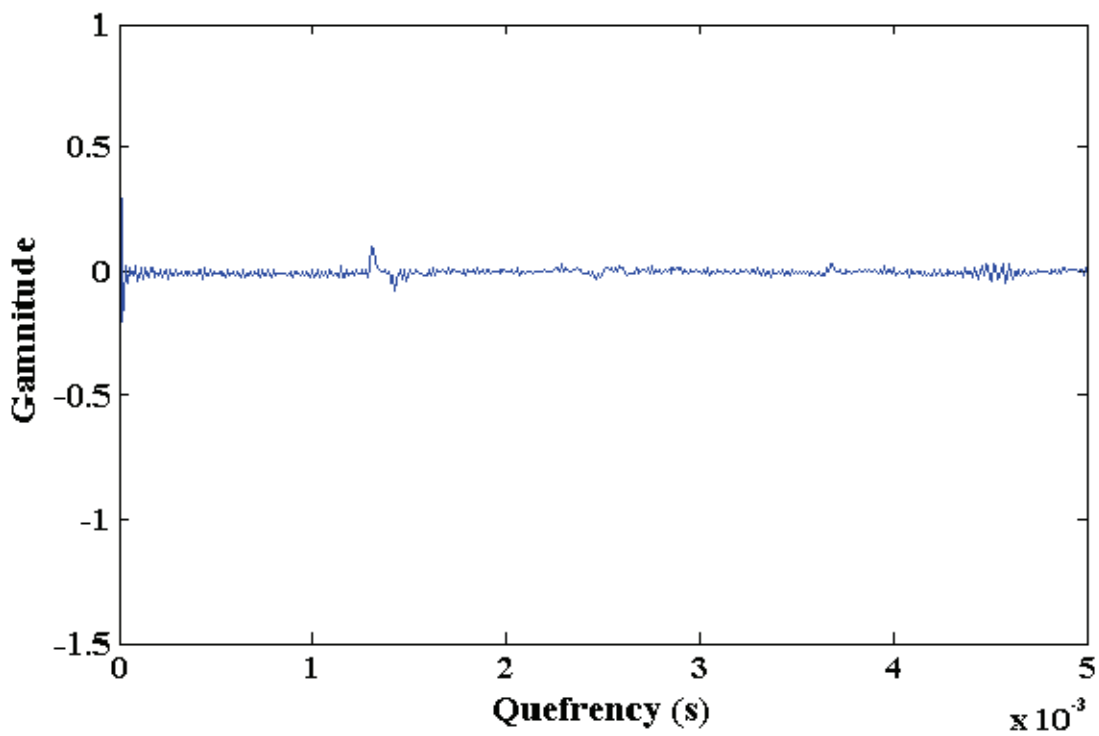


Figure D-42. Inverse Fourier transform of logarithmic magnitude spectrum from Figure D-41.

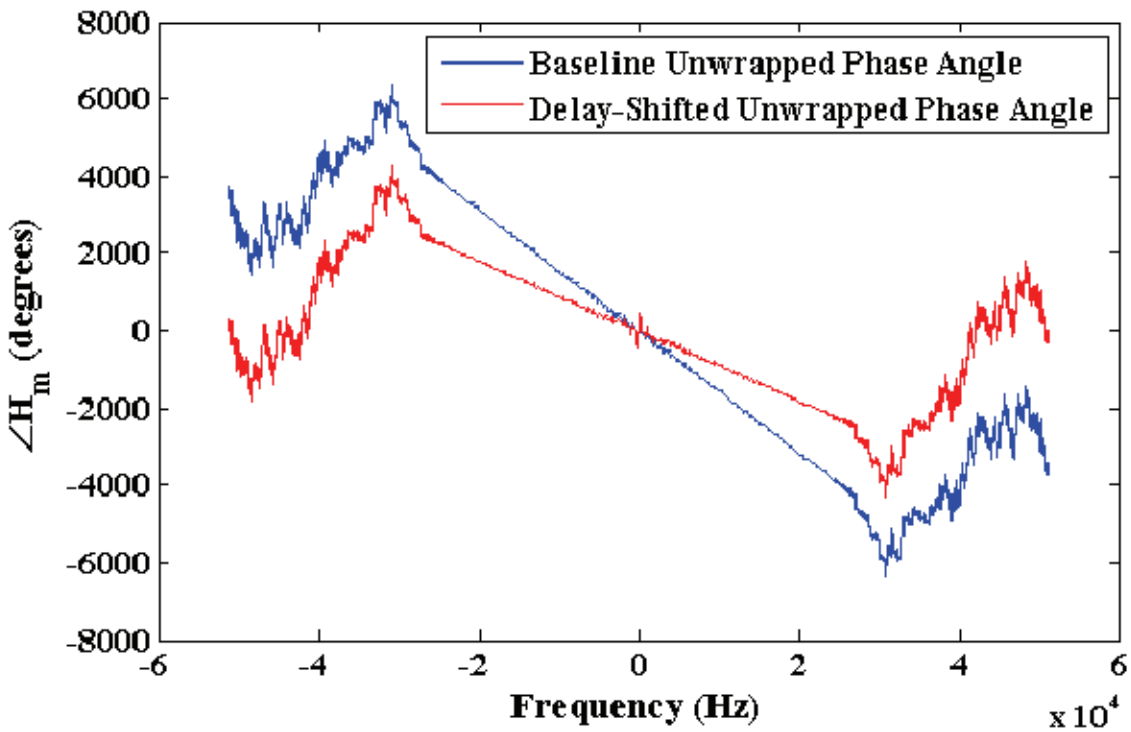


Figure D-43. Unwrapped two-sided FRF phase angle from B&K to electret 63.

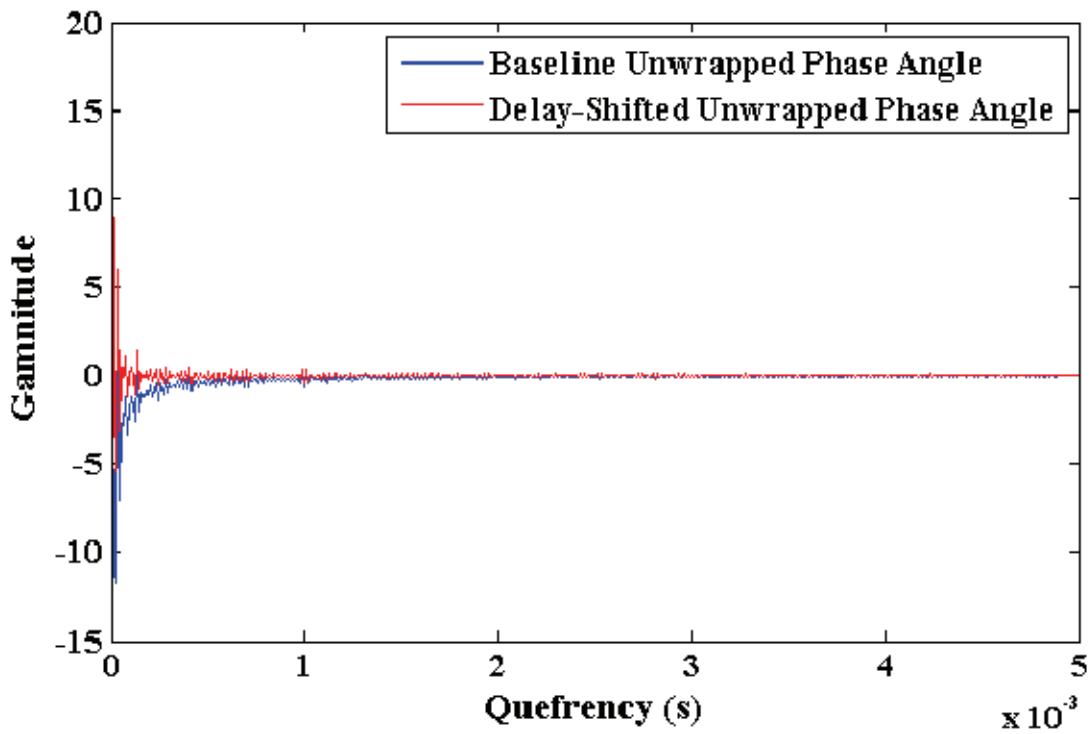


Figure D-44. Inverse Fourier transform of imaginary phase angle from Figure D-43.

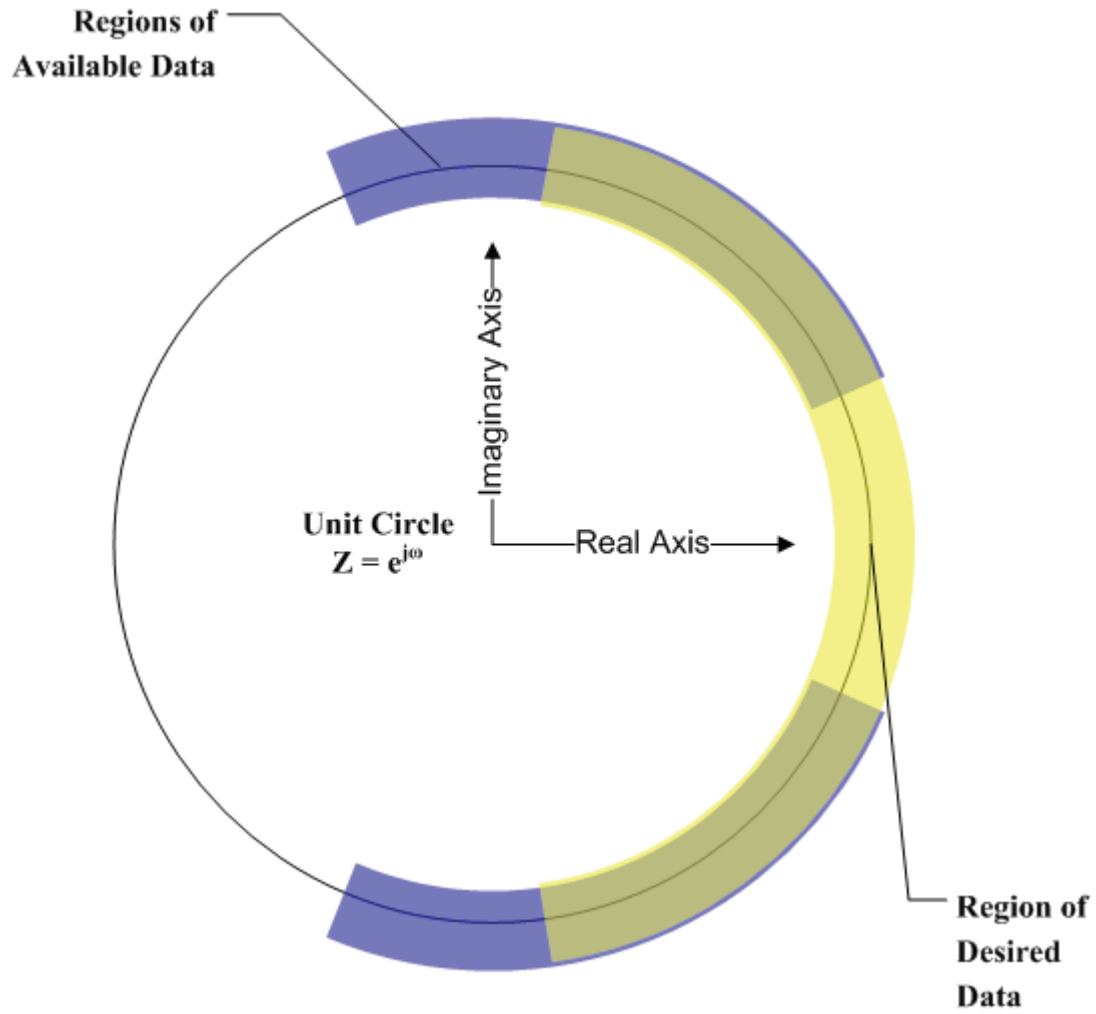


Figure D-45. Illustration of available FRF data (blue) and desired FRF calibration curve (yellow).

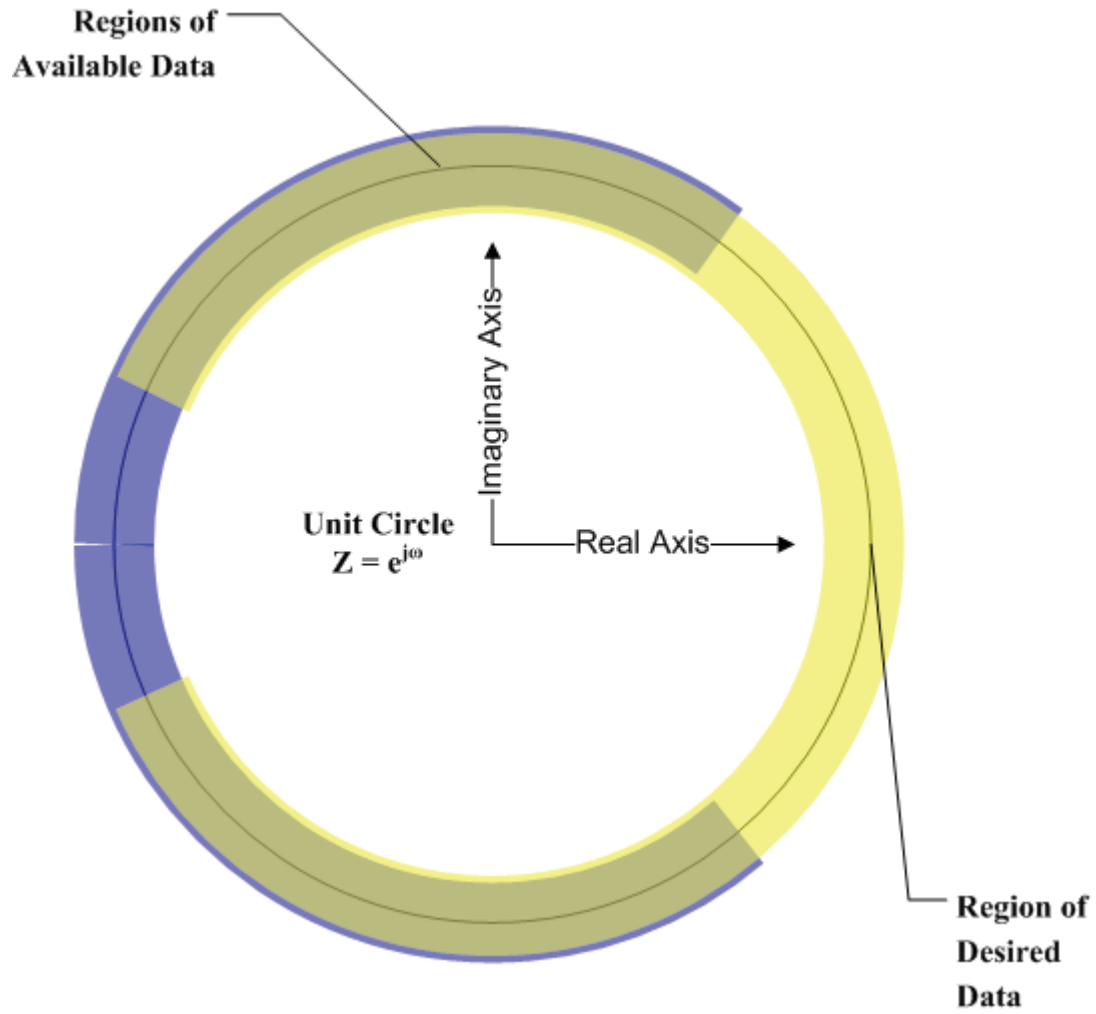


Figure D-46. Illustration of available FRF data and desired FRF calibration curve when decimated by 2.

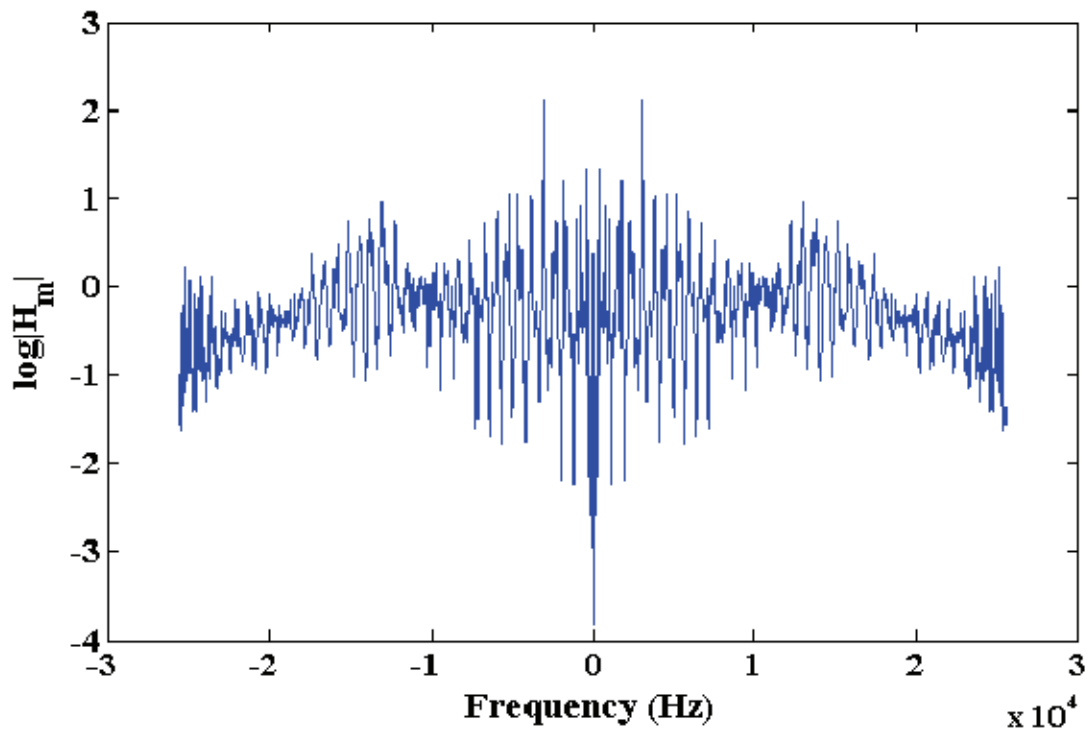


Figure D-47. Downsampled logarithm of two-sided FRF from B&K microphone to electret 63.

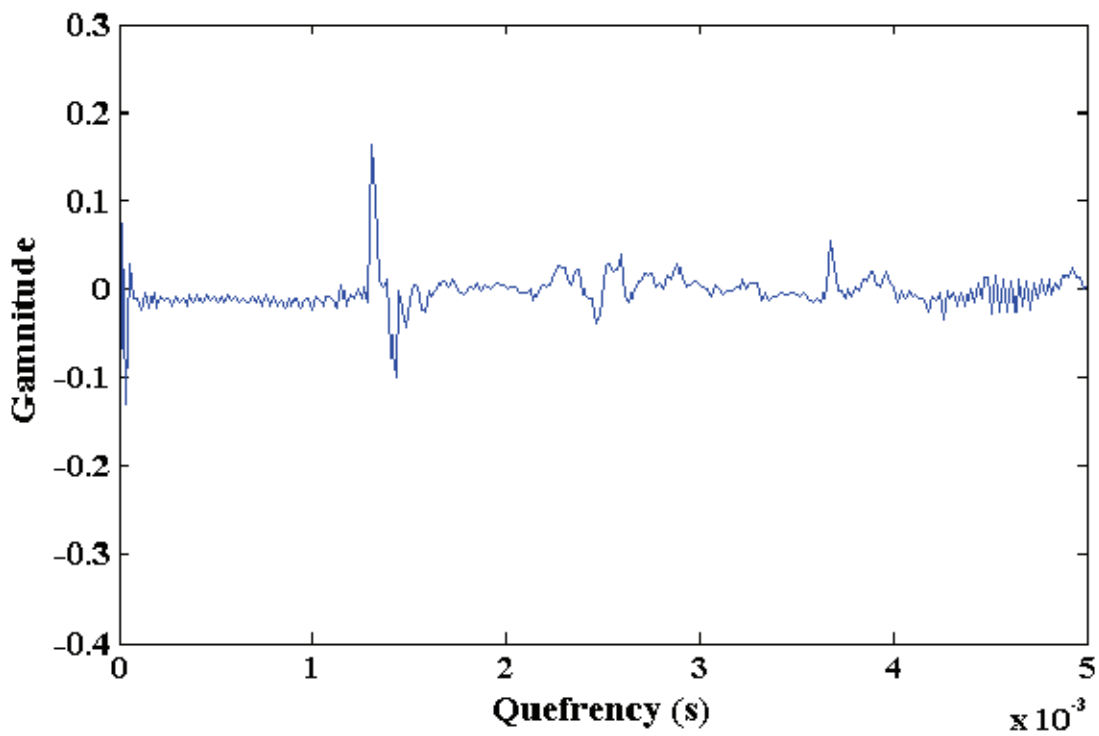


Figure D-48. Cepstrum corresponding to Figure D-47.

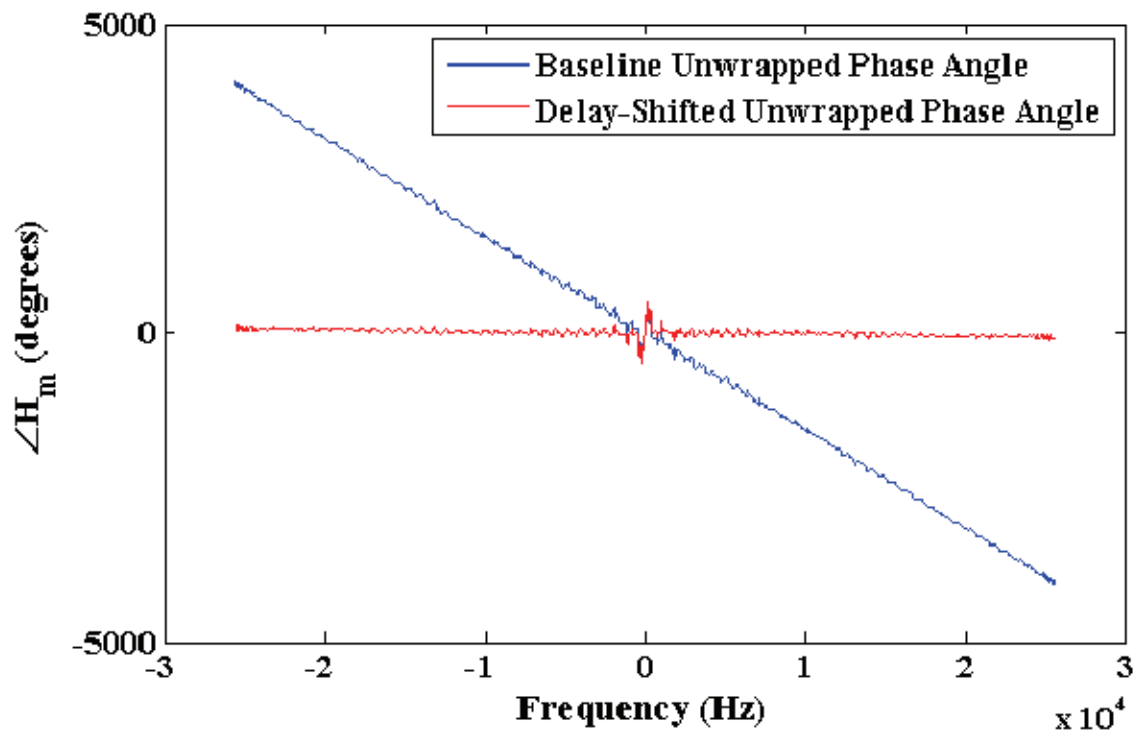


Figure D-49. Unwrapped downsampled phase angle from B&K to electret 63.

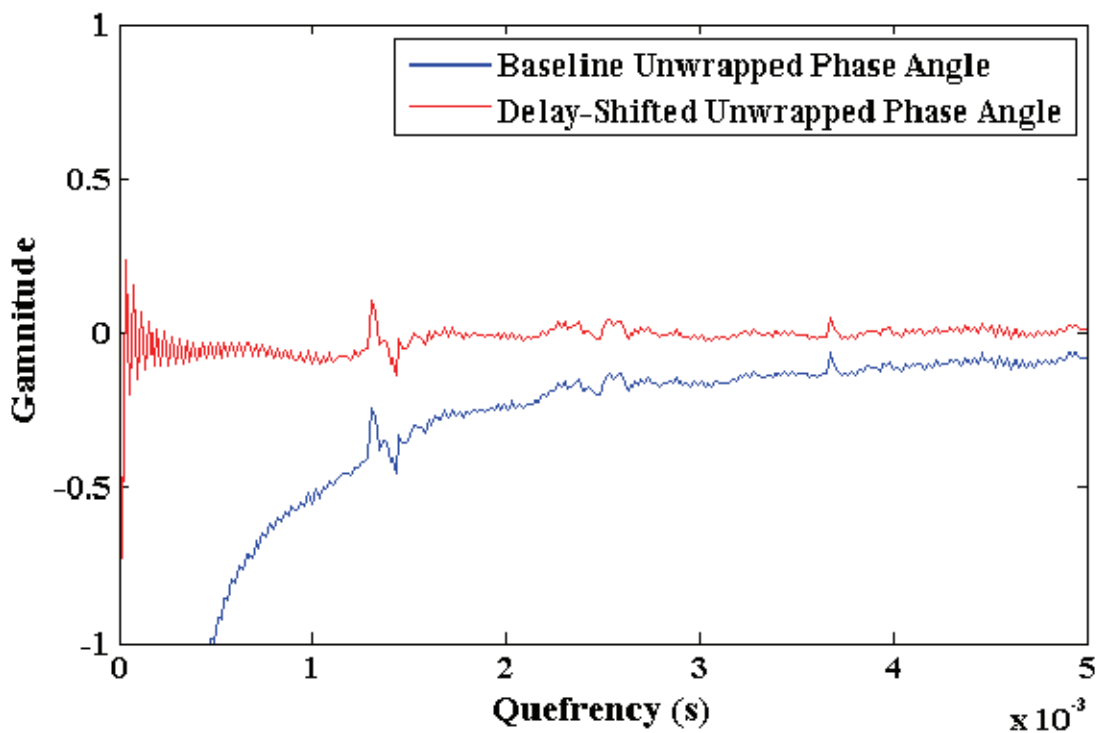


Figure D-50. Cepstrum corresponding to Figure D-49.

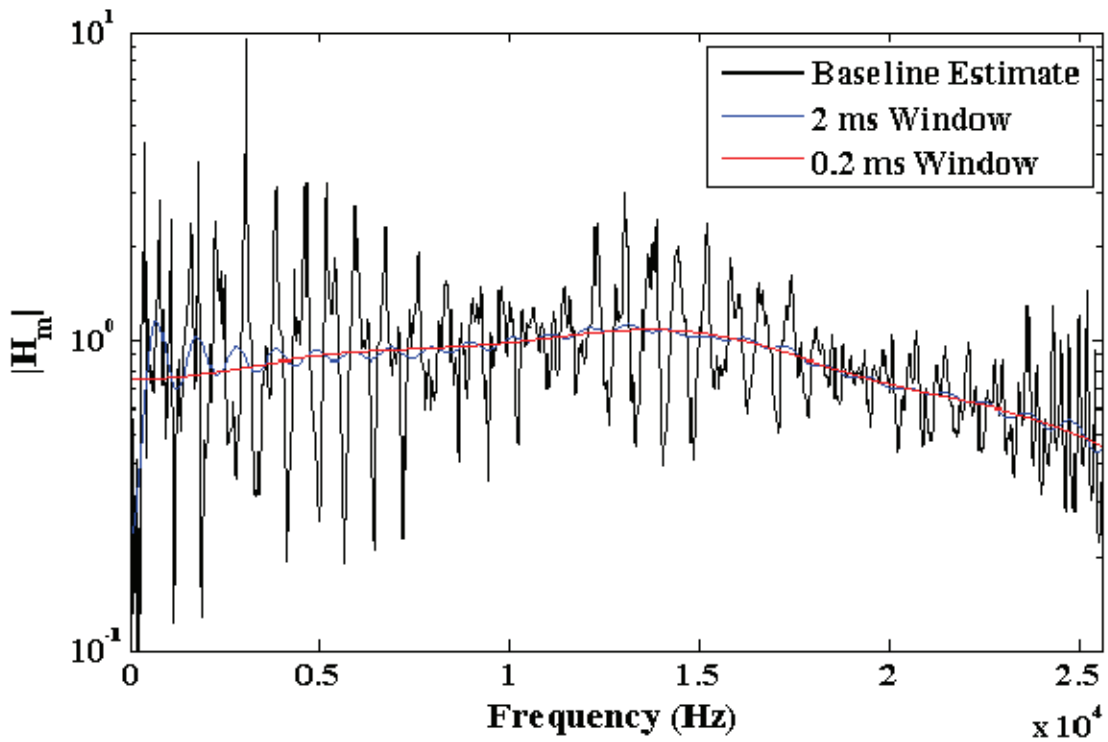


Figure D-51. Window length effects for original electret 63 FRF magnitude estimate.

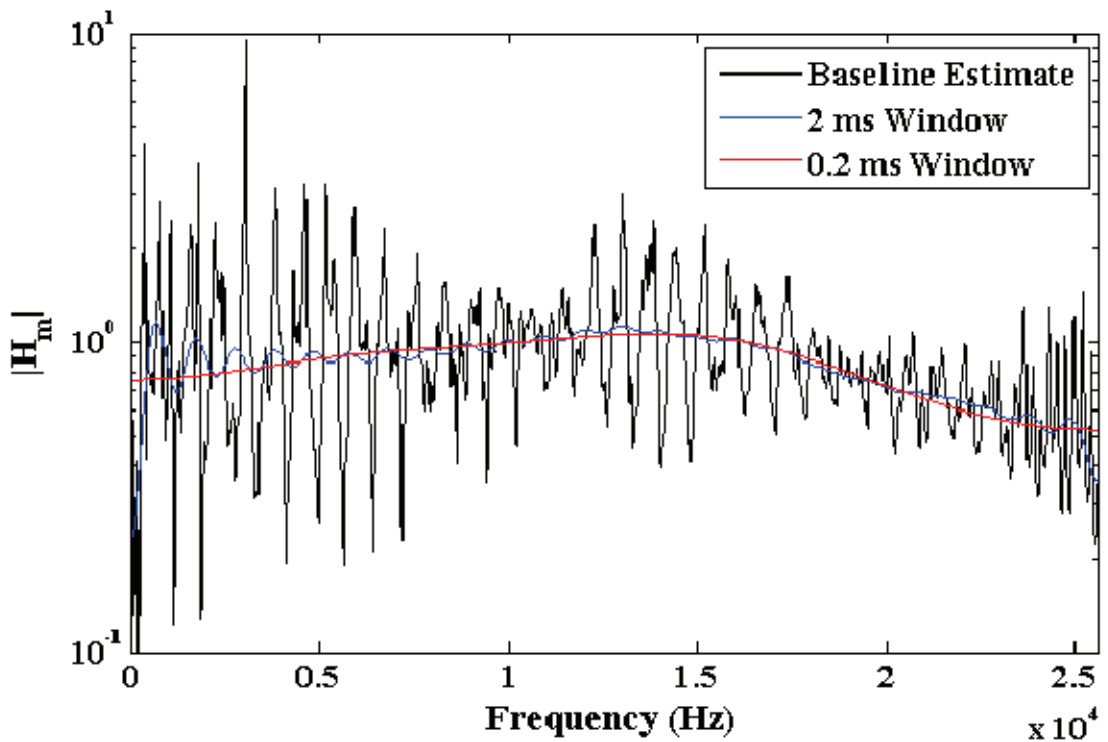


Figure D-52. Window length effects for downsampled electret 63 FRF magnitude estimate.

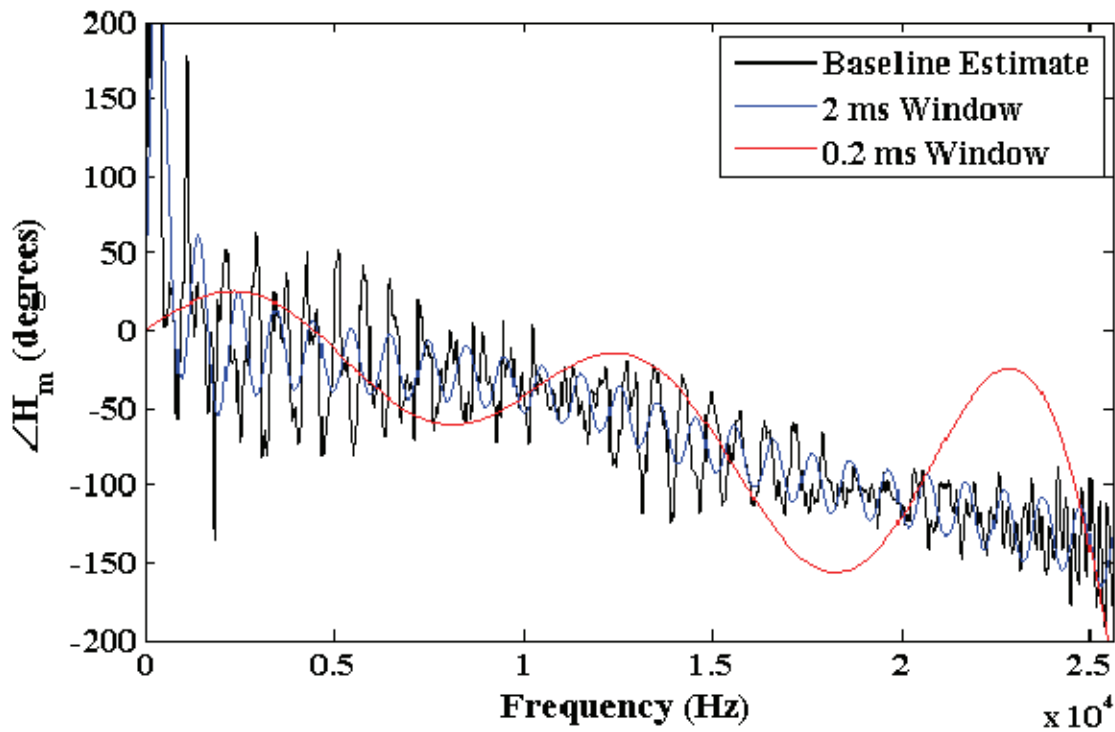


Figure D-53. Window length effects for original electret 63 FRF phase estimate.

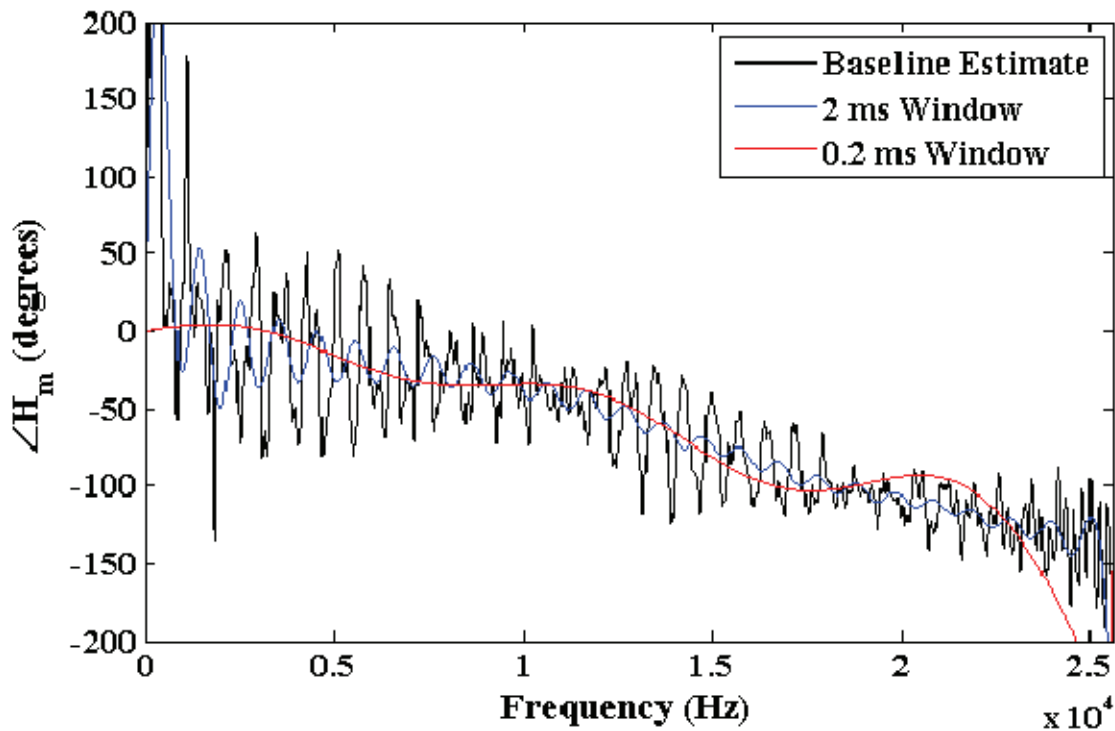


Figure D-54. Window length effects for downsampled electret 63 FRF phase estimate.

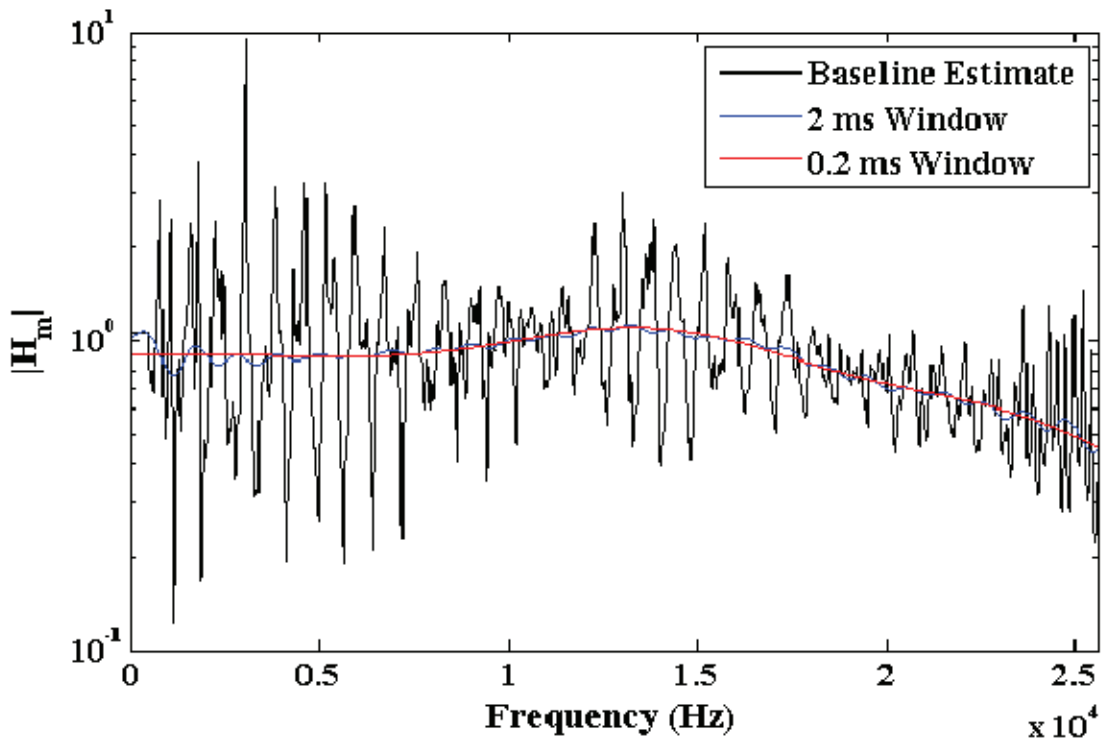


Figure D-55. Low-frequency fit effect for original electret 63 FRF magnitude estimate.

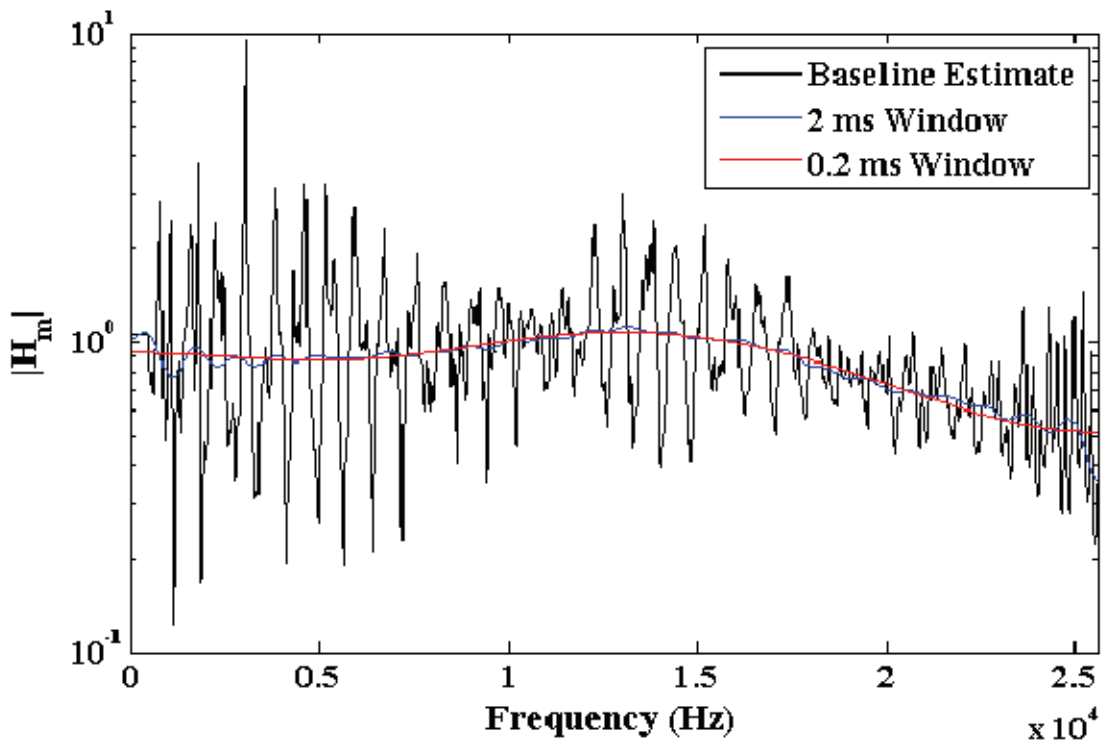


Figure D-56. Low-frequency fit effects for downsampled electret 63 FRF magnitude estimate.

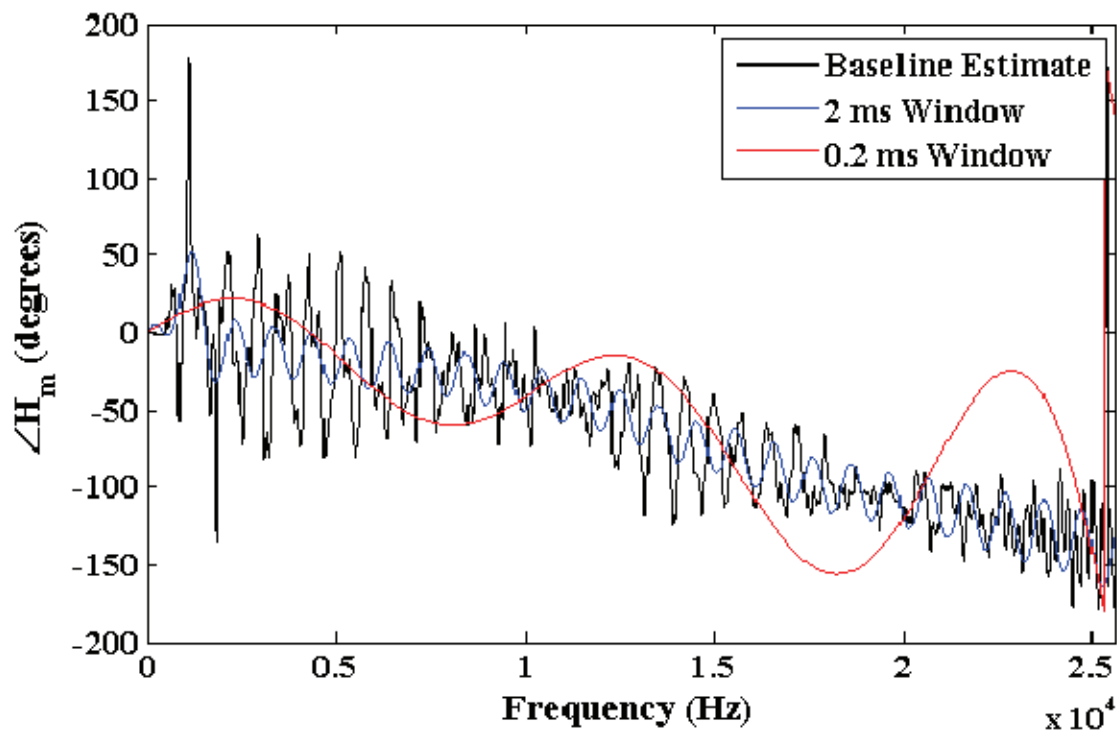


Figure D-57. Low-frequency fit effects for original electret 63 FRF phase estimate.

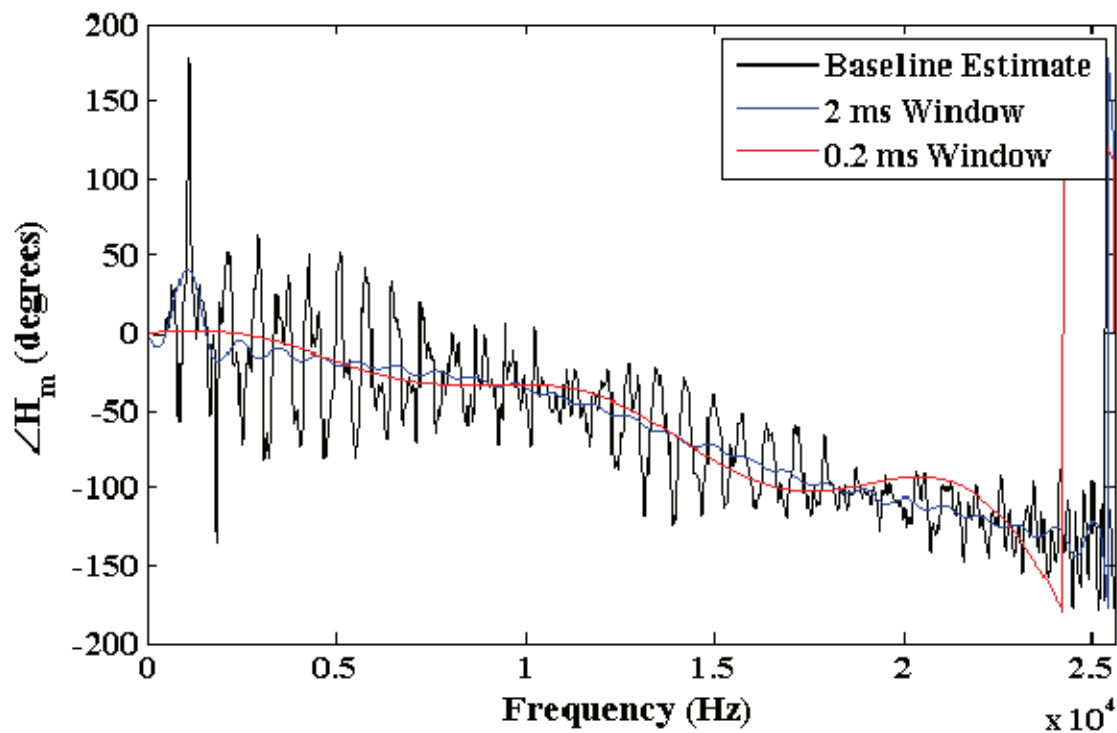


Figure D-58. Low-frequency fit effects for downsampled electret 63 FRF phase estimate.

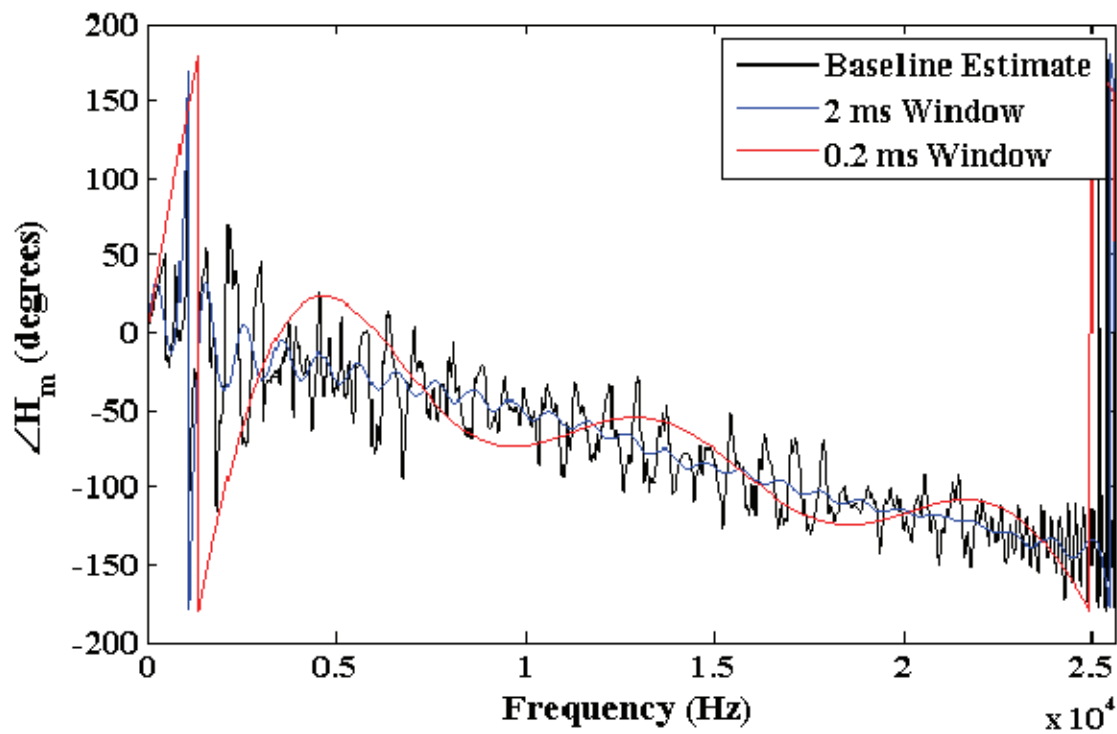


Figure D-59. Electret 43 phase angle estimates.

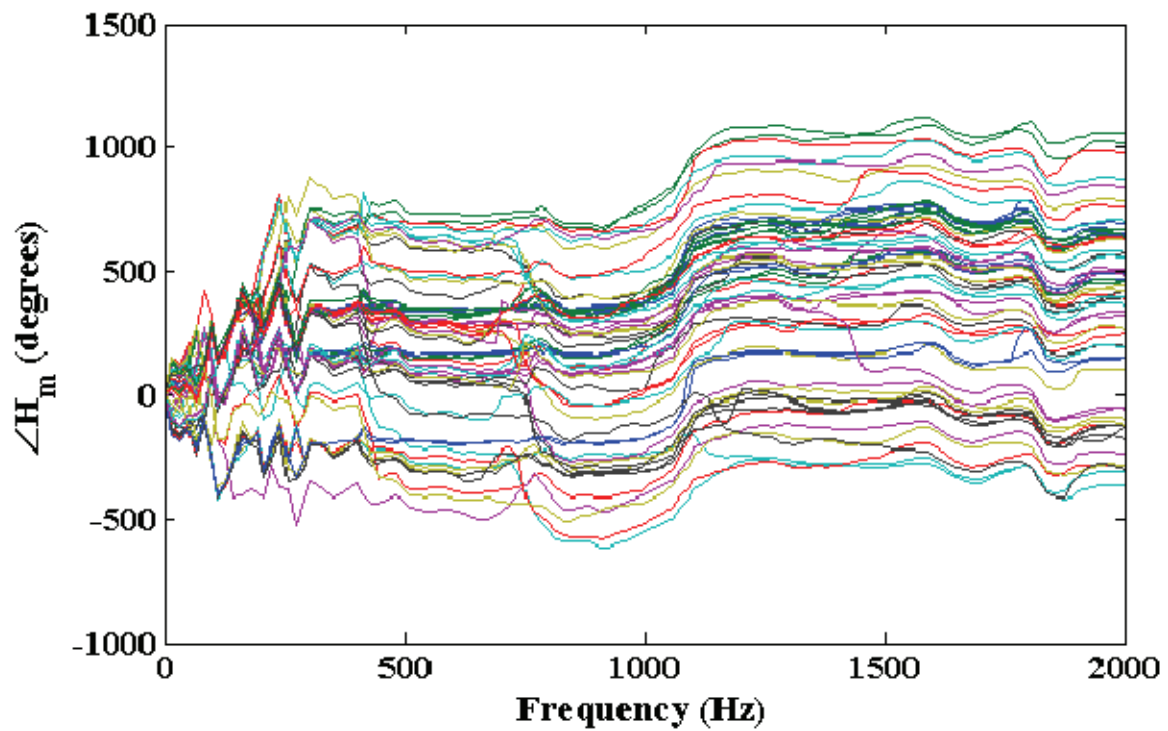


Figure D-60. Plot of phase angles for electrets 1 through 63.

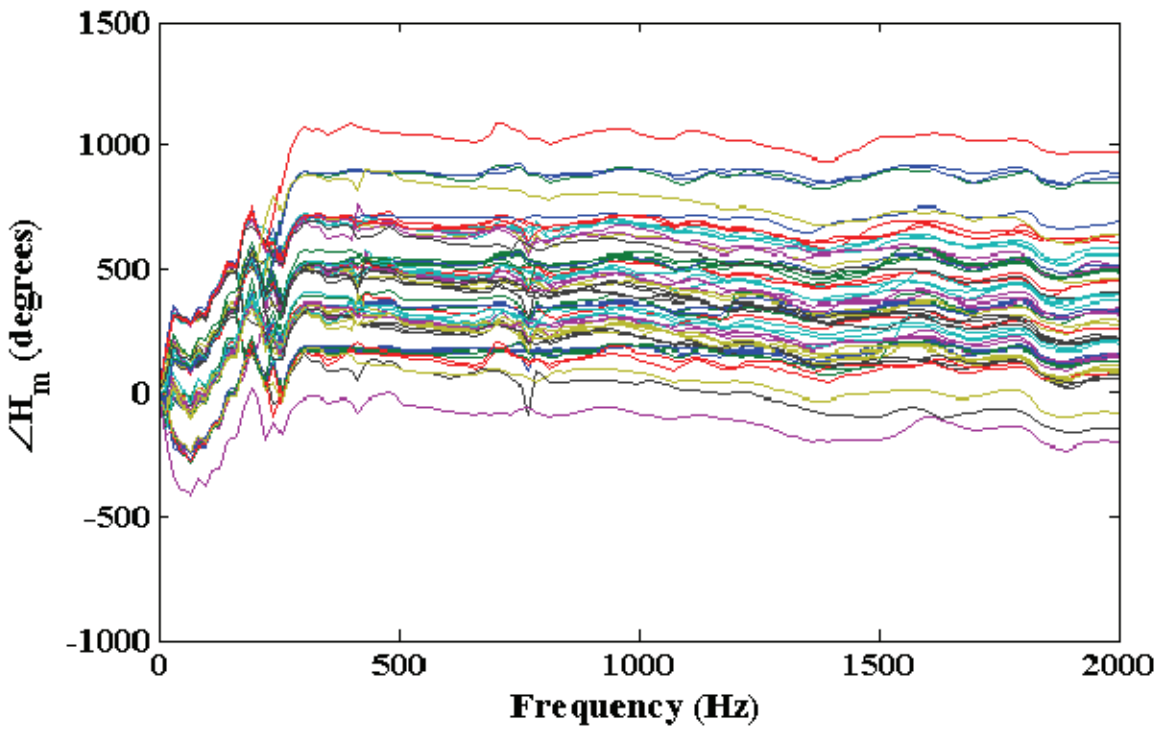


Figure D-61. Phase angles for electrets 1 through 63, additional acoustic treatment is applied.

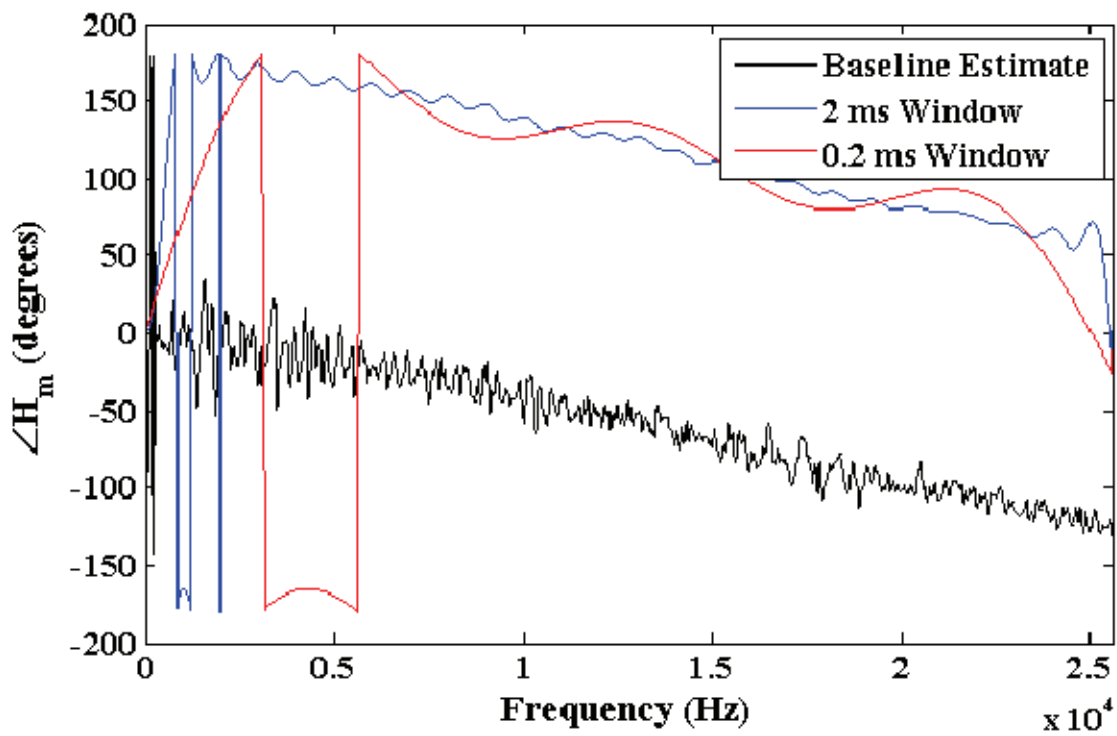


Figure D-62. Phase angle estimate for an acoustically-treated case.

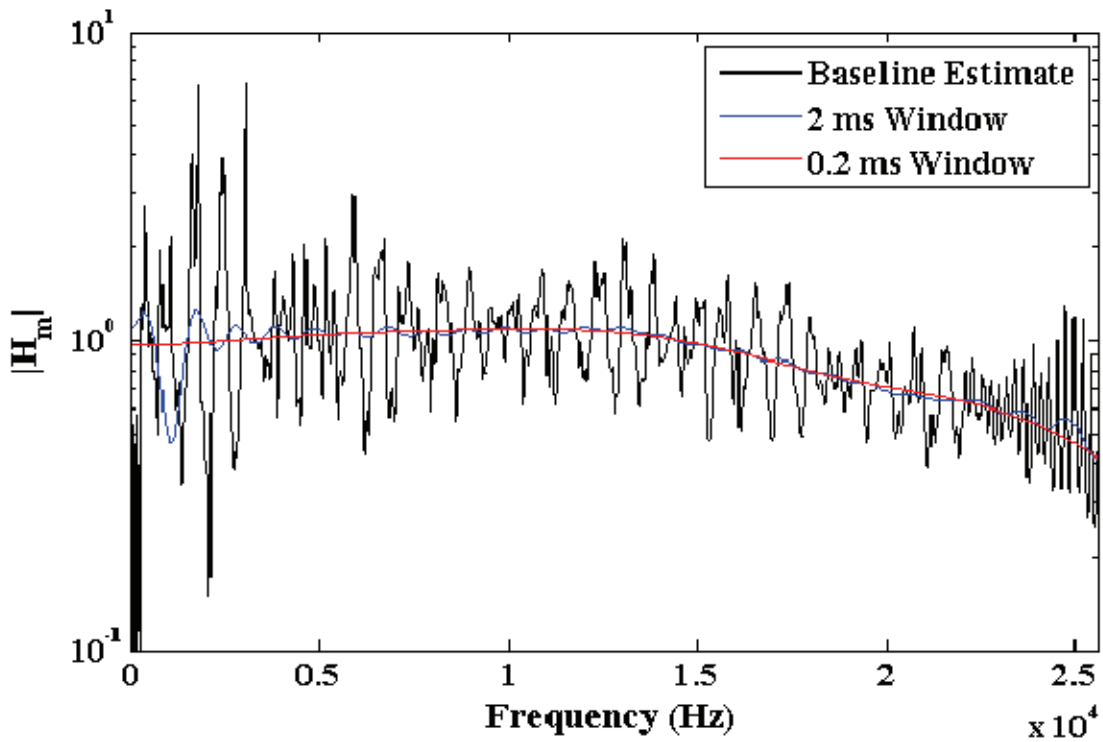


Figure D-63. Impulse response windowing magnitude estimate for electret 43.

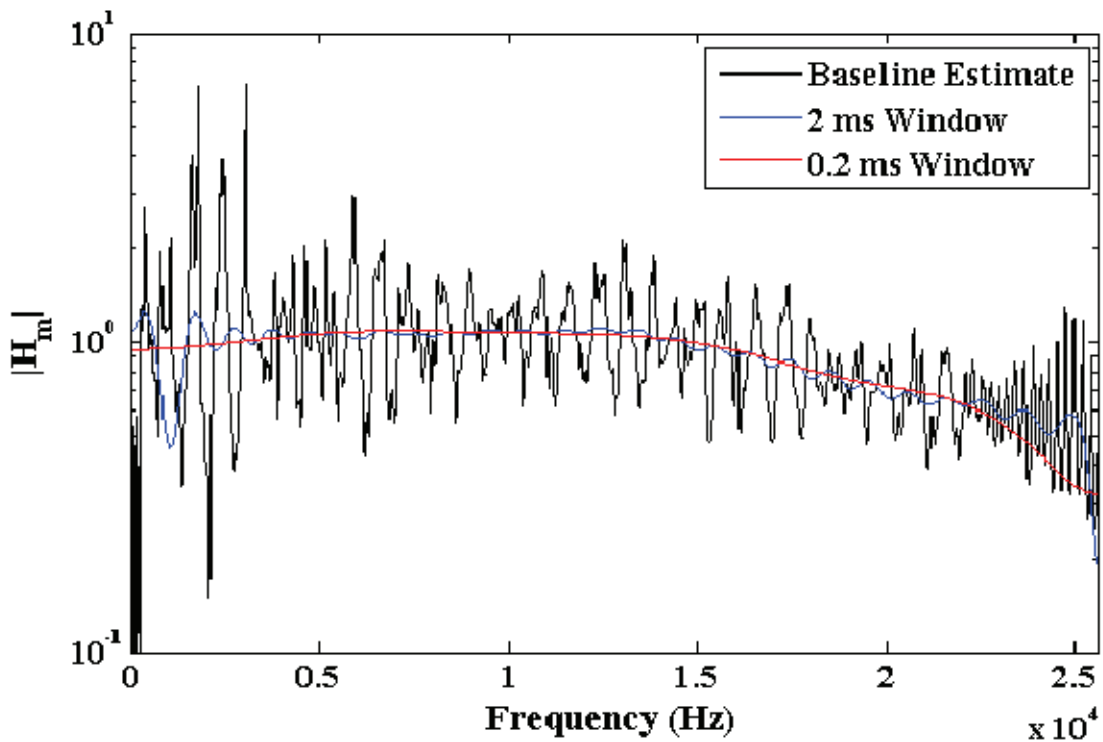


Figure D-64. Downsampled impulse response windowing magnitude estimate for electret 43.

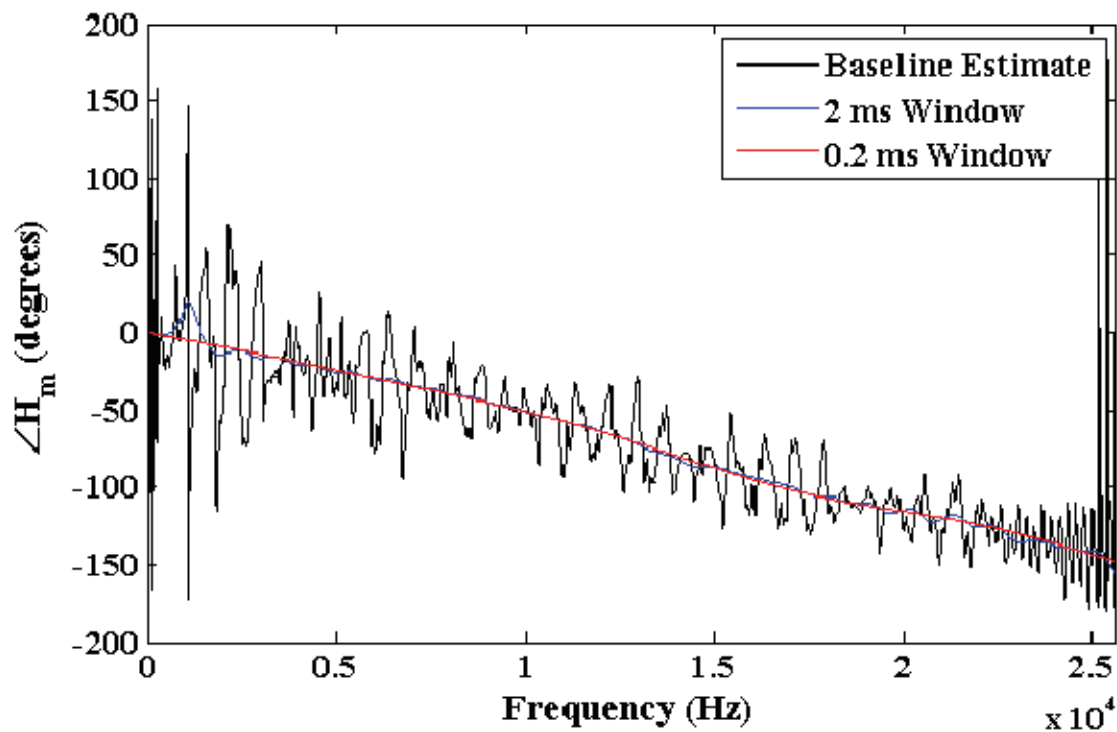


Figure D-65. Impulse response windowing phase estimate for electret 43.

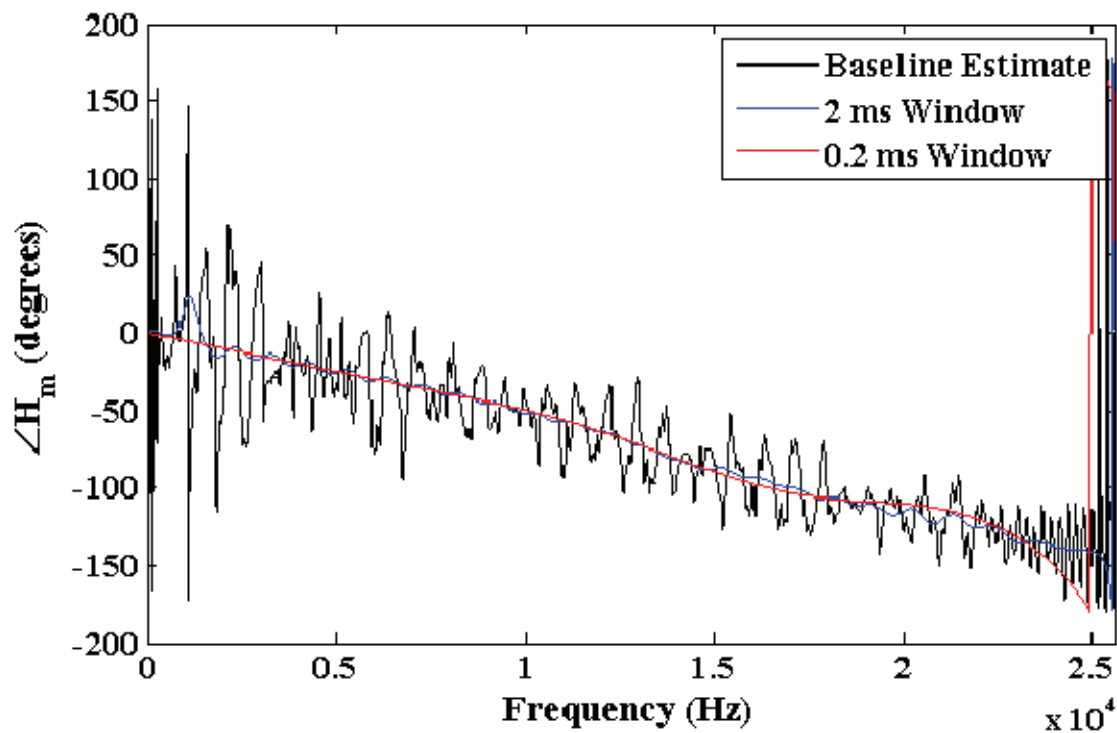


Figure D-66. Downsampled impulse response windowing phase estimate for electret 43.

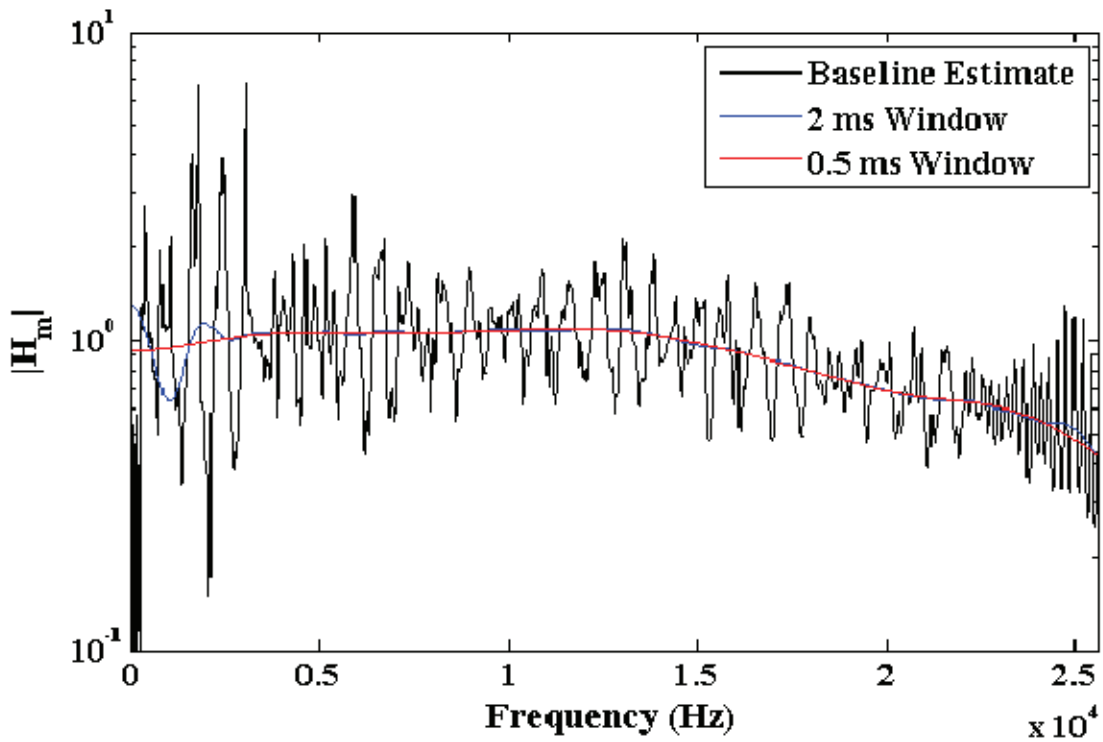


Figure D-67. Impulse response magnitude estimate with a 50% Tukey window.

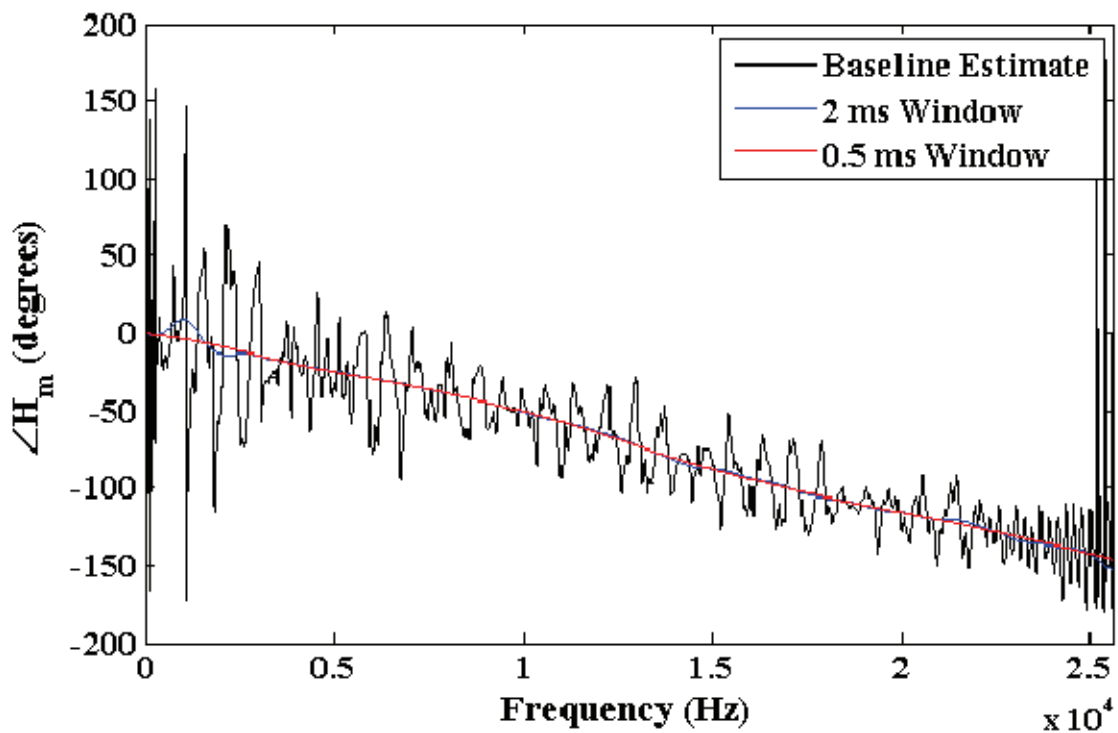


Figure D-68. Impulse response phase estimate with a 50% Tukey window.

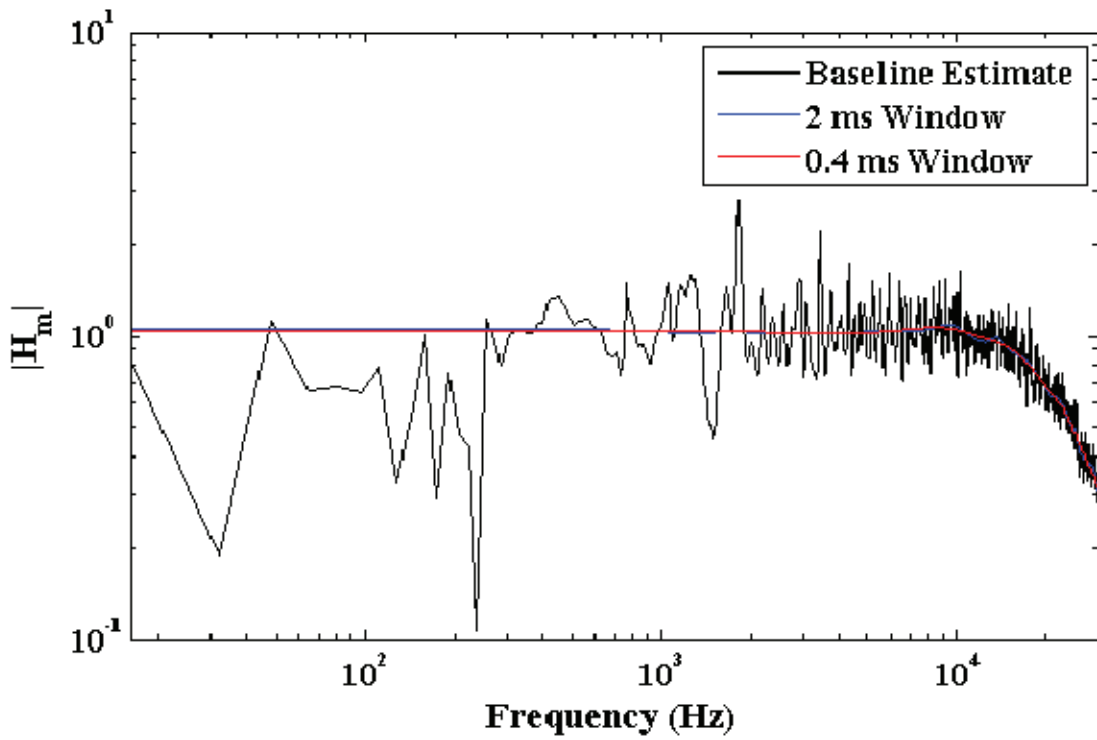


Figure D-69. Tukey-windowed magnitude estimate for treated calibration experiment.

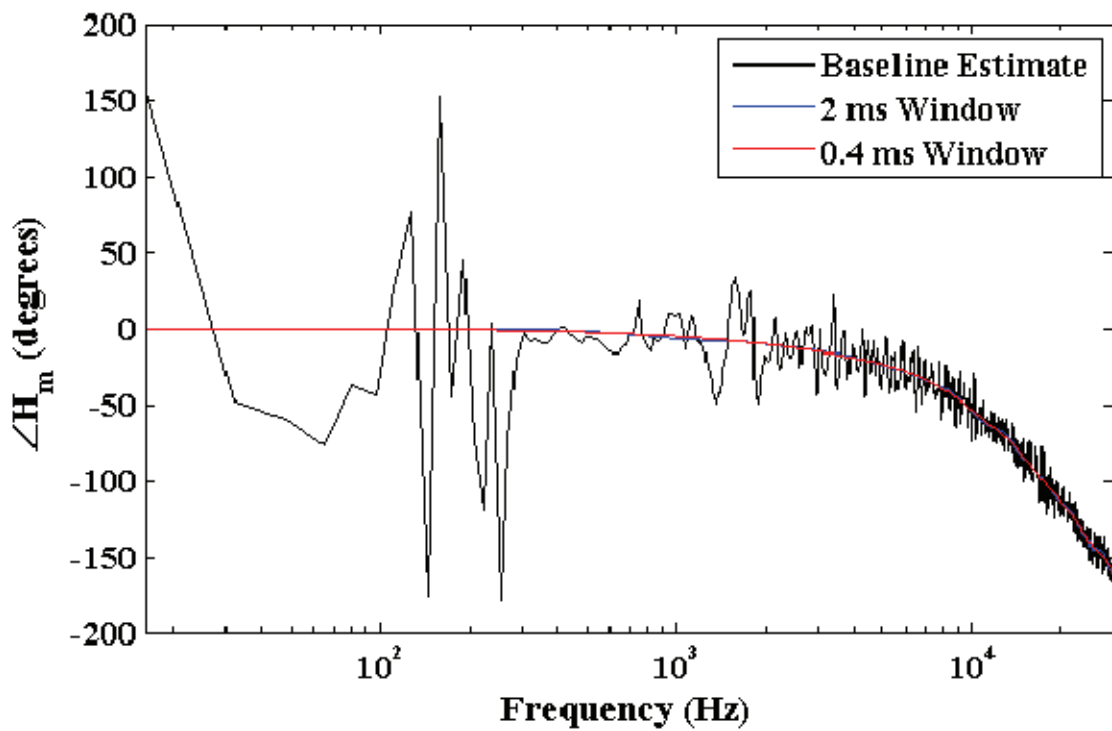


Figure D-70. Tukey-windowed phase estimate for treated calibration experiment.

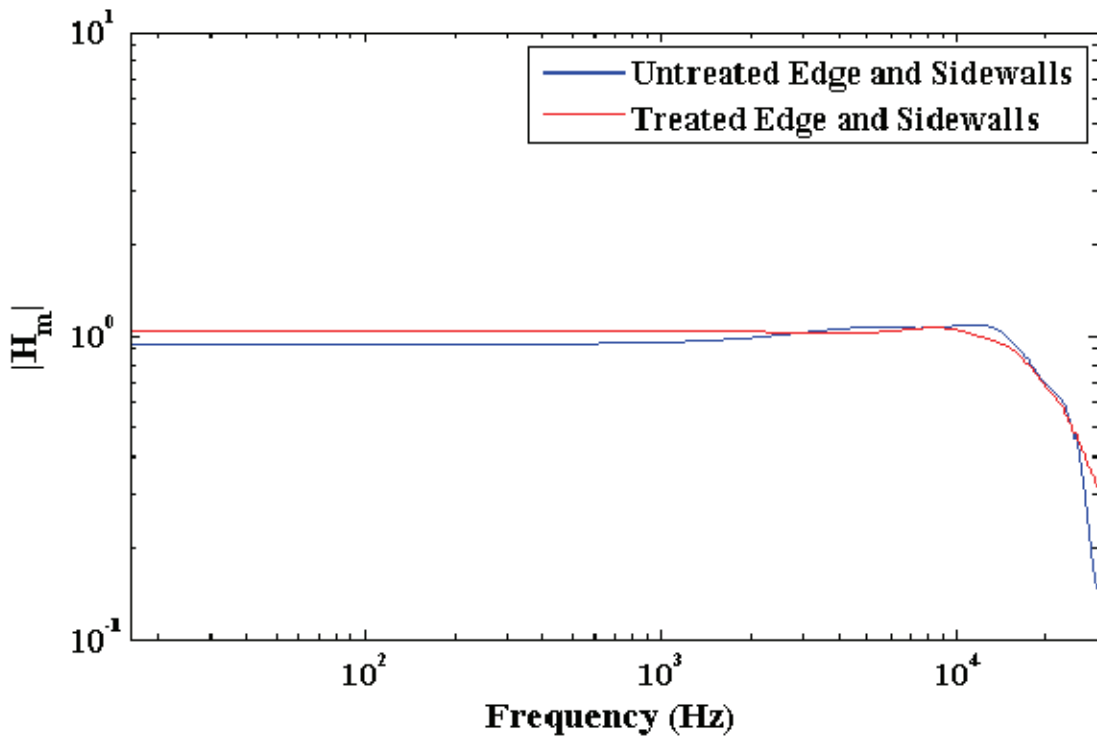


Figure D-71. Magnitude estimate comparison between untreated and treated experiments.

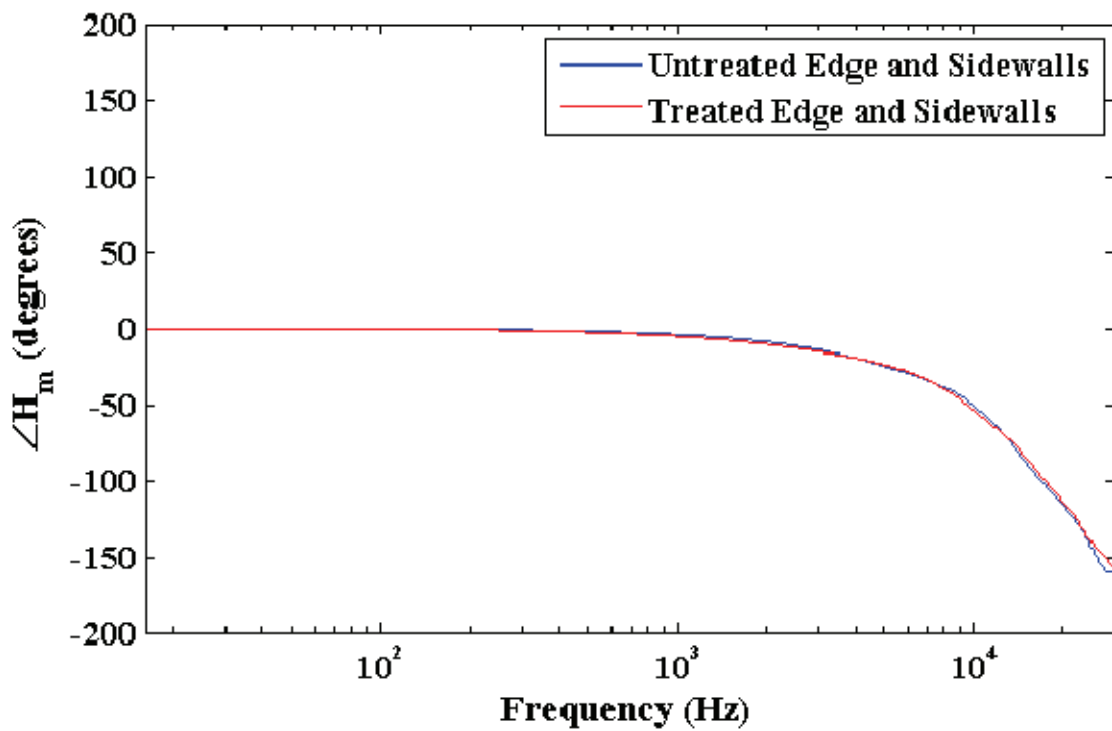


Figure D-72. Phase estimate comparison between untreated and treated experiments.

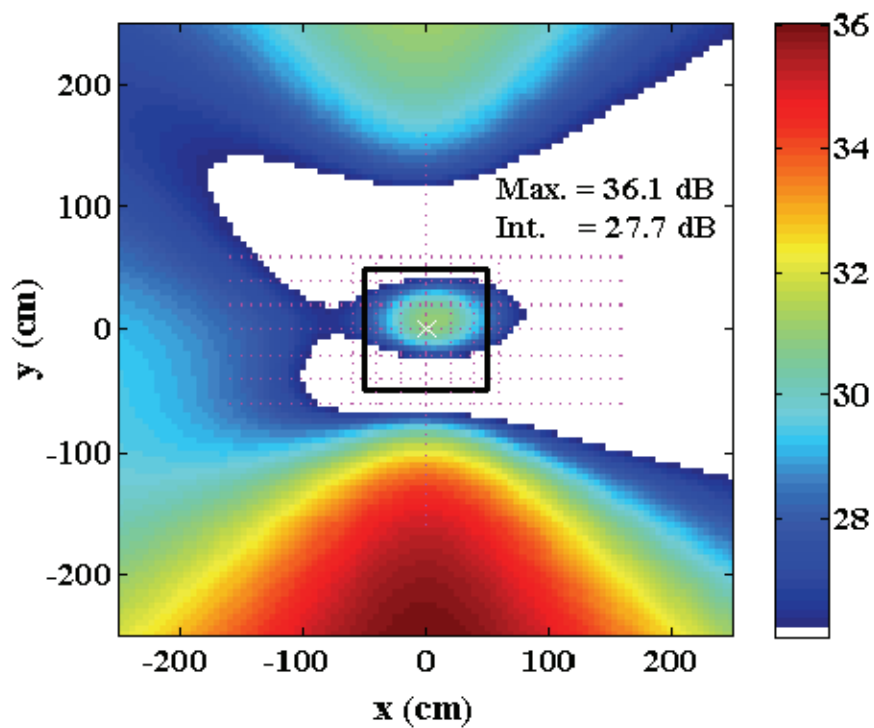


Figure D-73. Medium-aperture array calibration experiment beam map at 1120 Hz.

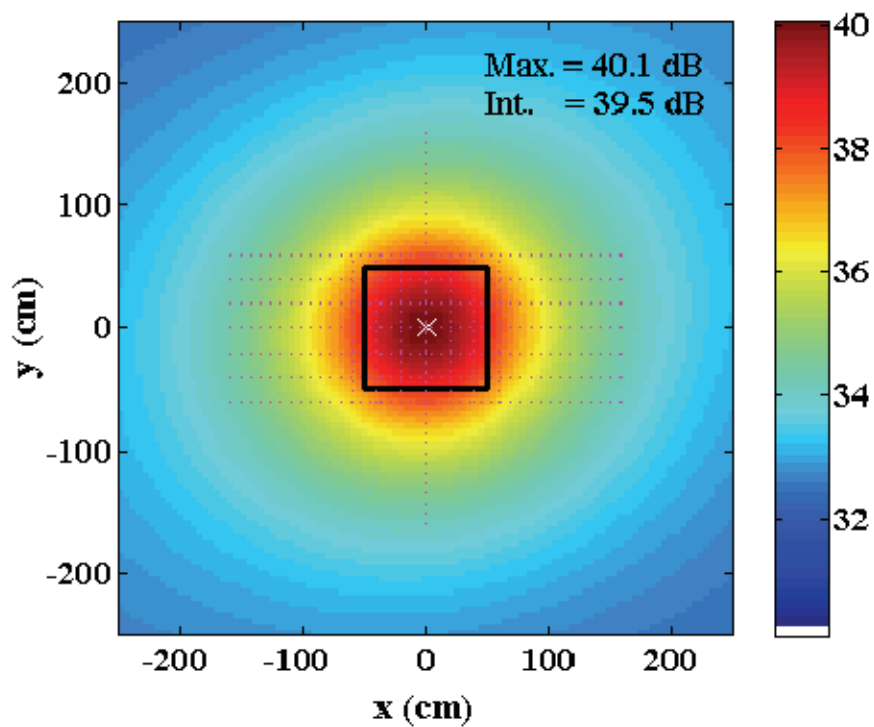


Figure D-74. Ideal calibrated response for experiment beam map at 1120 Hz.

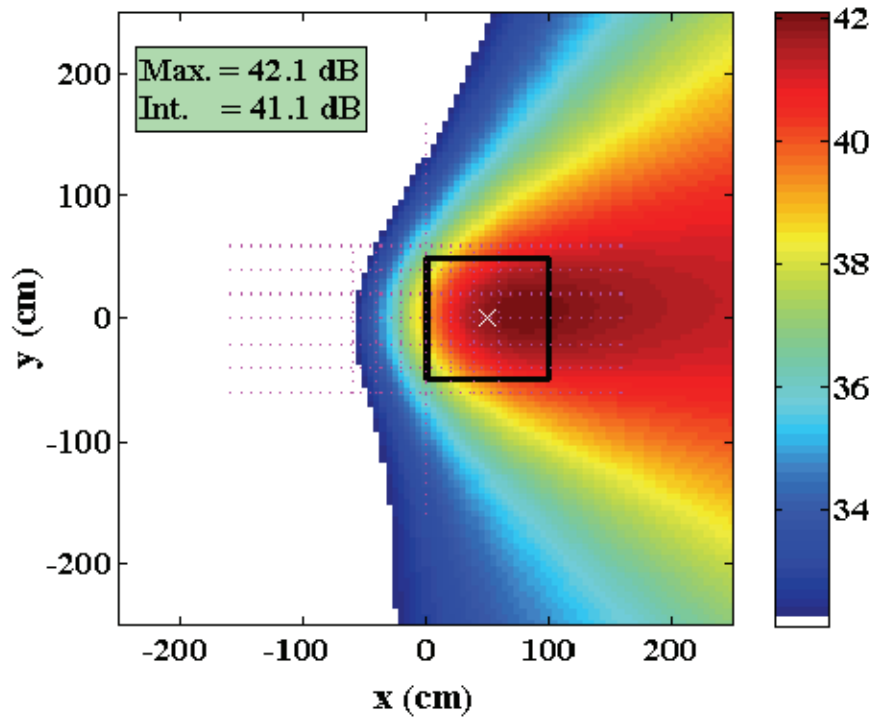


Figure D-75. Uncalibrated beam map of offset speaker at 1120 Hz.

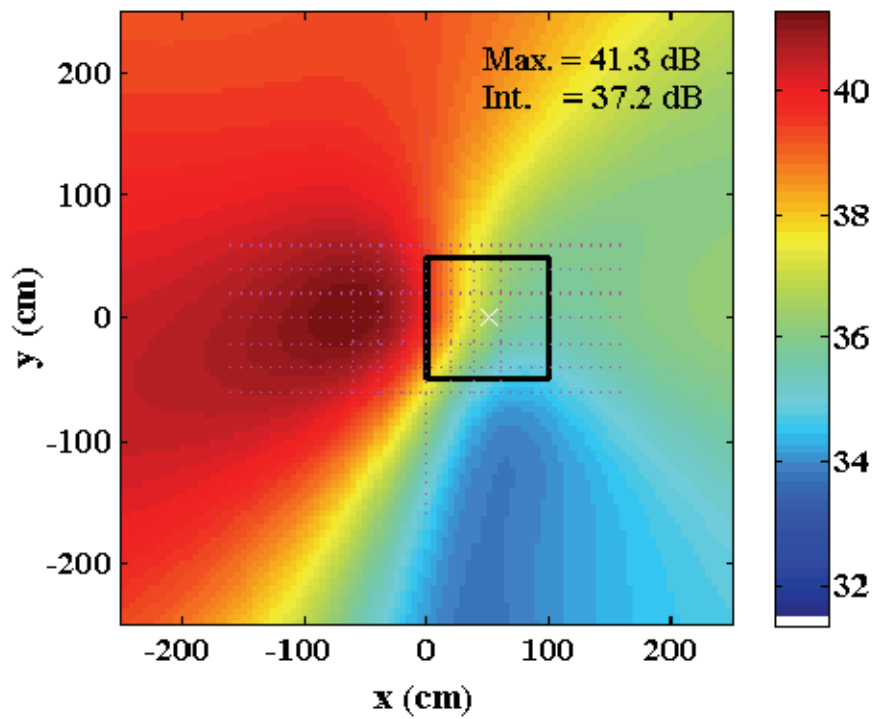


Figure D-76. Calibrated beam map of offset speaker at 1120 Hz.

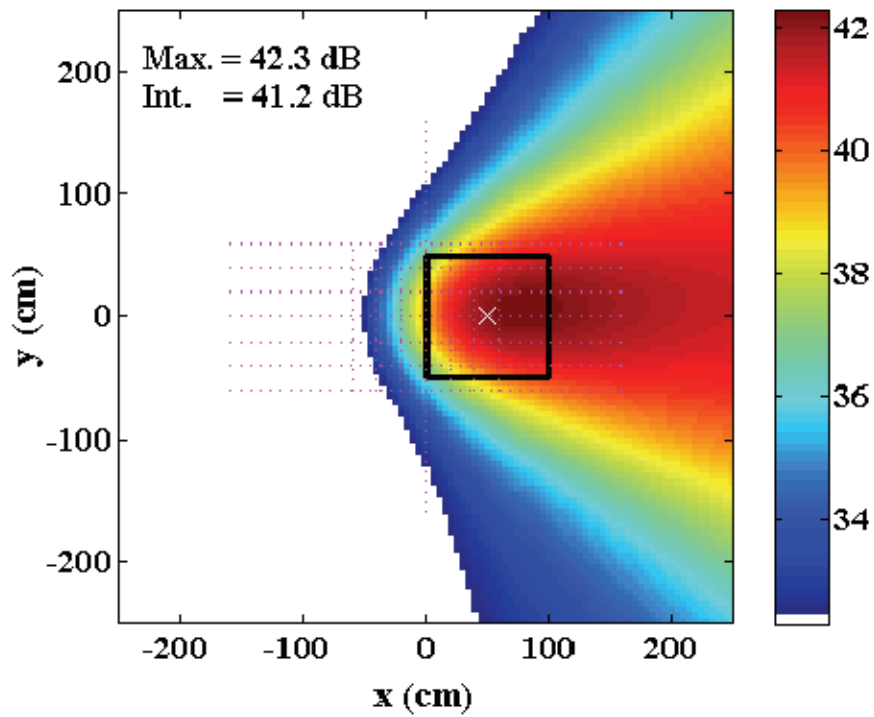


Figure D-77. Beam map of offset speaker at 1120 Hz, calibrated with new technique.

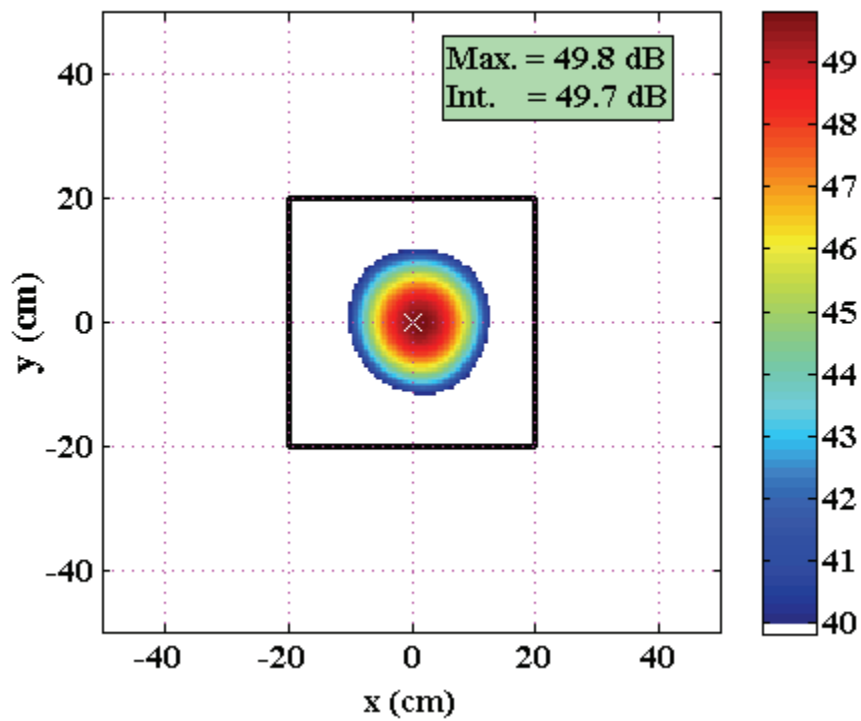


Figure D-78. Uncalibrated beam map of medium aperture array data at 10 kHz.

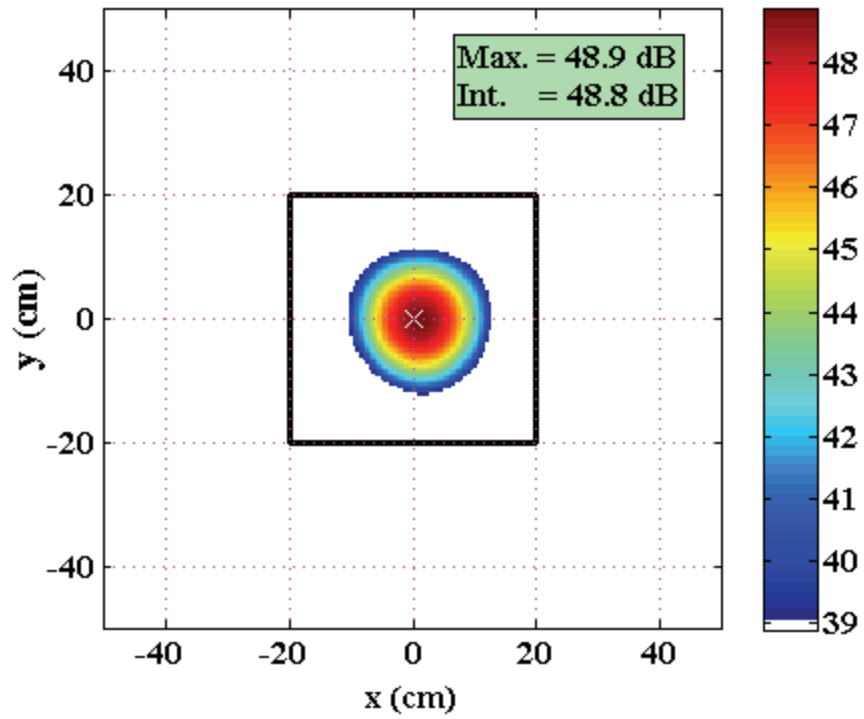


Figure D-79. Calibrated beam map of medium aperture array data at 10 kHz.

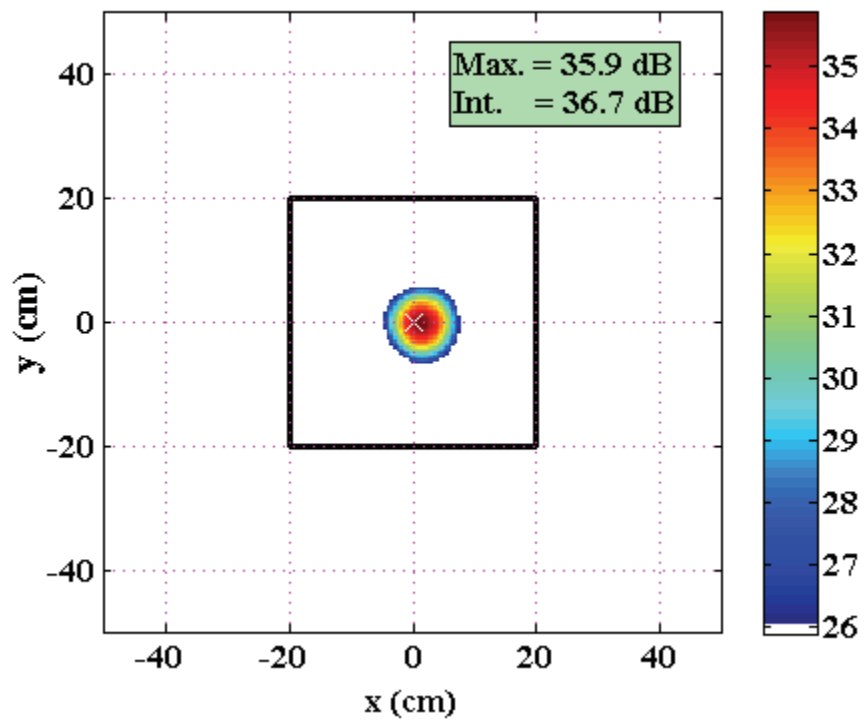


Figure D-80. Uncalibrated beam map of medium aperture array data at 20 kHz.

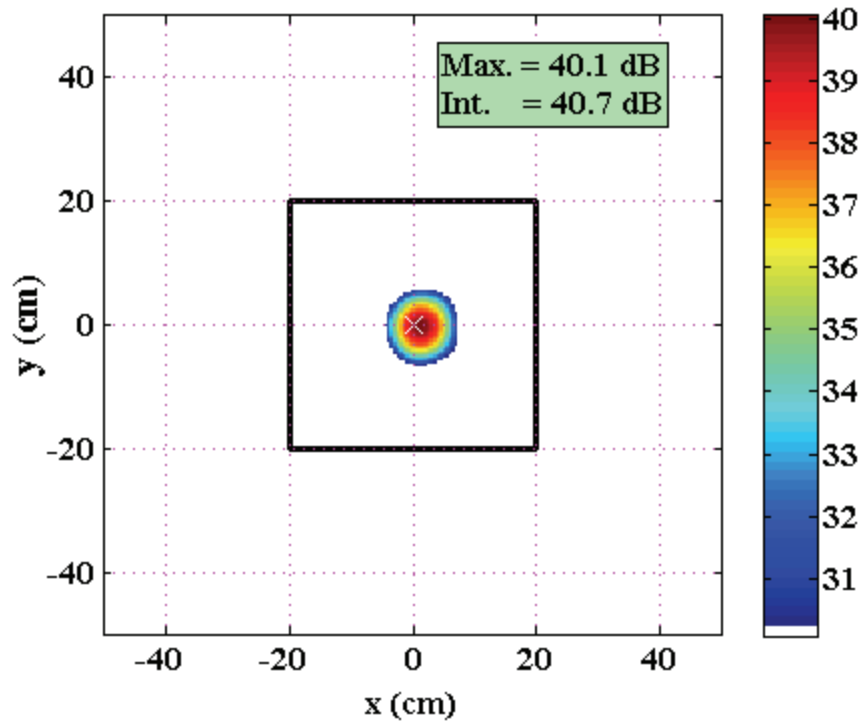


Figure D-81. Calibrated beam map of medium aperture array data at 20 kHz.

APPENDIX E COMPARISON OF DAS AND DAMAS RESULTS

A single experimental case is processed with a deconvolution algorithm, DAMAS [Brooks & Humphreys 2006a]. This method uses an iterative, and computationally expensive, procedure to attempt to remove the effects of an array's point spread function from a beam map. While expensive, it does see broad use as a comparator for DAS results, as well as other deconvolution algorithms. DAMAS is used with the same case for which a delay-and-sum integrated power uncertainty estimate is computed, that being the NACA 63-215 Mod-B model at a Mach number of 0.17 and 0 degree AoA. The initial scan plane selected is the same for that used with the DAS integration, having an extent of 0.4 m in the x-axis and 1.06 m in the y-axis, with 0.02 m steps in each direction. This was discussed previously as involving several trade-offs of computation time and noise rejection, balanced around admitting the majority of the trailing edge noise signature. This admittance is demonstrated at the shedding peak frequency of 2,512 Hz in Figure 5-45, as the integration region's black border bounds the majority of the trailing edge noise source. DAMAS is run for 1,000 iterations. The convergence behavior of this iteration count is discussed towards the end of this appendix.

Nominal integrated spectra from the two algorithms are shown in comparison to the array-centered B&K 4138 microphone in Figure E-1. As shown, for most of the measurement bandwidth the DAMAS solution is several decibels above the DAS solution, until just above 10 kHz when the two converge. A comparison of the DAMAS solution to the DAS 95% confidence region is shown in Figure E-2 to see if the uncertainty in the DAS prediction may actually overlap with the deconvolution prediction. This plot shows that below 3 kHz the DAMAS solution is just outside of the uncertainty bounds of DAS. Between 3 kHz and 10 kHz the DAMAS prediction is a bit higher, and above 10 kHz DAMAS falls within the DAS bounds.

However, the DAMAS data warrant further investigation. DAS integrated levels, with appropriate grid resolution, are only dependent on the integration bounds of the computation. Any scanning region grid points outside of the integration bounds have no effect on the integrated DAS solution. This is not so with DAMAS. As DAMAS is an inverse problem, the entire scan plane is used in the deconvolution process and the predicted levels within the integration region are very much dependent on the overall scan plane solution. While the integration region is selected for consistency's sake with DAS results, the current scan plane, which consists of only a fraction of the wind tunnel test section and as shown in Chapter 5 clearly excludes major noise sources, is selected for computational expediency. For this grid size, a single integrated spectrum from 512 Hz to 20 kHz required slightly over 24 hours on a modern workstation operating at 3.33 GHz in serial mode. For a grid encompassing the entire test section, the computational time would increase by a factor of approximately 32, as DAMAS computation time scales as the square of the number of grid points.

While a narrowband integrated spectrum could not be constructed to evaluate scan plane effects with DAMAS, individual frequency bins could be checked. A series of seven frequencies is evaluated. These frequencies are the same for which DAS beam maps are available in Chapter 5. For the DAMAS figures, the reduced integration region plots will have a dotted line representing the integration region, as well as the total beam map area. The full integration region plots will have a dotted line representing the integration region, and another dotted line representing the overall beam map area. This style is different from the previous DAS beam maps due to the point-like nature of the DAMAS predictions and data visibility issues.

The first frequency to be evaluated is 1,024 Hz, which has a DAS beam map plotted in Figure 5-43. The limited-region DAMAS beam map is shown in Figure E-3, while the full test

section beam map is shown in Figure E-4. In the smaller scan plane, most of the predicted sources lie on the very edge of the plane boundaries, while in the larger scan plane case sparse sources are present on the airfoil trailing edge, as well as some near the rear boundary. The larger scan plane level prediction is well below the DAS integrated level. It should be noted that physically neither of these beam maps resemble the DAS solution. Given the array's 3-dB beamwidth as plotted in Figure 4-47, the full test section scan plane may still be too small to properly resolve sources using DAMAS.

The second frequency evaluated is the shedding peak as noted in the free microphone cases previously at 2,512 Hz, with a DAS beam map in Figure 5-45. The reduced and full DAMAS scan plane beam maps are shown respectively in Figure E-5 and Figure E-6. These cases differ from each other by 1 dB, with the full scan plane predicting the lower value. This large scan plane data is only 0.1 dB off from the nominal DAS solution. In both cases, the trailing edge is the dominant visible noise source, with only a few sources falling outside of the integration bounds in the full scan plane plot. As with so many other analysis methods, when the trailing edge is the dominant noise source the methods tend to be well behaved and predict similar levels.

The third frequency, 5,008 Hz is evaluated next, with its DAS beam map shown in Figure 5-47. The reduced DAMAS beam map is shown in Figure E-7, while the full test section one is shown in Figure E-8. The reduced scan plane shows very few sources away from the integration region borders, while the full scan plane shows no significant sources within the integration region at all. This is consistent with the DAS beam map, which indicates diffuser and sidewall noise are the dominant sources at this frequency. The reduced scan plane beam map appears to attempt to resolve them by pushing its observed sources to the edge of the region. The full test section beam map appropriately locates them, and predicts an SPL significantly below DAS as

DAMAS is removing the lobe width effects from the sidewall and diffuser noise, preventing the noise from contaminating the integration region.

The frequency 7,600 Hz, with a DAS beam map shown in Figure 5-49, shows similar behavior to 5,008 Hz. The reduced and full DAMAS scan planes are shown in Figure E-9 and Figure E-10. Again, the reduced scan plane detects most sources on the very edge of its scan plane, and results in levels higher than those estimated with DAS. Again, the full scan plane DAMAS beam map shows that the sources are not within the integration region, and predicts a power lower than DAS as it removes the lobe effects from sidewall noise sources. The same behavior is seen at 8,800 Hz. The DAS beam map is given in Figure 5-51. The DAMAS reduced and full solutions are shown in Figure E-11 and Figure E-12.

15,008 Hz and 20,000 Hz array predictions both appear to be driven by the leading edge-sidewall noise source, as is clearly visible in the DAS beam maps of Figure 5-53 and Figure 5-55. In both of these cases, the DAS solution appears as if it may be contaminated by sidelobe effects of this noise source. In both of these cases, the reduced DAMAS solution shown in Figure E-13 and Figure E-15 interprets these possible sidelobes as major noise sources. This is likely because the main lobes of the noise sources are outside of the DAMAS solution region, and thus deconvolution fails to account for that behavior of the array's point spread function. As the full test section DAMAS beam maps of Figure E-14 and Figure E-16 show, these noise sources actually have little impact on the integration region when proper deconvolution occurs, and the resultant noise prediction is dramatically below the DAS output.

Briefly, the convergence of the DAMAS solutions will be checked. All of the cases shown were analyzed with 1,000 internal DAMAS iterations. A single case, the 20,000 Hz full test section beam map, was selected and run for 5,000 and 10,000 iterations. The 5,000 iteration case

is shown in Figure E-17, and the 10,000 iteration case is shown in Figure E-18. These figures show, in comparison to the 1,000 iteration solution of Figure E-16, that nominal convergence is achieved as the beam maps appear graphically to be the same, and the integrated levels match to within the displayed 0.1 dB precision.

Finally, a 1/3rd octave band analysis is conducted for the small and large beam map regions with DAMAS, and compared to the results from DAS and NAFNoise. The plot of these results is shown in Figure E-19. As with the narrowband integration, DAMAS with a small beam map tends to predict levels slightly above DAS. However, DAMAS with a full test section beam map predicts significantly lower than DAS for a large portion of the measurement bandwidth. While DAMAS still fails to reject much of the low frequency noise suspected to come from the diffuser, much of the higher-frequency contamination is eliminated..

The DAMAS algorithm appears to be able to more-finely resolve the acoustic sources in this data set than the standard DAS algorithm, and predicts significantly lower acoustic levels than DAS for frequencies where the airfoil trailing edge is not the dominant acoustic source, and background noise sources are physically located outside of the defined integration region. However, the required scan plane for the algorithm encompasses the entire test section, and a full integrated spectrum using such a domain is computationally infeasible. Using a reduced scan plane in an attempt to get a solution in a reduced amount of time leads to beam maps where incorrect acoustic fields are constructed, leading to erroneous integrated levels. If such a trade-off must be made, a DAS-based solution provides a more physically reasonable acoustic field, with the benefits of shorter computation time and existing uncertainty analysis codes. Alternative codes, such as SC-DAMAS, may provide a faster deconvolution alternative [Yardibi *et al.* 2008].

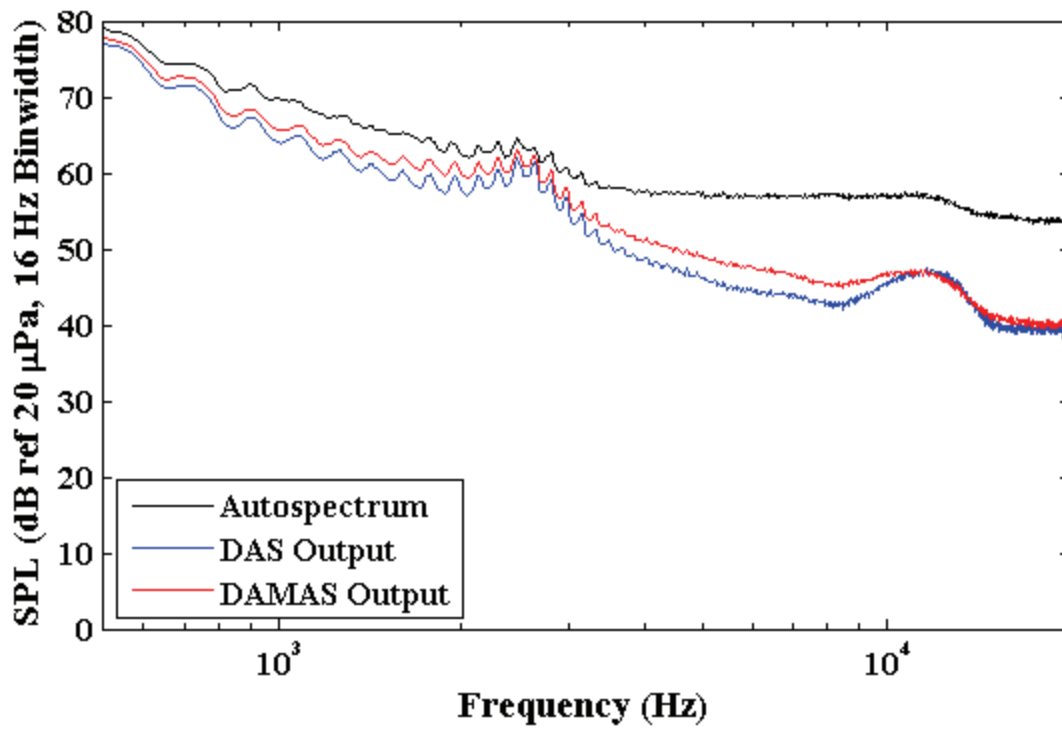


Figure E-1. Comparison of nominal DAS and DAMAS outputs.

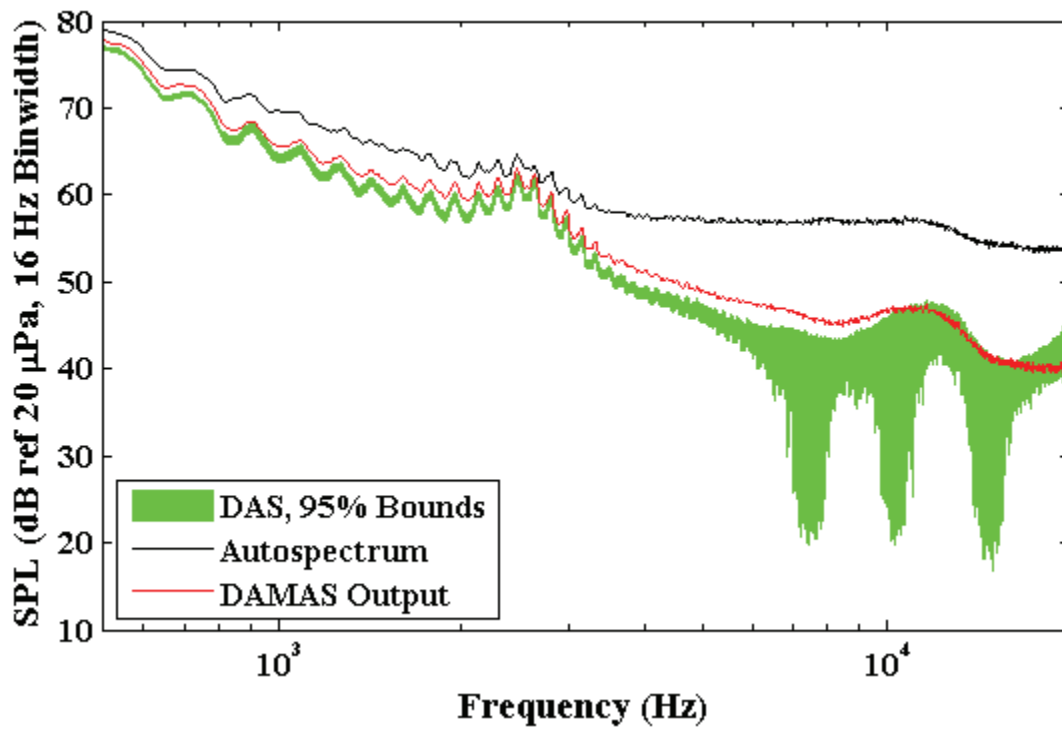


Figure E-2. Comparison of DAMAS output to DAS uncertainty bounds.

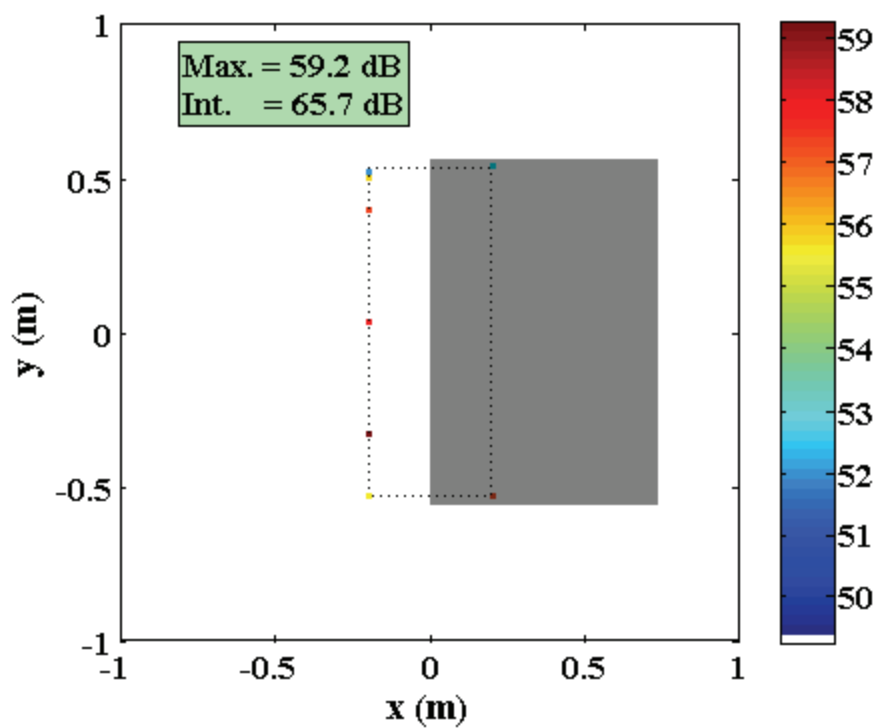


Figure E-3. Reduced scan plane DAMAS solution for 1,024 Hz.

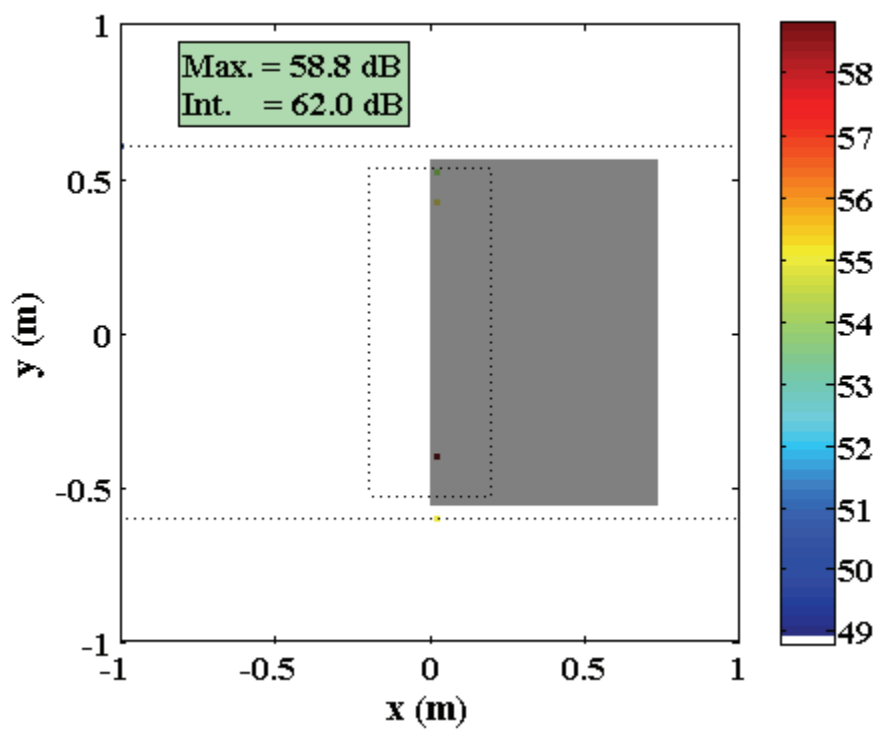


Figure E-4. Full test section scan plane DAMAS solution for 1,024 Hz.

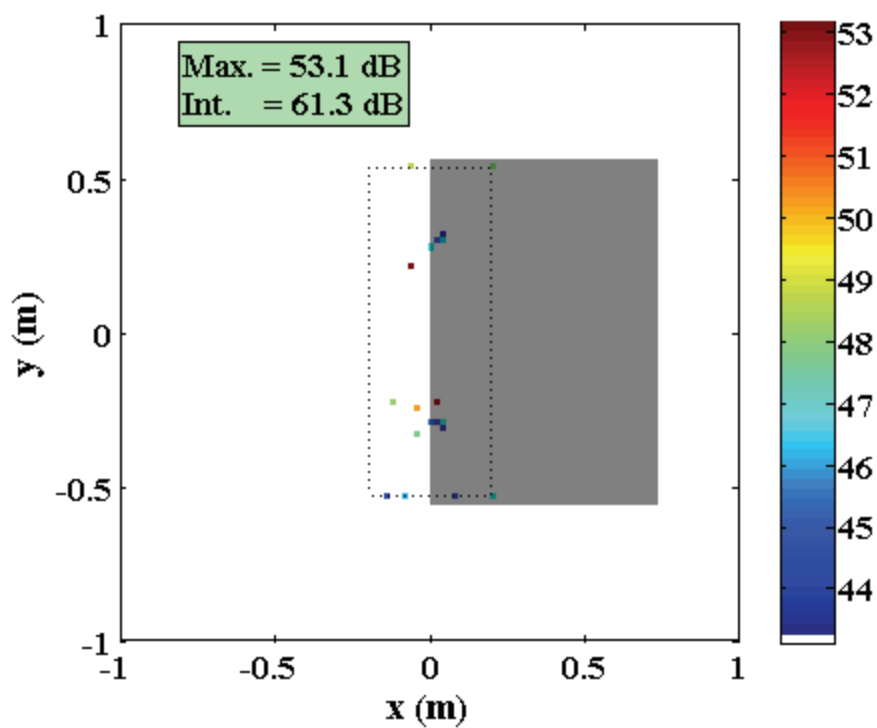


Figure E-5. Reduced scan plane DAMAS solution for 2,512 Hz.

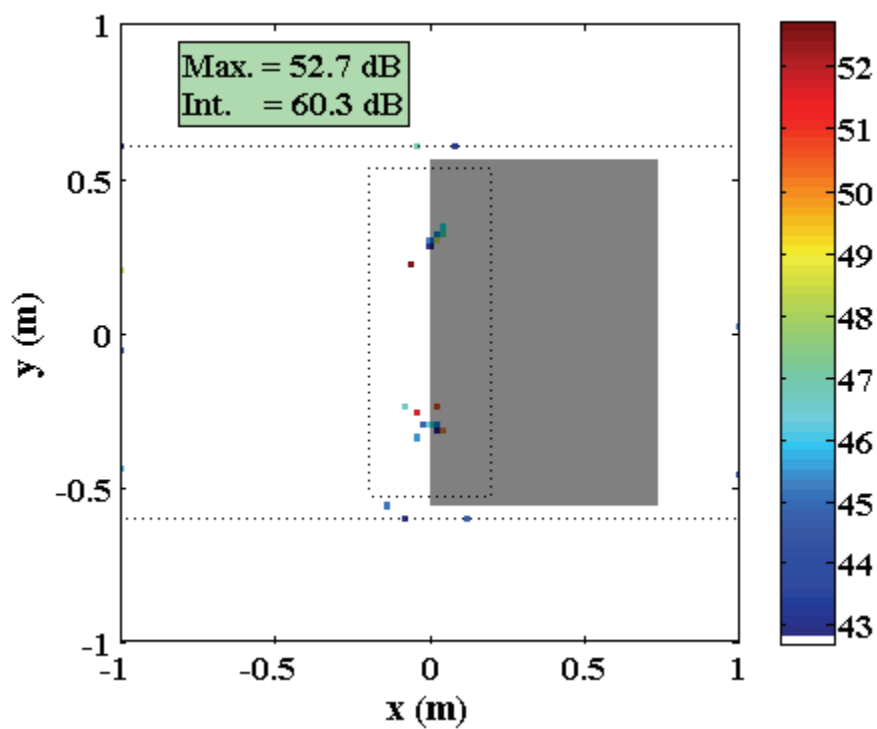


Figure E-6. Full test section scan plane DAMAS solution for 2,512 Hz.

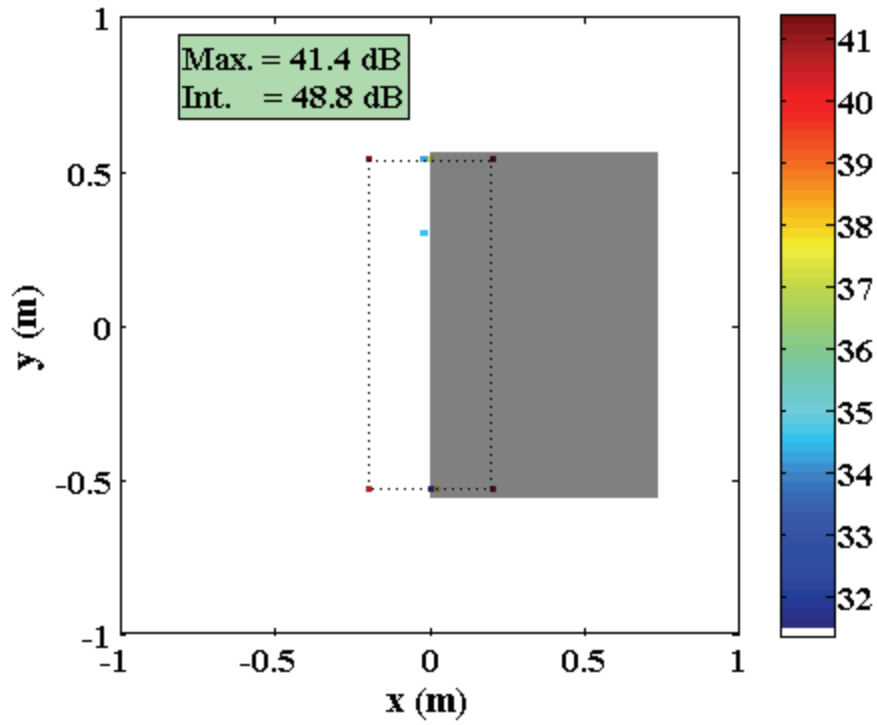


Figure E-7. Reduced scan plane DAMAS solution for 5,008 Hz.

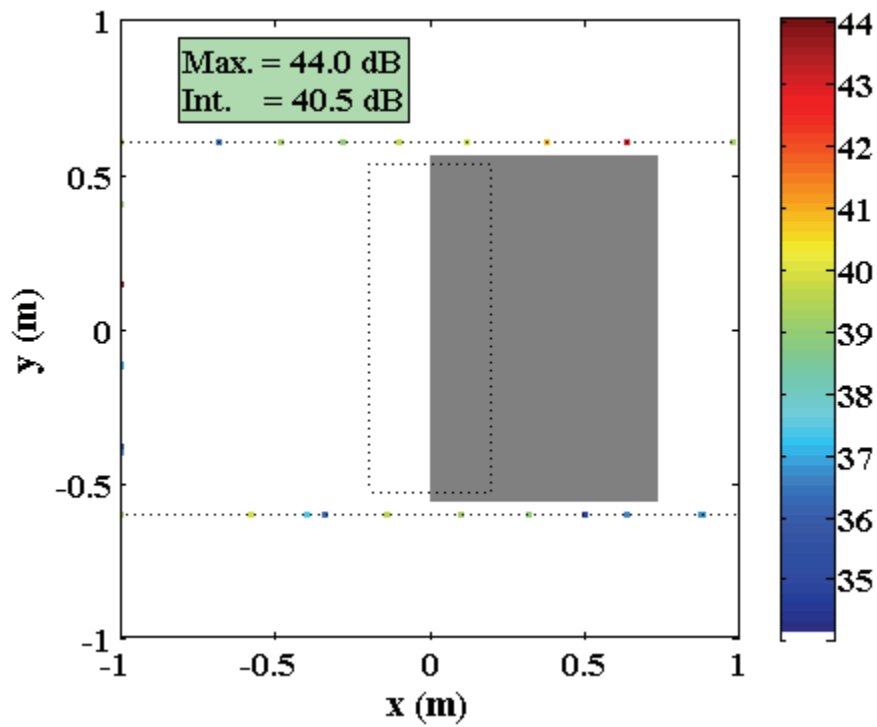


Figure E-8. Full test section scan plane DAMAS solution for 5,008 Hz.

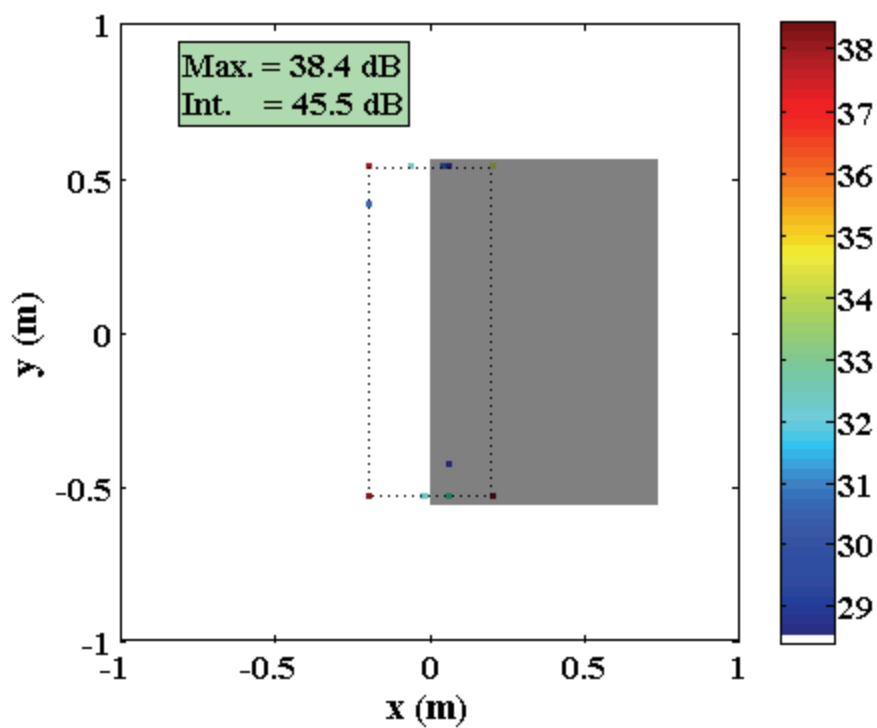


Figure E-9. Reduced scan plane DAMAS solution for 7,600 Hz.

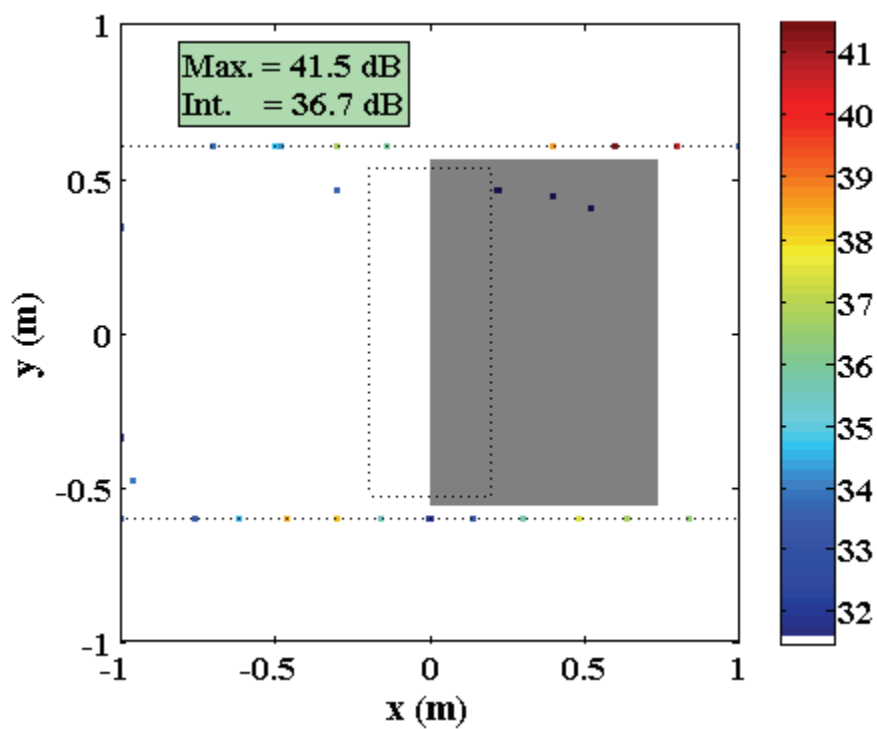


Figure E-10. Full test section scan plane DAMAS solution for 7,600 Hz.

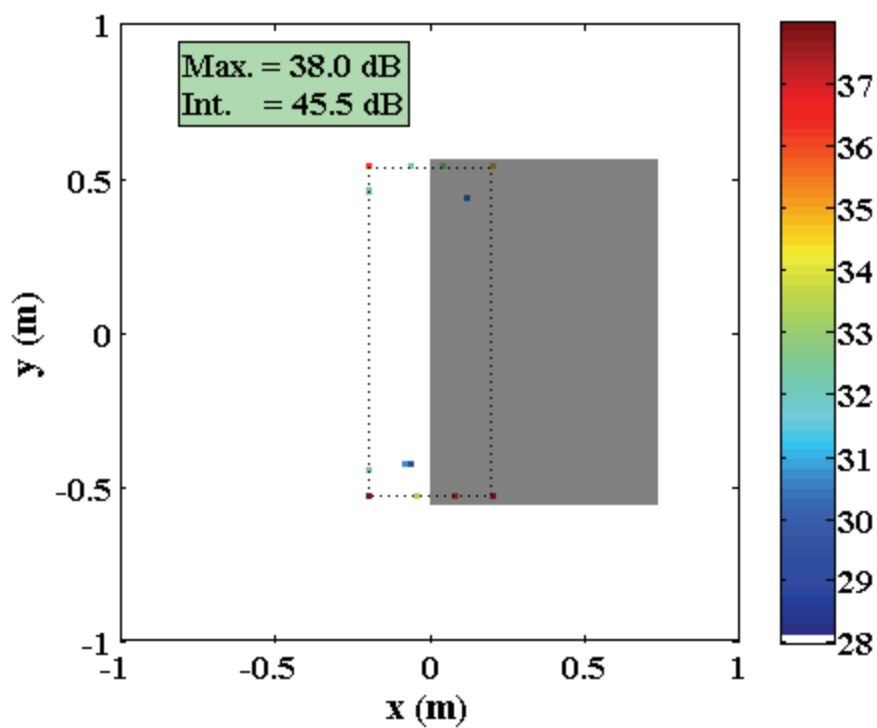


Figure E-11. Reduced scan plane DAMAS solution for 8,800 Hz.

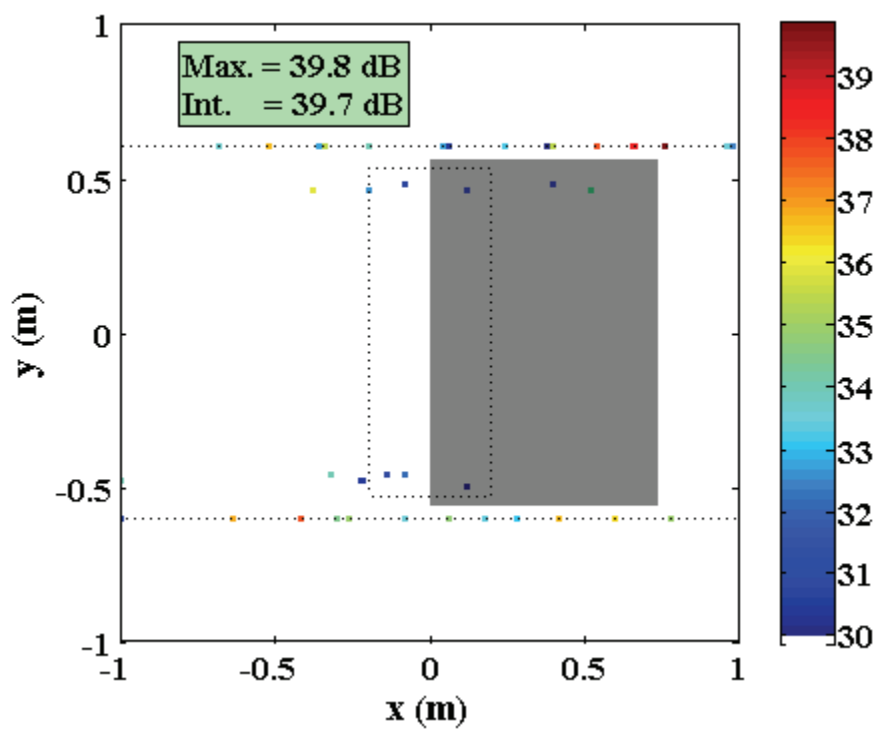


Figure E-12. Full test section scan plane DAMAS solution for 8,800 Hz.

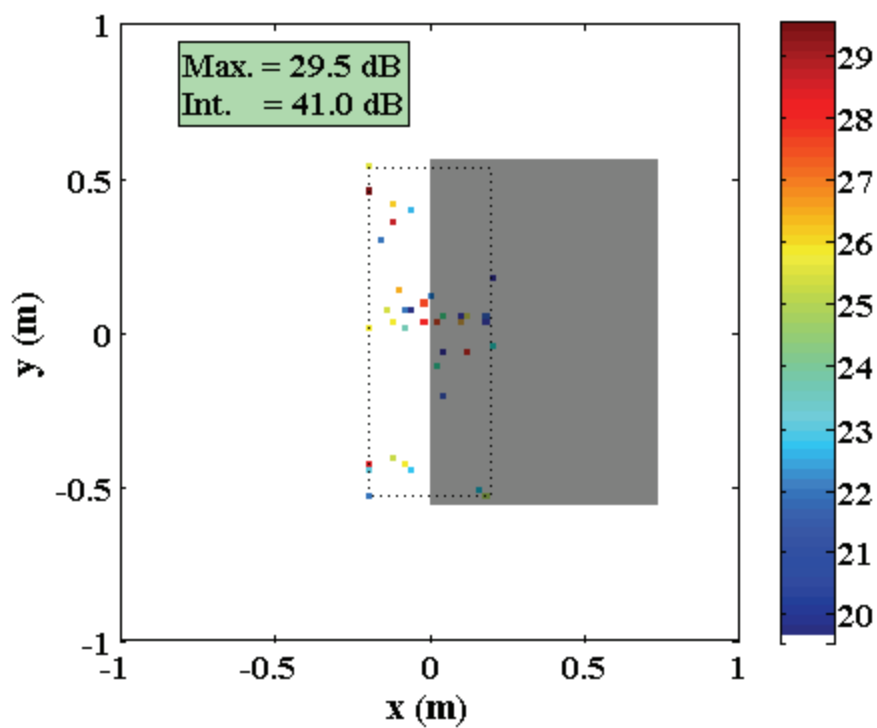


Figure E-13. Reduced scan plane DAMAS solution for 15,008 Hz.

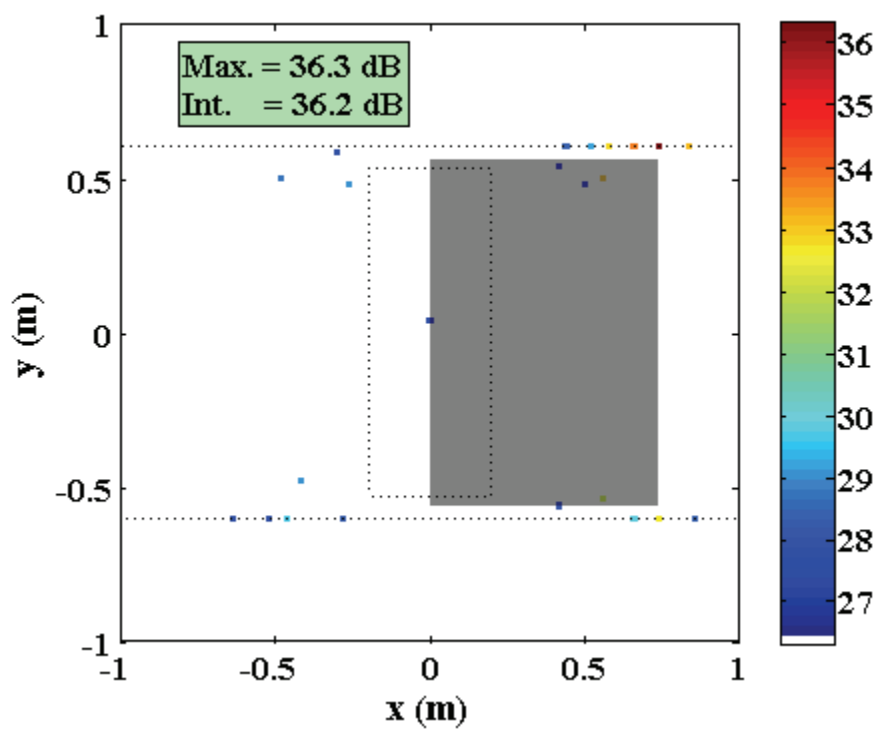


Figure E-14. Full test section scan plane DAMAS solution for 15,008 Hz.

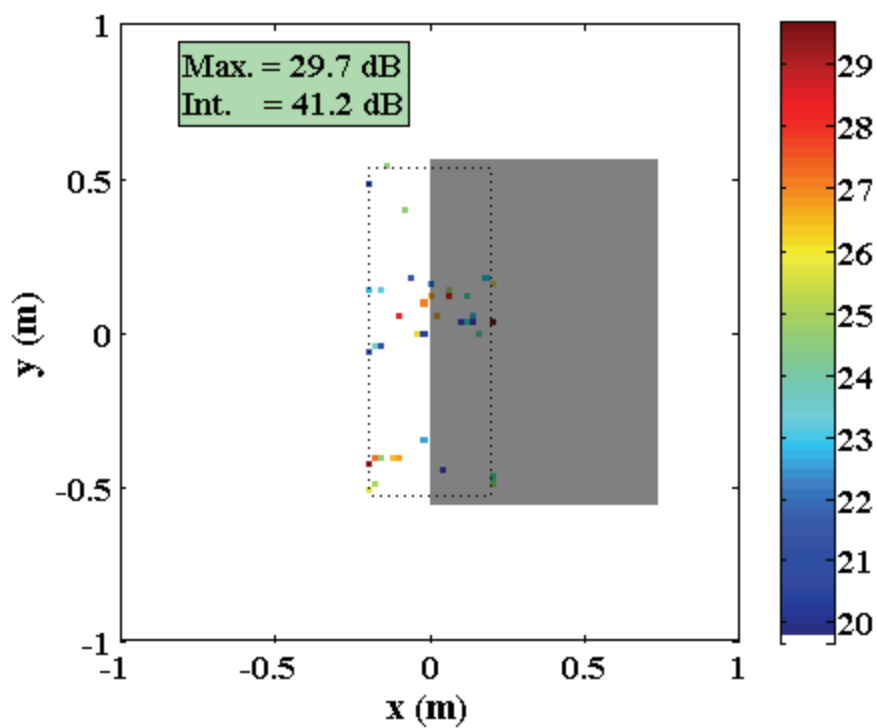


Figure E-15. Reduced scan plane DAMAS solution for 20,000 Hz.

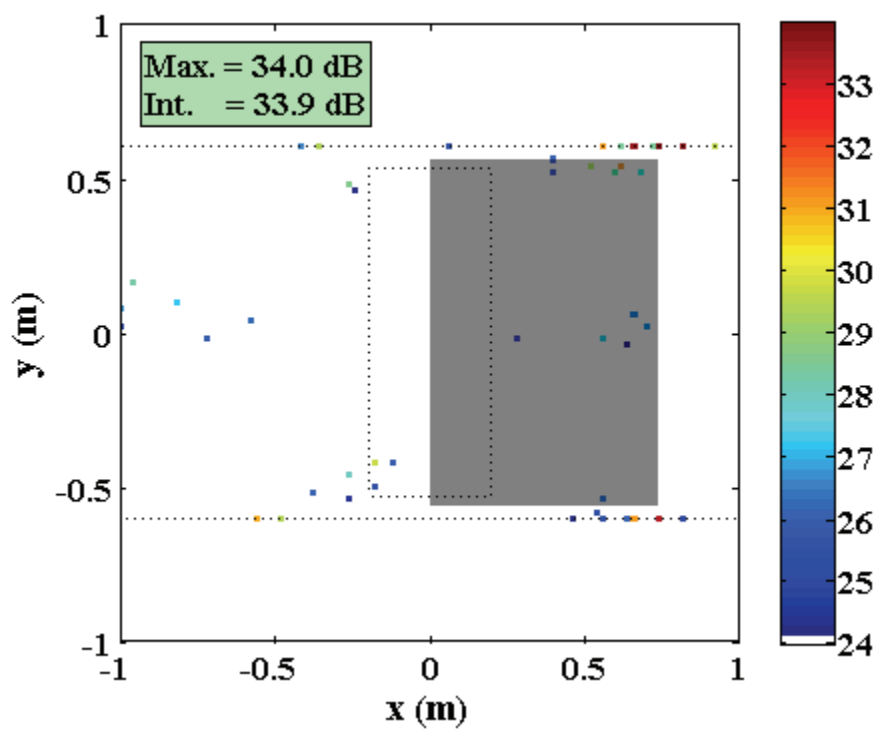


Figure E-16. Full test section scan plane DAMAS solution for 20,000 Hz.

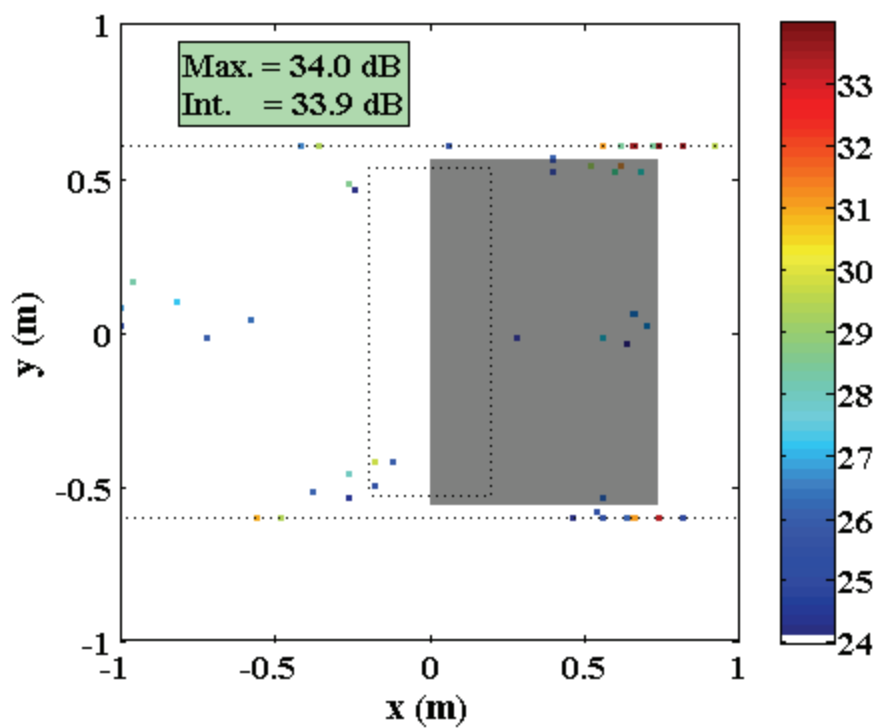


Figure E-17. Full test section scan plane DAMAS solution for 20,000 Hz with 5,000 iterations.

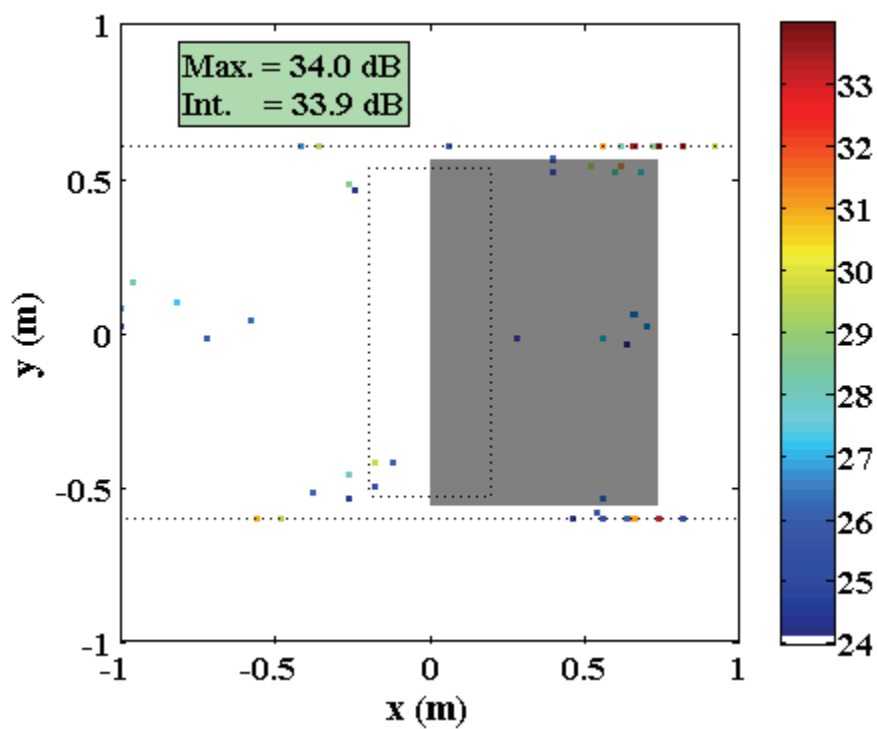


Figure E-18. Full test section scan plane DAMAS solution for 20,000 Hz with 10,000 iterations.

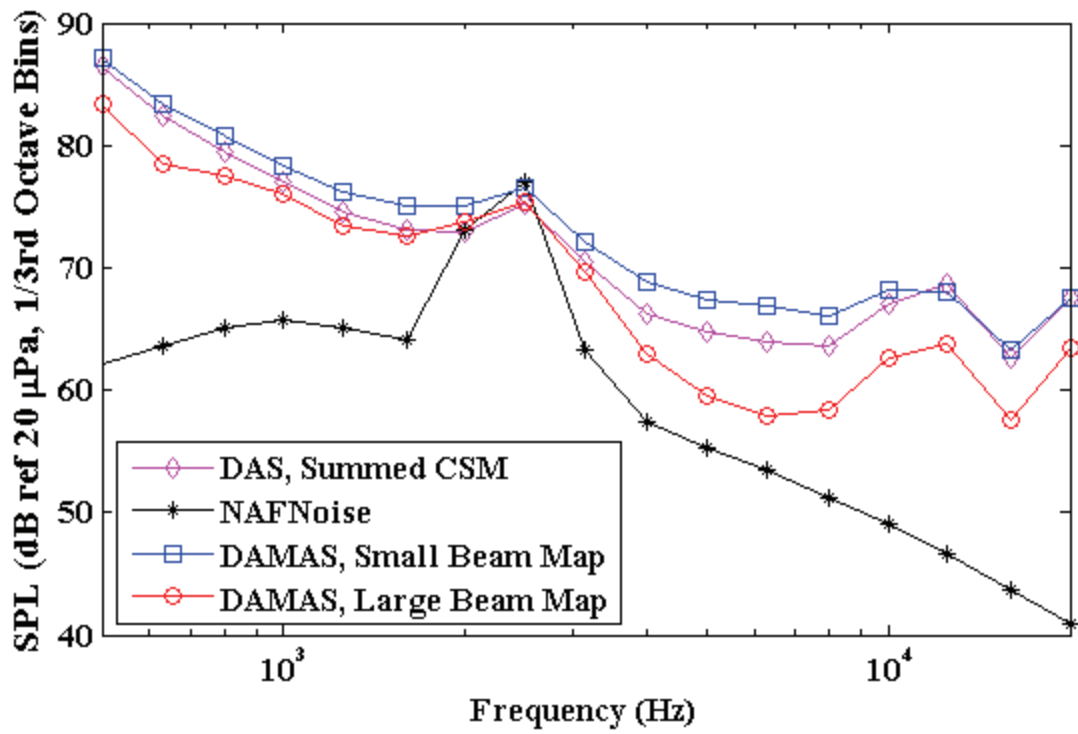


Figure E-19. 1/3rd octave comparison of DAMAS beam map regions with DAS and NAFNoise.

REFERENCES

- ABBOTT, I. H. & VON DOENHOFF, A. E. 1959 *Theory of Wing Sections*. 2nd ed. Dover Publications, Inc.: New York.
- ABRAMOWITZ, M. & STEGUN, I. 1965 *Handbook of Mathematical Functions*. 9th ed. Dover Publications, Inc.: New York.
- AMIET, R. K. 1975 Acoustic Radiation from an Airfoil in a Turbulent Stream. *Journal of Sound and Vibration* **41-4**, 407-420.
- AMIET, R. K. 1976 Noise Due to Turbulent Flow Past a Trailing Edge. *Journal of Sound and Vibration* **47-3**, 387-393.
- AMIET, R. K. 1978a Refraction of Sound by a Shear Layer. *Journal of Sound and Vibration* **58-3**, 467-482.
- AMIET, R. K. 1978b Effect of the Incident Surface Pressure Field on Noise Due to Turbulent Flow Past a Trailing Edge. *Journal of Sound and Vibration* **57-2**, 305-306.
- ARGUILLAT, B., RICOT, D., ROBERT, G. & BAILLY, C. 2005 *Measurements of the Wavenumber-Frequency Spectrum of Wall Pressure Fluctuations under Turbulent Flows*. 11th AIAA/CEAS Aeroacoustics Conference, Monterey, CA, May 23-25. AIAA-2005-2855.
- BAHR, C., YARDIBI, T., LIU, F. & CATTAFESTA, L. N. 2008 *An Analysis of Different Measurement Techniques for Airfoil Trailing Edge Noise*. 14th AIAA/CEAS Aeroacoustics Conference, Vancouver, BC, May 5-7. AIAA-2008-2957.
- BENDAT, J. S. & PIERSOL, A. G. 2000 *Random Data Analysis and Measurement Procedures*. 3rd ed. John Wiley and Sons, Inc.: New York.
- BERTSCH, L., DOBRZYNSKI, W. & GUERIN, S. 2008 *Tool Development for Low-Noise Aircraft Design*. 14th AIAA/CEAS Aeroacoustics Conference, Vancouver, BC, May 5-7. AIAA-2008-2995.
- BLACKSTOCK, D. T. 2000 *Fundamentals of Physical Acoustics*. John Wiley & Sons, Inc.: New York.
- BLAKE, W. K. 1986 "Complex Flow-Structure Interaction," in *Mechanics of Flow-Induced Sound and Vibration*, Academic Press: New York.
- BLAKE, W. K. & GERSHFELD, J. L. 1988 "The Aeroacoustics of Trailing Edges," in *Frontiers in Experimental Fluid Mechanics*, M. Gad-el-Hak, Editor, Springer-Verlag: Berlin & New York. p. 457-532.

- BOLDMAN, D. R., BRINICH, P. F. & GOLDSTEIN, M. 1976 Vortex Shedding from a Blunt Trailing Edge with Equal and Unequal External Mean Velocities. *Journal of Fluid Mechanics* **75**, 721-735.
- BOUCHARD, C., HAVELOCK, D. & BOUCHARD, M. 2009 Beamforming with Microphone Arrays for Directional Sources. *The Journal of the Acoustical Society of America* **125-4**, 2098-2104.
- BROOKS, T. F. & HODGSON, T. H. 1981 Trailing Edge Noise Prediction from Measured Surface Pressures. *Journal of Sound and Vibration* **78-1**, 69-117.
- BROOKS, T. F. & MARCOLINI, M. A. 1984 *Airfoil Trailing Edge Flow Measurements and Comparison with Theory Incorporating Open Wind Tunnel Corrections*. AIAA/NASA 9th Aeroacoustics Conference, Williamsburg, VA, October 15-17. AIAA-84-2266.
- BROOKS, T. F., POPE, D. S. & MARCOLINI, M. A. 1989 *Airfoil Self-Noise and Prediction*. NASA-RP-1218.
- BROOKS, T. F. & HUMPHREYS, W. M. 2006a A Deconvolution Approach for the Mapping of Acoustic Sources (Damas) Determined from Phased Microphone Arrays. *Journal of Sound and Vibration* **294**, 856-879.
- BROOKS, T. F. & HUMPHREYS, W. M. 2006b *Extension of Damas Phased Array Processing for Spatial Coherence Determination (Damas-C)*. 12th AIAA/CEAS Aeroacoustics Conference, Cambridge, MA, May 8-10. AIAA-2006-2654.
- BRUUN, H. H. 1995 *Hot-Wire Anemometry: Principles and Signal Analysis*. Oxford University Press: New York.
- CATTAFESTA, L. N. 2010 *Data Measurement and Analysis Course Notes (Chapter 5: Spectral Functions)*.
- CHASE, D. M. 1972 Sound Radiated by Turbulent Flow Off a Rigid Half-Plane as Obtained from a Wavevector Spectrum of Hydrodynamic Pressure. *The Journal of the Acoustical Society of America* **52**, 1011-1022.
- CHASE, D. M. 1975 Noise Radiated from an Edge in Turbulent Flow. *AIAA Journal* **13-8**, 1041-1047.
- CHOUDHARI, M., LOCKARD, D. P., MACARAEG, M. G., SINGER, B. A., STRETT, C. L., NEUBERT, G. R., STOKER, R. W., UNDERBRINK, J. R., BERKMAN, M. E., KHORRAMI, M. R. & SADOWSKI, S. S. 2002 *Aeroacoustic Experiments in the Langley Low-Turbulence Pressure Tunnel*. NASA-TM-2002-211432.
- CHUNG, J. Y. 1977 Rejection of Flow Noise Using a Coherence Function Method. *The Journal of the Acoustical Society of America* **62**, 388-395.

- CORCOS, G. M. 1964 The Structure of the Turbulent Pressure Field in Boundary-Layer Flows. *Journal of Fluid Mechanics* **18**, 353-378.
- CRIGHTON, D. G. & LEPPINGTON, F. G. 1971 On the Scattering of Aerodynamic Noise. *Journal of Fluid Mechanics* **46-03**, 577-597.
- CRIGHTON, D. G. 1972 Radiation from Vortex Filament Motion near a Half Plane. *Journal of Fluid Mechanics* **51**, 357-362.
- CURLE, N. 1955 The Influence of Solid Boundaries Upon Aerodynamic Sound. *Proceedings of the Royal Society of London. Series A, Mathematical and Physical Sciences (1934-1990)* **231-1187**, 505-514.
- DOUGHERTY, R. P. 2002 "Beamforming in Acoustic Testing," in *Aeroacoustic Measurements*, T. J. Mueller, Editor, Springer-Verlag: Berlin, Heidelberg & New York. p. 63-97.
- DOUGHERTY, R. P. & PODBOY, G. G. 2009 *Improved Phased Array Imaging of a Model Jet*. 15th AIAA/CEAS Aeroacoustics Conference, Miami, FL, May 11-13. AIAA 2009-3186.
- DOWLING, A. P. & FLOWCS WILLIAMS, J. E. 1983 *Sound and Sources of Sound*. Ellis Horwood Limited: West Sussex, England.
- DRELA, M. 2001 *Xfoil*, 6.94. MIT Aero & Astro, Boston.
- DU, L., XU, L., LI, J., GUO, B., STOICA, P. & CATTAFESTA, L. N. 2010 Covariance-Based Approaches to Aeroacoustic Noise Source Analysis. *The Journal of the Acoustical Society of America* **submitted, under review**.
- DUELL, E., WALTER, J., ARNETTE, S. & YEN, J. 2002 *Recent Advances in Large-Scale Aeroacoustic Wind Tunnels*. 8th AIAA/CEAS Aeroacoustics Conference, Breckenridge, CO, June 17-19. AIAA-2002-2503.
- EHRENFRIED, K. & KOOP, L. 2006 *A Comparison of Iterative Deconvolution Algorithms for the Mapping of Acoustic Sources*. 12th AIAA/CEAS Aeroacoustics Conference, Cambridge, MA, May 8-10. AIAA-2006-2711.
- FAA 2003 Stage 4 Aircraft Noise Standards; Proposed Rule. *Federal Register* **68-230**, 67330-67336.
- FFOWCS WILLIAMS, J. E. & HALL, L. H. 1969 Aerodynamic Sound Generation by Turbulent Flow in the Vicinity of a Scattering Half Plane. *Journal of Fluid Mechanics* **40-04**, 657-670.
- FFOWCS WILLIAMS, J. E. & HAWKINGS, D. L. 1969 Sound Generation by Turbulence and Surfaces in Arbitrary Motion. *Philosophical Transactions of the Royal Society of London. Series A, Mathematical and Physical Sciences (1934-1990)* **264-1151**, 321-342.

- FINK, M. R. 1975 Experimental Evaluation of Theories for Trailing Edge and Incidence Fluctuation Noise. *AIAA Journal* **13-11**, 1472-1477.
- GOLUB, R. A., RAWLS, J. W., JR. & RUSSELL, J. W. 2005 *Evaluation of the Advanced Subsonic Technology Program Noise Reduction Benefits*. NASA TM-2005-212144.
- GUIDATI, G., BAREIB, R. & WAGNER, S. 1996 *Wind Turbine Noise*. Springer-Verlag: Berlin, Heidelberg, New York.
- HEAVENS, S. N. 1978 An Experimental Study of Sound Diffraction at an Airfoil Trailing Edge. *Journal of Fluid Mechanics* **84**, 331-335.
- HOWE, M. S. 1978 *A Review of the Theory of Trailing Edge Noise*. NASA CR-3021.
- HOWE, M. S. 1988 The Influence of Surface Rounding on Trailing Edge Noise. *Journal of Sound and Vibration* **126-3**, 503-523.
- HOWE, M. S. 1991 Noise Produced by a Sawtooth Trailing Edge. *The Journal of the Acoustical Society of America* **90-1**, 482-487.
- HOWE, M. S. 1999 Trailing Edge Noise at Low Mach Numbers. *Journal of Sound and Vibration* **225-2**, 211-238.
- HOWE, M. S. 2001 Edge-Source Acoustic Green's Function for an Airfoil of Arbitrary Chord, with Application to Trailing-Edge Noise. *Quarterly Journal of Mechanics and Applied Mathematics* **54-1**, 139-155.
- HUMPHREYS, W. M., BROOKS, T. F., HUNTER, W. W. & MEADOWS, K. R. 1998 *Design and Use of Microphone Directional Arrays for Aeroacoustic Measurements*. 36th AIAA Aerospace Sciences Meeting, Reno, NV, January. AIAA-98-0471.
- HUTCHESON, F. V. & BROOKS, T. F. 2002 *Measurement of Trailing Edge Noise Using Directional Array and Coherent Output Power Methods*. 8th AIAA/CEAS Aeroacoustics Conference, Breckenridge, CO, June 17-19. AIAA-2002-2472.
- HUTCHESON, F. V. & BROOKS, T. F. 2004 *Effects of Angle of Attack and Velocity on Trailing Edge Noise*. 42nd AIAA Aerospace Sciences Meeting, Reno, NV, January 5-8. AIAA-2004-1031.
- JANSSON, D., MATHEW, J., HUBNER, J. P., SHEPLAK, M. & CATTAFESTA, L. N. 2002 *Design and Validation of an Aeroacoustic Test Facility*. 8th AIAA/CEAS Aeroacoustics Conference, Breckenridge, CO, June 17-19. AIAA-2002-2466.
- KHORRAMI, M. R., BERKMAN, M. E. & CHOUDHARI, M. 2000 Unsteady Flow Computations of a Slat with a Blunt Trailing Edge. *AIAA Journal* **38-11**, 2050-2058.

- KOOP, L. & EHRENFRIED, K. 2008 *Microphone-Array Processing for Wind-Tunnel Measurements with Strong Background Noise*. 14th AIAA/CEAS Aeroacoustics Conference, Vancouver, BC, May 5-7. AIAA-2008-2907.
- KUNZE, C., LYNCH, D. A. I., MUELLER, T. J. & BLAKE, W. K. 2002 *Effect of Trailing Edge Geometry on Vortex Shedding and Acoustic Radiation*. 8th AIAA/CEAS Aeroacoustics Conference, Breckenridge, CO, June 17-19. AIAA-2002-2435.
- LIGHTHILL, M. J. 1952 On Sound Generated Aerodynamically. I. General Theory. *Proceedings of the Royal Society of London. Series A, Mathematical and Physical Sciences (1934-1990)* **211-1107**, 564-587.
- LIGHTHILL, M. J. 1954 On Sound Generated Aerodynamically. II. Turbulence as a Source of Sound. *Proceedings of the Royal Society of London. Series A, Mathematical and Physical Sciences (1934-1990)* **222-1148**, 1-32.
- LIGHTHILL, M. J. 1962 The Bakerian Lecture, 1961. Sound Generated Aerodynamically. *Proceedings of the Royal Society of London. Series A, Mathematical and Physical Sciences (1934-1990)* **267-1329**, 147-182.
- LILLEY, G. M. 2001 The Prediction of Airframe Noise and Comparison with Experiment. *Journal of Sound and Vibration* **239-4**, 849-859.
- LOCKARD, D. P. & LILLEY, G. M. 2004 *The Airframe Noise Reduction Challenge*. NASA TM-2004-213013.
- MACARAEG, M. G. 1998 *Fundamental Investigations of Airframe Noise*. 4th AIAA/CEAS Aeroacoustics Conference, Toulouse, France, June 2-4. AIAA-98-2224.
- MANOHA, E., TROFF, B. & SAGAUT, P. 2000 Trailing-Edge Noise Prediction Using Large-Eddy Simulation and Acoustic Analogy. *AIAA Journal* **38-4**, 575-583.
- MATHEW, J., BAHR, C., CARROLL, B., SHEPLAK, M. & CATTAFESTA, L. N. 2005 *Design, Fabrication, and Characterization of an Anechoic Wind Tunnel Facility*. 11th AIAA/CEAS Aeroacoustics Conference, Monterey, CA, May 23-25. AIAA-2005-3052.
- MATHEW, J. 2006 *Design, Fabrication, and Characterization of an Anechoic Wind Tunnel Facility*. Mechanical and Aerospace Engineering. University of Florida, Gainesville, Ph.D.
- MCALPINE, A., NASH, E. C. & LOWSON, M. V. 1999 On the Generation of Discrete Frequency Tones by the Flow around an Aerofoil. *Journal of Sound and Vibration* **222-5**, 753-779.

- MENDOZA, J. M., BROOKS, T. F. & HUMPHREYS, W. M. 2002 *Aeroacoustic Measurements of a High-Lift Wing/Slat Model*. 8th AIAA/CEAS Aeroacoustics Conference, Breckenridge, CO, June 17-19. AIAA-2002-2604.
- MENDOZA, J. M., NANCE, D. K. & AHUJA, K. K. 2008 *Source Separation from Multiple Microphone Measurements in the Far Field of a Full Scale Aero Engine*. 14th AIAA/CEAS Aeroacoustics Conference, Vancouver, BC, May 5-7. AIAA-2008-2809.
- MOREAU, S., HENNER, M., IACCARINO, G., WANG, M. & ROGER, M. 2003 Analysis of Flow Conditions in Freejet Experiments for Studying Airfoil Self-Noise. *AIAA Journal* **41-10**, 1895-1905.
- MOREAU, S. & ROGER, M. 2005 Effect of Airfoil Aerodynamic Loading on Trailing-Edge Noise Sources. *AIAA Journal* **43-1**, 41-52.
- MOREAU, S. & ROGER, M. 2009 Back-Scattering Correction and Further Extensions of Amiet's Trailing-Edge Noise Model. Part 2: Application. *Journal of Sound and Vibration* **323-1-2**, 397-425.
- MORIARTY, P. J. 2005 *Nafnoise User's Guide*, National Renewable Energy Laboratory, Golden, CO.
- MORIARTY, P. J., GUIDATI, G. & MIGLIORE, P. 2005 *Prediction of Turbulent Inflow and Trailing-Edge Noise for Wind Turbines*. 11th AIAA/CEAS Aeroacoustics Conference, Monterey, CA, May 23-25. AIAA-2005-2881.
- MOSHER, M. 1996 *Phased Arrays for Aeroacoustic Testing - Theoretical Development*. 2nd AIAA/CEAS Aeroacoustics Conference, State College, PA, May. AIAA-96-1713.
- MUSKER, A. J. 1979 Explicit Expression for the Smooth Wall Velocity Distribution in a Turbulent Boundary Layer. *AIAA Journal* **17-6**, 655-657.
- NARK, D. M., BURLEY, C. L., TINETTI, A. & RAWLS, J. W., JR. 2008 *Initial Integration of Noise Prediction Tools for Acoustic Scattering Effects*. 14th AIAA/CEAS Aeroacoustics Conference, Vancouver, BC, May 5-7. AIAA-2008-2996.
- NASH, E. C., LOWSON, M. V. & MCALPINE, A. 1999 Boundary-Layer Instability Noise on Aerofoils. *Journal of Fluid Mechanics* **382**, 27-61.
- OBERAI, A. A., ROKNALDIN, R. & HUGHES, T. J. R. 2002 Computation of Trailing-Edge Noise Due to Turbulent Flow over an Airfoil. *AIAA Journal* **40-11**, 2206-2216.
- OERLEMANS, S. & SIJTSMA, P. 2000 *Effects of Wind Tunnel Side-Plates on Airframe Noise Measurements with Phased Arrays*. NLR-TP-2000-169.

- OERLEMANS, S. & SIJTSMA, P. 2002 *Determination of Absolute Levels from Phased Array Measurements Using Spatial Source Coherence*. NLR-TP-2002-226.
- OERLEMANS, S. 2004 *Wind Tunnel Aeroacoustic Tests of Six Airfoils for Use on Small Wind Turbines*. NREL/SR-500-35339.
- OERLEMANS, S., BROERSMA, L. & SIJTSMA, P. 2007a *Quantification of Airframe Noise Using Microphone Arrays in Open and Closed Wind Tunnels*. NLR-TP-2007-799.
- OERLEMANS, S., SIJTSMA, P. & MENDEZ-LOPEZ, B. 2007b *Location and Quantification of Noise Sources on a Wind Turbine*. NLR-TP-2007-798.
- OERLEMANS, S., FISHER, M., MAEDER, T. & KOGLER, K. 2008 *Reduction of Wind Turbine Noise Using Optimized Airfoils and Trailing-Edge Serrations*. 14th AIAA/CEAS Aeroacoustics Conference, Vancouver, BC, May 5-7. AIAA-2008-2819.
- PANTON, R. L. 1996 *Incompressible Flow*. 2nd ed. John Wiley & Sons: New York.
- PARCHEN, I. R. 1998 *Progress Report Draw, a Prediction Scheme for Trailing Edge Noise Based on Detailed Boundary-Layer Characteristics*. TNO-report HAG-RPT-980023.
- PATERSON, R. W., VOGT, P. G., FINK, M. R. & MUNCH, C. L. 1973 Vortex Noise of Isolated Airfoils. *Journal of Aircraft* **10-5**, 296-302.
- POPE, A. & HARPER, J. J. 1966 *Low Speed Wind Tunnel Testing*. John Wiley and Sons: New York.
- POWELL, A. 1959 On the Aerodynamic Noise of a Rigid Flat Plate Moving at Zero Incidence. *The Journal of the Acoustical Society of America* **31-12**, 1649-1653.
- RANDALL, R. B. & HEE, J. 1981 *Cepstrum Analysis*. Bruel & Kjaer Technical Review no. 3.
- RAVETTA, P. A., BURDISSO, R. A. & NG, W. F. 2009 Noise Source Localization and Optimization of Phased-Array Results. *AIAA Journal* **47-11**, 2520-2533.
- ROGER, M. & MOREAU, S. 2004 Broadband Self-Noise from Loaded Fan Blades. *AIAA Journal* **42-3**, 536-544.
- ROGER, M. & MOREAU, S. 2005 Back-Scattering Correction and Further Extensions of Amiet's Trailing-Edge Noise Model. Part 1: Theory. *Journal of Sound and Vibration* **286-3**, 477-506.
- SANDBERG, R. D., JONES, L. E., SANDHAM, N. D. & JOSEPH, P. F. 2007 *Direct Numerical Simulations of Noise Generated by Airfoil Trailing Edges*. 13th AIAA/CEAS Aeroacoustics Conference, Rome, May 21-23. AIAA-2007-3469.

- SANFORD, J. 2008 *Acoustic Refraction: A Three-Dimensional Shear Layer Correction for Microphone Measurements in an Open-Jet Acoustic Wind Tunnel*. Mechanical and Aerospace Engineering. University of Florida, Gainesville, B.S., Summa Cum Laude.
- SARRADJ, E. & GEYER, T. 2007 *Noise Generation by Porous Airfoils*. 13th AIAA/CEAS Aeroacoustics Conference, Rome, May 21-23. AIAA-2007-3719.
- SARRADJ, E. 2010 A Fast Signal Subspace Approach for the Determination of Absolute Levels from Phased Microphone Array Measurements. *Journal of Sound and Vibration* **329-9**, 1553-1569.
- SCHLINKER, R. H. & AMIET, R. K. 1981 *Helicopter Rotor Trailing Edge Noise*. NASA Contract NAS1-15730.
- SCHRODER, A., DIERKSHEIDE, U., WOLF, J., HERR, M. & KOMPENHANS, J. 2004 *Investigation on Trailing-Edge Noise Sources by Means of High-Speed Piv*. 12th International Symposium on Applications of Laser Techniques to Fluid Mechanics, Lisbon, Portugal, July 12-15.
- SHANNON, D. W., MORRIS, S. & MUELLER, T. J. 2005 *Trailing Edge Flow Physics and Acoustics*. 11th AIAA/CEAS Aeroacoustics Conference, Monterey, CA, May 23-25. AIAA-2005-2957.
- SHANNON, D. W. & MORRIS, S. 2008 Trailing Edge Noise Measurements Using a Large Aperture Phased Array. *International Journal of Aeroacoustics* **7-2**, 147-176.
- SIJTSMA, P. 2007 *Clean Based on Spatial Source Coherence*. 13th AIAA/CEAS Aeroacoustics Conference, Rome, May 21-23. AIAA-2007-3436.
- SIMON, G. & SCHOUKENS, J. 2000 Robust Broadband Periodic Excitation Design. *IEEE Transactions on Instrumentation and Measurement* **49-2**, 270-274.
- SINGER, B. A., BRENTNER, K. S., LOCKARD, D. P. & LILLEY, G. M. 2000a Simulation of Acoustic Scattering from a Trailing Edge. *Journal of Sound and Vibration* **230-3**, 541-560.
- SINGER, B. A., LOCKARD, D. P. & BRENTNER, K. S. 2000b Computational Aeroacoustic Analysis of Slat Trailing-Edge Flow. *AIAA Journal* **38-9**, 1558-1558.
- SZELAZEK, C. A. & HICKS, R. M. 1979 *Upper-Surface Modifications for $C_{l,Max}$ Improvement of Naca 6-Series Airfoils*. NASA TM-78603.
- TENNEKES, H. & LUMLEY, J. L. 1972 *A First Course in Turbulence*. The MIT Press: Cambridge, Massachusetts.
- UNDERBRINK, J. R. 1995 *Practical Considerations in Array Design for Passive Broad-Band Source Mapping Applications*. Acoustics Department. The Pennsylvania State University, State College, PA, M. E.

- WANG, M. & MOIN, P. 2000 Computation of Trailing-Edge Flow and Noise Using Large-Eddy Simulation. *AIAA Journal* **38-12**, 2201-2209.
- WHEELER, A. J. & GANJI, A. R. 1996 *Introduction to Engineering Experimentation*. Prentice Hall: Upper Saddle River, New Jersey.
- WILLSHIRE, B. 2003 *Quiet Aircraft Technology Program* (Presentation Slides). Doing the Wright Stuff: 100 Years of Aviation and the Environment.
- YARDIBI, T., LI, J., STOICA, P. & CATTAFESTA, L. N. 2008 *Sparsity Constrained Deconvolution Approaches for Acoustic Source Mapping*. 14th AIAA/CEAS Aeroacoustics Conference, Vancouver, BC, May 5-7. AIAA-2008-2956.
- YARDIBI, T., BAHR, C., ZAWODNY, N., LIU, F., CATTAFESTA, L. N. & LI, J. 2010a Uncertainty Analysis of the Standard Delay-and-Sum Beamformer and Array Calibration. *Journal of Sound and Vibration* **329-13**, 2654-2682.
- YARDIBI, T., LI, J., STOICA, P., ZAWODNY, N. & CATTAFESTA, L. N. 2010b A Covariance Fitting Approach for Correlated Acoustic Source Mapping. *The Journal of the Acoustical Society of America* **submitted, under review**.
- YARDIBI, T., ZAWODNY, N., BAHR, C., LIU, F., CATTAFESTA, L. N. & LI, J. 2010c Comparison of Microphone Array Processing Techniques for Aeroacoustic Measurements. *International Journal of Aeroacoustics* **Submitted, reviewed, and returned with corrections**.
- YU, J. C. & TAM, C. K. W. 1978 Experimental Investigation of the Trailing Edge Noise Mechanism. *AIAA Journal* **16-10**, 1046-1052.
- YU, J. C. & JOSHI, M. C. 1979 *On Sound Radiated from the Trailing Edge of an Isolated Airfoil in a Uniform Flow*. 5th AIAA Aeroacoustics Conference, Seattle, WA, March 12-14. AIAA-1979-0603.

BIOGRAPHICAL SKETCH

Chris Bahr was born and raised in Orlando, Florida. He attended the International Baccalaureate program at Winter Park High School, and graduated as a National Merit Scholar in the spring of 1999. He began attending the University of Florida in the fall of 1999, and received his Bachelor of Sciences degree in aerospace engineering in the spring of 2003. Along the way, he began working for Dr. Lou Cattafesta as an undergraduate researcher. Swayed by the stories of fame and glory coming from graduate students, Chris applied and was accepted to UF's graduate Mechanical and Aerospace Engineering program in the fall of 2003. He continued on with Dr. Cattafesta for seven years as a graduate student. During that time he met Stephanie Mecca, and married her in the summer of 2009. Upon completion of his degree in the spring of 2010, Chris will begin a post-doctoral position, working for Dr. Cattafesta.